

Tensor network states for 1+1 dimensional gauge field theories

Tensornetwerktoestanden voor 1+1 dimensionale ijkveldentheorieën

Boye Buyens

Supervisors: Dr. K. Van Acoleyen, Prof. Dr. H. Verschelde

Dissertation submitted in fulfillment of the requirements for the degree of
Doctor (Ph.D.) in Science: Physics

Department of Physics and Astronomy
Faculty of Sciences
Ghent University
Academic year 2016-2017



Members of the examination committee

Supervisors

Dr. Karel Van Acoleyen (Ghent University)

Prof. Dr. Henri Verschelde (Ghent University)

Chair

Prof. Dr. Jan Ryckebusch (Ghent University)

Reading Committee

Dr. Mari Carmen Bañuls (Max-Planck-Institute for Quantumoptics)

Prof. Dr. David Dudal (University of Leuven, Ghent University)

Dr. Jutho Haegeman (Ghent University)

Prof. Dr. Dimitri Van Neck (Ghent University)

Prof. Dr. Frank Verstraete (Ghent University, University of Vienna)

Prof. Dr. Uwe-Jens Wiese (University of Bern)

Dankwoord

Dank je zeggen is één van de moeilijkste dingen die er is, waarschijnlijk nog moeilijker dan kwantummechanica. Toch wil ik er de tijd voor nemen om dit te doen omdat het zonder deze mensen niet mogelijk zou geweest zijn dit punt te bereiken.

Eerst en vooral wil ik mijn ouders bedanken voor de steun en zorg die ze mij gegeven hebben. In het bijzonder wil ik mama bedanken om mij tijdens het middelbaar onderwijs in de juiste richting te duwen. Daarnaast wil ik ook de rest van mijn familie bedanken voor de leuke momenten en in het bijzonder Joris, Bea, Rika en Luc. Mijn voormalige en huidige viervoeter Snappy en Sam ben ik ook zeer erkentelijk omdat ze onvoorwaardelijk naar mij luisterden toen ik een presentatie oefende en omdat ze mij op tijd duidelijk maakten dat ik aan een pauze toe was (om met hun te spelen).

Dan zijn er nog vrienden die ik al lang ken en waar ik nog steeds bij terecht kan: Laurens en Sarah, Thomas, Sven en Jonathan. Uiteraard wil ik ook mijn collega's niet vergeten voor de vier fantastische jaren die ze me bezorgden alsook voor hun hulp tijdens mijn onderzoek: Laurens, Michaël, Nick, Matthias (1), Matthias (2), Vid, Jos, Volkher, Koenraad, Paul, Valentin, James, Damien, David en Hans. Ook wens ik nog eens uitdrukkelijk Laurens, Michaël en Matthias (2) te bedanken voor het nalezen van deze thesis. Daarnaast wil ik ook al mijn voetbalvrienden bedanken en mijn medespelers van de WE05/Maxwell's demons.

Ook wens ik Inge, Gerbrand en Katia te bedanken. Dankzij hun administratieve en technische ondersteuning kon ik mijn ten volle op mijn onderzoek toe leggen. Daarnaast wil ik ook Henri en het FWO bedanken omdat ze mij de kans gaven om dit onderzoek te doen.

Tenslotte zijn er nog drie mensen die ik in het bijzonder zou willen bedanken. Ten eerste Frank omdat hij hier in Gent een fantastische groep heeft opge-

bouwd met expertise in verschillende onderzoeksgebieden waardoor dit hier de ideale omgeving werd voor mijn onderzoek. Vervolgens wil ik ook Jutho bedanken omdat ik ten volle gebruik mocht maken van zijn ervaring met Matlab, met optimalisatiemethoden en met fysica in het algemeen.

Tenslotte is er nog iemand waar ik het meeste dank aan verschuldigd ben: Karel. Hij was al de promotor van mijn masterthesis en heeft ook de taak op zich willen nemen om mij te begeleiden gedurende mijn doctoraat. Dankzij hem heb ik veel geleerd, te veel om op te noemen, waarvoor ik hem heel dankbaar ben. Maar het meeste dankbaar ben ik hem voor de tijd die hij nam om mij te begeleiden en omdat ik altijd het gevoel had dat hij in mij geloofde.

Om te besluiten wens ik u, één van de weinigen die deze thesis ooit zal lezen, veel plezier en een boeiende ontdekking in de wereld van het Schwinger model.

Boye Buyens
Gent, 30 september 2016

Nederlandstalige samenvatting

Inleiding

In deze thesis bestuderen we het Schwinger model, QED in $(1+1)$ dimensies met één flavor, met behulp van Matrix Product Toestanden (MPS)¹. Schwinger bestudeerde dit model [1] omdat dit model een voorbeeld geeft van een ijkveld dat massa kon verwerven zonder de ijksymmetrie expliciet te breken [2]. Een paar maanden later zou Anderson zijn voorstel voor het Higgs mechanisme publiceren waarin ijkbosonen massa verwerven zonder dat de ijksymmetrie expliciet gebroken wordt [3]. Ondanks dat dit een relatief simpel model is, een Abelse $(1+1)$ -dimensionale ijktheorie, heeft dit model veel interessante fysische eigenschappen zoals confinement en chirale symmetriebreking. Daardoor is dit model zeer aantrekkelijk om analytische en numerieke methoden op te testen [4–34]. Ook vanuit de experimentele hoek krijgt dit model tegenwoordig veel aandacht in de context van kwantumsimulators, zie [35–38] en de referenties daarin.

MPS zijn een klasse van toestanden die een efficiënte en betrouwbare ansatz zijn voor grondtoestanden van Hamiltonianen met een mass gap. Tot op heden zijn er twee onderzoeksgroepen die MPS gebruikten om het Schwinger model te bestuderen. In 2003 heeft Byrnes [27] zijn doctoraat beëindigd waarin hij de fasetransitie gerelateerd aan de \mathcal{CT} -symmetrie onderzocht en ook het massaspectrum van de theorie bepaalde voor twee bijzondere waarden van het elektrisch achtergrondveld. Anderzijds hebben Bañuls *et al.* ook het massaspectrum bepaald en bestudeerden zij het chiraal condensaat op temperatuur nul alsook op eindige temperatuur.

1. De afkorting MPS komt van het Engels: Matrix Product States.

Hier gebruiken we een andere benadering door onmiddellijk in de thermodynamische limiet te werken. Dit heeft het voordeel dat we randeffecten vermijden. Een ander voordeel is dat we de translatiesymmetrie niet breken en bijgevolg de excitaties kunnen labelen met hun momentum. In tegenstelling tot hun methode gaan we de ijkvelden niet uitintegreren. Dit laatste is enkel mogelijk op een eindig rooster waar de Hamiltoniaan dan equivalent is met een spin-1/2 Hamiltoniaan met niet-lokale interacties. Deze truc lukt wel alleen maar in één dimensie. Daarentegen, omdat wij de ijkvelden dynamisch houden, kan onze methode veralgemeend worden naar hogere dimensies.

We hebben ook het feit dat het MPS-formalisme toelaat om het Schmidt-spectrum te berekenen volledig uitgebuit. In het laatste decennium is het duidelijk geworden dat de verstrengelingsentropie een interessante grootheid is voor het karakteriseren van veeldeeltjessystemen en kwantumveldentheorieën [39]. In tegenstelling tot oudere methoden zoals de Ads/CFT benadering [40] of de replica-truc [41], geven MPS directe toegang tot het hele Schmidt-spectrum en kunnen we alle Renyi-entropieën en de verstrengelingsentropie uitrekenen.

Voor de eerste keer ooit hebben we een volledige kwantumsimulatie gedaan van tijdsevolutie van het Schwinger model. Eerdere studies hiervan gebruikten de semi-klassieke benadering [16, 24, 31].

Overzicht van de thesis

Deze thesis bestaat uit twee delen. In deel I concentreren we ons voornamelijk op de systematiek van onze methode en op de resultaten. De details van onze simulaties worden uitgelegd in het technische deel II. De delen zijn zodanig geschreven dat ze onafhankelijk gelezen en begrepen kunnen worden.

Overzicht van deel I

In hoofdstuk 1 geven we eerst een historisch overzicht van het Standaardmodel om het onderzoek van deze thesis te kaderen. In dit hoofdstuk introduceren we ook de MPS ansatz voor de de grondtoestandsgolffunctie. We leggen een bepaalde blokstructuur op aan de tensoren zodat de MPS manifest ijkinvariant zijn. In de hoofdstukken 2-5 gebruiken we deze MPS voor enkele interessante toepassingen.

In hoofdstuk 2 bepalen we zeer nauwkeurig eigenschappen van de grondtoestand en de elementaire deeltjes van de theorie in de continuumlimiet. In het bijzonder vinden we een nieuwe excitatie onder de vorm van een massief vectorboson dat al eerder voorspeld was in perturbatietheorie. We verifiëren

Elitzurs theorema en tonen het voordeel aan van te werken met manifest ijk-invariante MPS door onze simulaties te vergelijken met simulaties in de volledige ijkvariante Hilbertruimte. Verder berekenen we ook nog het chiraal condensaat en vinden we de voorspelde UV-divergentie. We bestuderen ook de bipartite verstrengelingsentropie en vinden een logaritmische UV-divergentie met universele coëfficiënt. Dit is compatibel met de studies in [42]. Tenslotte bepalen we de elementaire excitaties van het Schwinger model wanneer er een elektrisch achtergrondveld is. Wanneer de massa van de fermionen klein is, bekomen we een schatting voor de waarde van het elektrisch achtergrondveld waar de elementaire excitatie met de grootste massa onstabiel wordt en kan vervallen in twee elementaire deeltjes met lagere massa.

In hoofdstuk 3 doen we een numerieke studie van het Schwinger model waarin we een externe statische ‘quark’ en ‘anti-quark’ in het vacuum plaatsen. We verkrijgen een gedetailleerd beeld van de transitie van een confining toestand voor kleine interquark afstanden naar de gebroken-string-gehadronizeerde toestand voor grote interquark afstanden. Naast de relevante grootheden, zoals het elektrisch veld en de lading, berekenen we ook de verstrengelingsentropie en tonen we aan dat het aftrekken van de vacuumwaarde resulteert in een UV-eindige grootheid. We vinden dat zowel stringvorming als stringbreking een karakteristieke afdruk laten op het ruimtelijk profiel van de gerenormalizeerde entropie. Tenslotte simuleren we ook voor de allereerste keer partiële stringbreking, het geval wanneer de quark en de anti-quark een niet-gehele lading hebben.

Gebruik makend van Matrix Product Operators (MPO) simuleren we het Schwinger model op eindige temperatuur in hoofdstuk 4. De variationele variëteit van ijk-invariante MPO die Gibbs states benaderen wordt geconstrueerd. Als een eerste toepassing berekenen we het chiraal condensaat in thermisch evenwicht. De resultaten komen overeen met eerdere studies. Als nieuwe toepassing bestuderen we ook het Schwinger model wanneer we een quark-antiquark paar in het systeem in thermisch evenwicht plaatsen met een fractionele lading. We detecteren een kritische temperatuur waarboven de string tension exponentieel afvalt. Dit is in overeenstemming met eerdere studies in de strong-coupling limiet. Tenslotte onderzoeken we het spontaan breken van de \mathcal{CT} -symmetrie op eindige temperatuur. Onze resultaten suggereren dat er op elke eindige temperatuur strikt groter dan nul geen spontane symmetriebreking is.

In hoofdstuk 5 bestuderen we reële tijdsevolutie ten gevolge van het aanleggen van een perturbatie in de vorm van een elektrisch achtergrondveld. Voor kleine waarden van de perturbatie kunnen we onze resultaten verklaren via het spectrum van de geperturbeerde Hamiltoniaan. Voor grotere waar-

den van de perturbatie zien we al vlug dat de toestand naar een stationaire oplossing convergeert. Gebruik makend van onze resultaten op eindige temperatuur onderzoeken we of de toestand thermalizeert of niet.

Ten slotte beëindigen we dit deel met conclusies en een vooruitblik. We leggen ook uit hoe dit formalisme uitgebreid zou kunnen worden naar hogere dimensies.

Overzicht van deel II

In deel II ontwikkelen we het formalisme voor de simulaties met ijk-invariante MPS. Zoals eerder vermeld is dit gedeelte zeer technisch en kan dit gerust overgeslagen worden. De nodige kennis over MPS en onze methode worden uitgelegd in deel I. Dit gedeelte is geschikt voor de lezer met interesse in numerieke methoden.

In hoofdstuk 1 hernemen we de definitie van MPS en vermelden we enkele eigenschappen. We introduceren ook de tensor netwerk diagrammen die een visuele manier bieden om verwachtingswaarden uit te rekenen. Nadien focussen we op de thermodynamische limiet en definiëren translatie-invariante MPS. Deze worden uniforme MPS genoemd. We doen ook een grondige studie van de raakruimte in uniforme MPS omdat de elementen van de raakruimte gebruikt zullen worden om elementaire excitaties te benaderen. Tenslotte wordt het formalisme uitgebreid voor \mathcal{CT} -invariante systemen waarbij \mathcal{C} een idempotente operator is en \mathcal{T} translatie is.

In hoofdstuk 2 bestuderen we enkele optimalizatietechnieken voor MPS uit de literatuur. Deze zullen gebruikt worden voor onze berekeningen. Concreet passeren de volgende methoden de revue: TDVP [43], DMRG [44] en iTEBD [45].

In hoofdstuk 3 construeren we manifest ijk-invariante MPS voor eindige roosters. De variationele vrijheidsgraden zijn gecodeerd in blokmatrixes. We bekijken het Schmidt-spectrum en vinden ten gevolge van de speciale structuur van de MPS dat we de Schmidt-waarden kunnen labelen met de eigenwaarden van het elektrisch veld. We bekijken ook hoe MPO benaderingen voor de Gibbs state in het ijk-invariante geval geconstrueerd kunnen worden. Tenslotte identificeren we de relevante matrix elementen van ijk-invariante observabelen door te projecteren op de ruimte van ijk-invariante toestanden.

In hoofdstuk 4 passen we de algoritmen bestudeerd in hoofdstuk 2 aan voor ons geval. Op die manier buiten we de ijk-invariante structuur van de MPS uit wat leidt tot efficiëntere algoritmen. Dit garandeert ons ook dat al onze berekeningen manifest ijk-invariant zijn. Hier kunnen alle algoritmen teruggevonden worden die geleid hebben tot de resultaten besproken in deel I.

Contents

Dankwoord	v
Nederlandstalige samenvatting	vii
I. The Schwinger model: the Hamiltonian picture	1
1. Introduction	3
1.1. Motivation	3
1.1.1. Brief history of the Standard Model	3
1.1.2. Lattice QCD	4
1.1.3. Tensor network states for Hamiltonian gauge theories	6
1.1.4. The Schwinger model	7
1.2. Overview	8
1.2.1. Overview of part I	8
1.2.2. Overview of part II	9
1.3. Matrix product states for the Schwinger model	10
1.3.1. Lagrangian and Hamiltonian quantization	10
1.3.2. Kogut-Susskind Hamiltonian	12
1.3.3. Gauge invariant MPS	14
2. Ground state properties and spectrum	19
2.1. $\alpha = 0$	19
2.1.1. Setup	19
2.1.2. Spectrum	24
2.1.3. Elitzurs' theorem	25

2.1.4.	Chiral condensate	27
2.1.5.	Entropy	29
2.2.	$\alpha \neq 0$	31
2.2.1.	Setup	31
2.2.2.	Spectrum for $\alpha \neq 0$	34
3.	Confinement and string breaking	39
3.1.	Introduction	39
3.2.	Lattice formulation and Hamiltonian	40
3.3.	Asymptotic confinement	42
3.3.1.	Setup	42
3.3.2.	Results	42
3.4.	From small to large distances	47
3.4.1.	MPS ground state approximation	47
3.4.2.	The case $m/g=0$: screening à la Higgs	51
3.4.3.	The case $Q = 1$: string breaking	54
3.4.4.	General Q : partial string breaking	59
3.5.	Conclusion	65
4.	Finite temperature	67
4.1.	Introduction	67
4.2.	Setup	68
4.2.1.	Hamiltonian and gauge invariance	68
4.2.2.	Gauge invariant MPO	69
4.2.3.	iTEBD for thermal evolution	70
4.3.	Chiral condensate	73
4.3.1.	Introduction	73
4.3.2.	The chiral limit $m/g = 0$	74
4.3.3.	$m/g \neq 0$: renormalization of $\Sigma(\beta)$	76
4.4.	Asymptotic confinement	78
4.4.1.	Introduction	78
4.4.2.	Deconfinement transition at large T	80
4.4.3.	$\mathcal{C}\mathcal{T}$ symmetry restoration at nonzero T	85
4.5.	Conclusion	90
5.	Real-time evolution	91
5.1.	Introduction	91
5.2.	Setup and systematics of the method	92
5.3.	Weak field regime	96
5.4.	Strong field regime	101
Conclusions and outlook		105

Appendices	109
A. Details on the continuum extrapolation for asymptotic confinement	111
A.1. String tension	111
A.2. Electric field	114
A.3. Renormalized entropy	116
B. Supplementary material for the Schwinger model at finite temperature	119
B.1. The chiral condensate for $\alpha = 0$	119
B.2. Asymptotic confinement: $\alpha \neq 0$	121
B.3. Simulations for $\alpha = 1/2$	123
B.4. Thermal corrections in the weak coupling limit	125
II. MPS for the Schwinger model: implementation	127
1. Matrix product states for quantum lattices	129
1.1. Matrix product states for finite lattices	129
1.1.1. Definition	129
1.1.2. Normalization and the transfer matrix	131
1.1.3. Schmidt spectrum of a MPS	132
1.1.4. Expectation values of MPS	133
1.1.5. Canonical form of MPS	136
1.2. uMPS in the thermodynamic limit	140
1.2.1. Definition	140
1.2.2. Calculus	141
1.3. The tangent space of uMPS	145
1.3.1. Definition	145
1.3.2. Gauge freedom and gauge fixing	147
1.3.3. Efficient computation of $(\mathbb{1} - e^{ik\mathbb{E}})^+$	148
1.3.4. Variational freedom in the tangent plane	150
1.3.5. Calculus	152
1.4. \mathcal{CT} invariant MPS	156
1.4.1. Ground state ansatz	156
1.4.2. Tangent space	159
2. Optimization methods for MPS	163
2.1. TDVP	163
2.1.1. Introduction	163
2.1.2. TDVP equations	164

2.1.3.	Efficient computation of $B(A)$	168
2.1.4.	TDVP algorithm for optimization	171
2.1.5.	TDVP for real-time evolution	172
2.1.6.	TDVP for \mathcal{CT} invariant MPS	174
2.2.	Excitations in the tangent plane	175
2.2.1.	Translational invariant Hamiltonian	176
2.2.2.	\mathcal{CT} invariant Hamiltonian	180
2.3.	iTEBD	181
2.3.1.	Introduction	182
2.3.2.	iTEBD algorithm	183
2.4.	DMRG for infinite boundary conditions	188
2.4.1.	Introduction	188
2.4.2.	MPS ansatz and calculus	189
2.4.3.	DMRG algorithm	194
2.4.4.	Pseudocode of the DMRG algorithm	198
3.	Matrix product states for the Schwinger model	205
3.1.	Hilbert space and gauge invariance	205
3.2.	Gauge invariant MPS with open boundary conditions	206
3.3.	Gauge invariant MPS in the thermodynamic limit	211
3.3.1.	Translation invariance over two sites	213
3.3.2.	\mathcal{CT} invariance	215
3.4.	Gauge invariant operators	217
3.4.1.	Purification of Gibbs states	217
3.4.2.	Local observables	221
4.	Gauge invariant MPS in the thermodynamic limit: calculus and algorithms	225
4.1.	Ground state properties and spectrum: \mathcal{CT} invariant case	225
4.1.1.	Introduction	225
4.1.2.	Normalization and Schmidt spectrum	226
4.1.3.	Calculus	231
4.1.4.	TDVP	235
4.1.5.	Excitations in the tangent plane	253
4.1.6.	Application to the Schwinger model	256
4.2.	Ground state properties and spectrum for $\alpha \neq 0$	258
4.2.1.	Introduction	258
4.2.2.	Normalization and Schmidt spectrum	260
4.2.3.	Calculus	263
4.2.4.	TDVP	266
4.2.5.	Excitations in the tangent plane	281
4.2.6.	Application to the Schwinger model	285

- 4.2.7. Real-time evolution within the coherent state approximation 287
- 4.3. iTEBD for the Schwinger model 292
 - 4.3.1. Real-time evolution 292
 - 4.3.2. Thermal evolution 297
- 4.4. Confinement: from small to large distances 306
 - 4.4.1. MPS ansatz 306
 - 4.4.2. DMRG 307

Bibliography **317**

I

**The Schwinger model: the Hamiltonian
picture**

1.1. Motivation

1.1.1. Brief history of the Standard Model

The Standard Model describes all fundamental forces except for gravity. Its history goes back to 1860 when Maxwell published his Maxwell's equations for classical electrodynamics. These equations survived two major revolutions of theoretical physics in the twentieth century: special relativity and quantum mechanics. Rewriting the Maxwell equations in the covariant form shows indeed that they are manifestly Lorentz invariant. Furthermore, two decades of research since the foundation of quantum mechanics in 1926 lead to a reliable quantum field theory describing the interaction of light and matter in the beginning of the 1950s. This theory is known as Quantum electrodynamics (QED) which is indeed described by a quantized version of the Maxwell equations. Perturbation theory using Feynman diagrams has produced physical predictions with unlevelled precision for QED.

QED also lies at the basis of the further development of the Standard Model. It was already recognized in 1929 by Weyl that the electromagnetic interaction of charged particles could be described by applying the 'gauge principle' to free particles [46]. The idea is that by making a global symmetry of a free theory local, we get the interactions of the theory. For QED it is the Lagrangian of the Dirac field, which exhibits a global $U(1)$ symmetry, that is gauged. This results in a Lagrangian where the fermions are coupled to a gauge field and that is invariant under time and space dependent $U(1)$ transformations. The quanta of this gauge field are the photons. Hence, starting from a free fermion theory with a global $U(1)$ symmetry we get the electromagnetic interactions by making this $U(1)$ symmetry local. These

ideas have been generalized to the unitary groups $SU(N)$ for $N > 1$, by Yang and Mills and have led to the famous $SU(N)$ Yang-Mills theories [47]. These theories describe the two other interactions of the Standard model: the weak interaction and the strong interaction.

In 1961 Sheldon Glashow published his proposal for the electroweak theory which unifies the electromagnetic and weak interaction as a $SU(2) \times U(1)$ Yang-Mills theory [48]. The model was however premature and did not obtain the masses for the gauge fields of the weak interactions, called the W^\pm and the Z boson. Abdus Salam and Steven Weinberg revised the model independently in 1967 and incorporated the Higgs mechanism [3, 49, 50] leading to the famous Glashow-Weinberg-Salam model for the electroweak interaction. The Higgs mechanism, in Belgium better known as the Brout-Englert-Higgs mechanism, predicted the existence of the Higgs boson. The experimental discovery of the Higgs boson in 2012, besides the discovery of the W and Z bosons in 1983, was then also the ultimate victory of this model.

After different attempts to find a model to describe the strong interaction, it were Fritzsche and Gell-Mann who presented Quantum Chromodynamics (QCD) to model the strong interaction [51, 52]. QCD is a $SU(3)$ Yang-Mills theory where the fermions, called the quarks, are coupled to the massless gauge bosons, called the gluons. Given the fact that QED and the electroweak model were successful, this model seems to be a straightforward and logic candidate for the strong interactions. However there was one main problem. The model predicts the existence of quarks, but these were never detected in experiments. So if QCD does describe the strong interaction, where are the quarks?

The answer to this question seemed to be ‘asymptotic freedom’ which was described by ’t Hooft in 1972 (unpublished) and Gross, Wilczek and Politzer [53, 54]. More specifically they showed that the beta function for QCD was negative, implying that the coupling increases with growing distance. This hinted towards an explanation for the absence of free quarks. It has also led to the acceptance of QCD as a plausible candidate to describe the strong interaction.

1.1.2. Lattice QCD

Asymptotic freedom did however not explain why free quarks do not appear in Nature. Also, asymptotic freedom implies that perturbation theory at low energies is not valid for QCD. This leads to another big problem: QCD seemed not to be well defined. A first reason is that the path integral is infinite if one does not fix the gauge. At the perturbative level one can overcome the gauge fixing problem with the introduction of the Fadeev-Popov ghosts [55]. At the non-perturbative level this approach fails and it is

impossible to fix the gauge. This problem is known as the Gribov-problem and is still a subject of research [56, 57]. A second problem was that methods for the regularization of UV and infrared divergencies were only known in perturbation theory. At the non-perturbative level there was thus no way of renormalizing divergencies.

Both problems were overcome in Wilsons' famous paper 'Confinement of quarks' [58]. In this paper, Wilson discretized the $SU(N)$ Yang-Mills path integral on an Euclidean lattice in order to explain confinement. In this formulation, the fermion fields live on the sites of the lattice and the gauge fields, which are now represented by $SU(N)$ elements, live on the links between the fermions. By employing a strong coupling expansion, Wilson explained why no free quarks appear. It is in this paper that he introduced his Wilson loop to distinguish the confined phase from the deconfined phase. Notably, in an anecdotal account for the thirtieth anniversary of his paper [59] Wilson said that 'the concept of confinement was nowhere in his thinking when starting his effort to construct lattice gauge theory'.

This paper did indeed not only attempt to explain the confinement of quarks but also regularized QCD in the non-perturbative regime. Indeed, on a finite lattice with a non-zero lattice spacing the path integral, in this context called the Wilsonian path integral, is manifestly finite and all quantities can be computed without the need of gauge fixing. The inverse lattice spacing and the volume of the lattice served as a natural cut-off of the theory. Therefore the Wilsonian path integral also enables to numerically compute expectation values. Although a full computation of the path integral, which requires computing an average sum over all possible field configurations, was impossible, the path integral could be estimated using the Monte-Carlo method [60]. With the increasing computing power, this method has since its first results at the end of the Seventies [61] produced by far the most impressive results for QCD [62, 63]. Examples include the determination of the light hadron masses [64], the determination of the quark masses [65] and obtaining the phase diagram at finite temperature [66].

Despite its success this method also has its drawbacks. When including a non-zero chemical potential, which is relevant for the physics of heavy-ion collisions, neutron stars and supernovae, simulations are troubled by the notorious sign problem. Recent efforts using the Taylor extrapolation method, reweighting or analytical continuation of the chemical potential has lead to results for small baryon densities and/or high temperatures [66, 67]. However, for large chemical potential and/or at zero temperature this problem cannot be overcome and an accurate description is still lacking. Another disadvantage of the Monte-Carlo method is that it is defined on an Euclidean lattice and hence does not enable to describe real-time evolution.

1.1.3. Tensor network states for Hamiltonian gauge theories

One month after Wilson submitted his paper, Kogut and Susskind, who were working in the same department at that time, presented Wilson's lattice approach in the Hamiltonian framework for $SU(2)$. In [68] they discretized now only the spatial dimensions and kept time continuous. Similar as in Wilson's framework, the fermions are defined on the lattice sites and the gauge fields live on the links between the sites. The Hilbert space representing the gauge fields is now determined by the irreducible representations of the Lie algebra corresponding to the gauge group. The so-called Kogut-Susskind Hamiltonian they obtained corresponds to the one that can be determined from the Wilsonian path integral with the transfer matrix formalism [69, 70]. This approach can in principle overcome the sign problem and enables the study of out-of-equilibrium physics. Unfortunately, exact diagonalization of the Kogut-Susskind Hamiltonian is impossible for large lattices due to the exponential increase of the dimension of the Hilbert space with the number of sites.

This problem described above is not specific to QCD only but holds for any strongly correlated many-body system: perturbative approaches such as mean-field theory fail and the Hilbert space describing the space of states is too large to simulate on a classical computer. For instance, with the present computing power one can diagonalize a spin-1/2 system of N sites with N at most 40. Fortunately, often one is only interested in the low-energy states of a system and it turns out that the area law for entanglement entropy [71–73] gives a universal identification of the physically relevant tiny corner of Hilbert space for these states. This is where Tensor Network States (TNS) [74, 75] come into play, these are a variational class of states that efficiently represent general low-energy states, by encoding the wave function into a set of tensors whose interconnections capture the proper entanglement behavior.

The most famous example of TNS are the Matrix Product States (MPS) [76] in one spatial dimension that underlie White's Density Matrix Renormalization Group (DMRG) [44]. Notably, it took quite long from the introduction of MPS until they were used as a variational ansatz for quantum many-body systems [77]. Historically they were mainly considered as an analytical tool. One well-known example that can be found in almost any introduction to MPS [74, 76] is the ground state of the AKLT model [78] which can be represented as an exact MPS. In 1992 Fannes, Nachtergaele and Werner [79] considered the MPS, in their paper called finitely correlated states, as an interesting class of states because one can easily impose translational invariance on them. The relation between DMRG and MPS only became clear to the majority of the community around the year 2000. Since the formulation

of DMRG in terms of MPS, the number of MPS algorithms for many-body systems has increased *exponentially*. In particular some algorithms have been developed for simulating real-time evolution. Some of these algorithms will be used in this thesis: the TDVP [43], the iTEBD [45] and of course the DMRG [44] albeit in a slightly different setting [80]. These algorithms enabled many physicists to obtain approximations of the low-energy states of a wide range of many-body states up to unlevelled precision. Also for lattice gauge theories MPS have been applied successfully [27, 30, 33, 34, 81–85]. Although MPS are these days mainly used for numerical purposes they are still interesting from the theoretical point of view. For instance they enabled the classifications of all gapped phases in one dimension [86].

1.1.4. The Schwinger model

In this dissertation we will use MPS to investigate the Schwinger model. The Schwinger model is one-flavor QED in one spatial dimension. Historically, Schwinger considered this model [1] as an example of a gauge vector field that can have a non-zero mass [2]. It was only a few months later that Anderson published his proposal for the Higgs mechanism where gauge fields acquire mass without breaking gauge invariance [3]. Despite its simplicity as an abelian gauge theory in one spatial dimension, it has many interesting physical features like for instance confinement and chiral symmetry breaking. This made this model very attractive to test analytical and numerical methods [4–34]. This model also gained interest from the experimentalists in the context of quantum simulators, see [35–38] and references therein.

Up to now two different groups considered the Schwinger model for MPS simulations. In 2003 Byrnes [27] finished his PhD where he investigated the phase transition related to the \mathcal{CT} symmetry and also determined the mass spectrum for two particular cases of the electric background field. On the other hand Bañuls *et al.* [30, 33, 34] determined the mass spectrum as well and considered the chiral condensate at zero and finite temperature.

Here we choose a different approach and work directly in the thermodynamic limit. This has the advantage that we avoid any possible finite size artifacts. Another advantage is that the translation symmetry will be maintained manifestly during our simulations and that we can label the eigenstates of the Hamiltonian with their momentum. Contrary to their approach we do not integrate out the gauge fields. Working on a finite lattice allows one to map the Hamiltonian to a long-range spin-1/2 system. This trick, however, is only possible in one spatial dimension. In contrary, because we keep the gauge fields dynamical, our method can be generalized to higher dimensions.

In addition to the earlier MPS studies we also exploit the fact that our TNS simulations allow for a direct calculation of the entanglement entropy between different regions. In the last decade it has become clear that entanglement entropy is a very useful quantity for the characterization of quantum many body systems and quantum field theories [39]. In contrast to earlier methods such as the AdS/CFT approach [40] or the replica trick [41], tensor network state simulations give access to the full Schmidt spectrum of the state, from which one can calculate all Renyi entropies easily, including the Von Neumann entropy.

We also perform for the first time a full quantum real-time evolution of the Schwinger model induced by a quench in the form of an electric background field, thereby showing the full potential of the MPS framework. Earlier studies were always in the semi-classical approximation e.g. [16, 24, 31].

1.2. Overview

The thesis is divided into two parts. In this part (part I) we mainly focus on the systematics of our simulations and the results. The details of the simulations are explained in the more technical part II. Both parts are written such that one should be able to read them independently.

1.2.1. Overview of part I

In the next section we introduce the Schwinger model and construct a MPS ansatz for the ground state wave function. By imposing a block structure on the tensors the state is manifestly gauge invariant. In chapter 2-5 we consider these gauge invariant MPS for some interesting applications.

In chapter 2 we are able to determine very accurately the ground state properties and elementary one-particle excitations in the continuum limit. In particular, a novel particle excitation in the form of a heavy vector boson is uncovered, compatible with the strong coupling expansion in the continuum. We verify Elitzur's theorem and demonstrate the advantage of working with gauge invariant MPS by comparing with MPS simulations on the full Hilbert space, that includes numerous non-physical gauge variant states. Furthermore, we compute the chiral condensate and recover the predicted UV-divergent behavior. We also consider the half chain entanglement entropy and find a logarithmic divergence with a universal coefficient, compatible with the result of [42]. Finally we determine the elementary excitations of the Schwinger model in the presence of an electric background field. For relatively small fermion masses we obtain an estimate for the value of the background field where the one-particle excitation with the largest energy becomes unstable and decays into two other elementary particles with smaller energy.

In chapter 3 MPS are used to perform a numerical study of the Schwinger model in the presence of an external static ‘quark’ and ‘antiquark’. We obtain a detailed picture of the transition from the confining state at short interquark distances to the broken-string ‘hadronized’ state at large distances and this for a wide range of couplings, recovering the predicted behavior both in the weak and strong coupling limit of the continuum theory. In addition to the relevant local observables like charge and electric field, we compute the (bipartite) entanglement entropy and show that subtraction of its vacuum value results in a UV-finite quantity. We find that both string formation and string breaking leave a clear imprint on the resulting entropy profile. Finally, we also study the case of fractional probe charges, simulating for the first time the phenomenon of partial string breaking in the Schwinger model.

Using Matrix Product Operators (MPO) the Schwinger model is simulated in thermal equilibrium in chapter 4. The variational manifold of gauge invariant MPO is constructed to represent Gibbs states. As a first application we compute the chiral condensate in thermal equilibrium and find agreement with earlier studies. Furthermore, as a new application we probe the Schwinger model with a fractionally charged static quark-antiquark pair separated infinitely far from each other. We find a critical temperature beyond which the string tension is exponentially suppressed, which is in qualitative agreement with analytical studies in the strong coupling limit. Finally, the \mathcal{CT} symmetry breaking is investigated and our results strongly suggest that the symmetry is restored at any nonzero temperature.

In chapter 5 we study non-equilibrium dynamics by simulating the real-time evolution of the system induced by a quench in the form of a uniform background electric field. For small quenches we can explain our results by investigating the one-particle spectrum of the quenched Hamiltonian. For larger values of the quench we observe that the state converges already at early times to a steady-state solution. By using our results from the finite temperature simulations we investigate whether the state thermalizes or not.

Finally we present our conclusion and discuss the generalization of our setup to higher dimensions.

1.2.2. Overview of part II

In part II we develop the formalism for performing simulations with gauge invariant MPS. It is not necessary to read this part to understand MPS and our approach as it is also briefly explained in part I. This part is in particular for the reader that is interested in numerical methods.

In chapter 1 we recall the definition of MPS and its properties. We introduce the tensor network diagram notation which visualizes the computation of expectation values with MPS. Furthermore we consider the thermodynamic limit and define translation invariant MPS, called uniform MPS. We study the tangent space of these uniform MPS as they will be used to approximate one-particle excitations with a particular momentum. Finally, the framework is extended to describe systems that exhibit \mathcal{CT} invariance, where \mathcal{C} can be any idempotent operator and \mathcal{T} is the translation over one site.

In chapter 2 we review some optimization methods for MPS in the thermodynamic limit from literature that will be used for our simulations. More specifically, we discuss the Time-Dependent Variational Principle (TDVP) [43] and the DMRG [44] for finding the optimal approximation of the ground state within the class of MPS. We also consider the method of [87] to find the optimal tangent vectors to approximate the one-particle excitations. Furthermore, we explain the infinite Time Evolving Block Decimation (iTEBD) algorithm [45] for real-time evolution.

In chapter 3 we construct the most general gauge invariant MPS on a finite lattice. The variational degrees of freedom of these MPS are encoded by block matrices. We discuss the Schmidt decomposition and find that the special structure of the MPS enables us to label the Schmidt values by the eigenvalues of the electric field. We extend the gauge invariant ansatz to systems in the thermodynamic limit by imposing translation symmetry or \mathcal{CT} symmetry on the state. Finally we construct gauge invariant MPO to approximate the Gibbs state at finite temperature. We also consider gauge invariant observables and identify the relevant matrix elements by projecting out the gauge variant part.

In chapter 4 we modify the MPS algorithms discussed in chapter 2 such that all computations are gauge invariant. This is done by exploiting the sparse structure of the gauge invariant MPS. This also leads to a huge speed up compared to when we should perform the computations in the full Hilbert space. We present the algorithms that are used to produce the results in part I.

1.3. Matrix product states for the Schwinger model

1.3.1. Lagrangian and Hamiltonian quantization

The Schwinger model is 1+1 dimensional QED with one fermion flavor. We start from the Lagrangian density in the continuum:

$$\mathcal{L} = \bar{\psi} (\gamma^\mu (i\partial_\mu + gA_\mu) - m) \psi - \frac{1}{4} F_{\mu\nu} F^{\mu\nu}, \quad (1.1)$$

where the sum over μ and ν runs from 0 to 1

$$\psi = \begin{pmatrix} \psi_1 \\ \psi_2 \end{pmatrix} \text{ and } F_{\mu\nu} = \partial_\mu A_\nu - \partial_\nu A_\mu.$$

Here the gamma matrices are (2×2) matrices:

$$\gamma^0 = \begin{pmatrix} 1 & 0 \\ 0 & -1 \end{pmatrix}, \gamma^1 = \begin{pmatrix} 0 & 1 \\ -1 & 0 \end{pmatrix}$$

and satisfy

$$\{\gamma^\mu, \gamma^\nu\} = 2g^{\mu\nu} \text{ with } g^{\mu\nu} = \begin{pmatrix} 1 & 0 \\ 0 & -1 \end{pmatrix}$$

the Lorentzian metric. The Lagrangian is invariant under the local gauge transformation

$$\psi(x) \longrightarrow e^{-ig\varphi(x)}\psi(x), A_\mu(x) \longrightarrow A_\mu(x) - \partial_\mu\varphi(x)$$

where $x = (x^0, x^1) = (t, z)$.

The Euler-Lagrange equations for A_μ read

$$\partial_\mu F^{\mu\nu} = gj^\nu, j^\nu = \bar{\psi}\gamma^\nu\psi.$$

We will now perform a Hamiltonian quantization. Therefore we use the gauge freedom to put $A_0 = 0$, this is the so-called temporal gauge. Introducing the electric field

$$E = -F^{01} = F^{10},$$

the Euler-Lagrange equation for A_0 becomes the well known Gauss' law

$$\partial_z E = gj^0. \tag{1.2}$$

The electric field is the canonical conjugate Π_{A_1} of A_1 :

$$E = \frac{\partial\mathcal{L}}{\partial(\partial_t A_1)} = \Pi_{A_1},$$

therefore the Hamiltonian in the temporal gauge becomes

$$\begin{aligned} \mathcal{H} &= \Pi_{A_1}\partial_t A_1 - \mathcal{L} \\ &= \frac{1}{2}E^2 - i\bar{\psi}\gamma^1(\partial_1 - igA_1)\psi + m\bar{\psi}\psi \end{aligned} \tag{1.3}$$

where one needs to include Gauss' law eq. (1.2) as an additional constraint. The fields are quantised by imposing

$$\{\psi_\alpha(t, z_1)^\dagger, \psi_\beta(t, z_2)\} = \delta(z_1 - z_2)\delta_{\alpha,\beta},$$

$$\begin{aligned} \{\psi_\alpha(t, z_1), \psi_\beta(t, z_2)\} &= 0, \\ [A_1(t, z_1), E(t, z_2)] &= i\delta(z_1 - z_2). \end{aligned}$$

For $m/g = 0$ the model can be solved through bosonization and reduces to the theory of a free boson with mass $g/\sqrt{\pi}$. When $m/g \neq 0$ there is no exact solution anymore. However for $m/g \ll 1$, the strong coupling limit, there are results available in mass perturbation theory [6, 21]. In the weak coupling limit, $m/g \gg 1$, there are also some results available about the mass spectrum [6, 27]. Some of these results will be used to benchmark our method and will be discussed in the next chapters.

1.3.2. Kogut-Susskind Hamiltonian

We will now briefly recall the Kogut-Susskind spatial discretization [7, 68] to turn this into a lattice system. Consider a lattice of $2N$ sites with lattice spacing a . To avoid the fermion doubling problem, the two-component fermions are sited on a staggered lattice:

$$\psi_1(2na) = \frac{1}{\sqrt{a}}\phi(2n) \text{ and } \psi_2((2n-1)a) = \frac{1}{\sqrt{a}}\phi(2n-1) \quad (1 \leq n \leq N)$$

where ϕ is a dimensionless fermion field:

$$\{\phi(n), \phi(m)\} = 0, \{\phi^\dagger(n), \phi(m)\} = \delta_{n,m}.$$

This can be turned into a spin-1/2 system by the Jordan-Wigner transformation

$$\phi(n) = \prod_{k < n} [i\sigma_z(k)]\sigma^-(n), \phi^\dagger(n) = \prod_{k < n} [-i\sigma_z(k)]\sigma^+(n).$$

The eigenvectors $\{|s_n\rangle_n : s_n \in \{-1, 1\}\}$ of $\sigma_z(n)$ will form the basis of the local Hilbert space at site n for our computations:

$$\begin{aligned} \sigma_z(n) |s\rangle_n &= s |s\rangle_n; \quad s = -1, 1; \\ \sigma^-(n) |1\rangle_n &= |-1\rangle_n, \quad \sigma^+(n) |-1\rangle_n = |1\rangle_n, \\ \sigma^-(n) |-1\rangle_n &= \sigma^+(n) |1\rangle_n = 0. \end{aligned}$$

On the links between the sites, we put the gauge field $\theta(n) = agA_1(na)$ and the electric field $E(n) \leftarrow E(na)$, with $[\theta(n), E(m)] = ig\delta_{n,m}$. The commutation relation determines the spectrum of $E(n)$ up to a constant: $E(n)/g = L(n) + \alpha(n)$, where $L(n)$ is the angular operator which has an integer spectrum and $\alpha(n) \in \mathbb{R}$ corresponds to the background electric field at link n . Therefore, at link n a basis is $\{|p_n\rangle_{[n]} : p_n \in \mathbb{Z}\}$ with

$$L(n) |p\rangle_{[n]} = p |p\rangle_{[n]} \text{ and } e^{\pm i\theta(n)} |p\rangle_{[n]} = |p \pm 1\rangle_{[n]} \quad (p \in \mathbb{Z})$$

As can be verified, the gauged spin Hamiltonian

$$H = \frac{g}{2\sqrt{x}} \left(\sum_{n=1}^{2N} \frac{1}{g^2} E(n)^2 + \frac{\sqrt{x}}{g} m \sum_{n=1}^{2N} (-1)^n (\sigma_z(n) + (-1)^n) + x \sum_{n=1}^{2N-1} (\sigma^+(n) e^{i\theta(n)} \sigma^-(n+1) + h.c.) \right),$$

where $x = 1/g^2 a^2$ is the inverse lattice spacing in units of g , corresponds in the continuum limit $x \rightarrow \infty$ to the Hamiltonian density eq. (1.3). Notice the different second (mass) term in the Hamiltonian for even and odd sites which originates from the staggered formulation of the fermions. In this formulation the odd sites are reserved for the charge $-g$ ‘quarks’, where spin up, $s = +1$, corresponds to an unoccupied site and spin down, $s = -1$, to an occupied site. The even sites are reserved for the charge $+g$ ‘antiquarks’ where now conversely spin up corresponds to an occupied site and spin down to an occupied site.

In the time-like axial gauge the Hamiltonian is still invariant under the residual time-independent local gauge transformations generated by:

$$gG_0(n) = E(n) - E(n-1) - \frac{g}{2} (\sigma_z(n) + (-1)^n).$$

As a consequence, if we restrict ourselves to physical gauge invariant operators O , with $[O, G_0(n)] = 0$, the Hilbert space decomposes into dynamically disconnected superselection sectors, corresponding to the different eigenvalues of $G_0(n)$. In the absence of any background charge ($\alpha(n) = 0$) the physical sector then corresponds to the $G(n) = 0$ sector where

$$G(n) = L(n) - L(n-1) - \frac{\sigma_z(n) + (-1)^n}{2}.$$

Imposing this condition (for every n) on the physical states is also referred to as the Gauss law constraint, as this is indeed the discretised version of eq. (1.2).

The other superselection sectors correspond to states with background charges. Specifically, if we want to consider two infinitely heavy probe charges, one with charge $-gQ$ at site m_L and one with opposite charge $+gQ$ at site m_R , we have to restrict ourselves to the sector:

$$gG_0(n) = gQ(\delta_{n,m_L} - \delta_{n,m_R}).$$

Notice that we will consider both integer and non-integer (fractional) charges Q . As in the continuum case [5], we can absorb the probe charges into

a background electric field string that connects the two sites. This amounts to taking $\alpha(n)$ only nonzero in between the sites: $\alpha(n) = -Q\Theta(m_L \leq n < m_R)$. The Gauss constraint,

$$gG_0(n) = E(n) - E(n-1) - \frac{g}{2}(\sigma_z(n) + (-1)^n) = gQ(\delta_{n,m_L} - \delta_{n,m_R}),$$

now becomes

$$G(n) = L(n) - L(n-1) - \frac{\sigma_z(n) + (-1)^n}{2} = 0, \quad (1.4)$$

and we finally find the Hamiltonian

$$\mathcal{H} = \frac{g}{2\sqrt{x}} \left(\sum_{n=1}^{2N} [L(n) + \alpha(n)]^2 + \frac{\sqrt{x}}{g} m \sum_{n=1}^{2N} (-1)^n (\sigma_z(n) + (-1)^n) + x \sum_{n=1}^{2N-1} (\sigma^+(n) e^{i\theta(n)} \sigma^-(n+1) + h.c.) \right), \quad (1.5)$$

in accordance with the continuum result of [5].

1.3.3. Gauge invariant MPS

Consider now the lattice spin-gauge system eq. (1.5) on $2N$ sites. On site n the matter fields are represented by the spin operators with basis $\{|s_n\rangle_n : s_n \in \{-1, 1\}\}$. The gauge fields live on the links and on link n their Hilbert space is spanned by the eigenkets $\{|p_n\rangle_n : p_n \in \mathbb{Z}\}$ of the angular operator $L(n)$. But notice that for our numerical scheme we only retain a finite range: $p_{n+1}^{\min} \leq p_n \leq p_{n+1}^{\max}$. We will address the issue of which values to take for p_{n+1}^{\min} and p_{n+1}^{\max} later in this subsection. Furthermore, it is convenient to block site n and link n into one effective site with local Hilbert space spanned by $\{|s_n, p_n\rangle_n\}$. Writing $\kappa_n = (s_n, p_n)$ we introduce the multi-index

$$\boldsymbol{\kappa} = ((s_1, p_1), (s_2, p_2), \dots, (s_{2N}, p_{2N})) = (\kappa_1, \dots, \kappa_{2N}).$$

With these notations we have that the effective site n is spanned by $\{|\kappa_n\rangle_n\}$. Therefore the Hilbert space of the full system of $2N$ sites and $2N$ links, which is the tensor product of the local Hilbert spaces, has basis $\{|\boldsymbol{\kappa}\rangle = |\kappa_1\rangle_1 \dots |\kappa_{2N}\rangle_{2N}\}$ and a general state $|\Psi\rangle$ is thus a linear combination of these $|\boldsymbol{\kappa}\rangle$:

$$|\Psi\rangle = \sum_{\boldsymbol{\kappa}} C^{\kappa_1, \dots, \kappa_{2N}} |\boldsymbol{\kappa}\rangle$$

with basis coefficients $C^{\kappa_1, \dots, \kappa_{2N}} \in \mathbb{C}$.

A general MPS $|\Psi[A]\rangle$ now assumes a specific form for the basis coefficients [79]:

$$|\Psi[A]\rangle = \sum_{\kappa} v_L^\dagger A_1^{\kappa_1} A_2^{\kappa_2} \dots A_{2N}^{\kappa_{2N}} v_R |\kappa\rangle, \quad (1.6)$$

where $A_n^{\kappa_n}$ is a complex $D_n \times D_{n+1}$ matrix with components $[A_n^{\kappa_n}]_{\alpha\beta}$ and where $v_L \in \mathbb{C}^{D_1 \times 1}$, $v_R \in \mathbb{C}^{D_{2N+1} \times 1}$ are boundary vectors. The MPS ansatz thus associates with each site n and every local basis state $|\kappa_n\rangle_n = |s_n, p_n\rangle_n$ a matrix $A_n^{\kappa_n} = A_n^{s_n, p_n}$. The indices α and β are referred to as virtual indices, and $D = \max_n(D_n)$ is called the bond dimension.

To better understand the role of the bond dimension in MPS simulations it is useful to consider the Schmidt decomposition with respect to the bipartition of the lattice consisting of the two regions $\mathcal{A}_1^n = \mathbb{Z}[1, \dots, n]$ and $\mathcal{A}_2^n = \mathbb{Z}[n+1, \dots, 2N]$ [76]:

$$|\Psi[A]\rangle = \sum_{\alpha=1}^{D_{n+1}} \sqrt{\sigma_{n,\alpha}} |\psi_{\alpha}^{\mathcal{A}_1^n}\rangle |\psi_{\alpha}^{\mathcal{A}_2^n}\rangle. \quad (1.7)$$

Here $|\Psi_{\alpha}^{\mathcal{A}_1^n}\rangle$ (resp. $|\Psi_{\alpha}^{\mathcal{A}_2^n}\rangle$) are orthonormal unit vectors living in the tensor product of the local Hilbert spaces belonging to the region \mathcal{A}_1^n (resp. \mathcal{A}_2^n) and $\sigma_{n,\alpha}$, called the Schmidt values, are non-negative numbers that sum to one. One can easily deduce that for a general MPS of the form eq. (1.6) at most D_{n+1} Schmidt values are nonzero (for the cut at site n eq. (1.7)). We refer to subsection 1.1.3 of part II for the computation of the Schmidt values for a MPS, see also [76, 88]. We thus see that taking a finite bond dimension for the MPS corresponds to a truncation in the Schmidt spectrum of a state. The success of MPS is then explained by the fact that ground states of local gapped Hamiltonians can indeed be approximated very efficiently in D [71] and that the computation time for expectation values of local observables scales only with D^3 , allowing for reliable simulations on an ordinary desktop.

Another advantage of MPS simulations is that one can work directly in the thermodynamic limit $N \rightarrow \infty$, see section 1.2 of part II and [43, 88], bypassing any possible finite size artifacts. In the following we will work in this limit. In section 2.1 where the Hamiltonian is invariant under the \mathcal{CT} transformation the tensors $A_n^{\kappa_n}$ are independent of n . In sections 2.2 and 3.3 the Hamiltonian is invariant under translations over two sites and therefore $A_n^{\kappa_n}$ only depends on the parity of n . While in section 3.4 the MPS ansatz is not translational invariant in the bulk. In that case the tensors are fixed asymptotically ($|n| \gg 1$) to their ground state value, anticipating that we approach the translational invariant ground state of the zero-background Hamiltonian. In both cases the MPS ansatz depends on a finite number of

parameters. Finally, we note that, in the thermodynamic limit, the expectation values of local observables are independent of the boundary vectors v_L and v_R .

To parameterize gauge invariant MPS, i.e. states that obey $G(n) |\Psi[A]\rangle = 0$ for every n , it is convenient to give the virtual indices a multiple index structure $\alpha \rightarrow (q, \alpha_q); \beta \rightarrow (r, \beta_r)$, where q resp. r labels the eigenvalues of $L(n-1)$ resp. $L(n)$. In section 3.2 of part II it is proven that the condition $G(n) = 0$, eq. (1.4), then imposes the following form on the matrices:

$$[A_n^{s,p}]_{(q,\alpha_q),(r,\beta_r)} = [a_n^{q,s}]_{\alpha_q,\beta_r} \delta_{q+(s+(-1)^n)/2,r} \delta_{r,p}, \quad (1.8)$$

where $\alpha_q = 1 \dots D_n^q$, $\beta_r = 1 \dots D_{n+1}^r$. The first Kronecker delta is Gauss' law, $G(n) = 0$, on the virtual level while the second Kronecker delta connects the virtual index r with the physical eigenvalue p of $L(n)$. Because the indices q (resp. r) label the eigenvalues of $L(n-1)$ (resp. $L(n)$) and we only retain the eigenvalues of $L(n-1)$ in the interval $\mathbb{Z}[p_n^{\min}, p_n^{\max}]$ (resp. of $L(n)$ in the interval $\mathbb{Z}[p_{n+1}^{\min}, p_{n+1}^{\max}]$) we have that $D_n^q = 0$ for $q > p_n^{\max}$ and $q < p_n^{\min}$. The formal total bond dimension of this MPS is $D_n = \sum_{q=p_n^{\min}}^{p_n^{\max}} D_n^q$, but notice that, as eq. (1.8) takes a very specific form, the true variational freedom lies within the matrices $a_n^{q,s} \in \mathbb{C}^{D_n^q \times D_{n+1}^r}$.

Gauge invariance is of course also reflected in the Schmidt decomposition eq. (1.7): for states of the form eq. (1.8) the Schmidt values can be labeled with the same double index $\alpha \rightarrow (q, \alpha_q)$. More specifically, the Schmidt decomposition eq. (1.7) now reads (see section 3.3 of II):

$$|\Psi[A]\rangle = \sum_{q=p_{n+1}^{\min}}^{p_{n+1}^{\max}} \sum_{\alpha_q=1}^{D_{n+1}^q} \sqrt{\sigma_{n,\alpha_q}^q} |\psi_{q,\alpha_q}^{\mathcal{A}_1^n}\rangle |\psi_{q,\alpha_q}^{\mathcal{A}_2^n}\rangle. \quad (1.9)$$

We observe that taking a finite bond dimension D_{n+1}^q corresponds to a truncation in the Schmidt spectrum, now of the charge sector q . The choice for the different bond dimensions D_{n+1}^q in the different simulations should then be such that the discarded Schmidt values for each charge sector are sufficiently small. Not surprisingly given the first term in the Hamiltonian eq. (1.5) – we will find the relevant eigenvalues sectors of $L(n)$ to be centered around a dominant sector p_0 that can be shifted away from $p_0 = 0$ for some sites n , see also [33] for a discussion. The largest Schmidt value in each q -sector decreases as we move farther away from $q = p_0$. Therefore, we found for $|q - p_0|$ sufficiently large that all the Schmidt values σ_{n,α_q}^q were sufficiently small and we could safely take $D^q = 0$ for these values of q . For each of our simulations we will provide details on the weight of the different sectors for the different simulations.

From the Schmidt spectrum eq. (1.9) one can extract different measures for the entanglement. In this thesis we will always use the Von Neumann entropy S . For the half chain cut at site n , to which we will associate the position $z = (n + 1/2)a$ in physical units, we then have:

$$S(z) = - \sum_{q=p_{n+1}^{\min}}^{p_{n+1}^{\max}} \sum_{\alpha_q=1}^{D_{n+1}^q} \sigma_{n,\alpha_q}^q \log(\sigma_{n,\alpha_q}^q). \quad (1.10)$$

Ground state properties and spectrum

B. Buyens, J. Haegeman, K. Van Acoleyen, H. Verschelde, F. Verstraete
 ‘MPS for gauge field theories’
 Physical Review Letters **113** 091601, arXiv:1312.6654 (2013)

B. Buyens, K. Van Acoleyen, J. Haegeman, F. Verstraete
 ‘Matrix product states for Hamiltonian lattice gauge theories’
 PoS(LATTICE2014)308, arXiv:1411.0020 (2014)

B. Buyens, J. Haegeman, F. Verstraete, K. Van Acoleyen
 ‘Tensor networks for gauge field theories’
 PoS(EPS-HEP2015)375, arXiv:1511.04288 (2015)

2.1. $\alpha = 0$

2.1.1. Setup

In this section we will consider the Schwinger model in a zero electric background field ($\alpha(n) = 0$), the Kogut-Susskind Hamiltonian eq. (1.5) thus becomes

$$\mathcal{H} = \frac{g}{2\sqrt{x}} \left(\sum_{n=1}^{2N} L(n)^2 + \frac{\sqrt{x}}{g} m \sum_{n=1}^{2N} (-1)^n (\sigma_z(n) + (-1)^n) \right. \\ \left. + x \sum_{n=1}^{2N-1} (\sigma^+(n) e^{i\theta(n)} \sigma^-(n+1) + h.c.) \right), \quad (2.1)$$

with $x = 1/g^2 a^2$ and a the lattice spacing.

In the thermodynamic limit ($N \rightarrow +\infty$) the Hamiltonian eq. (2.1) is invariant under \mathcal{T}^2 , a translation over two sites, and the corresponding eigenvalues read $\mathcal{T}^2 = e^{i2ka}$, where $k \in [-\pi/2a, \pi/2a[$ is the physical momentum of the state. Another symmetry that will be useful is \mathcal{CT} , obtained by a translation over one site, followed by a charge conjugation, $\mathcal{C} |s_n, p_n\rangle = |-s_n, -p_n\rangle$. Since $\mathcal{C}^2 = 1$, we will have $\mathcal{CT} = \pm e^{ika}$. The states with positive sign then correspond to the scalar sector, while the negative sign corresponds to the vector sector.

To obtain a ground state approximation in the thermodynamic limit ($N \rightarrow \infty$) and thereby anticipating $\mathcal{CT} = 1$, we use a \mathcal{CT} invariant MPS, see section 1.4 of part II:

$$|\Psi_{\mathcal{C}}[A]\rangle = \sum_{\kappa_n} v_L^\dagger \left(\prod_{n=1}^{2N} A^{\kappa_n} \right) v_R |\kappa^c\rangle \quad (N \rightarrow +\infty), \quad (2.2a)$$

where

$$|\kappa^c\rangle = |\{(-1)^{n+1} \kappa_n\}_{n=1 \dots 2N}, \kappa_n = (s_n, p_n) \in \{-1, 1\} \times \mathbb{Z}[p^{min}, p^{max}]\rangle,$$

$v_L, v_R \in \mathbb{C}^D$, and $A^\kappa \in \mathbb{C}^{D \times D}$. Gauge invariance,

$$G(n) |\Psi_{\mathcal{C}}[A]\rangle = 0 \text{ with } G(n) = L(n) - L(n-1) + \frac{\sigma_z(n) + (-1)^2}{2},$$

is imposed if A takes the form

$$[A^{s,p}]_{(q,\alpha_q);(r,\beta_r)} = [a^{q,s}]_{\alpha_q,\beta_r} \delta_{p,q+(s-1)/2} \delta_{r,-p} \quad (2.2b)$$

with $a^{q,s} \in \mathbb{C}^{D^q \times D^r}$. We refer to subsection 3.3.2 of part II for an explicit derivation of this MPS starting from the most general gauge invariant MPS eq. (1.8). The Schmidt decomposition eq. (1.9) with respect to the bipartition of the lattice consisting of the two regions $\mathcal{A}_1^n = \mathbb{Z}[1, \dots, n]$ and $\mathcal{A}_2^n = \mathbb{Z}[n+1, \dots, 2N]$ now reads

$$|\Psi_{\mathcal{C}}[A]\rangle = \sum_{q=p^{min}}^{p^{max}} \sum_{\alpha_q=1}^{D^q} \sqrt{\sigma_{\alpha_q}^q} |\psi_{q,\alpha_q}^{\mathcal{A}_1^n}\rangle |\psi_{q,\alpha_q}^{\mathcal{A}_2^n}\rangle.$$

Note that the Schmidt spectrum is independent of n . The computation of the Schmidt values $\sigma_{\alpha_q}^q$ is discussed in subsection 4.1.2 of part II.

In subsection 4.1.4 of part II it is explained how we implement the time-dependent variational principle (TDVP) [43] to obtain the optimal approximation for the ground state within the class of states eq. (2.2) with a fixed

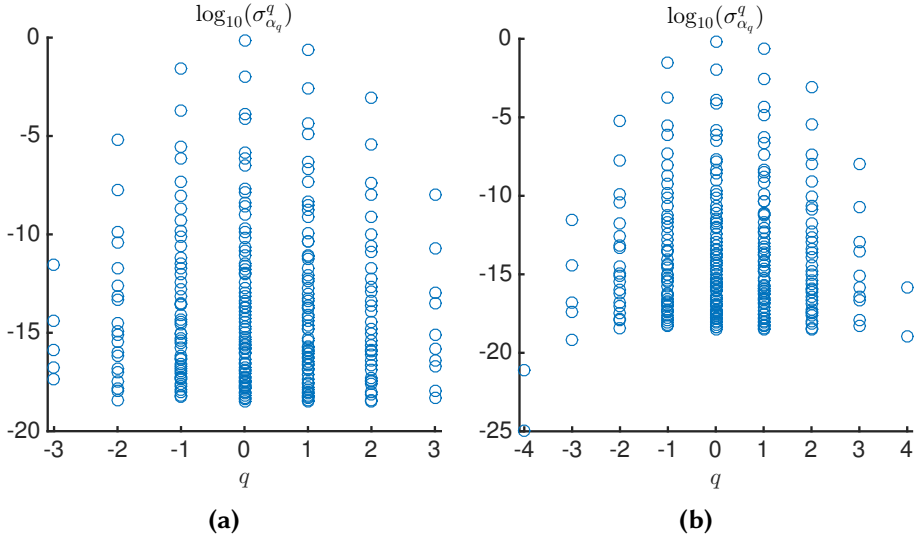


Figure 2.1: $m/g = 0.25$, $x = 100$. Distribution of the (base-10) logarithm of the Schmidt coefficients σ in every charge sector. (a) $p^{max} = -p^{min} = 3$ and $D^q = (5, 20, 48, 70, 62, 34, 10)$. (b) $p^{max} = 4 = -p^{min}$ and $D^q = (2, 5, 20, 48, 70, 62, 34, 10, 2)$.

bond dimension D^q . The variational freedom of these states $|\Psi_{\mathbb{C}}[A]\rangle$ lies within the matrices $a^{q,s} \in \mathbb{C}^{D^q \times D^r}$ and the formal bond dimension of this MPS equals $D = \sum_{q \in \mathbb{Z}} D^q$. It will be important to choose the distribution of D^q wisely, according to the relative weight of the different charge sectors. As illustrated in fig. 2.1a, this is done by looking at the Schmidt coefficients $\sigma_{\alpha_q}^q$, and demanding that the smallest coefficients of each sector coincide more or less. The resulting distribution of D^q is peaked around $q = 0$, and justifies our $p^{max} = 3$ truncation that corresponds to $D^q = 0$ for $|q| > 3$. Physically, this truncation hinges on the fact that the first term in the Hamiltonian eq. (2.1) ($\propto \sum_n L^2(n)$) punishes states with large eigenvalues of $L(n)$. As a consequence we expect such states not to be relevant for the low-energy physics at strong coupling. In fig. 2.1a we illustrate how one can check this assumption and determine the proper truncation by looking at the relative weight of the different charge sectors. As an extra check on our truncation we have performed another simulation, now with $p^{max} = 4$, again for $x = 100, m/g = 0.25$. In figure 2.1b we plot again the Schmidt coefficients for the ground state and by comparing fig. 2.1b with fig. 2.1a, we clearly see that we can indeed neglect the contributions from the $q = \pm 4$ charge sectors.

Once we have a good approximation for the ground state, we can use the

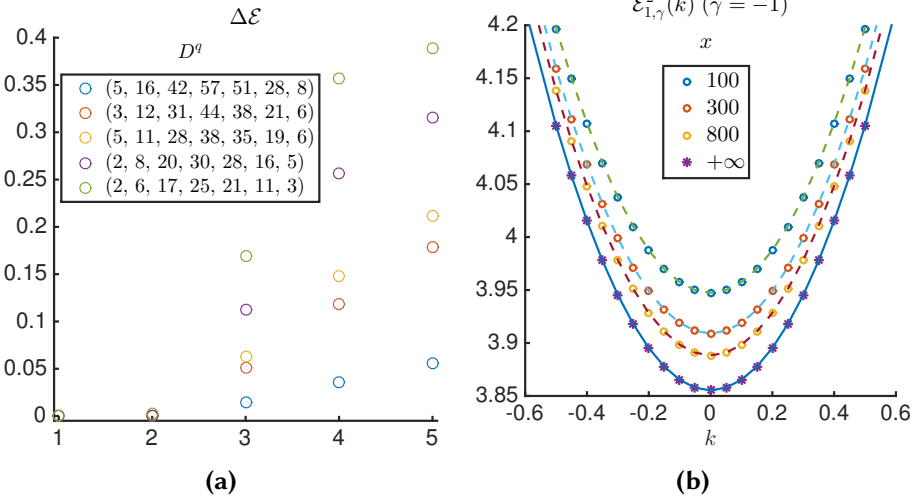


Figure 2.2.: $m/g = 0.25, x = 100, \alpha = 0$. (a): Difference for the estimated energies of the excited states for various bond dimension with respect to these with $D^q = (5, 20, 48, 70, 62, 34, 10)$ for the vector sector $\gamma = -1$. Only the first two excitations are stable under variation over D . (b): $m/g = 0.75$. Fit of the Einstein-dispersion relation $\mathcal{E}_{1,v}^2(k) = k^2 + \mathcal{E}_1, v^2(x)$ (dashed lines) to the data (small circles) for different values of x . The stars represent the estimated continuum values, the full line (lowest lying curve) is the curve $\mathcal{E}^2 = k^2 + \mathcal{E}_{1,v}^2$.

method of [87] to obtain the one-particle excited states. The excitations are labelled by their (physical) momentum $k \in [-\pi/2a, \pi/2a[$ and their \mathcal{CT} quantum number $\gamma = \pm 1$. For a given ground state approximation we then take the following ansatz state $|\Phi_{k,\gamma}^c[B, A]\rangle$ for the one-particle excitations (see also subsection 1.4.2 of part II):

$$\sum_{m=1}^{2N} e^{ikma} \gamma^m \sum_{q_n} v_L^\dagger \left(\prod_{1 < n < m} A^{\kappa_n} \right) B^{\kappa_m} \left(\prod_{m < n < 2N} A^{\kappa_n} \right) v_R |\kappa^c\rangle, \quad (2.3)$$

with $B^{q,s}$ again of the gauge invariant form eq. (2.2b) with general matrices $b^{q,s}$. These are determined variationally by minimizing their energy in the ansatz subspace which leads to a generalized eigenvalue problem (see subsection 4.2.5 of part II for the details). For a given momentum and \mathcal{CT} quantum number we typically find different local minima of which only one or two are stable under variation of the bond dimension D (see fig. 2.2a). It are these stable states that we can interpret as approximations to actual physical one-particle excitations.

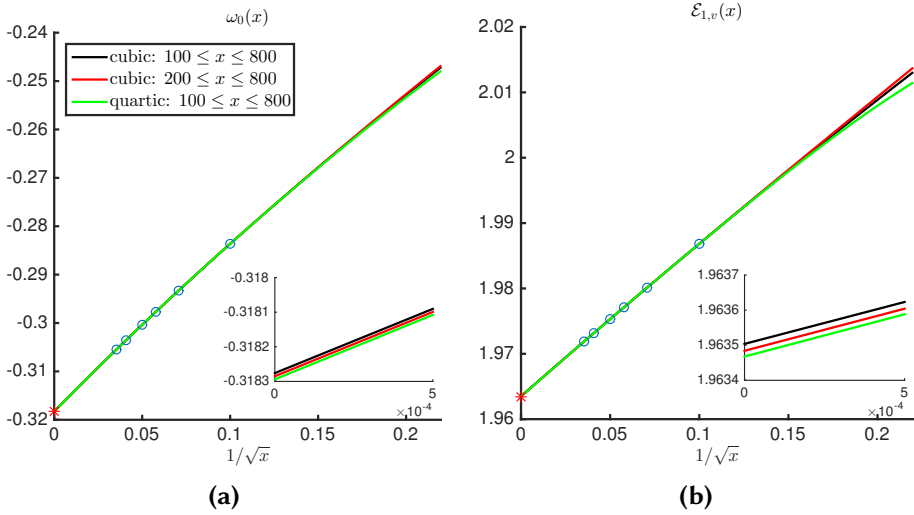


Figure 2.3.: $m/g = 0.75, \alpha = 0$. Continuum extrapolation through our data (bullets). We show here the cubic fit through all points (black), through the five largest x -values (red) and a quartic fit through all points (green). The star represents our final continuum estimate which is based on the cubic fit through the five largest x -values. Insets: zooming in on the interval $1/\sqrt{x} \in [0, 5 \times 10^{-4}]$. (a) $\omega_0(x)$. (b) $\mathcal{E}_{1,v}(x)$.

2.1.2. Spectrum

The continuum limit $a \rightarrow 0$ of the Schwinger model corresponds to the limit $x \rightarrow \infty$. To obtain the energies of the ground state and of the one-particle excitations in this limit, we have calculated these quantities for values of $x = 100, 200, 300, 400, 600, 800$. At every x we considered different values of D till convergence was reached at some D_{max} . We estimated the truncation error on D from comparison of the result for $D = D_{max}$ with the result for the next to largest value of D . Larger values of x typically required larger values of D for the same order of the error. For instance for $m/g = 0.5$ our maximal D varied from 185 for $x = 100$ to 358 for $x = 800$. This scaling of D is not surprising, as it is well known that MPS representations require larger D for systems with larger correlation lengths ξ (in units of the lattice spacing) [75]. For the Schwinger model ξ indeed diverges in the $x \rightarrow \infty$ limit.

To extrapolate towards $x \rightarrow \infty$ we used a third order polynomial fit in $1/\sqrt{x}$ through the largest five x -values. Similar to [27] our extrapolation error is then estimated by considering a third and fourth order polynomial through all six points, taking the error to be the maximal difference with the original inferred value. As can be observed from figs. 2.3a and 2.3b we indeed find that $\omega_0(x)$ and $\mathcal{E}_{1,v}(x)$ lie almost on a straight line as a function $1/\sqrt{x}$. This was also the case for $\mathcal{E}_{2,v}(x)$ and $\mathcal{E}_{1,s}(x)$. By fitting our data to higher order polynomials in $1/\sqrt{x}$ we take into account larger cut-off effects in x .

In table 2.1 we display our resulting values for the ground state energy density $\omega_0 = \mathcal{E}_0/2N\sqrt{x}$ with \mathcal{E}_0 the ground state energy, and the mass $\mathcal{E}_{k,\gamma} = \mathcal{E}_{k,\gamma} - \mathcal{E}_0$ of the different one-particle excitations. Because $\mathcal{H}/2\sqrt{x}$ reduces to the XY spin model in a staggered magnetic field in the limit $x \rightarrow +\infty$ we have that $\omega_0 = -1/\pi = -0.318310$.

For $m/g = 0$ the Schwinger model can be solved by bosonization [1] and reduces to a free theory, of one bosonic vector ($\gamma = -1$) particle with mass $\mathcal{E}_{1,v} = 1/\sqrt{\pi} = 0.56419$. In table 2.1 our results for $m/g = 0$ are compared with the analytical result. For $m/g \neq 0$ we find three excited states, one scalar and two vectors, with the hierarchy of masses $\mathcal{E}_{1,v} < \mathcal{E}_{1,s} < \mathcal{E}_{2,v}$ matching that of the strong coupling result [6, 21]. This is the first time that the second vector excitation has been found numerically. For the energy density and the two lowest mass excitations our results are consistent with the previous most precise simulations [27, 30], with a similar or sometimes better accuracy. Finally, a nice cross-check of our method follows from calculating the excitation energies for non-zero momenta k . The Schwinger model is Lorentz invariant in the continuum limit, so we should have an

m/g	ω_0	$\mathcal{E}_{1,v}$	$\mathcal{E}_{1,s}$	$\mathcal{E}_{2,v}$
0	-0.318320(4)	0.56418(2)		
0.125	-0.318319(4)	0.789491 (8)	1.472 (4)	2.10 (2)
0.25	-0.318316(3)	1.01917 (2)	1.7282 (4)	2.339(3)
0.3	-0.318316(3)	1.11210 (8)	1.82547 (3)	2.4285 (3)
0.5	-0.318305(2)	1.487473 (7)	2.2004 (1)	2.778 (2)
0.75	-0.318285 (9)	1.96347 (3)	2.658943(6)	3.2043(2)
1	-0.31826 (2)	2.44441 (1)	3.1182 (1)	3.640(4)

Table 2.1.: Energy density and masses of the one-particle excitations (in units $g = 1$) for different m/g . The last column displays the result for the heavy vector boson, compatible with the prediction of Coleman [6, 21]

approximate Einstein dispersion relation at finite lattice spacing a , for small momenta $ka \ll 1$. As shown in fig. 2.2b, this is precisely what we find.

2.1.3. Elitzur's theorem

By Elitzur's theorem [89], which states that a gauge symmetry cannot be spontaneously broken, one could argue that it is not necessary to impose the condition eq. (2.2b) for a variational calculation of the ground state. However, there will typically be many more non-physical (gauge variant) low-energy excitations in the full Hilbert space, and one would therefore expect a slower convergence rate for variational calculations that do not impose gauge invariance. Let us now examine this issue explicitly for the Schwinger model. To this end we do a comparative study where we approximate the ground state with a MPS eq. (2.2a), with and without imposing gauge invariance eq. (2.2b). We take the parameters $m/g = 0.25$, $x = 100$ and do the simulations for $D = 29$ and $D = 40$. As explained in the previous subsection, for the gauge invariant ansatz we have to distribute the variational freedom wisely among the charge sectors D^q ($D = \sum_q D^q$) according to the Schmidt values. We truncate the charges q on the links, $|q| \leq p^{max} = 2$ for $D = 29$ and $|q| \leq p^{max} = 3$ for $D = 40$. In all cases we used TDVP to find the ground state and stopped the algorithm when the norm of the gradient was below 10^{-6} . In the second and fourth column of table 2.2 we display the simulations where we did not impose gauge invariance and in the third and fifth column the simulations where the states were manifestly gauge invariant. For reference, for $D = 249$ with $D = (5, 20, 48, 70, 62, 34, 10)$, we found $\omega_0 = -3.048961$ and

$$\mathcal{E}_{1,v} = 1.04207, \mathcal{E}_{2,v} = 2.357 \text{ and } \mathcal{E}_{1,s} = 1.7516.$$

	without GI	with GI	without GI	with GI
p^{max}	2	2	3	3
D	29	[2 6 9 8 4]	40	[2 3 7 11 10 4 2]
steps	9645	278	12417	561
time	3 h 30 min	2 min	6 h 27min	5 min
$\langle G^2 \rangle$	3×10^{-9}	0	3×10^{-9}	0
ω_0	-3.048961	-3.048961	-3.048961	-3.048961
$\mathcal{E}_{1,v}$	1.04252{10}	1.04254	1.04194 {14}	1.04209
$\mathcal{E}_{2,v}$	2.455 {37}	2.455	2.385 {59}	2.386
$\mathcal{E}_{1,s}$	1.7719{20}	1.7719	1.7559 {31}	1.7565

Table 2.2.: Results of computations with and without imposing gauge invariance (GI). ($x = 100, m/g = 0.25$)

One immediately observes that the number of required steps is much larger in the gauge variant case. Furthermore, as the local dimension of the Hilbert space is larger, one TDVP iteration also takes more time in the gauge variant case. This leads to a huge difference in the total time: the gauge invariant simulations converged in a few minutes while the gauge variant simulations took a few hours. We can also explicitly verify Elitzur's theorem, by looking at the variance $\langle G^2 \rangle = \langle G(n)^2 \rangle, \forall n$, of the gauge transformation generators for our ground state approximations on the full Hilbert space. As $\langle G^2 \rangle \approx 0$ we indeed converge to the gauge invariant ground state, which is also confirmed by the agreement of the ground state energy per site ω_0 with the gauge invariant simulations.

We have also examined the low-energy states which are computed with the same MPS ansatz as in eq. (2.3), but now again with and without imposing gauge invariance. For the gauge invariant case, we found in the previous subsection three stable one-particle excitations: two with $\mathcal{CT} = -1$ and mass $\mathcal{E}_{1,v}, \mathcal{E}_{2,v}$ and one with $\mathcal{CT} = 1$ and mass $\mathcal{E}_{1,s}$. As expected, on the full Hilbert space we find many more non-physical excitations with $\langle G^2 \rangle \neq 0$. As illustrated in figure 2.4a we can identify the physical states by calculating $\langle G^2 \rangle$. The ranking (in increasing energy) where the physical excitations appear in the list of all excitations per sector ($\mathcal{CT} = \pm 1$) is indicated in table 2.2 with curly brackets $\{\dots\}$. There are indeed many gauge variant states lying between the ground state and low lying gauge invariant states. Moreover, the number of obtained gauge variant states increases with the bond dimension and we suspect that the Hamiltonian eq. (2.1) is gapless on the full Hilbert space.

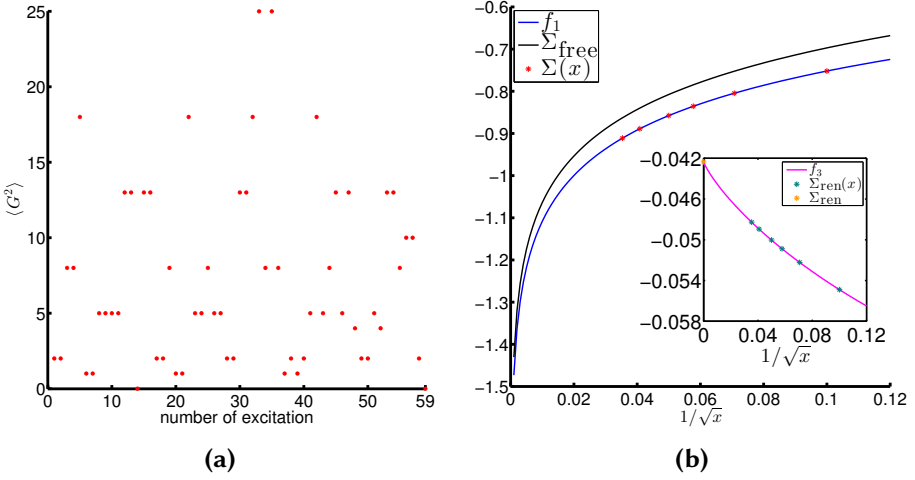


Figure 2.4.: (a): $m/g = 0.25$, $x = 100$, $D = 40$: one-particle excitations with $\mathcal{CT} = -1$, ranked according to increasing energy. Only those with $\langle G^2 \rangle = 0$ are gauge invariant. In this case, only the 14th and 59th excitations are physical and correspond to $\mathcal{E}_{1,v}$ and $\mathcal{E}_{2,v}$. (b): $m/g = 0.5$, $g = 1$. Optimal fit $f_1(x)$, eq. (2.5a), through the data points $\Sigma(x)$ for the five largest x . The divergence is removed by subtracting Σ_{free} . Inset: Optimal fit of $f_3(x)$, eq. (2.5c), through the data points $\Sigma_{ren}(x)$. The continuum value Σ_{ren} is the intersection with the y -axis.

2.1.4. Chiral condensate

For $m/g \neq 0$ the chiral condensate $\Sigma = \langle \bar{\psi}\psi \rangle$ is UV divergent ($x \rightarrow \infty$), and it has been argued that also at the non-perturbative level, this divergence originates solely from the free ($g = 0$) theory, leading to a logarithmic divergence, which is linear in m [23]. We now calculate the value of the chiral condensate with our MPS simulations and show that the scaling for large x does indeed show the predicted UV behavior. This problem was also studied in [34] with MPS-simulations for finite volumes. This allows us to compare results for the UV regulated chiral condensate.

On the lattice $\Sigma = \langle \bar{\psi}\psi \rangle$ reduces to

$$\frac{\Sigma(x)}{g} = \frac{\sqrt{x}}{2N} \sum_{n=1}^{2N} (-1)^n \left\langle \frac{\sigma_z(n) + 1}{2} \right\rangle,$$

which is easily computed from our MPS approximation eq. (2.2) for the ground state, see section 4.1 in part II. For the Hamiltonian eq. (2.1) the free chiral condensate $\Sigma_{free}(x)$, i.e. the chiral condensate for $g = 0$, can be

computed exactly [34]:

$$\frac{\Sigma_{free}(x)}{g} = -\frac{m}{\pi g} \frac{1}{\sqrt{1 + \frac{m^2}{g^2 x}}} K\left(\frac{1}{1 + \frac{m^2}{g^2 x}}\right) \quad (2.4)$$

where $K(z)$ is the complete elliptic integral of the first kind. As $x \rightarrow \infty$, we indeed have up to finite terms $\Sigma_{free}(x)/g \rightarrow -m/(2g\pi) \log(x)$. We now verify that this is the only UV divergence for all values of m/g . Thereto we compute $\Sigma(x)/g$ for $x = 100, 200, 300, 400, 600, 800$. We find that

$$f_1(x) = A_1 + B_1 \frac{\log(x)}{\sqrt{x}} + \left(-\frac{m}{2g\pi} - C_1\right) \log(x) + D_1 \frac{1}{\sqrt{x}} \quad (2.5a)$$

results in a good fit to the data $\Sigma(x)$, see figure 2.4b. Our estimate of C_1 is obtained by *i*) fitting $\Sigma(x)/g$ to $f_1(x)$ for the five largest x , *ii*) fitting all the data to $f_1(x)$, *iii*) fitting all the data to

$$f_2(x) = A_2 + B_2 \frac{\log(x)}{\sqrt{x}} + \left(-\frac{m}{2g\pi} - C_1\right) \log(x) + D_2 \frac{1}{\sqrt{x}} + E_2 \frac{1}{x}. \quad (2.5b)$$

The displayed value of C_1 in the second column of table 2.3 is the one with the largest magnitude of the fits *i*), *ii*) and *iii*). We observe that $C_1 \approx 0$, consistent with the claim [23] that the full non-perturbative UV divergence can indeed be traced back completely to the free chiral condensate eq. (2.4).

To compare our results with [34], we renormalize the chiral condensate by subtracting $\Sigma_{free}(x)$ from $\Sigma(x)$. As in [34] we fit

$$f_3(x) = A_3 + B_3 \frac{\log(x)}{\sqrt{x}} + C_3 \frac{1}{\sqrt{x}} + D_3 \frac{1}{x} \quad (2.5c)$$

to the renormalized chiral condensate $\Sigma_{ren}(x)/g = \Sigma(x)/g - \Sigma_{free}(x)/g$. Our estimate for Σ_{ren}/g is the A_3 obtained by a fit through the largest five x -values (see fig. 2.4b, inset). The error on this value is estimated as the maximum of the difference with the A_3 's we would obtain if we fitted all data to $f_3(x)$ and to

$$f_4(x) = A_3 + B_4 \frac{\log(x)}{\sqrt{x}} + C_4 \frac{1}{\sqrt{x}} + D_4 \frac{1}{x} + E_4 \frac{1}{x^{3/2}}. \quad (2.5d)$$

This error dominates the error due to the truncation of the bond dimension. The results can be found in the third column of table 2.3. We see that our results agree very well with [34] and with the exact strong coupling ($m/g = 0$) result: $\Sigma_0/g = -e^\gamma/(2\pi^{3/2}) \approx -0.1599288$.

m/g	C_1	Σ_{ren}/g	$\Sigma_{ren}/g[34]$	exact
0	3×10^{-6}	-0.159928 (1)	-0.159930 (8)	-0.1599288
0.125	3×10^{-5}	-0.092019 (2)	-0.092019 (4)	-
0.25	4×10^{-5}	-0.066647 (4)	-0.066660 (11)	-
0.5	1×10^{-4}	-0.042349 (2)	-0.042383 (22)	-
0.75	2×10^{-4}	-0.03062 (3)	-	-
1	3×10^{-4}	-0.023851 (8)	-	-
2	1×10^{-3}	-0.012463 (9)	-	-

Table 2.3.: Results for chiral condensate.

2.1.5. Entropy

We also computed the half chain (Von Neumann) entropy S_0 , eq. (1.10), for different values of m/g . Because the Schmidt spectrum $\{\sigma_{\alpha_q}^g\}$ is site independent, the half chain entropy will not depend on the position of the cut. As such the entropy is a UV divergent quantity, but one expects the divergence to come from the fermion kinetic term in the Hamiltonian eq. (2.1). Specifically, the general results of Cardy and Calbrese [90] predict for two fermionic degrees of freedom a UV divergence (with correlation length ξ in physical units)

$$S_0(x) \sim \frac{1}{6} \log\left(\frac{\xi}{a}\right) = -\frac{1}{6} \log(1/\sqrt{x}) + (\text{finite terms as } x \rightarrow +\infty)$$

where we denote with $S_0(x)$ the half chain entropy at lattice spacing $ga = 1/\sqrt{x}$.

This is precisely what we find in our simulations. When looking at $S_0(x) + \frac{1}{6} \log(1/\sqrt{x})$ as a function of $1/\sqrt{x}$, we observe that it behaves linear, see inset figs. 2.5a and 2.5b. Therefore, we should be able to fit $S_0(x)$ to a function of the form

$$f_1(x) = A_0 + B_0 \log\left(\frac{1}{\sqrt{x}}\right) + C_0 \frac{1}{\sqrt{x}} \quad (2.6)$$

and find $B_0 = 1/6$. Specifically, we fitted our data corresponding to the largest five x -values, $x = 200, 300, 400, 600, 800$, against f_1 to obtain a first estimate for B_0 . To have some robustness against the choice of fitting interval and the fitting function, we also included our result for $x = 100$ and fitted all our data against f_1 and against

$$f_2(x) = A_0 + B_0 \log\left(\frac{1}{\sqrt{x}}\right) + C_0 \frac{1}{\sqrt{x}} + D_0 \frac{1}{x}. \quad (2.7)$$

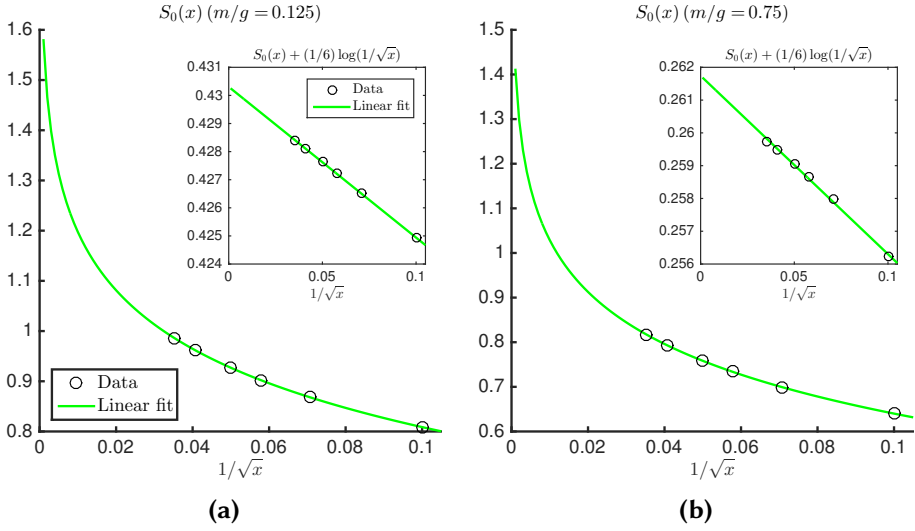


Figure 2.5.: Fit of the form $(-1/6) \log(1/\sqrt{x}) + A + B/\sqrt{x}$ through $S_0(x)$. Inset: linear extrapolation of $S_0(x) + (1/6) \log(1/\sqrt{x})$ based on the largest five x -values, $x = 200, 300, 400, 600, 800$, to obtain the coefficients A and B . (a) $m/g = 0.125$. (b): $m/g = 0.75$.

m/g	0.125	0.25	0.3	0.35	0.5	0.75	1
$(B_0 + 1/6) \times 10^3$	0.1	0.3	0.5	0.5	0.8	1.3	2

Table 2.4.: The largest value in magnitude of $B_0 + 1/6$ multiplied by 10^3 obtained from the fit eq. (2.6) through the largest five x -values and the fits eqs. (2.6) and (2.7) through all our data. According to [90] we should have $B_0 + 1/6 = 0$.

This gave us two other estimates for B_0 . In table 2.4 we give the results for $B_0 + 1/6$. The value that is shown is the largest value for $B_0 + 1/6$ (in magnitude) from the three fits, i.e. the largest error on the predicted result of [90]. As one observes these errors are at most 2×10^{-3} and for small values of m/g only of order 10^{-4} which is a nice cross-check on our results. In the insets of figs. 2.5a and 2.5b we show a linear fit of the form $f(x) = A + B \frac{1}{\sqrt{x}}$ through $S_0(x) + (1/6) \log(x)$. Here we estimated A and B by taking into account the largest five x -values. In the main figures we also show the fit $(-1/6) \log(x) + f(x)$ through $S_0(x)$.

2.2. $\alpha \neq 0$

2.2.1. Setup

Let us now turn on an electric background field, $\alpha(n) = \alpha \neq 0$. The Kogut-Susskind Hamiltonian eq. (1.5) then becomes

$$\mathcal{H} = \frac{g}{2\sqrt{x}} \left(\sum_{n=1}^{2N} [L(n) + \alpha]^2 + \frac{\sqrt{x}}{g} m \sum_{n=1}^{2N} (-1)^n (\sigma_z(n) + (-1)^n) \right. \\ \left. + x \sum_{n=1}^{2N-1} (\sigma^+(n) e^{i\theta(n)} \sigma^-(n+1) + h.c.) \right). \quad (2.8)$$

The \mathcal{CT} symmetry is broken for $\alpha \neq 1/2$. For $\alpha = 1/2$ the Hamiltonian exhibits again the \mathcal{CT} symmetry but now with $\mathcal{C}|s_n, p_n\rangle = |-s_n, -1 - p_n\rangle$ ($\mathcal{C}L(n)\mathcal{C} = -1 - L(n)$). Note however that contrary to the case $\alpha = 0$ this \mathcal{CT} symmetry is spontaneously broken for $m/g \gtrsim (m/g)_c \approx 0.33$ [6, 27]. At $m/g = (m/g)_c$ there is a phase transition which lies in the same universality class as the 2D classical, or equivalently the 1D quantum, transverse Ising model.

To obtain a ground state approximation in the thermodynamic limit ($N \rightarrow \infty$) we only need to anticipate \mathcal{T}^2 invariance. Therefore it is convenient to block the effective sites $2n - 1$ and $2n$ in one effective site n . Denoting

$$\zeta_n = (\kappa_{2n-1}, \kappa_{2n}) = (s_{2n-1}, p_{2n-1}, s_{2n}, p_{2n}) \\ \in \{-1, 1\} \times \mathbb{Z}[p_{2n-1}^{\min}, p_{2n-1}^{\max}] \times \{-1, 1\} \times \mathbb{Z}[p_{2n-1}^{\min}, p_{2n-1}^{\max}], \\ |\zeta\rangle = |\zeta_1\rangle \dots |\zeta_N\rangle$$

a MPS ansatz invariant under \mathcal{T}^2 is, see section 1.2 of part II,

$$|\Psi_u[A]\rangle = \sum_{\zeta} v_L^\dagger \left(\prod_{n=1}^N A^{\zeta_n} \right) v_R |\zeta\rangle \quad (N \rightarrow +\infty), \quad (2.9a)$$

where $v_L, v_R \in \mathbb{C}^D$, and $A^\zeta \in \mathbb{C}^{D \times D}$. Gauge invariance,

$$G(n) |\Psi_u[A]\rangle = 0 \text{ with } G(n) = L(n) - L(n-1) + \frac{\sigma_z(n) + (-1)^2}{2},$$

is imposed if A takes the form

$$[A^{s_1, p_1, s_2, p_2}]_{(q, \alpha_q); (r, \beta_r)} = [a^{q, s_1, s_2}]_{\alpha_q, \beta_r} \delta_{p_1, q+(s_1-1)/2} \delta_{p_2, q+(s_1+s_2)/2} \delta_{r, p_2}. \quad (2.9b)$$

We refer to subsection 3.3.1 of part II for an explicit derivation of this MPS starting from the most general gauge invariant MPS eq. (1.8). The Schmidt decomposition eq. (1.9) with respect to the bipartition of the lattice consisting of the two regions $\mathcal{A}_1^{2n} = \mathbb{Z}[1, \dots, 2n]$ and $\mathcal{A}_2^{2n} = \mathbb{Z}[2n + 1, \dots, 2N]$ now reads

$$|\Psi_u[A]\rangle = \sum_{q=p_{2n+1}^{min}}^{p_{2n+1}^{max}} \sum_{\alpha_q=1}^{D_{2n+1}^q} \sqrt{\sigma_{\alpha_q}^q} |\psi_{q,\alpha_q}^{\mathcal{A}_1^{2n}}\rangle |\psi_{q,\alpha_q}^{\mathcal{A}_2^{2n}}\rangle \quad (2.10)$$

where the Schmidt values now only depend on the parity of n : $\sigma_{\alpha}^q \equiv \sigma_{2n,\alpha_q}^q$. The computation of the Schmidt values $\sigma_{\alpha_q}^q$ is discussed in subsection 4.2.2 of part II.

In subsection 4.2.4 of part II one can find the details of the TDVP to obtain the optimal approximation for the ground state within the class of states eq. (2.9) with a fixed bond dimension D^q . As can be observed from eq. (2.10), truncating to a finite bond dimension corresponds to an effective truncation in the Schmidt decomposition of the ground state. Similar as for $\alpha = 0$, see the previous section, one would want a distribution of D^q -values such that the smallest retained Schmidt value is more or less equal for each eigenvalue sector of $L(2n)$. Then if we want a reliable MPS approximation for the ground state, these smallest retained Schmidt values should be sufficiently small, which corresponds to taking D^q sufficiently large. Similar to the case $\alpha = 0$ we did several simulations and adapted D^q until the smallest Schmidt value in each eigenvalue sector of $L(2n)$ was of order 10^{-17} , i.e. $\min_{\alpha_q} \sigma_{q,\alpha_q} \approx 10^{-17}$.

In figs. 2.6a and 2.6b we plot the distribution of the Schmidt values among the eigenvalue sectors of $L(2n)$ for the final MPS ground state approximations for $m/g = 0.75$, $x = 400$ and $\alpha = 0.2, 0.45$. As in subsection 2.1 we observe that the sectors corresponding to $q = 0, -1, 1$ are the most dominant ones which justifies our choice of taking $D^q = 0$ for $|q| > 3$. As for $\alpha = 0$ this can be understood from the term proportional to $[L(n) + \alpha]^2$ in eq. (2.8) which punishes large eigenvalues of $L(n)$. We also display the bond dimensions for each sector and for each simulated value of x in figs. 2.6c and 2.6d. One can observe that as x increases we need larger D^q for the same accuracy which is a consequence of the diverging correlation length as we approach the continuum limit ($x \rightarrow +\infty$). For the same reason we also need larger D^q when we are getting closer to the phase transition at $m/g = (m/g)_c \approx 0.33$ and $\alpha = 1/2$.

The properties of the ground state will be discussed in the next chapter in the context of confinement of static charges. Here we restrict ourselves to

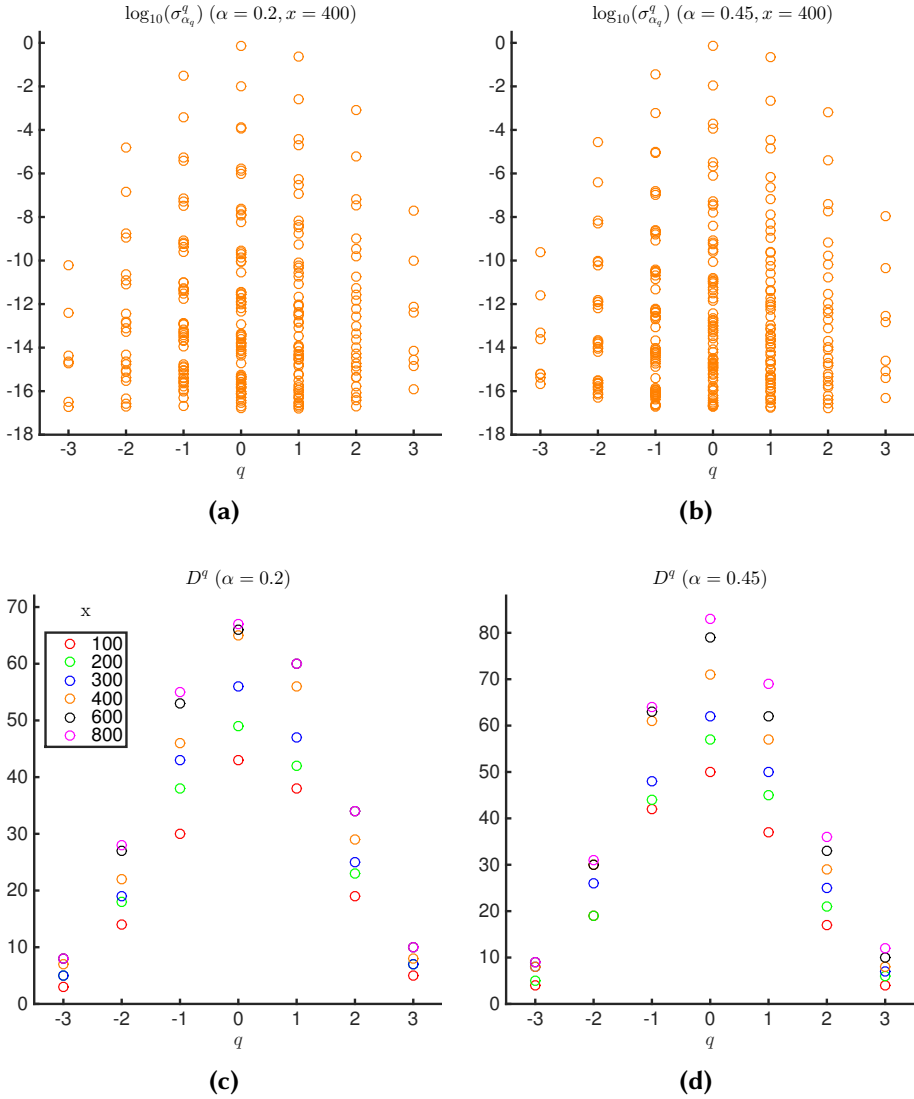


Figure 2.6: $m/g = 0.75$. (a): $\alpha = 0.2$, $x = 400$. Distribution of the 10–base logarithm of the Schmidt values $\sigma_{\alpha_q}^q$ among the eigenvalue sectors q of $L(2n)$. (b): Same as (a) but now for $\alpha = 0.45$. (c): $\alpha = 0.2$. Distribution of the bond dimension among the eigenvalue sectors of $L(2n)$ for different values of x . (d): Same as (c) but now for $\alpha = 0.45$.

the excitations. For the elementary excitations with momentum k we take the ansatz [88]:

$$|\Phi_k[B, A]\rangle = \sum_{m=1}^{N-M+1} e^{2ikn/\sqrt{x}} \sum_{\{\kappa_n\}} v_L^\dagger \left(\prod_{n=1}^m A^{\zeta_m} \right) B^{\zeta_{m+1}, \dots, \zeta_{m+M}} \left(\prod_{n=m+M+1}^N A^{\zeta_m} \right) v_R |\zeta\rangle, \quad (2.11a)$$

where A^ζ corresponds to the ground state eq. (2.9) and gauge invariance is imposed by

$$[B^{\zeta_1, \dots, \zeta_M}]_{(q, \alpha_q); (r, \beta_r)} = \left(\prod_{n=2}^{2M} \delta_{p_n, p_{n-1} + (s + (-1)^n)/2} \right) \delta_{p_1, q + (s_1 - 1)/2} \delta_{p_{2M}, r} [b_k^{q, s_1, \dots, s_{2M}}]_{\alpha_q, \beta_r}. \quad (2.11b)$$

where $\zeta_n = (s_{2n-1}, p_{2n-1}, s_{2n}, p_{2n})$ and $b_k^{q, s_1, \dots, s_{2M}} \in \mathbb{C}^{D^q \times D^r}$. The algorithm to find the optimal approximation $|\Phi_k[B, A]\rangle$ for the excited states is discussed in subsection 4.2.5 of part II for $M = 1$. The implementation for $M \geq 2$ is similar but a little bit more tedious. We refer to [88] for the details. For sufficiently large bond dimension this ansatz should converge exponentially fast as M increases to an elementary particle with momentum k [91]. The speed of convergence depends on how far this excitation is separated from the other excitations in the same momentum sector (in units of the Lieb-Robinson velocity). For $\alpha = 0$ we saw that $M = 1$ was already sufficient. Note that the computation time scales as $\mathcal{O}(4^M \max_p D_p^3)$ allowing only simulations for small M .

2.2.2. Spectrum for $\alpha \neq 0$

For a fixed value of x we approximate the excited states using the ansatz eq. (2.11) for $M = 2$. By comparing these energies with simulations for other values of the bond dimension D^q and for $M = 1$ we obtain an error for truncating the bond dimension and truncating M . Now we compute the excitation energies for $x = 25, 50, 60, 75, 90, 100$. Continuum estimates for the excitation energies are obtained similar as for $\alpha = 0$. Because the values of $ga = 1/\sqrt{x}$ are now larger than for $\alpha = 0$, i.e. we are farther away from the continuum, only the linear fits and quadratic fits in $1/\sqrt{x}$ are reliable. To have some robustness against the choice of fitting method and fitting interval we perform several fits: we fit the points corresponding to the largest four, five and six x -values against a quadratic function in $1/\sqrt{x}$

and we perform linear fits in $1/\sqrt{x}$ through the points corresponding to the largest three, four, five and six x -values, see fig. 2.7a. We take the mean of all these energies as our final estimate. The standard deviation of this mean serves as an error on this value and were of order 10^{-3} or smaller. This error dominates the error of taking a finite bond dimension D^q and taking $M \leq 2$.

Physics is periodic in α with period 1 and the excitations for $\alpha \in [1/2, 1]$ can be obtained from the excitations for $\alpha \in [0, 1/2]$ by a \mathcal{CT} transformation. Therefore we can restrict our computations to $\alpha \in [0, 1/2]$. Also, as the Schwinger model is a relativistic theory, the energy $\mathcal{E}(k)$ of a particle with momentum k can be obtained from the energy $\mathcal{E} = \mathcal{E}(0)$ of this excitation with momentum zero by the Einstein dispersion relation $\mathcal{E}^2(k) = \sqrt{k^2 + \mathcal{E}^2}$. Hence we only need to compute the excitations with momentum zero. In fig 2.7b we compare our numerical results for the energy \mathcal{E}_1 of the first excited state with mass perturbation theory [21]:

$$\mathcal{E}_1^2 = \mu_0^2 \left(1 + 3.5621 \frac{m}{\mu_0} \cos(2\pi\alpha) + 5.4807 \left(\frac{m}{\mu_0} \right)^2 - 2.0933 \left(\frac{m}{\mu_0} \right)^2 \cos(4\pi\alpha) \right) + \mathcal{O} \left(\left[\frac{m}{\mu_0} \right]^3 \right). \quad (2.12)$$

where $\mu_0 = \frac{g}{\sqrt{\pi}}$. The plot shows that our numerical results converge towards eq. (2.12) when $m/g \rightarrow 0$.

For $\alpha = 0$, we found in subsection 2.1.2 two elementary excitations with $\mathcal{CT} = -1$ and energy $\mathcal{E}_1 = \mathcal{E}_{1,v}$ and $\mathcal{E}_3 = \mathcal{E}_{2,v}$ and one elementary excitation with $\mathcal{CT} = 1$ and energy $\mathcal{E}_2 = \mathcal{E}_{1,s}$, see table 2.1. For these energies we had $\mathcal{E}_1 < \mathcal{E}_2 + \mathcal{E}_3$ and for $m/g = 0.125, 0.25$ and $m/g = 0.3$ we had $\mathcal{E}_3 > 2\mathcal{E}_1$ while for $m/g \gtrsim 0.5$ we had $\mathcal{E}_3 \leq 2\mathcal{E}_1$. This means that the decay of \mathcal{E}_3 into two elementary particles is only prevented by the \mathcal{CT} symmetry for $m/g = 0.125, 0.25, 0.3$. When $0 < \alpha < 1/2$ the \mathcal{CT} symmetry is broken and this decay is no longer forbidden. This is indeed what we observe in the one-particle spectrum: for $\alpha > 0$ only the excitations with energy \mathcal{E}_1 resp. \mathcal{E}_2 corresponding to $\mathcal{E}_{1,v}$ and $\mathcal{E}_{1,s}$ for $\alpha \rightarrow 0$ remain stable, see fig. 2.8(a)-(c). Furthermore, we observe that the binding energy $\mathcal{E}_{bind} = 2\mathcal{E}_1 - \mathcal{E}_2$ decreases as α tends towards $1/2$. When the binding energy becomes small, the convergence rate of the ansatz eq. (2.11) as a function of M to the excited state with energy \mathcal{E}_2 is rather slow.

For $m/g = 0.125$, see fig. 2.8a, the second particle is stable until $\alpha \lesssim 0.35$. For $\alpha = 0.38$ our estimates are $\mathcal{E}_1 = 0.4784(5)$ and $\mathcal{E}_2 = 0.965(2)$, indicating that the second excited state is unstable, $\mathcal{E}_2 > 2\mathcal{E}_1$. When $\alpha > 0.38$ we have $\mathcal{E}_2(x) > 2\mathcal{E}_1(x)$ for all the x -values we used. We conclude that

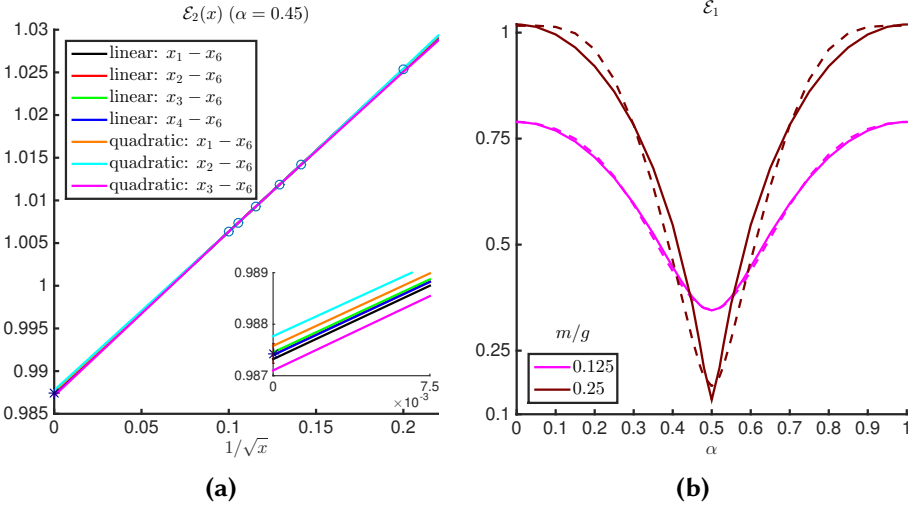


Figure 2.7.: (a): $m/g = 0.25$, $\alpha = 0.45$. Extrapolation of the energy \mathcal{E}_2 of the second excited state to $x = \infty$. We perform several linear and quadratic fits in $1/\sqrt{x}$ through the points with $x = (x_1, \dots, x_6) = (25, 50, 60, 75, 90, 100)$ (see legend). Inset: our continuum estimate is the mean of all the fits. The error is the standard deviation. (b): Comparison of \mathcal{E}_1 obtained by our numerical simulations (full line) with mass perturbation theory (dashed line).

there are two stable particles for $\alpha \lesssim 0.35$ and only one stable particle for $\alpha \gtrsim 0.38$. This agrees qualitatively with mass perturbation theory, $m/g \ll 1$, where there are two stable particles for $\alpha \leq 1/4$ and one stable particle for $1/4 < \alpha \leq 1/2$ [6].

For $m/g = 0.25$, see fig. 2.8b, our estimates for the energy \mathcal{E}_2 were unstable against variation of the bond dimension D and M for $\alpha \geq 0.47$. The errors on \mathcal{E}_2 are too large and prevent an extrapolation towards $x = \infty$. Nevertheless, in our simulations we have $\mathcal{E}_2(x) < 2\mathcal{E}_1(x)$ for $x = (25, 50, 60, 75, 90, 100)$ and the fact that $\mathcal{E}_2(x)$ decreases as the bond dimension and M increase might suggest that this particle is still stable but with very small binding energy. For $\alpha = 1/2$ the ground state is \mathcal{CT} invariant for $m/g \leq (m/g)_c \approx 0.33$ allowing us to classify the excitations according to their \mathcal{CT} number using an ansatz similar to eq. (2.3), see section 4.1 of part II for the details. We computed the excitation energies with and without classifying the states according to their \mathcal{CT} -number for $(m/g, \alpha) = (0.25, 1/2)$. In both cases, we found only one elementary particle. In the vector sector ($\mathcal{CT} = -1$) all other states had energies that were larger than $3\mathcal{E}_1$ and in the scalar sector ($\mathcal{CT} = 1$) the energies were larger than $2\mathcal{E}_1$. This corresponds to a theory with one stable particle. Therefore we estimate the value of the

electric background field where the second elementary particle disappears to be larger than 0.47 but smaller than 0.5 for $m/g = 0.25$. A similar picture is found for $m/g = 0.3$ as can be seen in fig. 2.8c. Here we estimate that the second elementary particle disappears between $\alpha = 0.48$ and $\alpha = 0.5$.

One also observes that the mass gap decreases as $(m/g, \alpha) \rightarrow ((m/g)_c, 1/2)$. This is a consequence of the fact that we are approaching a phase transition for these parameters and hence that the model becomes gapless. Because of that, the simulation for $(m/g, \alpha) = (0.3, 0.5)$ was extremely hard. Not only did we need a large bond dimension but the small mass gap also implied that the TDVP algorithm took long until it converged to the optimal approximation for the ground state.

For $m/g = 0.5$, we have for all values of α that $\mathcal{E}_3 < 2\mathcal{E}_1$ and thus at least three stable particles, see fig. 2.8d. When $\alpha \rightarrow 1/2$ we observe that the difference between the energies \mathcal{E}_1 , \mathcal{E}_2 and \mathcal{E}_3 becomes smaller. This requires in turn more variational parameters in our ansatz, i.e. larger values of D^q and M in eq. (2.11). For $\alpha \geq 0.4$ we could not perform a reliable continuum extrapolation anymore of \mathcal{E}_2 and \mathcal{E}_3 . We took as the continuum estimate their $x = 100$ values which we expect to be within 10% of its continuum value. Anyway, we found that \mathcal{E}_1 , \mathcal{E}_2 and \mathcal{E}_3 were stable for all values of x . Furthermore, for $\alpha \geq 0.45$ we found even another particle that seems to be stable. However, because its energy was very close to $2\mathcal{E}_1$ the errors on this energy using the ansatz eq. (2.11) for fixed values of x were too large to extrapolate its value to the continuum.

Our results thus show that the spectrum of $m/g = 0.5$ is clearly different than that for $m/g \leq (m/g)_c$. When $\alpha \rightarrow 1/2$ the number of stable particles seems rather to increase than to decrease for $m/g = 0.5$. This agrees with studies in the weak coupling limit $m/g \gg 1$ [6] where they found that for large values of m/g the number of stable particles is proportional with $1/(1/2 - \alpha)$. For $\alpha = 1/2$, due to spontaneous symmetry breaking of the \mathcal{CT} symmetry, there are two vacua and kinks which connect these two vacua [27]. The excitations with energy $\mathcal{E}_1, \mathcal{E}_2, \mathcal{E}_3$ are in this case larger than twice the energy of the kinks and hence they do not correspond to stable particles for $\alpha = 1/2$. Figure 2.8d should for $\alpha = 1/2$ thus only be interpreted in the limit $\alpha \xrightarrow{\neq} 0$.

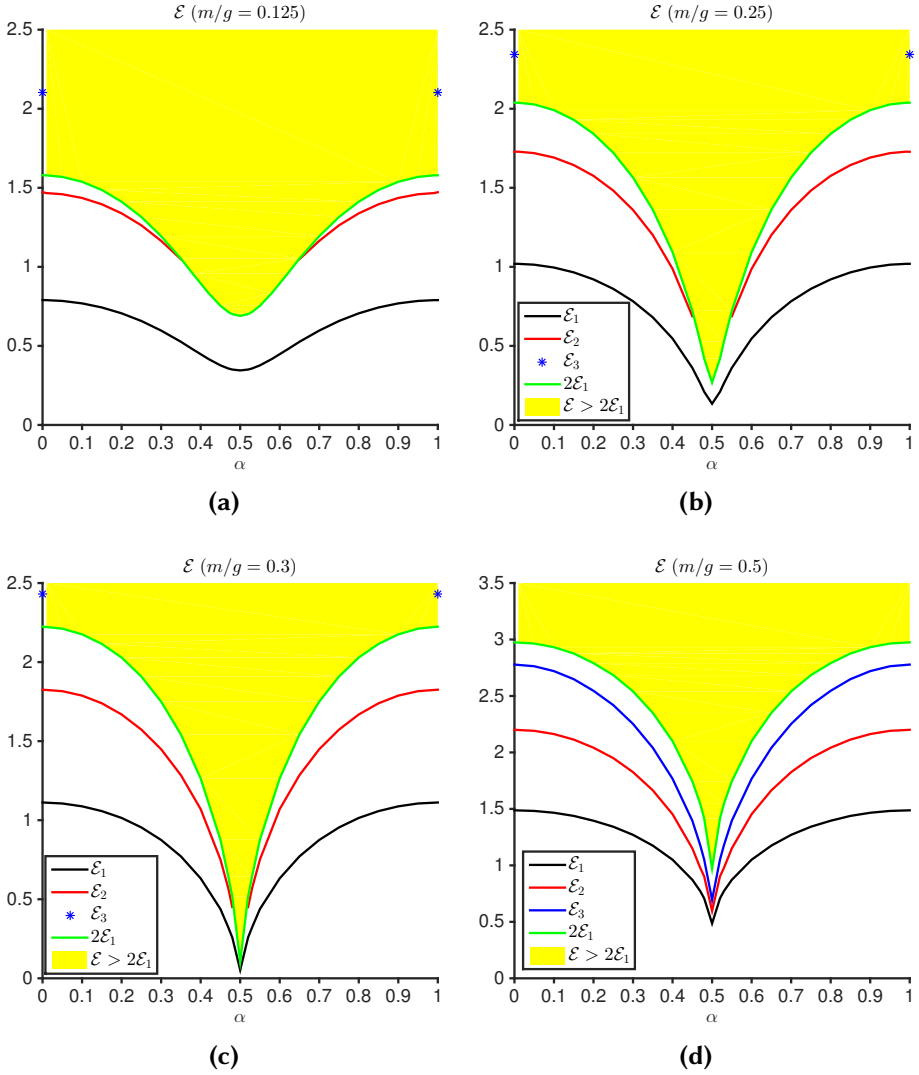


Figure 2.8.: Energy of the elementary particles \mathcal{E}_1 , \mathcal{E}_2 and \mathcal{E}_3 as a function of α . (a): $m/g = 0.125$. Only \mathcal{E}_1 and \mathcal{E}_2 are stable. For $\alpha \gtrsim 0.38$ only \mathcal{E}_1 is stable. (b): $m/g = 0.25$. Only \mathcal{E}_1 and \mathcal{E}_2 correspond to elementary particles for $\alpha \neq 0$. \mathcal{E}_2 is unstable for $\alpha \gtrsim 0.47$. (c): $m/g = 0.3$. Similar as (b) but now \mathcal{E}_2 disappears in the continuum for $\alpha \gtrsim 0.48$. (d): $m/g = 0.5$. For $\alpha < 0.5$ we find at least three elementary particles.

Confinement and string breaking

B. Buyens, J. Haegeman, H. Verschelde, F. Verstraete, K. Van Acoleyen
'Confinement and string breaking for QED₂ in the Hamiltonian picture'
arXiv:1509.00246v2 (2015)

3.1. Introduction

The confinement of color charge in quantum chromodynamics (QCD) is one of the beautiful key mechanisms of the Standard Model. Focussing on the static aspect of confinement, one can probe the theory with a heavy quark antiquark ($q\bar{q}$) pair and examine how the modified ground state evolves as a function of the interquark distance [92]. For small distances a color electric flux tube forms between the pair, resulting in a static potential (i.e. the surplus energy of the modified ground state) that grows linearly with the distance. This flux tube can therefore be conveniently modeled by an interquark string with a certain string tension. One can then describe a heavy quarkonium state as a $q\bar{q}$ pair that is kept together by this confining string. However, there exists a critical distance at which the string breaks. Beyond this distance the flux tube disappears and the potential flattens out to a constant. At this point it has become energetically favorable to excite light particles out of the vacuum that completely screen both the probe quark and antiquark, leading to two isolated color singlets. In a dynamical setting these would then be the two freely propagating jets of hadrons that emerge as final product of some particle collision.

This phenomenological picture is corroborated both by experiment and theoretical work. At the computational level, the static potential has been studied extensively over the years with lattice QCD. And one has indeed obtained

the linearly rising confining interquark potential, both in the quenched case [93–102] that excludes dynamical light quark degrees of freedom and in the unquenched case [103–105] that includes these degrees of freedom. In the latter case, where the dynamical quarks can screen the heavy probe charges, also the phenomenon of string breaking has been observed [106] as an asymptotic flattening of the calculated potential. Nevertheless our understanding of confinement is still not complete: the Euclidean space-time lattice Monte Carlo simulations can not access the real-time aspects of the dynamical string formation and string breaking. Furthermore, even in the static case, it is not settled yet [107–109] if one can fully describe the confinement mechanism - specifically the non-perturbative string formation - in terms of (semi-)local degrees of freedom such as for instance vortices and magnetic monopoles [110].

In this chapter we study how confinement and string breaking show up in the Hamiltonian set-up in the Schwinger model [1]. An important difference with QCD is that the Schwinger model already exhibits confinement at the perturbative level, as the Coulomb potential is linear in 1+1 dimensions. We make extensive use of both the strong and weak coupling results in the analysis of our numerical results. Our simulations of the lattice Hamiltonian are performed close to the continuum limit, indeed allowing for a quantitative check against these analytic continuum results in the appropriate regimes.

Specifically we simulate the modified vacuum structure in the presence of two probe charges and this for different distances and values of the charges. As we will show, already in this static case the Hamiltonian simulations give a complementary view on the confining properties of the theory. At the practical level, the direct access to the quantum state allows for a relatively easy calculation of all local observables. In this way we could not only extract the static interquark potential, but also for instance determine the detailed spatial profile of the electric string or the precise charge distribution of the light fermions around the probe charges. We also find that subtraction of the vacuum entropy results in a UV finite entanglement (Von Neumann) entropy and that both the string formation and string breaking leave characteristic imprints on this renormalized entropy.

3.2. Lattice formulation and Hamiltonian

We now consider the lattice with sites

$$\{-N_L, -N_L + 1, \dots, 1, \dots, M, \dots, M + N_R\}$$

(the meaning of N_L , M and N_R will become clear later) where the thermodynamic limit is obtained by taking the limits

$$N_L \rightarrow +\infty, N_R \rightarrow +\infty$$

while keeping M fixed. We start from the ground state $|\psi_0\rangle$ of the Hamiltonian eq. (2.1) in a zero background field ($\alpha = 0$):

$$\mathcal{H}_0 = \frac{g}{2\sqrt{x}} \left(\sum_{n=-N_L}^{M+N_R} L(n)^2 + \frac{\sqrt{x}}{g} m \sum_{n=-N_L}^{M+N_R} (-1)^n (\sigma_z(n) + (-1)^n) + x \sum_{n=-N_L}^{M+N_R-1} (\sigma^+(n)e^{i\theta(n)}\sigma^-(n+1) + h.c.) \right).$$

Then we consider an infinitely heavy quark-antiquark pair in this vacuum. The quark with charge $-gQ$ is put at site m_L and the antiquark with opposite charge gQ is put at site m_R with

$$-N_L \ll 1 \leq m_L \leq m_R \leq M \ll M + N_R.$$

As discussed in section 1.3, see in particular eqs. (1.4) and (1.5), these probe charges can be absorbed in the electric background field $\alpha(n) = -Q\Theta(m_L \leq n < m_R)$ and we thus arrive at the Hamiltonian

$$\mathcal{H} = \frac{g}{2\sqrt{x}} \left(\sum_{n=-N_L}^{M+N_R} [L(n) + \alpha(n)]^2 + \frac{\sqrt{x}}{g} m \sum_{n=-N_L}^{M+N_R} (-1)^n \sigma_z(n) + x \sum_{n=-N_L}^{M+N_R-1} (\sigma^+(n)e^{i\theta(n)}\sigma^-(n+1) + h.c.) \right), \quad (3.1)$$

where gauge invariance is imposed by the condition

$$G(n) = L(n) - L(n-1) - \frac{\sigma_z(n) + (-1)^n}{2} = 0. \quad (3.2)$$

In the following sections we will obtain ground state approximations of this Hamiltonian, for different values of m/g , different values of the probe charge Q and different distances $Lg = (m_R - m_L)/\sqrt{x}$ (in physical units $g = 1$) of the charge-pair, all this for different lattice-spacings $1/\sqrt{x}$, focussing on the continuum limit $x \rightarrow \infty$. Note that in the thermodynamic limit $N_R, N_L \rightarrow +\infty$ physics does not depend on M but on $m_R - m_L$. The parameter M will indeed only be considered for numerical purposes, see section 3.4.

An important point regarding the continuum limit is that the ground state energy of the Schwinger model is UV divergent but that this UV divergence does not depend on the background field $\alpha(n)$. If we write $\mathcal{E}_0 = 2N\epsilon_0$ (with $2N = M + N_L + N_R + 1$ the number of sites and $N \rightarrow +\infty$) for the ground state energy of \mathcal{H}_0 with zero background field $\alpha(n) = 0$, we have

$\sqrt{x}\epsilon_0 \rightarrow -x/\pi$ for the energy density in the $x \rightarrow \infty$ limit [10]. For the modified ground state energy in the presence of the probe charge gQ pair at distance L we can then write $\mathcal{E}_Q(L) = V_Q(L) + \mathcal{E}_0$, where the potential $V_Q(L)$ is now UV finite. Notice that $V_Q(L)$ will also be IR ($N \rightarrow \infty$) finite (for finite L).

3.3. Asymptotic confinement

3.3.1. Setup

We first study the large distance behavior of the potential as captured by the asymptotic string tension $\sigma_Q = \lim_{L \rightarrow +\infty} V_Q(L)/L$. This is the quantity that indicates whether the probe charges are asymptotically confined ($\sigma_Q \neq 0$) or not ($\sigma_Q = 0$). For the Schwinger model σ_Q has been computed analytically in the strong coupling expansion [5, 13, 22, 25]. At the numerical front the most successful computation up-to-date used finite-lattice scaling methods in a Hamiltonian formulation [10]. An advantage of our MPS simulations is that in contrast to [10] we can directly work in the thermodynamic limit, leaving only the $x \rightarrow \infty$ interpolation to extract the continuum results. The challenge of taking this continuum limit now lies in the diverging correlation length ξ/a (in lattice units), as MPS simulations require larger bond dimensions for growing correlation length [75].

To find the asymptotic string tension we put a probe charge $-gQ$ at $-\infty$ and a probe charge gQ at $+\infty$. As was explained in the previous section, a probe charge pair translates to a background electric field $\alpha(n)$ in the Hamiltonian eq. (3.1). In this case the background electric field will be uniform: $\alpha(n) = -Q, \forall n$. The Hamiltonian equals then the Hamiltonian eq. (2.8) with $\alpha = -Q$,

$$\mathcal{H}_Q = \frac{g}{2\sqrt{x}} \left(\sum_{n=1}^{2N} [L(n) - Q]^2 + \frac{\sqrt{x}}{g} m \sum_{n=1}^{2N} (-1)^n \sigma_z(n) + x \sum_{n=1}^{2N-1} (\sigma^+(n) e^{i\theta(n)} \sigma^-(n+1) + h.c.) \right) (N \rightarrow +\infty), \quad (3.3)$$

and is in particular \mathcal{T}^2 invariant. It is discussed in subsection 2.2.1 how we can obtain a faithful MPS approximation $|\Psi_u[A]\rangle$ for the ground state which is \mathcal{T}^2 invariant and gauge invariant.

3.3.2. Results

As explained in more detail in section A.1 of appendix A we computed values for $\sigma_Q(x)$ for $x = 100, 200, 300, 400, 600, 800$ and performed a polynomial

extrapolation in $1/\sqrt{x}$ similar to [10]. This indeed allowed us to recover a finite value for $\lim_{x \rightarrow \infty} \sigma_Q(x)$, thereby explicitly verifying that the UV divergencies in the energy densities $\sqrt{x}\epsilon_Q$ and $\sqrt{x}\epsilon_0$ cancel out.

In fig. 3.1a we plot our result for the continuum string tension σ_Q computed for different values of the mass m/g as a function of the charge gQ of the external quark-antiquark pair. Notice that we only consider Q -values $\in [0, 1[$ as the string tension is periodic in Q : $Q \rightarrow Q - p$ upon $L(n) \rightarrow L(n) + p$ for $p \in \mathbb{Z}$ in the Hamiltonian eq. (3.3). Notice also that one can combine this transformation for $p = 1$ with a \mathcal{CT} transformation. This transformation gives $Q \rightarrow 1 - Q$ in the Hamiltonian eq. (3.3) and therefore $\sigma_Q = \sigma_{1-Q}$. So for our calculations we could restrict ourselves to values $Q \in [0, 1/2]$. In practice we considered the explicit values: $Q = 0.05, 0.10, 0.15, \dots, 0.45, 0.47, 0.48, 0.5$ and performed an interpolating fit.

Our considered values for m/g interpolate between the strong and weak coupling regime. In the strong coupling regime $m/g \ll 1$ the string tension was computed in mass perturbation theory from the bosonized field theory up to order $\mathcal{O}((m/g)^3)$ [22]

$$\frac{\sigma_Q}{g^2} \approx \frac{m}{g} \Sigma (1 - \cos(2\pi Q)) + \frac{m^2 \Sigma^2 E_+ \pi}{4g^2} (1 - \cos(4\pi Q)) \quad (3.4)$$

where $\Sigma = 0.15993, E_+ = -8.9139$. As one can observe in fig. 3.1c for $m/g \rightarrow 0$ our results indeed converge to this analytic result which is plotted with a dashed line for $m/g = 0.125$ and for $m/g = 0.25$.

In the weak coupling regime $g/m \ll 1$ we can easily compute the string tension in standard perturbation theory from the continuum Lagrangian eq. (1.1). We include a current $j^\mu = g\epsilon^{\mu\nu}\partial_\nu Q$; with Q constant everywhere in the bulk, and $Q \rightarrow 0$ only at the boundaries at infinity (see [5]):

$$\begin{aligned} \mathcal{L} &= \bar{\psi} (\gamma^\mu (i\partial_\mu + gA_\mu) - m) \psi - \frac{1}{4} F_{\mu\nu} F^{\mu\nu} - A_\mu j^\mu \\ &= \bar{\psi} (\gamma^\mu (i\partial_\mu + gA_\mu) - m) \psi - \frac{1}{4} F_{\mu\nu} F^{\mu\nu} - \frac{1}{2} F_{\mu\nu} \bar{F}^{\mu\nu}, \end{aligned} \quad (3.5)$$

where on the last line we performed a partial integration and $\bar{F}^{\mu\nu} \equiv \epsilon^{\mu\nu} gQ$. The effective action, obtained by integrating out both the fermion and the gauge fields in the path integral, will then have the general form:

$$S_{eff} = \int d^2x \mathcal{L}_{eff} = \int d^2x C_0 \left(\frac{g}{m}\right) \bar{F}_{\mu\nu} \bar{F}^{\mu\nu} + C_1 \left(\frac{g}{m}\right) \frac{(\bar{F}_{\mu\nu} \bar{F}^{\mu\nu})^2}{m^2} + \dots, \quad (3.6)$$

where we can exclude derivative terms since $\bar{F}_{\mu\nu}$ is constant. At next to leading order we find for the first coefficient C_0 :

$$C_0 = -\frac{1}{4} + \frac{g^2}{24\pi m^2}. \quad (3.7)$$

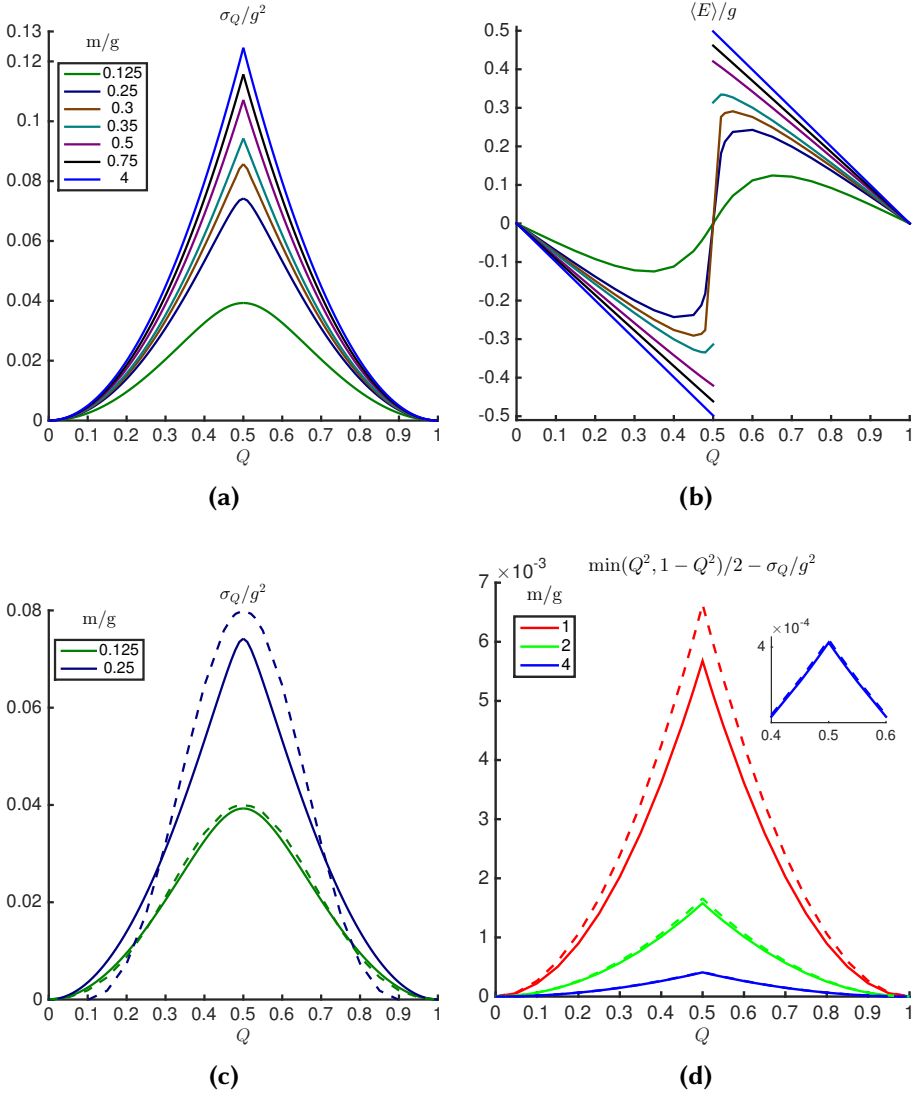


Figure 3.1.: (a): string tension σ_Q . (b): electric field per site. (c): comparison with the strong coupling result eq. (3.4) (dashed line) for $m/g = 0.125$ and $m/g = 0.25$. (d): comparison with the weak coupling result eq. (3.4) (dashed line) for $m/g = 1, 2, 4$. Inset: zooming in on the $m/g = 4$ curve.

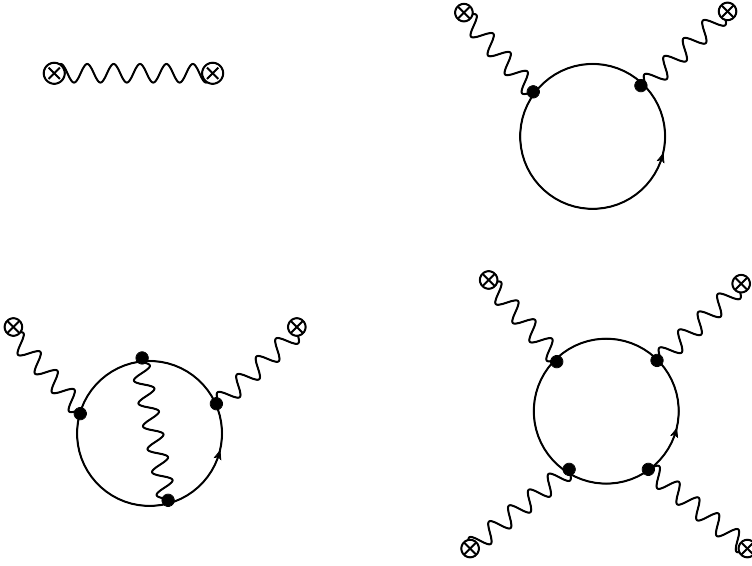


Figure 3.2.: Some diagrams for the effective action from eq. (3.5). On the first line we have the tree-level and the next to leading order g^2/m^2 contribution to C_0 eq. (3.7). Evaluation of the first diagram on the second line would give a g^4/m^4 correction to C_0 , while the other diagram would give the leading g^4/m^4 contribution to C_1 .

The zero order term here is the tree-level result while the g^2/m^2 term follows from the one loop Feynman diagram on the first line of fig. 3.2, which can be calculated with standard techniques (see e.g.[111]). Furthermore one can see that all other non-zero diagrams will lead to contributions to the coefficients C_i that are at least order g^4/m^4 . Finally, we can then identify $S_{eff} = \int d^2x \sigma_Q$, leading to the result

$$\frac{\sigma_Q}{g^2} \approx \frac{Q^2}{2} \left(1 - \frac{g^2}{m^2} \frac{1}{6\pi} \right), \quad (3.8)$$

with the value for $Q > 1/2$ following from the identification $\sigma_Q = \sigma_{1-Q}$ for the compact formulation of QED₂ that we are considering. In fig. 3.1d one can observe the convergence of our numerical results to this analytic result, now for $g/m \rightarrow 0$. Notice here that we subtracted the leading order term of eq. (3.8).

Comparing the strong and weak coupling regime we observe an important difference: in the strong coupling limit σ_Q is differentiable at $Q = 1/2$ whereas in the weak coupling limit this is not the case. Therefore there exists a critical mass $(m/g)_c$ with the property that σ_Q is differentiable at $Q = 1/2$ for $(m/g) < (m/g)_c$ and not differentiable at $Q = 1/2$ for $(m/g) > (m/g)_c$.

This point $(m/g)_c$ corresponds to the first order phase transition for the Hamiltonian \mathcal{H}_Q eq. (3.3) at $Q = 1/2$ [10]. $\mathcal{H}_{Q=1/2}$ is symmetric under the \mathcal{CT} transformation and the point $(m/g)_c$ separates the unbroken phase $m/g < (m/g)_c$ from the spontaneously broken phase $m/g > (m/g)_c$ that was originally predicted by Coleman [6]. This relationship of the breaking of \mathcal{CT} -symmetry with the non-differentiability of σ_Q can be made more concrete by noting that

$$\frac{d\sigma_Q}{dQ} = -\frac{1}{2} \left\langle \sum_{n=1,2} (L(n) - Q) \right\rangle_Q = -\frac{1}{2g} E_Q$$

where $\langle \dots \rangle_Q$ denotes the expectation values with respect to the ground state of \mathcal{H}_Q . We now have the relation $E_Q = -E_{1-Q}$ from the \mathcal{CT} -transformation, which indeed makes it a good order parameter for the \mathcal{CT} breaking at $Q = 1/2$.

We have performed an independent computation of E_Q , again for $Q = 0.05, 0.10, 0.15, \dots, 0.45, 0.47, 0.48, 0.5$, and now using values $x = 100, 200, 300, 400$ for our continuum extrapolation (see section A.2 of appendix A). Our results are displayed in fig. 3.1b. At $Q \rightarrow 1/2$ we find for $m/g = 0.3$, $E_Q/g = 0$ up to a numerical error of 4×10^{-3} while for $m/g = 0.35$ we find $E_Q/g = 0.314(2)$, consistent with the value $(m/g)_c \approx 0.33$ that was obtained in [27] and also consistent with the behavior of σ_Q in fig. 3.1a.

Finally we also computed the half chain entropy S_Q eq. (1.10) for different values of Q and m/g , which in this translational invariant case will not depend on the position of the cut. Similar as for $Q = 0$, see subsection 2.1.5, we find the predicted logarithmic divergence of Cardy and Calabrese [90]

$$S_Q(x) \sim \frac{1}{6} \log \left(\frac{\xi}{a} \right) = -\frac{1}{6} \log(1/\sqrt{x}) + (\text{finite terms as } x \rightarrow +\infty)$$

with ξ the correlation length. As an illustration, in fig. 3.3a we show a fit of the form $(-1/6) \log(1/\sqrt{x}) + A + B/\sqrt{x}$ through our data of $S_Q(x)$ for $Q = 0, Q = 0.45$ and $m/g = 0.25$. A and B have been obtained by a linear fit through $S_Q(x) + (1/6) \log(1/\sqrt{x})$.

The universality of the logarithmic UV-divergence then allows us to define a UV finite renormalized entropy $\Delta S_Q \equiv S_Q - S_0$, with a finite continuum value that can be obtained by a polynomial extrapolation in $1/\sqrt{x}$, see inset fig. 3.3a. Contrary to the string tension and the electric field, we found sometimes that the results at $x = 100$ and the continuum results differed by a factor of order one or had different sign. We refer to subsection A.3 in

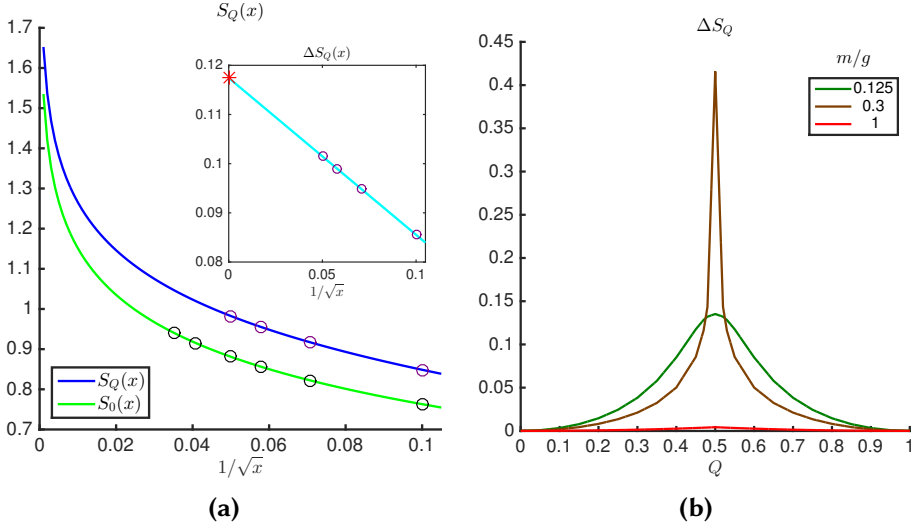


Figure 3.3.: (a): $m/g = 0.25$, $Q = 0.45$. Fit of the form $(-1/6) \log(1/\sqrt{x}) + A + B/\sqrt{x}$ to $S_Q(x)$ and $S_0(x)$. Inset: linear fit to $\Delta S_Q(x)$. (b): ΔS_Q for different values of m/g .

appendix A and in particular to fig. A.5 for the details about the continuum extrapolation. In fig. 3.3b we show this renormalized entropy ΔS_Q as a function of Q for different values of m/g . Most notably we observe an (almost) divergent behavior for $m/g = 0.3$ at $Q \rightarrow 1/2$ close to the critical point $Q = 1/2$, $(m/g)_c \approx 0.33$. From eq. (3.9) we indeed expect a growing entropy for growing correlation length. By the same argument one can understand the behavior at small Q -values: there the correlation length (inverse mass gap) increases with growing g/m (see subsection 2.2.2), which is indeed paralleled by the behavior of ΔS_Q .

3.4. From small to large distances

3.4.1. MPS ground state approximation

Let us now consider the situation where the external quark and antiquark pair are separated over a finite length L . On a lattice with spacing a and interquark distance $L = (m_R - m_L)a$, the pair introduces a non-uniform background electric field $\alpha(n) = -Q\Theta(m_L \leq n < m_R)$ in the Hamiltonian eq. (3.1). As ansatz for our MPS trial state $|\Psi[B]\rangle$ for the ground state we

now write [80, 112, 113]:

$$\sum_{\kappa} v_L^\dagger \left(\prod_{n=-N_L}^0 A_n^{\kappa_n} \right) \left(\prod_{n=1}^M B_n^{\kappa_n} \right) \left(\prod_{n=M+1}^{M+N_R} A_n^{\kappa_n} \right) v_R |\kappa\rangle, \quad (3.9)$$

where $-N_L \ll 1 \leq m_L \leq m_R \leq M \ll M + N_R$ and $A_n^\kappa = A_{n(\bmod 2)}^\kappa$ is obtained from the MPS approximation eq. (2.2) of the ground state of the zero-background Hamiltonian ($\alpha(n) = 0$) and only depends on the parity of n . This is a MPS of the form eq. (1.6) in the thermodynamic limit ($N_R, N_L \rightarrow +\infty$) where we take $A_n = B_n$ for $1 \leq n \leq M$ and take the A_n corresponding to the ground state eq. (2.2) for $\alpha(n) = 0$ to the left and to the right of the B_n 's ($n < 1$ and $n > M$).

The idea behind this ansatz is that the non-uniform background electric field changes the vacuum and breaks translation invariance (all B_n are different) but that asymptotically ($|n| \gg 1$) it does not affect the vacuum, see also section 2.4 of part II for a more detailed discussion. Again, gauge invariance eq. (1.4) is imposed if B_n takes the form eq. (1.8) with general matrices $b_n^{q,s} \in \mathbb{C}^{D_n^q \times D_{n+1}^r}$ ($q \in \mathbb{Z}[p_n^{\min}, p_n^{\max}]$; $p, r \in \mathbb{Z}[p_{n+1}^{\min}, p_{n+1}^{\max}]$). Note that we allow different bond dimensions on different sites. Also $A_n^{s,p}$ is of the form eq. (1.8) as we imposed this to determine the ground state of the zero-background electric field Hamiltonian. The Schmidt decomposition eq. (1.9) with respect to the bipartition of the lattice consisting of the two regions $\mathcal{A}_1^n = \mathbb{Z}[-N_L, \dots, n]$ and $\mathcal{A}_2^n = \mathbb{Z}[n+1, \dots, M+N_R]$ now reads

$$|\Psi[B]\rangle = \sum_{q=p_{n+1}^{\min}}^{p_{n+1}^{\max}} \sum_{\alpha_q=1}^{D_{n+1}^q} \sqrt{\sigma_{n,\alpha_q}^q} |\psi_{q,\alpha_q}^{\mathcal{A}_1^n}\rangle |\psi_{q,\alpha_q}^{\mathcal{A}_2^n}\rangle.$$

The computation of the Schmidt values σ_{n,α_q}^q is discussed in subsection 4.4.2 of part II.

Because eq. (3.9) is linear in each of the B_n we can use the DMRG-method [44, 80] to obtain the best approximation for the ground state within the manifold of gauge invariant states, by optimizing on the UV and IR finite quantity $V_Q(L)$, see section 4.4 of part II for the details on the implementation.

By looking at the Schmidt spectrum we were able to fix the values of the virtual dimension D_{n+1}^q and the minimum and maximum eigenvalues p_{n+1}^{\min} and p_{n+1}^{\max} of $L(n)$ we retained in our numerical scheme to obtain an accurate approximation of the ground state. In practice we started with a certain distribution of D^q -values for each n , anticipating that the dominant eigenvalue sector of $L(n)$ would shift from $q = 0$ at large n to $q \approx Q$ at the centre.

After a first full DMRG-optimization, the initial D^q values were updated: increased in case that the minimal retained Schmidt value in the particular eigenvalue sector was larger than $\sigma_{min} = 10^{-18}$, decreased in case that the minimal retained Schmidt value was smaller. This was repeated a few times until all retained minimal Schmidt values were smaller or of the same order than σ_{min} . As for the choice of m_L and M , which varied between $150 \leq m_L \leq 250$ and $m_R + 150 \leq M \leq m_R + 250$, we verified a posteriori that the inhomogeneous interval of the MPS eq. (3.9) was taken to be large enough, by verifying the convergence of local observables at large distances to their value for the homogenous ground state.

Let us give a specific example. In fig. 3.4 and fig. 3.5 we show some details on the simulation of the ground state for $m/g = 0.25$, $Q = 5$, $x = 100$, $Lg = 10.1$. In our setup with lattice spacing $1/g^2\sqrt{x} = 0.1/g$ this corresponds to a distance of 101 sites between the external quark with charge $-gQ$ and the external antiquark with charge gQ . Specifically, we put the antiquark at site $m_L = 151$ and the quark at site $m_R = 252$. And we reserved 150 sites on the left of the antiquark and 150 sites on the right for the non-uniform part of our MPS ansatz. In total we thus have $M = 151 + 101 + 150 = 402$ tensors B_n that need to be optimized. By looking at the 10-base logarithm of the expectation value of some local quantities with respect to the Schwinger vacuum, see fig. 3.4a, we observe that we took the range of the non-uniform part large enough: the errors by taking a finite range for the non-uniform part are of order 10^{-6} .

In fig. 3.4b we show the distribution of the minimum charge p_n^{min} and maximum charge p_n^{max} we used. For $q < p_n^{min}$ and $q > p_n^{max}$ we thus put $D_n^q = 0$. The p_n^{min} and p_n^{max} we took at the boundaries, i.e. $n \gtrsim 1$ and $n \lesssim 402$ correspond to the p^{min} and p^{max} of the Schwinger vacuum, i.e. the vacuum without external charges that we simulated in section 2.1. Between the boundaries and the external charges we anticipated the increasing electric field and raised p_n^{max} to $4 + Q = 9$ anticipating the dominant eigenvalue sector $q_0 \approx Q$ at the centre.

In figs. 3.4c and 3.4d we plot the distribution of the Schmidt values among the eigenvalues sector q of $L(n)$ at the sites $n = 150$ (c) and $n = 200$ (d). As explained above, we adapted the bond dimensions such that for each site n and at each eigenvalue sector p of $L(n)$: $\min_{\alpha_q} \sigma_{n,\alpha_q}^q \lesssim 10^{-18}$. Comparing with figs. 2.6a and 2.6b we observe that the dominant eigenvalue sector is shifted to $q = 2$ for $n = 150$ and to $q = 5$ for $n = 200$. One can also see that our p_n^{min} and p_n^{max} are not entirely optimal: for certain charge sectors the largest Schmidt-value is still well below 10^{-18} , and these sectors could have been discarded altogether. As we can see by looking at fig. 3.5a the most dominant eigenvalue sector of $L(n)$, i.e. the eigenvalue sector q with

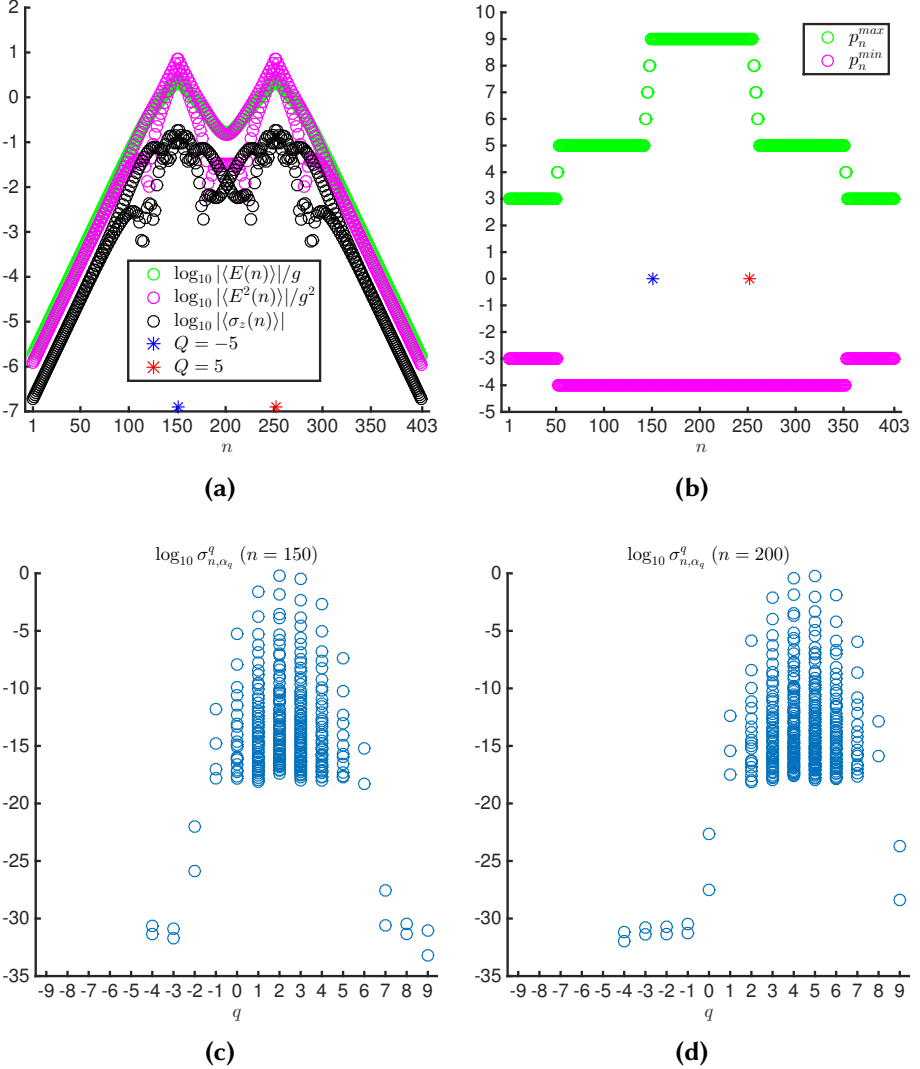


Figure 3.4: $m/g = 0.25, x = 100, Q = 5, Lg = 10.1$. The stars represent the external charges. Between them the electric background field $-Q = -5$ is applied. (a): 10-base logarithm of the expectation values of some local quantities with the Schwinger vacuum-value subtracted. At the boundaries one observes that they are sufficiently small indicating that we took the non-uniform range wide enough. (b): maximum and minimum eigenvalues p_n^{max} and p_n^{min} of $L(n-1)$ we took into account in our numerical scheme on every site. (c): Distribution of the 10-base logarithm of the Schmidt values σ_{n,α_q}^q among the eigenvalue sectors q of $L(n)$ for $n = 150$. (d): Distribution of the 10-base logarithm of the Schmidt values σ_{n,α_q}^q among the eigenvalue sectors q of $L(n)$ for $n = 200$.

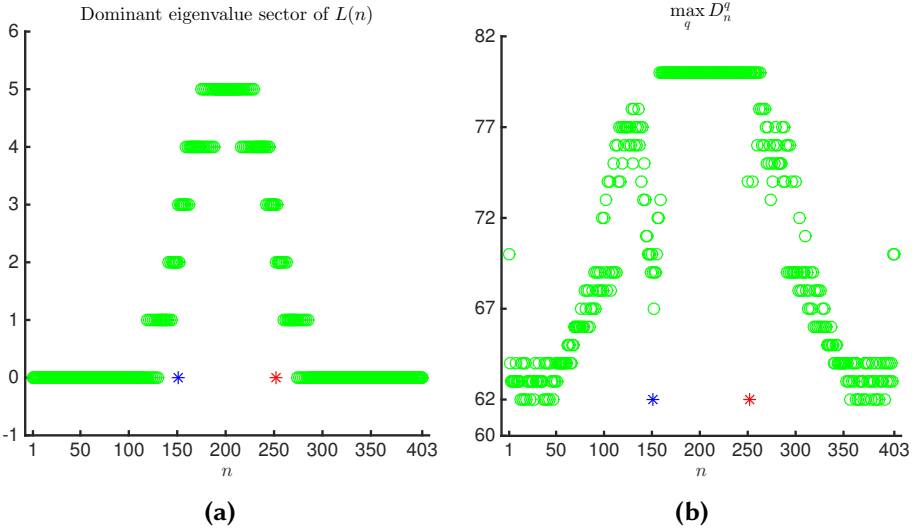


Figure 3.5.: $m/g = 0.25$, $x = 100$, $Q = 5$, $Lg = 10.1$. The stars represent the external charges. Between them the electric background field $-Q = -5$ is applied. (a): Dominant eigenvalue sector of $L(n)$, i.e. eigenvalue q of $L(n)$ with largest $\sum_{\alpha_q=1}^{D_n^q} \sigma_{n,\alpha_q}^q$. D_n^q is taken such that smallest Schmidt value is around 10^{-18} . (b): $\max_q D_n^q$: Largest bond dimension among the eigenvalue sectors of $L(n)$ at every site n .

the largest value for $\sum_{\alpha_q=1}^{D_n^q} \sigma_{n,\alpha_q}^q$ shifts from $q = 0$ to $q = 5$ as we go from the left boundary to the middle and then decreases to $q = 0$ as we go to the right boundary.

We also show the maximum bond dimension $\max_q D_n^q$ in fig. 3.5b. The largest bond dimension is required in the region where the electric background field is applied.

Physics is independent of the precise position of the quark and antiquark but depends on the distance $L = (m_R - m_L)\sqrt{x}/g$ between them. For our discussion of the results we will shift the system such that the quark with charge $-gQ$ is at position $z = -L/2$ and the antiquark with charge gQ is at position $z = L/2$.

3.4.2. The case $m/g=0$: screening à la Higgs

We will now first discuss our results for the $m/g = 0$ case. This is a special case, as the asymptotic string tension σ_Q vanishes for all values (integer or fractional) of the charge. Physically, this is interpreted as a manifestation of a Higgs mechanism [5], suppressing the long range Coulomb force and replacing it with a short range Yukawa force thereby effectively screening

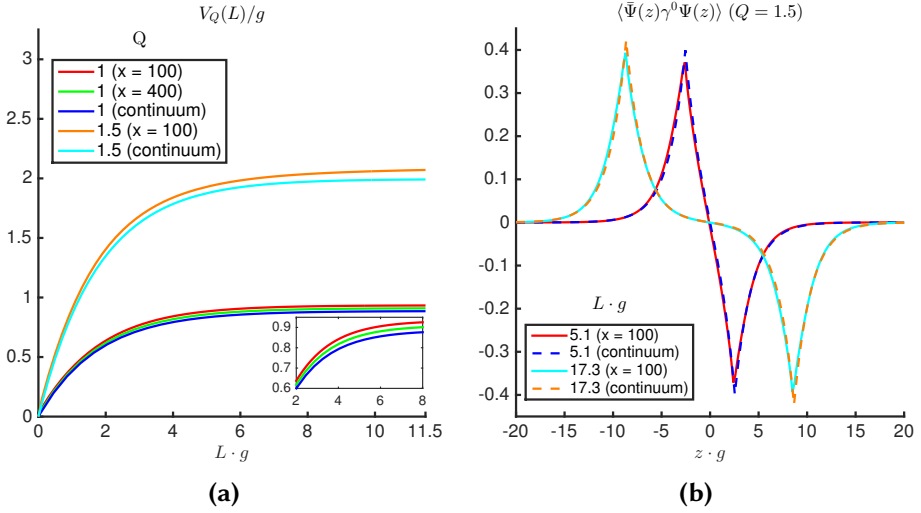


Figure 3.6.: $m/g = 0$. (a): Potential for $Q = 1$ and $Q = 1.5$ compared with exact result in the continuum eq. (3.10). Inset: convergence for $x \rightarrow +\infty$ to eq. (3.10) for $Q = 1$. (b): Distribution of fermion charge for $Q = 1.5$ for different separation lengths of the quark and antiquark for $x = 100$. The results are compared with the exact result eq. (3.11).

all charges. Another reason that makes the $m/g = 0$ case special is that it can be solved analytically [13], which allows for benchmarking of numerical results. Previous numerical calculations for this case were performed with Monte-Carlo simulations on the bosonized version of the theory [11].

In fig. 3.6a we have plotted our results for the potential for $m/g = 0$ for $Q = 1$ and $Q = 1.5$. This can be compared with the exact continuum result [13]:

$$V_Q(L) = \frac{\sqrt{\pi}gQ^2}{2} \left(1 - e^{-Lg/\sqrt{\pi}}\right), \quad (3.10)$$

which is indeed of the Yukawa-type. We find very good agreement already for $x = 100$ both for $Q = 1$ and $Q = 1.5$. For $Q = 1$ we also performed a computation for $x = 400$, in the inset one can observe the rate of convergence towards the continuum $x \rightarrow \infty$ in this case.

The charge density $\langle \bar{\psi}(z)\gamma^0\psi(z) \rangle$ of the light quarks is of course also an interesting quantity to compute, as it explicitly shows the screening of the external probe charges. The analytical result for the probe charge pair put at $\pm L/2$ reads [13]:

$$\langle \bar{\psi}(z)\gamma^0\psi(z) \rangle = \frac{gQ}{2\sqrt{\pi}} \left(e^{-g|z+L/2|/\sqrt{\pi}} - e^{-g|z-L/2|/\sqrt{\pi}} \right). \quad (3.11)$$

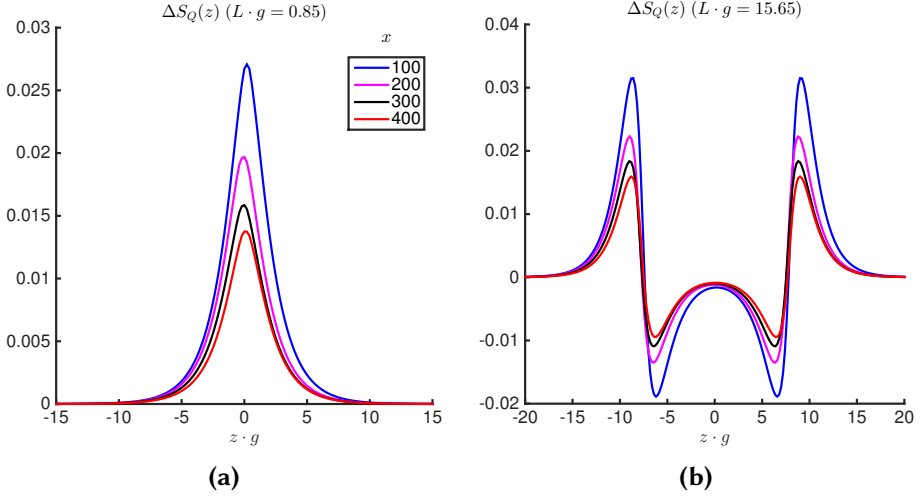


Figure 3.7.: $m/g = 0, Q = 1$. Spatial profile of ΔS_Q for different values of L and scaling to the continuum limit ($x \rightarrow +\infty$). (a) $Lg = 0.85$. (b): $Lg = 15.65$.

This indeed corresponds to a charge distribution with two ‘clouds’ of oppositely charged light (in this case massless) quarks, around the external quark and antiquark, that for large distance L have exactly the same total charge $\pm Q$ as the external pair. On the lattice the charge density at $z = (2n - 1/2)a$ is computed as $\sqrt{x}(\sigma_z(2n - 1) + \sigma_z(2n))/2$. In fig. 3.6b, we plot this density for $Q = 1.5$ where the charges are separated at distances $Lg = 5.1$ and $Lg = 17.3$. Here too our results for $x = 100$ are already very close to the continuum result.

In fig. 3.7 we show the spatial profile of the renormalized half chain Von Neumann entropy $\Delta S_Q(z) = S_Q(z) - S_0(z)$, see eq. (1.10), for different values of Lg . We computed this quantity for $z = (n + 1/2)a$ with n even and performed an interpolating fit. When the heavy quarks are close to each other, $\Delta S_Q(z)$ shows a peak in the middle between the charges and falls off very fast with $|z g|$. For larger values of Lg a cloud of light quarks forms around each of the heavy charges which clearly leaves its imprints on the spatial profile of the Von Neumann entropy, see fig. 3.7b. $\Delta S_Q(z)$ is non-zero around each of the heavy charges and is zero around $z g \approx 0$.

In fig. 3.7a and 3.7b we also show the scaling of $\Delta S_Q(z)$ to the continuum limit, $x \rightarrow +\infty$. Here we also needed to perform some interpolation because we can only take Lg to be an integer multiple of $1/\sqrt{x}$. Specifically, we performed simulations for $x = 400$ and $Lg = 0.85, 5.25, 15.65$. For $x = 100, 200, 300$ we first did simulations for $L_1 g < 0.85, 5.25, 15.65$ and $L_2 g >$

0.85, 5.25, 15.65. Afterwards we did a simple linear interpolation between L_1g and L_2g to obtain the curve for $Lg = 0.85, 5.25, 15.65$. We find the same qualitatively behavior for different values of x . In the continuum limit $x \rightarrow +\infty$ the entropy however becomes very small. For instance, in fig. 3.7a a continuum extrapolation of the maxima for $zg \approx 0$ yields the estimate $\Delta S_Q(0) \approx 5(7) \times 10^{-4}$, while extrapolating the maxima in fig. 3.7b around $zg = \pm 10$ gives $\Delta S_Q(\pm 10) \approx 2(5) \times 10^{-4}$.

3.4.3. The case $Q = 1$: string breaking

For $m/g \neq 0$, the asymptotic string tension σ_Q vanishes only for integer charges Q . This is taken to be an indication for a screening à la QCD [5], where the potential exhibits a string tension ($V_Q(L) \propto L$) at short distances, but flattens out completely at large distances, at least for integer charges Q . At these large distances it becomes energetically favorable to materialize light (yet massive) (anti-)fermions out of the vacuum that bind to the external quark and antiquark, resulting in two charge neutral mesons.

Historically, for QCD, lattice Monte-Carlo simulations succeeded first to calculate numerically the short distance confining behavior of the potential – both in the quenched and unquenched approximation – via the expectation value of the Wilson loop [106, 109]. The detection of string breaking has posed a larger challenge. A main problem with the use of the standard Wilson loop is the poor overlap with the broken-string two-meson state. This problem was finally overcome by including light quark propagators in the Wilson loop and analyzing its mixing with the standard Wilson loop [106, 114].

For the Schwinger model the string breaking phenomenon has been confirmed in mass perturbation theory [25] and in a semi-classical approximation of the bosonized version of the theory [9, 14]. At the numerical level, for $Q = 1$, lattice Monte-Carlo simulations have detected both the confining and string breaking behavior of the potential [11, 28]. In [11] the problem with the Wilson loop was avoided by computing instead the expectation value of the bosonized Hamiltonian, while [28] turned to very high statistics thereby explicitly showing the poor overlap of the Wilson loop with the broken-string ground state.

For the local quantities (charge density $= \bar{\psi}(z)\gamma^0\psi(z)$, electric field $= E(z)$) and the potential, we restrict ourselves from now on to lattice spacing $x = 100 (= 1/g^2a^2)$; from the previous subsection we can expect these results already to be quite close to the continuum. In fig. 3.8a we display our results for the potential, and this for different values of m/g . We computed explicitly the ground state energy at $Lg = 0.1, 0.3, \dots 15.3$ and performed an interpolating fit. We clearly find a transition from the confining behavior,

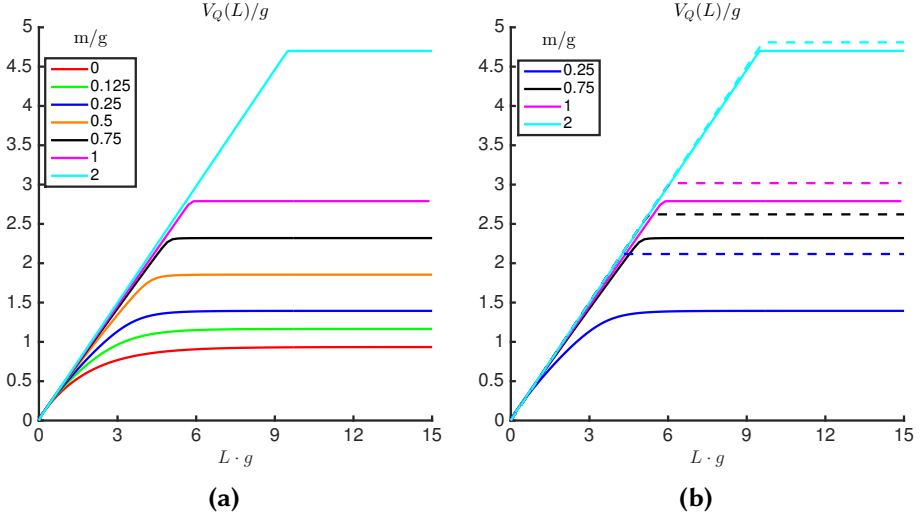


Figure 3.8.: $Q = 1, x = 100$. (a): Quark-antiquark potential for different values of m/g . (b): Comparison of potential with non-relativistic limit result eqs. (3.12) and (3.15) (dashed line) for $m/g = 0.25, 0.75, 1, 2$.

associated with the string state, towards the constant behavior associated with the broken-string two-meson state. This transition happens more sudden for larger values of m/g , which is in qualitative agreement with the semi-classical results from the bosonized theory [9, 14].

These results are also what one would expect from the non-relativistic weak coupling regime. In this non-relativistic limit one can obtain the ground state by diagonalizing the Hamiltonian in subspaces of the different (fermion) particle sectors. The zero particle sector simply consists of the Fock vacuum of the free Dirac-field and corresponds to the confining string state with an energy

$$\mathcal{E}_{string} = g^2 L/2, \quad (3.12)$$

for probe charge $Q = 1$ and separation length L . The broken-string state will correspond to the ground state in the subspace of all states containing one (light) quark antiquark pair. For this state the light antiquark will bind to the external probe quark and vice versa. We can make this more quantitative, by considering the effective Hamiltonian in the non-relativistic limit for this

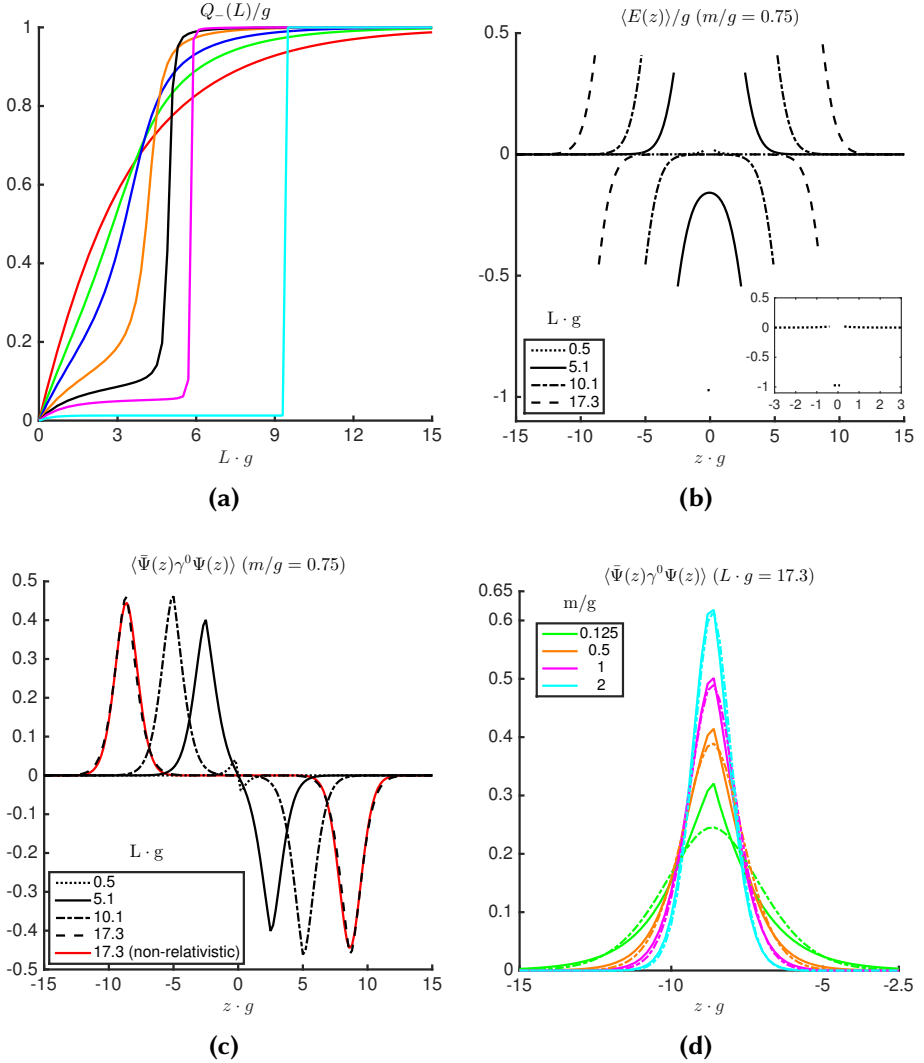


Figure 3.9.: $Q = 1$, $x = 100$. (a): The total charge of the light fermions on the negative axis $Q_-(L)$ for different values of m/g . (b): Electric field for $m/g = 0.75$. (c): Charge distribution for $m/g = 0.75$. For $Lg = 17.3$ we compare with the charge distribution of the non-relativistic meson state (full red line). (d): Comparison of the charge density of the left cloud (full line) with that of the non-relativistic meson state, eq. (3.17), (dashed line) for $Lg = 17.3$, now for $m/g = 0.125, 0.5, 1, 2$.

particle sector:

$$\mathcal{H}_{q\bar{q}} = 2m - \frac{\nabla_A^2}{2m} - \frac{\nabla_B^2}{2m} + \frac{g^2}{2}|x_A + L/2| + \frac{g^2}{2}|x_B - L/2| + \frac{g^2}{2}|x_A - x_B| - \frac{g^2}{2}|x_A - L/2| - \frac{g^2}{2}|x_B + L/2| + \frac{g^2}{2}L. \quad (3.13)$$

Here x_A and x_B are the coordinates for the light antiquark and quark, and we have put the probe quark at $x = -L/2$ and the probe antiquark at $x = L/2$. Anticipating binding of the light fermions to the probe charges for large L , we can assume $x_A < x_B$, $x_A < L/2$ and $x_B > -L/2$ leading to a cancellation of the last four potential terms $\mathcal{H}_{q\bar{q}} \approx \mathcal{H}_A + \mathcal{H}_B$ with

$$\mathcal{H}_A = m - \frac{\nabla_A^2}{2m} + \frac{g^2}{2}|x_A + L/2|, \mathcal{H}_B = m - \frac{\nabla_B^2}{2m} + \frac{g^2}{2}|x_B - L/2|.$$

A ground state solution will therefore be of the form

$$\Psi(x_A, x_B) = \phi_A(x_A)\phi_B(x_B)$$

where now $\phi_A(x_A)$ and $\phi_B(x_B)$ are both ground states of the non-relativistic one-particle problem for a linear potential. All eigenstates for this non-relativistic Hamiltonian \mathcal{H}_A (and similar for \mathcal{H}_B) can be written in terms of the so called Airy function Ai [115]:

$$\phi_A^{(n)}(x_A) = \mathcal{N} Ai \left((g^2 m)^{1/3} |x_A + L/2| - 2\mathcal{E}_n \frac{m^{1/3}}{g^{4/3}} \right), \quad (3.14)$$

where \mathcal{N} is the normalization factor and \mathcal{E}_n is the (kinetic) eigenenergy of the eigenstate. These energies follow from the continuity requirement on ϕ_A and ϕ'_A at $x_A = -L/2$, leading to either even or odd ϕ_A under $x_A + L/2 \rightarrow -(x_A + L/2)$. The ground state wave-function is even and the ground state energy \mathcal{E}_0 is related to the first zero of the first derivative of the Airy function, $Ai'(x_1) = 0$, at $x_1 \approx -1.0188$: $\mathcal{E}_0 = -\frac{x_1}{2} \frac{g^{4/3}}{m^{1/3}}$. So in the non-relativistic approximation we find:

$$\mathcal{E}_{2meson} = 2m + 1.0188 \frac{g^{4/3}}{m^{1/3}}. \quad (3.15)$$

Notice that relativistic corrections to this approximation will necessarily involve quantum field contributions from other particle sectors. The relativistic one-particle Dirac equation has no bound state solutions for a linear (vector) potential [116, 117].

Hence, in the non-relativistic approximation we can then understand the transition from the string state to the broken-string state as a level crossing

at the critical length L , where $\mathcal{E}_{string} = \mathcal{E}_{2meson}$. The dashed lines in fig. 3.8b corresponding to this non-relativistic result for $\mathcal{E}_{string} = Lg^2/2$ and $\mathcal{E}_{2meson} = 2m + 1.0188 \frac{g^{4/3}}{m^{1/3}}$ were plotted for comparison. We can indeed observe the convergence towards this result for increasing values of m/g . We further illustrate this behavior in fig. 3.9a, where we plot the total charge Q_- of the light fermions on the negative z -axis:

$$Q_- = g \int_{-\infty}^0 dz \langle \bar{\psi}(z) \gamma^0 \psi(z) \rangle. \quad (3.16)$$

One can observe indeed that the interpolation between $Q_- = 0$ (string state) for small L and $Q_- = 1$ (meson state) for large L becomes more and more discontinuous for growing m/g in accordance with the non-relativistic level crossing picture.

In figs. 3.9b and fig. 3.9c we investigate the interpolation from the string state to the string-broken state in more detail for $m/g = 0.75$ by plotting the charge density and electric field. For $L/g = 0.5$ there is only a very small charge cloud around the external quark and antiquark, notice also the very short electric field string displayed at the bottom of fig. 3.9b. At $L/g = 5.1$ the clouds start to build up, lowering the electric field value at the centre. At $L/g = 10.1$ the string is completely broken, the electric field at the centre has vanished, and we have two clouds of total charge ± 1 around the external quark and antiquark. At $L/g = 17.3$ the two isolated mesons are simply separated over a larger distance, with a quasi-identical charge distribution around the external quarks as for $L/g = 10.1$.

The full red line in fig. 3.9c is the charge distribution $\pm |\phi(z)|^2$ for the non-relativistic meson state for $Lg = 17.3$, with

$$\phi(z) = \mathcal{N} Ai \left((g^2 m)^{1/3} |z \pm L/2| - 1.0188 \right) \quad (3.17)$$

the ground state of the one-particle problem in a linear potential, see eq. (3.14). As one can observe, the charge distribution from this non-relativistic picture matches very well our exact (numerical) result. In fig. 3.9d we compare the charge cloud at the negative z -axis with the non-relativistic result for other values of m/g . One can again observe the convergence to the non-relativistic result for growing m/g , notice that already for $m/g = 0.5$ the match is quite good.

For the renormalized Von Neumann entropy $\Delta S_Q(z)$ we also find a characteristic picture, both for the string state and the string-broken state, see fig. 3.10 for the case $m/g = 2$. For the string state, $Lg \lesssim 9.5$, the entropy shows a constant surplus in between the probe charges, similar to the electric

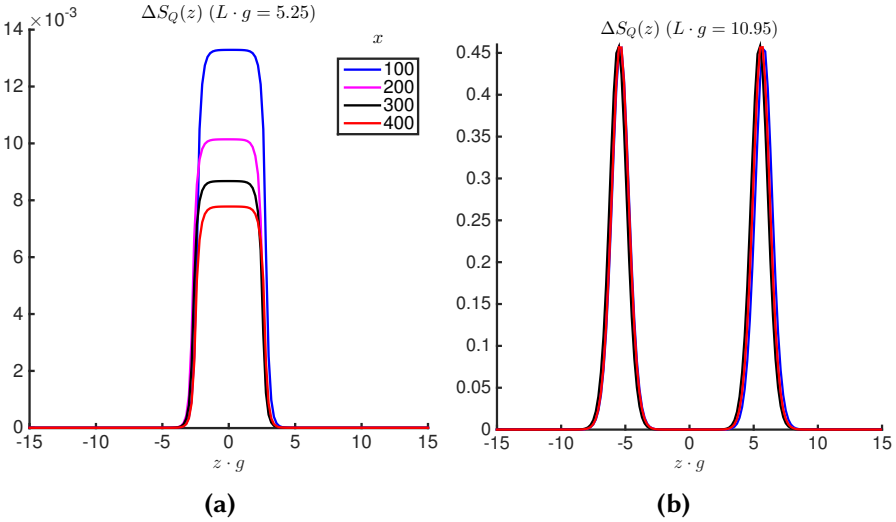


Figure 3.10.: $m/g = 2$, $Q = 1$. $\Delta S_Q(z)$ for different values of L and scaling to the continuum limit. (a) $Lg = 5.25$. (b) $Lg = 10.95$.

field. But notice that this effect vanishes in the continuum limit, we find an extrapolated value: $\Delta S_g(z) \approx 2.0(5) \times 10^{-3}$ for $zg \in [-2.5, 2.5]$. For the string-broken case $Lg \gtrsim 10$, see fig. 3.10b, we find that the entropy now shows two clouds around the heavy quark and the heavy antiquark, similar to the charge density. But notice that in contrast to the string state the entropy now survives the continuum limit, with the $x = 100$ value already close to the continuum extrapolation.

3.4.4. General Q : partial string breaking

We now finally turn our attention to the general case $Q \neq 1$. In this case we should have the interesting phenomenon of partial string breaking. Indeed, in the non-relativistic limit $m/g \rightarrow \infty$ of string breaking due to meson formation, probe charges Q can only be screened by an integer number: $Q \rightarrow \tilde{Q} = Q - n$, where n is the number of light (anti-)quarks that bind to the external charges. For nonzero \tilde{Q} this still leaves a string between the two separated meson configurations.

Our simulations allow us to verify to what extent this picture is realized for finite m/g . In fig. 3.11 we plot our results for different values of Q , both fractional and integer. We do indeed recover partial string breaking, largely following the non-relativistic picture. To our knowledge this is the first successful simulation of partial string breaking for the Schwinger model, a previous Monte-Carlo simulation [28] failed to detect the phenomenon. Note

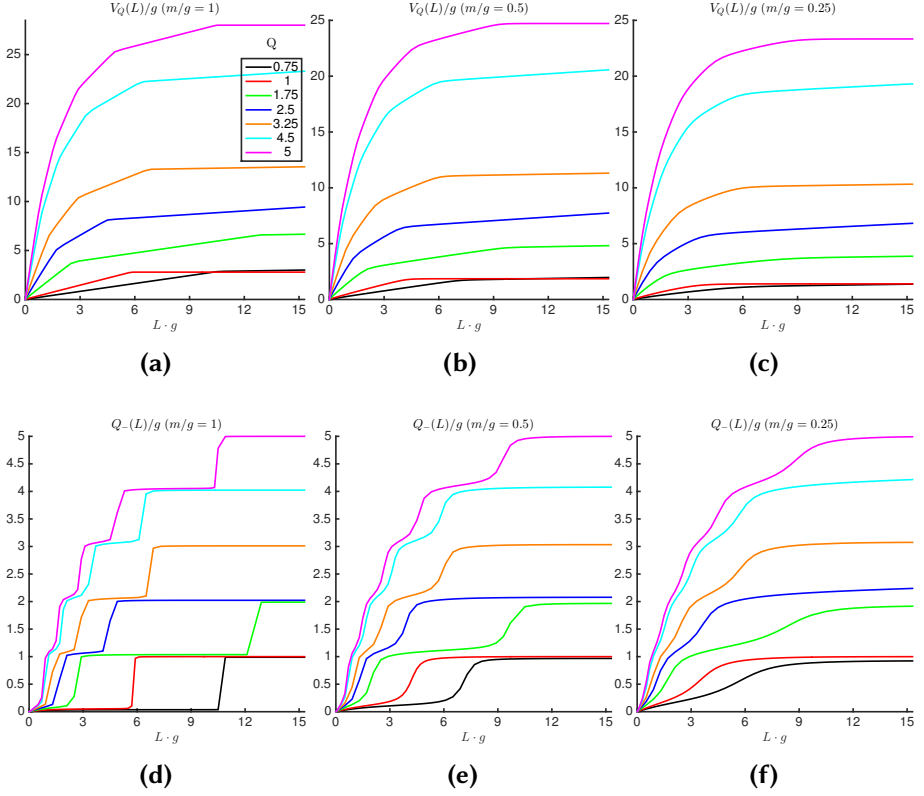


Figure 3.11.: $x = 100$. (a) - (c): Quark-antiquark potential for different values of Q . (a) $m/g = 1$. (b) $m/g = 0.5$ (c) $m/g = 1$. (d) - (f): $Q_-(L)$ for different values of Q . (d) $m/g = 1$. (e) $m/g = 0.5$ (f) $m/g = 0.25$.

however that for $SU(2)$ Yang-Mills theory Monte-Carlo simulations [118] were able to detect partial string breaking using the multi-level method.

In fig. 3.11d we plot, as in the previous section, the evolution of the total dynamical charge Q_- at the negative z -axis, for $m/g = 1$. For all values of Q this charge Q_- indeed makes quasi-discrete jumps of $\Delta Q_- \approx +1$ which should correspond to (partial) string breakings. As we see in fig. 3.11a these jumps indeed correlate with jumps in the string tensions in the different regions of the potentials. For $m/g = 0.5$ we still find jumps of Q_- but they are smoothed out, as can be seen in figs. 3.11b and 3.11e. For $m/g = 0.25$ the jumps are even more smoothed out as can be seen in figs. 3.11c and 3.11f. This smoothed behavior, similar to what we obtained in the $Q = 1$ case, is expected as we go further from the non-relativistic large m/g regime. But still notice the contrast with the behavior in the massless limit $m/g = 0$ of subsection 3.4.2, where the charge Q_- grows continuously to the external

Q	m/g		
	0.25	0.5	1
0.75	2.5×10^{-5} (6)	5×10^{-7} (2)	-7×10^{-10} (2)
1	8×10^{-7} (2)	5×10^{-9} (2)	-4×10^{-11} (4)
1.75	2.6×10^{-4} (7)	1.7×10^{-5} (7)	8×10^{-8} (8)
2.5	3.0×10^{-3} (1)	2.5×10^{-6} (5)	-1×10^{-9} (1)
3.25	2.2×10^{-5} (1)	2.1×10^{-7} (8)	-1×10^{-9} (1)
4.5	4.0×10^{-3} (2)	1.0×10^{-5} (2)	-1×10^{-9} (1)
5	2.1×10^{-4} (6)	1.0×10^{-5} (5)	-2×10^{-8} (1)

Table 3.1.: $x = 100$. Values for the difference $(\Delta V_Q/\Delta L - \sigma_Q)/g^2$ where $\Delta V_Q/\Delta L$ is the mean of the backward differences at $Lg = 15.3$ with $\Delta L g = 0.4, 0.8, 1.2, 1.6$.

value Q , assuring a complete screening.

For L going from 0 to ∞ , different partial string breakings should lead to the asymptotic behavior of the potential that we examined in section 3.3. In table 3.1 we show the difference of the slope of the potential around $Lg = 15.3$ with the asymptotic string tension at $x = 100$ that we calculated in the previous section. The former is estimated as the mean of the backward differences

$$\frac{1}{g^2} \frac{\Delta V_Q}{\Delta L} = \frac{V_Q(15.3g) - V_Q(Lg)}{Lg} \left(\approx \frac{1}{g^2} \frac{dV_Q}{dL} \right) \quad (3.18)$$

for $Lg = 13.7, 14.1, 14.5, 14.9$. The error is computed as the standard deviation of these backward differences. One observes that for $m/g = 1$ the string tension has already converged to the asymptotic result, almost up to the numerical precision, while for $m/g = 0.5$ we are already very close to the asymptotic result and for $m/g = 0.25$ there is a slightly larger (but still very small) difference.

For integer values of Q , the asymptotic string tension vanishes, so asymptotically we expect $Q_- \rightarrow Q$, corresponding to a complete screening. For the values $Q = 1$ and $Q = 5$ that we considered, this is already almost satisfied at $Lg = 15.3$, as can be seen in table 3.2. In the non-relativistic limit for general Q , the total dynamical charge Q_- that is produced asymptotically, will be the integer number that minimizes $|Q - Q_-|$. For finite m/g we expect corrections to the non-relativistic limit, but as one can see in the table these corrections are still very small for $m/g = 1$ and $m/g = 0.5$. Notice also that for the half-integer values $Q = 2.5$ and 4.5 , for which we have spontaneous symmetry breaking in the asymptotic limit (see section 3.3), we

Q	m/g		
	0.25	0.5	1
0.75	0.9225	0.9675	0.9891
1	0.9995	1.0000	1.0000
1.75	1.9157	1.9665	1.9891
2.5	2.2384	2.0778	2.0223
3.25	3.0748	3.0332	3.0111
4.5	4.2150	4.0770	4.0230
5	4.9922	4.9990	5.0000

Table 3.2.: $x = 100$. Values for Q_- at $Lg = 15.3$ for $m/g = 0.25$, $m/g = 0.5$ and $m/g = 1$.

find Q_- approaching the smallest of the two possible non-relativistic values $Q_- \approx Q - 1/2$.

In fig. 3.12 we show the spatial charge distribution and electric field for different distances of the probe quarks. For $Q = 1.75$ we have two partial string breakings. The first one, around $Lg \approx 1.7$ (see fig. 3.12a) brings the electric field string at the centre from $E/g \approx -1.7$ to $E/g \approx -0.7$. After the second partial string breaking, around $Lg \approx 9$, the probe charge is ‘overscreened’, $Q_- \approx 2$, leading to a final electric field string with opposite sign $E/g \approx +0.2$. Notice that in contrast to the $Q = 1$ case, the charge clouds at large separation of the probe quarks are not symmetric around the position of the probes. This is expected, as the remaining confining force between the two (charged) ‘mesons’ distorts the charge distribution. For $Q = 4.5$ we have a similar picture, but now, after the final partial string breaking, the probe charge is ‘underscreened’, $Q_- \approx 4$, resulting in a final negative electric field string $E/g \approx -0.4$. While for $Q = 5$ the final string breaking is complete: the probe charge is screened entirely $Q_- \approx 5$, leading to a complete neutralization of the electric field string $E/g \approx 0$ at the centre. In this case for large enough Lg we expect the charge distributions to become fully symmetric around the probe charge positions.

In fig. 3.13 we show the effect of different partial string breakings on the entropy profile $\Delta S_Q(z)$, for $m/g = 0.5$ and $Q = 4.5$. For the smallest interquark distance $Lg = 0.55$, the entropy peaks at the centre. At $Lg \gtrsim 2.55$ (after two string breakings, see fig. 3.11), we observe a profile with two peaks around the positions of the probe charges. At $Lg \gtrsim 7.35$ and $Lg \gtrsim 13.15$, after four string breakings, the profile now shows four peaks around the probe quark positions. In addition, we find an entropy surplus in the centre, which now seems to be stable under the continuum extrapolation.

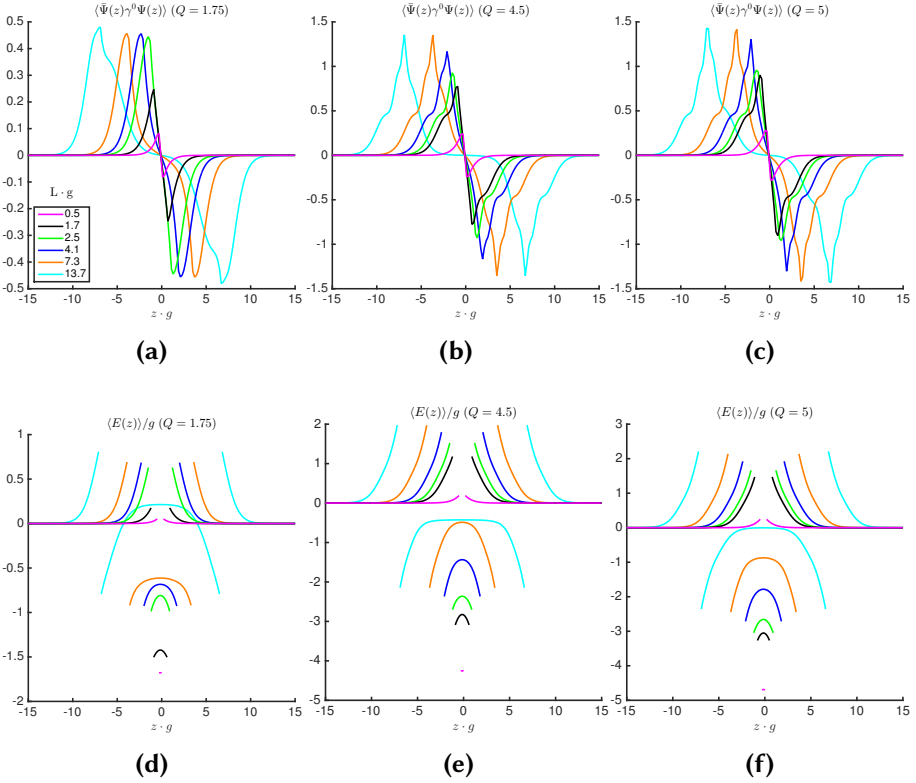


Figure 3.12.: $m/g = 0.5, x = 100$. (a) - (c): charge distribution for different values of Lg . (a) $Q = 1.75$. (b) $Q = 4.5$. (c) $Q = 5$. (d) - (f): Spatial profile of electric field for different values of Lg . (d) $Q = 1.75$ (e) $Q = 4.5$ (f) $Q = 5$.

In fig. 3.14 we show that this characteristic imprint on the entropy is generic. We plot $\Delta S_Q(z)$ for $Lg = 15.25$ and different values of Q . For $Lg = 15.25$ all the partial string breakings have occurred and the final meson configurations around the external charge positions are formed. By counting the peaks one can again deduce the number of light elementary quarks (corresponding to the number of partial string breakings) in the meson states. For instance, for $Q = 4.5$, fig. 3.14a, we observe that there were four partial string breakings and for $Q = 5$, fig. 3.14b, we observe that there were five partial string breakings. The spatial profiles do in fact only differ by one additional peak in each of the clouds for $Q = 5$ around $z \cdot g = \pm 5$. Notice also the difference in the spatial profile for $Q = 1.75$ and $Q = 2.5$, see figs. 3.14c and 3.14d. In both cases two partial string breakings lead to the asymptotic meson state, but in the former case the final electric field is ‘overscreened’ while in the latter case the final electric field is ‘underscreened’. Finally,

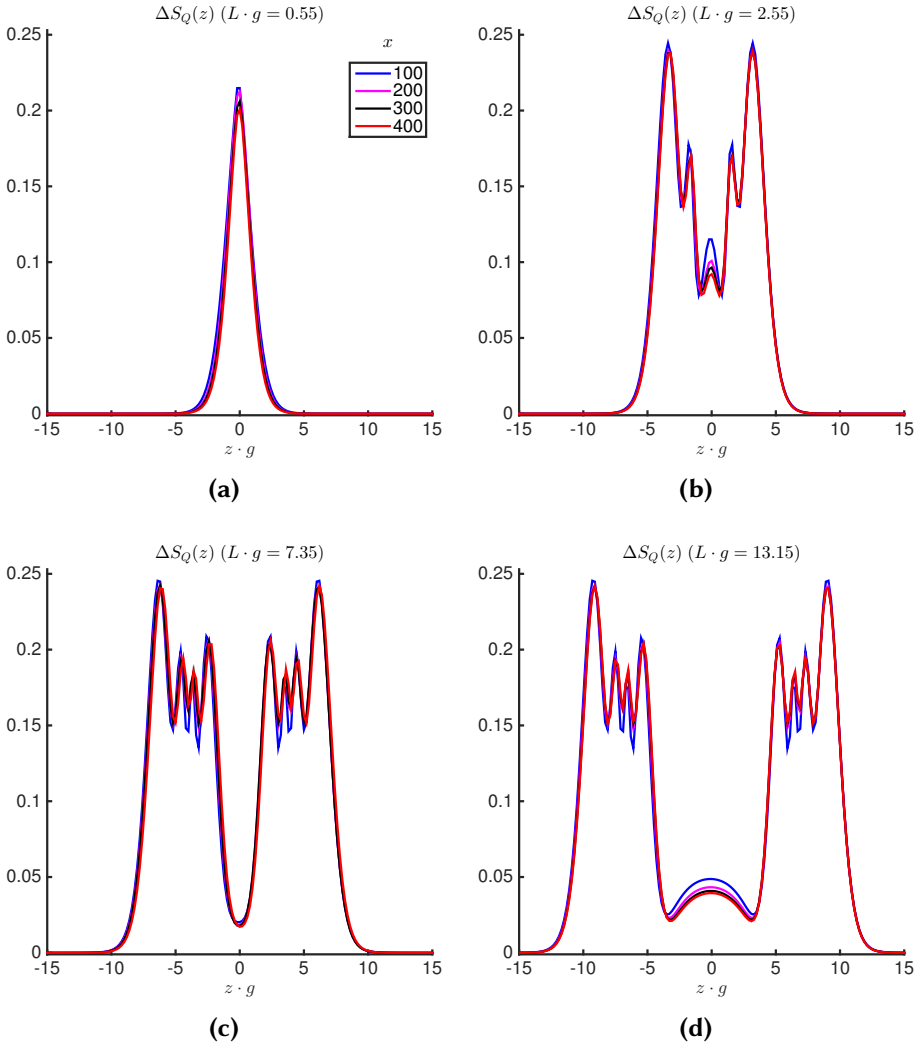


Figure 3.13.: $m/g = 0.5$, $Q = 4.5$. $\Delta S_Q(z)$ for different values of L . We also show the scaling to $x \rightarrow +\infty$. (a) $Lg = 0.55$. (b) $Lg = 2.55$. (c) $Lg = 7.35$ (d) $Lg = 13.25$.

notice that we can trust these results to be close to their continuum value, as the variation for the different x -values is very small.

3.5. Conclusion

In this chapter we employed the MPS formalism for a detailed numerical study of the confining mechanism in the static limit for the massive Schwinger model. Our Hamiltonian set-up gives us direct access to the modified vacuum state in presence of two probe charges. This allowed us, not only to compute the interquark potential, but also the spatial profile of the electric field between the probe charges and the charge concentration of the light fermions. Even for relatively small m/g the picture that emerged can be understood as a smoothed version of the non-relativistic limit, with a level crossing between the electric string state that is the ground state at short distances and the broken-string two meson state that is the ground state at large distances. Here the two isolated mesons each consist of a light (anti-)quark cloud around the heavy probe charge, that is well described by the solution to the Schrödinger equation of the appropriate one-particle problem.

In the case of fractional probe charges, we clearly observed the expected partial string breaking. Again in accordance with the non-relativistic picture we found the screening of the probe charges to happen in jumps $\Delta Q \approx 1$ of the light fermion charge; with these jumps becoming more and more discrete for growing m/g .

The tensor network simulations also give us direct access to the full Schmidt spectrum for the different bipartitions on the state. The numerical simulations show that the UV-divergence in the corresponding Von Neumann entropy is universal, allowing us to define a UV-finite renormalized entropy by subtracting the vacuum value. We have examined the imprint of both the string formation and string breaking on the profile of this renormalized entropy. Most notably we found that string breaking leaves a very distinct imprint on this entropy profile.

We have checked our results not only against the predictions from the one-particle Schrödinger equation eq. (3.13), but also against the weak coupling results from the original Lagrangian eq. (3.5) and against the strong coupling results from the bosonized field theory [6]. In the appropriate regimes we found nearly perfect agreement with these continuum analytic results. This not only demonstrates the potential of MPS simulations close to the continuum critical point of a lattice theory. But it also serves as a nice, if not unexpected, cross-check of the consistency of all different descriptions of the Schwinger model.

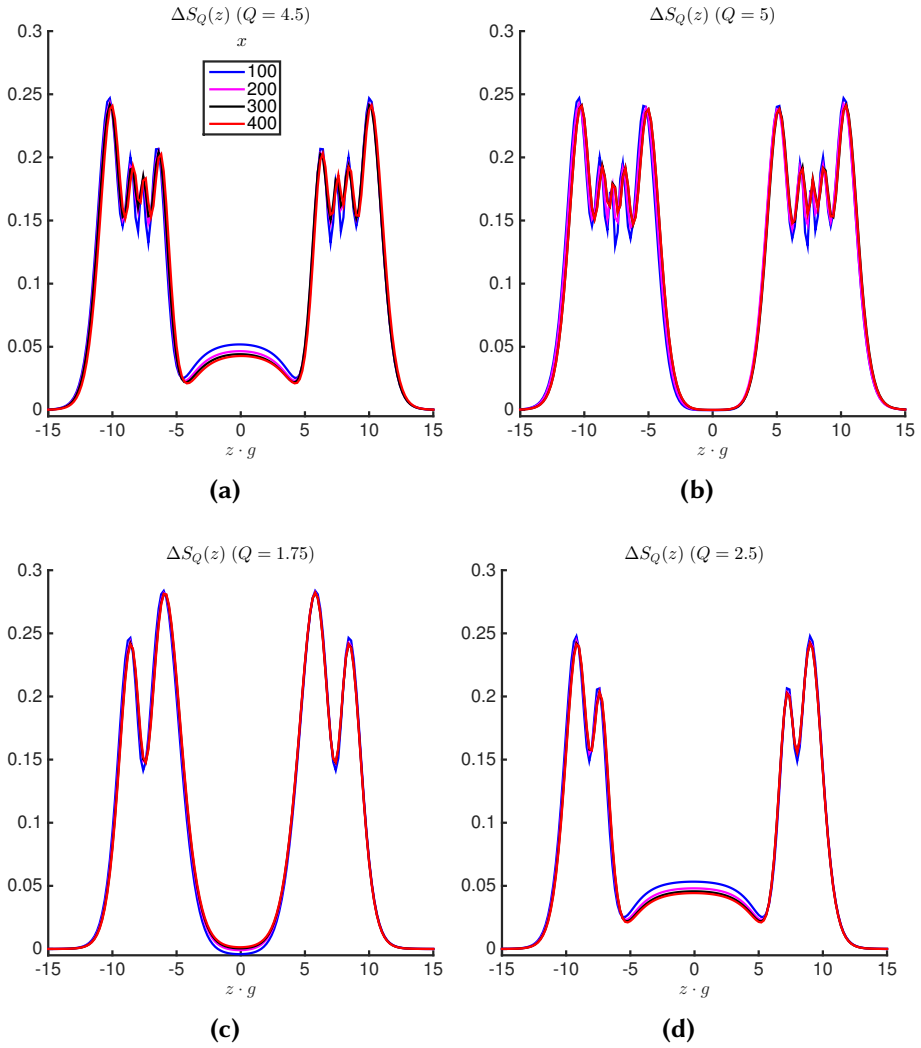


Figure 3.14.: $m/g = 0.5$, $Lg = 15.25$. $\Delta S_Q(z)$ for different values of Q and scaling to $x \rightarrow +\infty$. (a) $Q = 4.5$. (b) $Q = 5$. (c) $Q = 1.75$. (d) $Q = 2.5$.

Finite temperature

B. Buyens, F. Verstraete, K. Van Acoleyen

‘Hamiltonian simulation of the Schwinger model at finite temperature’
arXiv:1606.03385 (2016)

4.1. Introduction

When coupling a system to a heat bath it is described by mixed density operators instead of pure vector states. In one dimension the straightforward generalization of MPS to operators are the Matrix Product Operators (MPO) [119, 120]. Just like MPS are an efficient and faithful representation for ground states of local gapped Hamiltonians [71], MPO are an efficient approximation for Gibbs states [121, 122] which describe the system in thermal equilibrium. Therefore we expect TNS to be useful for investigating canonical and grand canonical ensembles for gauge field theories. This has recently been confirmed by a successful study of the chiral condensate of the Schwinger model at finite temperature [34].

In this chapter we also study the Schwinger model in thermal equilibrium, but now also focussing on asymptotic confinement and \mathcal{CT} symmetry breaking, thereby continuing our work at zero temperature of chapter 3. In the next section we discuss the setup of our simulations using MPO. To test our method, we compute in section 4.3 the chiral condensate and compare our results with earlier studies [15, 34]. In section 4.4 we turn our attention to the asymptotic aspects of confinement for a static quark-antiquark pair with fractional charge. At high temperatures we find that the string tension becomes exponentially small. Furthermore, we also study the \mathcal{CT} symmetry and find strong indications that the spontaneous symmetry breaking of the

ground state at zero temperature vanishes, as soon as a nonzero temperature is turned on.

4.2. Setup

4.2.1. Hamiltonian and gauge invariance

We start from the same setup as in subsection 2.2.1. The Hamiltonian is defined on a lattice of $2N$ sites

$$\mathcal{H} = \frac{g}{2\sqrt{x}} \left(\sum_{n=1}^{2N} [L(n) + \alpha]^2 + \frac{\sqrt{x}}{g} m \sum_{n=1}^{2N} (-1)^n (\sigma_z(n) + (-1)^n) + x \sum_{n=1}^{2N-1} (\sigma^+(n) e^{i\theta(n)} \sigma^-(n+1) + h.c.) \right), \quad (4.1)$$

taking into account that we are interested in the thermodynamic limit $N \rightarrow +\infty$. As mentioned in section 3.3, the electric background field can be interpreted to originate from an infinitely heavy quark-antiquark pair, separated infinitely far from each other, $N \rightarrow +\infty$, where the quark at site $n = 1$ has charge $g\alpha$ and the antiquark at site $n = 2N$ has charge $-g\alpha$.

Here we consider the system coupled to a heat reservoir with fixed temperature T . If the system only exchanges energy with this reservoir and it reaches thermal equilibrium it is represented by the canonical ensemble. The density operator that describes this canonical ensemble is the Gibbs state $\rho(\beta) = e^{-\beta\mathcal{H}}$, where $\beta = 1/T$ is the inverse temperature. The probability of finding the system in a particular eigenstate $|\mathcal{E}\rangle$ of \mathcal{H} is $e^{-\beta\mathcal{E}}/Z(\beta)$ where $Z(\beta) = \text{tr}(e^{-\beta\mathcal{H}})$ is the partition function. Because the physical sector corresponds to states with $G(n) = 0$,

$$G(n) = L(n) - L(n-1) + \frac{\sigma_z(n) + (-1)^n}{2},$$

we need to exclude the (micro)states that are not gauge invariant. In particular, the probability to find the system in an eigenstate $|\mathcal{E}\rangle$ of \mathcal{H} which is not gauge invariant, $G(n)|\mathcal{E}\rangle \neq 0$, should be zero: $\langle \mathcal{E} | \rho(\beta) | \mathcal{E} \rangle = 0$. Therefore we need to project \mathcal{H} onto the $(G(n) = 0)$ -subspace. If \mathcal{P} is the projector onto the $(G(n) = 0)$ -subspace, the canonical ensemble is thus described by the density operator

$$\rho(\beta) = \mathcal{P} e^{-\beta\mathcal{H}} (= \mathcal{P} e^{-\beta\mathcal{H}} \mathcal{P} = e^{-\beta\mathcal{H}} \mathcal{P}). \quad (4.2)$$

The ensemble average of a given gauge invariant observable \mathcal{Q} is computed as

$$\langle \mathcal{Q} \rangle_\beta = \frac{\text{tr}(\mathcal{P}\mathcal{Q}\mathcal{P}e^{-\beta\mathcal{H}})}{Z(\beta)} \text{ with } Z(\beta) = \text{tr}(\mathcal{P}e^{-\beta\mathcal{H}})$$

the partition function. Note that this expectation value indeed corresponds to the expectation value obtained from the Wilsonian path integral [70].

4.2.2. Gauge invariant MPO

A general operator ρ in the lattice system eq. (4.1) takes the form:

$$\rho = \sum_{\boldsymbol{\kappa}} C^{(\kappa_1, \kappa'_1), \dots, (\kappa_{2N}, \kappa'_{2N})} |\boldsymbol{\kappa}\rangle \langle \boldsymbol{\kappa}'|$$

with $C^{(\kappa_1, \kappa'_1), \dots, (\kappa_{2N}, \kappa'_{2N})} \in \mathbb{C}$, $\kappa_n = (s_n, p_n) \in \{-1, 1\} \times \mathbb{Z}[p_{n+1}^{\min}, p_{n+1}^{\max}]$ and $\boldsymbol{\kappa} = |\kappa_1\rangle \dots |\kappa_{2N}\rangle$. Note that we only retained a finite range for the eigenvalues p_n of $L(n)$ for our numerical scheme. We will address the issue of which values to take for p^{\min} and p^{\max} in subsection 4.2.3. The projector \mathcal{P} onto the $(G(n) = 0)$ -subspace equals

$$\mathcal{P} = \sum_{\boldsymbol{\kappa}} \left(\prod_{n=1}^{2N} \delta_{p_n - p_{n-1}, \frac{s_n + (-1)^n}{2}} \right) |\boldsymbol{\kappa}\rangle \langle \boldsymbol{\kappa}|. \quad (4.3)$$

To obtain a purification of the state \mathcal{P} we consider the Hilbert space

$$\mathcal{H}_{full} = \bigotimes_{n=1}^{2N} \mathcal{H}_n \otimes \mathcal{H}_n^a$$

where $\mathcal{H}_n^a = \text{span}\{|\kappa_n^a\rangle_n = |s_n^a\rangle_n |p_n^a\rangle\}$ is an auxiliary Hilbert space with the same dimension as \mathcal{H}_n . If we introduce the MPS [119]

$$|\Psi[A]\rangle = \sum_{\boldsymbol{\kappa}, \boldsymbol{\kappa}^a} \text{tr} \left(A_1^{\kappa_1, \kappa_1^a} \dots A_{2N}^{\kappa_{2N}, \kappa_{2N}^a} \right) |\boldsymbol{\kappa}, \boldsymbol{\kappa}^a\rangle \in \mathcal{H}_{full},$$

$$|\boldsymbol{\kappa}, \boldsymbol{\kappa}^a\rangle = |\kappa_1\rangle_1 |\kappa_1^a\rangle_1 \dots |\kappa_{2N}\rangle_{2N} |\kappa_{2N}^a\rangle_{2N},$$

where

$$[A_n^{(s,p), (s^a, p^a)}]_{(q, \alpha); (r, \beta)} = [a_n]_{\alpha q, \beta r} \delta_{r, q + [s + (-1)^n]/2} \delta_{p, r} \delta_{s, s^a} \delta_{p^a, q + [s^a + (-1)^n]/2}, \quad (4.4)$$

then tracing out the auxiliary Hilbert space $\mathcal{H}^a = \bigotimes_{n=1}^{2N} \mathcal{H}_n^a$ gives us \mathcal{P} up to a normalization factor:

$$\text{tr}_{\mathcal{H}^a} (|\Psi[A]\rangle \langle \Psi[\bar{A}]|) \propto \mathcal{P}.$$

We refer to subsection 3.4.1 of part II for a more detailed derivation.

For $\beta = 0$ we have that $\rho(0)$ is the projector \mathcal{P} on the $(G(n) = 0)$ -subspace. $[\mathcal{H}, \mathcal{P}] = 0$ implies that $\rho(\beta) = e^{-\beta\mathcal{P}\mathcal{H}\mathcal{P}} = e^{-\beta\mathcal{H}/2}\mathcal{P}e^{-\beta\mathcal{H}/2}$. As a consequence, if we evolve the purification $|\Psi[A(\beta)]\rangle$ according to

$$|\Psi[A(\beta)]\rangle = e^{-(\beta/2)\mathcal{H}} |\Psi[A(0)]\rangle. \quad (4.5)$$

we have for all values of β that

$$\rho(\beta) \propto \text{tr}_{\mathcal{H}^a} (|\Psi[A(\beta)]\rangle \langle\Psi[\bar{A}(\beta)]|).$$

Note that because $A_n(\beta = 0)$ takes the form eq. (4.4), gauge invariance of \mathcal{H} implies that during the evolution eq. (4.5) $A_n(\beta)$ will have a similar form:

$$[A_n^{(s,p),(s^a,p^a)}(\beta)]_{(q,\alpha);(r,\beta)} = [a_n^{q,s,s^a}(\beta)]_{\alpha q,\beta r} \delta_{r,q+[s+(-1)^n]/2} \delta_{p,r} \delta_{p^a,q+[s^a+(-1)^n]/2} \quad (4.6)$$

where $a_n^{q,s,s^a} \in \mathbb{C}^{D^q \times D^r}$ represents the variational freedom of the MPS $|\Psi[A(\beta)]\rangle$. Note that contrary to eq. (4.4) a_n^{q,s,s^a} now also depends on s, p and s^a . The total bond dimension of this MPS is $D = \sum_q D^q$. Finally we note that by restricting ourselves to finite eigenvalues of $L(n)$ we can not represent the initial state $\rho(0)$ exactly. Fortunately, as we will see later this does not spoil our results for non-zero β , see subsection 4.2.3 and in particular figs. 4.1a and 4.2a.

By performing our simulations in the thermodynamic limit $N \rightarrow +\infty$ we can impose translation invariance over two sites on our state by letting $a_n^{q,s,s^a}(\beta)$ only depend on the parity of n :

$$a_{2n-1}^{q,s,s^a}(\beta) = a_1^{q,s,s^a}(\beta) \text{ and } a_{2n}^{q,s,s^a}(\beta) = a_2^{q,s,s^a}(\beta), \forall n.$$

4.2.3. iTEBD for thermal evolution

In the previous subsection we purified the Gibbs state $\rho(\beta) = \mathcal{P}e^{-\beta\mathcal{H}}$ by the MPS $|\Psi[A(\beta)]\rangle$. Using gauge invariance and translation invariance over two sites we identified the variational degrees of freedom $a_1^{q,s,s^a}, a_2^{q,s,s^a} \in \mathbb{C}^{D^q \times D^r}$ of $|\Psi[A(\beta)]\rangle$, see eq. (4.6). There now only remains to solve eq. (4.5) within the MPS manifold which is performed by using the iTEBD [45]. Specifically, we perform a fourth order Trotter decomposition of $e^{-(d\beta/2)H}$ for small steps $d\beta$ [123]. Afterwards we project

$$|\Psi[A(\beta + d\beta)]\rangle = e^{-(\beta/2)\mathcal{H}} |\Psi[A(\beta)]\rangle$$

to a MPS with smaller bond dimensions D^q . In this way we avoid the bond dimensions to increase exponentially with β . This projection is performed as

an effective truncation in the Schmidt spectrum of $|\Psi[A(\beta)]\rangle$ with respect to the bipartition $\{\mathcal{A}_1^n = \mathbb{Z}[1, n], \mathcal{A}_2^n = \mathbb{Z}[n + 1, 2N]\}$.

The Schmidt decomposition with respect to the bipartition $\{\mathcal{A}_1^n, \mathcal{A}_2^n\}$ reads

$$|\Psi[A(\beta)]\rangle = \sum_{q=p^{\min}}^{p^{\max}} \sum_{\alpha_q=1}^{D^q} \sqrt{\sigma_{n,\alpha_q}^q} |\psi_{q,\alpha_q}^{\mathcal{A}_1^n}\rangle |\psi_{q,\alpha_q}^{\mathcal{A}_2^n}\rangle \quad (4.7)$$

where $|\psi_{q,\alpha_q}^{\mathcal{A}_k^n}\rangle$ are orthonormal unit vectors in the Hilbert space $\mathcal{H}_{\mathcal{A}_k^n} = \bigotimes_{j \in \mathcal{A}_k^n} (\mathcal{H}_j \otimes \mathcal{H}_j^a)$ ($k = 1, 2$) and the Schmidt values σ_{n,α_q}^q are non-negative numbers that sum to one. Note that the Schmidt values are labeled by the eigenvalues of $L(n)$ which is a consequence of eq. (3.25). Due to translation symmetry over two sites σ_{n,α_q}^q only depends on the parity of n : $\sigma_{2n-1,\alpha_q}^q = \sigma_{1,\alpha_q}^q$ and $\sigma_{2n,\alpha_q}^q = \sigma_{2,\alpha_q}^q, \forall n$. From eq. (4.7) one observes that the limit $D^q \rightarrow +\infty, p^{\min} \rightarrow -\infty$ and $p^{\max} \rightarrow +\infty$ yields an exact representation of the state $|\Psi[A(\beta)]\rangle$ and thus of the Gibbs state. The success of the approach using MPO is explained by the fact that by using relatively small values of D^q we can obtain very accurate approximations of the Gibbs state [121, 122]. After every Trotter step the iTEBD algorithm discards all Schmidt values $\sigma_{n,\alpha_q}^q < \epsilon^2$ with ϵ a preset tolerance. In particular, when all Schmidt values σ_{n,α_q}^q corresponding to an eigenvalue q are smaller than ϵ^2 this eigenvalue sector is discarded and p^{\min} is increased or p^{\max} is decreased. In this way p^{\min}, p^{\max} and D^q are adapted dynamically. We refer to subsection 4.3.2 of part II for the details on the implementation of the iTEBD algorithm.

In fig. 4.1a we plot p^{\max} and p^{\min} for our simulations with $m/g = 0.25$, $x = 200$, $\alpha = 0$, once with preset tolerance $\epsilon = 10^{-6}$ and once with preset tolerance $\epsilon = 5 \times 10^{-6}$. For $\epsilon = 10^{-6}$ we started with $p^{\max} = -p^{\min} = 25$ and for $\epsilon = 5 \times 10^{-6}$ we started with $p^{\max} = -p^{\min} = 20$. We observe that p^{\max} and p^{\min} decrease very fast in magnitude as a function of β to $p^{\max} = 3$ and $p^{\min} = -3$. The fact that we can accurately describe the system with a finite range of eigenvalues of the electric field should not come as a surprise. Physically, we do not expect it to be very likely to observe the system, which is in thermal equilibrium, in a state with extremely large electric field compared to the temperature. This follows from the first term in the Hamiltonian eq. (4.1) that appears in the Gibbs state $\rho(\beta) = \mathcal{P} \exp(-\beta\mathcal{H})$. Note that the p^{\min} and p^{\max} at $\beta g = 10$ corresponds to the values of p^{\max} and p^{\min} in our simulations at zero temperature in sections 2.1 and 2.2. In the inset we show the evolution of the maximum bond dimension over all the charge sectors. The bond dimension is an almost linearly increasing function of βg for $\beta g \lesssim 5$. When $\beta g \gtrsim 5$ the bond dimension remains almost constant, indicating that for these parameters $\beta g \gtrsim 5$ is already very close to

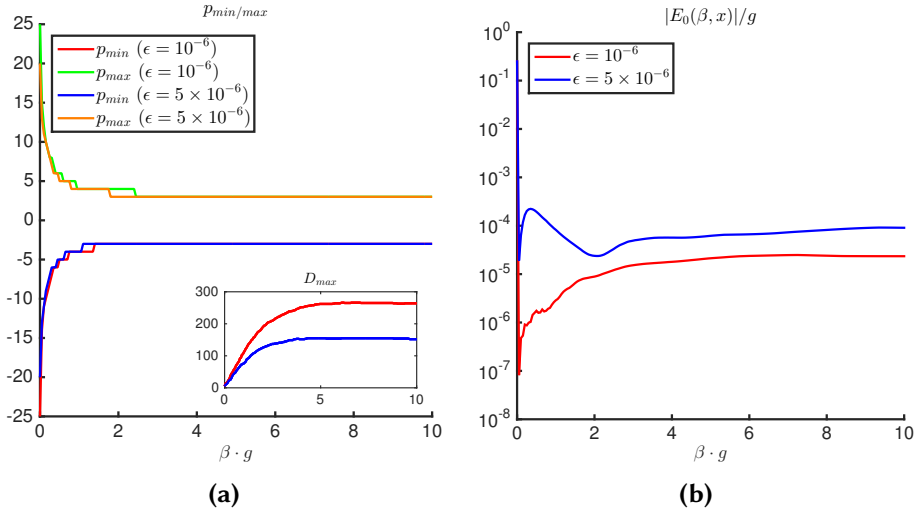


Figure 4.1.: $m/g = 0.25, x = 200, \alpha = 0$. (a) p^{\min} and p^{\max} for $\epsilon = 10^{-6}$ and $\epsilon = 5 \times 10^{-6}$. Inset: maximum bond dimension over all the charge sectors. (b): Electric field per site $E_0(\beta, x)$. Because $\alpha = 0$ we should have $E_0(\beta, x) = 0$.

zero temperature. If we want better accuracy one needs smaller values of ϵ . In the inset of 4.1a one observes that this requires more variational freedom in the MPS representation of $|\Psi[A(\beta)]\rangle$ and thus longer computation time.

As a first check on our method we show in fig. 4.1b the electric field $E_\alpha(\beta, x)$ at lattice spacing $a = 1/\sqrt{gx}$ where

$$E_\alpha(\beta, x) = \frac{g}{2} \text{tr} \left(\frac{\mathcal{P} e^{-\beta \mathcal{H}} \mathcal{P}}{\text{tr}(\mathcal{P} e^{-\beta \mathcal{H}})} (L(1) + L(2) + 2\alpha) \right).$$

For zero background field, $\alpha = 0$, this quantity should be zero which follows from \mathcal{CT} symmetry of the Hamiltonian (\mathcal{C} is charge conjugation: $\sigma^z \rightarrow -\sigma^z, L \rightarrow -L$, and \mathcal{T} is translation over one site). For very small values of βg the errors on $E_0(\beta, x)$ are relatively large. This is a consequence of taking finite values for p^{\min} and p^{\max} ; as we discussed in the previous section, for $\beta g = 0$ one should consider all possible electric field values ($p \in [-\infty, +\infty]$) to represent the Gibbs state $\rho(0) = \mathcal{P}$. Fortunately, discarding these Schmidt values for small values of βg does not spoil the results for larger values of βg . Indeed, for $\beta g > 0$ the errors on $E_0(\beta, x)/g$ are only of order 10^{-4} . In this plot one also observes that taking a smaller value for ϵ leads to better accuracy. From this example it is clear that, unless one is interested in the $\beta \rightarrow 0$ limit, one can safely neglect eigenvalue sectors q with $q + \alpha$ larger than 20 in magnitude.

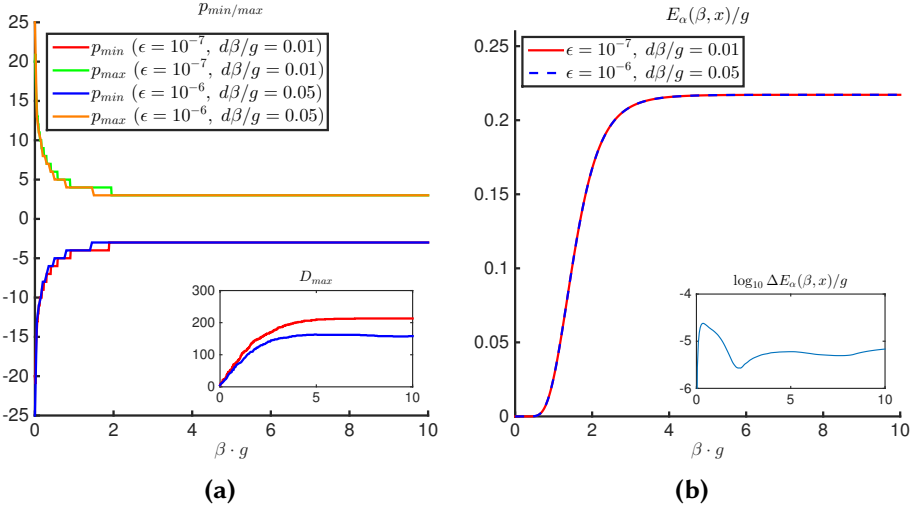


Figure 4.2.: $m/g = 0.5, x = 100, \alpha = 0.25$. (a) p^{min} and p^{max} for $\epsilon = 10^{-7}, d\beta = 0.01$ and $\epsilon = 10^{-6}, d\beta = 0.05$. Inset: maximum bond dimension over all the charge sectors. (b): Electric field per site $E_\alpha(\beta, x)/g$. Inset: 10-base logarithm of difference of $E_\alpha(\beta, x)/g$ between simulations with $\epsilon = 10^{-7}, d\beta = 0.01$ and $\epsilon = 10^{-6}, d\beta = 0.05$.

In fig. 4.2a and fig. 4.2b we compare two simulations for different values of the step size $d\beta$ and ϵ , now for nonzero background field $\alpha \neq 0$. The first one has $(d\beta, \epsilon) = (0.05, 10^{-6})$ and the second one has $(d\beta, \epsilon) = (0.01, 10^{-7})$. In fig. 4.2b we compare the electric field, which is non-zero for $\alpha \neq 0$, for both simulations and observe that the results are the same up to order 10^{-5} . For $\beta g \lesssim 2$ the difference is slightly larger, but still sufficiently small. This slightly larger error mainly originates from ignoring large eigenvalues of $L(n)$ at $\beta g = 0$. The fact that the results for different choices of $d\beta$ and ϵ are in agreement justifies taking $(d\beta, \epsilon) = (0.05, 10^{-6})$ for most of our simulations.

4.3. Chiral condensate

4.3.1. Introduction

In QCD with massless up and down quarks, the non-zero chiral quark condensate signals spontaneous symmetry breaking of the chiral symmetry. This spontaneous symmetry breaking occurs for relatively low temperatures and explains the existence of pions [124, 125]. For physical quark masses this chiral symmetry is explicitly broken. However, one can still distinguish two phases separated by a pseudo-critical temperature $T_c \approx 150 - 190$

MeV. For temperatures $T \ll T_c$ thermal expectation values are dominated by the pions which are a ‘remnant’ of the chiral symmetry, while at high temperatures the thermodynamics are well described by the quarks and the gluons. The pions can be interpreted as an example of confined quark bound states that dominate the physics only below T_c . Therefore, not so surprisingly, it is also suggested that around this pseudo-critical temperature QCD changes from the confined phase to the deconfined phase, although this is still a subject of debate [126, 127]. In the confined phase the gluons confine the quarks to baryons and mesons while in the deconfined phase QCD should resemble a quark-gluon plasma.

Here we will consider the chiral condensate of the Schwinger model to benchmark our method. In the one-flavor massless Schwinger model the non-zero chiral condensate is a consequence of the chiral symmetry being anomalous. The non-zero chiral condensate also determines the confining behavior of external charges in mass perturbation theory [20]. For $m/g = 0$, the chiral condensate is computed analytically by Sachs and Wipf [15]. Besides the studies in the exactly solvable case ($m/g = 0$) [15, 17], there are results available in mass perturbation theory ($m/g \ll 1$) [20, 26]. Furthermore, in [26] an approach using a generalized Hartree-Fock method beyond mass perturbation theory was studied. Recently, MPO simulations succeeded in recovering the analytical result of Sachs and Wipf for $m/g = 0$ and also obtained the chiral condensate in the non-perturbative regime [34].

On the lattice with spacing $ga = 1/\sqrt{x}$ and $2N$ sites the chiral condensate $\Sigma(\beta) = \langle \bar{\Psi}(z)\Psi(z) \rangle_\beta$ equals

$$\Sigma(\beta, x) = \frac{g\sqrt{x}}{2N} \sum_{n=1}^{2N} (-1)^n \text{tr} \left(\frac{\mathcal{P}e^{-\beta\mathcal{H}}}{\text{tr}(\mathcal{P}e^{-\beta\mathcal{H}})} \frac{\sigma_z(n) + 1}{2} \right) \quad (4.8)$$

and can be computed directly in the thermodynamic limit ($N \rightarrow +\infty$) using the ansatz eq. (4.5), see subsection 4.3.2 of part II for the details. For $m/g = 0$ we compare our simulations with the analytical result in subsection 4.3.2. In subsection 4.3.3 we compute a renormalized chiral condensate in the non-perturbative regime: $m/g \sim \mathcal{O}(1)$. The results are compared with the recent simulations of Bañuls *et al.* [34].

4.3.2. The chiral limit $m/g = 0$

Using path integral methods Sachs and Wipf [15] found that for $m/g = 0$:

$$\Sigma_{SW}(\beta) = \frac{g}{2\pi^{3/2}} e^{\gamma} e^{2I(\beta g/\sqrt{\pi})}, I(u) = \int_0^{+\infty} \frac{dt}{1 - e^{u \cosh(t)}}. \quad (4.9)$$

As will become clear later, it is convenient to remove the scaling in x originating from the ground state expectation value. More specifically, for a fixed

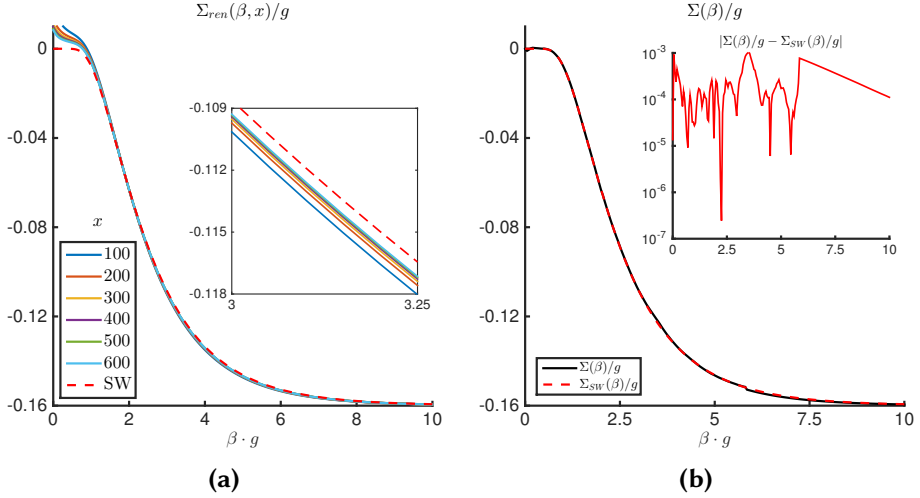


Figure 4.3.: $m/g = 0$. (a): $\Sigma_{ren}(\beta, x)$ for different values of x (full line) compared with the analytical result eq. (4.9) (SW, dashed line). (b): Chiral condensate in the continuum limit (full line) compared with the analytical result eq. (4.9). Inset: difference with the analytical result.

value of x we subtract the ground state expectation value $\Sigma(x) = \Sigma(+\infty, x)$ and add the ground state expectation value in the continuum limit $\Sigma = \Sigma(+\infty, +\infty)$, i.e. we consider

$$\Sigma_{ren}(\beta, x) = \Sigma(\beta, x) - \Sigma(x) + \Sigma. \quad (4.10)$$

The quantities $\Sigma(x)$ and Σ have already been computed before in subsection 2.1.4 (see also [34]). These changes won't affect the continuum limit: $\lim_{x \rightarrow +\infty} \Sigma(\beta, x) = \lim_{x \rightarrow +\infty} \Sigma_{ren}(\beta, x)$. In fig. 4.3a we plot the chiral condensate for $x = 100, 200, 300, 400, 500, 600$ and compare it with eq. (4.9). One indeed observes that even at $x = 100$ our result is close to the analytical result. This is a consequence of subtracting the scaling at zero temperature, i.e. using the chiral condensate Σ_{ren} defined in eq. (4.10), see also fig. B.1a and fig. B.1b in appendix B.1. Only at small values of βg a continuum extrapolation is necessary. As in [34] this is performed by fitting $\Sigma(\beta, x)$ to (see appendix B.1 for the details)

$$f_1(x) = A_1 + B_1 \frac{\log(x)}{\sqrt{x}} + C_1 \frac{1}{\sqrt{x}} \quad (4.11a)$$

and to

$$f_2(x) = A_2 + B_2 \frac{\log(x)}{\sqrt{x}} + C_2 \frac{1}{\sqrt{x}} + D_2 \frac{1}{x}. \quad (4.11b)$$

We show our continuum result in fig. 4.3b and we observe now also nice agreement with eq. (4.9) for small values of βg . In the inset we show the difference with this analytical result. For $\beta g \gtrsim 5$ the difference between $\Sigma(\beta, x)$ for different x -values becomes too small, only of order 10^{-4} , to obtain a reliable continuum extrapolation. Therefore we used for $\beta g \gtrsim 5$ our results at $x = 100$ as our continuum result. To have better precision for these values of βg one should lower ϵ and/or use a smaller time step $d\beta$. This would in turn require longer computation time. Note that for large values of βg the thermal corrections to the ground state expectation value are exponentially small anyway.

4.3.3. $m/g \neq 0$: renormalization of $\Sigma(\beta)$

At zero temperature the chiral condensate diverges for $m/g \neq 0$. By subtracting the free chiral condensate ($g = 0$) a UV finite quantity was obtained in subsection 2.1.4. At finite temperature it is sufficient to remove the divergent part at zero temperature. Like in the ($m/g = 0$)-case, for a fixed value of x , we subtract the ground state expectation value $\Sigma(x) = \Sigma(+\infty, x)$, but now we add the renormalized chiral condensate of the ground state $\Sigma_{ren} = \Sigma_{ren}(+\infty, +\infty)$ in the continuum limit. Eq. (4.10) thus becomes

$$\Sigma_{ren}(\beta, x) = \Sigma(\beta, x) - \Sigma(x) + \Sigma_{ren}$$

with

$$\Sigma_{ren} = \lim_{x \rightarrow +\infty} \Sigma(x) + \frac{m}{\pi g} \frac{1}{\sqrt{1 + \frac{m^2}{g^2 x}}} K\left(\frac{1}{1 + \frac{m^2}{g^2 x}}\right),$$

where K is the complete elliptic integral of the first kind, see eq. (2.4). The values of Σ_{ren} for different values of m/g have been computed in subsection 2.1.4, see table 2.3.

In fig. 4.4a we show the results for $x = 100$ (full line) and $x = 300$ (dashed line). As can be seen in the inset, the chiral condensate for $x = 100$ and $x = 300$ are almost on top of each other. This suggests that our results are already very close to the continuum limit $x \rightarrow +\infty$. For small values of βg a continuum estimate is obtained by performing a fit of the form eq. (4.11). For larger values of βg the difference between the results for different x -values becomes too small to obtain a reliable continuum estimate, so our results for $x = 100$ served as our continuum result. We refer to appendix B.1 for the details.

In fig. 4.4b we compare our continuum estimates (full line) with the results in [34] (dashed line). Clearly, the results are in very good agreement with each other. Note that this is a non-trivial check on MPO methods for gauge

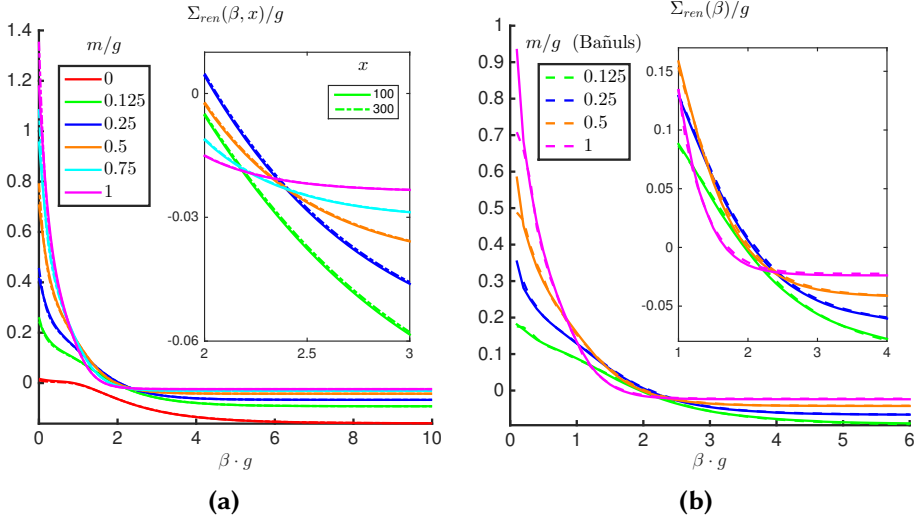


Figure 4.4. Chiral condensate for $m/g \neq 0$. Color legend left up applies to all plots. (a): Renormalized chiral condensate $\Sigma_{ren}(\beta, x)$ for $x = 100$ (full line) and $x = 300$ (dashed line). Inset: zooming in on the interval $\beta g \in [2, 3]$. (b): Continuum estimation for chiral condensate (full line) and comparison with [34] (dashed line). Inset: zooming in on the interval $\beta g \in [1, 4]$.

theories because in both approaches the optimization methods are different. In [34] they perform their simulations on a finite lattice and take the thermodynamic limit on the level of the expectation values. Also, instead of purifying the Gibbs state, they apply $\mathcal{P}e^{-\beta\mathcal{H}}$ immediately to the MPO. After every step they project this MPO to a MPO with smaller bond dimension D which has been fixed before. In contrast, we did our simulations immediately in the thermodynamic limit and adapted the bond dimension by investigating the Schmidt spectrum of the purified state.

Looking at the chiral condensate, one observes that it diverges for $\beta = 0$ which is a consequence of our renormalization scheme. Indeed, for $\beta = 0$ we have that $\Sigma(\beta, x) = 0$ while $\Sigma(x)$ diverges logarithmically in the limit $x \rightarrow +\infty$. For other values of βg the chiral condensate is UV finite and decreases to its ground state expectation value as a function of βg . The chiral condensate tends faster to its ground state expectation value for larger values of m/g . For instance, in fig. 4.4 we observe that for $m/g = 1$ the chiral condensate is already very close to its ground state expectation value for $\beta g \approx 2$ while for $m/g = 0$ even for $\beta g \approx 4$ there is still a significant difference with the ground state expectation value. This is explained by the fact that the mass gap of \mathcal{H} grows with m/g for $\alpha = 0$, see table 2.1 in

subsection 2.1.2.

4.4. Asymptotic confinement

4.4.1. Introduction

As mentioned in the previous section, QCD changes from the confined to the deconfined phase around a pseudo-critical temperature T_c . For infinitely heavy quark masses this phase transition is detected by the spontaneous breaking of the $SU(3)$ -center symmetry or equivalently by examining the free energy of an infinitely separated probe quark anti-quark pair, which diverges in the confining phase and is finite in the deconfining phase. In the case of physical QCD, with finite quark masses, the notion of confinement versus deconfinement is less clear [109]: the infinitely separated probe pair will always be screened by charge production out of the vacuum, leading to a finite free energy, already at zero temperature.

For the Schwinger model we have a similar situation: for integer probe charges the confining string will always be broken at large separation of the probe pair, due to screening by the dynamical fermions. However, this is not the case if we introduce fractional probe charges. In that case, at zero temperature, for $m/g \neq 0$ a confining string remains even at infinite separation [5]. So by probing the vacuum with fractional charge pairs at infinity we can examine the confining nature of the theory at finite temperatures.

At zero temperature we already elaborated on this in chapter 3 for finite and infinite distance Lg between the quark and antiquark. Our simulations confirmed the known results that for $m/g = 0$ the quark-antiquark potential is never confining for large Lg and that for $m/g \neq 0$ it is only confining if the charge of the heavy probe quarks is non-integer. A similar result has been shown when the system is in thermal equilibrium with a heat bath for $m/g = 0$ [19] and $m/g \ll 1$ [8, 12, 18]. But notice, that a critical temperature was found, above which the string tension is exponentially suppressed with the temperature. In the next subsection 4.4.2 we will focus on this phenomenon in the non-perturbative regime $m/g \sim \mathcal{O}(1)$. As we will discuss in subsection 4.4.3, our simulations in this mass regime also allow us to investigate the \mathcal{CT} symmetry restoration in the $\alpha \rightarrow 1/2$ limit. But let us now first discuss the general setup of the simulations.

Assuming that the quark has charge $g\alpha$ and the antiquark has charge $-g\alpha$, this setup can be translated to a uniform background field $g\alpha$ in the Hamiltonian \mathcal{H}_α , see eq. (4.1). Note that we denoted the α -dependence of \mathcal{H} in \mathcal{H}_α . The string tension at finite x , $\sigma_\alpha(\beta, x)$, is obtained from the partition

function $Z_\alpha(\beta, x) = \text{tr}(e^{-\beta\mathcal{H}_\alpha}\mathcal{P})$ as

$$\begin{aligned}\sigma_\alpha(\beta, x) &= -\frac{\sqrt{x}}{2N} \frac{1}{\beta} \log \left(\frac{Z_\alpha(\beta, x)}{Z_0(\beta, x)} \right) \\ &= \frac{\sqrt{x}}{2N} (F_\alpha(\beta, x) - F_0(\beta, x))\end{aligned}$$

where $F_\alpha(\beta, x) = -(1/\beta) \log(Z_\alpha(\beta, x))$ is the free energy for $Lg = +\infty$. The MPO framework enables us to compute the partition function $Z_\alpha(\beta, x)$ and thus the free energy per unit of length $\mathcal{F}_\alpha(\beta, x) = \frac{\sqrt{x}}{2N} F_\alpha(\beta, x)$ directly, also in the thermodynamic limit ($N \rightarrow +\infty$), see eq. (4.58) of subsection 4.3.2 in part II. This is in contrast to Monte-Carlo methods where the computation of the free energy is a difficult task [66, 128–130].

Other quantities that will be of interest here are the electric field and the Gibbs free entropy. The electric field,

$$E_\alpha(\beta, x) = \lim_{N \rightarrow +\infty} \frac{g}{2N} \sum_{n=1}^{2N} \text{tr} \left(\frac{e^{-\beta\mathcal{H}_\alpha}\mathcal{P}}{Z_\alpha(\beta, x)} (L(n) + \alpha) \right),$$

gives us more information about the α -dependence of the string tension because it equals $E_\alpha(\beta, x) = \partial_\alpha \sigma_\alpha(\beta, x)/g$. The (Gibbs) entropy per unit of length,

$$\mathcal{S}_\alpha(\beta, x) = -\frac{\sqrt{x}}{2N} \text{tr} \left(\frac{e^{-\beta\mathcal{H}_\alpha}\mathcal{P}}{Z_\alpha(\beta, x)} \log \left(\frac{e^{-\beta\mathcal{H}_\alpha}\mathcal{P}}{Z_\alpha(\beta, x)} \right) \right),$$

is a measure for thermal fluctuations in the Gibbs state. When the canonical ensemble behaves as the ground state and corrections to ground state expectation values are negligible, i.e. when the system is effectively at zero temperature, the entropy is very small and vice versa.

$\mathcal{S}_\alpha(\beta, x)$ is obtained from the average energy per unit of length $\mathcal{E}_\alpha(\beta, x) = \frac{\sqrt{x}}{2N} \frac{1}{Z_\alpha(\beta, x)} \text{tr}(\mathcal{H}_\alpha e^{-\beta\mathcal{H}_\alpha}\mathcal{P})$ via the standard relation $\mathcal{S}_\alpha(\beta, x) = -\beta(\mathcal{F}_\alpha(\beta, x) - \mathcal{E}_\alpha(\beta, x))$ for Gibbs states. For every value of βg we subtract its ($\alpha = 0$)-value from it and we thus consider $\Delta\mathcal{S}_\alpha(\beta, x) = \mathcal{S}_\alpha(\beta, x) - \mathcal{S}_0(\beta, x)$. Because retaining only a finite range of eigenvalues of $L(n)$ leads to the same errors in $\mathcal{S}_\alpha(\beta, x)$ and $\mathcal{S}_0(\beta, x)$, the quantity $\Delta\mathcal{S}_\alpha(\beta, x)$ can be obtained accurately at all temperatures. We will see later that $\Delta\mathcal{S}_\alpha(\beta, x)$ is actually still a good measure for characterizing the transition from the effective zero temperature behavior at small temperatures towards a thermal behavior at larger temperatures, see subsection 4.4.2 and in particular fig. 4.5d.

One can also compute the chiral condensate $\Sigma_\alpha(\beta, x)$. Contrary to the previous section, we will now renormalize it by subtracting its ($\alpha = 0$)-value and thus consider $\Delta\Sigma_\alpha(\beta, x) = \Sigma_\alpha(\beta, x) - \Sigma_0(\beta, x)$.

As shown in appendix B.2 for $m/g = (0.125, 0.25)$ and $\alpha = (0.1, 0.25, 0.45)$, all these quantities are UV finite quantities. There we extrapolate our results for $x = 100, 125, \dots, 300$ to the continuum limit for all values of $\beta g \in [0.5, 10]$. For all the quantities our data could be fitted against a simple polynomial function in $1/\sqrt{x}$, see fig. B.3 in appendix B.2. As an extra check on our results we observed convergence to the results of chapter 3 at large values of βg for the string tension and the electric field, see fig. B.4. We find that at $x = 100$ our results were already very close to the continuum limit. When $m/g \gtrsim 0.5$, the results for different x -values are very close to each other, see fig. B.5 in appendix B.2, and we can thus expect to be close to the continuum limit at $x = 100$. Therefore we will restrict ourselves in the main text to $x = 100$.

Physics is periodic in α with period 1 and due to \mathcal{CT} symmetry

$$\begin{aligned}\sigma_\alpha(\beta, x) &= \sigma_{1-\alpha}(\beta, x), \Delta\Sigma_\alpha(\beta, x) = \Delta\Sigma_{1-\alpha}(\beta, x) \\ E_\alpha(\beta, x) &= -E_{1-\alpha}(\beta, x), \mathcal{S}_\alpha(\beta, x) = \mathcal{S}_{1-\alpha}(\beta, x).\end{aligned}$$

Therefore we can restrict ourselves to $\alpha \in [0, 1/2]$. In subsection 4.4.2 we will investigate the temperature dependence of the string tension. In the high temperature regime we focus on the deconfinement of the heavy quarks when the temperature T becomes infinite: $T \rightarrow +\infty$. Then, in subsection 4.4.3, we treat the case when α tends to $1/2$ and investigate the spontaneous breaking of the \mathcal{CT} symmetry, see [6, 27] or subsection 3.3, for $\alpha = 1/2$ at finite temperature.

4.4.2. Deconfinement transition at large T

When α is small one can expand the string tension into a series of powers of α . Because σ_α is even in α , this yields an expansion in α^2 :

$$\sigma_\alpha(\beta) \approx f_2(\beta, m)\alpha^2 + \mathcal{O}(\alpha^4). \quad (4.12a)$$

For the electric field expectation value we then find:

$$E_\alpha(\beta, x) = \frac{\partial}{\partial(g\alpha)} (\sigma_\alpha(\beta, x)) = 2\alpha \frac{f_2(\beta, m)}{g} + \mathcal{O}(\alpha^3) \quad (4.12b)$$

and similarly for the entropy and chiral condensate:

$$\Delta\mathcal{S}_\alpha(\beta, x) = \beta^2 \frac{\partial f_2}{\partial \beta}(\beta, m)\alpha^2 + \mathcal{O}(\alpha^4), \quad (4.12c)$$

$$\Delta\Sigma_\alpha(\beta, x) = \frac{\partial f_2}{\partial m}(\beta, m)\alpha^2 + \mathcal{O}(\alpha^4). \quad (4.12d)$$

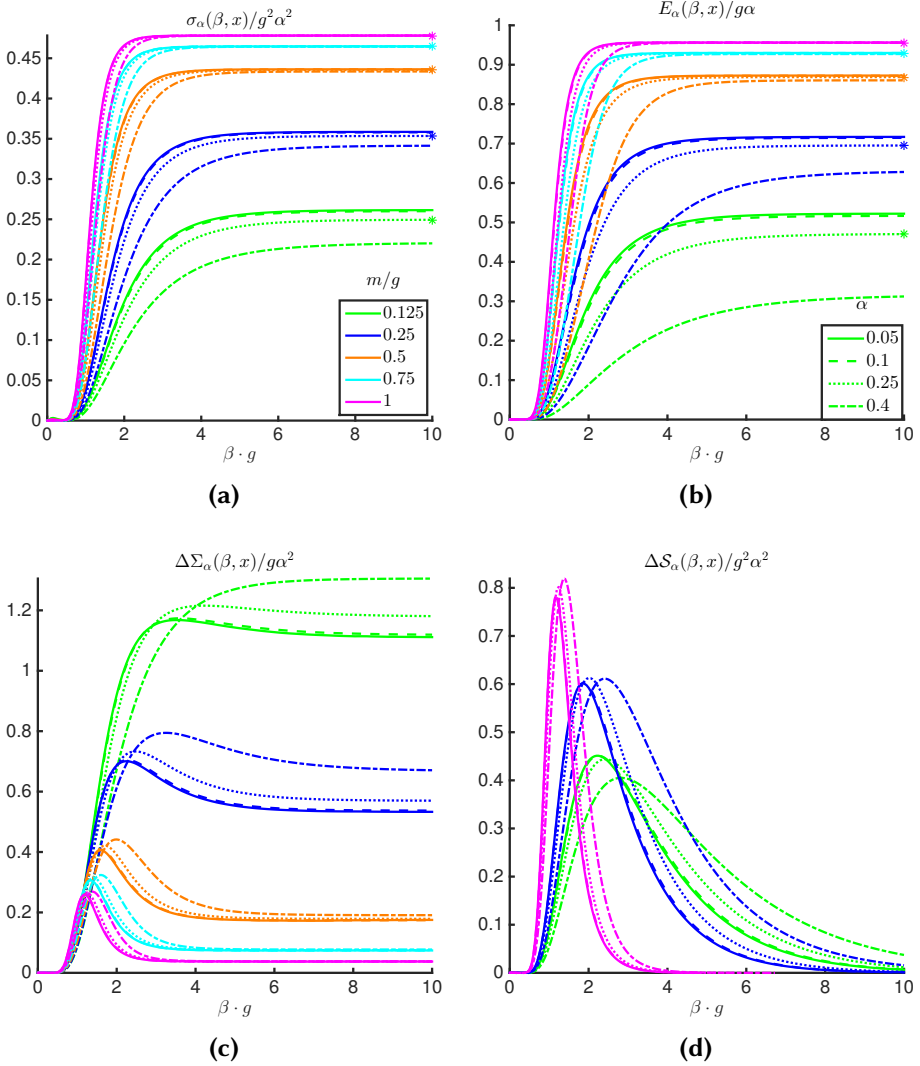


Figure 4.5.: $x = 100$. $\alpha = 0.05$ (full line), $\alpha = 0.1$ (dashed line), $\alpha = 0.25$ (dotted line) and $\alpha = 0.4$ (dashed dotted line). (a) $\sigma_\alpha(\beta, x)/g^2\alpha^2$. (b) $E_\alpha(\beta, x)/g\alpha$. (c) $\Delta\Sigma_\alpha(\beta, x)/g\alpha^2$. (d) $\Delta S_\alpha(\beta, x)/g^2\alpha^2$. The stars in (a) and (b) are the values at $\beta g = +\infty$ for $\alpha = 0.25$.

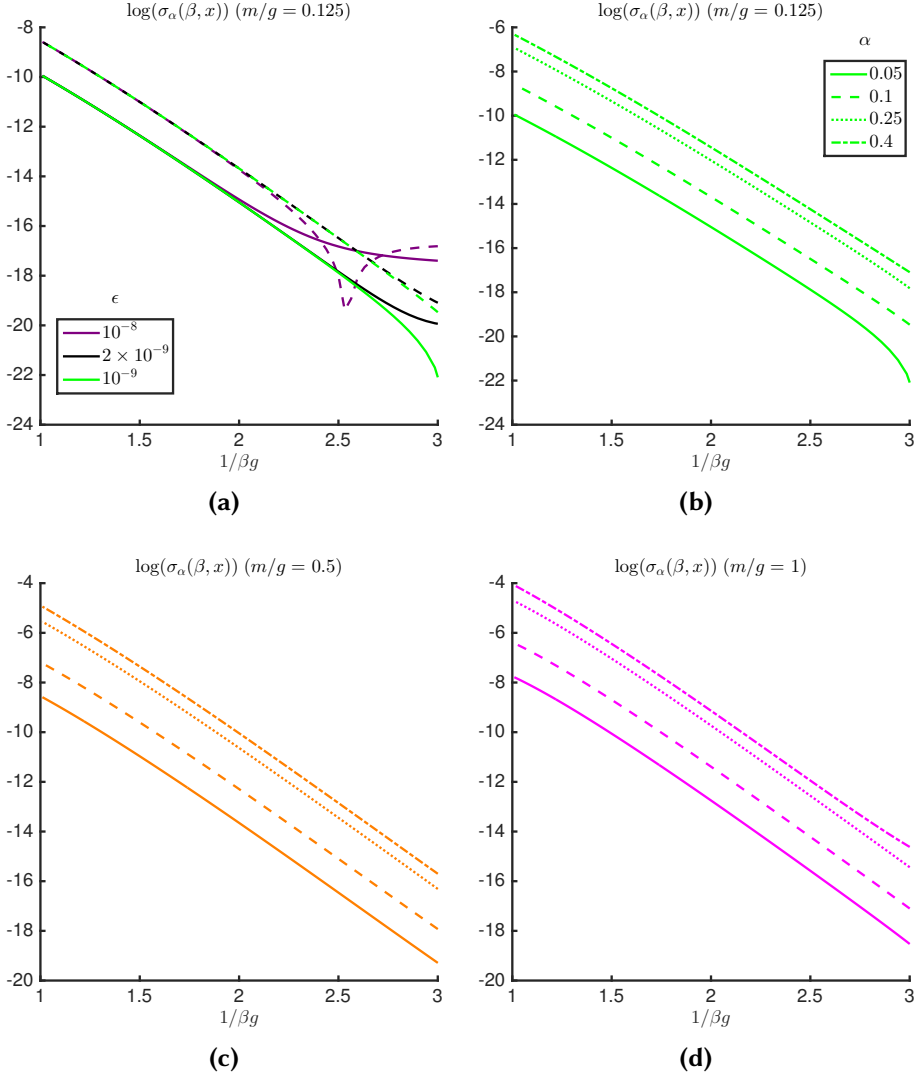


Figure 4.6.: $x = 100$. Logarithm of the string tension at larger temperatures $T = 1/\beta g$ as a function of T . (a) $m/g = 0.125$, $\alpha = 0.05$ (full line), $\alpha = 0.1$ (dashed line). Convergence of our results when improving the precision ϵ . (b) $m/g = 0.125$. Logarithm of string tension for $\alpha = 0.05$ (full line), $\alpha = 0.1$ (dashed line), $\alpha = 0.25$ (dotted line), $\alpha = 0.4$ (dashed dotted line). (c) Same as (b), now for $m/g = 0.25$. (d) Same as (b), now for $m/g = 1$.

We thus expect for α sufficiently small that the quantities $\sigma_\alpha(\beta, x)/g^2\alpha^2$, $E_\alpha(\beta, x)/g\alpha$, $\Delta\Sigma_\alpha(\beta, x)/g\alpha^2$ and $\Delta\mathcal{S}_\alpha(\beta, x)/g^2\alpha^2$ are independent of α up to order α^2 . This is precisely what we find in fig. 4.5 for $\alpha = 0.05$ and $\alpha = 0.1$. Note that as a consequence of eq. (4.12), the curves of the string tension and the electric field are similar, see figs. 4.5a and 4.5b. For $\alpha \gtrsim 0.25$ the expansion eq. (4.12) is in general not valid anymore and higher order corrections can become important.

When βg is large compared to the mass gap we find that all quantities have converged to their zero temperature value, i.e. the system is effectively at zero temperature. The value of $(\beta g)_0$ above which all ensemble averages are close to their ground state expectation agrees with the value of βg above which $\Delta\mathcal{S}_\alpha \approx 0$. This justifies taking the UV finite renormalized entropy $\Delta\mathcal{S}_\alpha$ as a measure to quantify thermal fluctuations in the Gibbs state. We observe that $(\beta g)_0$ is larger for smaller values of m/g . This is explained by the fact that for the values of α we considered here, the mass gap of \mathcal{H}_α increases with m/g , see fig. 2.8 in subsection 2.2.2 or [6]. For $\alpha = 0.25$ we observe in figs. 4.5a and 4.5b that the string tension and the electric field have converged to their ground state expectation values (stars) for $\beta g = 10$. In particular at low temperatures, large βg , the heavy probe charges are always confined when α is non-integer.

For $\beta g \lesssim 0.5$, the string tension is very small which suggests a transition from the confined phase to a deconfined plasma phase. In fact, we expect the string tension to decay exponentially with temperature at large values of $T = 1/\beta$ and the transition to occur exactly at infinite temperature $T/g = 1/\beta g = +\infty$. This is corroborated by studies in the strong coupling limit [8, 20] where they found that

$$\sigma_\alpha(\beta) \sim 2mT \sin(\pi\alpha)^2 e^{-\pi^3/2 T/g} + \mathcal{O}(m^2), \quad (4.13)$$

at high temperatures ($T/g = 1/\beta g \rightarrow +\infty$). In figs. 4.6b, 4.6c, 4.6d we indeed find that the logarithm of the string tension is almost linear as a function of T for $T/g \in [1, 3]$ or equivalently $\beta g \in [0.33, 1]$. Note that because for these values of βg the string tension is very small, we needed very small values of the tolerance ϵ and the step $d\beta \leq 5 \times 10^{-3}$ to investigate this regime, see fig. 4.6a.

In table 4.1 we show the coefficients for a fit of the form

$$\log(\sigma_\alpha(\beta, x)/g^2) = \log(A_\alpha \alpha^2) + B_\alpha \log(T/g) - C_\alpha T/g \quad (4.14)$$

to our data, which is equivalent to

$$\sigma_\alpha(\beta, x)/g^2 = \alpha^2 A_\alpha e^{-C_\alpha T/g} (T/g)^{B_\alpha}.$$

m/g	α	$\log(A_\alpha)$	B_α	C_α
0.125	0.05	2.53	1.91	6.45
	0.1	2.49	1.88	6.44
	0.25	2.31	1.86	6.43
	0.4	1.95	1.83	6.41
0.5	0.05	4.06	2.16	6.61
	0.1	4.03	2.14	6.6
	0.2	3.81	2.05	6.54
	0.4	3.42	1.94	6.49
1	0.05	5.38	2.97	7.1
	0.1	5.34	2.92	7.07
	0.25	5.05	2.67	6.93
	0.4	4.57	2.39	6.77

Table 4.1.: $x = 100$. Coefficients of the fit eq. (4.14) to our data for $m/g = 0.125, 0.5$ and $\alpha = 0.05, 0.1, 0.25$.

We performed these fits to our data $\log(\sigma_\alpha(\beta, x)/g^2)$ for $\epsilon = 10^{-9}$ and $\beta \in [\beta_1, \beta_2]$ with step $d\beta = 0.005$ for

$$(\beta_1, \beta_2) = (0.425, 0.965), (0.45, 0.94), (0.475, 0.915) \dots, (0.65, 0.75).$$

All these fits gave us estimates for A_α , B_α and C_α . As our final estimate we take the mean of all these A_α , B_α and C_α . The standard deviation on our estimates was at most of order 10^{-2} and the error of the fit was at most of order 10^{-3} .

For all values of m/g we observe that $A_{0.05} \approx A_{0.01}$ which is a consequence of eq. (4.12). Furthermore, we also find that B_α changes from $B_\alpha \approx 2$ for $m/g = 0.25, 0.5$ to $B_\alpha \approx 3$ for $m/g = 1$. The values of C_α obviously show that the string tension is exponentially suppressed for $T/g \gtrsim 2$. Note however that already for $m/g = 0.125$ the value of C_α deviates from the $C_\alpha^0 = \pi^{3/2} \approx 5.56$ in the strong coupling limit eq. (4.13).

We conclude that we have confinement for all finite values of the temperature T/g , but for $T/g \gtrsim 2$, or equivalently $\beta g \lesssim 0.5$, the string tension is exponentially suppressed with T/g . At high temperatures, the string tension can thus only be observed if we would separate the heavy charges by a distance which scales exponentially in the temperature. In an experimental setting, this means that the heavy charges are actually deconfined for $\beta g \lesssim 0.5$.

4.4.3. \mathcal{CT} symmetry restoration at nonzero T

As already discussed in section 3.3, at zero temperature there is a phase transition for $\alpha = 1/2$ and $m/g = (m/g)_c \approx 0.33$ [27]. For $m/g \leq (m/g)_c$ the ground state is \mathcal{CT} invariant whereas for $m/g \geq (m/g)_c$ the \mathcal{CT} symmetry is spontaneously broken to \mathcal{T}^2 . The vacuum is still invariant under translation over two sites and is two-fold degenerate. A detailed study of this phase transition was performed by Byrnes *et al.* [27]. Their results for the critical indices, $\nu = 0.99(1)$ and $\beta/\nu = 0.125(5)$, gave strong evidence that the phase transition lies in the universality class of the transverse Ising model or equivalently of the 2D classical Ising model [131]. For the transverse Ising model the phase transition is determined by the \mathbb{Z}_2 symmetry. When this symmetry is spontaneously broken, the magnetization gains a non-zero expectation value. Here the \mathcal{CT} symmetry of the Schwinger model for $\alpha = 1/2$ plays the role of the \mathbb{Z}_2 -symmetry and the electric field plays the role of the magnetization.

Besides this phase transition the pattern of the eigenvalues of the Schwinger model at $\alpha = 1/2$ in the symmetry broken regime bears a remarkable resemblance to the transverse Ising model [27]. Because of the similarities between both models, we might expect that also at finite temperature there are some analogies. In particular, because the spontaneous symmetry breaking in the transverse Ising model occurs only at zero temperature we might expect this also to be the case for the Schwinger model. Furthermore, general theorems like for instance the Mermin-Wagner theorem [132] or Peierls argument [133] suggest that at finite temperature no spontaneous symmetry breaking occurs in one spatial dimension. However the former is not applicable as the \mathcal{CT} transformation is discrete whereas the latter might not apply because the local dimension of the Hilbert space is infinite. Therefore it is a priori not sure whether the \mathcal{CT} symmetry is restored at any finite temperature.

The spontaneous symmetry breaking of the \mathcal{CT} symmetry is detected by investigating the left/right limits ($\alpha = 1/2 \pm \delta$):

$$\lim_{\delta \rightarrow 0^+} E_{1/2+\delta}(\beta) \text{ and } \lim_{\delta \rightarrow 0^+} E_{1/2-\delta}(\beta). \quad (4.15)$$

When these limits are different, the symmetry is spontaneously broken. Due to \mathcal{CT} symmetry we thus need to check whether

$$\lim_{\delta \rightarrow 0} E_{1/2-\delta}(\beta) = 0.$$

For $m/g = 0.125$ and $m/g = 0.25$ we find for all values of βg that $E_{1/2+\delta}(\beta)$

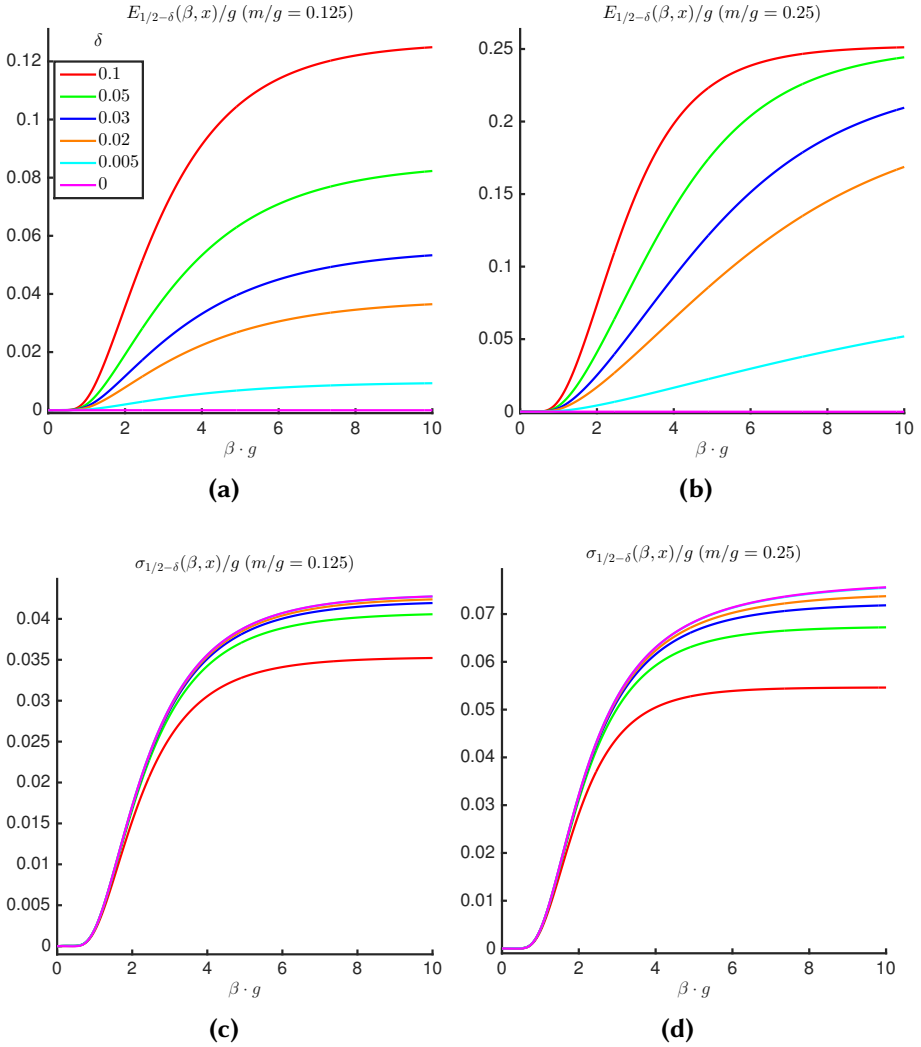


Figure 4.7.: $x = 100$. $\alpha = 1/2 - \delta$ for different values of δ . Left: $m/g = 0.125$. (a) Electric field. (c) String tension. Right: $m/g = 0.25$. (b) Electric field. (d) String tension.

decreases to zero as $|\delta| \rightarrow 0$, see figs. 4.7a and 4.7b. This leads us to the conclusion that $\lim_{\delta \rightarrow 0} E_{1/2-\delta}(\beta, x) = 0$. We can actually perform direct simulations for $\alpha = 1/2$ and find numerically that $|E_{1/2}(\beta, x)| \lesssim 5 \times 10^{-5}$. This can be improved by requiring better accuracy of our simulations, see appendix B.3. So similar as for zero temperature we observe for $m/g \lesssim (m/g)_c$ that $E_{1/2}(\beta, x) = 0$; implying that there is no \mathcal{CT} symmetry breaking. Because $E_\alpha(\beta, x) = \partial\sigma_\alpha(\beta, x)/\partial\alpha$, the string tension reaches its maximum for $\alpha = 1/2$. This is indeed what can be seen in figs. 4.7c and 4.7d: for all values of βg the string tension increases monotonically as a function of α to its value at $\alpha = 1/2$ when δ tends to zero. At large temperatures, the string tension shows similar as in subsection 4.4.2 deconfinement for $T \rightarrow +\infty$.

Contrary to the case $\alpha = 0.1$ and $\alpha = 0.25$, we find that neither the free energy nor the electric field has entirely converged to its ground state expectation value at $\beta g = 10$. This is what we would expect from our numerical simulations in subsection 2.2.2. There we found that for $m/g = 0.125$ and $m/g = 0.25$ the mass gap decreases when α tends to $1/2$, see fig. 2.8; consistent with the phase transition that occurs at $(m/g, \alpha) = ((m/g)_c, 1/2)$.

For $m/g \geq (m/g)_c$, at the exact value $\alpha = 1/2$, the simulations are not reliable anymore. Due to spontaneous symmetry breaking the ground state is now two-fold degenerate and for large values of βg the iTEBD algorithm pushes the Gibbs state during the evolution either to the ground state

$$|\Psi_{1/2-}\rangle \text{ of } H_{1/2-\delta}$$

or to the ground state

$$|\Psi_{1/2+}\rangle \text{ of } H_{1/2+\delta}$$

in the limit $\delta \rightarrow 0+$, see appendix B.3.

To examine the \mathcal{CT} symmetry breaking or restoration we need to consider nonzero $\delta > 0$. For small values of βg we find that the electric field converges to zero when $\delta \rightarrow 0$, see figs. 4.8a and 4.8b. This indicates that there is no spontaneous symmetry breaking for small values of βg .

For large values of βg however, we find that even for $\delta = 0.001$ the electric field and string tension are still very close to the values in the spontaneous broken ground state $|\Psi_{1/2-}\rangle$. But notice that the δ -dependence of the observables in the intermediate temperature region suggests that the $\delta \rightarrow 0$ limit has not been reached yet. This is corroborated by a study in the weak coupling limit, see appendix B.4, where we argue that thermal corrections to ground state expectation values can only be relevant if

$$\delta \lesssim K_m \frac{e^{-2\beta m}}{\beta} \tag{4.16}$$

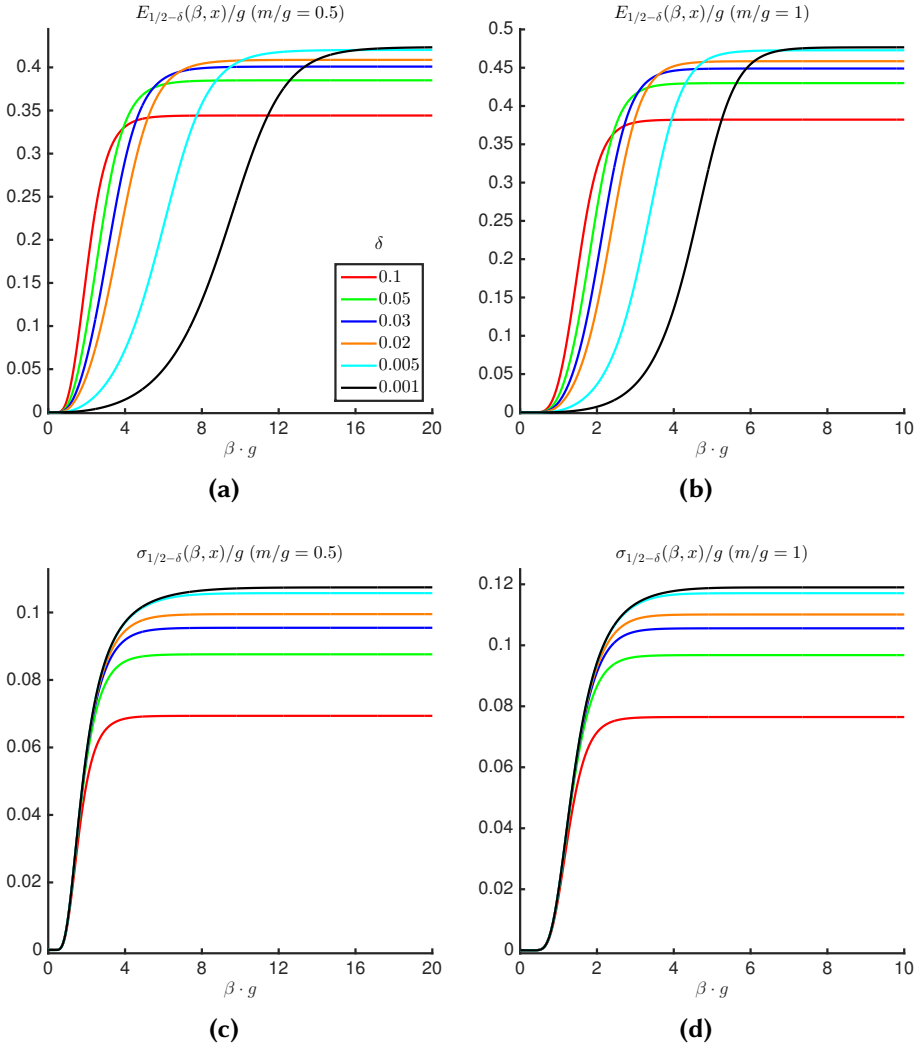


Figure 4.8: $x = 100$. $\alpha = 1/2 - \delta$ for different values of δ . Left: $m/g = 0.5$. (a) Electric field. (c) String tension. Right: $m/g = 1$. (b) Electric field. (d) String tension.

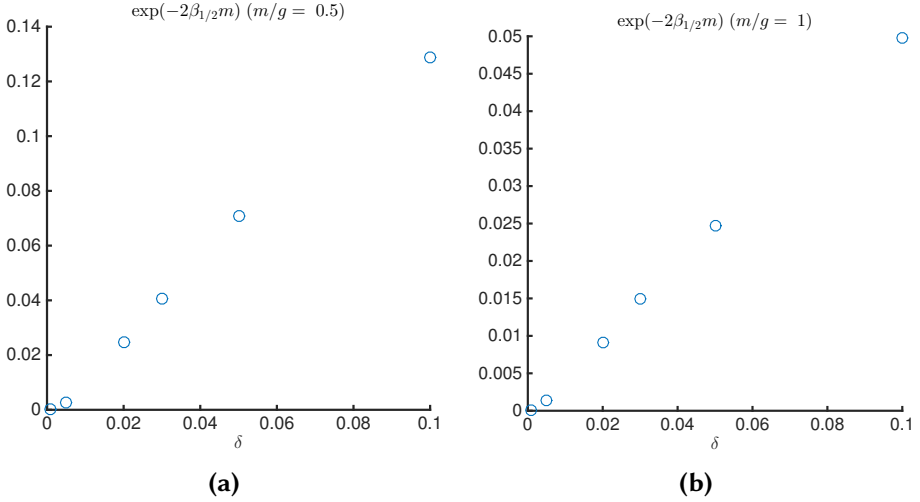


Figure 4.9.: $x = 100$. $\exp(-2\beta_{1/2}m)$ as a function of δ . (a) $m/g = 0.5$. (b) $m/g = 1$.

with K_m positive and independent of β . This implies that to observe thermal corrections to ground state expectation values we should take δ exponentially small in βm .

From the numerical point of view it is hard to simulate such small values of δ . For instance, for $(m/g, \delta) = (1, 0.001)$ we had to set $\epsilon = 10^{-7}$ and during the evolution the bond dimension of our MPS representation already reached 267. To examine the $\delta \rightarrow 0$ limit from our simulated δ -values we investigate the scaling of $\beta_{1/2}$, the value of β where the electric field $E_{1/2-\delta}(\beta_{1/2}, x)$ equals half of its ground state expectation value $E_{1/2-\delta}(\beta = +\infty, x)$. Motivated by eq. (4.16) we plot in fig. 4.9 $\exp(-2\beta_{1/2}m)$ as a function of δ . We seem to find there that $\exp(-2\beta_{1/2}m) \rightarrow 0$ as $\delta \rightarrow 0$, or equivalently that $\beta_{1/2} \rightarrow +\infty$ for $\delta \rightarrow 0$. This indicates that the curve of the electric field tends to a function which is zero for all finite values of β as $\delta \rightarrow 0$. Hence it seems, similar to the 1D quantum transverse Ising model, that the spontaneous symmetry breaking vanishes at all finite inverse temperatures and a phase transition would occur exactly at $T = 0$.

Similar as for $m/g = 0.125, 0.25$ the string tension, figs. 4.8c and 4.8d, converges nicely to its maximum for $\delta \rightarrow 0$ for all values of βg . At high temperatures we find again deconfinement for $T/g = 1/\beta g \rightarrow +\infty$.

To conclude, in this subsection we investigated the Schwinger model with an electric background field α close to $1/2$. We considered the values $m/g = 0.125, 0.25, 0.5$ and 1 . For all these values we find strong indications for

the existence of \mathcal{CT} symmetry at any nonzero temperature. In particular for $m/g > (m/g)_c \approx 0.33$, where the \mathcal{CT} symmetry is broken at zero temperature [27], our results imply a restoration of the \mathcal{CT} symmetry at any nonzero temperature. This is similar to what happens with the \mathbb{Z}_2 symmetry of the transverse Ising model and thus lends further support to the purported relationship between the Schwinger model at $\alpha = 1/2$ and the transverse Ising model, as suggested in [27].

4.5. Conclusion

In this chapter we investigated the Schwinger model in thermal equilibrium within the framework of MPO. We computed the chiral condensate and found agreement with the analytical result for $m/g = 0$ [15] and agreement with [34] in the non-perturbative regime. We also investigated the asymptotic aspects of confinement by considering a heavy quark-antiquark pair with fractional charge $g\alpha$, separated over an infinite distance. We find a nonzero string tension and therefore confinement for all values of m/g . However, at large temperatures $T \gtrsim 2g$ we find that the string tension decays exponentially with the temperature. We also considered the case when α tends to $1/2$ and investigated the spontaneous breaking of the \mathcal{CT} symmetry at finite temperature. Our results indicate that the spontaneous symmetry breaking vanishes at any nonzero temperature which implies that there is only a phase transition at zero temperature. We thus found two phase transitions that occur in limiting cases only: infinite temperature or zero temperature.

Our simulations show that the MPO framework offers a reliable approach to study the non-perturbative regime of one dimensional gauge field theories. However, even within the Schwinger model there remains a lot of fascinating things to explore. For instance one can investigate string breaking between the probe charges when they are separated by a finite distance, similar to section 3.4 but now at finite temperature.

Real-time evolution

5.1. Introduction

One of the main advantages of the TNS framework is that it allows for the full quantum simulation of real-time phenomena. Specifically we investigate the non-equilibrium dynamics induced by applying a uniform electric field $E_0 = g\alpha$ on the ground-state $|\Psi_0\rangle$ at time $t = 0$. Physically, the process corresponds to the so called Schwinger particle creation mechanism [134], but now for a confining theory. This process has been studied extensively in the past, either with some effective classical kinetic description [16, 24], in the semi-classical limit for the gauge fields [16, 31], in the context of ultracold atomic simulations [38] and with the AdS/CFT correspondence [135].

Here we investigate how the dynamics in earlier times depends on the magnitude of α . For relatively small values of α we observe oscillatory behavior of the local quantities. We find that the results can be reproduced by only considering the ground state and the one-particle excitations of the quenched Hamiltonian, also beyond the linear response regime. When increasing the values of α we find that these oscillations are damped over time which suggests that the state tends asymptotically to a steady-state solution. Using the finite temperature simulations of chapter 4 we investigate whether this steady-state is a Gibbs state.

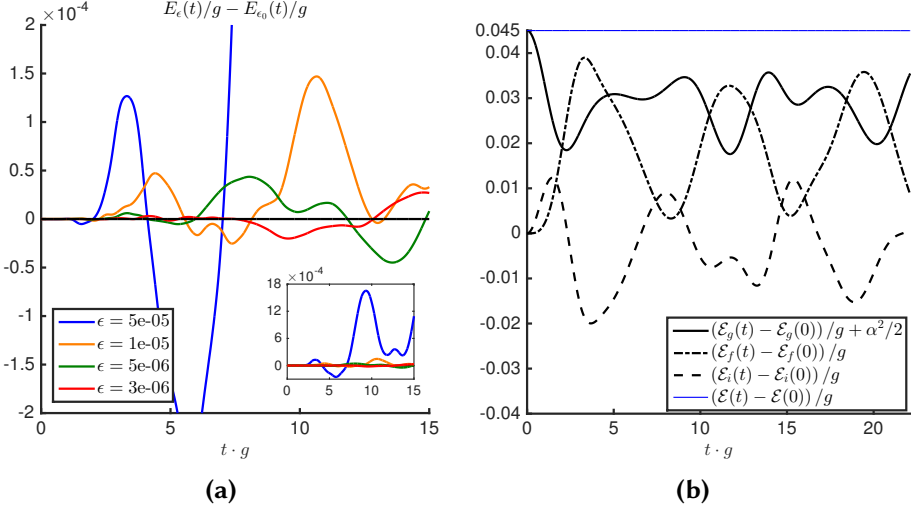


Figure 5.1.: Results for $m/g = 0.25$, $x = 100$, $\alpha = 0.3$. (a): Difference of $E(t)$ for various tolerances ϵ with respect to the estimated value for $\epsilon = \epsilon_0 = 2 \cdot 10^{-6}$ ($\alpha = 0.3$). (b): for $\alpha = 0.3$, the different energies per unit of length eq. (5.4). We subtracted the values at $t = 0$ without background field ($\alpha = 0$). The straight blue line is the total energy per unit of length obtained as the sum of the three terms.

5.2. Setup and systematics of the method

In our set-up the application of a uniform electric field is simulated by applying a uniform quench, i.e. evolving with the Hamiltonian

$$\mathcal{H}_\alpha = \frac{g}{2\sqrt{x}} \left(\sum_{n=1}^{2N} [L(n) + \alpha]^2 + \frac{\sqrt{x}}{g} m \sum_{n=1}^{2N} (-1)^n \sigma_z(n) + x \sum_{n=1}^{2N-1} (\sigma^+(n) e^{i\theta(n)} \sigma^-(n+1) + h.c.) \right). \quad (5.1)$$

At $t = 0$ we start from a \mathcal{CT} invariant MPS approximation for the ground state of $\mathcal{H}_0 = \mathcal{H}_{\alpha=0}$, see eq. (2.2a), and turn this into an MPS ansatz which takes the form (see eq. (3.19) in subsection 3.3.2 of part II)

$$|\Psi_u[A_1 A_2]\rangle = \sum_{\kappa} v_L^\dagger \left(\prod_{n=1}^N (A_1^{\kappa_{2n-1}} A_2^{\kappa_{2n}}) \right) v_R |\kappa\rangle (N \rightarrow +\infty) \quad (5.2)$$

where $\kappa_n = (s_n, p_n) \in \{-1, 1\} \times \mathbb{Z}[p_{n+1}^{min}, p_{n+1}^{max}]$ and gauge invariance imposes the following block structure:

$$[A_n^{s,p}]_{(q,\alpha_q);(r,\beta_r)} = [a_n^{q,s}]_{\alpha_q,\beta_r} \delta_{p,q+(s+(-1)^n)/2} \delta_{r,p},$$

with $a_n^{q,s} \in \mathbb{C}^{D_n^q \times D_{n+1}^r}$. We have implemented the iTEBD [136] using a fourth-order Trotter expansion [123] with time steps varying from $dt = 0.01/g$ until $dt = 0.05/g$ and during the whole evolution the structure of this uMPS is maintained. We refer to section 4.3.1 of part II for the details.

After every application of a Trotter gate the iTEBD truncates the Hilbert space by discarding the Schmidt coefficients lower than some fixed threshold ϵ^2 . More specifically, the Schmidt decomposition eq. (1.9) becomes now:

$$|\Psi_u[A_1 A_2]\rangle = \sum_{q=p_{n+1}^{min}}^{p_{n+1}^{max}} \sum_{\alpha_q=1}^{D_{n+1}^q} \sqrt{\sigma_{n,\alpha_q}^q} |\psi_{q,\alpha_q}^{\mathcal{A}_1^n}\rangle |\psi_{q,\alpha_q}^{\mathcal{A}_2^n}\rangle.$$

where $p_n^{min}, p_n^{max}, D_n^{min}, D_n^{max}$ and σ_{n,α_q}^q only depend on the parity of n . After every Trotter gate the Schmidt values σ_{n,α_q}^q smaller than ϵ^2 are discarded. This in turn determines the required bond dimensions D^q for every charge sector, that will evolve in time. For instance, for the value $\epsilon_0 = 2 \cdot 10^{-6}$ that we used for the simulations in fig 5.1, the maximal bond dimension goes from $D_0 = 18$ at $t = 0$ to $D_0 = 173$ at $t = 25$. It is this growth of the required bond dimensions, which can be traced back to the growth of entanglement [42], that makes the computations more costly at later times. As the simulation should be exact as $\epsilon \rightarrow 0$, the convergence in ϵ can be used to control the truncation error for a certain observable. We illustrate this in fig. 5.1a for the electric field $E(t)$ expectation value

$$E(t) = \frac{1}{2N} \sum_{n=1}^{2N} \langle \Psi(t) | L(n) + \alpha | \Psi(t) \rangle \quad (5.3)$$

where $|\Psi(t)\rangle = |\Psi_u[A_1 A_2]\rangle$ corresponds to our uMPS approximation of $e^{-i\mathcal{H}_\alpha t} |\Psi(0)\rangle$. Also notice that the convergence rate decreases in time. Keeping the truncation error small for larger time intervals will therefore require smaller values of the tolerance ϵ .

In fig. 5.1b we show the evolution of the energies per unit of length in the different sectors:

$$\mathcal{E}_g(t) = \frac{g}{4N} \sum_{n=1}^{2N} \langle \Psi(t) | [L(n) + \alpha]^2 | \Psi(t) \rangle, \quad (5.4a)$$

$$\mathcal{E}_f(t) = \frac{m\sqrt{x}}{4N} \sum_{n=1}^{2N} \langle \Psi(t) | \sigma_z(n) + (-1)^n | \Psi(t) \rangle, \quad (5.4b)$$

$$\mathcal{E}_i(t) = \frac{gx}{4N} \sum_{n=1}^{2N} \langle \Psi(t) | \sigma^+(n) e^{i\theta(n)} \sigma^-(n+1) + h.c. | \Psi(t) \rangle \quad (5.4c)$$

and the total energy per unit of length

$$\mathcal{E}(t) = \frac{\sqrt{x}}{2N} \langle \Psi(t) | \mathcal{H}_\alpha | \Psi(t) \rangle.$$

We see that the energy which is initially injected in the first gauge field term in eq. (5.1), partially leaks into the second fermionic mass term and third kinetic/interaction term, as we can again qualitatively understand from the fermionic particle creation picture. In [31] a similar behavior was observed in the semi-classical limit. A last cross-check of our real-time results is then provided by the total energy conservation which is indeed satisfied as can be seen from the blue line in fig. 5.1b.

Besides the electric field eq. (5.3) we will also investigate the ‘chiral condensate’

$$\Sigma(t) = \left\langle \Psi(t) \left| g \frac{\sqrt{x}}{2N} \sum_{n=1}^{2N} \frac{\sigma_z(n) + (-1)^n}{2} \right| \Psi(t) \right\rangle. \quad (5.5)$$

To obtain a UV finite quantity we subtract its contribution at $t = 0$ and thus consider

$$N(t) = \frac{\Sigma(t) - \Sigma(0)}{g}.$$

Here this quantity will be referred to as the (fermion) particle number. Indeed this quantity counts the number of electrons and positrons per unit of length that are created out of the vacuum or destroyed in the vacuum due to turning on the electric background field α at $t = 0$.

The MPS representation enables us to obtain the Schmidt spectrum, see eq. (4.55) of subsection 4.3.1 in part II. Therefore we can also compute the renormalized half chain Von Neumann entropy,

$$\Delta S(t) = S(t) - S(0).$$

which is obtained by computing the entropy of the state at time t , see eq. (1.10), and subtracting the entropy of the initial state computed in subsection 2.1.5. The cut for the half chain bipartition is taken on an even site. Note that due to \mathcal{T}^2 invariance it follows that this quantity is independent of the position.

By subtracting the $t = 0$ value of the entropy and the chiral condensate we expect that $N(t)$ and $\Delta S(t)$ are UV finite quantities. This is corroborated by figure 5.2 where we show the evolution of the electric field $E(t, x)$, the particle number $N(t, x)$ and the renormalized entropy $\Delta S(t, x)$ as a function of time for $x = 100, 200, 300, 400$. Note that we here explicitly denote the x -dependence of the quantities. We observe that for all these quantities the

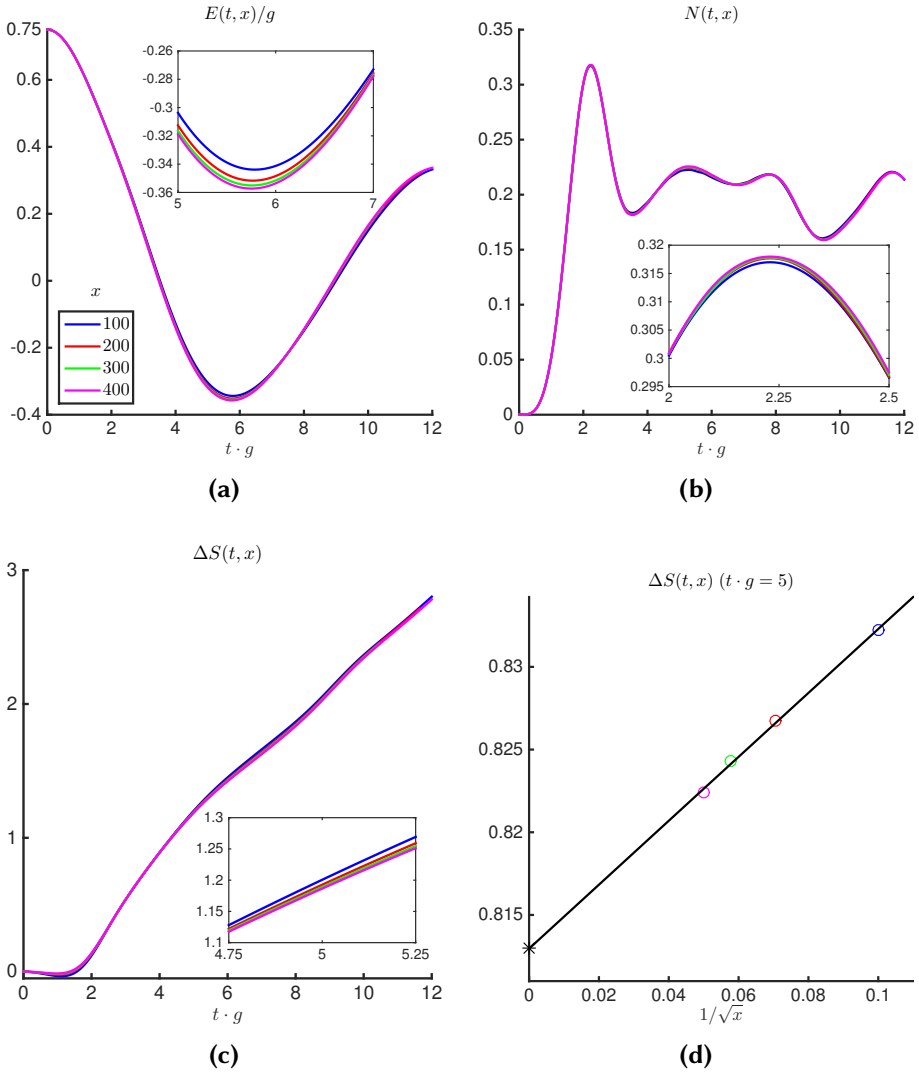


Figure 5.2: $m/g = 0.25, \alpha = 0.75$. Scaling of the quantities to $x \rightarrow +\infty$. (a) Electric field $E(t, x)$. (b) Particle number $N(t, x)$. (c) Renormalized entropy $\Delta S(t, x)$. (d) Polynomial extrapolation in $1/\sqrt{x}$ of the renormalized entropy to $x \rightarrow +\infty$.

graphs are almost on top of each other, see figs. 5.2 (a) - (c). This underlies the fact that these are UV finite quantities. One can also obtain a continuum estimate for these quantities by a polynomial extrapolation, see fig. 5.2d where we perform a polynomial extrapolation of $\Delta S(t)$ for $tg = 5$. It is also clear from this example that we can already expect at $x = 100$ to be close to the continuum limit. For the further simulations we will therefore restrict ourselves to $x = 100$, the x -dependence in the quantities $E(t, x)$, $N(t, x)$ and $\Delta S(t, x)$ will be omitted.

5.3. Weak field regime

In fig. 5.3a we display our results for the evolution of the electric field expectation value for different values of α . For early times we clearly find the α -scaling behavior as predicted from linear response theory. The $\alpha = 0.005$ and $\alpha = 0.01$ cases remain in the linear response regime throughout the entire depicted evolution; the periodic oscillations in this case can be traced back to the dominant production of the single-particle vector excitation in the linear response regime. Indeed, if we write \mathcal{H}_α eq. (5.1) as a perturbation on the Hamiltonian \mathcal{H}_0 :

$$\mathcal{H}_\alpha = \mathcal{H}_0 + \alpha \left(\frac{1}{\sqrt{x}} \sum_{n=1}^{2N} L(n) \right)$$

where we omitted the irrelevant constant $N\alpha^2/\sqrt{x}$, then from the Dyson series [111] it follows that up to first order in α :

$$E(t) \sim \alpha - \alpha \sum_m C_m \sin(\mathcal{E}_m t/2)^2$$

where the sum over m runs over all excitations of \mathcal{H}_0 with \mathcal{CT} number $(k, \gamma) = (0, -1)$ and C_m is a constant depending on the excitations. By truncating this sum to the first excitation $\mathcal{E}_{1,v}$ of \mathcal{H}_0 , see subsection 2.1.2, we find that

$$E(t) \sim \alpha (1 - C_1 \sin(\mathcal{E}_{1,v} t/2)^2).$$

For $x = 100$ and $m/g = 0.25$ the numerical value of $\mathcal{E}_{1,v}$ is 1.0421, hence within the linear response regime $E(t)$ should reach its minimum for $tg = \pi/\mathcal{E}_{1,v} = 3.0148$. From fig. 5.3a we can deduce for $\alpha = 0.005$ and $\alpha = 0.01$ that $E(t)$ reaches its minimum for $tg = 3.02(1)$ which indeed confirms that the periodic oscillations can be traced back to the single-particle vector excitation.

In fig. 5.3b we display the analogous result for the particle number $N(t)$. As $N(t)$ is now invariant under \mathcal{CT} the first order coefficients C_k in α vanish

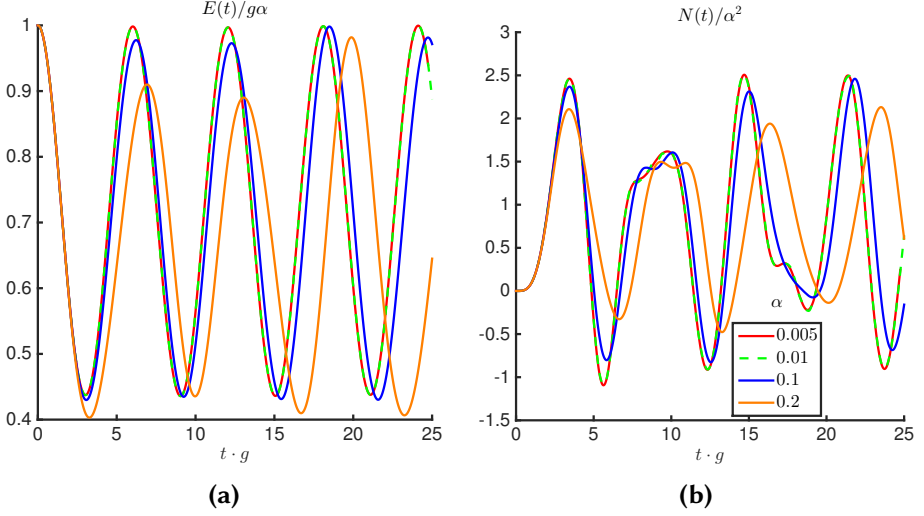


Figure 5.3.: $m/g = 0.25, x = 100$. (a) $E(t)/\alpha$. (b) $N(t)/\alpha^2$.

identically and hence $N(t)$ should scale as α^2 for early times, which is indeed what we find for $\alpha = 0.005$ and $\alpha = 0.1$.

The values $\alpha = 0.1$ and 0.2 depart from linear response theory, however the evolution can now be explained from the spectrum of the quenched Hamiltonian \mathcal{H}_α . Therefore we expand all operators, including the Hamiltonian \mathcal{H}_0 , in the creation and annihilation operators of \mathcal{H}_α up to second order. More specifically, we make the following approximation

$$\mathcal{H}_\alpha \approx \int dk \left(\sum_m \mathcal{E}_m(k) a_m^\dagger(k) a_m(k) \right). \quad (5.6a)$$

Here the integral goes over the momenta from $-\pi$ till π , the sum over m and n goes over all one-particle excitations and $\mathcal{E}_m(k)$ is positive. The operators a_m and a_m^\dagger are the annihilation and creation operators of the one-particle excitations $|\mathcal{E}_m(k)\rangle$ with energy $\mathcal{E}_m(k)$ and momentum k and satisfy the canonical bosonic commutation relations

$$[a_n(k'), a_m^\dagger(k)] = \delta(k' - k) \delta_{m,n}, [a_m(k'), a_n(k')] = 0, [a_n^\dagger(k'), a_m^\dagger(k)] = 0.$$

For any other operator \mathcal{O} we assume then that

$$\begin{aligned} \mathcal{O} \approx \int dk \left(\sum_m o_{2,m}(k) a_m(k) + \bar{o}_{2,m}(k) a_m^\dagger(k) \right) \\ + \int dk \int dk' \left(\sum_{m,n} o_{1,m,n}(k, k') a_m^\dagger(k) a_n(k') \right). \end{aligned} \quad (5.6b)$$

where the coefficients $o_{1,m,n}(k)$ and $o_{2,m}(k)$ can be obtained from the MPS approximations $|\Phi_k[B_m(k), A]\rangle$ eq. (2.11) of the excitations $|\mathcal{E}_m(k)\rangle$ obtained in subsection 2.2.2, see subsection 4.2.7 of part II for the details. For translation invariant operators we have that $o_{1,m,n}(k), o_{2,m}(k) \propto \delta(k)$ hence we only need the zero-momentum one-particle excitations.

Employing this approximation for \mathcal{H}_0 implies that the initial state $|\Psi(0)\rangle$, which is the ground state of \mathcal{H}_0 , is a coherent state, i.e. it is an eigenvector of $a_m(k)$ (see subsection 4.2.7 of part II):

$$a_m(k) |\Psi(0)\rangle = d_m(k) |\Psi(0)\rangle \quad (5.6c)$$

where $d_m(k) \propto d'_m \delta(k)$ for some constant $d'_m \in \mathbb{C}$. Within our approximation we interpret the initial state $|\Psi(0)\rangle$ thus as the ground state of \mathcal{H}_α with on top of it a density of zero-momentum one-particle excitations $|\mathcal{E}_m(0)\rangle$. This approximation is valid as long as this density of excitations is sufficiently small such that the elementary particles don't interact. This is what we would expect as the approximations eqs. (5.6a) and (5.6b) neglect the contribution of the scattering states of elementary excitations. The real-time evolution and the computation of expectation values of operators \mathcal{O} within the approximation eq. (5.6b) can now easily be performed, see subsection 4.2.7 of part II for the details.

For $m/g = 0.25$ and $\alpha = 0.1, 0.2$ we found in subsection 2.2.2 MPS approximations for the two one-particle excitations \mathcal{E}_1 and \mathcal{E}_2 of \mathcal{H}_α . This means that in eq. (5.6a) and eq. (5.6b) the sum over m and n runs from 1 to 2. Figs. 5.4a and figs. 5.4b show that the electric field $E(t)$ and the particle number $N(t)$ computed within the approximation eq. (5.6) are in very good agreement with the iTEBD simulations for $\alpha = 0.01$. In particular we find that the masses \mathcal{E}_1 and \mathcal{E}_2 of the one-particle excitations explain the frequencies of the oscillations in $E(t)$ and $N(t)$. This is also the case for $\alpha = 0.2$, figs. 5.4c and 5.4d, but now there is a larger discrepancy between the amplitudes of both curves. The approximation seems to systematically overestimate the amplitude of $E(t)$ with respect to $E(0)$ and the magnitude of $N(t)$. It would definitely be interesting to investigate whether including the two-particle scattering excitations [137, 138] in the approximation eq. (5.6) could damp the oscillations such that we would find even better agreement.

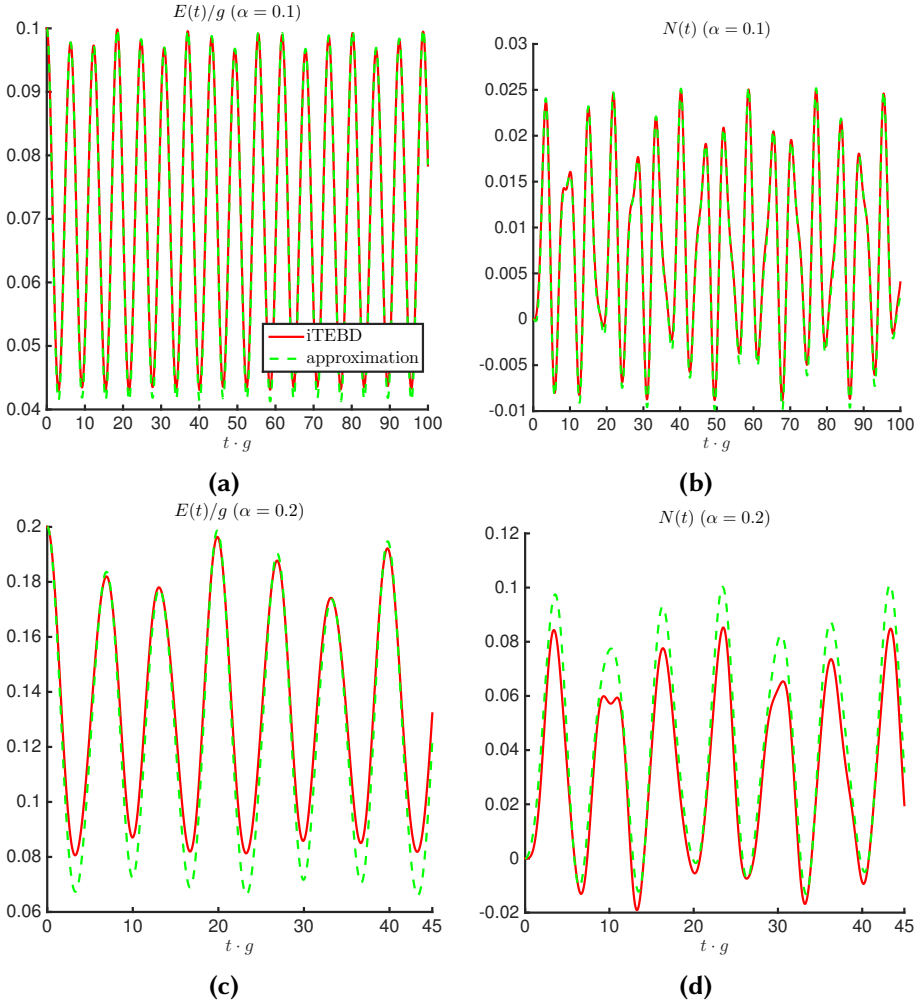


Figure 5.4: $m/g = 0.25$, $x = 100$. Comparison of the approximation eq. (5.6) (dashed line) with the (exact) iTEBD simulation (full line). (a)-(b): $\alpha = 0.1$ (a) $E(t)$. (b) $N(t)$. (c)-(d): $\alpha = 0.2$ (c) $E(t)$. (d) $N(t)$.

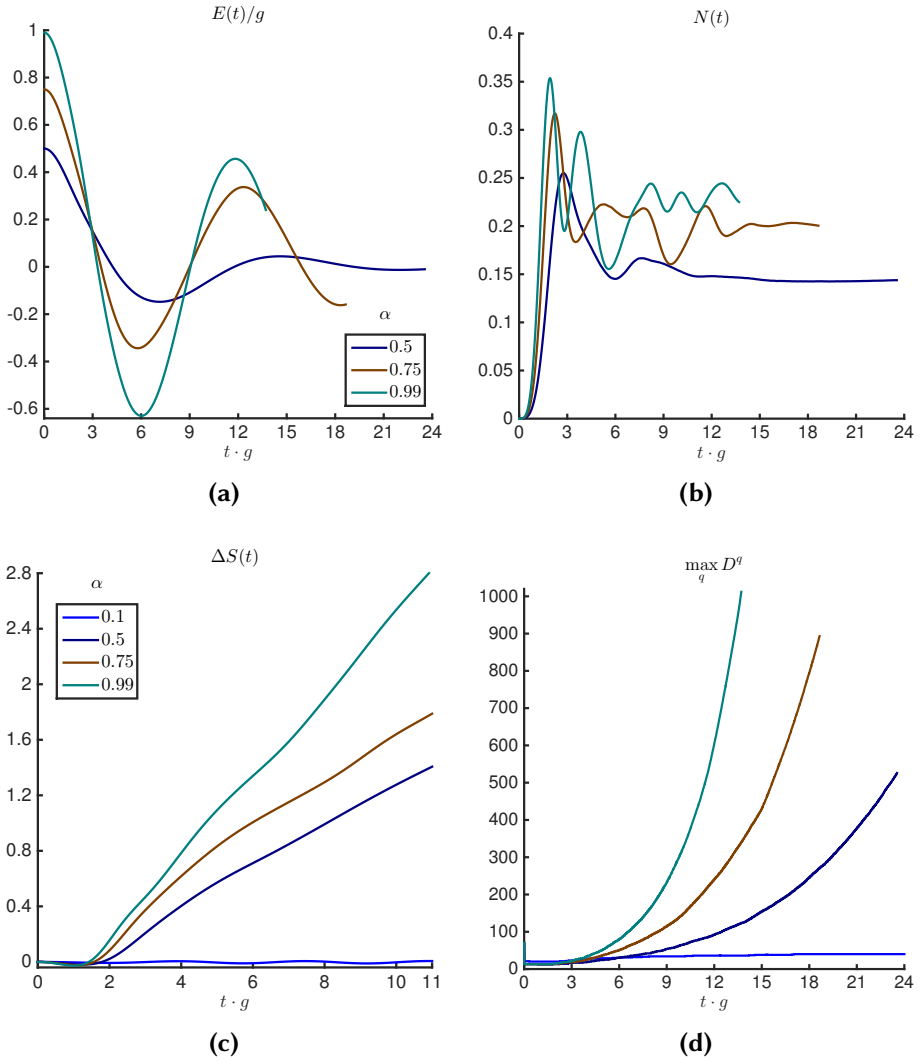


Figure 5.5.: $m/g = 0.25$, $x = 100$. (a) Electric field $E(t)$. (b) Particle number $N(t)$. (c) Renormalized von Neumann entropy $\Delta S(t)$. (d) Maximum bond dimensions over the eigenvalue sectors of $L(n)$.

5.4. Strong field regime

In the previous section we saw that we could explain the oscillatory behavior of the local quantities beyond linear response theory for relatively small values of α . However at very late times we expect that the physical picture discussed in the previous section doesn't hold anymore. It is accepted that in general a state that is brought out of equilibrium will relax and equilibrate at late times [139]. With this we mean that for any compact subsystem the reduced density operator of the state $|\psi(t)\rangle$ converges to a steady state. How these asymptotic states look like is less clear [140]. In general it is believed that this steady state is a Gibbs state of the quenched Hamiltonian at a certain temperature. This process, which is called thermalization, erases the local memory of the initial state. However there are also counterexamples like for instance integrable systems when the system has some local conserved quantities. In this case the steady state is believed to be a generalized Gibbs ensemble which is compatible with the conserved quantities [141]. Another counterexample is many-body localization [142] which occurs when all the eigenstates of the Hamiltonian obey an area law for the entanglement entropy. Even when some local quantities indicate thermalization it is still possible that the state as a whole doesn't become thermal, see for instance [143]. In this section we increase the magnitude of the background electric field and examine if it equilibrates to the predicted Gibbs state.

In figs. 5.5a and 5.5b we show the electric field and the particle number for $\alpha = 0.5, 0.75$ and $\alpha = 0.99$. The observed oscillatory behavior at earlier times can be seen as a remnant of the oscillations for smaller values of α , see figs. 5.4a and 5.4c. These oscillations are now damped over time and suggest that the state starts equilibrating. This is also corroborated by the half chain entropy, fig. 5.5c, which grows linearly in time. Note the difference with the case $\alpha = 0.1$ where the entropy oscillates around zero. It is precisely this growth of entropy that leads to an exponential increase of the bond dimension for a fixed tolerance. This is confirmed in fig. 5.5d where we show the maximum bond dimension $\max_q D^q$ for our simulations. For $\alpha = 0.5, 0.75$ and 0.99 we took $\epsilon = 10^{-5}$ and for $\alpha = 0.1$ we took $\epsilon = 10^{-6}$. This growth of the bond dimension limits the time we can follow the equilibration process.

If the state would eventually thermalize we can estimate its temperature from the results of chapter 4. The inverse temperature β_0 of the asymptotic Gibbs state $\rho(\beta_0) \propto \mathcal{P}e^{-\beta_0 \mathcal{H}_\alpha}$, see eq. (4.2), is determined from the requirement that

$$\langle \Psi(t) | \mathcal{H}_\alpha | \Psi(t) \rangle = \frac{\text{tr}(\mathcal{H}_\alpha \mathcal{P}e^{-\beta_0 \mathcal{H}_\alpha})}{\text{tr}(\mathcal{P}e^{-\beta_0 \mathcal{H}_\alpha})}.$$

In figs. 5.6a and 5.6d we show the energy per unit of length \mathcal{E}_β of the Gibbs state $\rho(\beta)$ as a function of β and the (conserved) energy per unit of length $\mathcal{E}(t)$ of the state $|\Psi(t)\rangle$. We subtracted from both quantities the energy per unit of length of $|\Psi(0)\rangle$. The intersection between the curves determines the value of $\beta_0 g$. Because we simulated the thermal evolution with steps $d\beta = 0.05$ we can only determine an interval $[\beta_0 g - 0.05, \beta_0 g + 0.05]$ for $\beta_0 g$. For $\alpha = 0.5$ we find $\beta_0 g \in [2.6, 2.7]$ and for $\alpha = 0.75$ we find $\beta_0 g \in [1.3, 1.4]$.

Figs. 5.6b and 5.6e suggest that the electric field expectation value indeed converges towards its thermal value for $\beta \approx \beta_0$ which might suggest that the state does thermalize. In contrast, the expectation value of the particle number has not entirely equilibrated yet and it is not clear whether it will converge to its thermal value or not. In figs. 5.6c and figs. 5.6f we find that the particle number at the depicted times is still relatively far away from its predicted thermal value. We would need a larger range of time to track the state to draw further conclusions about whether the state thermalizes or not.

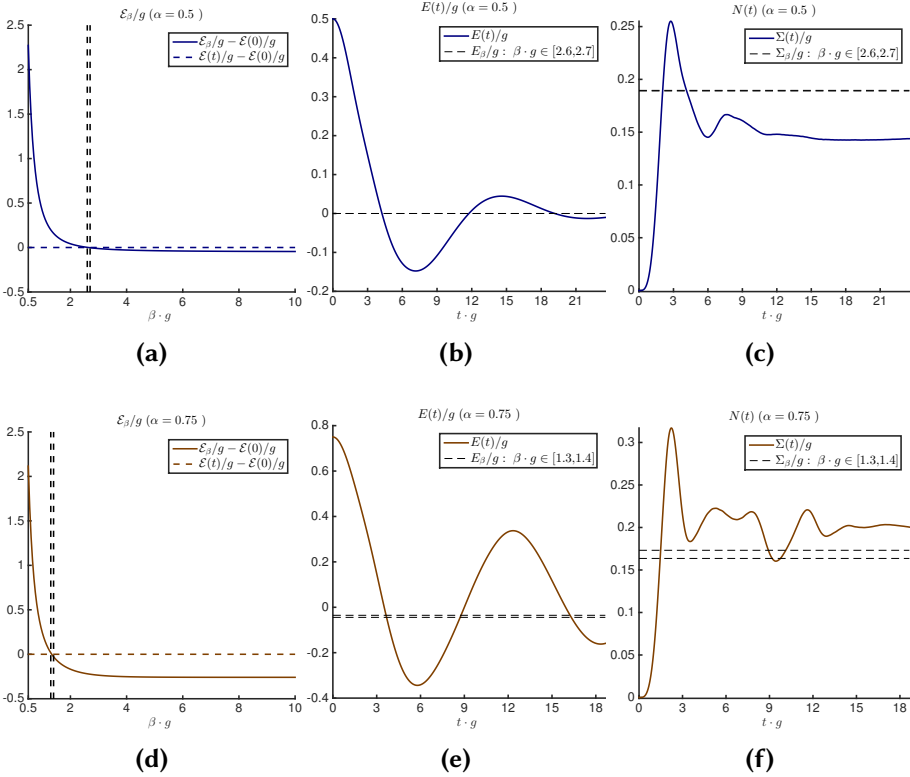


Figure 5.6.: $m/g = 0.25$, $x = 100$. (a) $\alpha = 0.5$. Estimating the temperature of the steady-state. (b) $\alpha = 0.5$. Electric field as a function of time (full line) and its predicted asymptotic thermal value (dashed line). (c) $\alpha = 0.5$. Particle number as a function of time (full line) and its predicted asymptotic thermal value (dashed line). (d) $\alpha = 0.75$. Estimating the temperature of the steady-state. (e) $\alpha = 0.75$. Electric field as a function of time (full line) and its predicted asymptotic thermal value (dashed line). (f) $\alpha = 0.75$. Particle number as a function of time (full line) and its predicted asymptotic thermal value (dashed line).

Conclusions and outlook

In this dissertation MPS are used to study a wide range of interesting aspects of the Schwinger model. I computed ground state quantities and determined the mass spectrum for a wide range of values of the background electric field α and the fermion mass m/g . I investigated confinement for static probe charges and performed finite temperature simulations. The simulation of out-of-equilibrium physics is considered as well. In all our studies I focussed on the continuum limit. By defining gauge invariant MPS all my computations were manifestly gauge invariant and I could speed up the computation time of existing MPS algorithms. Even within the Schwinger model there are a lot of interesting things to explore. Let me discuss a few topics which are still in progress:

- (a) The MPS simulations allow to determine the Schmidt spectrum. Here I used this for a direct computation of the half chain von Neumann entropy. Notice however that for gauge theories the full Von Neumann entropy is not equivalent to the LOCC distillable entanglement [144, 145]. Because the MPS simulations give direct access to the Schmidt spectrum I can compute the LOCC distillable entanglement. For the full Von Neumann entropy I was able to identify the UV divergence which allowed to define a renormalized entropy. I have already some preliminary results for the LOCC distillable entanglement, but it is not completely clarified yet how the LOCC distillable entanglement scales to the continuum limit.
- (b) In chapter 3 I investigated confinement for static probe charges. More challenging would be to investigate this in a dynamical setting. For instance, if I build two Gaussian wave packets with opposite charge and

give them opposite momentum such that they move away from each other. It is expected that, similar to the static case, a confining electric field string appears at early times when the packets are relatively close together. In contrast, at later times when the packets are farther away from each other, it would be interesting to find out whether the electric field string between the charges breaks or remains. Another interesting question is whether the dynamical string breaking would leave the same imprints on the Von Neumann entropy as in the static case. I have already performed some first simulations but I am troubled with the growth of entanglement between the charges. This leads in turn to an exponential increase in the variational parameters, similar as encountered in chapter 5. I am now looking for a reliable approximation where I can reduce the amount of entanglement I need to take into account in the simulations to have a faithful approximation.

- (c) In chapter 2 I determined the masses of the one-particle excitations. It would also be interesting to study the stationary scattering states and deduce the statistics of the particles. Therefore I can use the formalism developed in our group [137, 138, 146] which uses the MPS approximations of the one-particle excitations to determine the scattering states.

Of course I could also perform similar studies for non-abelian gauge theories like $SU(2)$ and $SU(3)$. Recently there were some studies of $SU(2)$ using MPS in the context of quantum link models [83, 84]. In [85] the nonabelian rotor models $O(2)$ and $O(4)$ were studied and the mass gap and the β -function were determined. It would definitely be interesting to perform similar studies within our framework for $SU(2)$ and $SU(3)$.

As the real world is not one-dimensional but three-dimensional the future goal is of course to bring this type of simulations to higher dimensions. The higher dimensional generalization of MPS go by the name of projected entangled pair states (PEPS) [147]. As a Hamiltonian method they are free of any sign problem although the fermions require a special treatment (see [148–150] for some examples) and also allow the simulation real-time evolution [151]. Despite the major progress in the last decade [148, 152–156], the current algorithms for PEPS simulations, however, scale unfavorably with the bond dimension [157] and I therefore expect that the successful simulation of specific microscopic gauge field Hamiltonians in the continuum limit will require new techniques. Nevertheless in the last years some promising results on PEPS and TNS in higher dimension for gauge theories have appeared [158–161]. This makes me confident that the needed faster algorithms will be developed soon and that TN will become useful to tackle gauge field theories.

Let me conclude by giving my personal opinion on the further development of TNS in the context of gauge theories. During this thesis I became convinced that TNS have the potential to become a worthy complementary approach to other methods for the study of gauge theories. In one spatial dimension the results are impressively accurate. But also in two dimensions, the PEPS can for some models already compete with state-of-the-art results of Monte-Carlo simulations [162]. Therefore I believe the TNS approach might really help in our understanding of the Standard Model where other approaches fail. I am however aware that TNS will only be able to really compete with lattice QCD in three dimensions within the next decades. Furthermore it is also important that we still consider other complementary approaches. Just like lattice QCD has its shortcomings, I believe there are also regimes that are harder or almost impossible to tackle with TNS.

But if the Standard Model is really describing Nature, I believe at one day we will finally reveal all her secrets.

Appendices

Details on the continuum extrapolation for asymptotic confinement

We provide here the details on the continuum extrapolation of the string tension, electric field and the renormalized entropy discussed in section 3.3.

A.1. String tension

Note that the string tension at $x = 1/g^2a^2$ is obtained from the energy density by:

$$\sigma_Q(x) = \sqrt{x}(\epsilon_Q(x) - \epsilon_0(x))$$

where $\epsilon_Q(x)$ is the ground state energy per site of the Schwinger Hamiltonian \mathcal{H}_Q (3.3). As for $x \rightarrow \infty$, $\mathcal{H}_Q/(2g\sqrt{x})$ reduces to the XY -model we have that

$$\lim_{x \rightarrow +\infty} \frac{\epsilon_Q(x)}{2g\sqrt{x}} = \lim_{x \rightarrow +\infty} \frac{\epsilon_0(x)}{2g\sqrt{x}} = \frac{-1}{\pi} \quad (\text{A.1})$$

and it is argued in [10] that $\epsilon_Q(x)/\sqrt{x}$ should behave polynomially as a function of $1/\sqrt{x}$ for large x , we have:

$$\sqrt{x} \frac{\epsilon_Q(x)}{g} = -\frac{2x}{\pi} + C_Q \sqrt{x} + A_Q + \mathcal{O}\left(\frac{1}{\sqrt{x}}\right) \quad (x \gg 1), \quad (\text{A.2a})$$

$$\sqrt{x} \frac{\epsilon_0(x)}{g} = -\frac{2x}{\pi} + C_0 \sqrt{x} + A_0 + \mathcal{O}\left(\frac{1}{\sqrt{x}}\right) \quad (x \gg 1). \quad (\text{A.2b})$$

This means that the energy densities $\sqrt{x}\epsilon_Q(x)$ and $\sqrt{x}\epsilon_0(x)$ are UV divergent. But as we will see, the string tension which is the difference of these quantities is UV finite and thus we should also have $C_Q = C_0$. However,

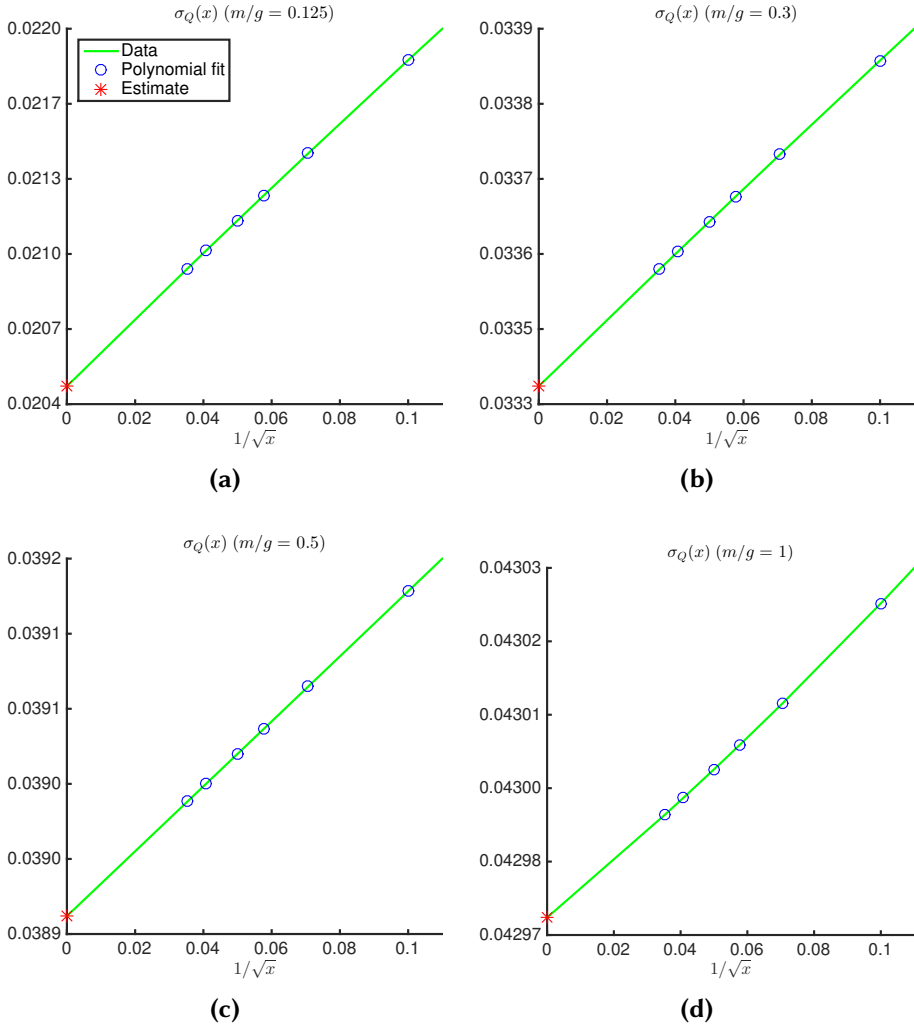


Figure A.1: $Q = 0.3$: Continuum extrapolation of the string tension σ_Q for different values of m/g .

from the numerical point of view it is clear that small errors in (A.1) or/and in C_Q and C_0 would lead to large errors in the extrapolated continuum value $\lim_{x \rightarrow \infty} \sigma_Q$. To avoid this problem we first calculate ϵ_0 and subtract it from the Hamiltonian (3.3): $\mathcal{H}_Q \leftarrow \mathcal{H}_Q - \sum_{n=1}^{2N} \epsilon_0$. The string tension is then computed as $\sigma_Q(x) = g\sqrt{x}\epsilon_Q(x)$ where $\epsilon_Q(x)$ is the ground state of the renormalized Hamiltonian. As follows from (A.2), for large x , $\sigma_Q(x)$ should scale as

$$\frac{\sigma_Q(x)}{g^2} = A_Q + \frac{B_Q}{\sqrt{x}} + \frac{C_Q}{x} + \frac{D_Q}{x^{3/2}} + \frac{E_Q}{x^2} + \mathcal{O}\left(\frac{1}{x^{5/2}}\right). \quad (\text{A.3})$$

In our simulations we computed $\sigma_Q(x)$ for $x = 100, 200, 300, 400, 600, 800$. Our estimate σ_Q^{est} is obtained by fitting the $\sigma_Q(x)$ corresponding to the five largest x to

$$f_1(x) = A_Q + \frac{B_Q}{\sqrt{x}} + \frac{C_Q}{x} + \frac{D_Q}{x^{3/2}} \quad (\text{A.4})$$

and taking $\sigma_Q^{est} = g^2 A_Q$.

In fig. A.1 we plot our results for the string tension as a function of $1/\sqrt{x}$ for $Q = 0.3$ and $m/g = 0.125, 0.3, 0.5, 1$. The numerical results are represented by circles and our polynomial fit (A.4) through the largest five x -values is shown by a full line. The star represents our continuum estimate. It is clear that the string tension indeed behaves polynomially as a function of $1/\sqrt{x}$. For larger values of m/g one can also deduce that we are already very close to the continuum limit at $1/\sqrt{x} = 0.1$. Indeed, for $m/g = 1$, the difference of our estimate with $\sigma_Q(x)$ at $x = 100$ is only of order 10^{-5} .

The continuum extrapolation depends on the chosen interval and the chosen fit. Therefore we also compute the continuum estimates by fitting all the data to $f_1(x)$ (see (A.4)) and all our data to

$$f_2(x) = A_Q + \frac{B_Q}{\sqrt{x}} + \frac{C_Q}{x} + \frac{D_Q}{x^{3/2}} + \frac{E_Q}{x^2}.$$

The error err_{σ_Q} is taken to be the maximum of the difference of σ_Q^{est} with these two other estimates. In fig. A.2a we show the \log_{10} of err_{σ_Q} as a function of Q for $m/g = 0.125, 0.3, 0.35, 0.5, 1$. It is clear that these errors are quite small. We have the largest error for $m/g = 0.3$ and $Q = 0.5$ which is explained by the fact that the gap is very small there as we are in the vicinity of a phase transition [27]. As mentioned above, it is well known that for smaller mass gaps, for a given bond dimension, the error on the ground state MPS approximation will be larger.

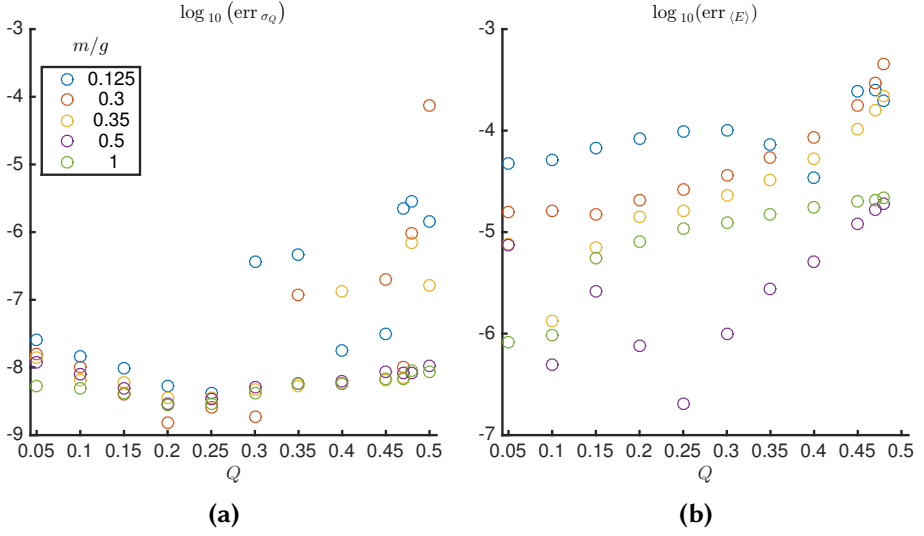


Figure A.2.: (a): $\log_{10}(\text{err}_{\sigma_Q})$ as a function of Q . (b): $\log_{10}(\text{err}_{\langle E \rangle})$ as a function of Q .

A.2. Electric field

The continuum extrapolation of the electric field,

$$\frac{\langle E \rangle}{g} = \frac{1}{2N} \left\langle \sum_{n=1}^{2N} (L(n) - Q) \right\rangle_Q, \quad (\text{A.5})$$

was found in a similar way. Now we used the values computed at $x = 100, 200, 300, 400$ and performed a linear fit,

$$g_1(x) = A_Q + \frac{B_Q}{\sqrt{x}}, \quad (\text{A.6})$$

through the three largest x -values. The fact that we again have analytical behavior as a function of $1/\sqrt{x}$ can be observed from fig. A.3 where we display the electric field as function of $1/\sqrt{x}$. It is also a consequence of the fact that $\langle E(x) \rangle = -d\sigma_Q(x)/dQ$ and we already argued that $\sigma_Q(x)$ is analytical as a function of x . To make our estimate more robust against the choice of the interval and the fitting function we compute estimates by a linear fit (A.6) through all the points ($x = 100, 200, 300, 400$) and a quadratic fit,

$$g_2(x) = A_Q + \frac{B_Q}{\sqrt{x}} + \frac{C_Q}{x},$$

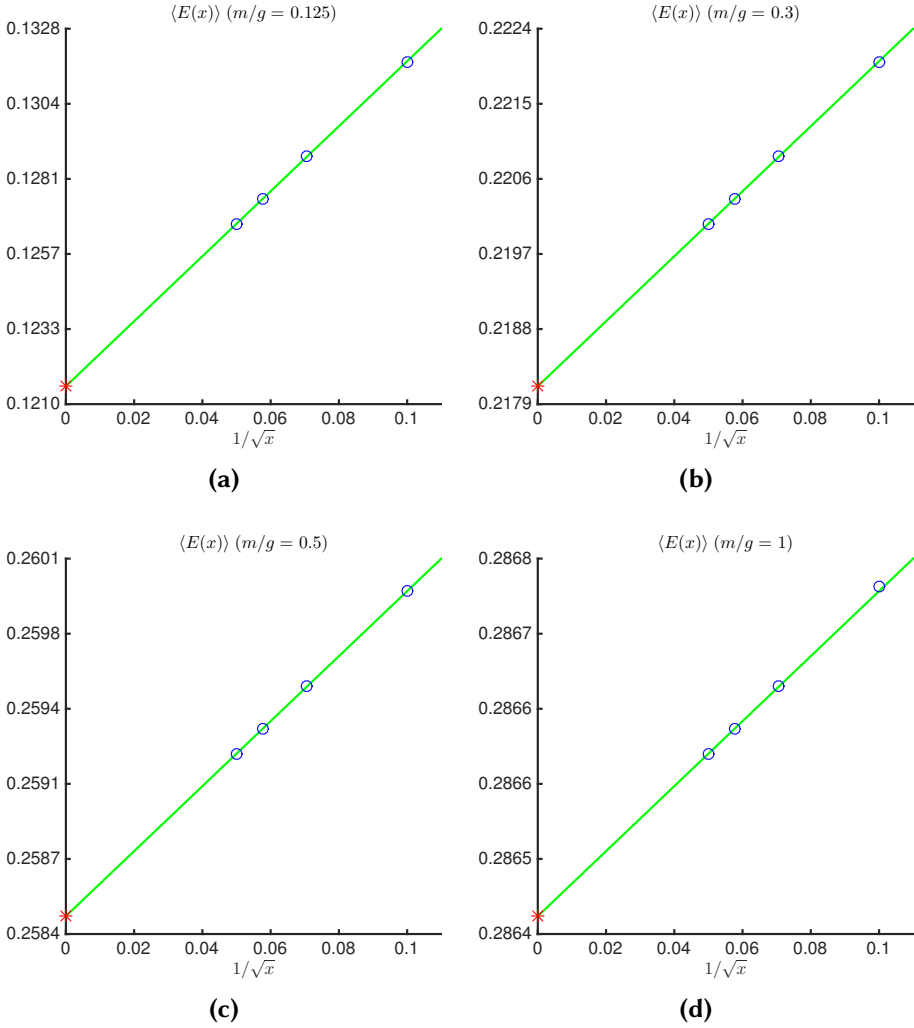


Figure A.3.: $Q = 0.3$. Continuum extrapolation of the electric field $\langle E \rangle$ for different values of m/g .

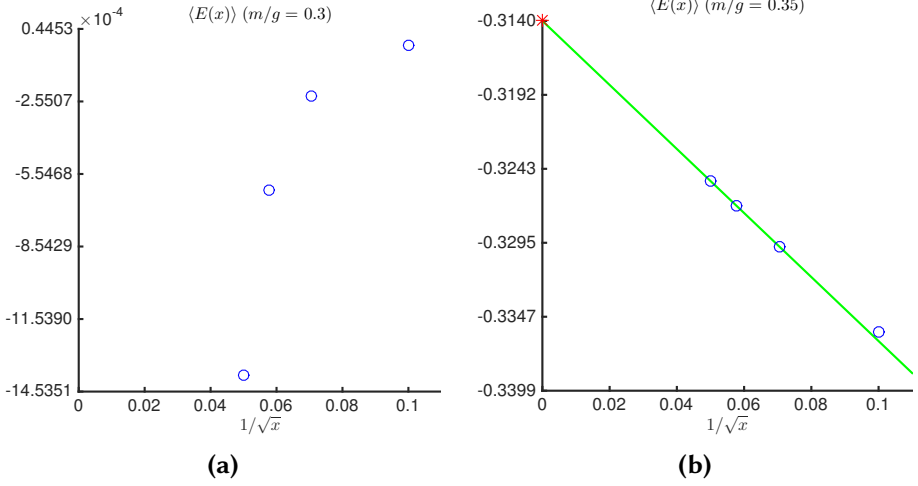


Figure A.4.: $Q = 1/2$. Continuum extrapolation of the electric field $\langle E \rangle$. (a): $m/g = 0.3$. (b): $m/g = 0.35$.

through all the points. Again, the error $\text{err}_{\langle E \rangle}$ is taken to be the maximum of the difference with these two estimates. The \log_{10} of $\text{err}_{\langle E \rangle}$ is displayed in fig. A.2b. The errors are quite small but become larger again around the phase transition at the critical mass $(m/g)_c \approx 0.33$ when going towards $Q = 1/2$.

At $Q = 1/2$ we did not display our error because this is a special case. For $m/g < (m/g)_c$ the \mathcal{CT} symmetry is not broken and thus we should have $\langle E \rangle = 0$, and this for all values of x . Therefore a continuum extrapolation of $\langle E \rangle$ is useless, see fig. A.4a. To obtain an error bound we take the largest value in magnitude of $\langle E(x) \rangle$ for $x = 100, 200, 300, 400$. It is displayed in table A.1. When $m/g > (m/g)_c$ we have two different vacua with opposite sign for the electric field. We will always take the negative sign which comes down to taking the vacuum in the limit $Q \rightarrow 1/2$ for $Q < 1/2$. In this case it is possible to perform a polynomial extrapolation, see fig. A.4b. The results are given in Table A.1. If possible we compare with [27].

A.3. Renormalized entropy

Using the Schmidt values $\sigma_{\alpha_q}^q$, see eq. (2.10), we can compute the half chain Von Neumann entropy $S_Q(x)$,

$$S_Q(x) = - \sum_{q=p_{min}}^{p_{max}} \sum_{\alpha_q=1}^{D_q} \sigma_{\alpha_q}^q \log(\lambda_{q,\alpha_q}),$$

m/g	$\langle E \rangle/g$	$\langle E \rangle/g$ [27]
0.125	3×10^{-4}	-
0.25	2×10^{-4}	-
0.3	0.0014	0.0(3)
0.35	-0.313(2)	-
0.5	-0.42041(3)	-0.421(1)
0.75	-0.46145(2)	-
1	-0.47692(2)	-0.4769 (5)
2	-0.49364(3)	-
4	-0.49834(3)	-

Table A.1.: Electric field at $Q = 1/2$ for different value of m/g .

for a particular value of x . As already mentioned in section 3.3, because the Schwinger model is equivalent to a non-critical boson theory [6], the half chain Von Neumann entropy should diverge as $(-1/6) \log(1/\sqrt{x})$ [90] when $x \rightarrow +\infty$. Because the coefficient of the logarithmic divergence of the Von Neumann entropy is universal, the renormalized entropy $\Delta S_Q = S_Q - S_0$ should be UV finite. In fig. A.5 we plot $\Delta S_Q(x)$ as a function of $1/\sqrt{x}$ and observe that this scales linearly in $1/\sqrt{x}$ to the continuum limit. A continuum result for different values of Q and m/g is obtained in exactly the same way as for the electric field. The errors originating of the choice of fitting interval and fitting function were relatively small.

For the electric field and the string tension we had that our results at $x = 100$, or equivalently $ga = 1/\sqrt{x} = 0.1$, only differed from the continuum result by at most 10 percent, see fig. A.1 and fig. A.3. Contrary, for the entropy this is not the case at all, see fig. A.5: the result at $x = 100$ and the continuum result differ by a factor of order one and sometimes also have a different sign. The main lesson is that, contrary to other quantities like the electric field and the string tension, we should be careful when extrapolating results at finite x of the renormalized entropy to the continuum limit. In particular, for the non-uniform case, see section 3.4, one should always check how the results scale for different values of x .

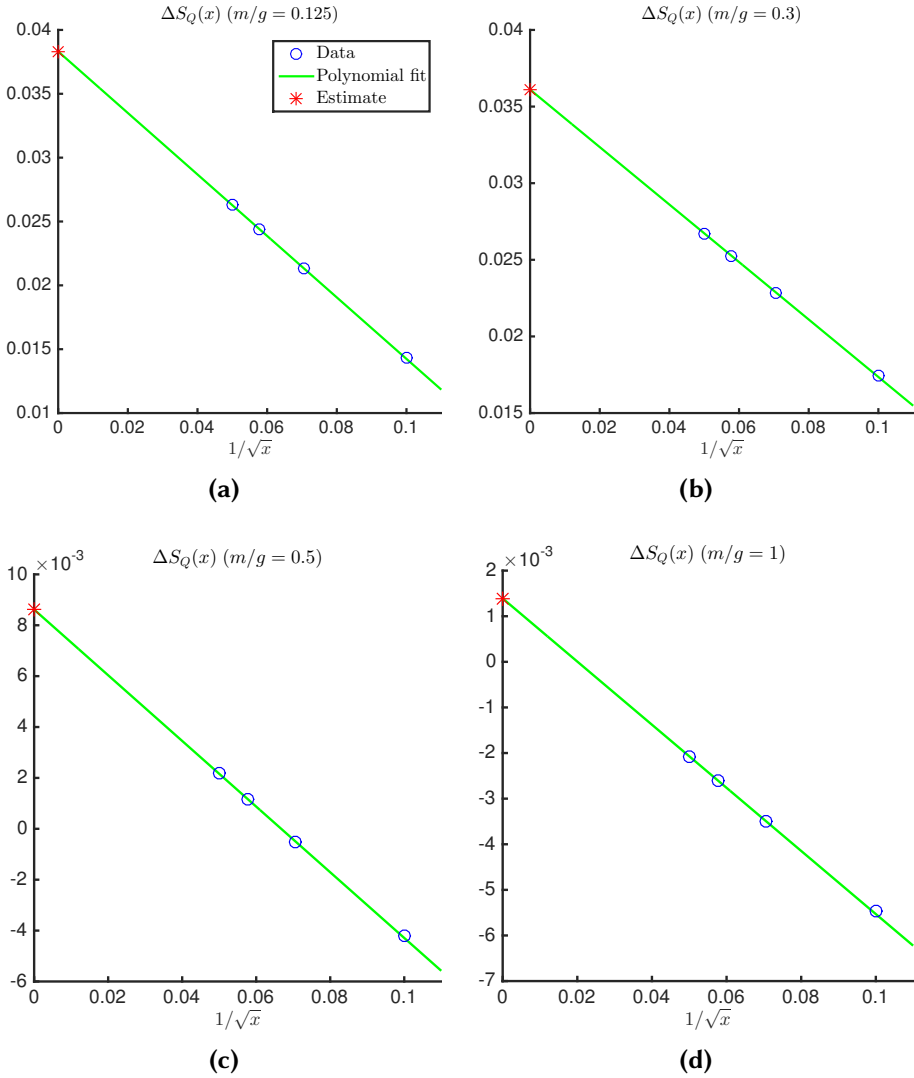


Figure A.5.: $Q = 0.3$. Continuum extrapolation of the renormalized half chain Von Neumann entropy for different values of m/g .

Supplementary material for the Schwinger model at finite temperature

Here we provide some additional information on the simulations at finite temperature, chapter 4.

B.1. The chiral condensate for $\alpha = 0$

Assume we computed the chiral condensate $\Sigma(\beta, x)$ for the x -values $x = x_1, \dots, x_n$ and we want to obtain a continuum value

$$\Sigma(\beta) = \lim_{x \rightarrow +\infty} \Sigma(\beta, x).$$

In our case we performed simulations for

$$x = 100, 125, 150, \dots, 300, 400, 500, 600.$$

When $\beta \rightarrow +\infty$ the chiral condensate diverges logarithmically in x for $m/g \neq 0$. Perturbative computations and numerical simulations pointed out, see [23, 34] and subsection 2.1.4, that this can be traced back to the free theory ($g = 0$). By subtracting the free chiral condensate eq. (2.4),

$$\Sigma_{free}(x) = -\frac{m}{\pi g} \frac{1}{\sqrt{1 + \frac{m^2}{g^2 x}}} K\left(\frac{1}{1 + \frac{m^2}{g^2 x}}\right),$$

where K is the complete elliptic integral of the first kind, the logarithmic divergence is removed. At finite temperature for a fixed value of x we will subtract the contribution of the ground state expectation value ($\beta g = +\infty$)

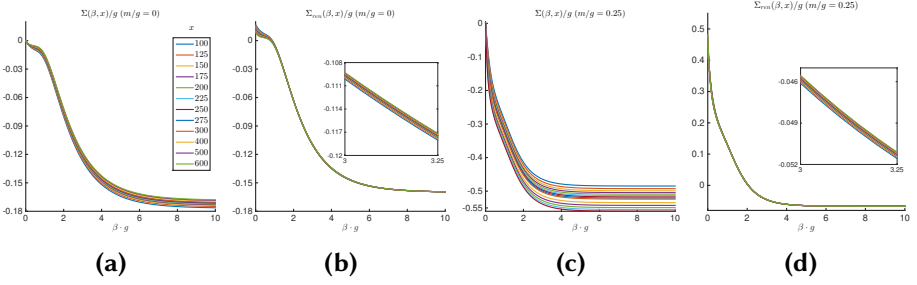


Figure B.1: Scaling of chiral condensate $\Sigma(\beta, x)$ and renormalized chiral condensate $\Sigma_{ren}(\beta, x)$ to $x \rightarrow +\infty$. (a) $\Sigma(\beta, x)$ for $m/g = 0$. (b) $\Sigma_{ren}(\beta, x)$ for $m/g = 0$. (c) $\Sigma(\beta, x)$ for $m/g = 0.25$. (d) $\Sigma_{ren}(\beta, x)$ for $m/g = 0.25$.

value and add the renormalized expectation value in the continuum limit, i.e. we will consider

$$\Sigma_{ren}(\beta, x) = \Sigma(\beta, x) - \Sigma(x) + \Sigma_{ren} \quad (\text{B.1})$$

where $\Sigma(x) = \Sigma(+\infty, x)$ corresponds to the chiral condensate of the ground state of H at finite x and $\Sigma = \Sigma(+\infty, +\infty)$ is the chiral condensate in the continuum limit. This quantity is UV finite. Note that in subsection 2.1.4 we already obtained Σ_{ren} to sufficient precision. Comparing fig. B.1a with fig. B.1b (resp. B.1c with fig. B.1d) it is clear that almost the full scaling in x of $\Sigma(\beta, x)$ is removed by considering $\Sigma_{ren}(\beta, x)$. Indeed, the graphs of $\Sigma_{ren}(\beta, x)$ for different values of x are almost on top of each other.

Like in [34] we perform a continuum extrapolation by fitting

$$f_1(x) = A_1 + B_1 \frac{\log(x)}{\sqrt{x}} + C_1 \frac{1}{\sqrt{x}} \quad (\text{B.2a})$$

and

$$f_2(x) = A_2 + B_2 \frac{\log(x)}{\sqrt{x}} + C_2 \frac{1}{\sqrt{x}} + D_2 \frac{1}{x} \quad (\text{B.2b})$$

to $\Sigma_{ren}(\beta, x)$. These fits were performed using all our data, using all our data excluding the smallest x -value, using all our data excluding the two smallest x -values, . . . , using all our data excluding the smallest five x -values. They give us all possible estimates for the continuum value. Our final value is the mean of all these estimates.

In figure B.2 we show the continuum extrapolation for $m/g = 0$ (a-d) and $m/g = 0.25$ (e-h) for different values of βg . The full line represents the fit f_1 to all our data and the dashed line represents the fit f_2 to all our data. For $m/g = 0$ the star represents the continuum value of the exact result of

Sachs and Wipf, for $m/g = 0.25$ the star represents the continuum estimate of [34]. For small values of βg , figs. B.2a and B.2e, the results are quit robust against the choice of fitting function. During the evolution, $\Sigma(\beta, x)$ changes from a decreasing function of $1/\sqrt{x}$ to an increasing function of $1/\sqrt{x}$ around a certain value of βg . Around this value of βg it is not possible to perform a reliable fit to the data, see figs. B.2b and B.2f. In this case we used our value of $x = 100$ as the estimated continuum value. Also, for larger values of βg the difference between the values of $\Sigma_{ren}(\beta, x)$ for different values of x becomes small, see B.2d and B.2h. In this case our continuum estimate is also the value for $x = 100$.

Comparing in fig. B.1 our results at finite x with the exact result for $m/g = 0$ and with the continuum estimates from [34] for $m/g = 0.25$, it is clear that we do not gain much accuracy by performing a continuum extrapolation: the difference between the continuum values and the value at $x = 100$ is only of order 10^{-3} . For larger values of m/g this difference is even smaller. This is because we renormalized $\Sigma(\beta, x)$ by adding $-\Sigma(+\infty, x) + \Sigma_{ren}(+\infty, +\infty)$. Apparently, most of the x -scaling in $\Sigma(\beta, x)$ is contained in the ground state expectation value $\Sigma(+\infty, x)$.

B.2. Asymptotic confinement: $\alpha \neq 0$

In this section we discuss the continuum extrapolation of several quantities for the case $\alpha \neq 0$. For a quantity \mathcal{Q}_α we will subtract its ($\alpha = 0$)-value at finite temperature and thus consider $\Delta\mathcal{Q}_\alpha(\beta, x) \equiv \mathcal{Q}_\alpha(\beta, x) - \mathcal{Q}_{\alpha=0}(\beta, x)$. For the quantities we will consider $\Delta\mathcal{Q}_\alpha(\beta, x)$ is a UV finite quantity and it scales linearly in $1/\sqrt{x}$ to $x = +\infty$. Therefore the following fits should be appropriate

$$f_1(x) = A_1 + B_1 \frac{1}{\sqrt{x}} \quad (\text{B.3a})$$

$$f_2(x) = A_2 + B_2 \frac{1}{\sqrt{x}} + C_2 \frac{1}{x} \quad (\text{B.3b})$$

$$f_3(x) = A_3 + B_3 \frac{1}{\sqrt{x}} + C_3 \frac{1}{x} + D_3 \frac{1}{x^{3/2}} \quad (\text{B.3c})$$

where higher order corrections in $1/\sqrt{x}$ should be sufficiently small, i.e. $C_2, C_3, D_3 \ll 1$. In figure B.3 we show the extrapolation of the string tension $\sigma_\alpha(\beta, x) = \Delta\mathcal{F}_\alpha(\beta, x) = \mathcal{F}_\alpha(\beta, x) - \mathcal{F}_0(\beta, x)$, fig. B.3a-B.3d, and the renormalized chiral condensate $\Delta\Sigma_\alpha(\beta, x) = \Sigma_\alpha(\beta, x) - \Sigma_0(\beta, x)$ for $m/g = 0.25$ and $\alpha = 0.25$, fig. B.3e-B.3h. We also show the fits f_1 , f_2 and f_3 , eq. (B.3) to all our data: $x = 100, 125, 150, \dots, 275, 300$. The electric field and the average energy per unit of length show similar behavior as

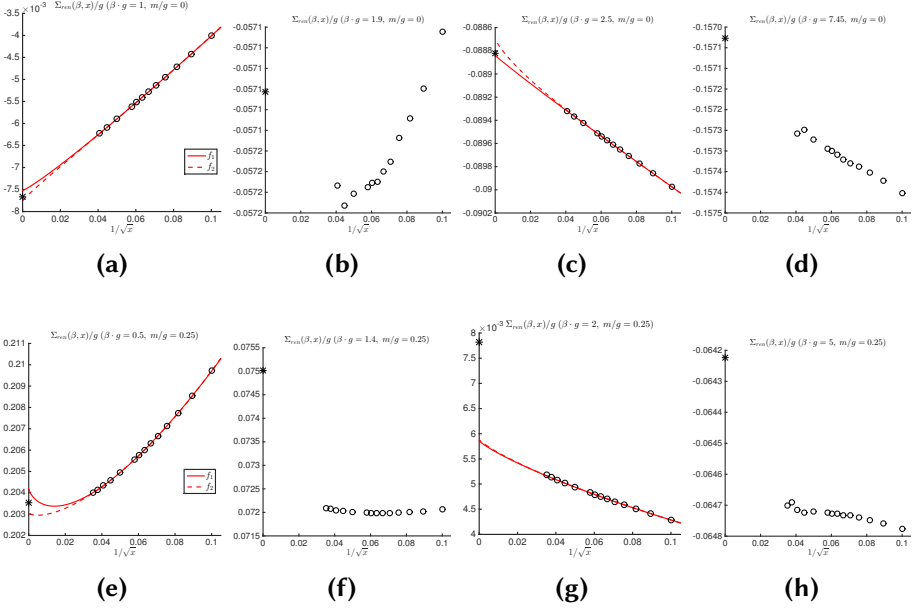


Figure B.2.: Continuum extrapolation of $\Sigma_{ren}(\beta, x)$ for different values of βg . The full line is the fit f_1 to all our data and the dashed line is the fit f_2 to all our data (see eq. (B.2)). (a-d) $m/g = 0$. (e-h) $m/g = 0.25$. For $m/g = 0$ the star represent the continuum result of Sachs and Wipf [15] while for $m/g = 0.25$ it represents the continuum estimate of [34].

a function of x . Our final estimate is obtained by taking the mean of the estimates obtained from

- (a) a linear fit (f_1) to the largest three x -values, the largest four x -values, ..., all x -values,
- (b) a quadratic fit (f_2) to the largest four x -values, the largest five x -values, ..., all x -values,
- (c) a cubic fit (f_3) to the largest five x -values, the largest six x -values, ..., all x -values.

The standard deviation on all these estimates serves as our error σ_{err} . Our estimates are shown by a star in fig. B.3. It is clear that for small values of βg our results are quite robust against the choice of fitting function f_1 or f_2 . For larger values of βg , the cubic fit seems to be less suitable, which can also be observed by inspecting the coefficient D_3 .

In fig. B.4 (a) - (d) we show the continuum results for $m/g = 0.125, 0.25$ and $\alpha = 0.1, 0.25, 0.45$ for the string tension, the electric field, the entropy per unit of length and the renormalized chiral condensate. The error σ_{err} for

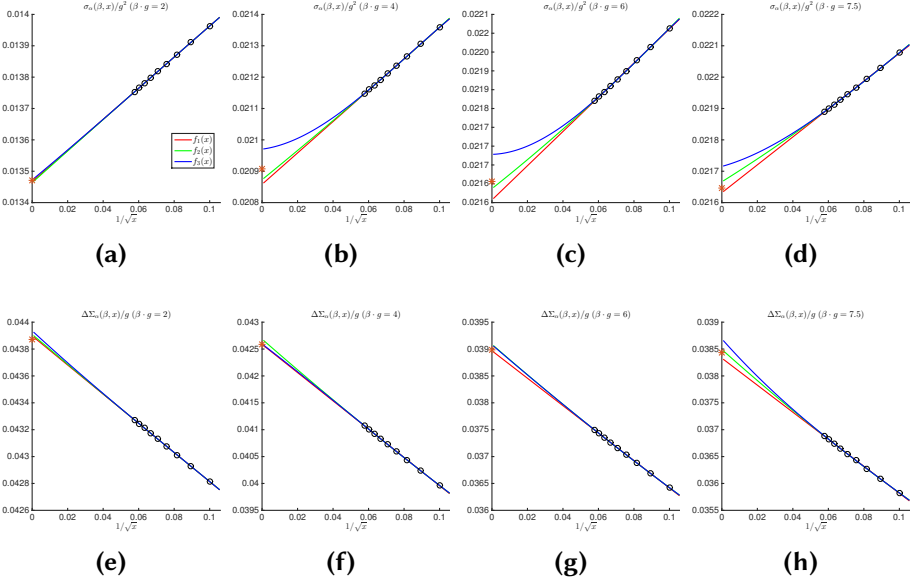


Figure B.3.: $m/g = 0.25, \alpha = 0.25$. Continuum extrapolation of the string tension $\sigma_\alpha(\beta)$ (a)-(d) and the renormalized chiral condensate $\Delta\Sigma_\alpha(\beta)$ (e)-(h) for different values of βg .

each of these quantities is shown in fig. B.4 (e) - (h). The entropy is obtained from the string tension $\sigma_\alpha(\beta)$ and the average energy $\mathcal{E}_\alpha(\beta)$ via the relation

$$\Delta S_\alpha(\beta) = -\beta \left(\sigma_\alpha(\beta) - \mathcal{E}_\alpha(\beta) \right),$$

therefore we display the error on $\mathcal{E}_\alpha(\beta)$ and $\sigma_\alpha(\beta)$ instead of the error on $S_\alpha(\beta)$. The errors are only of order 10^{-4} , so our fits are reliable. Note also that already at $x = 100$ our results are close to their continuum value. For $m/g \gtrsim 0.5$ the results for different x -values are even closer to each other. In fig. B.5 we show some quantities for $m/g = 0.5$ and $\alpha = 0.25$ and different values of x . Clearly, the results are almost on top of each other. Therefore, a continuum extrapolation is only necessary for $m/g = 0.125, 0.25$.

B.3. Simulations for $\alpha = 1/2$

Here we will discuss our results of the simulations for $\alpha = 1/2$. For $m/g \lesssim (m/g)_c \approx 0.33$, we already saw convergence of $E_{1/2-\delta}(\beta, x)$ to zero for $\delta \gtrsim 0$ for all values of $\beta g \in [0, 10]$. When performing simulations for $\alpha = 1/2$ we indeed observe that $E_{1/2}(\beta, x) = 0$, see figs. B.6a and B.6b. When imposing higher accuracy, which is obtained by lowering the tolerance ϵ

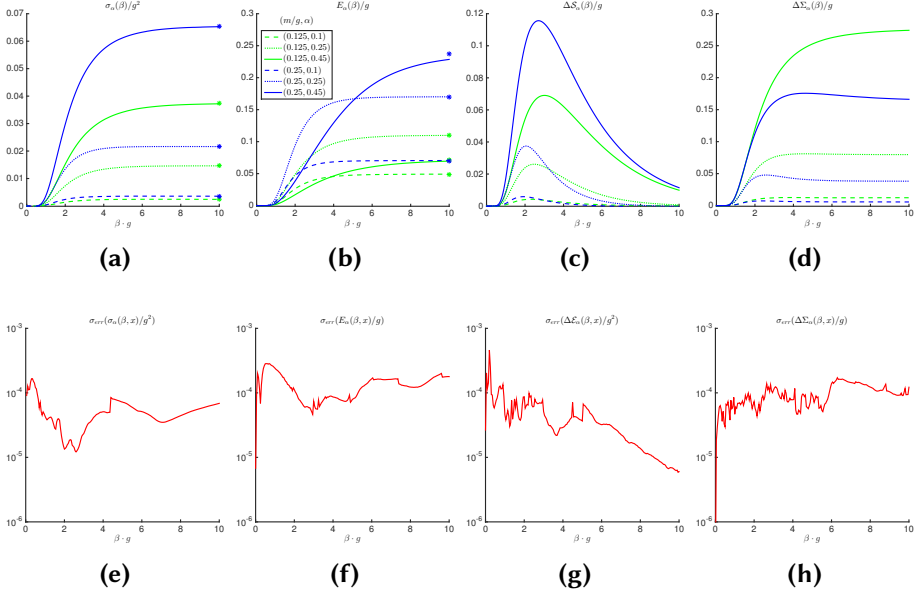


Figure B.4.: (a) - (d): Continuum results for $m/g = 0.125$ (green), 0.25 (blue) and $\alpha = 0.1$ (dotted line), $\alpha = 0.25$ (dashed line), $\alpha = 0.45$ (full line). The stars represent the value at $\beta g = +\infty$ computed in section 3.3. (a): String tension. (b) Electric field. (c): Entropy density. (d): Renormalized chiral condensate. (e) - (h): Errors σ_{err} on the continuum extrapolation for $m/g = 0.25$ and $\alpha = 0.25$. (e): String tension. (f) Electric field. (g) Average energy. (h) Chiral condensate.

(see subsection 4.2.3) we find that $E_{1/2}(\beta, x)$ becomes smaller in magnitude. However, even for $\epsilon = 10^{-6}$, we already have that $|E_{1/2}(\beta, x)| \lesssim 5 \times 10^{-5}$. This was expected because the Hamiltonian has for these values of m/g a unique CT invariant ground state which has a zero expectation value for the electric field.

In contrast, for $m/g \gtrsim (m/g)_c$ the electric field is not stable under variation of ϵ , see figs. B.6c and B.6d. Because the ground state is two-fold degenerate for $\alpha = 1/2$ and $m/g \gtrsim 0.33$ for a certain value of βg the evolution ‘picks’ out the ground state $|\Psi_{1/2-}\rangle$ corresponding to $\alpha = 1/2 - \delta$ in the limit $\delta \rightarrow 0$. The Gibbs states has evolved then to

$$\rho_{1/2-}(\beta) \propto |\Psi_{1/2-}\rangle \langle \Psi_{1/2-}| + \mathcal{O}(e^{-\beta\Delta})$$

for βg large where Δ is the mass gap of the Hamiltonian $H_{1/2-\delta}$ in the limit $\delta \rightarrow 0$. This artifact originates mainly from the fact that the iTEBD follows a path with minimal entanglement. Clearly, the state $\rho_{1/2-}(\beta)$ has less entanglement than the exact state ρ . One can also observe this by

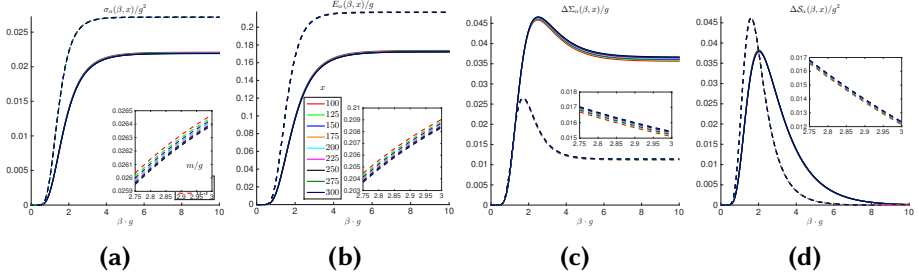


Figure B.5.: $\alpha = 0.25$. $m/g = 0.25$ (full line) and $m/g = 0.5$ (dashed line). Quantities for $x = 100, 125, 150, \dots, 300$. (a) String tension. (b) Electric field. (c) Renormalized chiral condensate. (d) Entropy.

investigating the maximum bond dimension D_{max} over the charge sectors, see insets figs. B.6 (a) - (d). We expect that D increases with βg and saturates when the system is effectively at zero temperature. For $m/g = 1$ we observe for $\beta g \gtrsim 6$ that D_{max} decreases with βg . This indicates that the iTEBD algorithm converges to a state with less entanglement.

It is clear that this leads to huge errors in the expectation values. Only for CT invariant observables, e.g. the free energy, the average energy, the chiral condensate, we can still find accurate results. In figs. B.6g and B.6h we indeed find that the free energy is stable under variation of ϵ .

B.4. Thermal corrections in the weak coupling limit

The Lagrangian for the Schwinger model is:

$$\mathcal{L} = \bar{\psi} (\gamma^\mu (i\partial_\mu + gA_\mu) - m) \psi - \frac{1}{4} F_{\mu\nu} F^{\mu\nu}.$$

In the weak coupling limit ($m/g \gg 1$) with an electric background field $g\alpha$ Coleman [6] considered the Hamiltonian for this Lagrangian in the semi-classical approximation and where he restricted to the two-particle subspace:

$$H_\alpha \approx \int_{-\infty}^{+\infty} dp \, 2\sqrt{p^2 + m^2} + \int_{-\infty}^{+\infty} dx \, \frac{g^2}{2} (|x| - 2\alpha x) + \mathcal{O}\left(\hbar, \frac{g}{m}\right),$$

with $[x, p] = i$.

The first term is the total energy of a fermion-antifermion pair. The second term gives the energy due to the separation of the fermion and the antifermion and yields an infinite number of bound states. Within this

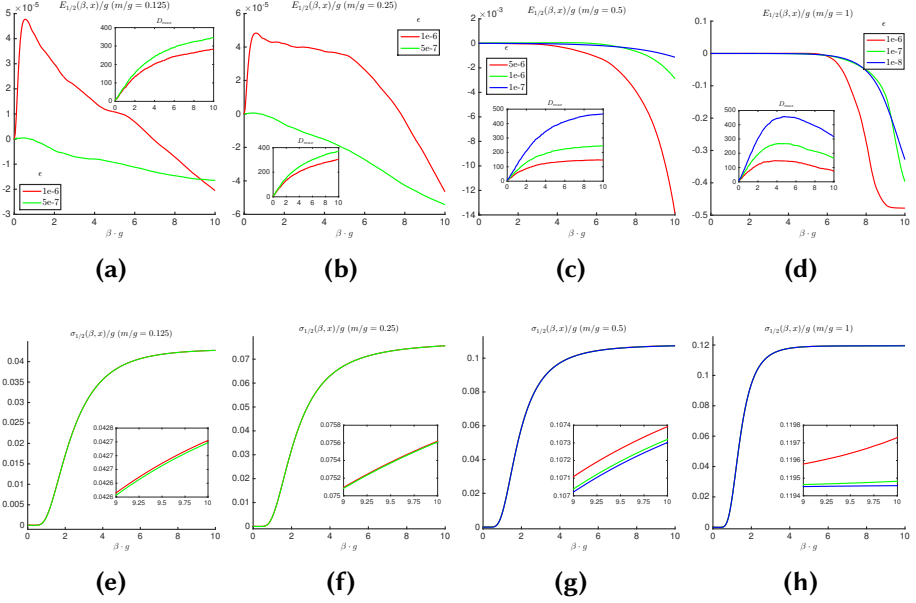


Figure B.6: $x = 100$, $\alpha = 0.5$. (a) - (d) Electric field $E_{1/2}(\beta, x)$ for different values of the tolerance ϵ . Inset: the maximum bond dimension over all charge sectors as a function of βg . (a): $m/g = 0.125$. (b): $m/g = 0.25$. (c) $m/g = 0.5$. (d) $m/g = 1$. (e) - (h) String tension $\sigma_{1/2}(\beta, x)$ for different values of the tolerance ϵ . Inset: zooming in on the interval $\beta g \in [9, 10]$. (e) $m/g = 0.125$. (f) $m/g = 0.25$. (g) $m/g = 0.5$. (h) $m/g = 1$.

semi-classical approximation Coleman then argued that the number of two-particle states with energy smaller than energy E is [6]

$$N(E) \approx \frac{E^2}{g^2 \pi (1 - 4\alpha^2)} \Theta(E - 2m) + \mathcal{O}\left(\frac{g}{m}\right),$$

where Θ is the Heaviside-function: $\Theta(x) = 1$ if $x > 0$ and $\Theta(x) = 0$ if $x < 0$. Therefore, thermal fluctuations to the ground state are only relevant if

$$\int_{2m}^{+\infty} dE \frac{dN}{dE}(E) e^{-\beta E} \sim C_m$$

for some constant C_m of order 1 depending on m but not on β . Hence, for a large fixed value of βg we will only observe significant thermal fluctuations to ground state expectation values if $\delta \lesssim K_m e^{-2\beta m} / \beta$ on, with K_m some positive constant which depends on m but is independent of β .

II

MPS for the Schwinger model: implementation

Matrix product states for quantum lattices

1.1. Matrix product states for finite lattices

In this section we recall the definition of Matrix Product States (MPS) on a one-dimensional finite lattice. We also explain how tensor network diagrams provide a way to visualize the contractions we need to compute expectation values. The Schmidt spectrum of a MPS is discussed here as well. Finally, we explain how the MPS can be brought in a canonical form. For a more extended overview we refer to [76].

1.1.1. Definition

Consider a one-dimensional system of N sites. Mathematically this is described by a lattice consisting of N sites with on each site n a local Hilbert space \mathcal{H}_n . Assuming that the quantum degrees of freedom of each of the particles is described by a q -dimensional Hilbert space, $\mathcal{H}_n \cong \mathbb{C}^q$, the total Hilbert space \mathcal{H} describing this system is the tensor product of these Hilbert spaces:

$$\mathcal{H} = \bigotimes_{n=1}^N \mathcal{H}_n \cong \mathbb{C}^{q^N}.$$

If $\{|d\rangle_n : d = 1, \dots, q\}$ is a basis for the local Hilbert space \mathcal{H}_n on site n the full Hilbert space \mathcal{H} has basis

$$\{|d_1, \dots, d_N\rangle = |d_1\rangle_1 \dots |d_N\rangle_N : d_n = 1, \dots, q\}$$

and a general state $|\Psi\rangle \in \mathcal{H}$ takes the form

$$|\Psi\rangle = \sum_{d_1=1}^q \dots \sum_{d_N=1}^q C^{d_1, \dots, d_N} |d_1, \dots, d_N\rangle$$

(mind here the order of α and β !) then

$$[(\mathbb{E}_n)^T(\Lambda)]_{\alpha,\beta} = \begin{array}{c} \beta \\ \text{---} \\ \Lambda \\ \text{---} \\ \alpha \end{array} \mathbb{E}_n = \begin{array}{c} \beta \\ \text{---} \\ A_n \\ \text{---} \\ \alpha \end{array} \Lambda_n = \left[\sum_{d=1}^q (A_n^d)^\dagger \Lambda A_n^d \right]_{\alpha,\beta} .$$

With these definitions, the diagram (1.2) becomes

$$\langle \Psi[\bar{A}] | \Psi[A] \rangle = \begin{array}{c} \Xi_0 \\ \text{---} \\ \mathbb{E}_1 \\ \text{---} \\ \mathbb{E}_2 \\ \text{---} \\ \dots \\ \mathbb{E}_n \\ \text{---} \\ \dots \\ \mathbb{E}_{N-1} \\ \text{---} \\ \mathbb{E}_N \\ \text{---} \\ \Lambda_n \end{array} \quad (1.3)$$

where $[\Xi_0]_{\alpha,\beta} = [v_L]_{\alpha,1} [\bar{v}_L]_{\beta,1}$ and $[\Lambda_N]_{\alpha,\beta} = [v_R]_{\alpha,1} [\bar{v}_R]_{\beta,1}$. Defining iteratively

$$\begin{array}{c} \Xi_n \\ \text{---} \\ \Xi_{n-1} \\ \text{---} \\ \mathbb{E}_n \end{array} \quad \text{and} \quad \begin{array}{c} \Lambda_{n-1} \\ \text{---} \\ \mathbb{E}_n \\ \text{---} \\ \Lambda_n \end{array} \quad (1.4)$$

we find for the diagram eq. (1.3)

$$\langle \Psi[\bar{A}] | \Psi[A] \rangle = \begin{array}{c} \Xi_n \\ \text{---} \\ \Lambda_n \end{array} = \text{tr}(\Xi_n \Lambda_n)$$

for any $n = 0, \dots, N$. To normalize the state it is thus sufficient to divide $A_n^{d_n}$ by $\sqrt{\text{tr}(\Xi_n \Lambda_n)}$. Note that the computation time of the norm of a MPS only scales as $\mathcal{O}(qND^3)$ with $D = \max_n D_n$.

1.1.3. Schmidt spectrum of a MPS

The matrices Ξ_n and Λ_n contain information about the Schmidt spectrum of $|\Psi[A]\rangle$. Consider the bipartition $\{\mathcal{A}_1^n, \mathcal{A}_2^n\}$ of the lattice where

$$\mathcal{A}_1^n = \{1, 2, \dots, n\} \text{ and } \mathcal{A}_2^n = \{n+1, \dots, N\}.$$

If one traces out the local Hilbert spaces living on the sites in the region \mathcal{A}_2^n one obtains the reduced density matrix $\rho_{\mathcal{A}_1^n}$,

$$\rho_{\mathcal{A}_1^n} = \text{tr}_{\mathcal{A}_2^n} (|\Psi[A]\rangle \langle \Psi[\bar{A}]|)$$

with components

$$[\rho_{\mathcal{A}_1^n}]_{(d_1, \dots, d_N); (d'_1, \dots, d'_n)} =$$

$d_n, d'_n = 1, \dots, q$. The non-zero Schmidt values with respect to this bipartition are given by the non-zero eigenvalues of $\rho_{\mathcal{A}_1^n}$. Using the property that for any two matrices A and B the non-zero eigenvalues of AB are the non-zero eigenvalues of BA , the non-zero Schmidt values are the eigenvalues of

$$= \Xi_n \Lambda_n,$$

where we assumed that the state $|\Psi[A]\rangle$ is normalized to one, $\text{tr}(\Xi_n \Lambda_n) = 1$. Denoting the eigenvalues of $\Xi_n \Lambda_n$ by $\sigma_{n,1}, \dots, \sigma_{n,D_{n+1}}$ with

$$1 \geq \sigma_{n,1} \geq \sigma_{n,2} \geq \dots \geq \sigma_{n,D_{n+1}} \geq 0, \quad \sum_{\alpha=1}^{D_{n+1}} \sigma_{n,\alpha} = 1,$$

the Schmidt decomposition with respect to the bipartition $\{\mathcal{A}_1^n, \mathcal{A}_2^n\}$ of the lattice reads

$$|\Psi[A]\rangle = \sum_{\alpha=1}^{D_{n+1}} \sqrt{\sigma_{n,\alpha}} |\Phi_{\alpha}^{\mathcal{A}_1^n}\rangle \otimes |\Phi_{\alpha}^{\mathcal{A}_2^n}\rangle \quad (1.5)$$

where

$$|\Phi_{\alpha}^{\mathcal{A}_1^n}\rangle \in \bigotimes_{j \in \mathcal{A}_1^n} \mathcal{H}_j \quad \text{and} \quad |\Phi_{\alpha}^{\mathcal{A}_2^n}\rangle \in \bigotimes_{j \in \mathcal{A}_2^n} \mathcal{H}_j$$

are orthonormal unit vectors,

$$\langle \Phi_{\alpha}^{\mathcal{A}_1^n} | \Phi_{\beta}^{\mathcal{A}_1^n} \rangle = \delta_{\alpha,\beta}, \quad \langle \Phi_{\alpha}^{\mathcal{A}_2^n} | \Phi_{\beta}^{\mathcal{A}_2^n} \rangle = \delta_{\alpha,\beta}.$$

Conversely, starting from this Schmidt decomposition, one shows that any state can be written as a MPS with bond dimensions $D_{n+1} \leq q^{\lfloor N/2 \rfloor}$ [76].

1.1.4. Expectation values of MPS

Consider a local observable \mathcal{O} , i.e. a Hermitian operator of the form

$$\mathcal{O} = \sum_{n=1}^{N-K+1} o_{n,n+1, \dots, n+K-1}.$$

Here $o_{n,n+1,\dots,n+K-1}$ is a Hermitian operator that acts non-trivially on sites $n, \dots, n + K - 1$ only, i.e. it is a shorthand notation for

$$o_{n,n+1,\dots,n+K-1} \leftarrow \mathbb{1}_{\mathcal{H}_1} \otimes \dots \otimes \mathbb{1}_{\mathcal{H}_{n-1}} \otimes o_{n,n+1,\dots,n+K-1} \otimes \mathbb{1}_{\mathcal{H}_{n+K}} \otimes \dots \otimes \mathbb{1}_{\mathcal{H}_N}$$

where $\mathbb{1}_{\mathcal{H}_n}$ is the identity operator on \mathcal{H}_n and the $o_{n,n+1,\dots,n+K-1}$ appearing on the right-hand side can be any Hermitian operator on $\mathcal{H}_n \otimes \mathcal{H}_{n+1} \otimes \dots \otimes \mathcal{H}_{n+K-1}$. For our applications we can restrict ourselves to $K = 2$ and thus to operators of the form

$$\mathcal{O} = \sum_{n=1}^{N-1} o_{n,n+1} \tag{1.6}$$

where $o_{n,n+1}$ acts only non-trivially on $\mathcal{H}_n \otimes \mathcal{H}_{n+1}$. With tensor network diagrams we represent an operator by

$$\langle d'_1, \dots, d'_n | \mathcal{O} | d_1, \dots, d_N \rangle = \begin{array}{c} d_1 \quad \dots \quad d_N \\ | \quad | \quad | \\ \text{---} \text{---} \text{---} \\ | \quad | \quad | \\ d'_1 \quad \dots \quad d'_N \end{array}, d_n, d'_n = 1, \dots, q$$

and eq. (1.6) becomes

$$\begin{array}{c} d_1 \quad \dots \quad d_N \\ | \quad | \quad | \\ \text{---} \text{---} \text{---} \\ | \quad | \quad | \\ d'_1 \quad \dots \quad d'_N \end{array} = \sum_{n=1}^{N-1} \begin{array}{c} d_1 \quad \dots \quad d_{n-1} \\ | \quad | \quad | \\ \text{---} \text{---} \text{---} \\ | \quad | \quad | \\ d'_1 \quad \dots \quad d'_{n-1} \end{array} \begin{array}{c} d_n \quad d_{n+1} \\ | \quad | \\ \text{---} \text{---} \\ | \quad | \\ d'_n \quad d'_{n+1} \end{array} \begin{array}{c} d_{n+2} \quad \dots \quad d_N \\ | \quad | \quad | \\ \text{---} \text{---} \text{---} \\ | \quad | \quad | \\ d'_{n+2} \quad \dots \quad d'_N \end{array} \tag{1.7}$$

where we introduced the following notation for the identity operator $\mathbb{1}_{\mathcal{H}_n}$ on \mathcal{H}_n :

$$\begin{array}{c} d_n \\ | \\ d'_n \end{array} = \delta_{d_n, d'_n}.$$

The expectation value $\langle \Psi[\bar{A}] | \mathcal{O} | \Psi[A] \rangle$ becomes

$$\begin{aligned}
 \langle \Psi[\bar{A}] | \mathcal{O} | \Psi[A] \rangle &= \text{Diagram 1} \\
 &= \sum_{n=1}^{N-1} \text{Diagram 2} \\
 &= \sum_{n=1}^{N-1} \Xi_{n-1} \Lambda_{n+1}, \tag{1.8}
 \end{aligned}$$

Diagram 1: A tensor network with two horizontal chains of tensors $A_1, \dots, A_n, A_{n+1}, \dots, A_N$. The top chain has left and right boundary vectors v_L^\dagger and v_R . The bottom chain has left and right boundary vectors v_L^T and \bar{v}_R . A central box labeled \mathcal{O} is connected to the top chain at site $n+1$ and the bottom chain at site $n+1$.

Diagram 2: Similar to Diagram 1, but the central box is labeled $o_{n,n+1}$ and is connected to the top chain at site n and the bottom chain at site n .

Diagram 3: A circular diagram with two nodes Ξ_{n-1} and Λ_{n+1} . Ξ_{n-1} is connected to Λ_{n+1} by two paths: one through tensors A_n and A_{n+1} on top, and another through tensors A_n and A_{n+1} on the bottom. A central box labeled o is connected to both Ξ_{n-1} and Λ_{n+1} .

where Λ_n and Ξ_n are defined in eq. (1.4).

The most efficient way to compute the diagrams in the right-hand side of eq. (1.8) is by first computing

$$\alpha - \text{Diagram } C_{n,n+1} - \beta = \alpha - \text{Diagram } A_n A_{n+1} - \beta = \left[A_n^{d_1} A_{n+1}^{d_2} \right]_{\alpha, \beta}, \tag{1.9a}$$

Diagram $C_{n,n+1}$: A box with two horizontal legs labeled α and β , and two vertical legs labeled d_1 and d_2 .

Diagram $A_n A_{n+1}$: Two boxes labeled A_n and A_{n+1} connected horizontally, with vertical legs d_1 and d_2 below them.

then performing the following contraction

$$\begin{aligned}
 \alpha - \text{Diagram } D_{n,n+1} - \beta &= \alpha - \text{Diagram } D_{n,n+1} - \beta \\
 &= \sum_{d'_1, d'_2=1}^q \langle d_1, d_2 | o_{n,n+1} | d'_1, d'_2 \rangle \left[C_{n,n+1}^{d'_1, d'_2} \right]_{\alpha, \beta}. \tag{1.9b}
 \end{aligned}$$

Diagram $D_{n,n+1}$: A box with two horizontal legs labeled α and β , and two vertical legs labeled d_1 and d_2 . Inside the box, there is a smaller box labeled $o_{n,n+1}$ connected to the vertical legs.

and finally computing

$$\alpha - \text{Diagram } \Omega_{n-1} - \beta = \alpha - \text{Diagram } D_{n,n+1} - \beta = \sum_{d_1, d_2=1}^q \left[D_{n,n+1}^{d_1, d_2} \Lambda_{n+1} \left(C_{n,n+1}^{d_1, d_2} \right)^\dagger \right]_{\alpha, \beta}. \tag{1.9c}$$

Diagram Ω_{n-1} : A circle with two legs labeled α and β .

Diagram $D_{n,n+1}$: A box with two horizontal legs labeled α and β , and two vertical legs labeled d_1 and d_2 . Inside the box, there is a smaller box labeled $C_{n,n+1}$ connected to the vertical legs.

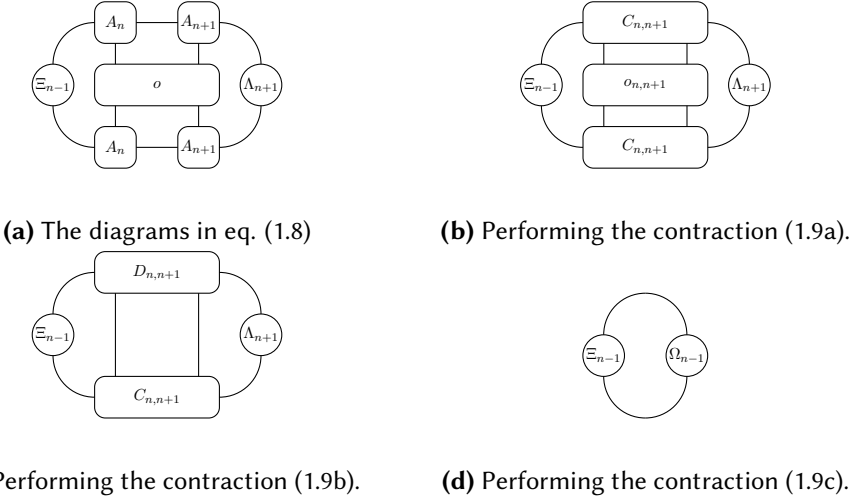


Figure 1.1.: Right order of performing the contractions to compute the diagram eq. (1.8): 1.1a \rightarrow 1.1d.

By performing the contractions in this order, see also fig. 1.1, the expectation value becomes

$$\langle \Psi[\bar{A}] | \mathcal{O} | \Psi[A] \rangle = \sum_{n=1}^N \text{tr}(\Xi_{n-1} \Omega_{n-1}).$$

and can be computed in $\mathcal{O}(Nq^2D^3)$ time. Here we assumed that $q \ll D$ which is the case for our applications.

1.1.5. Canonical form of MPS

There is some freedom in the representation eq. (1.1) of a MPS $|\Psi[A]\rangle$. If we define the tensors $\tilde{A}_n^{d_n} \in \mathbb{C}^{\tilde{D}_n \times \tilde{D}_{n+1}}$ by

$$\begin{array}{c} \text{---} \tilde{A}_n \text{---} \\ | \\ \text{---} U_n \text{---} A_n \text{---} V_{n+1} \text{---} \\ | \end{array}$$

with $U_n \in \mathbb{C}^{\tilde{D}_n \times D_n}$, $V_n \in \mathbb{C}^{D_n \times \tilde{D}_n}$ and $V_n U_n = \mathbb{1}_{D_n \times D_n}$, then it is clear that if we define the boundary vectors

$$\tilde{v}_L^\dagger = v_L^\dagger V_1, \tilde{v}_R = U_{N+1} v_R,$$

that $|\Psi[A, v_L, v_R]\rangle = |\Psi[\tilde{A}, \tilde{v}_L, \tilde{v}_R]\rangle$. Here we explicitly denoted the dependence of a MPS on its boundary vectors. This **gauge freedom** can be used to bring the MPS in a so-called canonical form. Consider again the matrices Ξ_n and Λ_n , see eq. (1.4), then we say that a MPS is in the **left**

canonical form if $\Xi_n = \mathbb{1}_{D_{n+1} \times D_{n+1}}$ for all $n = 0, \dots, N$. Similarly, we say that a MPS is in the **right canonical form** if $\Lambda_n = \mathbb{1}_{D_{n+1} \times D_{n+1}}$ for all $n = 0, \dots, N$.

Before we discuss how to bring a general MPS in such a canonical form it is convenient to get rid of the boundary vectors. Therefore we absorb v_L^\dagger into the definition of A_1 : $A_1^d \rightarrow v_L^\dagger A_1^d$ and v_R into the definition of A_N^d : $A_N^d \rightarrow A_N^d v_R$. In this case we have $D_1 = D_{N+1} = 1$ and $\Xi_0 = \Lambda_N = 1$. The MPS (1.1) then takes the form

$$|\Psi[A]\rangle = \sum_{d_1=1}^q \dots \sum_{d_N=1}^q A_1^{d_1} \dots A_N^{d_N} |d_1, \dots, d_N\rangle, A_n \in \mathbb{C}^{D_n \times D_{n+1}} \quad (1.10)$$

with $D_1 = D_{N+1} = 1$.

(a) Left canonical form

We now discuss how one brings a general MPS $|\Psi[A]\rangle$, eq. (1.10), in the left canonical form. Therefore we apply a QR-decomposition of $A'_1 \in \mathbb{C}^{qD_1 \times D_2}$ with components $[A'_1]_{(d,\alpha);\beta} = [A_1^d]_{\alpha,\beta}$:

$$A'_1 = Q'_1 M_1, Q'_1 \in \mathbb{C}^{qD_1 \times \tilde{D}_2}, M_1 \in \mathbb{C}^{\tilde{D}_2 \times D_2}, (Q'_1)^\dagger Q'_1 = \mathbb{1}_{\tilde{D}_2}.$$

Next, we define $L_1^d \in \mathbb{C}^{D_1 \times \tilde{D}_2}$ with components $[L_1^d]_{\alpha,\beta} = [Q'_1]_{(d,\alpha);\beta}$ and define $\tilde{A}_2^d = M_1 A_2^d \in \mathbb{C}^{\tilde{D}_2 \times D_3}$. These transformations do not affect the MPS (1.10) which now becomes

$$|\Psi[A]\rangle = \sum_{d_1=1}^q \dots \sum_{d_N=1}^q L_1^{d_1} \tilde{A}_2^{d_2} A_3^{d_3} \dots A_N^{d_N} |d_1, \dots, d_N\rangle.$$

Note that $(Q'_1)^\dagger Q'_1 = \mathbb{1}_{\tilde{D}_2}$ implies that

$$\begin{array}{c} \text{---} \Xi_1 \text{---} \\ \text{---} \mathbb{1}_{\tilde{D}_2} \text{---} \\ \text{---} L_1 \text{---} \\ \text{---} L_1 \text{---} \end{array} = \mathbb{1}_{\tilde{D}_2}. \quad (1.11)$$

With tensor network diagrams, we depict this transformation symbolically as

$$\begin{array}{c} \text{---} A_1 \text{---} \stackrel{(QR)}{=} \text{---} L_1 \text{---} M_1 \text{---} \\ \text{---} \tilde{A}_2 \text{---} = \text{---} M_1 \text{---} A_2 \text{---} \end{array}$$

Assume now that the MPS has been written in the form

$$|\Psi[A]\rangle = \sum_{d_1=1}^q \dots \sum_{d_N=1}^q L_1^{d_1} \dots L_k^{d_k} \tilde{A}_{k+1}^{d_{k+1}} A_{k+2}^{d_{k+2}} \dots A_N^{d_N} |d_1, \dots, d_N\rangle$$

where $L_1^{d_1}, \dots, L_k^{d_k}$ are in the left canonical form:

$$\Xi_n = \begin{array}{c} \text{---} \\ \text{---} \end{array} \text{---} \text{---} \begin{array}{c} L_n \\ L_n \end{array} = \mathbb{1}_{\tilde{D}_{n+1}} \text{ for } n \leq k.$$

Then one performs a QR-decomposition of \tilde{A}_{k+1} :

$$\text{---} \text{---} A_{k+1} \text{---} \stackrel{(QR)}{=} \text{---} \text{---} L_{k+1} \text{---} \text{---} M_{k+1} \text{---}$$

and one defines

$$\text{---} \text{---} \tilde{A}_{k+2} \text{---} = \text{---} \text{---} M_{k+1} \text{---} \text{---} A_{k+2} \text{---}$$

The MPS then takes the form

$$|\Psi[A]\rangle = \sum_{d_1=1}^q \dots \sum_{d_N=1}^q L_1^{d_1} \dots L_{k+1}^{d_{k+1}} \tilde{A}_{k+2}^{d_{k+2}} A_{k+3}^{d_{k+3}} \dots A_N^{d_N} |d_1, \dots, d_N\rangle$$

with

$$\Xi_n = \begin{array}{c} \text{---} \\ \text{---} \end{array} \text{---} \text{---} \begin{array}{c} L_n \\ L_n \end{array} = \mathbb{1}_{\tilde{D}_{n+1}} \text{ for } n \leq k+1.$$

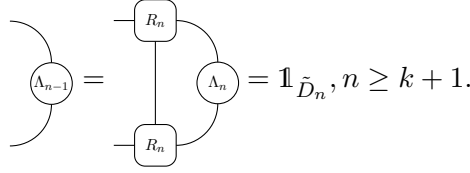
Doing this procedure for $k = 1, \dots, N$ leads to a MPS in the left canonical form.

(b) Right canonical form

Bringing a general MPS, eq. (1.10), in the right canonical form is done in a similar way as for the left canonical form, but instead of going from left to right, we proceed from right to left. More specifically, assume the MPS representation (1.10) is put in the form

$$|\Psi[A]\rangle = \sum_{d_1=1}^q \dots \sum_{d_N=1}^q A_1^{d_1} \dots A_{k-1}^{d_{k-1}} \tilde{A}_k^{d_k} R_{k+1}^{d_{k+1}} \dots R_N^{d_N} |d_1, \dots, d_N\rangle$$

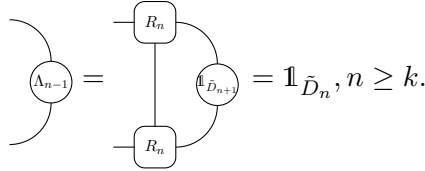
with $A_n^{d_n} \in \mathbb{C}^{D_n \times D_{n+1}}$ ($n < k$), $\tilde{A}_k^{d_k} \in \mathbb{C}^{D_k \times \tilde{D}_{k+1}}$, $R_n^{d_n} \in \mathbb{C}^{\tilde{D}_n \times \tilde{D}_{n+1}}$ ($n \geq k+1$) and where $R_{k+1}^{d_{k+1}}, \dots, R_N^{d_N}$ are in the right canonical form:



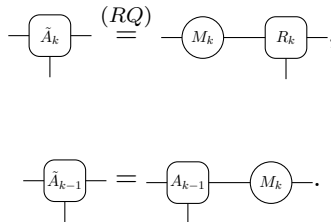
Then one performs a QR-decomposition of $A_k^\dagger \in \mathbb{C}^{q \tilde{D}_{k+1} \times D_k}$ with components $[A_k^\dagger]_{\alpha;(d,\beta)} = [\tilde{A}_k^d]_{\alpha,\beta}$: $A_k^\dagger = Q_k' M_k$, $Q_k' \in \mathbb{C}^{q \tilde{D}_{k+1} \times \tilde{D}_k}$, $M_k \in \mathbb{C}^{\tilde{D}_k \times D_k}$, $(Q_k')^\dagger Q_k' = \mathbb{1}_{\tilde{D}_k}$. Then one defines $R_k^d \in \mathbb{C}^{\tilde{D}_k \times \tilde{D}_{k+1}}$ with components $[R_k^d]_{\alpha,\beta} = [Q_k'^\dagger]_{\beta;(d,\alpha)}$ and one puts $\tilde{A}_{k-1}^d = A_{k-1}^d M_k^\dagger \in \mathbb{C}^{D_{k-1} \times \tilde{D}_k}$. The MPS representation then becomes

$$|\Psi[A]\rangle = \sum_{d_1=1}^q \dots \sum_{d_N=1}^q A_1^{d_1} \dots A_{k-2}^{d_{k-2}} \tilde{A}_{k-1}^{d_{k-1}} R_k^{d_k} \dots R_N^{d_N} |d_1, \dots, d_N\rangle$$

and because $(Q_k')^\dagger Q_k' = \mathbb{1}_{\tilde{D}_k}$, R_k is also in the right canonical form:

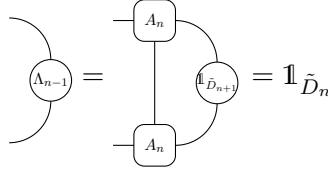


By applying this procedure for $k = N, N-1, \dots, 1$, one brings the MPS in the right canonical form. Symbolically, this transformation is represented with tensor network diagrams as

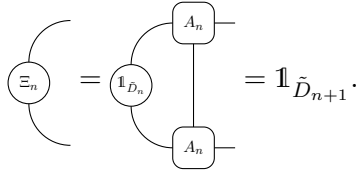


(c) Centered canonical form

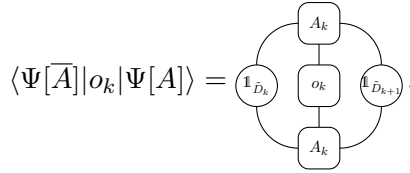
One can now combine the left and right canonical form to put a MPS in a so-called centered canonical form. More specifically, given a site k one uses the previous procedures to put for $n \geq k + 1$:



and for $n < k$:



This form is convenient for the DMRG algorithm. For a local operator o_k that acts only non-trivial on site k we find for the expectation value



1.2. uMPS in the thermodynamic limit

In this section we focus on one-dimensional quantum systems in the thermodynamic limit. We define translational invariant states, the uniform MPS (uMPS), which were introduced for the first time in [79]. Contrary to their approach, we are not concerned here with a rigorous treatment but rather follow [88, 136]. As for the finite-size case, we discuss the normalization, the Schmidt spectrum and the computation of expectation values of these states.

1.2.1. Definition

On a one-dimensional quantum system with N particles ($N \rightarrow +\infty$), a **uniform MPS** (uMPS) takes the form

$$|\Psi_u[A]\rangle = \lim_{N \rightarrow +\infty} \sum_{d_1=1}^q \dots \sum_{d_N=1}^q v_L^\dagger A^{d_1} \dots A^{d_N} v_R |d_1, \dots, d_N\rangle. \quad (1.12)$$

- (iv) Using an iterative procedure, like the Arnoldi iteration [165] or the Jacobi-Davidson method [166], the leading eigenvalue η and the corresponding left and right eigenvector Ξ and Λ can be found in

$$\mathcal{O}(N_{iter}qD^3)$$

time, with N_{iter} the number of iterations needed of the chosen method. This is because for these iterative methods we only need the action of the transfer matrix \mathbb{E} on a matrix Λ , see (1.13).

- (v) The definitions of Ξ and Λ coincide with the definitions (1.4) in the sense that

$$(a) \quad \lim_{n \rightarrow +\infty} \mathbb{E}^n(v_R v_R^\dagger) \sim \left(\lim_{n \rightarrow +\infty} \eta^n \right) \Lambda,$$

$$(b) \quad \lim_{n \rightarrow +\infty} [\mathbb{E}^T]^n(\bar{v}_L v_L^T) \sim \left(\lim_{n \rightarrow +\infty} \eta^n \right) \Xi.$$

To normalize the state to one, we need to divide A^d by $\sqrt{\eta}$ and rescale Ξ and Λ such that $\text{tr}(\Xi\Lambda) = 1$. The singular values of $\Xi\Lambda$ are the Schmidt values associated to any half chain cut of the lattice. Note that due to translation invariance, these Schmidt values are also independent of the site n . Denoting the eigenvalues of $\Xi\Lambda$ by $\sigma_1, \dots, \sigma_D$ with

$$1 \geq \sigma_1 \geq \sigma_2 \geq \dots \geq \sigma_D \geq 0, \quad \sum_{\alpha=1}^D \sigma_\alpha = 1,$$

the Schmidt decomposition eq. (1.5) with respect to the bipartition $\{\mathcal{A}_1^n = \mathbb{Z}[1, \dots, n], \mathcal{A}_2^n = \mathbb{Z}[n+1, \dots, N]\}$ of the lattice now becomes

$$|\Psi[A]\rangle = \sum_{\alpha=1}^D \sqrt{\sigma_\alpha} \left| \Phi_\alpha^{\mathcal{A}_1^n} \right\rangle \otimes \left| \Phi_\alpha^{\mathcal{A}_2^n} \right\rangle.$$

Consider now an observable of the form $\mathcal{O} = \sum_{n=r_1}^{r_2} o_{n,n+1}$ ($1 \ll r_1 \leq r_2 \ll N = +\infty$) where $o_{n,n+1}$ acts only non-trivially on sites n and $n+1$, then

$$\langle \Psi_u[\bar{A}] | \mathcal{O} | \Psi_u[A] \rangle = \sum_{n=r_1}^{r_2} \left(\Xi \begin{array}{c} \text{---} \text{A} \text{---} \text{A} \text{---} \\ \text{---} o_{n,n+1} \text{---} \\ \text{---} \text{A} \text{---} \text{A} \text{---} \end{array} \Lambda \right). \quad (1.14)$$

Following the scheme in fig. 1.1, this can be performed in $\mathcal{O}(|r_2 - r_1|q^2D^3)$ time. Consider now the special case, when $r_1 = 1, r_2 = +\infty$ and $o_{n,n+1} = o$:

$$\mathcal{O} = \lim_{N \rightarrow +\infty} \sum_{n=1}^{N-1} \mathcal{T}^{n-1} o \mathcal{T}^{-n+1}$$

with \mathcal{T} the translation operator over one site and where o acts only non-trivially on sites 1 and 2. In this case the expectation value diverges with the length of the lattice N . However, the expectation value per site is finite and equals

$$\lim_{N \rightarrow +\infty} \frac{1}{N} \langle \Psi_u[\bar{A}] | \mathcal{O} | \Psi_u[A] \rangle = \text{Diagram}, \quad (1.15)$$

which can be computed in $\mathcal{O}(q^2 D^3)$ time.

It is also possible to put the uMPS in a canonical form. Like in the non-uniform case we can put $\Lambda = \mathbb{1}_D$ (right canonical form) and $\Xi = \mathbb{1}_D$ (left canonical form). We also consider the **symmetric canonical form**: $\Xi = \Lambda$. In algorithm 1.1 we give the pseudocode for an implementation in for instance C++, Matlab or Python. As input we give the tensor $A = \{[A^d]_{\alpha,\beta}\}_{d=1\dots d; \alpha,\beta=1\dots d}$ representing the uMPS $|\Psi[A]\rangle$ eq. (1.12) and a string *stringCanForm*. The string ‘stringCanForm’ indicates the desired canonical form: ‘left’ for the left canonical form, ‘right’ for the right canonical form and ‘symmetric’ for the symmetric canonical form. The output of the algorithm is again a tensor A corresponding to the same uMPS but now with norm 1. The left and right eigenvector Ξ and Λ of the transfer matrix corresponding to the leading eigenvalue $\eta = 1$ are in the desired canonical form. In either way Ξ and Λ are diagonal. The algorithm is straightforward and can also be found in [136]. Essentially, it constructs the matrix Γ to bring the uMPS in the desired form by the MPS gauge transformation

$$\text{Diagram: } \left[\text{A} \right] \leftarrow \left[\Gamma \right] \left[\text{A} \right] \left[\Gamma^{-1} \right] / \sqrt{\eta}.$$

Let us conclude this part by some giving comments on the algorithm

- (i) As already mentioned, we use an interactive procedure to find leading η of the transfer matrix and the corresponding left and right eigenvectors Ξ and Λ . This is what happens in line 2 and 3. We invoke the iterative eigensolver ‘eigs’¹ and apply it on the functions ‘ApplyTransferLeft’ and ‘ApplyTransferRight’. These functions, see lines 26-28 and lines 29-31, compute the right and left action of the transfer matrix on a matrix, which can be performed in $\mathcal{O}(qD^3)$ time. Therefore, finding

1. This nomenclature stems from matlab where the routine for the Arnoldi iteration is called ‘eigs’. But more general ‘eigs’ can be any iterative eigensolver.

the leading eigenvalue η and the corresponding left and right eigenvectors Ξ and Λ takes $\mathcal{O}(N_{iter}qD^3)$ time, where N_{iter} is the number of iterations needed by the iterative procedure. We can expect that N_{iter} is proportional with the correlation length. The correlation length ξ can be computed from the leading eigenvalue η and the second leading eigenvalue η_2 of the transfer matrix as $\xi = -\log(\eta_2/\eta)$.

- (ii) Because Ξ and Λ are positive-definite, the matrices X and Y in line 7 exist.
- (iii) In line 8, $[U, \Sigma, V] = \text{SVD}(YX)$ means a singular value decomposition of YX :

$$YX = U\Sigma V^\dagger, U^\dagger U = \mathbb{1}, VV^\dagger = \mathbb{1}, \Sigma \text{ diagonal and positive definite.}$$

Algorithm 1.1 Normalization of a uMPS

Input: A , stringCanForm

Output: A, Ξ, Λ .

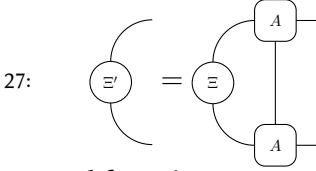
```

1: function  $[A, \Xi, \Lambda, \eta, \Gamma] = \text{NORMALIZEUMPS}(A, \text{stringCanForm})$ 
2:    $[\Xi, \eta] = \text{eigs}(@(\Xi)\text{ApplyTransferLeft}(\Xi, A))$ 
3:    $[\Lambda, \eta] = \text{eigs}(@(\Lambda)\text{ApplyTransferRight}(\Lambda, A))$ 
4:    $A \leftarrow A/\sqrt{\eta}$ 
5:    $\Xi \leftarrow \Xi/\text{tr}(\Xi)$ 
6:    $\Lambda \leftarrow \Lambda/\text{tr}(\Lambda)$ 
7:   Find matrices  $X$  and  $Y$  such that  $\Xi = XX^\dagger, \Lambda = Y^\dagger Y$ 
8:    $[U, \Sigma, V] = \text{SVD}(YX)$ 
9:    $\Sigma \leftarrow \Sigma/\sqrt{\text{tr}(\Sigma^2)}$ 
10:  switch stringCanForm do
11:    case 'left'
12:       $\Gamma = \Sigma V^\dagger X^{-1} = U^\dagger Y$ 
13:       $\Xi = \mathbb{1}_D$ 
14:       $\Lambda = \Sigma^2$ 
15:    case 'right'
16:       $\Gamma = V^\dagger X^{-1} = \Sigma^{-1} U^\dagger Y$ 
17:       $\Xi = \Sigma^2$ 
18:       $\Lambda = \mathbb{1}_D$ 
19:    case 'symmetric'
20:       $\Gamma = \Sigma^{1/2} V^\dagger X^{-1} = \Sigma^{-1/2} U^\dagger Y$ 
21:       $\Xi = \Sigma$ 
22:       $\Lambda = \Sigma$ 
23:  end switch
24:  

```

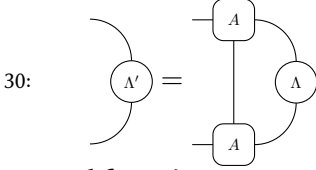

25: **end function**

26: **function** $\Xi' = \text{APPLYTRANSFERLEFT}(\Xi, A)$



28: **end function**

29: **function** $\Lambda' = \text{APPLYTRANSFERRIGHT}(\Lambda, A)$



31: **end function**

1.3. The tangent space of uMPS

Here we study the tangent space of the uMPS. They provide a variational class of states to approximate one-particle excitations with a given momentum [87, 91]. The calculus of these states is discussed here as well, see also [88] for a nice overview .

1.3.1. Definition

If \mathcal{T} is the translation operator over one site on a lattice with N sites,

$$\mathcal{T} |d_1, d_2, \dots, d_N\rangle = |d_2, \dots, d_N, d_1\rangle$$

then it is obvious that in the limit $N \rightarrow +\infty$ uMPS are invariant under \mathcal{T} : $\mathcal{T} |\Psi_u[A]\rangle = |\Psi_u[A]\rangle$. Furthermore, because $\mathcal{T}^N = \mathbb{1}$ its spectrum equals all the N^{th} roots of unity, i.e.

$$\text{spec}(\mathcal{T}) = \left\{ e^{ik} : k = 2\pi \frac{0}{N}, 2\pi \frac{1}{N}, \dots, 2\pi \frac{N-1}{N} \right\}.$$

When considering the thermodynamic limit, the spectrum of \mathcal{T} becomes continuous, $\text{spec}(\mathcal{T}) : \{e^{ik} : k \in [0, 2\pi[. \}$. Note that k is only determined up to an integer multiple of 2π , so one can also take $k \in [-\pi, \pi[. \}$ k is called the momentum and an eigenstate of \mathcal{T} with eigenvalue e^{ik} is called a momentum- k eigenstate.

Starting from a uMPS $|\Psi_u[A]\rangle$, see eq. (1.12), an example of a momentum- k eigenstate of the translation operator \mathcal{T} is $|\Phi_k[B, A]\rangle$ which is defined by

$$\lim_{N \rightarrow +\infty} \sum_{n=1}^N \sum_{d_1, \dots, d_N=1}^q e^{ikn} v_L^\dagger A^{d_1} \dots A^{d_{n-1}} B^{d_n} A^{d_{n+1}} \dots A^{d_N} v_R |d_1, \dots, d_N\rangle,$$

or with tensor network diagrams:

$$|\Phi_k[B, A]\rangle = \lim_{N \rightarrow +\infty} \sum_{n=1}^N e^{ikn} \text{Diagram} \quad (1.16)$$

We indeed have that $\mathcal{T}|\Phi_k[B, A]\rangle = e^{ik}|\Phi_k[B, A]\rangle$, hence these states can be used as a variational ansatz for momentum- k eigenstates. More specifically, we use the uMPS $|\Psi_u[A]\rangle$ to approximate the ground states. The states $|\Phi_k[B, A]\rangle$ serve then as a variational ansatz to approximate the one-particle eigenstates. Note that this ansatz is linear in the tensors B . For any $k \in [0, 2\pi[$ the set

$$\mathcal{T}_A^k = \{|\Phi_k[B, A]\rangle : B^d \in \mathbb{C}^{D \times D}, d = 1 \dots q\}$$

is called the (boosted) **tangent space** with momentum k in the uMPS $|\Psi_u[A]\rangle$. For $k = 0$, this definition exactly coincides with the definition of tangent space in differential geometry in the sense that

$$|\Phi_0[B, A]\rangle = \sum_{d=1}^q \sum_{\alpha=1}^D \sum_{\beta=1}^D [B^d]_{\alpha,\beta} \left(\frac{\partial}{\partial [A^d]_{\alpha,\beta}} |\Psi_u[A]\rangle \right).$$

From now on we assume that $|\Psi_u[A]\rangle$ is normalized and that the left and right eigenvector Ξ and Λ corresponding to the largest eigenvalue $\eta = 1$ of the transfer matrix are positive diagonal matrices, see algorithm 1.1.

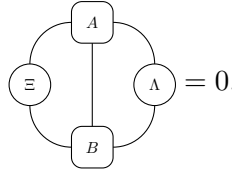
The overlap of the tangent vectors $|\Phi_k[B, A]\rangle$ with $|\Psi_u[A]\rangle$ can easily be computed:

$$\langle \Phi_k[\bar{B}, \bar{A}] | \Psi_u[A] \rangle = 2\pi\delta(k) \text{Diagram}$$

where the delta-Dirac function for momentum $k = 2\pi m/N$ ($m = 0, \dots, N-1$) is regularized as

$$2\pi\delta(2\pi m/N) = \lim_{N \rightarrow +\infty} \sum_{n=1}^N e^{i2\pi nm/N} = \lim_{N \rightarrow +\infty} N\delta_{m,0}.$$

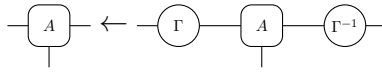
The prefactor $2\pi\delta(k)$ thus originates from the infinite number of sites N . Note that for $k \neq 0$ the states are automatically orthogonal to $|\Psi_u[A]\rangle$, while for $k = 0$ $|\Psi_u[A]\rangle$ is only orthogonal to $|\Phi_0[B, A]\rangle$ if



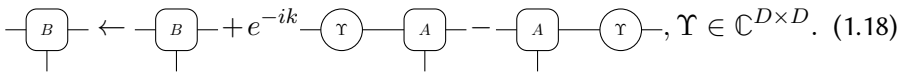
$$= 0. \tag{1.17}$$

1.3.2. Gauge freedom and gauge fixing

The uMPS $|\Psi_u[A]\rangle$ has the gauge freedom

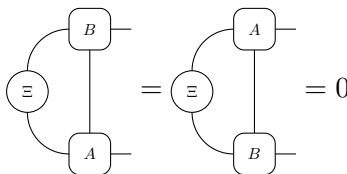


in its representation. When fixing the gauge of the tensor A (left, right or symmetric) one still has an additional freedom in the tensor B : it is clear that $|\Phi_k[B, A]\rangle$ is invariant under the transformation



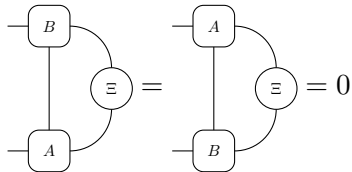
$$, \Upsilon \in \mathbb{C}^{D \times D}. \tag{1.18}$$

When $k \neq 0$ this freedom can be used to let B obey the **left gauge fixing condition**,



$$= 0 \tag{1.19}$$

or the **right gauge fixing condition**,



$$= 0. \tag{1.20}$$

When $k = 0$ one can still impose the left gauge or right gauge fixing condition if $|\Phi_0(B, A)\rangle$ is orthogonal to $|\Psi[A]\rangle$, i.e. if eq. (1.17) is satisfied.

Let us now discuss how we can let B obey the left gauge fixing condition. Given B , it follows from eq. (1.19), that Υ , see eq. (1.18), must satisfy:

Diagram (1.21) shows a rectangular box labeled $\mathbb{1} - e^{-ik}\mathbb{E}$ with two horizontal lines on the left and two on the right. A circle labeled $\Xi\Upsilon$ is connected to the left lines. This is equal to a circle labeled Ξ connected to the left lines, and a vertical line connecting two boxes labeled B and A on the right lines.

Because the leading eigenvalue of the transfer matrix \mathbb{E} equals $\eta = 1$, $\mathbb{1} - e^{-ik}\mathbb{E}$ is invertible for $k \neq 0$. For $k = 0$, we can still solve eq. (1.21) if B satisfies eq. (1.17). Therefore we introduce the orthogonal projector \mathbb{P} onto the kernel of $1 - \mathbb{E}$:

Diagram showing a vertical rectangular box labeled \mathbb{P} with two horizontal lines on each side. This is equal to a circle labeled Λ connected to the left lines, and a circle labeled Ξ connected to the right lines.

When considering $\mathbb{Q} = \mathbb{1} - \mathbb{P}$, it follows from eq. (1.17) that eq. (1.21) is solved as

Diagram (1.22) shows a circle labeled Υ connected to the left lines of a rectangular box labeled $(\mathbb{1} - e^{-ik}\mathbb{E})^+$. The box has two horizontal lines on the left and two on the right. A circle labeled Ξ^{-1} is connected to the right lines. A vertical line connects two boxes labeled B and A on the right lines, which are also connected to the Ξ circle.

where $(\mathbb{1} - e^{-ik}\mathbb{E})^+$ is a pseudo inverse of $\mathbb{1} - e^{-ik}\mathbb{E}$ defined as:

$$(\mathbb{1} - e^{-ik}\mathbb{E})^+ = (\mathbb{1} - e^{-ik}\mathbb{E})^{-1}, k \neq 0 \text{ and } (\mathbb{1} - \mathbb{E})^+ = \mathbb{Q}(\mathbb{Q}(\mathbb{1} - e^{-ik}\mathbb{E})\mathbb{Q})^{-1}\mathbb{Q}.$$

Similarly, when $k \neq 0$ or eq. (1.17) is satisfied, taking

Diagram (1.23) shows a circle labeled Υ connected to the left lines of a rectangular box labeled $(\mathbb{1} - e^{ik}\mathbb{E})^+$. The box has two horizontal lines on the left and two on the right. A circle labeled Λ^{-1} is connected to the left lines. A vertical line connects two boxes labeled B and A on the right lines, which are also connected to a circle labeled Λ .

imposes the right gauge fixing condition eq. (1.20) on B .

1.3.3. Efficient computation of $(\mathbb{1} - e^{ik}\mathbb{E})^+$

In the previous subsection we saw that to impose the right gauge fixing or the left gauge fixing condition on B , we need to compute the (pseudo) inverse of $\mathbb{1} - e^{ik}\mathbb{E}$. Note that this is a $(D^2 \times D^2)$ matrix and that the computation time to compute the inverse exactly would scale as D^6 . Fortunately,

the action of $\mathbb{1} - e^{ik}\mathbb{E}$ on a vector can be implemented in $\mathcal{O}(D^3)$ time. Hence we can use iterative methods to solve eq. (1.22) and eq. (1.23).

More specifically, assume we want to determine

This is equivalent to solving the following equation for K

The action on K in the left-hand side can be implemented in $\mathcal{O}(qD^3)$ time. Using an iterative method like the generalized minimal residual method [167] or the biconjugate gradient stabilized method [168] a solution K can be found in $\mathcal{O}(N_{iter}qD^3)$ time where N_{iter} is the number of iterations needed for the iterative solver.

A pseudocode for this algorithm is presented in algorithm 1.2 and essentially solves eq. (1.24) using the iterative method ‘bigstab’². The command ‘ $K = \text{bigstab}(@(\text{K})\text{ApplyTransRight}(K,A),\Omega)$ ’ means that the biconjugate gradient stabilized method is applied to the linear map ‘ApplyTransRight’, which maps K to K' as shown in line 8, and gives the solution K of $\text{ApplyTransRight}(K) = \Omega$.

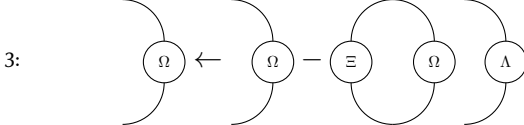
Algorithm 1.2 Determine $(\mathbb{1} - e^{ik}\mathbb{E})^+$ acting on the right

Input: $A, \Omega, k, \Xi, \Lambda$

Output: K .

1: **function** $K = \text{INVTRANSRIGHT}(A, \Omega, k, \Xi, \Lambda)$

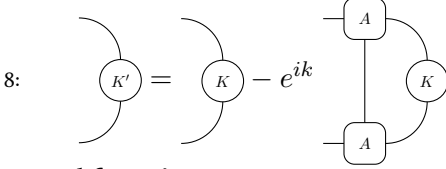
2: **if** $k = 0$ **then**



4: **end if**

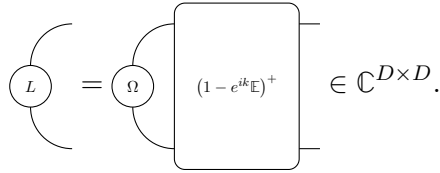
2. This is the matlab command to invoke the biconjugate gradient stabilized method. Of course, one could choose another method.

5: $K = \text{bicgstab}(@\langle K \rangle \text{ApplyTransRight}(K, A, k), \Omega)$
 6: **end function**
 7: **function** $K' = \text{APPLYTRANSRIGHT}(K, A, k)$



9: **end function**

Similarly, we provide in algorithm 1.3 the pseudocode for the efficient computation of



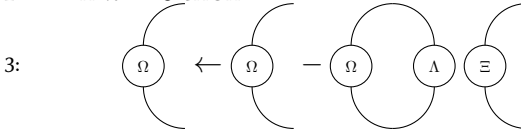
Algorithm 1.3 Determine $(\mathbb{1} - e^{ik} \mathbb{E})^+$ acting on the left

Input: $A, \Omega, k, \Xi, \Lambda$

Output: L .

1: **function** $L = \text{INVTRANSLEFT}(A, \Omega, k, \Xi, \Lambda)$

2: **if** $k = 0$ **then**

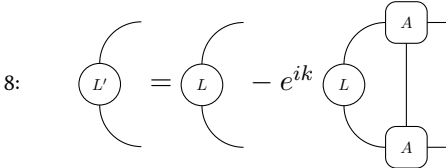


4: **end if**

5: $L = \text{bicgstab}(@\langle L \rangle \text{ApplyTransLeft}(L, A, k), \Omega)$

6: **end function**

7: **function** $L' = \text{APPLYTRANSLEFT}(L, A, k)$



9: **end function**

1.3.4. Variational freedom in the tangent plane

In subsection 1.3.2 we discussed how we can use the freedom eq. (1.18) in B in the representation of $|\Phi_k[B, A]\rangle$ to impose the left gauge fixing condition

where $X \in \mathbb{C}^{n_L \times D}$,

$$\text{Diagram 1} = \text{Diagram 2} \quad \text{and} \quad \text{Diagram 3} = 0. \quad (1.26b)$$

Any B satisfying the left gauge fixing condition (1.19) can thus be parametrized by a matrix $X \in \mathbb{C}^{n_L \times D}$ and vice versa.

1.3.5. Calculus

In the previous subsection, we focussed on the gauge freedom and how this can be used to impose the left gauge fixing condition eq. (1.19) or the right gauge fixing condition eq. (1.20) on B . In this subsection we discuss how expectation values of tangent vectors $|\Phi_k[B, A]\rangle$ are computed. In order that these expectation values are well-defined it is important that the tangent vector $|\Phi_k[B, A]\rangle$ is orthogonal to $|\Psi_u[A]\rangle$, i.e. that $k \neq 0$ or that

$$\text{Diagram} = 0.$$

As we discussed in subsection 1.3.2, we can take B such that it obeys either the left gauge fixing condition or the right gauge fixing condition. From now on, we assume that this is the case:

$$\text{Diagram 1} = 0 \quad \text{or} \quad \text{Diagram 2} = 0.$$

The overlap between two different tangent vectors equals

$$\langle \Phi_{k'}[\overline{B'}, \overline{A}] | \Phi_k[B, A] \rangle = 2\pi \delta(k - k') \text{Diagram} \quad (1.27)$$

Notice that the tangent vectors satisfy a delta-Dirac normalization in the thermodynamic limit. Also, two tangent vectors with different momentum

are automatically orthogonal as it should. When B and B' are parametrized as in eq. (1.25) or eq. (1.26): $B = B(X)$ and $B' = B(Y)$, we have that

$$\langle \Phi_{k'}[\overline{B'}, \overline{A}] | \Phi_k[B, A] \rangle = 2\pi\delta(k - k') \text{tr}(Y^\dagger X). \quad (1.28)$$

Consider now an operator of the form $\mathcal{O} = \lim_{N \rightarrow +\infty} \sum_{n=1}^{N-1} \mathcal{T}^{n-1} o \mathcal{T}^{-n+1}$ where o acts non-trivially on site 1 and site 2. One can show that [43]

$$\langle \Phi_k[\overline{B}, \overline{A}] | \mathcal{O} | \Psi_u[A] \rangle = 2\pi\delta(k) \left(\begin{array}{c} \text{Diagram 1} \\ + \text{Diagram 2} \\ + \text{Diagram 3} \end{array} \right) \quad (1.29a)$$

where

$$L_0 = \begin{array}{c} \text{Diagram 1} \\ \text{Diagram 2} \end{array} \quad (1.29b)$$

$$K_0 = \begin{array}{c} \text{Diagram 1} \\ \text{Diagram 2} \end{array} \quad (1.29c)$$

can be computed efficiently using algorithms 1.2 and 1.3. The inverse

$$(1 - \mathbb{E})^+$$

that appears here originates from the geometric series:

$$(1 - \mathbb{E})^+ = \lim_{N \rightarrow +\infty} \sum_{n=0}^N (\mathbb{Q}\mathbb{E}\mathbb{Q})^n.$$

Note that if B obeys the right gauge fixing condition resp. the left gauge fixing condition, the first resp. second term drops out of the expression.

Finally, we compute expectation values of the form $\langle \Phi_{k'}[B', A] | \mathcal{O} | \Phi_k[B, A] \rangle$. For these expectation values, to be well-defined, we need to subtract the expectation value of \mathcal{O} with respect to $|\Psi_u[A]\rangle$ from it: if

$$\mathcal{O} = \lim_{N \rightarrow +\infty} \sum_{n=1}^{N-1} \mathcal{T}^{n-1} o \mathcal{T}^{-n+1}$$

then we need to subtract $\langle \Psi_u[\bar{A}] | o | \Psi_u[A] \rangle$:

$$o \leftarrow o - \langle \Psi_u[\bar{A}] | o | \Psi_u[A] \rangle.$$

If one computes the following matrices iteratively (algorithms 1.2 and 1.3):

Diagram (1.30a) shows a circle labeled L_1 with a cross Ξ inside. This is equal to a tensor product of a circle with a cross Ξ and a rectangular box labeled $(1 - e^{-ik\epsilon})^+$. The box has two vertical lines on its left side and two on its right side. A vertical line connects a box labeled B at the top to a box labeled A at the bottom, passing through the box.

Diagram (1.30b) shows a circle labeled L_2 with a cross Ξ inside. This is equal to a tensor product of a circle with a cross Ξ and a rectangular box labeled $(1 - e^{-ik\epsilon})^+$. The box has two vertical lines on its left side and two on its right side. Inside the box, there are two boxes labeled B and A at the top, and two boxes labeled A and A at the bottom. A central box labeled o is connected to the B and A boxes above and the A and A boxes below.

Diagram (1.30c) shows a circle labeled L_3 with a cross Ξ inside. This is equal to a tensor product of a circle with a cross Ξ and a rectangular box labeled $(1 - e^{-ik\epsilon})^+$. The box has two vertical lines on its left side and two on its right side. Inside the box, there are two boxes labeled A and B at the top, and two boxes labeled A and A at the bottom. A central box labeled o is connected to the A and B boxes above and the A and A boxes below.

Diagram (1.30d) shows a circle labeled L_4 with a cross Ξ inside. This is equal to a tensor product of a circle labeled L_0 with a cross Ξ and a rectangular box labeled $(1 - e^{-ik\epsilon})^+$. The box has two vertical lines on its left side and two on its right side. A vertical line connects a box labeled B at the top to a box labeled A at the bottom, passing through the box.

Diagram (1.30e) shows a circle labeled K_1 with a cross Ξ inside. This is equal to a tensor product of a rectangular box labeled $(1 - e^{ik\epsilon})^+$ and a circle with a cross Ξ . The box has two vertical lines on its left side and two on its right side. A vertical line connects a box labeled B at the top to a box labeled A at the bottom, passing through the box.

(1.30f)

(1.30g)

(1.30h)

invariant under \mathcal{CT} :

$$|\Psi_{\mathcal{C}}[A]\rangle = \begin{array}{c} \textcircled{v_L^\dagger} \text{---} \text{A} \text{---} \text{A} \text{---} \dots \text{---} \text{A} \text{---} \text{A} \text{---} \dots \text{---} \text{A} \text{---} \text{A} \text{---} \textcircled{v_R} \\ | \quad | \quad | \quad | \quad | \quad | \quad | \quad | \\ d_1 \quad \textcircled{c} \quad d_{2n-1} \quad \textcircled{c} \quad d_{2N-1} \quad \textcircled{c} \quad d_{2N} \end{array} \quad (1.31)$$

in the limit $N \rightarrow +\infty$ where $A^d \in \mathbb{C}^{D \times D}$. By construction this state is obtained from the uMPS

$$|\Psi_u[A]\rangle = \textcircled{v_L^\dagger} \text{---} \text{A} \text{---} \text{A} \text{---} \dots \text{---} \text{A} \text{---} \text{A} \text{---} \dots \text{---} \text{A} \text{---} \text{A} \text{---} \textcircled{v_R}$$

by applying \mathcal{C} on the even sites. In this context we call $|\Psi_u[A]\rangle$ the ‘uniform counterpart’ of $|\Psi_{\mathcal{C}}[A]\rangle$. As will become clear later, all computations can be performed on the level of its uniform counterpart $|\Psi_u[A]\rangle$. In particular, we can apply the whole formalism developed for uMPS to these states as well. For instance, concerning the normalization we find because $\mathcal{C}^2 = \mathbb{1}_{\mathbb{C}^q}$ that

$$\langle \Psi_{\mathcal{C}}[A] | \Psi_{\mathcal{C}}[A] \rangle = \langle \Psi_u[A] | \Psi_u[A] \rangle = \text{tr}(\Xi \Lambda)$$

where Ξ and Λ are the left and right eigenvector corresponding to the leading eigenvalue of the transfer matrix $\mathbb{E} = \mathbb{E}_A^A$, see subsection 1.2.2. They are also obtained via the algorithm 1.1. Note that we here also assumed the leading eigenvalue of the transfer matrix to be normalized to one.

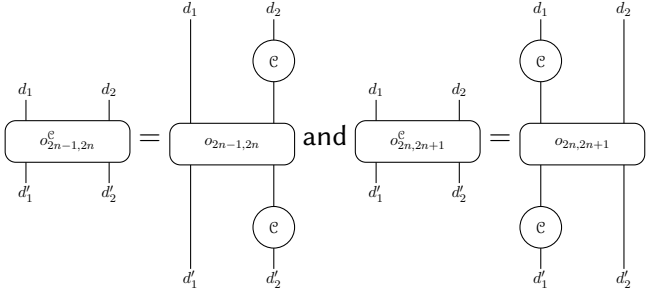
Furthermore, for any local operator

$$\textcircled{\mathcal{O}} = \sum_{n=1}^{2N-1} \begin{array}{c} d_1 \quad \dots \quad d_{2N} \\ | \quad | \quad | \quad | \quad | \quad | \quad | \quad | \\ \textcircled{\mathcal{O}} \\ | \quad | \quad | \quad | \quad | \quad | \quad | \quad | \\ d'_1 \quad \dots \quad d'_{2N} \end{array} \quad \dots \quad \begin{array}{c} d_{n-1} \quad d_n \quad d_{n+1} \quad d_{n+2} \quad d_{2N} \\ | \quad | \quad | \quad | \quad | \\ \textcircled{o_{n,n+1}} \\ | \quad | \quad | \quad | \quad | \\ d'_{n-1} \quad d'_n \quad d'_{n+1} \quad d'_{n+2} \quad d'_{2N} \end{array}$$

we have that

$$\begin{aligned} \langle \Psi_{\mathcal{C}}[A] | \textcircled{\mathcal{O}} | \Psi_{\mathcal{C}}[A] \rangle &= \sum_{n=1}^N \begin{array}{c} \textcircled{\Xi} \text{---} \text{A} \text{---} \text{A} \text{---} \text{A} \text{---} \text{A} \text{---} \text{A} \text{---} \textcircled{\Lambda} \\ | \quad | \quad | \quad | \quad | \\ o_{2n-1,2n}^{\mathcal{C}} \end{array} + \sum_{n=1}^{N-1} \begin{array}{c} \textcircled{\Xi} \text{---} \text{A} \text{---} \text{A} \text{---} \text{A} \text{---} \text{A} \text{---} \text{A} \text{---} \textcircled{\Lambda} \\ | \quad | \quad | \quad | \quad | \\ o_{2n,2n+1}^{\mathcal{C}} \end{array} \\ &= \sum_{n=1}^N \langle \Psi_u[A] | o_{2n-1,2n}^{\mathcal{C}} | \Psi_u[A] \rangle \\ &\quad + \sum_{n=1}^{N-1} \langle \Psi_u[A] | o_{2n,2n+1}^{\mathcal{C}} | \Psi_u[A] \rangle \end{aligned}$$

where



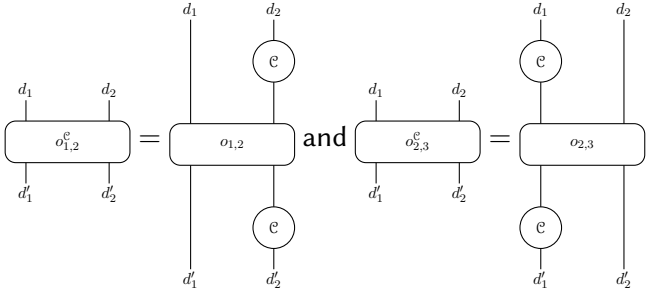
For our simulations, we are interested in the case when $o_{n,n+1}$ only depends on the parity of n :

$$o_{2n-1,2n} = o_{1,2} \text{ and } o_{2n,2n+1} = o_{2,3}.$$

In this case, we find in the thermodynamic limit for the expectation value per site

$$\begin{aligned}
 \lim_{N \rightarrow +\infty} \frac{1}{2N} \langle \Psi_c[A] | \mathcal{O} | \Psi_c[A] \rangle &= \frac{1}{2} \left(\begin{array}{c} \textcircled{\Xi} \\ | \quad | \\ \boxed{o_{1,2}^c + o_{2,3}^c} \\ | \quad | \\ \textcircled{\Lambda} \end{array} \right) \\
 &= \left\langle \Psi_u[A] \left| \frac{o_{1,2}^c + o_{2,3}^c}{2} \right| \Psi_u[A] \right\rangle
 \end{aligned}$$

with



We thus find that if we absorb \mathcal{C} on the even sites in the operators that the expectation value with respect to $|\Psi_c[A]\rangle$ reduces to the expectation value with respect to its uniform counterpart $|\Psi_u[A]\rangle$.

One observes that the state $|\Phi_{k,\gamma}^{\mathcal{C}}[B, A]\rangle$ is quite similar to the state $|\Phi_k[B, A]\rangle$, see subsection 1.3, considering the last one also defined on a lattice consisting of $2N$ sites. In fact, the state $|\Phi_{k,\gamma}^{\mathcal{C}}[B, A]\rangle$ is obtained from the state $|\Phi_{[k]_{\gamma}}[B, A]\rangle$ where

$$[k]_{\gamma} = k/2, \text{ if } \gamma = 1, [k]_{\gamma} = k/2 + \pi, \text{ if } \gamma = -1,$$

by applying \mathcal{C} on the even sites. Therefore, all expectation values with respect to $|\Phi_{k,\gamma}^{\mathcal{C}}[B, A]\rangle$ can be reduced to expectation values with respect to $|\Phi_{[k]_{\gamma}}[B, A]\rangle$. For the overlap with $|\Psi_{\mathcal{C}}[A]\rangle$ we find

$$\langle \Phi_{k,\gamma}^{\mathcal{C}}[\overline{B}, \overline{A}] | \Psi_{\mathcal{C}}[A] \rangle = 2\pi\delta(k)\delta_{\gamma,1} \langle \Xi | \begin{array}{c} \text{A} \\ | \\ \text{B} \end{array} | \Lambda \rangle = \langle \Phi_{[k]_{\gamma}}[\overline{B}, \overline{A}] | \Psi_u[A] \rangle$$

where the delta-Dirac function for momentum $k = 2\pi m/N$ ($m = 0, \dots, N-1$) is regularized as

$$2\pi\delta(2\pi m/N) = \lim_{N \rightarrow +\infty} \sum_{n=1}^{2N} e^{i2\pi nm/N} = \lim_{N \rightarrow +\infty} 2N\delta_{m,0}.$$

The prefactor $2\pi\delta(k)$ thus originates from the infinite lattice size $2N$ ($N \rightarrow +\infty$). Note that for $k \neq 0$ or $\gamma = -1$, the states are automatically orthogonal to $|\Psi_{\mathcal{C}}[A]\rangle$, while for $(k, \gamma) = (0, 1)$ $|\Psi_{\mathcal{C}}[A]\rangle$ is orthogonal to $|\Phi_{k,\gamma}^{\mathcal{C}}[B, A]\rangle$ if we impose eq. (1.17) on B .

Similar to eq. (1.18) we have the following freedom in the representation of B :

$$B^d \leftarrow B^d + e^{-i[k]_{\gamma}} \Upsilon A^d - A^d \Upsilon; \quad d = 1, \dots, q; \quad \Upsilon \in \mathbb{C}^{D \times D}. \quad (1.33)$$

As explained in subsection 1.3.2, when $[k]_{\gamma} \neq 0$ or eq. (1.17) is satisfied this freedom can be used to let B obey the left gauge fixing condition, see eq. (1.19), or the right gauge fixing condition, see eq. (1.20). Therefore we can also parameterize B by a matrix X , see eq. (1.25) for the right gauge fixing condition and see eq. (1.26) for the left gauge fixing condition.

When B obeys either the right or left gauge fixing condition, the overlap between different tangent vectors is

$$\langle \Phi_{k',\gamma'}^{\mathcal{C}}[\overline{B}', \overline{A}] | \Phi_{k,\gamma}^{\mathcal{C}}[B, A] \rangle = \langle \Phi_{[k']_{\gamma'}}[\overline{B}', \overline{A}] | \Phi_{[k]_{\gamma}}[B, A] \rangle \quad (1.34)$$

$$= 2\pi\delta(k - k')\delta_{\gamma,\gamma'} \langle \Xi | \begin{array}{c} \text{B} \\ | \\ \text{B}' \end{array} | \Lambda \rangle,$$

as follows from eq. (1.27). We thus find again that tangent vectors with different quantum numbers (k, γ) are automatically orthogonal.

For our purposes it is sufficient to consider operators of the form

$$\begin{array}{c} d_1 \quad \dots \quad d_{2N} \\ \text{---} \\ \text{---} \\ \text{---} \\ \text{---} \\ \text{---} \\ d'_1 \quad \dots \quad d'_{2N} \end{array} \text{---} \mathcal{O} = \lim_{N \rightarrow +\infty} \sum_{n=1}^{2N-1} \begin{array}{c} d_1 \\ \text{---} \\ \text{---} \\ \text{---} \\ \text{---} \\ d'_1 \end{array} \dots \begin{array}{c} d_{n-1} \\ \text{---} \\ \text{---} \\ \text{---} \\ \text{---} \\ d'_{n-1} \end{array} \begin{array}{c} d_n \quad d_{n+1} \\ \text{---} \\ \text{---} \\ \text{---} \\ \text{---} \\ d'_n \quad d'_{n+1} \end{array} \text{---} \mathcal{O}_{n,n+1} \dots \begin{array}{c} d_{n+2} \\ \text{---} \\ \text{---} \\ \text{---} \\ \text{---} \\ d'_{n+2} \end{array} \dots \begin{array}{c} d_{2N} \\ \text{---} \\ \text{---} \\ \text{---} \\ \text{---} \\ d'_{2N} \end{array}$$

where

$$\begin{array}{c} d_1 \quad d_2 \\ \text{---} \\ \text{---} \\ \text{---} \\ \text{---} \\ d'_1 \quad d'_2 \end{array} \text{---} \mathcal{O}_{2n-1,2n} = \begin{array}{c} d_1 \\ \text{---} \\ \text{---} \\ \text{---} \\ \text{---} \\ d'_1 \end{array} \text{---} \mathcal{O} \begin{array}{c} d_2 \\ \text{---} \\ \text{---} \\ \text{---} \\ \text{---} \\ d'_2 \end{array} \text{---} \mathcal{O}_{2n,2n+1} \text{ and } \begin{array}{c} d_1 \quad d_2 \\ \text{---} \\ \text{---} \\ \text{---} \\ \text{---} \\ d'_1 \quad d'_2 \end{array} \text{---} \mathcal{O}_{2n,2n+1} = \begin{array}{c} d_1 \\ \text{---} \\ \text{---} \\ \text{---} \\ \text{---} \\ d'_1 \end{array} \text{---} \mathcal{O} \begin{array}{c} d_2 \\ \text{---} \\ \text{---} \\ \text{---} \\ \text{---} \\ d'_2 \end{array} \text{---} \mathcal{O}_{2n-1,2n}$$

for some local operator \mathcal{O} . Note that this operator is \mathcal{CT} invariant. If we now define its ‘uniform counterpart’ \mathcal{O}_u by

$$\mathcal{O}_u = \lim_{N \rightarrow +\infty} \sum_{n=1}^{2N-1} \mathcal{T}^{n-1} \mathcal{O} \mathcal{T}^{-n+1},$$

then we find that

$$\langle \Phi_{k,\gamma}^{\mathcal{C}}[\overline{B'}, \overline{A}] | \mathcal{O} | \Psi_{\mathcal{C}}[A] \rangle = \langle \Phi_{[k]_{\gamma}}[\overline{B'}, \overline{A}] | \mathcal{O}_u | \Psi_u[A] \rangle.$$

The value of $\langle \Phi_{[k]_{\gamma}}[\overline{B'}, \overline{A}] | \mathcal{O}_u | \Psi_u[A] \rangle$ can be found in eq. (1.29a) and contains now an overall $\delta(k) \delta_{\gamma,1}$ factor. Similarly, we find that

$$\langle \Phi_{k',\gamma'}^{\mathcal{C}}[\overline{B'}, \overline{A}] | \mathcal{O} | \Phi_{k,\gamma}^{\mathcal{C}}[B, A] \rangle = \langle \Phi_{[k']_{\gamma'}}[\overline{B'}, \overline{A}] | \mathcal{O}_u | \Phi_{[k]_{\gamma}}[B, A] \rangle. \quad (1.35)$$

If we subtract the expectation value of \mathcal{O} with respect to $|\Psi_{\mathcal{C}}[A]\rangle$ from \mathcal{O} , i.e.

$$\mathcal{O} \leftarrow \mathcal{O} - \langle \Psi_u[A] | \mathcal{O} | \Psi_u[A] \rangle \mathbb{1}_{\mathcal{C}^q} \otimes \mathbb{1}_{\mathcal{C}^q},$$

we can use eq. (1.30) to evaluate the right-hand side. The delta-Dirac appearing there needs to be replaced by $\delta(k - k') \delta_{\gamma,\gamma'}$.

Optimization methods for MPS

2.1. TDVP

The Time-Dependent Variational Principle (TDVP), introduced in [169], provides a tool to evolve the Schrödinger equation within a variational manifold of states in an optimal way. Starting from the action principle for the Schrödinger equation, applying the Euler-Lagrange equations with respect to the variational parameters gives the TDVP equations. They have also a nice geometric interpretation [170].

Here we review the method of [43, 87] to apply the TDVP to the manifold of uMPS with a fixed bond dimension. We give the main ideas and construct the TDVP equations. With these equations the steepest descent method is reformulated to find the optimal approximation for the ground state within the class of uMPS with a fixed bond dimension. The TDVP equations can also be applied to perform real-time evolution of the Schrödinger equation. Finally, we generalize this framework to \mathcal{CT} invariant MPS.

Note that recently it has been shown that the TDVP unifies a lot of optimization methods for MPS [171].

2.1.1. Introduction

The goal is to evolve the Schrödinger equation

$$i\partial_t |\Psi_u[A]\rangle = \mathcal{H} |\Psi_u[A]\rangle,$$

where $|\Psi_u[A]\rangle$ is a uMPS eq. (1.12) with $A^d \in \mathbb{C}^{D \times D}$ ($d = 1 \dots q$) and \mathcal{H} the Hamiltonian, within the manifold of uMPS with the same bond dimension D . For the left-hand side we can write

$$\partial_t |\Psi_u[A]\rangle = |\Phi_0[\dot{A}, A]\rangle$$

where $|\Phi_0[\dot{A}, A]\rangle$ is a tangent vector introduced in section 1.3. Clearly, $\mathcal{H}|\Psi_u[A]\rangle$ does not belong to the tangent plane. Therefore, we will approximate $\mathcal{H}|\Psi_u[A]\rangle$ by a tangent vector in an optimal way, i.e. we want to find B such that

$$\| \mathcal{H}|\Psi_u[A]\rangle - |\Phi_0[B, A]\rangle \|_2$$

is minimal. The Schrödinger equation yields norm conservation of the state. By projecting $\mathcal{H}|\Psi_u[A]\rangle$ to a tangent vector, we will lose this unitarity. However, we can still impose norm conservation up to first order in the time step. Therefore we need to project $\mathcal{H}|\Psi_u[A]\rangle$ orthogonal to $|\Psi_u[A]\rangle$. We thus need to find B such that it minimizes

$$\| \mathcal{H}|\Psi_u[A]\rangle - |\Phi_0[B, A]\rangle \|_2 \text{ with } \langle \Phi_0[\bar{B}, \bar{A}] | \Psi_u[A] \rangle = 0.$$

We assume that \mathcal{H} is translational invariant and takes the form

$$\mathcal{H} = \lim_{N \rightarrow +\infty} \sum_{n=1}^{N-1} \mathcal{T}^{n-1} h \mathcal{T}^{-n+1}$$

with h a hermitian operator acting non-trivially on the sites 1 and 2 only.

2.1.2. TDVP equations

As discussed in subsection 1.3.2, if $\langle \Phi_0[\bar{B}, \bar{A}] | \Psi_u[A] \rangle = 0$ we can impose either the left gauge fixing condition eq. (1.19) or the right gauge fixing condition eq. (1.20) on B . In this case we can parametrize B by a matrix X , see eq. (1.25) for right gauge fixing condition and eq. (1.26) for left gauge fixing condition in subsection 1.3.4.

(a) Equations when B obeys the right gauge fixing condition

Assume now B obeys the right gauge fixing condition and we use the parametrization eq. (1.25): $B = B(X)$ with $X \in \mathbb{C}^{D \times n_R}$. With this parametrization the complete freedom in the representation of B is removed and we thus need to minimize

$$\begin{aligned} f(\bar{X}, X) &= (\| \mathcal{H}|\Psi_u[A]\rangle - |\Phi_0[B(X), A]\rangle \|_2)^2 \\ &= \langle \Phi_0[\bar{B}(\bar{X}), \bar{A}] | \Phi_0[B(X), A] \rangle - \langle \Phi_0[\bar{B}(\bar{X}), \bar{A}] | \mathcal{H}|\Psi_u[A]\rangle \\ &\quad + \text{terms independent of } \bar{X} \\ &= 2\pi\delta(0) \left(N(\bar{X}, X) - H(\bar{X}, X) \right) \\ &\quad + \text{terms independent of } \bar{X} \end{aligned} \tag{2.1}$$

Omitting the virtual indices and physical indices in the tensor network diagrams and denoting

$$\gamma \text{---} \left[\begin{array}{c} \nabla_{\overline{B}} f \\ | \\ d \end{array} \right] \text{---} \delta = \frac{\partial f}{\partial \overline{B}_{\gamma, \delta}^d}.$$

we find

$$\left[\begin{array}{c} \nabla_{\overline{B}} f \\ | \\ d \end{array} \right] = \left[\begin{array}{c} \nabla_{\overline{B}} N \\ | \\ d \end{array} \right] - \left[\begin{array}{c} \nabla_{\overline{B}} H \\ | \\ d \end{array} \right]$$

where

$$\left[\begin{array}{c} \nabla_{\overline{B}} N \\ | \\ d \end{array} \right] = \left[\begin{array}{c} B(X) \\ \text{---} \Xi \text{---} \Lambda \\ \text{---} \text{---} \end{array} \right]$$

and

$$\left[\begin{array}{c} \nabla_{\overline{B}} H \\ | \\ d \end{array} \right] = \left[\begin{array}{c} A \\ \text{---} \Xi \text{---} K_0 \\ \text{---} \text{---} \end{array} \right] + \left[\begin{array}{c} A \quad A \\ \text{---} \Xi \text{---} h \text{---} \Lambda \\ \text{---} \text{---} A \end{array} \right] + \left[\begin{array}{c} A \quad A \\ \text{---} \Xi \text{---} h \text{---} \Lambda \\ \text{---} \text{---} A \end{array} \right]. \tag{2.5}$$

From eq. (1.25) and eq. (2.4) we find that

$$\left[\begin{array}{c} \nabla_{\overline{X}} f \\ \text{---} \end{array} \right] = \left[\begin{array}{c} \Xi^{-1/2} \nabla_{\overline{B}} f \\ | \\ V_R \\ \text{---} \Lambda^{-1/2} \end{array} \right] = \left[\begin{array}{c} X \\ \text{---} \end{array} \right] - \left[\begin{array}{c} \nabla_{\overline{X}} H \\ \text{---} \end{array} \right]$$

where

$$\left[\begin{array}{c} \nabla_{\overline{X}} H \\ \text{---} \end{array} \right] = \left[\begin{array}{c} \Xi^{-1/2} \nabla_{\overline{B}} H \\ | \\ V_R \\ \text{---} \Lambda^{-1/2} \end{array} \right]. \tag{2.6}$$

Note that the parametrization eq. (1.25) implied that $\nabla_{\overline{X}} N(\overline{X}, X) = X$, i.e. $\nabla_{\overline{X}} \nabla_X N(\overline{X}, X) = \mathbb{1}_{n_R \times n_R}$. This has a nice interpretation when considering the manifold of uMPS as a Kähler manifold and the overlap of two

tangent vectors as a metric, see [172]. The equation $\nabla_{\bar{X}} f = 0$ is easily solved as

$$\left(\begin{array}{c} \text{---} \\ \text{---} \end{array} \right) X = \left(\begin{array}{c} \text{---} \\ \text{---} \end{array} \right) \nabla_{\bar{X}} H.$$

Therefore, the optimal approximation $|\Phi_0[B, A]\rangle$ for $\mathcal{H}|\Psi_u[A]\rangle$ is obtained for

$$\left(\begin{array}{c} \text{---} \\ \text{---} \end{array} \right) B = \left(\begin{array}{c} \text{---} \\ \text{---} \end{array} \right) \Xi^{-1/2} \nabla_{\bar{X}} H V_R \Lambda^{-1/2}.$$

Note that both V_R and $\nabla_{\bar{X}} H$ depend on A , therefore the TDVP yields a highly non-linear ordinary differential equation of the form $\dot{A} = B(A)$.

(b) Equations when B obeys the left gauge fixing condition

Assume B obeys the left fix-gauge condition and we use the parametrization eq. (1.26): $B = B(X)$ with $X \in \mathbb{C}^{n_L \times D}$. In this case we have

$$\left(\begin{array}{c} \text{---} \\ \text{---} \end{array} \right) \nabla_{\bar{B}} H = \left(\begin{array}{c} \text{---} \\ \text{---} \end{array} \right) L_0 + \left(\begin{array}{c} \text{---} \\ \text{---} \end{array} \right) \Xi + \left(\begin{array}{c} \text{---} \\ \text{---} \end{array} \right) \Xi \quad (2.7)$$

with L_0 defined in eq. (1.29b). $\|\mathcal{H}|\Psi_u[A]\rangle - |\Phi_0[B(X), A]\rangle\|_2$ is thus minimized if we take

$$\left(\begin{array}{c} \text{---} \\ \text{---} \end{array} \right) X = \left(\begin{array}{c} \text{---} \\ \text{---} \end{array} \right) \nabla_{\bar{X}} H = \left(\begin{array}{c} \text{---} \\ \text{---} \end{array} \right) \Xi^{-1/2} \nabla_{\bar{B}} H V_L \Lambda^{-1/2}. \quad (2.8)$$

Therefore, the optimal approximation $|\Phi_0[B, A]\rangle$ for $\mathcal{H}|\Psi_u[A]\rangle$ is obtained by taking

$$\left(\begin{array}{c} \text{---} \\ \text{---} \end{array} \right) B = \left(\begin{array}{c} \text{---} \\ \text{---} \end{array} \right) \Xi^{-1/2} V_L \nabla_{\bar{X}} H \Lambda^{-1/2}.$$

2.1.3. Efficient computation of $B(A)$

Looking at eq. (2.5) and (2.7) we observe that we need to compute diagrams of the form

(2.9)

We will now discuss how this is performed in the most efficient way when $q \ll D$. For both diagrams one first defines

$$\alpha - \begin{array}{c} \text{---} C_{1,2} \text{---} \\ | \quad | \\ d_1 \quad d_2 \end{array} - \beta = \alpha - \begin{array}{c} \text{---} A_1 \text{---} A_2 \text{---} \\ | \quad | \\ d_1 \quad d_2 \end{array} - \beta = \left[A_1^{d_1} A_2^{d_2} \right]_{\alpha, \beta},$$

and then performs the following contraction

$$\begin{aligned} \alpha - \begin{array}{c} \text{---} D_{1,2} \text{---} \\ | \quad | \\ d_1 \quad d_2 \end{array} - \beta &= \alpha - \begin{array}{c} \text{---} D_{1,2} \text{---} \\ \text{---} o \text{---} \\ | \quad | \\ d_1 \quad d_2 \end{array} - \beta \\ &= \sum_{d'_1, d'_2=1}^q \langle d_1, d_2 | o | d'_1, d'_2 \rangle \left[C_{1,2}^{d'_1, d'_2} \right]_{\alpha, \beta}. \end{aligned}$$

With these definitions, the diagrams (2.9) reduce to resp.

Now one performs the following contractions

$$\alpha - \begin{array}{c} \text{---} E \text{---} \\ | \\ d \end{array} - \beta = \alpha - \begin{array}{c} \text{---} D_{1,2} \text{---} \\ | \quad | \quad | \\ \quad \quad \quad \Lambda \\ \quad \quad \quad | \\ \quad \quad \quad A_3 \\ \quad \quad \quad | \\ \quad \quad \quad \beta \end{array} = \sum_{d'=1}^q \left[D_{1,2}^{d, d'} \Lambda \left(A_3^{d'} \right)^\dagger \right]_{\alpha, \beta},$$

$$\alpha - \boxed{F} - \beta \underset{d}{=} \Xi = \sum_{d'=1}^q \left[\left(A_3^{d'} \right)^\dagger \Xi D_{1,2}^d \right]_{\alpha, \beta},$$

and one arrives at

$$\alpha - \Xi - \boxed{o} - \beta \underset{d}{=} \Lambda = \alpha - \Xi - \boxed{E} - \beta \underset{d}{=} \left[\Xi E^d \right]_{\alpha, \beta},$$

$$\alpha - \Xi - \boxed{o} - \beta \underset{d}{=} \Lambda = \alpha - \boxed{F} - \beta \underset{d}{=} \left[F^d \Lambda \right]_{\alpha, \beta}.$$

Performing the contractions in this order yields a computational cost of

$$\mathcal{O} \left(\max(q^4 D^2, q^2 D^3) \right) = \mathcal{O}(q^2 D^3)$$

because we assume that in our simulations D is larger than q .

Now we have discussed how one efficiently computes the contractions, we can present the algorithm to compute

$$B(A) = \arg \min_B \left\{ \left\| |\mathcal{H}|\Psi_u[A]\right\rangle - |\Phi_0[B, A]\right\rangle \right\|_2 : \langle \Phi_0[\overline{B}, \overline{A}] | \Psi_u[A] \rangle = 0 \}. \quad (2.10)$$

The pseudocode is shown in algorithm 2.1 and is justified by the discussion in subsection 2.1.2. We assume that A is normalized such that the leading eigenvalue η of the transfer matrix equals one and that the matrices Ξ and Λ corresponding to the left and right eigenvector are positive definite. We also pass the string 'stringGaugeFix' to the function which tells us what gauge fixing condition we need to impose: 'right' if we want $B = B(A)$ in the right gauge fixing condition and 'left' if we want $B = B(A)$ in the left gauge fixing condition. The output of the function gives the gradient $X = \nabla_{\overline{X}} H$, eq. (2.6) or (2.8), and $B = B(A)$ eq. (2.10).

Algorithm 2.1 Compute gradient TDVP

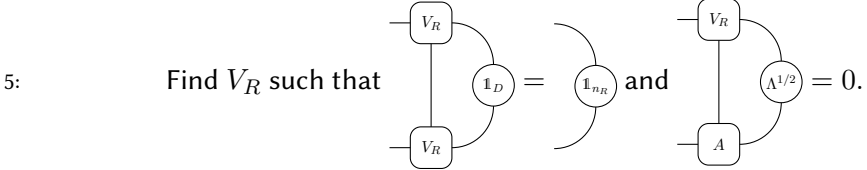
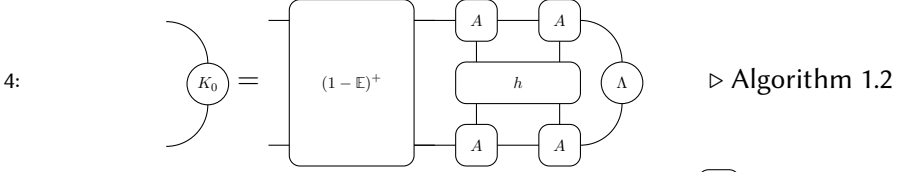
Input: A, Ξ, Λ, h , stringGaugeFix

Output: X, B

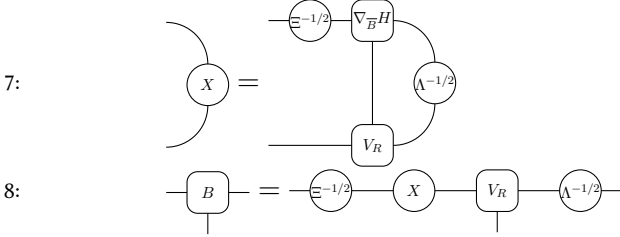
1: **function** $[X, B] = \text{TDVP}_{\text{DIRECTION}}(A, \Xi, \Lambda, h, \text{stringGaugeFix})$

2: **switch** stringGaugeFix **do**

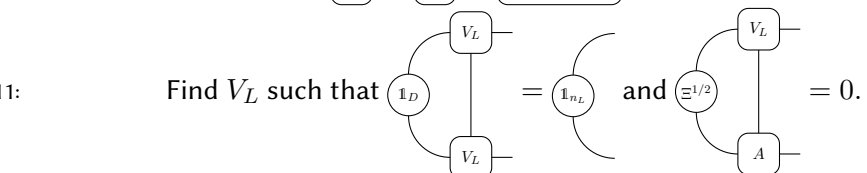
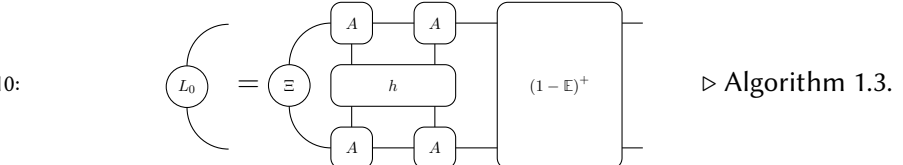
3: **case** 'right'



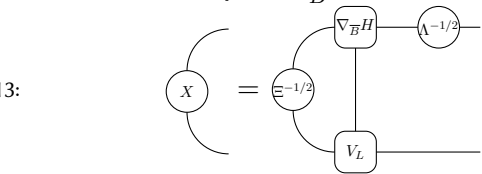
6: Compute $\nabla_{\bar{B}} H$ $\triangleright \text{Eq. (2.5)}$

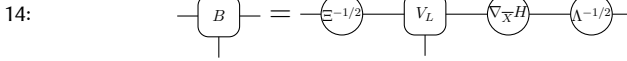


9: **case** 'left'



12: Compute $\nabla_{\bar{B}} H$ $\triangleright \text{Eq. (2.7)}$





15: **end switch**

16: **end function**

2.1.4. TDVP algorithm for optimization

Here we discuss how the TDVP can be used to find an optimal approximation for the ground state. Therefore we evolve the Schrödinger equation in imaginary time $d\tau = -idt$,

$$|\Psi_u[A(\tau)]\rangle = -\mathcal{H} |\Psi_u[A(\tau)]\rangle,$$

which evolves any state not orthogonal to the ground state of \mathcal{H} to the ground state of \mathcal{H} as $\tau \rightarrow +\infty$. As discussed in the previous subsection, the evolution is performed within the manifold of uMPS by evolving A according to

$$\dot{A}(\tau) = -B(A(\tau))$$

where the computation of $B(A(\tau))$ follows from algorithm 2.1. Solving this ordinary differential equation with an Euler integrator gives the following equation:

$$A(\tau + d\tau) = A(\tau) - B(A(\tau)) d\tau + \mathcal{O}(d\tau^2).$$

For $d\tau$ small enough this equation will evolve towards the optimal approximation of the ground state. The convergence criterium is that

$$\| |\Phi_0[B(A), A] \rangle \|_2$$

is small enough, i.e. that

$$\text{normGrad} = \sqrt{\text{tr} \left(\begin{array}{c} \nabla_{\bar{X}}H \\ \nabla_{\bar{X}}H \end{array} \right)} = \sqrt{\text{tr} (\nabla_{\bar{X}}H (\nabla_{\bar{X}}H)^\dagger)} \leq \epsilon_{grad} \quad (2.11)$$

where ϵ_{grad} is a preset tolerance and $\nabla_{\bar{X}}H$ is defined in eq. (2.6) or (2.8) depending on whether you choose the left gauge fixing or right gauge fixing condition for B .

The pseudocode is given in algorithm 2.2 and resembles a simple steepest descent algorithm [173]. Note however that the TDVP equation does not yield a steepest descent in parameter space, but produces the best approximation to a gradient descent in the full Hilbert space. This steepest descent can also be extended to a naive variational conjugate gradient method, see [174] for an example.

Algorithm 2.2 Steepest descent TDVP

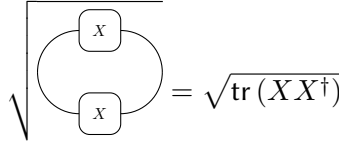
Input: $A_0, \epsilon_{grad}, d\tau, h$

Output: A

```

1: function  $A = \text{TDVP}_{\text{FLOW}}(\epsilon_{grad}, d\tau, A_0, h)$ 
2:    $A \leftarrow A_0$ 
3:    $normGrad = 1$ 
4:   while  $normGrad \geq \epsilon_{grad}$  do
5:      $[A, \Xi, \Lambda, \eta, \Gamma] = \text{normalizeUmps}(A)$  ▷ Algorithm 1.1
6:      $[X, B] = \text{TDVP}_{\text{direction}}(A, \Xi, \Lambda, h)$  ▷ Algorithm 2.1
7:      $normGrad = \sqrt{\text{tr}(XX^\dagger)}$ 
8:      $A \leftarrow A - Bd\tau$ 
9:   end while
10: end function

```



2.1.5. TDVP for real-time evolution

In the previous subsection we used the TDVP to perform imaginary time evolution of the Schrödinger equation, but of course we can also use the TDVP for simulating real-time evolution. In that case the TDVP equation becomes

$$\dot{A}(t) = -iB(A(t))$$

where the computation of $B(A(t))$ is discussed in algorithm 2.1. To solve this differential equation numerically we need to improve the Euler integration which is only correct up to order dt^2 . We will use the Runge-Kutta fourth-order method (RK4) [175]. Given a general ordinary differential equation of the form $\dot{x} = f(t, x)$ with x a vector, one defines

$$k_1 = f(t, x(t)) \tag{2.12a}$$

$$k_2 = f(t + dt/2, x(t) + k_1 dt/2) \tag{2.12b}$$

$$k_3 = f(t + dt/2, x(t) + k_2 dt/2) \tag{2.12c}$$

$$k_4 = f(t + dt, x(t) + k_3 dt) \tag{2.12d}$$

and one advances $x(t)$ with time step dt using the following update rule

$$x(t + dt) = x(t) + \frac{h}{6}(k_1 + 2k_2 + 2k_3 + k_4) + \mathcal{O}(dt^5) \quad (2.12e)$$

which is correct up to order dt^5 . Making now the replacements $x(t) \rightarrow [A^d(t)]_{\alpha,\beta}$ and $f(x(t)) \rightarrow -iB(A(t))$ one can easily write down the algorithm for real-time evolution. There is however one thing one needs to take care of. For the computation of $B(A)$ one should first normalize A , i.e. we compute $B_{\Gamma,\eta} = B(A_{\Gamma,\eta})$ with

$$\text{---} \boxed{A_{\Gamma,\eta}} \text{---} = \frac{1}{\sqrt{\eta}} \text{---} (\Gamma) \text{---} \boxed{A} \text{---} (\Gamma^{-1}) \text{---},$$

see algorithm 2.1. Because

$$B(A) = \arg_B \min \{ \| |\Phi_0[B, A]\rangle - H |\Psi_u[A]\rangle \|_2 : \langle \Phi_0[\bar{B}, \bar{A}] | \Psi_u[A] \rangle = 0 \}$$

it follows that

$$\text{---} \boxed{B_{\Gamma,\eta}} \text{---} = \text{---} (\Gamma) \text{---} \boxed{B(A)} \text{---} (\Gamma^{-1}) \text{---} / \sqrt{\eta}.$$

Therefore, if we first normalize A ,

$$\text{---} \boxed{A} \text{---} \leftarrow \text{---} \boxed{A_{\Gamma,\eta}} \text{---} = \frac{1}{\sqrt{\eta}} \text{---} (\Gamma) \text{---} \boxed{A} \text{---} (\Gamma^{-1}) \text{---},$$

and we compute $B_{\Gamma,\eta} = B(A_{\Gamma,\eta})$ via the TDVP, algorithm 2.1, we need to transform it back:

$$\text{---} \boxed{B(A)} \text{---} = \sqrt{\eta} \text{---} (\Gamma^{-1}) \text{---} \boxed{B_{\Gamma,\eta}} \text{---} (\Gamma) \text{---}. \quad (2.13)$$

In algorithm 2.3 we give the pseudocode for advancing a state $|\Psi_u[A_0]\rangle$ at time t to the state $|\Psi_u[A(t + dt)]\rangle$ at time $t + dt$ using TDVP and RK4. For simplicity, we assume that the Hamiltonian is time-independent. The algorithm is an implementation of the steps eq. (2.12) with $x(t) \rightarrow [A^d(t)]_{\alpha,\beta}$ and $f(x(t)) \rightarrow -iB(A(t))$ and taking into account that we need to transform B back after normalizing A , see eq. (2.13).

Algorithm 2.3 Real-time with TDVP and RK4

Input: A_0, dt, h

Output: A, Ξ, Λ

1: **function** $A = \text{TDVPRK4}(dt, A_0, t_0, h)$

it is known that this symmetry is not spontaneously broken, one can use the ansatz $|\Psi_{\mathcal{C}}[A]\rangle$, see eq. (1.31), to approximate the ground state. The Schrödinger equation,

$$i\partial_t |\Psi_{\mathcal{C}}[A]\rangle = \mathcal{H} |\Psi_{\mathcal{C}}[A]\rangle \quad (2.15)$$

is then equivalent to

$$i\partial_t |\Psi_u[A]\rangle = \mathcal{H}_u |\Psi_u[A]\rangle \quad (2.16)$$

where $|\Psi_u[A]\rangle$ is the ‘uniform counterpart’ of $|\Psi_{\mathcal{C}}[A]\rangle$, see section 1.4, and \mathcal{H}_u is the uniform counterpart of \mathcal{H} :

$$\mathcal{H}_u = \lim_{N \rightarrow +\infty} \sum_{n=1}^{2N-1} \mathcal{T}^{n-1} h \mathcal{T}^{-n+1}. \quad (2.17)$$

This equivalence follows from applying \mathcal{C} on the even sites of the Schrödinger equation eq. (2.15). As a consequence, if we want to find the optimal solution of the Schrödinger equation (2.15) within the manifold of \mathcal{CT} invariant MPS, we need to apply the TDVP algorithm for the Schrödinger equation (2.16). Therefore, to find the optimal approximation of the ground state we can apply algorithm 2.2, while if we want to perform real-time evolution we can use algorithm 2.3. In both cases, the A that comes out of the algorithm corresponds to the desired \mathcal{CT} invariant state. The expectation values have to be computed as explained in section 1.4.

2.2. Excitations in the tangent plane

In the previous section we discussed how one can use the TDVP to find an optimal uMPS approximation $|\Psi_u[A]\rangle$ for the ground state of a translational invariant Hamiltonian. Here we consider the tangent vectors $|\Phi_k[B, A]\rangle$ [87], see section 1.3, to find an optimal approximation for the one-particle excitations with momentum k . These tangent vectors are an extension of the Feynman-Bijl ansatz [176, 177], the single mode approximation [178] and the Rommer-Östlund ansatz [179] for one-particle excitations to the thermodynamic limit. Motivated by [91, 180], where it is proven that the momentum- k eigenstates with energy separated from the rest of the spectrum in that momentum sector can be created by acting with local operators on the vacuum, we expect that these tangent vectors are a good ansatz for elementary excitations.

We follow the method of [87] and find the optimal tangent vector that approximates the elementary excitations by solving an eigenvalue equation. The method is also extended to \mathcal{CT} invariant Hamiltonians (\mathcal{C} idempotent) where we optimize the tangent vectors $|\Phi_{k,s}^{\mathcal{C}}[B, A]\rangle$.

2.2.1. Translational invariant Hamiltonian

Once we have a good uMPS approximation $|\Psi_u[A]\rangle$ for the ground state we use the tangent vectors $|\Phi_k[B, A]\rangle$ to approximate the one-particle excitations with momentum k , see section 1.3. Because the excitations should be orthogonal to the ground state we can impose either the left gauge fixing condition eq. (1.19) or the right gauge fixing condition eq. (1.20) on B . In both cases, it is then possible to parametrize B by a matrix X , see eq. (1.26) for the left gauge fixing condition and eq. (1.25) for the right gauge fixing condition. The variational freedom lies thus within the matrices $X \in \mathbb{C}^{D \times n_R}$ or $X \in \mathbb{C}^{n_L \times D}$. Finally, we note that the ansatz $|\Phi_k[B(X), A]\rangle$ is linear in X . Therefore, the optimal approximation $|\Phi_k[B(X), A]\rangle$ for the excited states are found by minimizing

$$H_k(\bar{X}, X) = \frac{\langle \Phi_k[\bar{B}(\bar{X}), \bar{A}] | H | \Phi_k[B(X), A] \rangle}{\langle \Phi_k[\bar{B}(\bar{X}), \bar{A}] | \Phi_k[B(X), A] \rangle} \quad (2.18)$$

with respect to \bar{X} . This is equivalent to solving the generalized eigenvalue problem

$$H_k^{eff}(X) = \mathcal{E}_k N_k^{eff}(X)$$

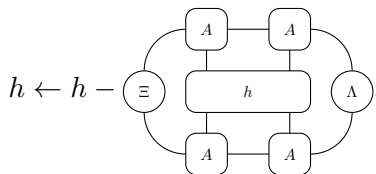
where

$$\begin{aligned} \left[H_k^{eff}(X) \right]_{(\alpha, \beta)} &= \frac{\partial}{\partial \bar{X}_{\alpha, \beta}} \langle \Phi_k[\bar{B}(\bar{X}), \bar{A}] | H | \Phi_k[B(X), A] \rangle, \\ \left[N_k^{eff}(X) \right]_{(\alpha, \beta)} &= \frac{\partial}{\partial \bar{X}_{\alpha, \beta}} \langle \Phi_k[\bar{B}(\bar{X}), \bar{A}] | \Phi_k[B(X), A] \rangle. \end{aligned}$$

This generalized eigenvalue system can also be recognized as the Rayleigh-Ritz equation. As we are only interested in the difference of the energy of the excited state with respect to the ground state energy, we subtract the (divergent) ground state energy from the Hamiltonian. More specifically, if

$$\mathcal{H} = \lim_{N \rightarrow +\infty} \sum_{n=1}^{N-1} \mathcal{T}^{n-1} h \mathcal{T}^{-n+1}$$

then we renormalize \mathcal{H} by



which implies that $\langle \Psi_u[A] | \mathcal{J} \mathcal{C} | \Psi_u[A] \rangle = 0$. As a consequence, from eq. (1.30i) it follows that

$$H_k^{eff}(X) = 2\pi\delta(0)\tilde{H}_k^{eff}(X)$$

with $\tilde{H}_k^{eff}(X)$ finite, see eq. (1.30i). Furthermore, eq. (1.28) implies that

$$N_k^{eff}(X) = 2\pi\delta(0)X$$

so we need to solve the eigenvalue problem

$$\tilde{H}_k^{eff}(X) = \mathcal{E}_k X.$$

Because we are only interested in the smallest eigenvalues, we can solve this eigenvalue problem iteratively. Therefore we need to implement the action of \tilde{H}_k^{eff} on X efficiently. We can use similar tricks as for the TDVP equations, see subsection 2.1.2. If B obeys the left gauge fixing condition and we parametrize B :

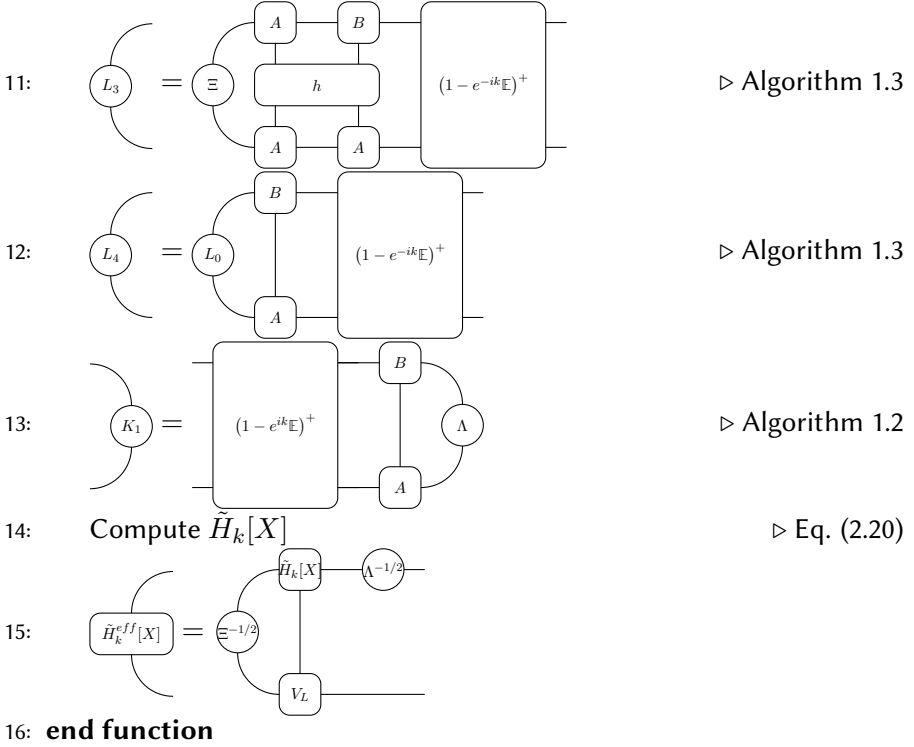
$$\text{---} \boxed{B(X)} \text{---} = \text{---} \bigcirc^{\varepsilon^{-1/2}} \text{---} \boxed{V_L} \text{---} \bigcirc^X \text{---} \bigcirc^{\Lambda^{-1/2}} \text{---} \quad (2.19)$$

with $X \in \mathbb{C}^{n_L \times D}$ and $V_L^d \in \mathbb{C}^{D \times n_L}$, see eq. (1.26), then one first defines

$$\begin{aligned}
 \tilde{H}_k[X] = & \Xi \left(\text{Diagram 1} + \text{Diagram 2} \right) \\
 + e^{ik} & \left(\text{Diagram 3} + \text{Diagram 4} + \text{Diagram 5} \right) \\
 + & \left(\text{Diagram 6} + e^{ik} \text{Diagram 7} + e^{-ik} \text{Diagram 8} \right) \\
 + e^{ik} & \left(\text{Diagram 9} + e^{-ik} \text{Diagram 10} \right) \\
 + e^{i2k} & \left(\text{Diagram 11} + e^{-i2k} \text{Diagram 12} \right) \quad (2.20)
 \end{aligned}$$

where K_0 and L_0 are defined in eqs. (1.29b) and (1.29c) and $K_1(X)$, $L_2(X)$, $L_3(X)$, $L_4(X)$ are defined in eq. (1.30). $\tilde{H}_k[X]$ is obtained by taking the partial derivative of the right-hand side of eq. (1.30i) with respect to $\overline{B'}$ and taking into account that B' obeys the left gauge fixing condition. $\tilde{H}_k^{eff}[X]$ is now found as

$$\tilde{H}_k^{eff}[X] = \Xi^{-1/2} \left(\text{Diagram} \right) \quad (2.21)$$



2.2.2. \mathcal{CT} invariant Hamiltonian

Let us now focus on the case when \mathcal{H} is of the form (2.14) and thus in particular \mathcal{CT} invariant ($\mathcal{C}^2 = \mathbb{1}_{C^g}$). If the ground state is \mathcal{CT} invariant and $|\Psi_{\mathcal{C}}[A]\rangle$ is a \mathcal{CT} invariant MPS approximation for the ground state, see subsection 2.1.6, we can use the tangent vectors $|\Phi_{k,\gamma}^{\mathcal{C}}[B, A]\rangle$ to approximate the one-particle excitations with quantum numbers $(k, \gamma) \in [-\pi, \pi] \times \{-1, 1\}$, see subsection 1.4.2. Again, because the excitations should be orthogonal to the ground state we can impose either the right gauge fixing condition eq. (1.20) or the left gauge fixing condition eq. (1.19) on B . In both cases, it is then possible to parametrize B by a matrix X , see eq. (1.25) for the right gauge fixing condition and eq. (1.26) for the left gauge fixing condition. The variational freedom lies thus within the matrix X . Finally, we note that the ansatz $|\Phi_{k,\gamma}^{\mathcal{C}}[B(X), A]\rangle$ is linear in X . Therefore, the optimal approximations $|\Phi_{k,\gamma}^{\mathcal{C}}[B(X), A]\rangle$ for the excited states are found by minimizing

$$H_{k,\gamma}^{\mathcal{C}}(\bar{X}, X) = \frac{\langle \Phi_{k,\gamma}^{\mathcal{C}}[\bar{B}(\bar{X}), \bar{A}] | \mathcal{H} | \Phi_{k,\gamma}^{\mathcal{C}}[B(X), A] \rangle}{\langle \Phi_{k,\gamma}^{\mathcal{C}}[\bar{B}(\bar{X}), \bar{A}] | \Phi_{k,\gamma}^{\mathcal{C}}[B(X), A] \rangle}$$

with respect to \bar{X} .

Using eq. (1.34) and eq. (1.35), we find that

$$\begin{aligned} H_{(k,\gamma)}^{\mathcal{C}}(\bar{X}, X) &= \frac{\langle \Phi_{[k]_{\gamma}}[\bar{B}(\bar{X}), \bar{A}] | \mathcal{H}_u | \Phi_{[k]_{\gamma}}[B(X), A] \rangle}{\langle \Phi_{[k]_{\gamma}}[\bar{B}(\bar{X}), \bar{A}] | \Phi_{[k]_{\gamma}}[B(X), A] \rangle} \\ &= H_{[k]_{\gamma}}(\bar{X}, X) \end{aligned}$$

where \mathcal{H}_u is defined in eq. (2.17), $H_{[k]_{\gamma}}(\bar{X}, X)$ is defined in eq. (2.18) and

$$[k]_{\gamma} = k/2 \text{ if } \gamma = 1 \text{ and } [k]_{\gamma} = k/2 + \pi \text{ if } \gamma = -1.$$

The minimization of $H_{[k]_{\gamma}}(\bar{X}, X)$ with respect to \bar{X} is discussed in the previous subsection. We can thus apply algorithm 2.4 to find the matrix X corresponding to the optimal approximation $|\Phi_{k,\gamma}^{\mathcal{C}}[B(X), A]\rangle$ of the excited states. The algorithm also gives (an estimate for) the energy $\mathcal{E}_{k,\gamma} = \mathcal{E}_{[k]_{\gamma}}$ of the excited state.

2.3. iTEBD

The Time-Evolving Block Decimation (TEBD) algorithm, for the first time published in [45], provides another way to evolve a MPS according to the Schrödinger equation. Contrary to the TDVP it enables a dynamical expansion of the variational manifold, i.e. one can increase or decrease the bond dimension of the matrices representing the MPS. As we will see, decreasing the bond dimension results in an effective truncation in the Schmidt spectrum. The fact that we can dynamically adapt the variational freedom makes it very attractive to use it for real-time evolution. Indeed, when evolving a state in real-time it is known that in general the entanglement grows [42], hence we need small bond dimension at early times and large bond dimension at later times.

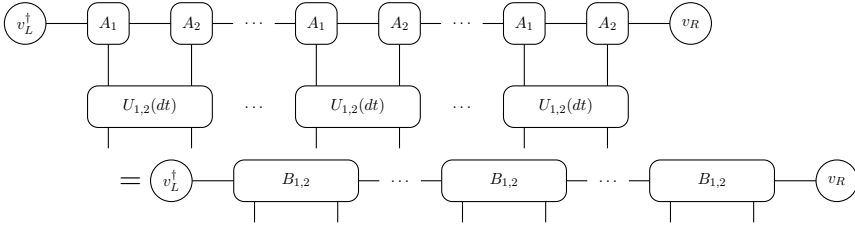
Two drawbacks of the method are that the way of updating the MPS representation might not be (globally) optimal and that it breaks translation symmetry down to translation symmetry over two sites. However by increasing the number of variational parameters we can always improve our approximation and thus we can always control the error in our truncation. Also, for our purpose the Hamiltonian is only translation invariant over two sites, therefore the second drawback of TEBD is not a stumbling-block as well. Here we focus on the TEBD algorithm for infinite lattices, called the infinite Time-Evolving Block Decimation (iTEBD), and follow mainly the considerations of [136].

2.3.2. iTEBD algorithm

The Trotter-Suzuki decomposition eq. (2.23) implies that we need to apply the gates $\mathcal{V}_1(dt)$ and $\mathcal{V}_2(dt)$ to a uMPS. We will now discuss how each of the gates are applied to a uniform MPS and how a new uniform MPS is obtained.

(a) Application of V_1

Applying the Trotter-gate $\mathcal{V}_1(dt)$ to a uniform MPS $|\Psi_u[A_1 A_2]\rangle$, see eq. (2.22), gives us $\mathcal{V}_1(dt) |\Psi(A_1 A_2)\rangle$ which equals



where

$$\begin{aligned}
 \text{---} B_{1,2} \text{---} &= \begin{array}{c} \text{---} A_1 \text{---} A_2 \text{---} \\ | \quad | \\ \text{---} U_{1,2}(dt) \text{---} \\ | \quad | \end{array}, & (2.24) \\
 \begin{array}{c} d_1 \quad d_2 \\ | \quad | \\ \text{---} U_{1,2}(dt) \text{---} \\ | \quad | \\ d'_1 \quad d'_2 \end{array} &= [\exp(-ih_{1,2}dt)]_{(d'_1, d'_2); (d_1, d_2)}.
 \end{aligned}$$

Note that if $A_{1,2}^{d_1, d_2} = A_1^{d_1} A_2^{d_2}$ is normalized, see algorithm 1.1, where Ξ resp. Λ is the normalized positive matrix corresponding to the left resp. right eigenvector of the leading eigenvalue η of the transfer matrix, then $B_{1,2}$ is also normalized with the same matrices Ξ and Λ . This is a consequence of the fact that $\mathcal{U}_{1,2}(dt)$ is a unitary gate. In order to reobtain a uMPS of the form (2.22) one performs the decomposition

$$\text{---} \Xi^{1/2} \text{---} B_{1,2} \text{---} \Lambda^{1/2} \text{---} \stackrel{(SVD)}{=} \begin{array}{c} \text{---} U_1 \text{---} \Sigma_{1,2} \text{---} V_2 \text{---} \\ | \quad | \quad | \end{array} \quad (2.25)$$

with

$$\begin{array}{c} \text{---} U_1 \text{---} \\ | \quad | \\ \text{---} \mathbb{1}_{qD} \text{---} \\ | \quad | \\ \text{---} U_1 \text{---} \end{array} = \text{---} \mathbb{1}_{qD} \text{---} \quad \text{and} \quad \begin{array}{c} \text{---} V_2 \text{---} \\ | \quad | \\ \text{---} \mathbb{1}_{qD} \text{---} \\ | \quad | \\ \text{---} V_2 \text{---} \end{array} = \text{---} \mathbb{1}_{qD} \text{---} \quad (2.26)$$

with

(2.29)

The diagonal elements of $\Sigma_{2,1}^2$ are the Schmidt values associated to the bipartition $\{\mathcal{A}_1^{2n}, \mathcal{A}_2^{2n}\}$ of the lattice, where

$$\mathcal{A}_1^{2n} = \{1, 2, \dots, 2n\} \text{ and } \mathcal{A}_2^{2n} = \{2n + 1, \dots, 2N\}.$$

Denoting the eigenvalues of $\Sigma_{2,1}^2$ by $\sigma_1, \dots, \sigma_{qD}$ with

$$1 \geq \sigma_1 \geq \sigma_2 \geq \dots \geq \sigma_{qD} \geq 0, \sum_{\alpha=1}^{qD} \sigma_\alpha = 1,$$

the Schmidt decomposition with respect to the bipartition $\{\mathcal{A}_1^{2n}, \mathcal{A}_2^{2n}\}$ of the lattice reads

$$|\Psi_u[B_{2,1}]\rangle = \sum_{\alpha=1}^{qD} \sqrt{\sigma_\alpha} |\Phi_\alpha^{\mathcal{A}_1^{2n}}\rangle \otimes |\Phi_\alpha^{\mathcal{A}_2^{2n}}\rangle$$

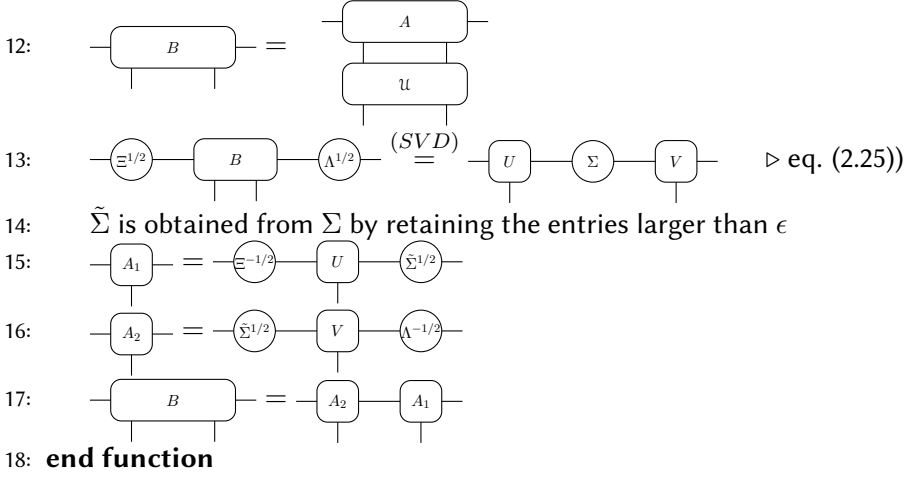
where

$$|\Phi_\alpha^{\mathcal{A}_1^{2n}}\rangle \in \bigotimes_{j \in \mathcal{A}_1^{2n}} \mathcal{H}_j \text{ and } |\Phi_\alpha^{\mathcal{A}_2^{2n}}\rangle \in \bigotimes_{j \in \mathcal{A}_2^{2n}} \mathcal{H}_j$$

are orthonormal unit vectors.

The bond dimension between the sites $2n$ and $2n + 1$ is now qD . Again one can reduce the bond dimension by discarding the Schmidt values with respect to this bipartition smaller than a preset tolerance ϵ : if $\tilde{\Sigma}_{2,1} \in \mathbb{C}^{\tilde{D} \times \tilde{D}}$ is the diagonal matrix which contains the \tilde{D} diagonal elements of $\tilde{\Sigma}_{2,1}$ larger than ϵ (in decreasing order), we define

Hence, we have approximated $V_2 |\Psi_u[A_2 A_1]\rangle$ by the uMPS $|\Psi_u[\tilde{A}_2 \tilde{A}_1]\rangle$ with bond dimension \tilde{D} :



2.4. DMRG for infinite boundary conditions

2.4.1. Introduction

Now we consider the thermodynamic limit ($N \rightarrow +\infty$) for a Hamiltonian that is only asymptotically translation invariant. More specifically, the lattice now consists of the sites

$$\{-N_L, -N_L + 1, \dots, 0, 1, \dots, M, M + 1, \dots, M + N_R\}$$

where the meaning of N_L , M and N_R will become clear soon.

\mathcal{H} takes the form

$$\mathcal{H} = \sum_{n=-N_L}^{M+N_R-1} h_{n,n+1}$$

where

$$h_{2n-1,2n} = \mathcal{T}^{2n-2} h_{1,2}^R \mathcal{T}^{-2n+2} \text{ for } m_R < 2n - 1 < M + N_R$$

$$h_{2n,2n+1} = \mathcal{T}^{2n-1} h_{2,3}^R \mathcal{T}^{-2n+1} \text{ for } m_R < 2n < M + N_R$$

$$h_{2n-1,2n} = \mathcal{T}^{2n-2} h_{1,2}^L \mathcal{T}^{-2n+2} \text{ for } -N_L \leq 2n - 1 < m_L$$

$$h_{2n,2n+1} = \mathcal{T}^{2n-1} h_{2,3}^L \mathcal{T}^{-2n+1} \text{ for } -N_L < 2n \leq m_L$$

and $h_{n,n+1}$ can be any Hermitian operator acting on two sites for $m_L \leq n \leq m_R - 1$, with $-N_L \ll 1 \leq m_L \leq m_R \leq M \ll M + N_R$ and where $h_{n,n+1}^L$ and $h_{n,n+1}^R$ are Hermitian operator that act only non-trivially on sites n and $n + 1$. The thermodynamic limit is obtained by $N_L, N_R \rightarrow +\infty$ while keeping $m_R - m_L$ fixed. $m_R - m_L$ is the length of the non-uniform part of the

Hamiltonian. For all sites $n \leq 1$ the Hamiltonian generates the interaction $h_{n,n+1}^L$ which only depends on the parity of n and on all sites $n \geq m_R$ the Hamiltonian generates the interaction $h_{n,n+1}^R$ which only depends on the parity of n as well. For convenience we assume that N_L is odd and that M and N_R are even.

2.4.2. MPS ansatz and calculus

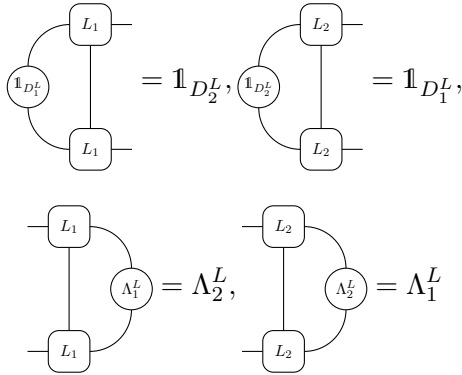
We will now construct a MPS ansatz for the ground state. Because \mathcal{H} has for $n \leq m_L$ and $n \geq m_R$ the same interactions we can assume that the ground state of \mathcal{H} converges on the left (i.e. for $n \ll m_L$) to the ground state of

$$\mathcal{H}_L = \lim_{K \rightarrow +\infty} \sum_{n=1}^{K-1} \mathcal{T}^{n-1} h_{n,n+1}^L \mathcal{T}^{-n+1} \text{ with } h_{2n-1,2n}^L = h_{1,2}^L, h_{2n,2n+1}^L = h_{2,3}^L$$

while the ground state of \mathcal{H} on the right (i.e. for $n \gg m_R$) will converge to the ground state of

$$\mathcal{H}_R = \lim_{K \rightarrow +\infty} \sum_{n=1}^{K-1} \mathcal{T}^{n-1} h_{n,n+1}^R \mathcal{T}^{-n+1} \text{ with } h_{2n-1,2n}^R = h_{1,2}^R, h_{2n,2n+1}^R = h_{2,3}^R.$$

More specifically, if $|\Psi_u[L_1 L_2]\rangle$ is the uniform MPS (for translation over two sites) corresponding to the ground state of \mathcal{H}_L , where $L_1 \in \mathbb{C}^{D_1^L \times D_2^L}$ and $L_2 \in \mathbb{C}^{D_2^L \times D_1^L}$ are in the left canonical form,



with $\Lambda_1^L \in \mathbb{C}^{D_2^L \times D_2^L}$ and $\Lambda_2^L \in \mathbb{C}^{D_1^L \times D_1^L}$ positive matrices, then we put in the MPS ansatz the tensors L_1 and L_2 on sites $n \leq 1$. When applying the TDVP algorithm we get a uMPS $|\Psi_u[L_{1,2}]\rangle$ where the sites $2n - 1$ and $2n$ are blocked, i.e.

$$\alpha \begin{array}{c} \text{---} L_{1,2} \text{---} \beta \\ | \\ (d_1, d_2) \end{array} = \alpha \begin{array}{c} \text{---} L_{1,2} \text{---} \beta \\ | \quad | \\ d_1 \quad d_2 \end{array}$$

with

$$\begin{array}{c} \text{---} L_{1,2} \text{---} \\ | \\ \text{---} L_{1,2} \text{---} \end{array} \text{---} \mathbb{1}_{D_2^L} = \mathbb{1}_{D_2^L}, \quad \begin{array}{c} \text{---} L_{1,2} \text{---} \\ | \\ \text{---} L_{1,2} \text{---} \end{array} \text{---} \Lambda_2^L = \Lambda_2^L.$$

Then one applies a SVD eq. (2.25)

$$\text{---} L_{1,2} \text{---} \stackrel{(SVD)}{=} \text{---} U_1 \text{---} \text{---} \Sigma_{1,2} \text{---} \text{---} V_2 \text{---}$$

and one puts

$$\text{---} L_1 \text{---} = \text{---} U_1 \text{---}, \quad \text{---} L_2 \text{---} = \text{---} \Sigma_{1,2} \text{---} \text{---} V_2 \text{---}$$

Defining

$$\text{---} \Omega \text{---} = \begin{array}{c} \text{---} V_2 \text{---} \\ | \\ \text{---} V_2 \text{---} \end{array} \text{---} \Lambda_2^L$$

it follows that $\Lambda_1^L = \Sigma_{1,2} \Omega \Sigma_{1,2}$. Note that one can discard the irrelevant Schmidt values in $\Sigma_{1,2}$ to reduce the bond dimension.

Similarly, if $|\Psi_u[R_1 R_2]\rangle$ is the uniform MPS corresponding to the ground state of \mathcal{H}_2 where $R_1 \in \mathbb{C}^{D_1^R \times D_2^R}$ and $R_2 \in \mathbb{C}^{D_2^R \times D_1^R}$ are in the right canonical form,

$$\begin{array}{c} \text{---} R_1 \text{---} \\ | \\ \text{---} R_1 \text{---} \end{array} \text{---} \mathbb{1}_{D_1^R} = \mathbb{1}_{D_1^R}, \quad \begin{array}{c} \text{---} R_2 \text{---} \\ | \\ \text{---} R_2 \text{---} \end{array} \text{---} \mathbb{1}_{D_2^R} = \mathbb{1}_{D_2^R}$$

$$\begin{array}{c} \text{---} R_1 \text{---} \\ | \\ \text{---} R_1 \text{---} \end{array} \text{---} \Xi_2^R = \Xi_1^R, \quad \begin{array}{c} \text{---} R_2 \text{---} \\ | \\ \text{---} R_2 \text{---} \end{array} \text{---} \Xi_1^R = \Xi_2^R,$$

with $\Xi_1^R \in \mathbb{C}^{D_2^R \times D_2^R}$ and $\Xi_2^R \in \mathbb{C}^{D_1^R \times D_1^R}$ positive matrices, then we put in the MPS ansatz the tensors R_1 and R_2 on sites $n > M$. When applying the

TDVP algorithm we get a uMPS $|\Psi_u[R_{1,2}]\rangle$ approximation for the ground state of \mathcal{H}_R where the sites $2n - 1$ and $2n$ are blocked, i.e.

$$\alpha - \text{R}_{1,2} - \beta = \alpha - \text{R}_{1,2} - \beta$$

with

$$\text{R}_{1,2} = \mathbb{1}_{D_1^R}, \Xi_2^R = \Xi_2^R$$

Then one applies a SVD eq. (2.25)

$$\text{R}_{1,2} \stackrel{(SVD)}{=} U_1 - \Sigma_{1,2} - V_2$$

and one puts

$$\text{R}_1 = U_1 - \Sigma_{1,2}, \text{R}_2 = V_2$$

Defining

$$\Omega = \Xi_2^R$$

it follows that $\Xi_2^R = \Sigma_{1,2}\Omega\Sigma_{1,2}$. Note that one can discard the irrelevant Schmidt values in $\Sigma_{1,2}$ to reduce the bond dimension D_2^R .

On the remaining sites we will put some new tensors B_n that have to be determined with a variational method. The MPS trial state for the ground state of \mathcal{H} takes then the form [80, 112, 113]

$$|\Psi[B]\rangle = B_0 - B_1 - B_2 - \dots - B_n - \dots - B_{M-1} - B_M - B_{M+1}$$

(2.30a)

with $B_n^{d_n} \in \mathbb{C}^{D_n \times D_{n+1}}$ ($D_1 = D_1^L, D_{M+1} = D_1^R$),

$$B_0 = v_L^\dagger - L_1 - L_2 - \dots - L_1 - L_2$$

(2.30b)

and

$$\begin{array}{c} \circlearrowleft B_{M+1} \\ | \\ (d_{M+1}, \dots, d_{M+N_R}) \end{array} = \begin{array}{c} \text{---} \text{---} \text{---} \text{---} \text{---} \text{---} \text{---} \text{---} \\ | \quad | \quad | \quad | \\ \text{---} R_1 \text{---} R_2 \text{---} \dots \text{---} R_1 \text{---} R_2 \text{---} \text{---} \\ | \quad | \quad | \quad | \\ d_{M+1} \quad d_{M+2} \quad d_{M+N_R-1} \quad d_{M+N_R} \end{array} \cdot \begin{array}{c} \circlearrowright v_R \end{array} \quad (2.30c)$$

In the thermodynamic limit ($N_R, N_L \rightarrow +\infty$) all the expectation values are independent of the boundary vectors v_R and v_L . Because the tensors L_n and R_n are already fixed, the freedom of this ansatz lies within the tensors B_1, \dots, B_M . In this form we blocked sites $-N_L, \dots, 0$ into the effective site 0 and we blocked the sites $M+1, \dots, M+N_R$ into the effective site $M+1$. Therefore this MPS ansatz can be interpreted on a finite lattice and thus indeed resembles the state (1.1) but on site 0 and site $M+1$ the local Hilbert space is infinite dimensional.

Consider now an operator of the form

$$\mathcal{O} = \sum_{n=-n_L}^{M+N_R} o_{n,n+1}$$

where $o_{n,n+1}$ acts only non-trivially on sites n and $n+1$ with

$$o_{2n-1,2n} = \mathcal{T}^{2n-2} o_{1,2}^R \mathcal{T}^{-2n+2} \text{ for } M < 2n-1 < M+N_R$$

$$o_{2n,2n+1} = \mathcal{T}^{2n-2} o_{2,3}^R \mathcal{T}^{-2n+2} \text{ for } M < 2n < M+N_R$$

$$o_{2n-1,2n} = \mathcal{T}^{2n-2} o_{1,2}^L \mathcal{T}^{-2n+2} \text{ for } -N_L \leq 2n-1 < 0$$

$$o_{2n,2n+1} = \mathcal{T}^{2n-2} o_{2,3}^L \mathcal{T}^{-2n+2} \text{ for } -N_L < 2n \leq 0$$

where $o_{1,2}^R$ and $o_{1,2}^L$ resp. $o_{2,3}^R$ and $o_{2,3}^L$ are Hermitian operators acting on sites 1 and 2 resp. 2 and 3. To avoid divergences originating from the infinite lattice we subtract from $o_{n,n+1}^L$ and $o_{n,n+1}^R$ its ground state expectation value, i.e.

$$\begin{array}{c} \circlearrowleft L_n \text{---} L_{n+1} \text{---} \circlearrowright L_{n+1} \\ | \quad | \\ \text{---} o_{n,n+1}^L \text{---} \\ | \quad | \\ \circlearrowleft L_n \text{---} L_{n+1} \text{---} \circlearrowright L_{n+1} \end{array} \mathbb{1} \otimes \mathbb{1} \quad (2.31a)$$

$$\begin{array}{c} \circlearrowleft R_n \text{---} R_{n+1} \text{---} \circlearrowright R_{n+1} \\ | \quad | \\ \text{---} o_{n,n+1}^R \text{---} \\ | \quad | \\ \circlearrowleft R_n \text{---} R_{n+1} \text{---} \circlearrowright R_{n+1} \end{array} \mathbb{1} \otimes \mathbb{1} \quad (2.31b)$$

with $n = 1, 2; n + 1 = n + 1 \bmod 2 \in \{1, 2\}$.

To compute the expectation value $\langle \Psi[\bar{B}] | \mathcal{O} | \Psi[B] \rangle$ we first compute $L_0 \in \mathbb{C}^{D_1^L \times D_1^L}$:

$$\Theta_1 = \text{[Diagram]}, \quad \text{[Diagram]} = \text{[Diagram]}, \quad (2.32a)$$

$$\Theta_2 = \text{[Diagram]}, \quad \text{[Diagram]} = \text{[Diagram]}, \quad (2.32b)$$

$$L_0 = \Theta_1 + \Theta_2 + \text{[Diagram]}, \quad (2.32c)$$

which can be computed efficiently by using algorithm 1.3 for the inverses of $(1 - \mathbb{E}_{L_{1,2}}^{L_{1,2}})^+$ and $(1 - \mathbb{E}_{L_{2,1}}^{L_{2,1}})^+$. We also need to compute a similar matrix $K_0 \in \mathbb{C}^{D_1^R \times D_1^R}$ for the right uniform part:

$$\Theta_1 = \text{[Diagram]}, \quad \text{[Diagram]} = \text{[Diagram]}, \quad (2.33a)$$

$$\Theta_2 = \text{[Diagram]}, \quad \text{[Diagram]} = \text{[Diagram]}, \quad (2.33b)$$

$$\begin{array}{c} \text{---} \\ \text{---} \end{array} \left(K_0 \right) = \begin{array}{c} \text{---} \\ \text{---} \end{array} \left(\Theta_1 \right) + \begin{array}{c} \text{---} \\ \text{---} \end{array} \left(\Theta_2 \right) \quad (2.33c)$$

which can be computed efficiently by using algorithm 1.2 for the inverses of $\left(1 - \mathbb{E}_{R_{1,2}}^{R_{1,2}}\right)^+$ and $\left(1 - \mathbb{E}_{R_{2,1}}^{R_{2,1}}\right)^+$. Finally we compute iteratively

$$\begin{array}{c} \text{---} \\ \text{---} \end{array} \left(\Xi_0 \right) = \mathbb{1}_{D_1^L}, \quad \begin{array}{c} \text{---} \\ \text{---} \end{array} \left(\Xi_n \right) = \begin{array}{c} \text{---} \\ \text{---} \end{array} \left(\Xi_{n-1} \right) \begin{array}{c} B_n \\ B_n \end{array} \quad (2.34a)$$

$$\begin{array}{c} \text{---} \\ \text{---} \end{array} \left(\Lambda_M \right) = \mathbb{1}_{D_1^R}, \quad \begin{array}{c} \text{---} \\ \text{---} \end{array} \left(\Lambda_{n-1} \right) = \begin{array}{c} B_n \\ B_n \end{array} \left(\Lambda_n \right) \quad (2.34b)$$

and we arrive at

$$\begin{aligned}
 \langle \Psi[\bar{B}] | \mathcal{O} | \Psi[\bar{B}] \rangle &= \begin{array}{c} \text{---} \\ \text{---} \end{array} \left(L_0 \right) \left(\Lambda_0 \right) + \begin{array}{c} L_2 \quad B_1 \\ \text{---} \quad \text{---} \\ \text{---} \quad \text{---} \\ L_2 \quad B_1 \\ \text{---} \quad \text{---} \end{array} \left(o_{0,1} \right) \left(\Lambda_1 \right) \\
 + \sum_{n=1}^{M-1} &\begin{array}{c} B_n \quad B_{n+1} \\ \text{---} \quad \text{---} \\ \text{---} \quad \text{---} \\ B_n \quad B_{n+1} \\ \text{---} \quad \text{---} \end{array} \left(\Xi_{n-1} \right) \left(o_{n,n+1} \right) \left(\Lambda_{n+1} \right) + \begin{array}{c} B_M \quad R_1 \\ \text{---} \quad \text{---} \\ \text{---} \quad \text{---} \\ B_M \quad R_1 \\ \text{---} \quad \text{---} \end{array} \left(\Xi_{M-1} \right) \left(o_{M,M+1} \right) \left(\mathbb{1}_{D_2^R} \right) + \begin{array}{c} \text{---} \\ \text{---} \end{array} \left(\Xi_M \right) \left(K_0 \right). \quad (2.35)
 \end{aligned}$$

2.4.3. DMRG algorithm

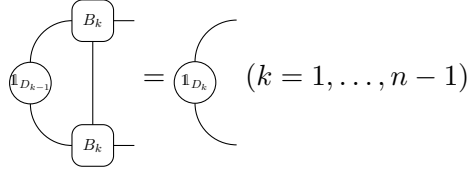
The MPS $|\Psi[B]\rangle$ is linear in each of the B_n ($1 \leq n \leq M$) and thus we can apply the DMRG algorithm [44, 80] to find the optimal approximation for the ground state. The DMRG algorithm minimizes

$$H(B_1, \dots, B_M) = \frac{\langle \Psi[\bar{B}] | \mathcal{H} | \Psi[B] \rangle}{\langle \Psi[\bar{B}] | \Psi[B] \rangle}$$

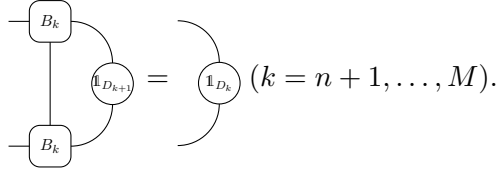
by first minimizing $H(B_1, \dots, B_M)$ with respect to \bar{B}_1 while keeping B_2, \dots, B_M fixed, then minimizing $H(B_1, \dots, B_M)$ with respect to \bar{B}_2 while keeping B_1, B_3, \dots, B_M fixed and so on until B_M . After this ‘sweep’ it will

‘sweep back’: first the DMRG algorithm minimizes $H(B_1, \dots, B_M)$ with respect to \overline{B}_M while keeping B_1, \dots, B_{M-1} fixed, then it minimizes $H(B_1, \dots, B_M)$ with respect to \overline{B}_{M-1} while keeping B_1, \dots, B_{M-2}, B_M fixed and so on until B_1 .

Let us now discuss how $H(B_1, \dots, B_M)$ is minimized with respect to B_n ($n = 1, \dots, M$). Therefore we assume that B_1, \dots, B_{n-1} are in the left canonical form



and that B_{n+1}, \dots, B_N are in the right canonical form,



Because L_1 and L_2 are in the left canonical form and R_1 and R_2 are in the right canonical form, we can use the procedure described in subsection 1.1.5 to bring B_1, \dots, B_{n-1} in the left canonical form and B_{n+1}, \dots, B_N in the right canonical form. Minimizing $H(B_1, \dots, B_M)$ with respect to \overline{B}_n is then equivalent to finding the smallest eigenvalue \mathcal{E}_0 of \mathbb{H}_n with components

$$[\mathbb{H}_n]_{(d', \gamma, \delta); (d, \alpha, \beta)} = \frac{\partial}{\partial [B_n^d]_{\alpha, \beta}} \frac{\partial}{\partial [\overline{B}_n^{d'}]_{\gamma, \delta}} H(B_1, \dots, B_M). \quad (2.36)$$

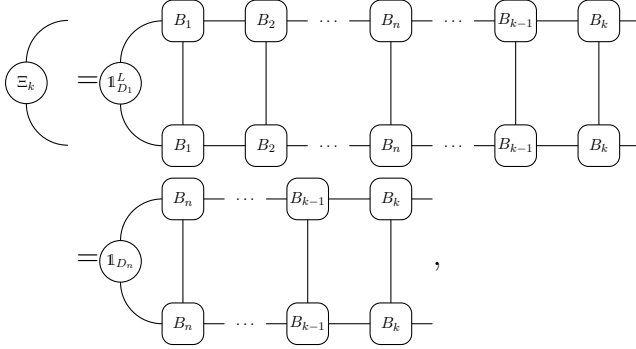
An exact diagonalization of \mathbb{H}_n would take $\mathcal{O}(q^3 D^6)$ computation time. However, because we are only interested in the smallest eigenvalue we can use an iterative procedure and we only need the action of \mathbb{H}_n on B_n , i.e. we only need to compute

$$[\mathbb{H}_n(B_n)]_{(d', \gamma, \delta)} = \frac{\partial}{\partial [\overline{B}_n^{d'}]_{\gamma, \delta}} H(B_1, \dots, B_M).$$

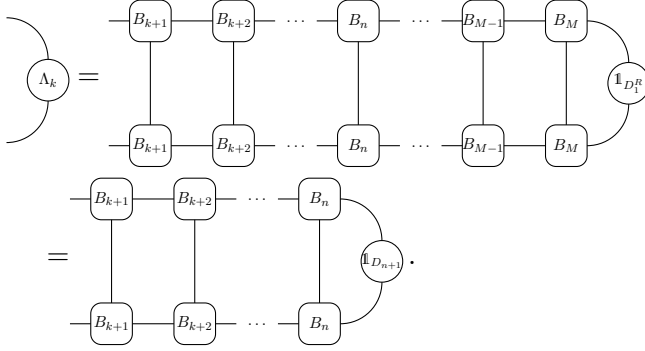
The computation of $\mathbb{H}_n(B_n)$ can be performed efficiently [80] and follows from taking the partial derivative with respect to \overline{B}_n of the expression eq. (2.35) for $\mathcal{O} = \mathcal{H}$, i.e.

$$o_{1,2}^L = h_{1,2}^L, o_{2,3}^L = h_{2,3}^L, o_{1,2}^R = h_{1,2}^R, o_{2,3}^R = h_{2,3}^R, o_{n,n+1} = h_{n,n+1}$$

and taking into account that Ξ_k depends on B_n for $k \geq n$,



and that Λ_k depends on B_n for $k \leq n - 1$,



Here we used that B_1, \dots, B_{n-1} are in the left canonical form and that B_{n+1}, \dots, B_M are in the right canonical form. $\mathbb{H}_n(B_n)$ can be constructed as follows. First one computes K_0 and L_0 as in eqs. (2.32) and (2.33) with

$$o_{1,2}^L = h_{1,2}^L, o_{2,3}^L = h_{2,3}^L, o_{1,2}^R = h_{1,2}^R, o_{2,3}^R = h_{2,3}^R.$$

Then one computes

$$\begin{aligned} [F_1^{d',d}]_{\alpha,\beta} &= \text{Diagram with } F_1 \text{ tensor} = \text{Diagram with } L_0 \text{ tensor} + \text{Diagram with } 1_{D_2}^L \text{ and } h_{0,1} \text{ tensors} \\ &= [L_0]_{\alpha,\beta} \delta_{d,d'} + \sum_{d_1, d_2=1}^q [(L_2^{d_1})^\dagger L_2^{d_2}]_{\alpha,\beta} \langle d_1, d' | h_{0,1} | d_2, d \rangle, \end{aligned} \quad (2.37a)$$

$$\begin{aligned}
 [G_M^{d',d}]_{\alpha\beta} &= \text{Diagram of } G_M \text{ with inputs } d, d' \text{ and outputs } \alpha, \beta \\
 &= \text{Diagram of } K_0 \text{ with inputs } d, d' \text{ and outputs } \alpha, \beta \\
 &\quad + \text{Diagram of } h_{M,M+1} \text{ with inputs } d, d' \text{ and outputs } \alpha, \beta \\
 &\quad \quad \quad \text{Diagram of } \mathbb{1}_{D_2^\beta} \text{ with inputs } \alpha, \beta \\
 &= \delta_{d,d'} [K_0]_{\alpha,\beta} + \sum_{d_1, d_2=1}^q \langle d', d_1 | h_{M,M+1} | d, d_2 \rangle [R_1^{d_2} (R_1^{d_1})^\dagger]_{\alpha,\beta}.
 \end{aligned} \tag{2.37b}$$

and one computes for $k = 2, \dots, n$

$$\begin{aligned}
 [F_k^{d',d}]_{\alpha,\beta} &= \text{Diagram of } F_k \text{ with inputs } d, d' \text{ and outputs } \alpha, \beta \\
 &= \text{Diagram of } F_{k-1} \text{ with inputs } d, d' \text{ and outputs } \alpha, \beta \\
 &\quad \quad \quad \text{Diagram of } B_{k-1} \text{ with inputs } \alpha, \beta \\
 &\quad \quad \quad \text{Diagram of } h_{k-1,k} \text{ with inputs } d, d' \text{ and outputs } \alpha, \beta \\
 &\quad \quad \quad \text{Diagram of } \mathbb{1}_{D_{k-1}} \text{ with inputs } \alpha, \beta \\
 &= \sum_{d_1, d_2=1}^q [(B_{k-1}^{d_1})^\dagger F_{k-1}^{d_1, d_2} B_{k-1}^{d_2}]_{\alpha,\beta} \delta_{d,d'} \\
 &\quad + \sum_{d_1, d_2=1}^q \langle d_1, d' | h_{k-1,k} | d_2, d \rangle [(B_{k-1}^{d_1})^\dagger B_{k-1}^{d_2}]_{\alpha,\beta}
 \end{aligned} \tag{2.37c}$$

and for $k = M - 1, M - 2, \dots, n$

$$\begin{aligned}
 [G_k^{d',d}]_{\alpha,\beta} &= \text{Diagram of } G_k \text{ with indices } \alpha, \beta, d, d' \\
 &= \text{Diagram of } G_{k+1} \text{ with } B_{k+1} \text{ tensors} + \text{Diagram of } h_{k,k+1} \text{ with } B_{k+1} \text{ tensors and } \mathbb{1}_{D_{k+2}} \\
 &= \delta_{d,d'} \sum_{d_1, d_2} [B_{k+1}^{d_1} G_{k+1}^{d_2, d_1} (B_{k+1}^{d_2})^\dagger]_{\alpha,\beta} \\
 &\quad + \langle d', d_1 | h_{k,k+1} | d, d_2 \rangle [B_{k+1}^{d_2} (B_{k+1}^{d_1})^\dagger]_{\alpha,\beta} . \quad (2.37d)
 \end{aligned}$$

Once we have constructed F_n and G_n one easily obtains $\mathbb{H}_n(B_n)$:

$$\begin{aligned}
 \alpha - \mathbb{H}_n(B_n) - \beta &= \text{Diagram of } F_n \text{ with } B_n \text{ tensor} + \text{Diagram of } G_n \text{ with } B_n \text{ tensor} \\
 &= \sum_{d_0=1}^q [F_n^{d, d_0} B_n^{d_0}]_{\alpha\beta} + \sum_{d_0=1}^q [B_n^{d_0} G_n^{d, d_0}]_{\alpha\beta} . \quad (2.38)
 \end{aligned}$$

Assuming that $q \ll D$, the computation time of $\mathbb{H}_n(B_n)$ scales like $\mathcal{O}(Mq^2D^3)$ with $D = \max_n(D_n)$.

2.4.4. Pseudocode of the DMRG algorithm

The pseudocode for the DMRG algorithm [44, 80] is presented in algorithm 2.6. As input we give the tensors $A_{1,2}^L$ and $A_{1,2}^R$ corresponding to the MPS approximations of the ground states $|\Psi_u[A_{1,2}^L]\rangle$ and $|\Psi_u[A_{1,2}^R]\rangle$ of $\mathcal{H}_L = \sum_{n=1}^{K-1} \mathcal{T}^{n-1} h_L \mathcal{T}^{-n+1}$ and $\mathcal{H}_R = \sum_{n=1}^{K-1} \mathcal{T}^{n-1} h_R \mathcal{T}^{-n+1}$ ($K \rightarrow +\infty$). The tensors do not need to be normalized, this will be done in the algorithm (lines 2-7). Furthermore, we also pass a desired tolerance ϵ to the function. This will be the error on the ground state energy \mathcal{E}_0 of \mathcal{H} . We also give an initial ansatz for the ground state B_1, \dots, B_M . We have also transformed B_2, \dots, B_M in the right canonical form, see lines 18-23, using the procedure from subsection 1.1.5 and normalized the state to norm 1.

As output we get the tensors B_1, \dots, B_M corresponding to the optimal approximation of the ground state \mathcal{H} with the class of states defined in eq. (2.30). Furthermore the algorithm gives the vectors $\Sigma_1, \dots, \Sigma_M$ which contain the square roots of the Schmidt values of $|\Psi[B]\rangle$ with respect to the bipartition $\{\mathcal{A}_1^n, \mathcal{A}_2^n\}$ of the lattice, where

$$\mathcal{A}_1^n = \{-N_L, 2, \dots, n\} \text{ and } \mathcal{A}_2^n = \{n+1, \dots, M+N_R\}.$$

Finally we also get the estimate \mathcal{E}_0 for the smallest eigenvalue of \mathcal{H} . To obtain a IR finite quantity for \mathcal{E}_0 one should subtract the ground state expectation values from the left uniform part $h_{n,n+1}^L$ and the right uniform part $h_{n,n+1}^R$ of \mathcal{H} as in eq. (2.31).

The main function ‘DMRG’, line 1 - 33, performs the sweeps where $H(B_1, \dots, B_M)$ is optimized with respect to B_n . After the sweep from left to right (i.e. from $n = 1$ until $n = M$) by using the function ‘SweepLeft2Right’ we get an estimate \mathcal{E}_1 for the ground state energy and after a sweep from right to left (by using the function ‘SweepRight2Left’) we get another (and smaller) estimate \mathcal{E}_2 for the ground state energy. When the difference between \mathcal{E}_1 and \mathcal{E}_2 in magnitude is small enough, i.e. smaller than our desired tolerance ϵ , the DMRG algorithm has converged and our estimate for the ground state energy is $\mathcal{E}_0 = \mathcal{E}_2$. This is what happens if the algorithm executes the while loop, lines 27-31.

In this while loop, the algorithm invokes the functions ‘SweepLeft2Right’ and ‘SweepRight2Left’ which are presented in lines 34-51 and 52-69. Both algorithms are similar. Let us therefore focus on the function ‘SweepLeft2Right’. This function first minimizes $H(B_1, \dots, B_M)$ with respect to \bar{B}_1 while keeping B_2, \dots, B_M fixed, then minimizes $H(B_1, \dots, B_M)$ with respect to \bar{B}_2 while keeping B_1, B_3, \dots, B_M fixed and so on until B_M . As explained in the previous subsection we therefore need to find the smallest eigenvalue of \mathbb{H}_n , see eq. (2.36). To implement the action of \mathbb{H}_n on B_n we need to compute F_n and G_n , see eqs. (2.37) and (2.38).

First of all, note that F_1 and G_M are independent of B_1, \dots, B_M and thus only need to be computed once, see lines 24 and 25. Hence they can be passed via an extra argument to the function ‘SweepLeft2Right’. When sweeping from left to right one deduces that G_n only depends on B_{n+1}, \dots, B_M and that these tensors are not optimized yet in this sweep. Therefore, one can compute all the tensors G_n before optimizing, see line 35-37. In contrast, F_n can only be computed when B_1, \dots, B_{n-1} are optimized. The for loop, line 38-50, exactly performs the optimization of B_n for $n = 1, \dots, N$ assuming that B_1, \dots, B_{n-1} are optimized. First, F_n is computed in line 40. This allows to implement the action of \mathbb{H}_n on B_n . As before the command in line 42 means that you have to use an iterative eigensolver which gives you

the tensor B_n corresponding to the eigenvector \mathbb{H}_n with smallest eigenvalue \mathcal{E}_0 . The function ‘HeffDMRG’, lines 70-72, computes the action of \mathbb{H}_n on B_n and has to be passed as an argument to ‘eigs’.

After applying this iterative eigensolver we have optimized B_n . Note however that all our formulas use the fact that B_k is in the left canonical form for $k < n$ and B_k is in the right canonical form for $k > n$. Before proceeding we need to put B_n in the left canonical form. This can be performed with the method discussed in subsection 1.1.5, see lines 43-48. As a nice byproduct we also get the Schmidt values associated with the bipartition $\{\mathcal{A}_1^n, \mathcal{A}_2^n\}$ of the lattice, where

$$\mathcal{A}_1^n = \{-N_L, 2, \dots, n\} \text{ and } \mathcal{A}_2^n = \{n + 1, \dots, M + N_R\}.$$

The square roots of these Schmidt values are stored in the vector Σ_n .

The function ‘SweepRight2Left’, lines 52-69, is similar but now one first optimizes B_M , then B_{M-1} and so on. In this case F_n will depend on B_1, \dots, B_{n-1} which are not optimized yet and can thus be computed before starting the sweep. When now sweeping from right to left we have to update G_n after every step. By applying an iterative eigensolver to \mathbb{H}_n we have update B_n . Afterwards we need to transform B_n in the right canonical form in the way that is discussed in subsection 1.1.5.

We have now discussed the pseudocode of algorithm 2.6 and this can be used as a basis for implementing the DMRG algorithm.

Algorithm 2.6 DMRG for infinite open boundary conditions

Input: $B = (B_1, \dots, B_M), A_{1,2}^L, A_{1,2}^R, \epsilon, h_{n,n+1}, h_{1,2}^L, h_{2,3}^L, h_{1,2}^R, h_{2,3}^R$

Output: $B = (B_1, \dots, B_M), \Sigma = (\Sigma_1, \dots, \Sigma_M), \mathcal{E}_0$

1: **function** $[B, \Sigma, \mathcal{E}_0] = \text{DMRG}(B, A_{1,2}^L, A_{1,2}^R, \epsilon, h_{n,n+1}, h_{1,2}^L, h_{2,3}^L, h_{1,2}^R, h_{2,3}^R)$

2: $[L_{1,2}, \mathbb{1}_{D_1^L}, \Lambda_2^L] = \text{normalizeUmeps}(A_{1,2}^L, \text{‘left’}) \quad \triangleright \text{Algorithm 1.1}$

3: $\begin{array}{c} \text{---} L_{1,2} \text{---} \\ | \\ \text{---} U_1 \text{---} \Sigma_{1,2} \text{---} V_2 \text{---} \end{array} \stackrel{(SVD)}{=} \begin{array}{c} \text{---} U_1 \text{---} \Sigma_{1,2} \text{---} V_2 \text{---} \\ | \quad | \quad | \\ \text{---} U_1 \text{---} \Sigma_{1,2} \text{---} V_2 \text{---} \end{array} \quad \triangleright \text{Eq. (2.25)}$

4: $\begin{array}{c} \text{---} L_1 \text{---} \\ | \\ \text{---} U_1 \text{---} \end{array} = \begin{array}{c} \text{---} U_1 \text{---} \\ | \\ \text{---} U_1 \text{---} \end{array}$

5: $\begin{array}{c} \text{---} L_2 \text{---} \\ | \\ \text{---} \Sigma_{1,2} \text{---} V_2 \text{---} \end{array} = \begin{array}{c} \text{---} \Sigma_{1,2} \text{---} V_2 \text{---} \\ | \quad | \\ \text{---} \Sigma_{1,2} \text{---} V_2 \text{---} \end{array}$

6: $\Lambda_1^L = \Sigma_{1,2} \Omega \Sigma_{1,2}$ with $\begin{array}{c} \text{---} \Omega \text{---} \\ | \\ \text{---} V_2 \text{---} \Lambda_2^L \text{---} \\ | \\ \text{---} V_2 \text{---} \end{array} = \begin{array}{c} \text{---} V_2 \text{---} \\ | \\ \text{---} \Lambda_2^L \text{---} \\ | \\ \text{---} V_2 \text{---} \end{array}$

7: $[R_{1,2}, \Xi_1^R, \mathbb{1}_{D_2^R}] = \text{normalizeUmeps}(A_{1,2}^R, \text{‘right’}) \quad \triangleright \text{Algorithm 1.1}$

8: $\begin{array}{c} \text{---} R_{1,2} \text{---} \\ \text{---} \end{array} \stackrel{(SVD)}{=} \begin{array}{c} U_1 \\ \text{---} \end{array} \text{---} \Sigma_{1,2} \text{---} \begin{array}{c} V_2 \\ \text{---} \end{array}$ ▷ Eq. (2.25)

9: $\begin{array}{c} \text{---} R_1 \text{---} \\ \text{---} \end{array} = \begin{array}{c} U_1 \\ \text{---} \end{array} \text{---} \Sigma_{1,2} \text{---}$

10: $\begin{array}{c} \text{---} R_2 \text{---} \\ \text{---} \end{array} = \begin{array}{c} V_2 \\ \text{---} \end{array}$

11: $\Xi_2^R \leftarrow \Sigma_{1,2} \Omega \Sigma_{1,2}, \Omega = \begin{array}{c} U_1 \\ \text{---} \\ U_1 \\ \text{---} \end{array}$

12: $\Theta_1 = \begin{array}{c} \mathbb{1}_{D_1^L} \\ \text{---} \end{array} \begin{array}{c} L_1 \\ \text{---} \\ L_1 \\ \text{---} \end{array} \begin{array}{c} o_{1,2}^L \\ \text{---} \end{array} \begin{array}{c} L_2 \\ \text{---} \\ L_2 \\ \text{---} \end{array} \begin{array}{c} (1 - \mathbb{E}_{L_{1,2}}^{L_{1,2}})^+ \\ \text{---} \end{array}$ ▷ algorithm 1.3.

13: $\Theta_2 = \begin{array}{c} \mathbb{1}_{D_2^L} \\ \text{---} \end{array} \begin{array}{c} L_2 \\ \text{---} \\ L_2 \\ \text{---} \end{array} \begin{array}{c} o_{2,3}^L \\ \text{---} \end{array} \begin{array}{c} L_1 \\ \text{---} \\ L_1 \\ \text{---} \end{array} \begin{array}{c} (1 - \mathbb{E}_{L_{2,1}}^{L_{2,1}})^+ \\ \text{---} \end{array}$ ▷ algorithm 1.3.

14: $L_0 = \Theta_1 + \Theta_2$

15: $\Theta_1 = \begin{array}{c} (1 - \mathbb{E}_{R_{1,2}}^{R_{1,2}})^+ \\ \text{---} \end{array} \begin{array}{c} R_1 \\ \text{---} \\ R_1 \\ \text{---} \end{array} \begin{array}{c} o_{1,2}^R \\ \text{---} \end{array} \begin{array}{c} R_2 \\ \text{---} \\ R_2 \\ \text{---} \end{array} \begin{array}{c} \mathbb{1}_{D_1^R} \\ \text{---} \end{array}$ ▷ algorithm 1.2.

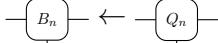
16: $\Theta_2 = \begin{array}{c} (1 - \mathbb{E}_{R_{2,1}}^{R_{2,1}})^+ \\ \text{---} \end{array} \begin{array}{c} R_2 \\ \text{---} \\ R_2 \\ \text{---} \end{array} \begin{array}{c} o_{2,3}^R \\ \text{---} \end{array} \begin{array}{c} R_1 \\ \text{---} \\ R_1 \\ \text{---} \end{array} \begin{array}{c} \mathbb{1}_{D_2^R} \\ \text{---} \end{array}$ ▷ algorithm 1.2.


17: $K_0 = \Theta_1 + \Theta_2$

18: **for** $n = M : -1 : 2$ **do**

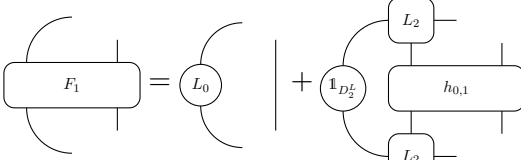
19: $\begin{array}{c} \text{---} B_n \text{---} \\ \text{---} \end{array} \stackrel{(RQ)}{=} \begin{array}{c} M_n \\ \text{---} \end{array} \text{---} Q_n \text{---}$

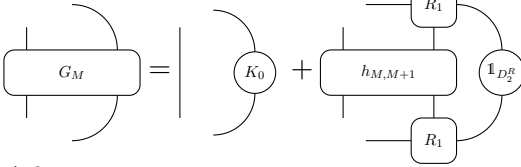
20:
$$M_n \leftarrow M_n / \text{tr}(M_n M_n^\dagger)$$

21: 

22: 

 23: **end for**

24: 

25: 

26:
$$\Delta \mathcal{E} = 1$$

 27: **while** $\Delta \mathcal{E} > \epsilon$ **do**

28:
$$[B, \Sigma, \mathcal{E}_1] = \text{SweepLeft2Right}(B, F_1, G_N)$$

29:
$$[B, \Sigma, \mathcal{E}_2] = \text{SweepRight2Left}(B, F_1, G_N)$$

30:
$$\Delta \mathcal{E} = |\mathcal{E}_2 - \mathcal{E}_1|$$

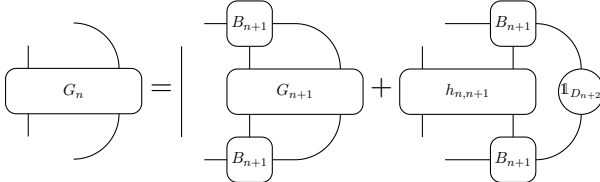
 31: **end while**

32:
$$\mathcal{E}_0 = \mathcal{E}_2$$

 33: **end function**

 34: **function** $[A, \Sigma, \mathcal{E}] = \text{SWEEPLEFT2RIGHT}(B, F_1, G_N)$

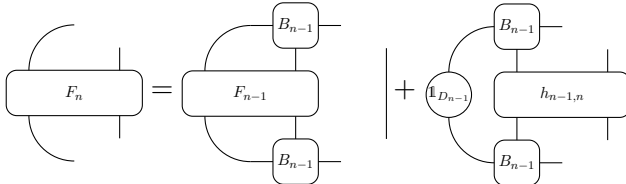
 35: **for** $n = M - 1 : -1 : 1$ **do**

36: 

 37: **end for**

 38: **for** $n = 1 : M$ **do**

 39: **if** $n > 1$ **then**

40: 

 41: **end if**

42:
$$[B_n, \mathcal{E}] = \text{eigs}(@ (B_n) \text{HeffDMRG}(B_n, F_n, G_n))$$

```

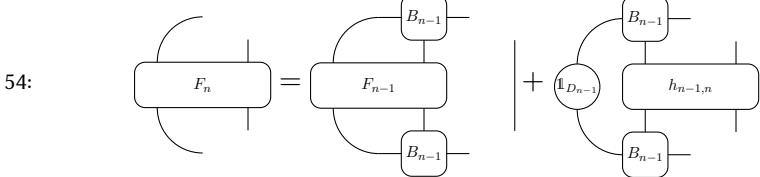
43: 
44:  $M_n \leftarrow M_n / \text{tr}(M_n M_n^\dagger)$ 
45:  $\Sigma_n \leftarrow$  singular values of  $M_n$ 
46: if  $n < M$  then
47: 
48: 
49: end if
50: end for
51: end function

```

```

52: function  $[B, \Sigma, \mathcal{E}] = \text{SWEEP\_RIGHT2LEFT}(B, F_1, G_N)$ 
53: for  $n = 2 : M$  do

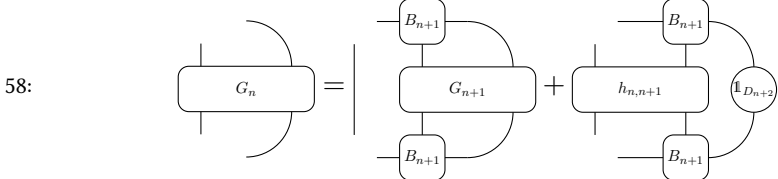
```



```

55: end for
56: for  $n = M : -1 : 1$  do
57: if  $n < M$  then

```



```

59: end if
60:  $[B_n, \mathcal{E}] = \text{eigs}(@(\text{HeffDMRG})(B_n, F_n, G_n))$ 

```

```

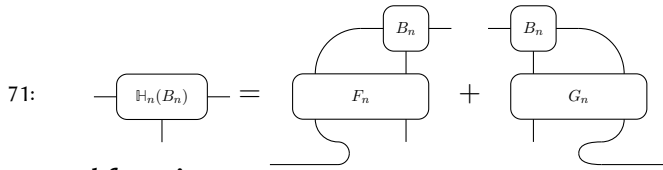
61: 
62:  $M_n \leftarrow M_n / \text{tr}(M_n M_n^\dagger)$ 
63:  $\Sigma_{n-1} \leftarrow$  singular values of  $M_n$ 
64: if  $n > 1$  then
65: 
66: 
67: end if
68: end for

```

```

69: end function
70: function  $\mathbb{H}_n(B_n) = \text{HEFFDMRG}(B_n, F_n, G_n)$ 

```



72: **end function**

Matrix product states for the Schwinger model

3.1. Hilbert space and gauge invariance

We briefly recall the lattice formulation of the Schwinger model. A more extended discussion can be found in subsection 1.3.2 of part I. In the Kogut-Susskind formulation [68] the eigenvectors $\{|s_n\rangle_n : s_n \in \{-1, 1\}\}$ of $\sigma_z(n)$ will form the basis of the local Hilbert space at site n for our computations:

$$\begin{aligned} \sigma_z(n) |s\rangle_n &= s |s\rangle_n, \quad s = -1, 1; \\ \sigma^-(n) |-1\rangle_n &= \sigma^+(n) |1\rangle_n = 0, \quad \sigma^-(n) |1\rangle_n = |-1\rangle_n, \quad \sigma^+(n) |-1\rangle_n = |1\rangle_n. \end{aligned}$$

On the links between the sites, we put the gauge field $\theta(n) = agA_1(na)$ and the electric field $E(n) \leftarrow E(na)$, with a the lattice spacing, g the coupling constant and $[\theta(n), E(m)] = ig\delta_{n,m}$. The commutation relation determines the spectrum of $E(n)$ up to a constant: $E(n)/g = L(n) + \alpha(n)$, where $L(n)$ is the angular operator which has an integer spectrum and $\alpha(n) \in \mathbb{R}$ corresponds to the background electric field at link $[n]$. Therefore, at link $[n]$ a basis is $\{|p_n\rangle_{[n]} : p_n \in \mathbb{Z}\}$ with

$$L(n) |p\rangle_{[n]} = p |p\rangle_{[n]} \quad \text{and} \quad e^{\pm i\theta(n)} |p\rangle_{[n]} = |p \pm 1\rangle_{[n]} \quad (p \in \mathbb{Z}).$$

The Kogut-Susskind Hamiltonian [7] defined on $2N$ sites reads now, see eq. (1.5) in part I,

$$\begin{aligned} \mathcal{H} = \frac{g}{2\sqrt{x}} \left(\sum_{n=1}^{2N} [L(n) + \alpha(n)]^2 + \frac{\sqrt{x}}{g} m \sum_{n=1}^{2N} (-1)^n (\sigma_z(n) + (-1)^n) \right. \\ \left. + x \sum_{n=1}^{2N-1} (\sigma^+(n) e^{i\theta(n)} \sigma^-(n+1) + h.c.) \right), \quad (3.1) \end{aligned}$$

where m is the fermion mass and $x = 1/(g^2 a^2)$ is the inverse lattice spacing squared in units $g = 1$.

In our formalism we block site n and link $[n]$ into one effective site n . Writing $\kappa_n = (s_n, p_n)$ we introduce the multi-index

$$\boldsymbol{\kappa} = ((s_1, p_1), (s_2, p_2), \dots, (s_{2N}, p_{2N})) = (\kappa_1, \dots, \kappa_{2N}).$$

With these notations we have that the effective site n is spanned by $\{|\kappa_n\rangle_n\}$. Therefore the Hilbert space \mathcal{H} of the full system of $2N$ sites and $2N$ links, which is the tensor product of the local Hilbert spaces, has basis $\{|\boldsymbol{\kappa}\rangle = |\kappa_1\rangle_1 \dots |\kappa_{2N}\rangle_{2N}\}$ and a general state $|\Psi\rangle$ is thus a linear combination of these $|\boldsymbol{\kappa}\rangle$:

$$|\Psi\rangle = \sum_{\boldsymbol{\kappa}} C^{\kappa_1, \dots, \kappa_{2N}} |\boldsymbol{\kappa}\rangle$$

with basis coefficients $C^{\kappa_1, \dots, \kappa_{2N}} \in \mathbb{C}$.

Because QED is a gauge theory we have to restrict to \mathcal{H}_{phys} , the set of all gauge invariant states that satisfy $G(n)|\Psi\rangle = 0, \forall n = 1, \dots, 2N$, where

$$G(n) = L(n) - L(n-1) + \frac{\sigma_z(n) + (-1)^n}{2},$$

see eq. (1.4) of part I.

3.2. Gauge invariant MPS with open boundary conditions

Every state in \mathcal{H} can be written as a MPS with open boundary conditions [76]

$$|\Psi[B, C]\rangle = \left[\begin{array}{ccccccc} B_1 & C_1 & \dots & B_n & C_n & \dots & B_{2N} & C_{2N} \\ \downarrow & \downarrow & & \downarrow & \downarrow & & \downarrow & \downarrow \\ s_1 & p_1 & & s_n & p_n & & s_{2N} & p_{2N} \end{array} \right], \quad (3.2)$$

with $B_n^{s_n} \in \mathbb{C}^{D_n \times D'_n}$, $C_n^{p_n} \in \mathbb{C}^{D'_n \times D_{n+1}}$, $s_n \in \{-1, 1\}$, $p_n \in \mathbb{Z}$ and $D_1 = D'_{2N+1} = 1$, and where B_n and C_n are in the right canonical form:

$$\begin{array}{c} \begin{array}{c} \text{---} B_n \text{---} \\ | \\ \text{---} B_n \text{---} \\ | \\ \text{---} \mathbb{1}_{D'_n} \text{---} \end{array} = \begin{array}{c} \text{---} \mathbb{1}_{D_n} \text{---} \\ \text{---} \end{array} \text{ and } \begin{array}{c} \text{---} B_n \text{---} \\ | \\ \text{---} B_n \text{---} \\ | \\ \text{---} \mathbb{1}_{D_{n+1}} \text{---} \end{array} = \begin{array}{c} \text{---} \mathbb{1}_{D_n} \text{---} \\ \text{---} \end{array} \end{array} \quad (3.3)$$

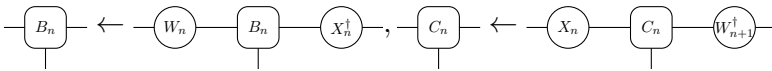
that $C_{2N}^s = V_{2N} \tilde{C}_{2N}^s$ which implies that $V_{2N} V_{2N}^\dagger = \mathbb{1}_{D'_{2N}}$. Using this, $\tilde{B}_{2N}^p = U_{2N}^{-1} B_{2N}^p V_{2N}^p$ and the fact that B_{2N}^p and \tilde{B}_{2N}^p obey eq. (3.3) it follows that $U_{2N} U_{2N}^\dagger = \mathbb{1}_{D_{2N}}$. Proceeding in the same way from $k = 2N$ till $k = 1$ one finds that all the matrices U_k and V_k are unitary.

Now we will prove that $U_k = \mathbb{1}_{D_k}, V_k = \mathbb{1}_{D'_k}$ for $k \neq n$. If $k < n$ we can assume that $n > 1$. Note that $U_1 = 1$ and that $B_1^s = \tilde{B}_1^s = B_1^s V_1$. Using eq. (3.4) it follows that $V_1 = (\Xi_1^C)^{-1} \sum_s B_1^{s\dagger} \Xi_1^B B_1^s = \mathbb{1}_{D'_1}$. Assume now $V_{k-1} = \mathbb{1}_{D'_{k-1}}$ ($k < n - 1$) then $C_{k-1}^p = \tilde{C}_{k-1}^p = C_{k-1}^p U_k$, which implies $U_k = (\Xi_k^B)^{-1} \sum_p C_{k-1}^p \dagger \Xi_{k-1}^C C_{k-1}^p = \mathbb{1}_{D_k}$, i.e. $V_{k-1} = \mathbb{1}_{D'_{k-1}}$ implies that $U_k = \mathbb{1}_{D_k}$ for $k < n - 1$. In a similar way, one proves that $U_k = \mathbb{1}_{D_k}$ implies $V_k = \mathbb{1}_{D'_k}$ ($k < n$). This concludes the case $k < n$. For $k > n$ one starts from $\tilde{C}_{2N}^p = C_{2N}^p = V_{2N} C_{2N}^p$. From eq. (3.3), we obtain that $V_{2N} = \mathbb{1}_{D'_{2N}}$. As a consequence $\tilde{B}_{2N-1}^s = B_{2N-1}^s = U_{2N} B_{2N}^s$ holds. By eq. (3.3) it follows that $U_{2N} = \mathbb{1}_{D_{2N}}$. One can now repeat this reasoning and find that $U_k = \mathbb{1}_{D_k}, V_k = \mathbb{1}_{D'_k}$ for all $k > n$.

Hence, the MPS eq. (3.2) is gauge invariant iff for every $n = 1, \dots, 2N$ there exist unitary matrices U_n and V_n (depending on $\varphi(n)$) such that

$$U_n^\dagger B_n^s V_n = e^{-i\varphi(n)[\frac{s+(-1)^n}{2}]} B_n^s, \\ C_{n-1}^p U_n = e^{-i\varphi_n p} C_{n-1}^p (n > 1), V_n^\dagger C_n^p = e^{i\varphi_n p} C_n^p. \quad (3.7)$$

Let us now choose $\varphi(n) = 1$, then the matrices U_n and V_n do not depend on $\varphi(n)$ anymore. The unitary matrices can be diagonalized (as exponential of a Hermitian matrix): $U_n = W_n^\dagger \Delta_{U_n} W_n$, $V_n = X_n^\dagger \Delta_{V_n} X_n$, where W_n, X_n are unitary matrices and Δ_{U_n} and Δ_{V_n} are diagonal matrices where all the diagonal elements have modulus one. If we perform the following MPS gauge transformation:



($W_1 = W_{2N+1} = 1$), the MPS eq. (3.2) is unaffected and the conditions eq. (3.7) now read

$$\Delta_{U_n}^\dagger B_n^s \Delta_{V_n} = e^{-i(s+(-1)^n)/2} B_n^s, \\ C_{n-1}^p \Delta_{U_n} = e^{-ip} C_{n-1}^p (n > 1), \Delta_{V_n}^\dagger C_n^p = e^{ip} C_n^p. \quad (3.8)$$

The property eq. (3.3) will also hold for the ‘new’ B and C , however the property eq. (3.4) is modified in the sense that Ξ_n^B and Ξ_n^C are not diagonal anymore, but they are still positive definite. As already mentioned, the

entries of the diagonal matrices Δ_{U_n} and Δ_{V_n} are complex phase factors. Let $e^{-i\lambda_{n,j}}$, $j = 1, \dots, n_{U_n}$, respectively $e^{-i\mu_{n,j}}$, $j = 1, \dots, n_{V_n}$ be the eigenvalues of Δ_{U_n} with multiplicity $m(\lambda_{n,j})$ respectively of Δ_{V_n} with multiplicity $m(\mu_{n,j})$,

$$\Delta_{U_n} = \sum_{j=1}^{n_{U_n}} \sum_{\alpha_j=1}^{m(\lambda_{n,j})} e^{-i\lambda_{n,j}} |\lambda_{n,j}, \alpha_j\rangle \langle \lambda_{n,j}, \alpha_j| \quad (3.9a)$$

$$\Delta_{V_n} = \sum_{j=1}^{n_{V_n}} \sum_{\alpha_j=1}^{m(\mu_{n,j})} e^{-i\mu_{n,j}} |\mu_{n,j}, \alpha_j\rangle \langle \mu_{n,j}, \alpha_j| \quad (3.9b)$$

then we can write B and C as

$$B_n^s = \sum_{j=1}^{n_{U_n}} \sum_{k=1}^{n_{V_n}} \sum_{\alpha_j=1}^{m(\lambda_{n,j})} \sum_{\beta_k=1}^{m(\mu_{n,k})} [B_n^s]_{(\lambda_{n,j}, \alpha_j); (\mu_{n,k}, \beta_k)} |\lambda_{n,j}, \alpha_j\rangle \langle \mu_{n,k}, \beta_k| \quad (3.10a)$$

for $n > 1$,

$$C_n^p = \sum_{j=1}^{n_{V_n}} \sum_{k=1}^{n_{U_{l+1}}} \sum_{\alpha_j=1}^{m(\mu_{n,j})} \sum_{\beta_k=1}^{m(\lambda_{l+1,k})} [C_n^p]_{(\mu_{n,j}, \alpha_j); (\lambda_{n+1,k}, \beta_k)} |\mu_{n,j}, \alpha_j\rangle \langle \lambda_{n+1,k}, \beta_k|, \quad (3.10b)$$

for $n < 2N$, whereas

$$B_1^s = \sum_{k=1}^{n_{V_1}} \sum_{\beta_k=1}^{m(\mu_{1,k})} [B_1^s]_{1; (\mu_{1,k}, \beta_k)} \langle \mu_{1,k}, \beta_k|, \quad (3.10c)$$

$$C_{2N}^p = \sum_{j=1}^{n_{V_{2N}}} \sum_{\alpha_j=1}^{m(\mu_{2N,j})} [C_{2N}^p]_{(\mu_{2N,j}, \alpha_j); 1} |\mu_{2N,j}, \alpha_j\rangle. \quad (3.10d)$$

Using eq. (3.8) it follows that

$$\begin{aligned} (e^{-i(p-\lambda_{l+1,k})} - 1)[C_n^p]_{(\mu_{n,j}, \alpha_j); (\lambda_{n+1,k}, \beta_k)} &= 0 \\ (e^{-i(p-\mu_{n,j})} - 1)[C_n^p]_{(\mu_{n,j}, \alpha_j); (\lambda_{n+1,k}, \beta_k)} &= 0, \\ (e^{-i(p-\mu_{2N,j})} - 1)[C_{2N}^p]_{(\mu_{2N,j}, \alpha_j); 1} &= 0, \end{aligned}$$

hence

$$[C_n^p]_{(\mu_{n,j}, \alpha_j); (\lambda_{n+1,k}, \beta_k)} = \delta_{p, \mu_{n,j}} \delta_{p, \lambda_{n+1,k}} [c_n^p]_{\alpha_j, \beta_k}, \quad (3.11a)$$

$$[C_{2N}^p]_{(\mu_{2N,j}, \alpha_j); 1} = \delta_{p, \mu_{2N,j}} [c_{2N}^p]_{\alpha_j, 1}, \quad (3.11b)$$

Note that $\lambda_{n,j}$ and $\mu_{n,j}$ are only unique up to a multiple of 2π . By writing $\delta_{p,\mu_{n,j}}$ we mean that we must take $\mu_{n,j}$ equal to p modulo 2π .

Assume now that there would exist a λ_{n+1,k_0} ($n < 2N$) with $\lambda_{n+1,k_0} \neq p$, $\forall p \in \mathbb{Z}$. Then it follows by eq. (3.11) that

$$[C_n^p]_{(\mu_{n,j}, \alpha_j); (\lambda_{n+1,k_0}, \beta_{k_0})} = 0,$$

$\forall p \in \mathbb{Z}, \forall j = 1, \dots, n_{v_n}, \forall \alpha_j = 1, \dots, m(\mu_{n,j})$. If we now consider the non-singular matrix Ξ_n^C , see eq. (3.4), then

$$\left(\sum_{p \in \mathbb{Z}} (C_n^p)^\dagger \Xi_n^C C_l^p \right)_{(\lambda_{n+1,k_0}, \alpha_{k_0}), (\lambda_{n+1,k}, \beta_k)} = 0,$$

$\forall \alpha_{k_0} = 1, \dots, m(\lambda_{n,k_0}), \forall k = 1, \dots, n_{u_{n+1}}, \forall \beta_k = 1, \dots, m(\lambda_{\lambda_{n+1,k}})$. By eq. (3.4) this would mean that Ξ_{n+1}^B has a zero-row and would be singular which is a contradiction because Ξ_{n+1}^B is positive definite. As a consequence all the $\lambda_{n,k}$ are integers. In the same way, but now by using the condition eq. (3.3) one proves that all the $\mu_{n,j}$ are integers.

We can thus write eq. (3.9) as

$$\Delta_{U_n} = \sum_{q \in \mathbb{Z}} \sum_{\alpha_q=1}^{D_n^q} e^{-iq} |q, \alpha_q\rangle \{q, \alpha_q\}, \quad (3.12a)$$

$$\Delta_{V_n} = \sum_{q \in \mathbb{Z}} \sum_{\alpha_q=1}^{D'_n{}^q} e^{-iq} |q, \alpha_q\rangle \{q, \alpha_q\}, \quad (3.12b)$$

and expand B and C :

$$\begin{aligned} B_n^s &= \sum_{q,r \in \mathbb{Z}} \sum_{\alpha_q=1}^{D_n^q} \sum_{\beta_r=1}^{D'_n{}^q} [B_n^s]_{(q,\alpha_q);(r,\beta_r)} |q, \alpha_q\rangle \{r, \beta_r\}, \\ C_n^p &= \sum_{q,r \in \mathbb{Z}} \sum_{\alpha_q=1}^{D'_n{}^q} \sum_{\beta_r=1}^{D_{n+1}^r} [C_n^p]_{(q,\alpha_q);(r,\beta_r)} |q, \alpha_q\rangle \{r, \beta_r\}, \\ B_1^s &= \sum_{r \in \mathbb{Z}} \sum_{\beta_r=1}^{D'_n{}^r} [\bar{B}_1^s]_{1;(r,\beta_r)} \{r, \beta_r\}, \\ C_{2N}^p &= \sum_{q \in \mathbb{Z}} \sum_{\alpha_q=1}^{D'_{2N}{}^q} [\bar{C}_{2N}^p]_{(q,\alpha_q);1} |q, \alpha_q\rangle \end{aligned}$$

where D_n^q respectively $D_n'^q$ denotes the multiplicity of the eigenvalue q in the matrix U_n respectively V_n . Note that $D_n = \sum_q D_n^q$ and $D_n' = \sum_q D_n'^q$. We have already proven, see eq. (3.11), that

$$[C_n^p]_{(q,\alpha_q);(r,\beta_r)} = \delta_{q,p}\delta_{q,r}[c_n^p]_{\alpha_q,\beta_r}, [C_n^p]_{(q,\alpha_q);1} = \delta_{q,p}[c_n^p]_{\alpha_q,1}, \quad (3.13a)$$

where $c_n^p \in \mathbb{C}^{D_n^p \times D_{n+1}^p}$. Finally, if we substitute eq. (3.12) in eq. (3.10a), we obtain

$$(e^{-i[(s+(-1)^n)/2+q-r]} - 1)[B_n^s]_{(q,\alpha_q);(r,\beta_r)} = 0, (n > 1), \\ (e^{-i[(s-1)/2-r]} - 1)[\tilde{B}_n^s]_{1;(r,\beta_r)} = 0$$

implying that

$$[B_n^s]_{(q,\alpha_q);(r,\beta_r)} = \delta_{r,q+(s+(-1)^n)/2}[b_n^{q,s}]_{\alpha_q,\beta_r} (n > 1), \\ [B_1^s]_{1;(r,\beta_r)} = \delta_{r,(s-1)/2}[b_1^{q=0,s}]_{1,\beta_r} \quad (3.13b)$$

where $b_n^{q,s} \in \mathbb{C}^{D_n^q \times D_n^{q+(s+(-1)^n)/2}}$ is random.

We have now proven that every MPS that is invariant under local gauge transformations with $\varphi(n) = 1$ can be brought in the form eq. (3.13) by a MPS gauge transformation. A state in this form is also invariant under any gauge transformation. Indeed, according to eq. (3.8), we need to find unitary matrices U_n and V_n such that

$$e^{-i\varphi(n)p}C_{n-1}^p = \tilde{C}_{n-1}^p U_n, e^{i\varphi(n)p}C_n^p = V_n^\dagger C_n^p, \\ e^{-i\varphi(n)(s+(-1)^n)/2}\tilde{B}_n^s = U_n^\dagger B_n^s V_n,$$

where B and C take the form of eq. (3.13). The choice

$$[U_n]_{(q,\alpha_q);(r,\beta_r)} = \delta_{q,r}\delta_{\alpha_q,\beta_r}e^{-i\varphi(n)q}, [V_n]_{(q,\alpha_q);(r,\beta_r)} = \delta_{q,r}\delta_{\alpha_q,\beta_r}e^{-i\varphi(n)q},$$

solves this problem. This proves that every gauge invariant state can be brought in the form eq. (3.13) by a MPS-gauge transformation and, conversely, that every MPS in the form eq. (3.13) is gauge invariant.

3.3. Gauge invariant MPS in the thermodynamic limit

In the previous subsection we have constructed the most general MPS for open boundary conditions that are gauge invariant. For our simulations we will block site n and link $[n]$ into one effective site. The local Hilbert space on the effective site n is then spanned by the set

$$\{|\kappa_n\rangle = |s_n, p_n\rangle_n : (s_n, p_n) \in \{-1, 1\} \times \mathbb{Z}\}.$$

In terms of the MPS representation (3.2) this means that we define

$$[A_n^\kappa]_{\alpha,\beta} = [A_n^{s,p}]_{\alpha,\beta} = \alpha \text{---} \begin{array}{c} \text{---} A_n \text{---} \\ | \quad | \\ s \quad p \end{array} \text{---} \beta = \alpha \text{---} \begin{array}{c} \text{---} B_n \text{---} \\ | \\ s \end{array} \text{---} \begin{array}{c} \text{---} C_n \text{---} \\ | \\ p \end{array} \text{---} \beta = [B_n^s C_n^p]_{\alpha,\beta}$$

and the MPS ansatz then reads

$$|\Psi[A]\rangle = \begin{array}{c} \text{---} A_1 \text{---} \\ | \quad | \\ s_1 \quad p_1 \end{array} \text{---} \cdots \text{---} \begin{array}{c} \text{---} A_n \text{---} \\ | \quad | \\ s_n \quad p_n \end{array} \text{---} \cdots \text{---} \begin{array}{c} \text{---} A_{2N} \text{---} \\ | \quad | \\ s_{2N} \quad p_{2N} \end{array} \text{---}$$

From (3.13) it follows that this MPS is gauge invariant if and only if A_n can be brought in the form

$$(q, \alpha_q) \text{---} \begin{array}{c} \text{---} A_n \text{---} \\ | \quad | \\ s \quad p \end{array} \text{---} (r, \beta_r) = [a_n^{q,s}]_{\alpha_q, \beta_r} \delta_{p, q+(s+(-1)^n)/2} \delta_{r,p} \quad (3.14)$$

where $a_n^{q,s} \in \mathbb{C}^{D_n^q \times D_{n+1}^r}$.

The interpretation is that q labels the eigenvalues of $L(n-1)$ while r labels the eigenvalues of $L(n)$, which is reflected in the last Kronecker-delta that identifies the physical index p with the virtual index r . The first Kronecker-delta is then equivalent with Gauss' law $G(n) = 0$. The virtual indices α_q and β_r give the state $|\Psi[A]\rangle$ some additional variational freedom. Note that we have chosen to label the matrices $a_n^{q,s}$ by the virtual index q but equivalently one could also label it by the physical index p . This is only a choice of convention. The multiple-index structure of the tensors A_n implies that the Schmidt decomposition eq. (1.5) with respect to the bipartition $\{\mathcal{A}_1^n = \mathbb{Z}[1, \dots, n], \mathcal{A}_2^n = \mathbb{Z}[n+1, 2N]\}$ of the lattice reads

$$|\Psi[A]\rangle = \sum_{q \in \mathbb{Z}} \sum_{\alpha_q=1}^{D_{n+1}^q} \sqrt{\sigma_{n,\alpha_q}^q} \left| \Phi_{q,\alpha_q}^{\mathcal{A}_1^n} \right\rangle \otimes \left| \Phi_{q,\alpha_q}^{\mathcal{A}_2^n} \right\rangle$$

where

$$1 \geq \sigma_{n,1}^q \geq \sigma_{n,2}^q \geq \dots \geq \sigma_{n,D_{n+1}^q}^q \geq 0, \quad \sum_{q \in \mathbb{Z}} \sum_{\alpha_q=1}^{D_{n+1}^q} \sigma_{n,\alpha_q}^q = 1$$

and

$$\left| \Phi_{q,\alpha_q}^{\mathcal{A}_1^n} \right\rangle \in \bigotimes_{j \in \mathcal{A}_1^n} \mathcal{H}_j \quad \text{and} \quad \left| \Phi_{q,\alpha_q}^{\mathcal{A}_2^n} \right\rangle \in \bigotimes_{j \in \mathcal{A}_2^n} \mathcal{H}_j$$

are orthonormal unit vectors,

$$\left\langle \Phi_{q,\alpha_q}^{\mathcal{A}_1^n} \left| \Phi_{r,\beta_r}^{\mathcal{A}_1^n} \right. \right\rangle = \delta_{q,r} \delta_{\alpha_q, \beta_r}, \quad \left\langle \Phi_{q,\alpha}^{\mathcal{A}_2^n} \left| \Phi_{r,\beta_r}^{\mathcal{A}_2^n} \right. \right\rangle = \delta_{q,r} \delta_{\alpha_q, \beta_r}.$$

For our numerical scheme we can only retain a finite number of eigenvalues p of $L(n)$, say $p_{n+1}^{\min} \leq p \leq p_{n+1}^{\max}$ for some integers p_{n+1}^{\min} and p_{n+1}^{\max} . This implies that we set $D_{n+1}^q = 0$ for $q \notin \mathbb{Z}[p_{n+1}^{\min}, p_{n+1}^{\max}]$. In particular, the Schmidt decomposition now becomes

$$|\Psi[A]\rangle = \sum_{q=p_{n+1}^{\min}}^{p_{n+1}^{\max}} \sum_{\alpha_q=1}^{D_{n+1}^q} \sqrt{\sigma_{n,\alpha_q}^q} \left| \Phi_{q,\alpha_q}^{\mathcal{A}_1^n} \right\rangle \otimes \left| \Phi_{q,\alpha_q}^{\mathcal{A}_2^n} \right\rangle$$

and it is clear that any state can be approximated faithfully if we take p_n^{\min} , p_n^{\max} and D_{n+1}^q large enough. The power of this approach is of course that for our studies we can take these parameters relatively small and still have a very good approximation. We will not always explicitly denote the truncation in the eigenvalues of $L(n)$. In particular we write $q \in \mathbb{Z}$ instead of $q \in \mathbb{Z}[p_{n+1}^{\min}, p_{n+1}^{\max}]$ but one has to keep in mind that for our numerical simulations we consider a finite range of eigenvalues of $L(n)$, i.e. when $q \notin \mathbb{Z}[p_{n+1}^{\min}, p_{n+1}^{\max}]$ or $q + (s + (-1)^n)/2 \notin \mathbb{Z}[p_{n+1}^{\min}, p_{n+1}^{\max}]$ we put by definition $a_n^{q,s} = 0$. One also define $a_n^{q,s} = a^q \bmod p_{n+1}^{max,s}$ where $q \bmod p_{n+1}^{max} \in \mathbb{Z}[p_{n+1}^{\min}, p_{n+1}^{\max}]$.

For our applications we are interested in the thermodynamic limit $N \rightarrow +\infty$. Physically this means that we only want to consider the bulk properties of our system. As we already discussed in chapter 1, the MPS formalism allows to perform the computations directly in the thermodynamic limit, thereby bypassing any finite size effects. This also has the advantage that we can take into account translation symmetry. In the following subsections we discuss some special types of MPS in the thermodynamic limit and make them gauge invariant.

3.3.1. Translation invariance over two sites

In the thermodynamic limit ($N \rightarrow +\infty$) and when the electric background field $\alpha(n)$ is independent of n , i.e. $\alpha(n) = \alpha$, the Hamiltonian (3.1) is invariant under \mathcal{T}^2 , i.e. translation invariant over two sites. For the Schwinger model this symmetry is not spontaneously broken and the ground state has the same symmetry. As an ansatz for the ground state we can choose the A_n to depend only on the parity of n :

$$A_{2n-1}^\kappa = A_1^\kappa, A_{2n}^\kappa = A_2^\kappa, \forall n = 1, \dots, N.$$

We then arrive at the MPS eq. (2.22):

$$|\Psi_u[A_1 A_2]\rangle = \begin{array}{c} \textcircled{v_L^\dagger} \text{---} \textcircled{A_1} \text{---} \textcircled{A_2} \text{---} \dots \text{---} \textcircled{A_1} \text{---} \textcircled{A_2} \text{---} \dots \text{---} \textcircled{A_1} \text{---} \textcircled{A_2} \text{---} \textcircled{v_R} \\ \kappa_1 \quad \kappa_2 \quad \quad \quad \kappa_{2n-1} \quad \kappa_{2n} \quad \quad \quad \kappa_{2N-1} \quad \kappa_{2N} \end{array} \quad (3.15a)$$

$(N \rightarrow +\infty)$ with $\kappa_n = (s_n, p_n) \in \{-1, 1\} \times \mathbb{Z}$,

$$\begin{array}{c} (q, \alpha_q) \text{---} \boxed{A_n} \text{---} (r, \beta_r) \\ \text{---} \downarrow \text{---} \\ (s, p) \end{array} = [a_n^{q,s}]_{\alpha_q, \beta_r} \delta_{r, q+(s+(-1)^n)/2} \delta_{r,p}. \quad (3.15b)$$

where $a_1^{q,s} \in \mathbb{C}^{D_1^q \times D_2^r}$ and $a_2^{q,s} \in \mathbb{C}^{D_2^q \times D_1^r}$. In the thermodynamic limit all our computations are independent of the boundary vectors v_R and v_L . This form will be useful when using the iTEBD algorithm for performing real-time evolution, see subsection 4.3.1.

When we want to apply the TDVP to find the optimal approximation for the ground state it is convenient to block the effective sites $2n - 1$ and $2n$ into one effective site. More specifically, we define

$$\begin{aligned} [A^\zeta]_{(q, \alpha_q), (r, \beta_r)} &= [A^{\kappa_1, \kappa_2}]_{(q, \alpha_q), (r, \beta_r)} = \begin{array}{c} (q, \alpha_q) \text{---} \boxed{A} \text{---} (r, \beta_r) \\ \text{---} \downarrow \quad \downarrow \text{---} \\ \kappa_1 \quad \kappa_2 \end{array} \\ &= \begin{array}{c} (q, \alpha_q) \text{---} \boxed{A_1} \text{---} \boxed{A_2} \text{---} (r, \beta_r) \\ \text{---} \downarrow \quad \downarrow \text{---} \\ \kappa_1 \quad \kappa_2 \end{array} = [A_1^{\kappa_1} A_2^{\kappa_2}]_{(q, \alpha_q), (r, \beta_r)} \end{aligned}$$

where $\zeta = (\kappa_1, \kappa_2) = (s_1, p_1, s_2, p_2) \in \{-1, 1\} \times \mathbb{Z} \times \{-1, 1\} \times \mathbb{Z}$. The uMPS ansatz then has the form

$$|\Psi_u[A]\rangle = \begin{array}{c} \textcircled{v_L^\dagger} \text{---} \boxed{A} \text{---} \boxed{A} \text{---} \dots \text{---} \boxed{A} \text{---} \dots \text{---} \boxed{A} \text{---} \boxed{A} \text{---} \textcircled{v_R} \\ \text{---} \downarrow \quad \downarrow \quad \quad \quad \downarrow \quad \quad \quad \downarrow \quad \quad \quad \downarrow \\ \zeta_1 \quad \zeta_2 \quad \quad \quad \zeta_n \quad \quad \quad \zeta_{N-1} \quad \zeta_N \end{array} \quad (3.16a)$$

and gauge invariance is imposed by

$$\begin{aligned} \begin{array}{c} (q, \alpha_q) \text{---} \boxed{A} \text{---} (r, \beta_r) \\ \text{---} \downarrow \text{---} \\ \zeta \end{array} &= \begin{array}{c} (q, \alpha_q) \text{---} \boxed{A} \text{---} (r, \beta_r) \\ \text{---} \downarrow \text{---} \\ (s_1, p_1, s_2, p_2) \end{array} \\ &= [a^{q, s_1, s_2}]_{\alpha_q, \beta_r} \delta_{p_1, q+(s_1-1)/2} \delta_{p_2, q+(s_1+s_2)/2} \delta_{r, p_2}. \quad (3.16b) \end{aligned}$$

with $a^{q, s_1, s_2} \in \mathbb{C}^{D^q \times D^r}$ ($D^q = D_1^q$) as follows from (3.15b).

Once we have a good approximation $|\Psi_u[A]\rangle$ for the ground state we can use the states $|\Phi_k[B, A]\rangle$, eq. (1.16), to approximate the momentum- k excitations ($k \in [-\pi, \pi]$):

$$\begin{aligned} |\Phi_k[B, A]\rangle &= \lim_{N \rightarrow +\infty} \\ \sum_{n=1}^N e^{ikn} &\begin{array}{c} \textcircled{v_L^\dagger} \text{---} \boxed{A} \text{---} \dots \text{---} \boxed{A} \text{---} \boxed{B} \text{---} \boxed{A} \text{---} \dots \text{---} \boxed{A} \text{---} \textcircled{v_R} \\ \text{---} \downarrow \quad \downarrow \quad \quad \quad \downarrow \quad \downarrow \quad \quad \quad \downarrow \quad \downarrow \\ \zeta_1 \quad \zeta_{n-1} \quad \zeta_n \quad \zeta_{n+1} \quad \zeta_N \end{array}, \quad (3.17a) \end{aligned}$$

the projector onto the $(G(n) = 0)$ -subspace, the canonical ensemble is thus described by the density operator $\rho(\beta) = \mathcal{P}e^{-\beta\mathcal{H}} (= \mathcal{P}e^{-\beta\mathcal{H}}\mathcal{P} = e^{-\beta\mathcal{H}}\mathcal{P})$. The ensemble average of a given gauge invariant observable \mathcal{Q} is computed as

$$\langle \mathcal{Q} \rangle_\beta = \frac{\text{tr}(\mathcal{P}\mathcal{Q}\mathcal{P}e^{-\beta\mathcal{H}})}{Z(\beta)} \text{ with } Z(\beta) = \text{tr}(\mathcal{P}e^{-\beta\mathcal{H}})$$

the partition function.

Let us now construct a Matrix Product Operator (MPO) to approximate the Gibbs state $\mathcal{P}e^{-\beta\mathcal{H}}$. Therefore we will use the method discussed in [119]. The main idea is that we purify the MPO ansatz by a MPS in a higher dimensional Hilbert space. Starting from the identity on the $(G(n) = 0)$ -subspace for $\beta = 0$, we obtain the state for finite β by evolving this purification in imaginary time using the iTEBD algorithm, see section 2.3. In addition to [119], we need to take gauge invariance into account when constructing the MPS purification by imposing a block structure similar to eq. (3.14) on the tensors describing the MPS.

On a lattice of $2N$ effective sites we denote the local Hilbert space with \mathcal{H}_n :

$$\mathcal{H}_n = \text{span}\{|\kappa_n\rangle = |s_n, p_n\rangle_n : s_n \in \{-1, 1\}, p_n \in \mathbb{Z}[p_{n+1}^{\min}, p_{n+1}^{\max}]\}.$$

By introducing the multi-index

$$\boldsymbol{\kappa} = ((s_1, p_1), (s_2, p_2), \dots, (s_{2N}, p_{2N})) = (\kappa_1, \dots, \kappa_{2N}).$$

it follows that the Hilbert space of the full system of $2N$ sites and $2N$ links,

$$\mathcal{H} = \bigotimes_{n=1}^{2N} \mathcal{H}_n,$$

has basis

$$\{|\boldsymbol{\kappa}\rangle = |\kappa_1\rangle_1 \dots |\kappa_{2N}\rangle_{2N}\}$$

and a general operator ρ thus takes the form:

$$\rho = \sum_{\boldsymbol{\kappa}, \boldsymbol{\kappa}'} C^{(\kappa_1, \kappa'_1), \dots, (\kappa_{2N}, \kappa'_{2N})} |\boldsymbol{\kappa}\rangle \langle \boldsymbol{\kappa}'|$$

with $C^{(\kappa_1, \kappa'_1), \dots, (\kappa_{2N}, \kappa'_{2N})} \in \mathbb{C}$.

In this basis, the projector \mathcal{P} on the $(G(n) = 0)$ -subspace reads

$$\mathcal{P} = \sum_{\boldsymbol{\kappa}} \left(\prod_{n=1}^{2N} \delta_{p_n - p_{n-1}, \frac{s_n + (-1)^n}{2}} \right) |\boldsymbol{\kappa}\rangle \langle \boldsymbol{\kappa}| \quad (3.21)$$

where we take periodic boundary conditions ($p_0 = p_{2N}$). For $\beta = 0$ we have that $\rho(0) = \mathcal{P}$. We will now write this state as a MPO [119, 120]:

$$\rho(0) = \sum_{\boldsymbol{\kappa}, \boldsymbol{\kappa}'} \text{tr} \left(W_1^{\kappa_1 \kappa'_1} \dots W_{2N}^{\kappa_{2N} \kappa'_{2N}} \right) |\boldsymbol{\kappa}\rangle \langle \boldsymbol{\kappa}'| \quad (3.22)$$

where $W_n^{\kappa_n \kappa'_n} \in \mathbb{C}^{D_n \times D_{n+1}}$ are complex matrices. Thereto we put

$$W_n^{\kappa_1, \kappa_2} = \sum_{\kappa^a} A_n^{\kappa_1, \kappa^a} \otimes \bar{A}_n^{\kappa_2, \kappa^a}$$

with $\kappa^a = (s^a, p^a)$ and $A_n^{(\kappa), (\kappa^a)} = A_n^{(s,p), (s^a, p^a)} \in \mathbb{C}^{D_n \times D_{n+1}}$ complex matrices. In order that $\rho(0) = \mathcal{P}$ we give, similar as in eq. (3.14), the virtual indices (α, β) of $[A_n^{(s,p), (s^a, p^a)}]_{\alpha, \beta}$ a multiple index structure: $\alpha \rightarrow (q, \alpha_q)$, $\beta \rightarrow (r, \beta_r)$ where $q, r \in \mathbb{Z}$ label the eigenvalues of $L(n)$. If we put

$$[A_n^{(s,p), (s^a, p^a)}]_{(q, \alpha); (r, \beta)} = [a_n]_{\alpha_q, \beta_r} \delta_{r, q + [s + (-1)^n]/2} \delta_{p, r} \delta_{s, s^a} \delta_{p^a, q + [s^a + (-1)^n]/2}, \quad (3.23)$$

where $a_n \in \mathbb{C}^{D_n \times D_{n+1}}$ can be any non-zero matrix, then it follows that $\rho(0)$ equals (3.21) up to a normalization factor.

To obtain a purification of the state $\rho(0)$ we need to consider the Hilbert space

$$\mathcal{H}_{full} = \bigotimes_{n=1}^{2N} \mathcal{H}_n \otimes \mathcal{H}_n^a$$

where $\mathcal{H}_n^a = \text{span}\{|\kappa_n^a\rangle_n = |s_n^a\rangle_n |p_n^a\rangle\}$ is an auxiliary Hilbert space with the same dimension as \mathcal{H}_n . Then we introduce the MPS [119]

$$|\Psi[A]\rangle = \sum_{\boldsymbol{\kappa}, \boldsymbol{\kappa}^a} \text{tr} \left(A_1^{\kappa_1, \kappa_1^a} \dots A_{2N}^{\kappa_{2N}, \kappa_{2N}^a} \right) |\boldsymbol{\kappa}, \boldsymbol{\kappa}^a\rangle \in \mathcal{H}_{full},$$

$$|\boldsymbol{\kappa}, \boldsymbol{\kappa}^a\rangle = |\kappa_1\rangle_1 |\kappa_1^a\rangle_1 \dots, |\kappa_{2N}\rangle_{2N} |\kappa_{2N}^a\rangle_{2N},$$

where $A_n^{\kappa_n, \kappa_n^a}$ is defined in (3.23). By contracting the κ_n^a we obtain up to a normalization factor $\rho(0)$:

$$\text{tr}_{\mathcal{H}^a} (|\Psi[A]\rangle \langle \Psi[\bar{A}]|) \propto \rho(0).$$

Because $\rho(0)$ is the projector \mathcal{P} on the ($G(n) = 0$)-subspace, $[\mathcal{H}, \mathcal{P}] = 0$ implies that $\rho(\beta) = \mathcal{P} e^{-\beta \mathcal{H}} = e^{-\beta \mathcal{H}/2} \mathcal{P} e^{-\beta \mathcal{H}/2}$. As a consequence, if we evolve the purification $|\Psi[A(\beta)]\rangle$ according to

$$|\Psi[A(\beta)]\rangle = e^{-(\beta/2)\mathcal{H}} |\Psi[A(0)]\rangle, \quad (3.24)$$

we have for all values of β that

$$\rho(\beta) = \text{tr}_{\mathcal{H}^a} (|\Psi[A(\beta)]\rangle \langle \Psi[\bar{A}(\beta)]|).$$

Note that the Hamiltonian \mathcal{H} here only acts on \mathcal{H}_n but not on the auxiliary Hilbert spaces \mathcal{H}_n^a .

Because $A_n(\beta = 0)$ takes the form (3.23), gauge invariance of \mathcal{H} and the fact that it act as the identity on \mathcal{H}_n^a implies that during the evolution (3.24) $A_n(\beta)$ will have a similar form:

$$[A_n^{(s,p),(s^a,p^a)}(\beta)]_{(q,\alpha);(r,\beta)} = [a_n^{q,s,s^a}(\beta)]_{\alpha q,\beta r} \delta_{r,q+[s+(-1)^n]/2} \delta_{p,r} \delta_{p^a,q+[s^a+(-1)^n]/2} \quad (3.25)$$

where $a_n^{q,s,s^a} \in \mathbb{C}^{D_n^q \times D_{n+1}^r}$ represents the variational freedom of the MPS $|\Psi[A(\beta)]\rangle$. Note that contrary to (3.23) a_n^{s,p,s^a} now also depends on q, s and s^a . The interpretation is quite simple: q labels the eigenvalue of $L(n)$. The physical index p is updated according to Gauss' law similar as in eq. (3.14) : $p = q + (s + (-1)^n)/2$. We also need to consider the auxiliary system \mathcal{H}_a and here also p^a is updated according to Gauss' law: $p^a = q + (s^a + (-1)^n)/2$. Note thus that once (q, s, s^a) are fixed that (p, p^a, r) are also known and thus the variational parameters must only be labeled by (q, s, s^a) .

The virtual dimensions of this MPS are $D_n = \sum_q D_n^q$. Finally we note that by restricting ourselves to finite eigenvalues of $L(n)$ we can not represent the initial state $\rho(0)$ exactly. Fortunately, as we will see later this does not spoil our results for non-zero β .

In the thermodynamic limit ($N \rightarrow +\infty$) the Hamiltonian (3.1) in a uniform background field α is translation invariant over an even number of sites. By starting from a state which has this symmetry, i.e. by taking in (3.25) all a_n equal for $\beta = 0$, we have for all values of β that $a_n^{s,p,s^a}(\beta)$ depends only on the parity of n : $a_{2n-1}^{s,p,s^a}(\beta) = a_1^{s,p,s^a}(\beta)$ and $a_{2n}^{s,p,s^a}(\beta) = a_2^{s,p,s^a}(\beta), \forall n$.

We have thus reduced the problem of approximating the Gibbs state to evolving the Schrödinger equation in imaginary time $dt = -i\beta/2$ within the manifold of uniform MPS $|\Psi_u[A_1 A_2]\rangle$ which takes a form similar to eq. (3.15):

$$|\Psi_u[A_1 A_2]\rangle = \begin{array}{c} \textcircled{v_L^1} \text{---} \textcircled{A_1} \text{---} \textcircled{A_2} \text{---} \dots \text{---} \textcircled{A_1} \text{---} \textcircled{A_2} \text{---} \dots \text{---} \textcircled{A_1} \text{---} \textcircled{A_2} \text{---} \dots \text{---} \textcircled{A_1} \text{---} \textcircled{A_2} \text{---} \textcircled{v_R} \\ \text{(\kappa_1, \kappa_1^a)} \quad \text{(\kappa_2, \kappa_2^a)} \quad \text{(\kappa_{2n-1}, \kappa_{2n-1}^a)} \quad \text{(\kappa_{2n}, \kappa_{2n}^a)} \quad \text{(\kappa_{2N-1}, \kappa_{2N-1}^a)} \quad \text{(\kappa_{2N}, \kappa_{2N}^a)} \end{array} \quad (3.26a)$$

hence, by taking into account that

$$\begin{aligned} & \langle s_1, p_1, \dots, s_{2N}, p_{2N} | o_{k,k+1,\dots,k+K-1} | s'_1, p'_1, \dots, s'_{2N}, p'_{2N} \rangle = \\ & \quad \left(\prod_{j < k, j \geq k+K}^{2N} \delta_{s_j, s'_j} \delta_{p_j, p'_j} \right) \\ & \langle s_k, p_k, \dots, s_{k+K-1}, p_{k+K-1} | \tilde{o}_{k,\dots,k+K-1} | s'_k, p'_k, \dots, s'_{k+K-1}, p'_{k+K-1} \rangle \end{aligned}$$

we find that

$$\begin{aligned} & \langle s_1, p_1, \dots, s_{2N}, p_{2N} | o_{k,k+1,\dots,k+K-1} | s'_1, p'_1, \dots, s'_{2N}, p'_{2N} \rangle = \\ & \quad \left(\prod_{j < k, j \geq k+K}^{2N} \delta_{s_j, s'_j} \delta_{p_j, p'_j} \right) \delta_{s_k + s_{k+1} + \dots + s_{k+K-1}, s'_k + s'_{k+1} + \dots + s'_{k+K-1}} \\ & \quad \langle s_k, \dots, s_{k+K-1} | o_{k,k+1,\dots,k+K-1}^{p_{k-1}} | s'_k, \dots, s'_{k+K-1} \rangle \\ & \quad \left(\prod_{j=k}^{k+K-1} \delta_{p_j, p_{k-1} + \sum_{l=k}^j (s_l + (-1)^l) / 2} \delta_{p'_j, p'_{k-1} + \sum_{l=k}^j (s'_l + (-1)^l) / 2} \right) \\ & \quad \delta_{p_{k+K-1}, p'_{k+K-1}} \quad (3.27a) \end{aligned}$$

where

$$\begin{aligned} & \langle s_k, \dots, s_{k+K-1} | o_{k,k+1,\dots,k+K-1}^{p_{k-1}} | s'_k, \dots, s'_{k+K-1} \rangle = \\ & \langle s_k, p_k, \dots, s_{k+K-1}, p_{k+K-1} | \tilde{o}_{k,\dots,k+K-1} | s'_k, p'_k, \dots, s'_{k+K-1}, p'_{k+K-1} \rangle \\ & \quad \left(\prod_{j=k}^{k+K-1} \delta_{p_j, p_{k-1} + \sum_{l=k}^j (s_l + (-1)^l) / 2} \delta_{p'_j, p'_{k-1} + \sum_{l=k}^j (s'_l + (-1)^l) / 2} \right) \\ & \quad \delta_{p_{k+K-1}, p'_{k+K-1}}. \quad (3.27b) \end{aligned}$$

What is the interpretation of this result? The locality of $o_{k,k+1,\dots,k+K-1}$ implies that at site $k-1$ we have the eigenvalues $p_{k-1} = p'_{k-1}$ of $L(k-1)$. Because $o_{k,k+1,\dots,k+K-1}$ is gauge invariant, Gauss' law tells us how to compute p_j and p'_j for $j \geq k$ given $p_{k-1} = p'_{k-1}$ and the charges s_j and s'_j on the matter sites:

$$p_j = p_{k-1} + \sum_{l=k}^j \frac{s_l + (-1)^l}{2}, \quad p'_j = p'_{k-1} + \sum_{l=k}^j \frac{s'_l + (-1)^l}{2}. \quad (3.28)$$

At sites n with $n \geq k+K$ the operator $o_{k,k+1,\dots,k+K-1}$ acts trivially and therefore we have that $s_n = s'_n$ and $p_n = p'_n$ for $n \geq k+K$, but we also

have, again Gauss' law, that

$$\begin{aligned} p_{k+K} &= p_{k+K-1} + \frac{s_{k+K} + (-1)^{k+K}}{2} \\ &= p'_{k+K-1} + \frac{s'_{k+K} + (-1)^{k+K}}{2} = p'_{k+K}, \end{aligned}$$

hence $p_{k+K-1} = p'_{k+K-1}$. Notice that this implies conservation of the overall charge in the non-trivial sector of $o_{k,k+1,\dots,k+K-1}$:

$$s_k + s_{k+1} + \dots + s_{k+K-1} = s'_k + s'_{k+1} + \dots + s'_{k+K-1}.$$

The matrix elements

$$\langle s_k, \dots, s_{k+K-1} | O_{k,k+1,\dots,k+K-1}^{p_{k-1}} | s'_k, \dots, s'_{k+K-1} \rangle$$

are obtained by the matrix elements

$$\langle s_k, p_k, \dots, s_{k+K-1}, p_{k+K} | \tilde{O}_{k,\dots,k+K-1} | s'_k, p'_k, \dots, s'_{k+K-1}, p'_{k+K-1} \rangle$$

where we take into account eq. (3.28).

We will see later that the expectation values of gauge invariant observables indeed only depend on the matrix elements

$$\langle s_k, \dots, s_{k+K-1} | O_{k,k+1,\dots,k+K-1}^{p_{k-1}} | s'_k, \dots, s'_{k+K-1} \rangle.$$

For $K = 2$ we find that

$$\begin{aligned} \langle s_1, p_1, \dots, s_{2N}, p_{2N} | O_{k,k+1} | s'_1, p'_1, \dots, s'_{2N}, p'_{2N} \rangle &= \\ & \left(\prod_{j \neq k, k+1} \delta_{s_j, s'_j} \delta_{p_j, p'_j} \right) \\ & \langle s_k, s_{k+1} | O_{k,k+1}^{p_{k-1}} | s'_k, s'_{k+1} \rangle \delta_{s_k + s_{k+1}, s'_k + s'_{k+1}} \delta_{p_{k+1}, p'_{k+1}} \\ & \delta_{p_k, p_{k-1} + (s_k + (-1)^k)/2} \delta_{p_k, p_{k-1} + (s_k + s_{k+1})/2} \\ & \delta_{p'_k, p_{k-1} + (s'_k + (-1)^k)/2} \delta_{p'_k, p_{k-1} + (s'_k + s'_{k+1})/2} \end{aligned} \quad (3.29a)$$

where

$$\begin{aligned} & \langle s_k, s_{k+1} | O_{k,k+1}^{p_{k-1}} | s'_k, s'_{k+1} \rangle \\ &= \left\langle s_k, p_{k-1} + \frac{s_k + (-1)^k}{2}, s_{k+1}, p_{k-1} + \frac{s_k + s_{k+1}}{2} \right| \\ & \left| \tilde{O}_{k,k+1} \left| s'_k, p_{k-1} + \frac{s'_k + (-1)^k}{2}, s'_{k+1}, p_{k-1} + \frac{s'_k + s'_{k+1}}{2} \right. \right\rangle. \end{aligned} \quad (3.29b)$$

Gauge invariant MPS in the thermodynamic limit: calculus and algorithms

In this chapter we finally discuss the algorithms that will lead to our results in part I. In addition to the optimization methods discussed in chapter 2, we will now incorporate gauge invariance by imposing the block structure eq. (3.13) on our tensors. As we will see, we can use the same algorithms as before but now we have to perform the contractions on the level of the non-zero blocks that represent the variational freedom of a gauge invariant MPS. Besides a speed up in computation time this also guarantees that all our states are manifestly gauge invariant.

4.1. Ground state properties and spectrum: \mathcal{CT} invariant case

4.1.1. Introduction

Here we will discuss the implementation of the algorithms needed in section 2.1 of part I. We start from the Hamiltonian

$$\mathcal{H} = \frac{g}{2\sqrt{x}} \left(\sum_{n=1}^{2N} [L(n) + \alpha]^2 + \frac{\sqrt{x}}{g} m \sum_{n=1}^{2N} (-1)^n (\sigma_z(n) + (-1)^n) + x \sum_{n=1}^{2N-1} (\sigma^+(n) e^{i\theta(n)} \sigma^-(n+1) + h.c.) \right), \quad (4.1)$$

where $\alpha = 0$ or $\alpha = 1/2$. Note that we here also allow the case $\alpha = 1/2$. This Hamiltonian is \mathcal{CT} invariant, with \mathcal{C} charge conjugation

$$\begin{aligned} \mathcal{C}L(n)\mathcal{C} &= -2\alpha - L(n), \mathcal{C}\theta(n)\mathcal{C} = -\theta(n), \\ \mathcal{C}\sigma_z(n)\mathcal{C} &= -\sigma_z(n), \mathcal{C}\sigma^\pm(n)\mathcal{C} = \sigma^\mp(n). \end{aligned}$$

When the ground state is also \mathcal{CT} invariant we can use the \mathcal{CT} invariant MPS ansatz (3.18) constructed in subsection 3.3.2 to approximate the ground state:

$$|\Psi_{\mathcal{C}}[A]\rangle = \begin{array}{c} \textcircled{v_L^\dagger} \text{---} \boxed{A} \text{---} \boxed{A} \text{---} \cdots \text{---} \boxed{A} \text{---} \boxed{A} \text{---} \cdots \text{---} \boxed{A} \text{---} \boxed{A} \text{---} \textcircled{v_R} \\ | \\ \textcircled{c} \\ \kappa_2 \\ | \\ \textcircled{c} \\ \kappa_{2n} \\ | \\ \textcircled{c} \\ \kappa_{2N} \end{array}, \quad (4.2a)$$

$$\begin{array}{c} (q, \alpha_q) \text{---} \boxed{A} \text{---} (r, \beta_r) \\ | \\ \kappa \\ (s, p) \end{array} = [a^{q,s}]_{\alpha_q, \beta_r} \delta_{p, q+(s-1)/2} \delta_{r, -p-2\alpha}. \quad (4.2b)$$

with $\kappa_n = (s_n, p_n) \in \{-1, 1\} \times \mathbb{Z}[p^{\min}, p^{\max}]$.

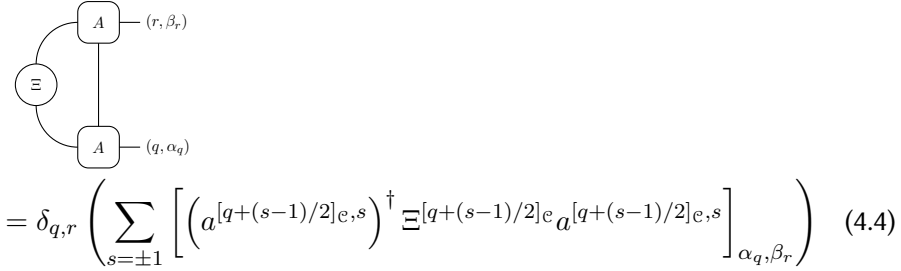
4.1.2. Normalization and Schmidt spectrum

As discussed in section 1.4, to normalize $|\Psi_{\mathcal{C}}[A]\rangle$ we can investigate its ‘uniform counterpart’ $|\Psi_u[A]\rangle$. We thus need to apply algorithm 1.1 to normalize $|\Psi_{\mathcal{C}}[A]\rangle = |\Psi_{\mathcal{C}}[A(a)]\rangle$ and to bring it in a desired canonical form. Let us now discuss in full detail how we can exploit the block structure in eq. (4.2b) to speed up the algorithm and to maintain gauge invariance after every step. The pseudocode is given in algorithm 4.1. As input we pass the matrices $a^{q,s} \in \mathbb{C}^{D^q \times D^{-(q+(s-1)/2)-2\alpha}}$ representing the variational freedom of the gauge invariant state $|\Psi_{\mathcal{C}}[A]\rangle$ to the function. The string ‘stringCanForm’ contains the desired canonical form: ‘left’ if we want A in the left canonical form, ‘right’ if we want A in the right canonical form and ‘symmetric’ if we want A in the symmetric canonical form.

The first step, lines 2 and 3, is to find the leading eigenvalue η of the transfer matrix \mathbb{E} and the corresponding left and right eigenvectors Ξ and Λ :

$$\begin{array}{c} \boxed{A} \\ | \\ \boxed{A} \end{array} \text{---} \textcircled{\Lambda} = \eta \textcircled{\Lambda} \quad \text{and} \quad \textcircled{\Xi} \text{---} \begin{array}{c} \boxed{A} \\ | \\ \boxed{A} \end{array} = \eta \textcircled{\Xi}. \quad (4.3)$$

The tensors A take the special form (4.2b) and therefore we find that



$$= \delta_{q,r} \left(\sum_{s=\pm 1} \left[(a^{[q+(s-1)/2]e,s})^\dagger \Xi^{[q+(s-1)/2]e} a^{[q+(s-1)/2]e,s} \right]_{\alpha_q, \beta_r} \right) \quad (4.4)$$

where $\Xi^q \in \mathbb{C}^{D^q \times D^q}$ has components

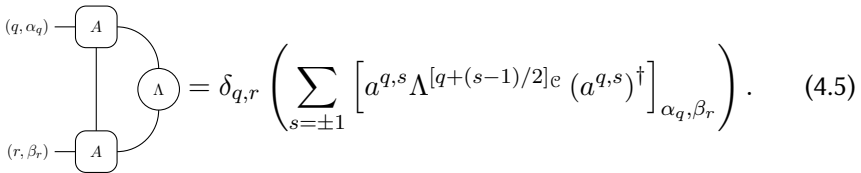
$$[\Xi^q]_{\alpha_q, \beta_q} = [\Xi]_{(q, \alpha_q); (q, \beta_q)}$$

and we introduced the notation $[\dots]_e$ to indicate that we apply a charge conjugation:

$$[q]_e = -q - 2\alpha, [q + (s - 1)/2]_e = -q - (s - 1)/2 - 2\alpha.$$

One observes that the outcome is a matrix which is block diagonal in the different sectors corresponding to the eigenvalues q of $L(n)$. Also, the result only depends on the diagonal blocks Ξ^q of Ξ corresponding to the eigenvalues q of $L(n)$. Note that the computation time of this diagram scales linearly in $P \equiv p^{\max} - p^{\min} + 1$, the number of eigenvalues of $L(n)$ we retain in our numerical scheme. As we will see later, this is the main advantage of our formalism: the overall computation time will scale linearly in P . In contrast, a full computation of this diagram, without taking into account the block structure (4.2b), would take $\mathcal{O}(P^4)$ time.

In a similar way we find that



$$= \delta_{q,r} \left(\sum_{s=\pm 1} \left[a^{q,s} \Lambda^{[q+(s-1)/2]e} (a^{q,s})^\dagger \right]_{\alpha_q, \beta_r} \right). \quad (4.5)$$

To solve the eigenvalue problems eq. (4.3), the iterative eigensolver ‘eigs’ computes the left resp. right action of the transfer matrix on Ξ^q by applying the functions ‘ApplyTransferLeft’, line 37, and ‘ApplyTransferRight’, line 42. Now the diagrams are computed according to eqs. (4.4) and (4.5). In particular we thus only need to consider the action of the transfer matrix on the diagonal blocks Ξ^q and Λ^q of Ξ and Λ , see eq. (4.4) and eq. (4.5). When implementing this algorithm one can store the $(D^q \times D^r)$ matrices $a^{q,s}$ in a

$(P \times 2)$ cell array. Similarly, the diagonal blocks Λ^q and Ξ^q can be stored in a $(P \times 1)$ cell array. Note that the eigenvalue equations,

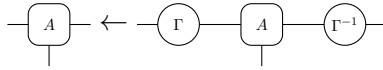
$$\sum_{s=\pm 1} \left[\left(a^{[q+(s-1)/2]e,s} \right)^\dagger \Xi^{[q+(s-1)/2]e} a^{[q+(s-1)/2]e,s} \right] = \eta \Xi^q$$

$$\sum_{s=\pm 1} \left[a^{q,s} \Lambda^{[q+(s-1)/2]e} \left(a^{q,s} \right)^\dagger \right] = \eta \Lambda^q$$

for $q = p^{min}, \dots, p^{max}$ and $\Xi^q, \Lambda^q \in \mathbb{C}^{D^q \times D^q}$, connect different eigenvalue sectors of $L(n)$. This is important, because otherwise we could not apply the quantum Perron-Frobenius theorem [163] and we would not be guaranteed that the blocks Ξ^q and Λ^q are non-singular.

The other steps in the algorithm 4.1 are also performed on the level of the blocks in each of the sectors corresponding to the eigenvalues of $L(n)$. Indeed, the algorithm is exactly the same as for the general case, algorithm 1.1. The only difference is that we now have to transform each of the blocks Ξ^q and Λ^q , this explains the for-loop, line 4-30.

After the for-loop over the eigenvalue sectors q of $L(n)$ we have the matrix $\Gamma \in \mathbb{C}^{D \times D}$ to perform the MPS gauge transformation with, see line 33. Here also this diagram can be computed on the level of the blocks: because $[\Gamma]_{(q,\alpha_q);(r,\beta_r)} = \delta_{q,r} [\Gamma^q]_{\alpha,\beta}$, it follows that



is equivalent to

$$a^{q,s} \leftarrow \Gamma^q a^{q,s} \left(\Gamma^{[q+(s-1)/2]e} \right)^{-1}.$$

Remember that after applying this algorithm Ξ^q and Λ^q are diagonal positive definite matrices. In further discussions we will assume that Ξ^q and Λ^q are positive definite matrices (it is not really necessary that they are diagonal but it is certainly convenient).

Hence, by taking the block structure eq. (4.2b) into account we can normalize the state $|\Psi_e[A]\rangle$ in

$$\mathcal{O} \left(N_{iter} \sum_q \sum_s \max \left(D^q \left(D^{[q+(s-1)/2]e} \right)^2, (D^q)^2 D^{[q+(s-1)/2]e} \right) \right)$$

$$\sim \mathcal{O} \left(2N_{iter} P \max_q (D_q)^3 \right)$$

time where N_{iter} is the number of iterations needed by the iterative eigensolver ‘eigs’ and the factor 2 originates from the number of spins on a site.

Algorithm 4.1 Normalization of a gauge and \mathcal{CT} invariant MPS

Input: a , stringCanForm

Output: a, Ξ, Λ .

```

1: function [ $a, \Xi, \Lambda, \eta, \Gamma$ ] = NORMALIZEUMPS( $a$ , stringCanForm)
2:   [ $\Xi, \eta$ ] = eigs(@( $\Xi$ )ApplyTransferLeft( $\Xi, a$ ))
3:   [ $\Lambda, \eta$ ] = eigs(@( $\Lambda$ )ApplyTransferRight( $\Lambda, a$ ))
4:   for  $q = p^{min} : p^{max}$  do
5:     for  $s = -1, 1$  do
6:        $a^{q,s} \leftarrow a^{q,s} / \sqrt{\eta}$ 
7:     end for
8:      $\Xi^q \leftarrow \Xi^q / \text{tr}(\Xi^q)$ 
9:      $\Lambda^q \leftarrow \Lambda^q / \text{tr}(\Lambda^q)$ 
10:    Find matrices  $X^q$  and  $Y^q$  such that  $\Xi^q = X^q(X^q)^\dagger$ ,  $\Lambda^q = (Y^q)^\dagger Y^q$ 
11:    [ $U^q, \Sigma^q, V^q$ ] = SVD( $Y^q X^q$ )
12:  end for
13:   $\chi = \sqrt{\text{tr} \left( \sum_{q=p^{min}}^{p^{max}} (\Sigma^q)^2 \right)}$ 
14:  for  $q = p^{min} : p^{max}$  do
15:     $\Sigma^q \leftarrow \Sigma^q / \chi$ 
16:    switch stringCanForm do
17:      case 'left'
18:         $\Gamma^q = \Sigma^q (V^q)^\dagger (X^q)^{-1} = (U^q)^\dagger Y^q$ 
19:         $\Xi^q = \mathbf{1}_{D^q}$ 
20:         $\Lambda^q = (\Sigma^q)^2$ 
21:      case 'right'
22:         $\Gamma^q = (V^q)^\dagger (X^q)^{-1} = (\Sigma^q)^{-1} (U^q)^\dagger Y^q$ 
23:         $\Xi^q = (\Sigma^q)^2$ 
24:         $\Lambda^q = \mathbf{1}_{D^q}$ 
25:      case 'symmetric'
26:         $\Gamma^q = (\Sigma^q)^{1/2} (V^q)^\dagger (X^q)^{-1} = (\Sigma^q)^{-1/2} (U^q)^\dagger Y^q$ 
27:         $\Xi^q = \Sigma^q$ 
28:         $\Lambda^q = \Sigma^q$ 
29:    end switch
30:  end for
31:  for  $q = p^{min} : p^{max}$  do
32:    for  $s = -1, 1$  do
33:       $a^{q,s} \leftarrow \Gamma^q a^{q,s} (\Gamma^{[q+(s-1)/2]c})^{-1}$ 
34:    end for
35:  end for
36: end function

```

```

37: function  $\Xi' = \text{APPLYTRANSFERLEFT}(\Xi, a)$ 
38:   for  $q = p^{\min} : p^{\max}$  do
39:      $[\Xi']^q = \sum_{s=\pm 1} \left[ \left( a^{[q+(s-1)/2]_e, s} \right)^\dagger \Xi^{[q+(s-1)/2]_e} a^{[q+(s-1)/2]_e, s} \right]$ 
40:   end for
41: end function
42: function  $\Lambda' = \text{APPLYTRANSFERRIGHT}(\Lambda, a)$ 
43:   for  $q = p^{\min} : p^{\max}$  do
44:      $[\Lambda']^q = \sum_{s=\pm 1} \left[ a^{q, s} \Lambda^{[q+(s-1)/2]_e} (a^{q, s})^\dagger \right]$ 
45:   end for
46: end function
    
```

As explained in subsection 1.1.3, we can compute from Λ and Ξ the Schmidt spectrum of the state $|\Psi_e[A]\rangle$. Denoting the eigenvalues of $\Xi^q \Lambda^q$ by $\sigma_1^q, \dots, \sigma_{D^q}^q$ with

$$1 \geq \sigma_1^q \geq \sigma_2^q \geq \dots \geq \sigma_{D^q}^q \geq 0, \quad \sum_{q=p^{\min}}^{p^{\max}} \sum_{\alpha_q=1}^{D^q} \sigma_{\alpha_q}^q = 1,$$

the Schmidt decomposition with respect to the bipartition

$$\{\mathcal{A}_1^n = \mathbb{Z}[1, \dots, n], \mathcal{A}_2^n = \mathbb{Z}[n+1, \dots, 2N]\}$$

of the lattice reads

$$|\Psi[A]\rangle = \sum_{q=p^{\min}}^{p^{\max}} \sum_{\alpha_q=1}^{D^q} \sqrt{\sigma_{\alpha_q}^q} |\Phi_{q, \alpha_q}^{\mathcal{A}_1^n}\rangle \otimes |\Phi_{q, \alpha_q}^{\mathcal{A}_2^n}\rangle$$

where

$$|\Phi_{q, \alpha_q}^{\mathcal{A}_1^n}\rangle \in \bigotimes_{j \in \mathcal{A}_1^n} \mathcal{H}_j \quad \text{and} \quad |\Phi_{q, \alpha_q}^{\mathcal{A}_2^n}\rangle \in \bigotimes_{j \in \mathcal{A}_2^n} \mathcal{H}_j$$

are orthonormal unit vectors,

$$\langle \Phi_{q, \alpha_q}^{\mathcal{A}_1^n} | \Phi_{r, \beta_r}^{\mathcal{A}_1^n} \rangle = \delta_{q,r} \delta_{\alpha_q, \beta_r}, \quad \langle \Phi_{q, \alpha}^{\mathcal{A}_2^n} | \Phi_{r, \beta_r}^{\mathcal{A}_2^n} \rangle = \delta_{q,r} \delta_{\alpha, \beta_r}.$$

Due to \mathcal{CT} symmetry we find that the Schmidt spectrum is independent of the site n . However, the Schmidt values $\sigma_{\alpha_q}^q$ in a particular eigenvalue sector q of $L(2n-1)$ on the odd sites will correspond to the Schmidt values $\sigma_{\alpha_q}^{-q}$ in the eigenvalue sector q of $L(2n)$ on the even sites. As a measure of the entanglement we can compute for instance the Von Neumann entropy S

$$S = - \sum_{q=p^{\min}}^{p^{\max}} \sum_{\alpha=1}^{D^q} \sigma_{\alpha}^q \log(\sigma_{\alpha}^q)$$

which is site independent.

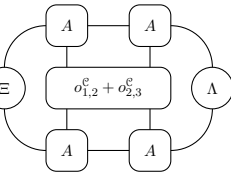
4.1.3. Calculus

Once we normalized the \mathcal{CT} invariant state $|\Psi_{\mathcal{C}}[A]\rangle$ we can compute expectation values of observables. We are interested in observables \mathcal{O} that take the form

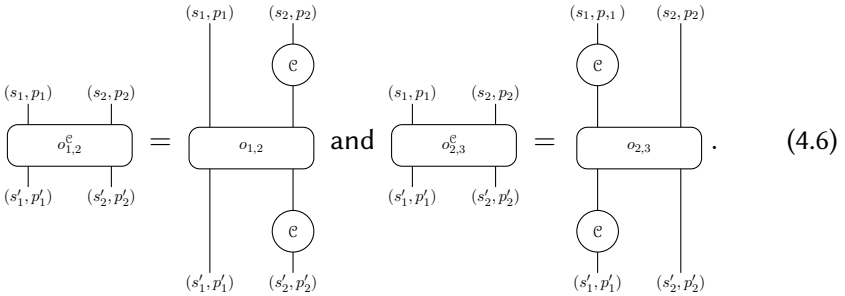
$$\mathcal{O} = \sum_{n=1}^{2N-1} o_{n,n+1},$$

$$o_{2n-1,2n} = \mathcal{T}^{2n-2} o_{1,2} \mathcal{T}^{2n-2}, o_{2n,2n+1} = \mathcal{T}^{2n-2} o_{2,3} \mathcal{T}^{-2n+2},$$

with $o_{1,2}$ resp. $o_{2,3}$ Hermitian observables acting only non-trivially on the sites 1 and 2 resp. 2 and 3. In that case we have for the expectation value per site, see subsection 1.4.1,

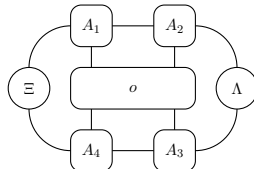
$$\lim_{N \rightarrow +\infty} \frac{1}{2N} \langle \Psi_{\mathcal{C}}[A] | \mathcal{O} | \Psi_{\mathcal{C}}[A] \rangle = \frac{1}{2} \langle \Xi | o_{1,2}^{\mathcal{C}} + o_{2,3}^{\mathcal{C}} | \Lambda \rangle$$


with



$$(4.6)$$

To compute this diagram efficiently we need to perform the contractions as discussed in fig. 1.1 in subsection 1.1.4. Here the block structure of A , Ξ and Λ leads to some simplifications. Let us discuss this for more general diagrams of the form



$$(4.7)$$

where A_n has the block structure eq. (4.2b)

$$[A_n^{s,p}]_{(q,\alpha_q),(r,\beta_r)} = [a_n^{q,s}]_{\alpha_q,\beta_r} \delta_{p,q+(s-1)/2} \delta_{r,-p-2\alpha} \quad (n = 1, 2, 3, 4) \quad (4.8)$$

and Ξ and Λ are block diagonal

$$[\Xi]_{(q,\alpha_q),(r,\beta_r)} = [\Xi^q]_{\alpha_q,\beta_r} \delta_{q,r}, \quad [\Lambda]_{(q,\alpha_q),(r,\beta_r)} = [\Lambda^q]_{\alpha_q,\beta_r} \delta_{q,r} \quad (4.9)$$

and o can be any operator acting on two sites. First one defines the tensors $C_{k,l}$ ($(k,l) = (1,2), (4,3)$) that are obtained by blocking the tensors A_k and A_l :

$$(q,\alpha_q) \text{---} \boxed{C_{k,l}} \text{---} (r,\beta_r) = (q,\alpha_q) \text{---} \boxed{A_k} \text{---} \boxed{A_l} \text{---} (r,\beta_r) \quad \kappa_i = (s_i, p_i) \quad (i = 1, 2).$$

Eq. (4.31) implies now that $C_{k,l}$ has a similar block structure

$$(q,\alpha_q) \text{---} \boxed{C_{k,l}} \text{---} (r,\beta_r) = \delta_{p_1, q+(s_1-1)/2} \delta_{p_2, [q+(s_1-s_2)/2]_c} \delta_{r, q+(s_1-s_2)/2} \left[C_{k,l}^{q, s_1, s_2} \right]_{\alpha_q, \beta_r}$$

with

$$C_{k,l}^{q, s_1, s_2} = a_k^{q, s_1} a_l^{[q+(s_1-1)/2]_c, s_2}. \quad (4.10)$$

Hence, we have

$$\begin{array}{c} \Xi \\ \circlearrowleft \\ \Lambda \end{array} \begin{array}{c} A_1 \\ \text{---} \\ A_2 \\ \text{---} \\ o \\ \text{---} \\ A_4 \\ \text{---} \\ A_3 \end{array} = \begin{array}{c} \Xi \\ \circlearrowleft \\ \Lambda \end{array} \begin{array}{c} C_{1,2} \\ \text{---} \\ o \\ \text{---} \\ C_{4,3} \end{array}. \quad (4.11)$$

Next we apply the operator o to $C_{1,2}$:

$$(q,\alpha_q) \text{---} \boxed{D_{1,2}} \text{---} (r,\beta_r) = (q,\alpha_q) \text{---} \boxed{C_{1,2}} \text{---} (r,\beta_r) \text{---} \boxed{o} \text{---} (r,\beta_r).$$

When o is of the form eq. (4.6) with $o_{1,2}$ and $o_{2,3}$ a gauge invariant operator, then $D_{1,2}$ is also of the form (4.10). This follows from eq. (3.29) and applying a charge conjugation on the even or the odd sites. When we allow $o_{1,2}$ and $o_{2,3}$ to be gauge variant, $D_{1,2}$ is not necessarily of the form (4.10). However, because of the block structure of $C_{4,3}$, the fact that Ξ and Λ are block diagonal and because we are interested in the expectation value eq. (4.11),

and we easily find that

$$[\Omega]_{(q,\alpha_q);(r,\beta_r)} = [\Omega^q]_{\alpha_q,\beta_r} \delta_{q,r}$$

with

$$\Omega^q = \sum_{s_1, s_2 = -1, 1} a_{1,2}^{q, s_1, s_2} \Lambda^{q+(s_1-s_2)/2} (c_{4,3}^{q, s_1, s_2})^\dagger.$$

After performing these contractions, the expectation value is obtained as

$$\Xi \text{---} \begin{array}{c} A_1 \text{---} A_2 \\ | \quad | \\ o \\ | \quad | \\ A_4 \text{---} A_3 \end{array} \text{---} \Lambda = \Xi \text{---} \Omega = \sum_{q=p^{\min}}^{p^{\max}} \text{tr}(\Xi^q \Omega^q).$$

These steps are summarized in the pseudocode of algorithm 4.2. The input are the tensors a_1, a_2, a_3, a_4 , see eq. (4.31), the blocks Ξ^q and Λ^q , see eq. (4.9) and the local observable o . After executing the algorithm we have the outcome of the diagram (4.7). Assuming that $\max_q D^q \gg 2, P$; the overall computation time scales with

$$\mathcal{O} \left(2^2 P \max_q (D_q)^3 \right)$$

where the factor 2^2 originates from the dimension of the tensor product of two spin-1/2 bases.

We conclude this subsection with two comments on the algorithm:

- i. In line 10 $\langle s_1, s_2 | o^q | s'_1, s'_2 \rangle$ is defined in eq. (4.13).
- ii. $\sum_{\{s'_k\}}, \sum_{\{s_k\}}$ are shorthand notations for $\sum_{s'_1, s'_2 = -1, 1}, \sum_{s_1, s_2 = -1, 1}$.

Algorithm 4.2 Expectation value of a gauge and \mathcal{CT} invariant MPS

Input: $a_1, a_2, a_3, a_4, \Xi, \Lambda, o$

Output: Outcome of the diagram (4.7)

- 1: **function** $\langle o \rangle = \text{EXPVALMPS}(a_1, a_2, a_3, a_4, \Xi, \Lambda, o)$
- 2: **for** $q = p^{\min} : p^{\max}$ **do**
- 3: **for** $s_1, s_2 = -1, 1$ **do**
- 4: $c_{1,2}^{q, s_1, s_2} = a_1^{q, s_1} a_2^{[q+(s_1-1)/2]e, s_2}$
- 5: $c_{4,3}^{q, s_1, s_2} = a_4^{q, s_1} a_3^{[q+(s_1-1)/2]e, s_2}$
- 6: **end for**
- 7: **end for**
- 8: **for** $q = p^{\min} : p^{\max}$ **do**

```

9:      for  $s_1, s_2 = -1, 1$  do
10:          $d_{1,2}^{q,s_1,s_2} = \sum_{\{s'_k\}} \langle s_1, s_2 | o^q | s'_1, s'_2 \rangle c_{1,2}^{q,s'_1,s'_2}$ 
11:      end for
12:       $\Omega^q = \sum_{\{s_k\}} d_{1,2}^{q,s_1,s_2} \Lambda^{q+(s_1-s_2)/2} \left( c_{4,3}^{q,s_1,s_2} \right)^\dagger$ 
13: end for
14:  $\langle o \rangle = \sum_{q=p^{min}}^{p^{max}} \text{tr} (\Xi^q \Omega^q)$ 
15: end function

```

From our discussion it also follows that if o is gauge invariant, we can efficiently compute the following contractions:

$$\sum_{s_1, s_2 = -1, 1} \left[\left(c_{4,3}^{q+(s_2-s_1)/2, s_1, s_2} \right)^\dagger \Xi^{q+(s_2-s_1)/2} d_{1,2}^{q+(s_2-s_1)/2, s_1, s_2} \right]_{\alpha_q, \beta_r}, \quad (4.14a)$$

and

$$\sum_{s_1, s_2 = -1, 1} \left[d_{1,2}^{q,s_1,s_2} \Lambda^{q+(s_1-s_2)/2} \left(c_{4,3}^{q,s_1,s_2} \right)^\dagger \right]_{\alpha_q, \beta_r} \quad (4.14b)$$

in $\mathcal{O}(2^2 P \max_q (D^q)^3)$ time. The $\delta_{q,r}$ factor is a consequence of gauge invariance of o .

4.1.4. TDVP

Here we will formulate the TDVP algorithm, see section 2.1, for gauge invariant MPS $|\Psi_{\mathcal{C}}[A]\rangle$. The objective is to find B such that it minimizes

$$\| \mathcal{H}_u |\Psi_u[A]\rangle - |\Phi_0[B, A]\rangle \|_2 \text{ with } \langle \Phi_0[\bar{B}, \bar{A}] | \Psi_u[A] \rangle = 0,$$

$$[W_R^q]_{(\alpha_r, s), \beta_q} = \left[\left(\Lambda^{[q+(s-1)/2]e} \right)^{1/2} (a^{q,s})^\dagger \right]_{\alpha_r, \beta_q}$$

with

$$F^q = \sum_{s=-1,1} D^{[q+(s-1)/2]e}$$

then the right gauge fixing condition is equivalent with

$$\tilde{b}^q W_R^q = 0.$$

Let $\tilde{V}_R^q \in \mathbb{C}^{n_R^q \times F^q}$ be a matrix such that the rows of \tilde{V}_R^q form an orthonormal basis for the left zero space of $W_R^q \in \mathbb{C}^{F^q \times D^q}$, i.e. $\tilde{V}_R^q W_R^q = 0$ and $\tilde{V}_R^q \left(\tilde{V}_R^q \right)^\dagger = \mathbb{1}_{n_R^q}$ where n_R^q is the dimension of the kernel of W_R^q . We expect that $n_R^q = F^q - D^q$ but we also allow for the more general case $n_R^q \geq F^q - D^q$ as well. $\tilde{b}^q W_R^q = 0$ implies that there exists a matrix $X^q \in \mathbb{C}^{D^q \times n_R^q}$ such that

$$\tilde{b}^q = (\Xi^q)^{-1/2} X^q \tilde{V}_R^q,$$

the $(\Xi^q)^{-1/2}$ is only a matter of convention. It follows that

$$b^{q,s}(X) = (\Xi^q)^{-1/2} X^q v_R^{q,s} (\Lambda^{[q+(s-1)/2]e})^{-1/2} \quad (4.15)$$

where $v_R^{q,s} \in \mathbb{C}^{n_R^q \times D^{[q+(s-1)/2]e}}$ has components

$$[v_R^{q,s}]_{\alpha_q, \beta_r} = [\tilde{V}_R^q]_{\alpha_q, (s, \beta_r)}.$$

The parameterization eq. (1.25),

$$\boxed{B(X)} = \bigcirc_{\Xi^{-1/2}} - \bigcirc_X - \boxed{V_R} - \bigcirc_{\Lambda^{-1/2}},$$

can be recovered from eq. (4.15) by noting that

$$[B^{s,p}]_{(q, \alpha_q); (r, \beta_r)} = [b^{q,s}]_{\alpha_q, \beta_r} \delta_{p, q+(s-1)/2} \delta_{r, [q+(s-1)/2]e} \quad (4.16a)$$

$$[\Xi]_{(q, \alpha_q), (r, \beta_r)} = \delta_{q,r} [\Xi^q]_{\alpha_q, \beta_r}, \quad [\Lambda]_{(q, \alpha_q), (r, \beta_r)} = \delta_{q,r} [\Lambda^q]_{\alpha_q, \beta_r}, \quad (4.16b)$$

and by putting

$$[X]_{(q, \alpha_q), (r, \beta_r)} = \delta_{q,r} [X^q]_{\alpha_q, \beta_r}, \quad (4.16c)$$

$$[V_R^{s,p}]_{(q, \alpha_q); (r, \beta_r)} = [v_R^{q,s}]_{\alpha_q, \beta_r} \delta_{p, q+(s-1)/2} \delta_{r, [q+(s-1)/2]e}. \quad (4.16d)$$

Note that $\tilde{V}_R^q (\tilde{V}_R^q)^\dagger = \mathbb{1}_{n_R^q}$ implies that

$$\sum_{s=-1,1} v_R^{q,s} (v_R^{q,s})^\dagger = \mathbb{1}_{n_R^q}.$$

The pseudocode to determine \tilde{V}_R is presented in algorithm 4.3 and is basically a summary of the steps discussed before. In line 12 the command 'nullLeft' determines the matrix $\tilde{V}_R^q \in \mathbb{C}^{n_R^q \times F^q}$ such that the rows of \tilde{V}_R^q form an orthonormal basis for the left zero space of $W_R^q \in \mathbb{C}^{F^q \times D^q}$. In Matlab one has to apply the command 'null', which determines the right zero space, to $(W_R^q)^\dagger$, and take the Hermitian conjugate.

Algorithm 4.3 Compute v_R for gauge and \mathcal{CT} invariant MPS

Input: a, Ξ, Λ

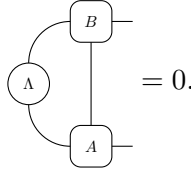
Output: Tensor v_R which allows parameterization eq. (4.15)

```

1: function  $v_R = \text{COMPUTEVR}(a, \Xi, \Lambda)$ 
2:   for  $q = p^{\min} : p^{\max}$  do
3:     for  $s = -1, 1$  do
4:       for  $\beta_q = 1 : D^q$  do
5:         for  $\alpha_r = 1 : D^{\lfloor q+(s-1)/2 \rfloor}$  do
6:            $[W_R^q]_{(\alpha_r, s), \beta_q} = [(\Lambda^{\lfloor q+(s-1)/2 \rfloor})^{1/2} (a^{q,s})^\dagger]_{\alpha_r, \beta_q}$ 
7:         end for
8:       end for
9:     end for
10:  end for
11:  for  $q = p^{\min} : p^{\max}$  do
12:     $\tilde{V}_R^q = \text{nullLeft}(W_R^q)$ 
13:  end for
14:  for  $q = p^{\min} : p^{\max}$  do
15:    for  $s = -1, 1$  do
16:      for  $\alpha_q = 1 : n_R^q$  do  $\triangleright n_R^q$  is rank of  $\tilde{V}_R^q$ 
17:        for  $\beta_r = 1 : D^{\lfloor q+(s-1)/2 \rfloor}$  do
18:           $[v_R^{q,s}]_{\alpha_q, \beta_r} = [\tilde{V}_R^q]_{\alpha_q, (\beta_r, s)}$ 
19:        end for
20:      end for
21:    end for
22:  end for
23: end function

```

We can find a similar parameterization when we want B to obey the left gauge fixing condition,



Now we define $W_L^q \in \mathbb{C}^{D^q \times F^q}$ with components

$$[W_L^q]_{\alpha_q, (\beta_r, s)} = \left[\left(a^{[q+(s-1)/2]e, s} \right)^\dagger \left(\Xi^{[q+(s-1)/2]e, s} \right)^{1/2} \right]_{\alpha_q, \beta_r}$$

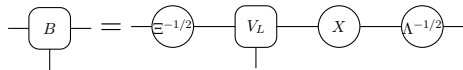
and consider $\tilde{V}_L^q \in \mathbb{C}^{F^q \times n_L^q}$, a matrix such that the columns of \tilde{V}_L^q form an orthonormal basis for the right zero space of $W_L^q \in \mathbb{C}^{D^q \times F^q}$. We thus have that $W_L^q \tilde{V}_L^q = 0$ and $(\tilde{V}_L^q)^\dagger \tilde{V}_L^q = \mathbb{1}_{n_L^q}$. In general, we expect that $n_L^q = F^q - D^q$, but we allow for the more general case $n_L \geq F^q - D^q$ as well. Defining now the matrix $v_L^{q,s} \in \mathbb{C}^{D^q \times n_L^{[q+(s-1)/2]e}}$ with components

$$[v_L^{q,s}]_{\alpha_q, \beta_r} = \left[\tilde{V}_L^{[q+(s-1)/2]e, s} \right]_{(\alpha_q, s), \beta_r}$$

we find that $B = B(b)$ can now be parameterized by a matrix $X \in \mathbb{C}^{n_L^q \times D^q}$:

$$b^{q,s} = (\Xi^q)^{-1/2} v_L^{q,s} X^{[q+(s-1)/2]e} \left(\Lambda^{[q+(s-1)/2]e} \right)^{-1/2}. \quad (4.17)$$

This agrees with the parameterization (1.26),



if we note that

$$[\Xi]_{(q, \alpha_q), (r, \beta_r)} = \delta_{q,r} [\Xi^q]_{\alpha_q, \beta_r}, \quad [\Lambda]_{(q, \alpha_q), (r, \beta_r)} = \delta_{q,r} [\Lambda^q]_{\alpha_q, \beta_r}, \quad (4.18a)$$

and we put

$$[X]_{(q, \alpha_q), (r, \beta_r)} = \delta_{q,r} [X^q]_{\alpha_q, \beta_r}, \quad (4.18b)$$

$$[V_L^{s,p}]_{(q, \alpha_q); (r, \beta_r)} = [v_L^{q,s}]_{\alpha_q, \beta_r} \delta_{p, q+(s-1)/2} \delta_{r, [q+(s-1)/2]e}. \quad (4.18c)$$

From $(\tilde{V}_L^q)^\dagger \tilde{V}_L^q = \mathbb{1}_{n_L^q}$ it follows that

$$\sum_{s=-1,1} (v_L^{q,s})^\dagger v_L^{q,s} = \mathbb{1}_{n_L^q}.$$

The pseudocode is presented below, algorithm 4.4. Here the command ‘null-Right’, line 12, determines $\tilde{V}_L^q \in \mathbb{C}^{F^q \times n_L^q}$ such that the columns of \tilde{V}_L^q form an orthonormal basis for the right zero space of $W_L^q \in \mathbb{C}^{D^q \times F^q}$. In Matlab this coincides with the command ‘null(\tilde{V}_L^q)’.

Algorithm 4.4 Compute v_L for gauge and \mathcal{CT} invariant MPS

Input: a, Ξ, Λ

Output: Tensor v_L which allows parameterization (4.17)

```

1: function  $v_L = \text{COMPUTEVL}(a, \Xi, \Lambda)$ 
2:   for  $q = p^{\min} : p^{\max}$  do
3:     for  $s = -1, 1$  do
4:       for  $\alpha_q = 1 : D^q$  do
5:         for  $\beta_r = 1 : D^{\lfloor q+(s-1)/2 \rfloor e}$  do
6:            $X^q = [W_L^q]_{\alpha_q, (\beta_r, s)} = \left[ \begin{array}{c} \left( a^{\lfloor q+(s-1)/2 \rfloor e, s} \right)^\dagger \\ \left( \Xi^{\lfloor q+(s-1)/2 \rfloor e, s} \right)^{1/2} \end{array} \right]_{\alpha_q, \beta_r}$ 
7:         end for
8:       end for
9:     end for
10:  end for
11:  for  $q = p^{\min} : p^{\max}$  do
12:     $\tilde{V}_L^q = \text{nullRight}(W_R^q)$ 
13:  end for
14:  for  $q = p^{\min} : p^{\max}$  do
15:    for  $s = -1, 1$  do
16:      for  $\alpha_q = 1 : D^q$  do
17:        for  $\beta_r = 1 : n_L^{\lfloor q+(s-1)/2 \rfloor e}$  do  $\triangleright n_L^q$  is rank of  $\tilde{V}_L^q$ 
18:           $[v_L^{q,s}]_{\alpha_q, \beta_r} = [\tilde{V}_L^{q+(s-1)/2 e, s}]_{(\alpha_q, s), \beta_r}$ 
19:        end for
20:      end for
21:    end for
22:  end for
23: end function

```

(b) TDVP equations

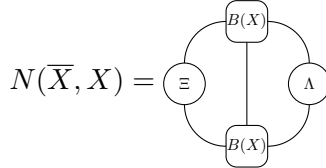
Once we have parameterized $b^{q,s}$ with the block diagonal matrix X , see eq. (4.15) or eq. (4.17), we have identified the variational freedom in the representation of $|\Phi_0[B, A]\rangle$. The TDVP dictates that we have to minimize

$$f(\bar{X}, X) = (|\mathcal{J}\mathcal{t}_u |\Psi_u[A]\rangle - |\Phi_0[B(X), A]\rangle) \|^2$$

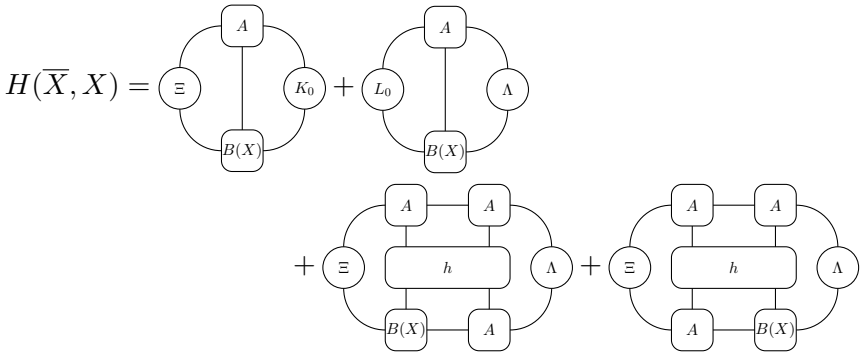
with respect to the complex conjugate of $[X]_{(q,\alpha_q);(r,\beta_r)} = [X^q]_{\alpha_q,\beta_q} \delta_{q,r}$. We can now follow the method from subsection 2.1.2. Because of eq. (1.27), we have that

$$f(\bar{X}, X) = 2\pi\delta(0) \left(N(\bar{X}, X) - H(\bar{X}, X) \right) - \text{terms independent of } \bar{X}$$

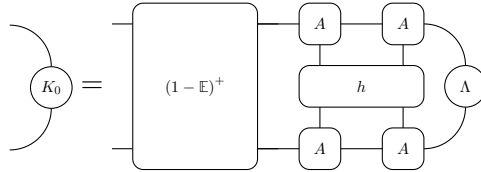
where



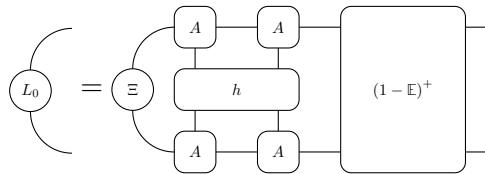
and



with



and



The computation of K_0 and L_0 will be discussed in (c). The only property that is important for now is that K_0 and L_0 are block diagonal:

$$[K_0]_{(q,\alpha_q);(r,\beta_r)} = \delta_{q,r} [K_0^q]_{\alpha_q,\beta_r}, [L_0]_{(q,\alpha_q);(r,\beta_r)} = \delta_{q,r} [L_0^q]_{\alpha_q,\beta_r}$$

with $K_0^q, L_0^q \in \mathbb{C}^{D^q \times D^q}$.

As can be verified easily, the parameterization eq. (4.15) or eq. (4.17) implies that

$$N(\bar{X}, X) = \sum_{q=p^{min}}^{p^{max}} \text{tr} \left((X^q)^\dagger X^q \right).$$

This is also a consequence of eq. (1.28). When B obeys the right gauge fixing condition it follows from eq. (2.6) that $f(\bar{X}, X)$ is minimized with respect to \bar{X} if and only if

$$[X^q]_{\alpha_q, \beta_q} = \frac{\partial H}{\partial [\bar{X}^q]_{\alpha_q, \beta_q}}(\bar{X}, X), \quad (4.19a)$$

$$= \sum_{s=-1,1} \left[(\Xi^q)^{-1/2} (\nabla_{\bar{b}} H)^{q,s} \left(\Lambda^{[q+(s-1)/2]_e} \right)^{-1/2} (v_R^{q,s})^\dagger \right]_{\alpha_q, \beta_q} \quad (4.19b)$$

with

$$[(\nabla_{\bar{b}} H)^{q,s}]_{\alpha_q, \beta_r} = [(\nabla_{\bar{B}} H)^{s,p}]_{(q, \alpha_q), (r, \beta_r)} \delta_{r, [q+(s-1)/2]_e} \delta_{p, q+(s-1)/2} \quad (4.19c)$$

and

$$= \Xi + K_0 + \Xi + h + \Lambda + \Xi + h + A + \Lambda. \quad (4.19d)$$

Here we used the block structure of Ξ , Λ and V_R , see eq. (4.16). Contrary to the TDVP for general states we only need to compute the ‘gauge invariant part’ of $\nabla_{\bar{B}} H$, see eq. (4.19c). Note that, because \mathcal{H} is gauge invariant and because of the block structure of $A^{s,p}$, Ξ and Λ we have also conversely that

$$[(\nabla_{\bar{B}} H)^{s,p}]_{(q, \alpha_q), (r, \beta_r)} = \delta_{r, [q+(s-1)/2]_e} \delta_{p, q+(s-1)/2} [(\nabla_{\bar{b}} H)^{q,s}]_{\alpha_q, \beta_r}.$$

The efficient computation of the matrix $(\nabla_{\bar{b}} H)^{q,s} \in \mathbb{C}^{D^q \times D^{[q+(s-1)/2]_e}}$ will be discussed in (d). Once we obtain $(\nabla_{\bar{b}} H)^{q,s}$, the optimal approximation of $\mathcal{H}_u |\Psi_u[A]\rangle$ is $|\Phi_0[B, A]\rangle$ with

$$[B^{s,p}]_{(q, \alpha_q), (r, \beta_r)} = [b^{q,s}]_{\alpha_q, \beta_r} \delta_{p, q+(s-1)/2} \delta_{r, [q+(s-1)/2]_e}$$

and

$$b^{q,s} = (\Xi^q)^{-1/2} X^q v_R^{q,s} \left(\Lambda^{[q+(s-1)/2]e} \right)^{-1/2}$$

with $[X^q]_{\alpha_q, \beta_q} = [\nabla_{\bar{X}} H]_{(q, \alpha_q); (q, \beta_q)}$.

If B obeys the left gauge fixing condition it follows from eq. (2.8) that

$$\begin{aligned}
 & \text{Diagram: } \text{circle}(\nabla_{\bar{X}} H) \text{ with } (q, \beta_q) \text{ top and } (q, \alpha_q) \text{ bottom} \\
 &= \text{Diagram: } \Xi^{-1/2} \text{ circle}(\nabla_{\bar{B}} H) \text{ with } \Lambda^{-1/2} \text{ circle}(\Lambda^{-1/2}) \text{ top and } V_L \text{ circle}(V_L) \text{ bottom} \\
 &= \sum_{s=-1,1} \left[\left(v_L^{[q+(s-1)/2]e, s} \right)^\dagger \left(\Xi^{[q+(s-1)/2]e} \right)^{-1/2} \right. \\
 & \quad \left. (\nabla_{\bar{B}} H)^{[q+(s-1)/2]e, s} (\Lambda^q)^{-1/2} \right]_{\alpha_q, \beta_q} \tag{4.20a}
 \end{aligned}$$

where we used eq. (4.18) and where

$$\text{Diagram: } \text{circle}(\nabla_{\bar{B}} H) = \text{Diagram: } L_0 \text{ circle}(L_0) \text{ with } A \text{ circle}(A) \text{ top and } \Lambda \text{ circle}(\Lambda) \text{ right} + \Xi \text{ circle}(\Xi) \text{ with } h \text{ rectangle}(h) \text{ top and } \Lambda \text{ circle}(\Lambda) \text{ right} + \Xi \text{ circle}(\Xi) \text{ with } h \text{ rectangle}(h) \text{ top and } A \text{ circle}(A) \text{ bottom} \tag{4.20b}$$

Like for the right gauge fixing condition, gauge invariance of \mathcal{H} and the block structure of $A^{s,p}$, Ξ and Λ implies that

$$\left[(\nabla_{\bar{B}} H)^{s,p} \right]_{(q, \alpha_q), (r, \beta_r)} = \delta_{r, [q+(s-1)/2]e} \delta_{p, q+(s-1)/2} \left[(\nabla_{\bar{B}} H)^{q,s} \right]_{\alpha_q, \beta_r} \tag{4.20c}$$

The computation of $(\nabla_{\bar{B}} H)^{q,s}$ is discussed in (d). Hence, the optimal approximation of $\mathcal{H}_u |\Psi_u[A]\rangle$ is $|\Phi_0[B, A]\rangle$ with

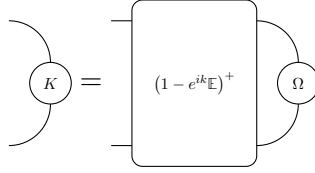
$$b^{q,s} = (\Xi^q)^{-1/2} v_L^{q,s} X^{[q+(s-1)/2]e} \left(\Lambda^{[q+(s-1)/2]e} \right)^{-1/2} .$$

and $[X^q]_{\alpha_q, \beta_q} = [\nabla_{\bar{X}} H]_{(q, \alpha_q); (q, \beta_q)}$.

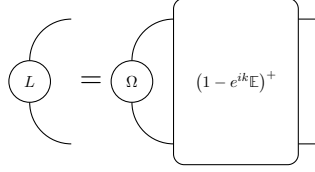
(c) Computing $(1 - e^{ik}\mathbb{E})^+$

To compute K_0 and L_0 we need to take the (pseudo) inverse of $(\mathbb{1} - e^{ik}\mathbb{E})^+$. As already discussed in subsection 1.3.3 this is done by an iterative method

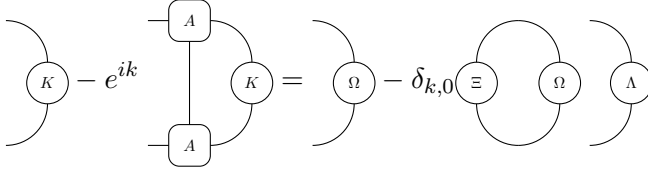
for which we only need the action of $\mathbb{1} - e^{ik}\Xi$ on a matrix. In fact for the computation of matrices that take the form



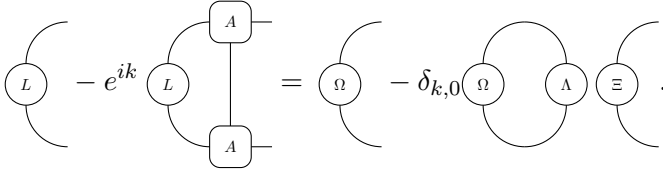
or



we can use the algorithms 1.2 and 1.3. The previous equations are equivalent with



and



For our applications Ω will also be block diagonal: $[\Omega]_{(q,\alpha);(r,\beta)} = \delta_{q,r}[\Omega^q]_{\alpha_q,\beta_r}$. Using the block structure of $A^{s,p}$, Ξ and Λ , it immediately follows that we need to find K^q and L^q such that

$$K^q - e^{ik} \sum_{s=-1,1} a^{q,s} K^{[q+(s-1)/2]} e^{(a^{q,s})^\dagger} = \Omega^q - \delta_{k,0} \left(\sum_{q'=p^{min}}^{p^{max}} \text{tr} \left(\Xi^{q'} \Omega^{q'} \right) \right) \Lambda^q$$

and

$$L^q - e^{ik} \sum_{s=-1,1} \left(a^{[q+(s-1)/2]e,s} \right)^\dagger L^{[q+(s-1)/2]} e^{a^{[q+(s-1)/2]e,s}} = \Omega^q - \delta_{k,0} \left(\sum_{q'=p^{min}}^{p^{max}} \text{tr} \left(\Omega^{q'} \Lambda^{q'} \right) \right) \Xi^q.$$

The algorithms for computing these inverses are presented in algorithms 4.5 and 4.6 and are just resuming algorithms 1.2 and 1.3 with taking into account the previous discussion. The overall computation time scales like

$$\mathcal{O}\left(2N_{iter}P \max_q (D^q)^3\right).$$

Algorithm 4.5 Determine $(\mathbb{1} - e^{ik}\mathbb{E})^+$ acting on the right (\mathcal{CT} and gauge invariant case)

Input: $a, \Omega, k, \Xi, \Lambda$

Output: K .

```

1: function  $K = \text{INVTRANSRIGHT}(a, \Omega, k, \Xi, \Lambda)$ 
2:   if  $k = 0$  then
3:     for  $q = p^{\min} : p^{\max}$  do
4:        $\Omega^q \leftarrow \Omega^q - \delta_{k,0} \left( \sum_{q'=p^{\min}}^{p^{\max}} \text{tr} \left( \Xi^{q'} \Omega^{q'} \right) \right) \Lambda^q$ 
5:     end for
6:   end if
7:    $K = \text{bicgstab}(@K)\text{ApplyTransRight}(K, a, k, \Omega)$ 
8: end function
9: function  $K' = \text{APPLYTRANSRIGHT}(K, a, k)$ 
10:  for  $q = p^{\min} : p^{\max}$  do
11:     $K'^q = K^q - e^{ik} \sum_{s=-1,1} a^{q,s} K^{[q+(s-1)/2]e} (a^{q,s})^\dagger$ 
12:  end for
13: end function

```

Algorithm 4.6 Determine $(\mathbb{1} - e^{ik}\mathbb{E})^+$ acting on the left (\mathcal{CT} and gauge invariant case)

Input: $a, \Omega, k, \Xi, \Lambda$

Output: L .

```

1: function  $L = \text{INVTRANSLEFT}(a, \Omega, k, \Xi, \Lambda)$ 
2:   if  $k = 0$  then
3:     for  $q = p^{\min} : p^{\max}$  do
4:        $\Omega^q \leftarrow \Omega^q - \delta_{k,0} \left( \sum_{q'=p^{\min}}^{p^{\max}} \text{tr} \left( \Omega^{q'} \Lambda^{q'} \right) \right) \Xi^q$ 
5:     end for
6:   end if
7:    $L = \text{bicgstab}(@L)\text{ApplyTransLeft}(L, a, k, \Omega)$ 

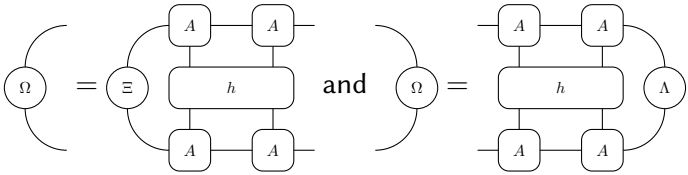
```

```

8: end function
9: function  $L' = \text{APPLYTRANSLEFT}(L,a,k)$ 
10:   for  $q = p^{\min} : p^{\max}$  do
11:      $L'^q = L^q$ 
            $-e^{ik} \sum_{s=-1,1} \left( a^{[q+(s-1)/2]_c, s} \right)^\dagger L^{[q+(s-1)/2]_c} a^{[q+(s-1)/2]_c, s}$ 
12:   end for
13: end function

```

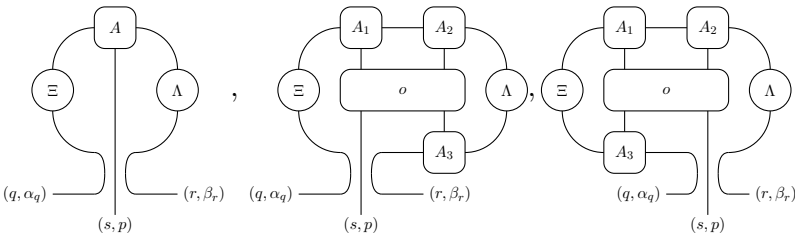
For the computation of K_0 and L_0 we need to apply the algorithms for



Because of eq. (4.14) it follows in both cases that Ω has the required block structure: $[\Omega]_{(q,\alpha_q);(r,\beta_r)} = \delta_{q,r} [\Omega^q]_{\alpha_q, \beta_r}$.

(d) Efficient computation of $\nabla_{\bar{b}} H$

For the computation of $\nabla_{\bar{b}} H$ we need to compute the following type of diagrams:

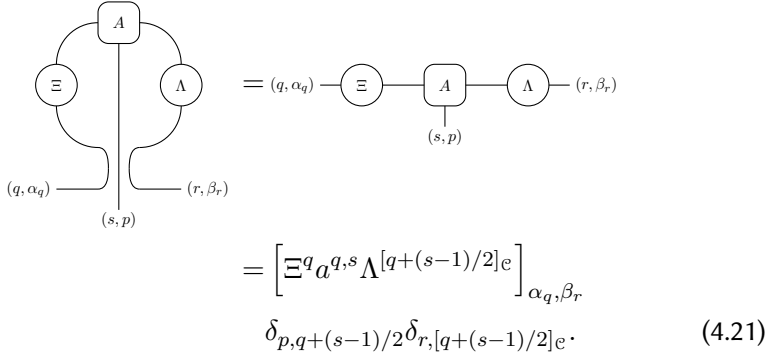


where $p = q + (s - 1)/2$ and $r = [q + (s - 1)/2]_c$, Ξ and Λ are block diagonal and A_n take the form eq. (4.31):

$$[\Xi]_{(q,\alpha_q);(r,\beta_r)} = \delta_{q,r} [\Xi^q]_{\alpha_q, \beta_r}, [\Lambda]_{(q,\alpha_q);(r,\beta_r)} = \delta_{q,r} [\Lambda^q]_{\alpha_q, \beta_r}$$

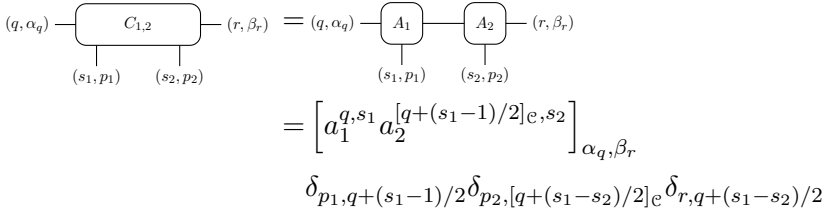
$$[A_n^{s,p}]_{(q,\alpha_q);(r,\beta_r)} = \delta_{p,q+(s-1)/2} \delta_{r,[q+(s-1)/2]_c} [a_n^{q,s}]_{\alpha_q, \beta_r}.$$

The first diagram can be obtained immediately by noting that



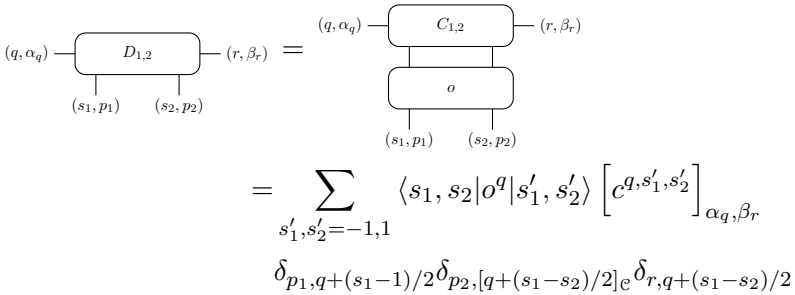
$$\begin{aligned}
 &= \left[\Xi^q a^{q,s} \Lambda^{q+(s-1)/2} \right]_{\alpha_q, \beta_r} \\
 &\quad \delta_{p, q+(s-1)/2} \delta_{r, [q+(s-1)/2]} e. \tag{4.21}
 \end{aligned}$$

For the other two diagrams, we follow the procedure described in subsection 2.1.3, but take now into account the special structure of the matrices. First we compute



$$\begin{aligned}
 &= \left[a_1^{q, s_1} a_2^{[q+(s_1-1)/2] e, s_2} \right]_{\alpha_q, \beta_r} \\
 &\quad \delta_{p_1, q+(s_1-1)/2} \delta_{p_2, [q+(s_1-s_2)/2]} e \delta_{r, q+(s_1-s_2)/2}
 \end{aligned}$$

and apply o :



$$\begin{aligned}
 &= \sum_{s'_1, s'_2 = -1, 1} \langle s_1, s_2 | o^q | s'_1, s'_2 \rangle \left[c^{q, s'_1, s'_2} \right]_{\alpha_q, \beta_r} \\
 &\quad \delta_{p_1, q+(s_1-1)/2} \delta_{p_2, [q+(s_1-s_2)/2]} e \delta_{r, q+(s_1-s_2)/2}
 \end{aligned}$$

(o^q is defined in eq. (4.13)).

Next, we perform the following contractions

$$\begin{aligned}
 & \begin{array}{c} (q, \alpha_q) \text{---} E \text{---} (r, \beta_r) \\ | \\ (s, p) \end{array} = \begin{array}{c} (q, \alpha_q) \text{---} D_{1,2} \\ | \quad | \quad | \\ | \quad | \quad | \\ (s, p) \quad A_3 \quad \Lambda \\ | \quad | \\ (r, \beta_r) \end{array} \\
 &= \sum_{s'=-1,1} \left[d_{1,2}^{q,s,s'} \Lambda^{q+(s-s')/2} \left(a_3^{[q+(s-1)/2]e,s'} \right)^\dagger \right]_{\alpha_q, \beta_r} \\
 & \quad \delta_{p,q+(s-1)/2} \delta_{r,[q+(s-1)/2]e},
 \end{aligned}$$

$$\begin{aligned}
 & \begin{array}{c} (q, \alpha_q) \text{---} F \text{---} (r, \beta_r) \\ | \\ (s, p) \end{array} = \begin{array}{c} D_{1,2} \text{---} (r, \beta_r) \\ | \quad | \\ | \quad | \\ (s, p) \quad A_3 \\ | \\ (q, \alpha_q) \end{array} \\
 &= \sum_{s'=-1,1} \left[\left(a_3^{[q+(s'-1)/2]e,s'} \right)^\dagger \Xi^{q+(s'-1)/2} e \right. \\
 & \quad \left. d_{1,2}^{[q+(s'-1)/2]e,s',s} \right]_{\alpha_q, \beta_r} \delta_{p,q+(s-1)/2} \delta_{r,[q+(s-1)/2]e},
 \end{aligned}$$

hence

$$\begin{aligned}
 & \begin{array}{c} A_1 \quad A_2 \\ | \quad | \\ \Xi \quad o \quad \Lambda \\ | \quad | \quad | \\ (q, \alpha_q) \quad A_3 \quad (r, \beta_r) \\ | \\ (s, p) \end{array} = \begin{array}{c} (q, \alpha_q) \text{---} \Xi \text{---} E \text{---} (r, \beta_r) \\ | \\ (s, p) \end{array} \\
 &= [\Xi^q e^{q,s}]_{\alpha_q, \beta_r} \delta_{p,q+(s-1)/2} \delta_{r,[q+(s-1)/2]e},
 \end{aligned}$$

$$\begin{aligned}
 &= (q, \alpha_q) - F - (s, p) \quad \Lambda - (r, \beta_r) \\
 &= \left[f^{q,s} \Lambda^{[q+(s-1)/2]e} \right]_{\alpha_q, \beta_r} \delta_{p, q+(s-1)/2} \delta_{r, [q+(s-1)/2]e} .
 \end{aligned}$$

The steps are summarized in algorithms 4.7 and 4.8. Algorithm 4.7 concerns the computation of the diagram

$$\text{Diagram (4.22)} \tag{4.22}$$

and algorithm 4.8 concerns the computation of the diagram

$$\text{Diagram (4.23)} \tag{4.23}$$

Both diagrams result in a tensor A_* which has the same form as the A_n

$$[A_*^{s,p}]_{(q, \alpha_q); (r, \beta_r)} = \delta_{p, q+(s-1)/2} \delta_{r, [q+(s-1)/2]e} [a_*^{q,s}]_{\alpha_q, \beta_r} .$$

The computation time is of order

$$\mathcal{O} \left(2^2 N_{iter} P \max_q (D^q)^3 \right) .$$

Algorithm 4.7 Diagram eq. (4.22) for gauge and $\mathbb{C}\mathbb{J}$ invariant MPS

Input: $a_1, a_2, a_3, \Xi, \Lambda, o$

Output: Outcome a_* of the diagram (4.22)

```

1: function  $a_* = \text{COMPUTEDIAGRAM1}(a_1, a_2, a_3, \Xi, \Lambda, o)$ 
2:   for  $q = p^{\min} : p^{\max}$  do
3:     for  $s_1, s_2 = -1, 1$  do
4:        $c_{1,2}^{q, s_1, s_2} = a_1^{q, s_1} a_2^{[q+(s_1-1)/2]_{e, s_2}}$ 
5:     end for
6:   end for
7:   for  $q = p^{\min} : p^{\max}$  do
8:     for  $s_1, s_2 = -1, 1$  do
9:        $d_{1,2}^{q, s_1, s_2} = \sum_{\{s'_k\}} \langle s_1, s_2 | o^q | s'_1, s'_2 \rangle c_{1,2}^{q, s'_1, s'_2}$ 
10:    end for
11:  end for
12:  for  $q = p^{\min} : p^{\max}$  do
13:    for  $s = -1, 1$  do
14:       $e^{q, s} = \sum_{s'=-1,1} \left[ d_{1,2}^{q, s, s'} \Lambda^{q+(s-s')/2} \left( a_3^{[q+(s-1)/2]_{e, s'}} \right)^\dagger \right]$ 
15:       $a_*^{q, s} = \Xi^q e^{q, s}$ 
16:    end for
17:  end for
18: end function

```

Algorithm 4.8 Diagram (4.23) for gauge and \mathcal{CT} invariant MPS

Input: $a_1, a_2, a_3, \Xi, \Lambda, o$

Output: Outcome a_* of the diagram (4.23)

```

1: function  $a_* = \text{COMPUTEDIAGRAM2}(a_1, a_2, a_3, \Xi, \Lambda, o)$ 
2:   for  $q = p^{\min} : p^{\max}$  do
3:     for  $s_1, s_2 = -1, 1$  do
4:        $c_{1,2}^{q, s_1, s_2} = a_1^{q, s_1} a_2^{[q+(s_1-1)/2]_{e, s_2}}$ 
5:     end for
6:   end for
7:   for  $q = p^{\min} : p^{\max}$  do
8:     for  $s_1, s_2 = -1, 1$  do
9:        $d_{1,2}^{q, s_1, s_2} = \sum_{\{s'_k\}} \langle s_1, s_2 | o^q | s'_1, s'_2 \rangle c_{1,2}^{q, s'_1, s'_2}$ 
10:    end for
11:  end for
12:  for  $q = p^{\min} : p^{\max}$  do
13:    for  $s = -1, 1$  do

```

```

14:       $f^{q,s} = \sum_{s'=-1,1} \left( a_3^{[q+(s'-1)/2]e,s'} \right)^\dagger \Xi^{[q+(s'-1)/2]e}$ 
15:       $a_*^{q,s} = f^{q,s} \Lambda^{[q+(s-1)/2]e}$ 
16:      end for
17: end for
18: end function

```

(e) TDVP algorithm for gauge and \mathcal{CT} invariant MPS

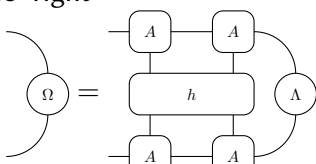
We are finally ready to present the algorithm for the TDVP for gauge and \mathcal{CT} invariant MPS. In algorithm 4.9 we present the ‘gauged \mathcal{CT} invariant version’ of algorithm 2.1. The input is also the same as in algorithm 2.1, but now $A = A(a), \Xi, \Lambda$, have the block structure. ‘stringGaugeFix’ tells us the desired form of b : ‘left’ if we want b to obey the left gauge fixing condition and ‘right’ if we want b to obey the right gauge fixing condition.

Algorithm 4.9 Compute gradient TDVP for gauge and \mathcal{CT} invariant MPS

Input: $a, \Xi, \Lambda, h, \text{stringGaugeFix}$

Output: X, b

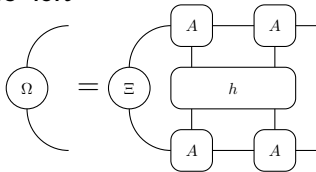
```

1: function  $[X, b] = \text{TDVP}_{\text{DIRECTION}}(a, \Xi, \Lambda, h, \text{stringGaugeFix})$ 
2:    $a_1 = \text{computeDiagram1}(a, a, a, \Xi, \Lambda, h)$  ▷ Algorithm 4.7
3:    $a_2 = \text{computeDiagram2}(a, a, a, \Xi, \Lambda, h)$  ▷ Algorithm 4.8
4:   switch stringGaugeFix do
5:     case ‘right’
6:        ▷ Eq. (4.14)
7:        $K_0 = \text{invTransRight}(A, \Omega, 0, \Xi, \Lambda)$  ▷ Algorithm 4.5
8:       for  $q = p^{\min} : p^{\max}$  do
9:         for  $s = -1, 1$  do
10:           $a_3^{q,s} = \Xi^q a^{q,s} K_0^{[q+(s-1)/2]e}$ 
11:           $(\nabla_b H)^{q,s} = a_1^{q,s} + a_2^{q,s} + a_3^{q,s}$ 
12:        end for
13:      end for
14:       $v_R = \text{computeVR}(a, \Xi, \Lambda)$  ▷ Algorithm 4.3
15:      for  $q = p^{\min} : p^{\max}$  do

```

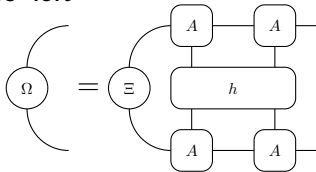
```

16:      
$$X^q = \sum_{s=-1,1} \left[ (\Xi^q)^{-1/2} (\nabla_{\bar{b}} H)^{q,s} \right. \\
\left. \left( \Lambda^{[q+(s-1)/2]e} \right)^{-1/2} \left( v_R^{q,s} \right)^\dagger \right]$$

17:      end for
18:      for  $q = p^{min} : p^{max}$  do
19:          for  $s = -1, 1$  do
20:               $b^{q,s} = (\Xi^q)^{-1/2} X^q v_R^{q,s} \left( \Lambda^{[q+(s-1)/2]e} \right)^{-1/2}$ 
21:          end for
22:      end for
23:      case 'left'
24:          

$\Omega = \Xi$







$\triangleright$  Eq. (4.14)


25:           $L_0 = \text{invTransLeft}(a, \Omega, 0, \Xi, \Lambda)$   $\triangleright$  Algorithm 4.6
26:          for  $q = p^{min} : p^{max}$  do
27:              for  $s = -1, 1$  do
28:                   $a_3^{q,s} = L_0^q a^{q,s} \Lambda^{[q+(s-1)/2]e}$ 
29:                   $(\nabla_{\bar{b}} H)^{q,s} = a_1^{q,s} + a_2^{q,s} + a_3^{q,s}$ 
30:              end for
31:          end for
32:           $v_L = \text{computeVL}(a, \Xi, \Lambda)$   $\triangleright$  Algorithm 4.4
33:          for  $q = p^{min} : p^{max}$  do
34:              
$$X^q = \sum_{s=-1,1} \left[ \left( v_L^{[q+(s-1)/2]e,s} \right)^\dagger \left( \Xi^{[q+(s-1)/2]e} \right)^{-1/2} \right. \\
\left. \left( \nabla_{\bar{b}} H \right)^{[q+(s-1)/2]e,s} \left( \Lambda^q \right)^{-1/2} \right]$$

35:          end for
36:          for  $q = p^{min} : p^{max}$  do
37:              for  $s = -1, 1$  do
38:                   $b^{q,s} = (\Xi^q)^{-1/2} v_L^{q,s} X^{[q+(s-1)/2]e} \left( \Lambda^{[q+(s-1)/2]e} \right)^{-1/2}$ 
39:              end for
40:          end for
41:      end switch
42: end function

```

Now we have rewritten the function ‘TDVPdirection’ we can use the algorithms 2.2 and 2.3 to perform a steepest descent or to perform real-time evolution. For our purpose we want to use 2.2 to find an optimal approximation

$|\Psi_{\mathcal{C}}[A]\rangle$ of the ground state of \mathcal{H} where A is automatically gauge invariant:

$$\begin{array}{c} (q, \alpha_q) \text{---} \boxed{A} \text{---} (r, \beta_r) \\ | \\ (s, p) \end{array} = [a^{q,s}]_{\alpha_q, \beta_r} \delta_{p, q+(s-1)/2} \delta_{r, -p-2\alpha}.$$

The steepest descent just keeps on computing $[X, b] = \text{TDVPdirection}(a, \Xi, \Lambda, h)$ and updates a according to

$$a^{q,s} \leftarrow a^{q,s} - b^{q,s} d\tau$$

for $d\tau$ small. The algorithm has converged to its optimal approximation when

$$\text{normGrad} = \sqrt{\sum_{q=p^{\min}}^{p^{\max}} \text{tr} \left((X^q)^\dagger X^q \right)}$$

is sufficiently small. Instead of normalizing with the general algorithm 1.1, we now have to use algorithm 4.1. With these comments, we conclude that we can apply algorithm 2.2 in exactly the same way, we refer to the pseudocode for the details.

4.1.5. Excitations in the tangent plane

Assume now we have found $|\Psi_{\mathcal{C}}[A]\rangle$ with

$$\begin{array}{c} (q, \alpha_q) \text{---} \boxed{A} \text{---} (r, \beta_r) \\ | \\ (s, p) \end{array} = [a^{q,s}]_{\alpha_q, \beta_r} \delta_{p, q+(s-1)/2} \delta_{r, [p]_{\mathcal{C}}},$$

which is a \mathcal{CT} and gauge invariant MPS approximation for the ground state of \mathcal{H} . Then we can use the tangent vectors $|\Phi_{k,\gamma}^{\mathcal{C}}[B, A]\rangle$, see eq. (3.20), to approximate the one-particle excitations with quantum numbers $(k, \gamma) \in [-\pi, \pi] \times \{-1, 1\}$, see subsection 1.4.2. Gauge invariance is imposed by

$$\begin{array}{c} (q, \alpha_q) \text{---} \boxed{B} \text{---} (r, \beta_r) \\ | \\ (s, p) \end{array} = [b^{q,s}]_{\alpha_q, \beta_r} \delta_{p, q+(s-1)/2} \delta_{r, [p]_{\mathcal{C}}}.$$

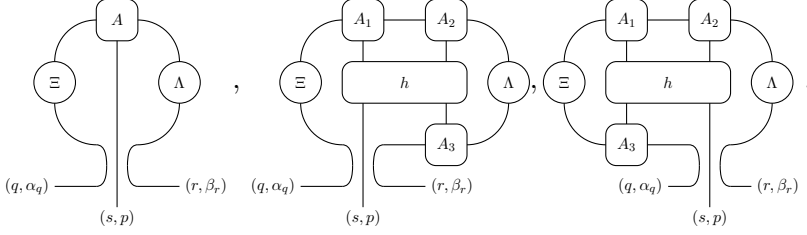
As in the general case, because the excitations should be orthogonal to the ground state we can impose either the left gauge fixing condition eq. (1.19) or the right gauge fixing condition eq. (1.20) on B . In both cases, it is then possible to parameterize B by a matrix X , see eq. (4.17) for the left gauge fixing condition and eq. (4.15) for the right gauge fixing condition. As discussed in section 2.2, the optimal approximation $|\Phi_{k,\gamma}^{\mathcal{C}}[B, A]\rangle$ for the excited states is found by solving the eigenvalue problem

$$\tilde{H}_{[k]_{\gamma}}^{eff}(X) = E_{[k]_{\gamma}} X$$

where $\tilde{H}_{[k]_\gamma}^{eff}(X)$ can be found in eqs. (2.20) and (2.21) and

$$[k]_\gamma = k/2 + \pi \text{ if } \gamma = -1, [k]_\gamma = k/2 \text{ if } \gamma = 1.$$

Let us now assume that B obeys the left gauge fixing condition and thus that b is parameterized as in eq. (4.17). Then in eq. (2.20) $\tilde{H}_{[k]_\gamma}$ is computed and this involves computing diagrams of the form:



These can be computed as discussed in equation eq. (4.21) and algorithms 4.7 and 4.8. Note also that eq. (2.20) involves the computation of the pseudo inverses $(\mathbb{1} - e^{ik}\mathbb{E})^+$ which can be performed using the algorithms 4.5 and 4.6. After performing the contractions in eq. (2.20) we obtain the tensor $\tilde{H}_{[k]_\gamma}[X]$ which takes the form

$$\left[\left(\tilde{H}_{[k]_\gamma}[X] \right)^{s,p} \right]_{(q,\alpha_q),(r,\beta_r)} = \left[\left(\tilde{h}_{[k]_\gamma}[X] \right)^{q,s} \right]_{\alpha_q,\beta_r} \delta_{p,q+(s-1)/2} \delta_{r,-p-2\alpha}.$$

Computing the diagram eq. (2.21) yields then that

$$\left[\tilde{H}_{[k]_\gamma}^{eff}(X) \right]_{(q,\alpha_q),(r,\beta_r)} = \delta_{q,r} \left[\left(\tilde{H}_{[k]_\gamma}^{eff}(X) \right)^q \right]_{\alpha_q,\beta_r}$$

with

$$\left(\tilde{H}_{[k]_\gamma}^{eff}(X) \right)^q = \sum_{s=-1,1} \left[\left(v_L^{[q+(s-1)/2]e,s} \right)^\dagger \left(\Xi^{[q+(s-1)/2]e} \right)^{-1/2} \left(\tilde{h}_{[k]_\gamma}[X] \right)^{[q+(s-1)/2]e,s} \left(\Lambda^q \right)^{-1/2} \right].$$

The eigenvalue equation $\tilde{H}_{[k]_\gamma}^{eff}(X) = E_{[k]_\gamma} X$ thus boils down to finding the blocks $X^q \in \mathbb{C}^{D^q \times D^q}$ of the block diagonal matrix X such that ,

$$\left(\tilde{H}_{[k]_\gamma}^{eff}(X) \right)^q = E_{[k]_\gamma} X^q, q = p^{min}, \dots, p^{max}.$$

The pseudocode is presented in algorithm 4.10 and in fact resumes algorithm 2.4 but takes now into account the special structure of the tensors as discussed above. Again the main function 'ElementaryExcitation' invokes the

iterative eigensolver 'eigs' to find the smallest eigenvalues of 'ApplyHeff'. As discussed above, 'ApplyHeff' computes, given the block diagonal matrix X , $(\tilde{H}_{[k]_\gamma}^{eff}(X))^q$ in

$$\mathcal{O}\left(2^2 P N_{iter} \max_q (D^q)^3\right)$$

time where N_{iter} originates from the computation of L_0, L_2, L_3, L_4 and K_1 that also need an iterative method, see algorithms 4.5 and 4.6. Note that in our case we need to give as input $k \leftarrow [k]_\gamma$.

Algorithm 4.10 Excitations in the tangent plane for \mathcal{CT} and gauge invariant MPS

Input: a, k, h

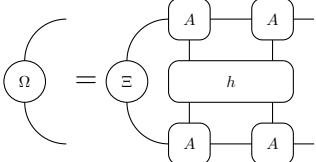
Output: $\{X_k\}, \{\mathcal{E}_k\}$

1: **function** $\{\{X_k\}, \{\mathcal{E}_k\}\} = \text{ELEMENTARYEXCITATION}(a, k, h)$

2: $[a, \Xi, \Lambda] = \text{normalizeUmps}(a)$ ▷ Algorithm 4.1

3:  ▷ Eq. (4.14)

4: $K_0 = \text{invTransRight}(a, \Omega, 0, \Xi, \Lambda)$ ▷ Algorithm 4.5

5:  ▷ Eq. (4.14)

6: $L_0 = \text{invTransLeft}(a, \Omega, 0, \Xi, \Lambda)$ ▷ Algorithm 4.6

7: $v_L = \text{computeVL}(a, \Xi, \Lambda)$ ▷ Algorithm 4.4

8: $\{\{X_k\}, \{\mathcal{E}_k\}\} = \text{eigs}(@X)\text{ApplyHeff}(X, a, K_0, L_0, \Lambda, \Xi, v_L, h, k)$

9: **end function**

10: **function** $H_k^{eff}[X] = \text{APPLYHEFF}(X, a, K_0, L_0, \Lambda, \Xi, v_L, h, k)$

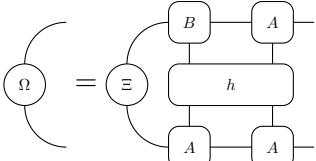
11: **for** $q = p^{min} : p^{max}$ **do**

12: **for** $s = -1, 1$ **do**

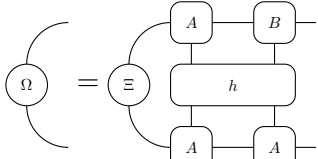
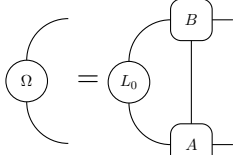
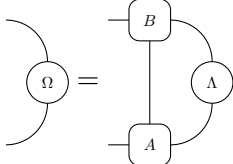
13: $b^{q,s} = (\Xi^q)^{-1/2} v_L^{q,s} X^{[q+(s-1)/2]} e (\Lambda^{[q+(s-1)/2]} e)^{-1/2}$

14: **end for**

15: **end for**

16:  ▷ Eq. (4.14)

17: $L_2 = \text{invTransLeft}(a, \Omega, -k, \Xi, \Lambda)$ ▷ Algorithm 4.6

- 18:  ▷ Eq. (4.14)
- 19: $L_3 = \text{invTransLeft}(a, \Omega, -k, \Xi, \Lambda)$ ▷ Algorithm 4.6
- 20:  ▷ Eq. (4.4)
- 21: $L_4 = \text{invTransLeft}(a, \Omega, -k, \Xi, \Lambda)$ ▷ Algorithm 4.6
- 22:  ▷ Eq. (4.5)
- 23: $K_1 = \text{invTransRight}(a, \Omega, k, \Xi, \Lambda)$ ▷ Algorithm 4.5
- 24: Compute $\tilde{H}_k[X]$, eq. (2.20) ▷ Eq. (4.21), algorithms 4.7 and 4.8
- 25: **for** $q = p^{\min} : p^{\max}$ **do**
- 26:
$$\left(\tilde{H}_k^{\text{eff}}(X) \right)^q = \sum_{s=-1,1} \left[\left(v_L^{[q+(s-1)/2]e,s} \right)^\dagger \right. \\ \left. \left(\Xi^{[q+(s-1)/2]e} \right)^{-1/2} \left(\tilde{h}_k[X] \right)^{[q+(s-1)/2]e,s} \left(\Lambda^q \right)^{-1/2} \right]$$
- 27: **end for**
- 28: **end function**

4.1.6. Application to the Schwinger model

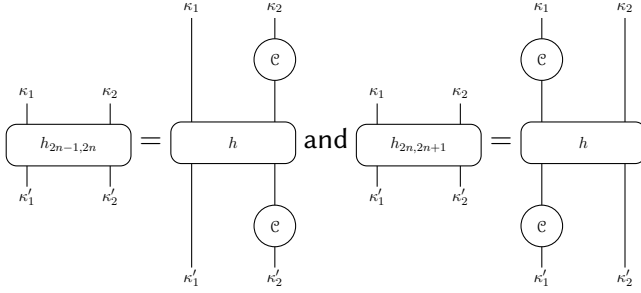
In section 2.1 of part I we apply this formalism to the Schwinger model with $\alpha = 0$, i.e. to the Hamiltonian

$$\mathcal{H} = \frac{g}{2\sqrt{x}} \left(\sum_{n=1}^{2N} L(n)^2 + \frac{\sqrt{x}}{g} m \sum_{n=1}^{2N} (-1)^n (\sigma_z(n) + (-1)^n) \right. \\ \left. + x \sum_{n=1}^{2N-1} (\sigma^+(n) e^{i\theta(n)} \sigma^-(n+1) + h.c.) \right).$$

This Hamiltonian can be rewritten in the form

$$\begin{array}{c} \kappa_1 \quad \dots \quad \kappa_{2N} \\ \text{---} \\ \mathcal{H} \\ \text{---} \\ \kappa_1 \quad \dots \quad \kappa_{2N} \end{array} = \lim_{N \rightarrow +\infty} \sum_{n=1}^{2N-1} \begin{array}{c} \kappa_1 \\ \text{---} \\ \kappa_1' \\ \text{---} \\ \kappa_{n-1} \end{array} \dots \begin{array}{c} \kappa_n \quad \kappa_{n+1} \\ \text{---} \\ h_{n,n+1} \\ \text{---} \\ \kappa_n' \quad \kappa_{n+1}' \end{array} \dots \begin{array}{c} \kappa_{n+2} \\ \text{---} \\ \kappa_{n+2}' \\ \text{---} \\ \kappa_{2N} \end{array}$$

where



if we set

$$h = \frac{g}{2\sqrt{x}} \left(L(1)^2 - \frac{\sqrt{x}}{g} m(\sigma_z(1) - 1) + x(\sigma^+(1)e^{i\theta(1)}\sigma^+(2) + h.c.) \right).$$

By applying the TDVP as in subsection 4.1.4 we obtain the ground state approximation $|\Psi_{\mathcal{C}}[A]\rangle$, with

$$[A^{s,p}]_{(q,\alpha_q);(r,\beta_r)} = [a^{q,s}]_{\alpha_q,\beta_r} \delta_{p,q+(s-1)/2} \delta_{r,-q-(s+1)/2}.$$

In our computations we stopped the steepest descent method when

$$normGrad \approx 5 \times 10^{-9} - 10^{-9}.$$

By normalizing the state we can obtain the Schmidt spectrum and compute entanglement properties like for instance the Von Neumann half chain entropy, see subsection 4.1.2. The energy density ω_0 is computed as

$$\omega_0 = \frac{1}{2\sqrt{x}} \text{Tr} \left(\begin{array}{c} \text{---} A \text{---} A \text{---} \\ | \\ \Xi \text{---} h \text{---} \Lambda \\ | \\ \text{---} A \text{---} A \text{---} \end{array} \right). \tag{4.24}$$

Another quantity that will be discussed is the chiral condensate

$$\Sigma = \langle \bar{\psi} \psi \rangle = \frac{1}{2\sqrt{x}} \text{Tr} \left(\begin{array}{c} \text{---} A \text{---} A \text{---} \\ | \\ \Xi \text{---} o_{\Sigma} \text{---} \Lambda \\ | \\ \text{---} A \text{---} A \text{---} \end{array} \right).$$

with

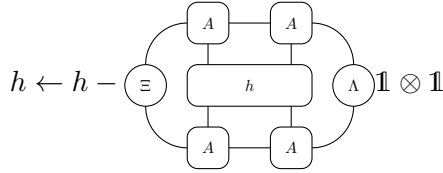
$$o_{\Sigma} = -\frac{1}{2}(\sigma_z(1) + 1).$$

These diagrams can be computed using algorithm 4.2. Therefore we only need the matrix elements

$$\begin{aligned} \langle s_1, s_2 | h^q | s'_1, s'_2 \rangle &= \frac{g}{2\sqrt{x}} \left(\delta_{s_1, s'_1} \delta_{s_2, s'_2} \left((q + s_1 - 1)/2 \right)^2 - \frac{\sqrt{x}}{g} m (s_1 - 1) \right) \\ &\quad + x \delta_{s_1, s_2} \delta_{s'_1, s'_2} \delta_{s_1, -s'_1} \delta_{s_2, -s'_2} \\ \langle s_1, s_2 | o_{\Sigma}^q | s'_1, s'_2 \rangle &= -\delta_{s_1, s'_1} \delta_{s_2, s'_2} \frac{m}{2} (s_1 - 1) \end{aligned}$$

see eq. (4.13)

To find the excitations we set the ground state energy equal to zero, i.e.



and we apply then algorithm 4.10 to find the excitation energies \mathcal{E}_k and the corresponding approximations for the eigenstates $|\Phi_{k,\gamma}^{\mathbb{C}}[B, A]\rangle$ with

$$[B^{s,p}]_{(q,\alpha_q);(r,\beta_r)} = [b^{q,s}]_{\alpha_q,\beta_r} \delta_{p,q+(s-1)/2} \delta_{r,-q-(s+1)/2}.$$

If we want to have a state with physical momentum k_{phys} we need to take $k = k_{phys} \sqrt{x}/2$ in the ansatz $|\Phi_{k,\gamma}^{\mathbb{C}}[B, A]\rangle$.

4.2. Ground state properties and spectrum for $\alpha \neq 0$

4.2.1. Introduction

Let us now turn our attention to the simulation of the Schwinger model with a uniform non-zero background: $\alpha(n) = \alpha \neq 0$. The Hamiltonian now reads

$$\begin{aligned} \mathcal{H} = \frac{g}{2\sqrt{x}} \left(\sum_{n=1}^{2N} [L(n) + \alpha]^2 + \frac{\sqrt{x}}{g} m \sum_{n=1}^{2N} (-1)^n (\sigma_z(n) + (-1)^n) \right. \\ \left. + x \sum_{n=1}^{2N-1} (\sigma^+(n) e^{i\theta(n)} \sigma^-(n+1) + h.c.) \right). \end{aligned}$$

Clearly this Hamiltonian is \mathcal{T}^2 invariant. To approximate the ground state we use the MPS ansatz $|\Psi_u[A]\rangle$ eq. (3.16):

$$|\Psi_u[A]\rangle = \left(v_L^\dagger \right) \text{---} \left(A \right) \text{---} \left(A \right) \text{---} \dots \text{---} \left(A \right) \text{---} \dots \text{---} \left(A \right) \text{---} \left(A \right) \text{---} \left(v_R \right) \quad (4.25a)$$

ζ_1 ζ_2 ζ_n ζ_{N-1} ζ_N

where $\zeta = (s_1, p_1, s_2, p_2)$, $s_i \in \{-1, 1\}$, $p_1 \in \mathbb{Z}[p_2^{\min}, p_2^{\max}]$, $p_2 \in \mathbb{Z}[p_1^{\min}, p_1^{\max}]$. Remember that this ansatz is obtained by blocking the effective sites $2n - 1$ and $2n$ into one effective site n , see subsection 3.3.1. Gauge invariance is imposed as

$$\begin{aligned}
 (q, \alpha_q) \text{---} \boxed{A} \text{---} (r, \beta_r) &= (q, \alpha_q) \text{---} \boxed{A} \text{---} (r, \beta_r) \\
 \downarrow \zeta & \qquad \qquad \downarrow (s_1, p_1, s_2, p_2) \\
 &= [a^{q, s_1, s_2}]_{\alpha_q, \beta_r} \delta_{p_1, q+(s_1-1)/2} \delta_{p_2, q+(s_1+s_2)/2} \delta_{r, p_2}. \quad (4.25b)
 \end{aligned}$$

where $a^{q, s_1, s_2} \in \mathbb{C}^{D^q \times D^r}$. From now we denote $p^{\min} = p_1^{\min}$ and $p^{\max} = p_1^{\max}$. Due to Gauss' law we have that, if we restrict on the even links to the eigenvalues $p \in \mathbb{Z}[p^{\min}, p^{\max}]$ that at the even sites we must restrict to $p \in \mathbb{Z}[p_2^{\min}, p_2^{\max}]$ with $p_2^{\min} \geq p^{\min}$ and $p_2^{\max} \leq p^{\max} + 1$.

Comparing this ansatz with the ansatz in the \mathcal{CT} invariant case from the previous section, see eq. (4.2b), we observe that they are similar. In both cases the variational degrees of freedom are labeled by only one of the physical or virtual indices related to the operator $L(n)$. Starting from the eigenvalue q of $L(2n - 1)$ we can obtain the others by updating them according to Gauss' law. For the \mathcal{CT} invariant case we had to flip the eigenvalues in between, which was related to the \mathcal{CT} eigenvalue; here it is even more straightforwardly. The blocking of the sites comes at the price that the local dimension of the Hilbert space is squared: on each effective site we have now two spin systems corresponding to the matter.

Like in the previous section, we now want to reformulate the TDVP and the search for the excitations using the tangent vectors $|\Phi_k[B, A]\rangle$ on the level of the blocks a^{q, s_1, s_2} . It should be clear that we can use exactly the same ideas as in the previous section. In particular we will find again that the computation time of all the algorithms scales linearly in $P = p^{\max} - p^{\min} + 1$. A difference is now that the outgoing virtual index r of $[A^{s_1, p_1, s_2, p_2}]_{(q, \alpha_q, r, \beta_r)}$ equals $r = p_2 = q + (s_1 + s_2)/2$ instead of $r = [q + (s - 1)/2]_c$. Similar we have that the outgoing index for $\left[(A^{s_1, p_1, s_2, p_2})^\dagger \right]_{(q, \alpha_q, r, \beta_r)}$ is $r = q - (s_1 + s_2)/2$:

$$\left[(A^{s_1, p_1, s_2, p_2})^\dagger \right]_{(q, \alpha_q, r, \beta_r)} = \delta_{r, q-(s_1+s_2)/2} \delta_{p_2, q} \delta_{p_1, q-(s_2+1)/2} a^{q-(s_1+s_2)/2, s_1, s_2}.$$

Therefore, as a rule of thumb, we can just copy all the algorithms and formulas from the previous section by performing the following substitutions:

$$s \rightarrow (s_1, s_2), t \rightarrow (t_1, t_2) \quad (4.26a)$$

$$a^{q, s} \rightarrow a^{q, s_1, s_2}, \left(a^{[q+(s-1)/2]_c, s} \right)^\dagger \rightarrow \left(a^{q-(s_1+s_2)/2, s_1, s_2} \right)^\dagger \quad (4.26b)$$

$$a_1^{q,s} a_2^{[q+(s-1)/2]_{\mathbb{C},t}} \rightarrow a_1^{q,s_1,s_2} a_2^{q+(s_1+s_2)/2,t_2,t_1} \quad (4.26c)$$

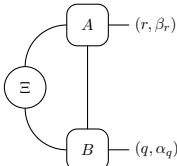
$$\begin{aligned} (a_2^{q+(t-s)/2,t})^\dagger a_1^{[q+(s-1)/2]_{\mathbb{C},s}}^\dagger \rightarrow \\ \left(a_2^{q-(t_1+t_2+s_1+s_2)/2,t_1,t_2} \right)^\dagger \left(a_1^{q-(s_1+s_2)/2,s_1,s_2} \right)^\dagger \end{aligned} \quad (4.26d)$$

with $q = p^{\min}, \dots, p^{\max}$, $s, s_1, s_2, t, t_1, t_2 \in \{-1, 1\}$.

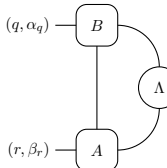
In the next subsections we discuss the optimization methods to find the optimal ground state approximation with TDVP and the optimal tangent vectors to approximate one-particle excitations. Because of the similarities with the $\mathbb{C}\mathcal{T}$ invariant case in the previous section we won't go into full detail and mainly restrict ourselves to the pseudocodes of the algorithms.

4.2.2. Normalization and Schmidt spectrum

To normalize the state we need the action of the transfer matrix Ξ on the block matrices $[\Xi]_{(q,\alpha_q);(r,\beta_r)} = \delta_{q,r} [\Xi^q]_{\alpha_q,\beta_r}$ and $[\Lambda]_{(q,\alpha_q);(r,\beta_r)} = \delta_{q,r} [\Lambda^q]_{\alpha_q,\beta_r}$. For any two tensors A and B of the form eq. (4.25b) with general matrices $a^{q,s_1,s_2}, b^{q,s_1,s_2} \in \mathbb{C}^{D^q \times D^r}$ we have similar to eqs. (4.4) and (4.5):



$$= \delta_{q,r} \left(\sum_{\{s_k\}} \left[\left(a^{q-(s_1+s_2)/2,s_1,s_2} \right)^\dagger \Xi^{q-(s_1+s_2)/2} b^{q-(s_1+s_2)/2,s_1,s_2} \right]_{\alpha_q,\beta_r} \right) \quad (4.27)$$

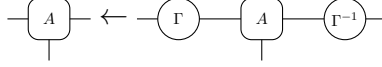


$$= \delta_{q,r} \left(\sum_{\{s_k\}} \left[b^{q,s_1,s_2} \Lambda^{q+(s_1+s_2)/2} \left(a^{q,s_1,s_2} \right)^\dagger \right]_{\alpha_q,\beta_r} \right). \quad (4.28)$$

where $\sum_{\{s_k\}} = \sum_{s_1,s_2=\pm 1}$.

Therefore, to normalize a state and bring it in a desired canonical form, the only difference with respect to algorithm 4.1 is that we need to redefine the

functions ‘ApplyTransferLeft’ and ‘ApplyTransferRight’ which implement the action of the transfer matrix. Now we need to compute the left and right action on the block diagonal matrices according to eqs. (4.27) and eq. (4.28). Another small modification is that now



is equivalent to

$$a^{q,s_1,s_2} \leftarrow \Gamma^q a^{q,s_1,s_2} \left(\Gamma^{q+(s_1+s_2)/2} \right)^{-1}.$$

The pseudocode is presented below in algorithm 4.11.

Algorithm 4.11 Normalization of a gauge and \mathcal{T}^2 invariant MPS

Input: a , stringCanForm

Output: a, Ξ, Λ .

```

1: function  $[a, \Xi, \Lambda, \eta, \Gamma] = \text{NORMALIZEUMPS}(a, \text{stringCanForm})$ 
2:    $[\Xi, \eta] = \text{eigs}(@(\Xi)\text{ApplyTransferLeft}(\Xi, a))$ 
3:    $[\Lambda, \eta] = \text{eigs}(@(\Lambda)\text{ApplyTransferRight}(\Lambda, a))$ 
4:   for  $q = p^{\min} : p^{\max}$  do
5:     for  $s_1, s_2 = -1, 1$  do
6:        $a^{q,s_1,s_2} \leftarrow a^{q,s_1,s_2} / \sqrt{\eta}$ 
7:     end for
8:      $\Xi^q \leftarrow \Xi^q / \text{tr}(\Xi^q)$ 
9:      $\Lambda^q \leftarrow \Lambda^q / \text{tr}(\Lambda^q)$ 
10:    Find matrices  $X^q$  and  $Y^q$  such that  $\Xi^q = X^q (X^q)^\dagger$ ,  $\Lambda^q = (Y^q)^\dagger Y^q$ 
11:     $[U^q, \Sigma^q, V^q] = \text{SVD}(Y^q X^q)$ 
12:     $\Sigma^q \leftarrow \Sigma^q / \sqrt{\text{tr}((\Sigma^q)^2)}$ 
13:    switch stringCanForm do
14:      case ‘left’
15:         $\Gamma^q = \Sigma^q (V^q)^\dagger (X^q)^{-1} = (U^q)^\dagger Y^q$ 
16:         $\Xi^q = \mathbf{1}_{D^q}$ 
17:         $\Lambda^q = (\Sigma^q)^2$ 
18:      case ‘right’
19:         $\Gamma^q = (V^q)^\dagger (X^q)^{-1} = (\Sigma^q)^{-1} (U^q)^\dagger Y^q$ 
20:         $\Xi^q = (\Sigma^q)^2$ 
21:         $\Lambda^q = \mathbf{1}_{D^q}$ 
22:      case ‘symmetric’
23:         $\Gamma^q = (\Sigma^q)^{1/2} (V^q)^\dagger (X^q)^{-1} = (\Sigma^q)^{-1/2} (U^q)^\dagger Y^q$ 
24:         $\Xi^q = \Sigma^q$ 

```

```

25:            $\Lambda^q = \Sigma^q$ 
26:       end switch
27:   end for
28:   for  $q = p^{min} : p^{max}$  do
29:       for  $s_1, s_2 = -1, 1$  do
30:            $a^{q,s} \leftarrow \Gamma^q a^{q,s_1,s_2} (\Gamma^{q+(s_1+s_2)/2})^{-1}$ 
31:       end for
32:   end for
33: end function
34: function  $\Xi' = \text{APPLYTRANSFERLEFT}(\Xi, a)$ 
35:   for  $q = p^{min} : p^{max}$  do
36:        $[\Xi']^q = \sum_{\{s_k\}} \left[ \left( a^{q-(s_1+s_2)/2, s_1, s_2} \right)^\dagger \Xi^{q-(s_1+s_2)/2} a^{q-(s_1+s_2)/2, s_1, s_2} \right]$ 
37:   end for
38: end function
39: function  $\Lambda' = \text{APPLYTRANSFERRIGHT}(\Lambda, a)$ 
40:   for  $q = p^{min} : p^{max}$  do
41:        $[\Lambda']^q = \sum_{\{s_k\}} \left[ a^{q, s_1, s_2} \Lambda^{q+(s_1+s_2)/2} (a^{q, s_1, s_2})^\dagger \right]$ 
42:   end for
43: end function

```

The Schmidt spectrum of the state $|\Psi_u[A]\rangle$ follows now from computing the eigenvalues of $\Xi^q \Lambda^q$ denoted by $\sigma_1^q, \dots, \sigma_{D^q}^q$ with

$$1 \geq \sigma_1^q \geq \sigma_2^q \geq \dots \geq \sigma_{D^q}^q \geq 0, \quad \sum_{q=p^{min}}^{p^{max}} \sum_{\alpha_q=1}^{D^q} \sigma_{\alpha_q}^q = 1.$$

Note that these are the Schmidt values with respect to the bipartition

$$\{\mathcal{A}_1^{2n} = \mathbb{Z}[1, \dots, 2n], \mathcal{A}_2^{2n} = \mathbb{Z}[2n + 1, \dots, 2N]\}$$

of the lattice. The Schmidt spectrum is now independent of the parity of the site where we take the half chain cut. The Schmidt spectrum with respect to a bipartition of the form

$$\{\mathcal{A}_1^{2n-1} = \mathbb{Z}[1, \dots, 2n - 1], \mathcal{A}_2^{2n-1} = \mathbb{Z}[2n, \dots, 2N]\}$$

is obtained by decomposing the effective site consisting of the sites and links $2n - 1$ and $2n$. This will be discussed in subsection 4.3.1. Here we will refer the Schmidt values corresponding to the bipartition \mathcal{A}_1^{2n} and \mathcal{A}_2^{2n} as ‘the’

Schmidt values. ‘The’ Schmidt decomposition reads

$$|\Psi_u[A]\rangle = \sum_{q=p^{\min}}^{p^{\max}} \sum_{\alpha_q=1}^{D^q} \sqrt{\sigma_{\alpha_q}^q} \left| \Phi_{q,\alpha_q}^{2n} \right\rangle \otimes \left| \Phi_{q,\alpha_q}^{2n} \right\rangle$$

where

$$\left| \Phi_{q,\alpha_q}^{2n} \right\rangle \in \bigotimes_{j \in \mathcal{A}_1^{2n}} \mathcal{H}_j \text{ and } \left| \Phi_{q,\alpha_q}^{2n} \right\rangle \in \bigotimes_{j \in \mathcal{A}_2^{2n}} \mathcal{H}_j$$

are orthonormal unit vectors. The quantity S

$$S = - \sum_{q=p^{\min}}^{p^{\max}} \sum_{\alpha=1}^{D^q} \sigma_{\alpha}^q \log(\sigma_{\alpha}^q)$$

then corresponds to the Von Neumann entropy associated to a cut of the lattice between link $[2n]$ and site $2n + 1$.

4.2.3. Calculus

Consider now a local operator of the form:

$$\mathcal{O} = \sum_{n=1}^{2N-1} \tilde{o}_{n,n+1},$$

$$\tilde{o}_{2n-1,2n} = \mathcal{T}^{2n-2} \tilde{o}_{1,2} \mathcal{T}^{2n-2}, \tilde{o}_{2n,2n+1} = \mathcal{T}^{2n-2} \tilde{o}_{2,3} \mathcal{T}^{-2n+2}$$

with $\tilde{o}_{1,2}$ resp. $\tilde{o}_{2,3}$ a local operator acting on sites 1 and 2 resp. 2 and 3. Because we are working on the effective site n consisting of sites $2n - 1$, $2n$ and links $[2n - 1]$ and $[2n]$ we rewrite this sum as

$$\mathcal{O} = \sum_{n=1}^{N-1} o_{n,n+1}$$

where

$$o_{n,n+1} = \mathcal{T}^{n-1} o \mathcal{T}^{n-1}$$

with $o = \tilde{o}_{1,2} + \tilde{o}_{2,3}$ defined on the effective sites 1 and 2 (i.e. on sites 1, 2, 3, 4 and link $[1]$, $[2]$, $[3]$, $[4]$). In components we have

$$\langle \zeta'_1, \zeta'_2 | o | \zeta_1, \zeta_2 \rangle = \langle \kappa'_1, \kappa'_2 | o_{1,2} | \kappa_1, \kappa_2 \rangle \delta_{\zeta'_2, \zeta_2} + \delta_{\kappa'_1, \kappa_1} \delta_{\kappa'_4, \kappa_4} \langle \kappa'_2, \kappa'_3 | o_{2,3} | \kappa_2, \kappa_3 \rangle$$

with

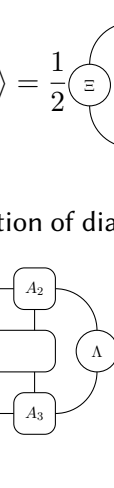
$$\zeta_k = (\kappa_{2k-1}, \kappa_{2k}) = ((s_{2k-1}, p_{2k-1}), (s_{2k}, p_{2k})) = (s_{2k-1}, p_{2k-1}, s_{2k}, p_{2k}),$$

$\zeta'_k = (\kappa'_{2k-1}, \kappa'_{2k}) = ((s'_{2k-1}, p'_{2k-1}), (s'_{2k}, p'_{2k})) = (s'_{2k-1}, p'_{2k-1}, s'_{2k}, p'_{2k})$
 $(s_i, s'_i \in \{-1, 1\}, p_i, p'_i \in \mathbb{Z})$. For further use we define the matrix elements
 (with the notations from above)

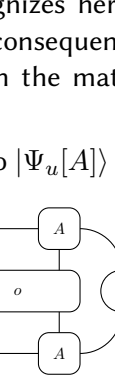
$$\begin{aligned}
 \langle s'_1, s'_2, s'_3, s'_4 | o^q | s_1, s_2, s_3, s_4 \rangle &= \langle \zeta'_1, \zeta'_2 | o | \zeta_1, \zeta_2 \rangle \\
 \delta_{p'_1, q+(s'_1-1)/2} \delta_{p'_2, q+(s'_1+s'_2)/2} \delta_{p'_3, q+(s'_1+s'_2+s'_3-1)/2} \delta_{p'_4, q+(s'_1+s'_2+s'_3+s'_4)/2} \\
 \delta_{p_1, q+(s_1-1)/2} \delta_{p_2, q+(s_1+s_2)/2} \delta_{p_3, q+(s_1+s_2+s_3-1)/2} \delta_{p_4, q+(s_1+s_2+s_3+s_4)/2} \\
 \delta_{s_1+s_2+s_3+s_4, s'_1+s'_2+s'_3+s'_4} \delta_{p_4, p'_4} \quad (4.29)
 \end{aligned}$$

The interpretation of the matrix elements $\langle s'_1, s'_2, s'_3, s'_4 | o^q | s_1, s_2, s_3, s_4 \rangle$ is that they equal the general matrix elements $\langle \zeta'_1, \zeta'_2 | o | \zeta_1, \zeta_2 \rangle$ where we take into account Gauss' law. Thereby we interpret the q as the incoming eigenvalue of $L(n)$. Given the charges s_i and s'_i on the matter sites, the Kronecker delta's indeed reflect Gauss' law which tells us to compute p_i from p_{i-1} and s_i as $p_i = p_{i-1} + (s_i + (-1)^i)/2$. One recognizes here the matrix elements occurring in eq. (3.27) for $K = 4$. As a consequence, the computation of the expectation values only depends on the matrix elements $\langle s'_1, s'_2, s'_3, s'_4 | o^q | s_1, s_2, s_3, s_4 \rangle$.

For the expectation value per site of \mathcal{O} with respect to $|\Psi_u[A]\rangle$ we have

$$\lim_{N \rightarrow +\infty} \frac{1}{2N} \langle \Psi_u[A] | \mathcal{O} | \Psi_u[A] \rangle = \frac{1}{2} \langle \Xi | \mathcal{O} | \Lambda \rangle$$


Let us therefore consider the computation of diagrams of the form



$$\langle \Xi | \mathcal{O} | \Lambda \rangle \quad (4.30)$$

where A_n has the block structure

$$[A_n^{s_1, p_1, s_2, p_2}]_{(q, \alpha_q), (r, \beta_r)} = [a^{q, s_1, s_2}]_{\alpha_q, \beta_r} \delta_{p_1, q+(s_1-1)/2} \delta_{p_2, q+(s_1+s_2)/2} \delta_{r, p_2} \quad (4.31)$$

and Ξ and Λ are block diagonal

$$[\Xi]_{(q, \alpha_q), (r, \beta_r)} = [\Xi^q]_{\alpha_q, \beta_r} \delta_{q, r}, [\Lambda]_{(q, \alpha_q), (r, \beta_r)} = [\Lambda^q]_{\alpha_q, \beta_r} \delta_{q, r} \quad (4.32)$$

and o can be any operator acting on two effective sites.

which is similar to eq. (4.14). The expectation value can now be computed easily:

$$= \sum_{q=p^{\min}}^{p^{\max}} \text{tr}(\Xi^q \Omega^q).$$

The pseudocode is given below

Algorithm 4.12 Expectation value of a gauge and \mathcal{T}^2 invariant MPS

Input: $a_1, a_2, a_3, a_4, \Xi, \Lambda, o$

Output: Outcome of the diagram (4.30)

```

1: function  $\langle o \rangle = \text{EXPVALMPS}(a_1, a_2, a_3, a_4, \Xi, \Lambda, o)$ 
2:   for  $q = p^{\min} : p^{\max}$  do
3:     for  $s_1, s_2, s_3, s_4 = -1, 1$  do
4:        $c_{1,2}^{q, s_1, s_2, s_3, s_4} = a_1^{q, s_1, s_2} a_2^{q + (s_1 + s_2)/2, s_3, s_4}$ 
5:        $c_{4,3}^{q, s_1, s_2, s_3, s_4} = a_4^{q, s_1, s_2} a_3^{q + (s_1 + s_2)/2, s_3, s_4}$ 
6:     end for
7:   end for
8:   for  $q = p^{\min} : p^{\max}$  do
9:     for  $s_1, s_2, s_3, s_4 = -1, 1$  do
10:       $d_{1,2}^{q, s_1, s_2, s_3, s_4} = \sum_{\{s'_k\}} \langle s_1, s_2, s_3, s_4 | o^q | s'_1, s'_2, s'_3, s'_4 \rangle c_{1,2}^{q, s'_1, s'_2, s'_3, s'_4}$ 
11:    end for
12:     $\Omega^q = \sum_{\{s_k\}} d_{1,2}^{q, s_1, s_2, s_3, s_4} \Lambda^{q + (s_1 + s_2 + s_3 + s_4)/2} \left( c_{4,3}^{q, s_1, s_2, s_3, s_4} \right)^\dagger$ 
13:  end for
14:   $\langle o \rangle = \sum_{q=p^{\min}}^{p^{\max}} \text{tr}(\Xi^q \Omega^q)$ 
15: end function
    
```

4.2.4. TDVP

According to the TDVP, see section 2.1, given a state $|\Psi_u[A]\rangle$, we have to find B such that it minimizes

$$\| |\mathcal{H}|\Psi_u[A]\rangle - |\Phi_0[B, A]\rangle \|_2 \text{ with } \langle \Phi_0[\bar{B}, \bar{A}] | \Psi_u[A] \rangle = 0.$$

Now A and B take the form eq. (4.25b):

$$[A^{s_1, p_1, s_2, p_2}]_{(q, \alpha_q); (r, \beta_r)} = [a^{q, s_1, s_2}]_{\alpha_q, \beta_r} \delta_{p_1, q + (s_1 - 1)/2} \delta_{p_2, q + (s_1 + s_2)/2} \delta_{r, p_2}, \quad (4.34a)$$

$$[B^{s_1,p_1,s_2,p_2}]_{(q,\alpha_q);(r,\beta_r)} = [b^{q,s_1,s_2}]_{\alpha_q,\beta_r} \delta_{p_1,q+(s_1-1)/2} \delta_{p_2,q+(s_1+s_2)/2} \delta_{r,p_2}, \quad (4.34b)$$

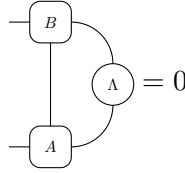
Here we assume that \mathcal{H} is gauge invariant and of the form

$$\mathcal{H} = \sum_{n=1}^{N-1} \mathcal{T}^{n-1} h \mathcal{T}^{-n+1}$$

where h acts only non-trivially on the effective sites 1 and 2 (i.e. on sites 1, 2, 3, 4 and link [1], [2], [3] and [4]).

(a) Gauge fixing in the tangent plane

Because of eq. (4.28), when B obeys the right gauge fixing condition



we can parameterize b^{q,s_1,s_2} by a block diagonal matrix with blocks $X^q \in \mathbb{C}^{D^q \times n_R^q}$:

$$b^{q,s_1,s_2} = (\Xi^q)^{-1/2} X^q v_R^{q,s_1,s_2} \left(\Lambda^{q+(s_1+s_2)/2} \right)^{-1/2} \quad (4.35)$$

where $v_R^q \in \mathbb{C}^{n_R^q \times D^{q+(s_1+s_2)/2}}$ can be obtained from algorithm 4.13. This algorithm is similar to algorithm 4.3 for the \mathcal{CT} invariant case. As discussed in that algorithm the command 'nullLeft', line 12, determines the matrix $\tilde{V}_R^q \in \mathbb{C}^{n_R^q \times F^q}$ such that the rows of \tilde{V}_R^q form an orthonormal basis for the left zero space of $W_R^q \in \mathbb{C}^{F^q \times D^q}$. Here we have that

$$F^q = \sum_{q=p^{min}}^{p^{max}} \sum_{\{s_k\}} D^{q+(s_1+s_2)/2}$$

and $n_R^q \geq F^q - D^q$ is the dimension of the kernel of W_r^q .

Algorithm 4.13 Compute v_R for gauge and \mathcal{T}^2 invariant MPS

Input: a, Ξ, Λ

Output: Tensor v_R which allows parameterization eq. (4.35)

1: **function** $v_R = \text{COMPUTEVR}(a, \Xi, \Lambda)$

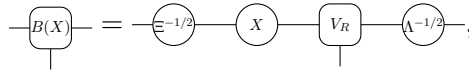
2: **for** $q = p^{min} : p^{max}$ **do**

```

3:   for  $s_1, s_2 = -1, 1$  do
4:     for  $\beta_q = 1 : D^q$  do
5:       for  $\alpha_r = 1 : D^{q+(s_1+s_2)/2}$  do
6:          $[W_R^q]_{(\alpha_r, s_1, s_2), \beta_q} = \left[ (\Lambda^{q+(s_1+s_2)/2})^{1/2} (a^{q, s_1, s_2})^\dagger \right]_{\alpha_r, \beta_q}$ 
7:       end for
8:     end for
9:   end for
10:  end for
11:  for  $q = p^{min} : p^{max}$  do
12:     $\tilde{V}_R^q = \text{nullLeft}(W_R^q)$ 
13:  end for
14:  for  $q = p^{min} : p^{max}$  do
15:    for  $s_1, s_2 = -1, 1$  do
16:      for  $\alpha_q = 1 : n_R^q$  do  $\triangleright n_R^q$  is rank of  $\tilde{V}_R^q$ 
17:        for  $\beta_r = 1 : D^{q+(s_1+s_2)/2}$  do
18:           $[v_R^{q, s_1, s_2}]_{\alpha_q, \beta_r} = [\tilde{V}_R^q]_{\alpha_q, (\beta_r, s_1, s_2)}$ 
19:        end for
20:      end for
21:    end for
22:  end for
23: end function

```

The parameterization eq. (1.25),



is recovered if we put

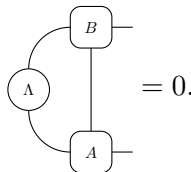
$$[X]_{(q, \alpha_q), (r, \beta_r)} = \delta_{q,r} [X^q]_{\alpha_q, \beta_r},$$

$$[V_R^{s_1, p_1, s_2, p_2}]_{(q, \alpha_q); (r, \beta_r)} = [v_R^{q, s_1, s_2}]_{\alpha_q, \beta_r} \delta_{p_1, q+(s_1-1)/2} \delta_{p_2, q+(s_1+s_2)/2} \delta_{r, p_2}.$$

Note that $\tilde{V}_R^q (\tilde{V}_R^q)^\dagger = \mathbb{1}_{n_R^q}$ implies that

$$\sum_{\{s_k\}} v_R^{q, s_1, s_2} (v_R^{q, s_1, s_2})^\dagger = \mathbb{1}_{n_R^q}.$$

Similarly, if B obeys the left gauge fixing condition,



b^{q,s_1,s_2} can be parameterized by $X^q \in \mathbb{C}^{n_L^q \times D^q}$:

$$b^{q,s_1,s_2} = (\Xi^q)^{-1/2} v_L^{q,s_1,s_2} X^{q+(s_1+s_2)/2} \left(\Lambda^{q+(s_1+s_2)/2} \right)^{-1/2}. \quad (4.36)$$

The pseudocode to obtain $v_L^{q,s_1,s_2} \in \mathbb{C}^{D^q \times n_L^{q+(s_1+s_2)/2}}$ is presented below, algorithm 4.14. Here the command ‘nullRight’, determines $\tilde{V}_L^q \in \mathbb{C}^{F^q \times n_L^q}$ such that the columns of \tilde{V}_L^q form an orthonormal basis for the right zero space of $W_L^q \in \mathbb{C}^{D^q \times F^q}$, with

$$F^q = \sum_{q=p^{min}}^{p^{max}} \sum_{\{s_k\}} D^{q-(s_1+s_2)/2}$$

and $n_L^q \geq F^q - D^q$.

Algorithm 4.14 Compute v_L for gauge and \mathcal{T}^2 invariant MPS

Input: a, Ξ, Λ

Output: Tensor v_L which allows parameterization (4.36)

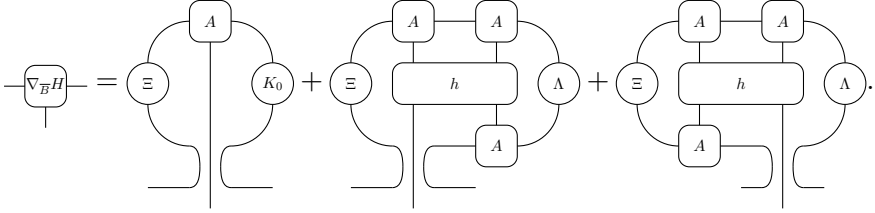
```

1: function  $v_L = \text{COMPUTEVL}(a, \Xi, \Lambda)$ 
2:   for  $q = p^{min} : p^{max}$  do
3:     for  $s_1, s_2 = -1, 1$  do
4:       for  $\alpha_q = 1 : D^q$  do
5:         for  $\beta_r = 1 : D^{q-(s_1+s_2)/2}$  do
6:            $[W_L^q]_{\alpha_q, (\beta_r, s_1, s_2)} = \left[ \begin{array}{l} \left( a^{q-(s_1+s_2)/2, s_1, s_2} \right)^\dagger \\ \left( \Xi^{q-(s_1+s_2)/2, s_1, s_2} \right)^{1/2} \end{array} \right]_{\alpha_q, \beta_r}$ 
7:         end for
8:       end for
9:     end for
10:  end for
11:  for  $q = p^{min} : p^{max}$  do
12:     $\tilde{V}_L^q = \text{nullRight}(W_R^q)$ 
13:  end for
14:  for  $q = p^{min} : p^{max}$  do
15:    for  $s_1, s_2 = -1, 1$  do
16:      for  $\alpha_q = 1 : D^q$  do
17:        for  $\beta_r = 1 : n_L^{q+(s_1+s_2)/2}$  do  $\triangleright n_L^q$  is rank of  $\tilde{V}_L^q$ 
18:           $[v_L^{q,s_1,s_2}]_{\alpha_q, \beta_r} = \left[ \tilde{V}_L^{q+(s_1+s_2)/2, s_1, s_2} \right]_{(\alpha_q, s_1, s_2), \beta_r}$ 
19:        end for

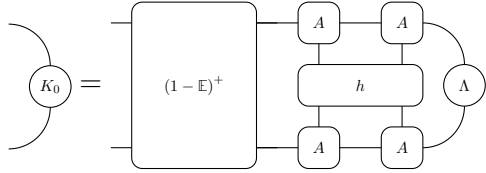
```


$$[(\nabla_{\bar{b}}H)^{q,s_1,s_2}]_{\alpha_q,\beta_r} = [(\nabla_{\bar{B}}H)^{s_1,p_1,s_2,p_2}]_{(q,\alpha_q),(r,\beta_r)} \delta_{p_1,q+(s_1-1)/2} \delta_{p_2,q+(s_1+s_2)/2} \delta_{r,p_2}$$

and



As usual we introduced



The computation of K_0 will be discussed in (c) and the computation of $(\nabla_{\bar{b}}H)^{q,s_1,s_2}$ will be discussed in (d).

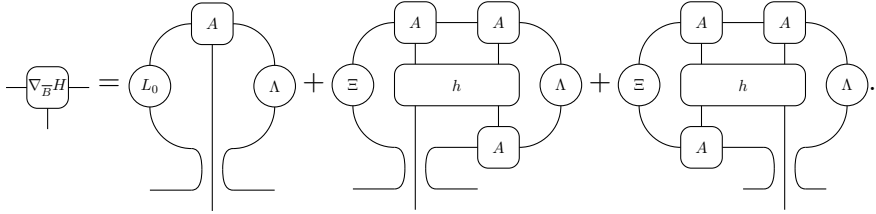
If B obeys the left gauge fixing condition, we find as in eq. (4.20) that the solution X equals

$$[X^q]_{\alpha_q,\beta_q} = [\nabla_X H]_{(q,\alpha_q);(q,\beta_q)},$$

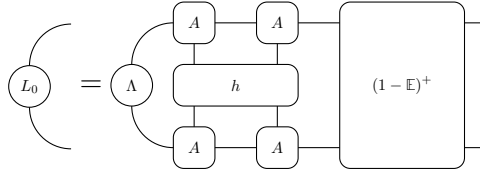
with

$$\begin{aligned} & \left(\nabla_{\bar{X}} H \right)_{(q,\alpha_q);(q,\beta_q)} = \Xi^{-1/2} \left(\nabla_{\bar{B}} H \right)_{(q,\alpha_q);(q,\beta_q)} \Lambda^{-1/2} \\ & = \sum_{\{s_k\}} \left[\left(v_L^{q-(s_1+s_2)/2,s_1,s_2} \right)^\dagger \left(\Xi^{q-(s_1+s_2)/2} \right)^{-1/2} \right. \\ & \quad \left. \left(\nabla_{\bar{b}} H \right)^{q-(s_1+s_2)/2,s_1,s_2} (\Lambda^q)^{-1/2} \right]_{\alpha_q,\beta_q}, \end{aligned}$$

$$[(\nabla_{\bar{b}}H)^{q,s_1,s_2}]_{\alpha_q,\beta_r} = [(\nabla_{\bar{B}}H)^{s_1,p_1,s_2,p_2}]_{(q,\alpha_q),(r,\beta_r)} \delta_{p_1,q+(s_1-1)/2} \delta_{p_2,q+(s_1+s_2)/2} \delta_{r,p_2},$$



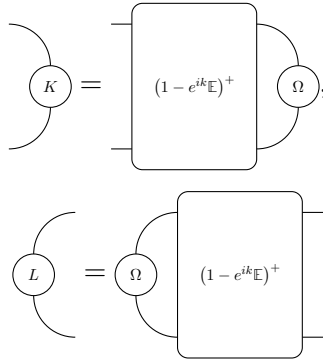
The computation of L_0 ,



will be discussed in (c) and the computation of $(\nabla_{\bar{b}} H)^{q, s_1, s_2}$ in (d).

(c) Computing $(1 - e^{ik}\mathbb{E})^+$

If Ω is block diagonal, $[\Omega]_{(q,\alpha);(r,\beta)} = \delta_{q,r} [\Omega^q]_{\alpha_q, \beta_r}$, the equations



are equivalent to

$$K^q - e^{ik} \sum_{\{s_k\}} a^{q, s_1, s_2} K^{q+(s_1+s_2)/2} (a^{q, s_1, s_2})^\dagger = \Omega^q - \delta_{k,0} \left(\sum_{q'=p^{min}}^{p^{max}} \text{tr} \left(\Xi^{q'} \Omega^{q'} \right) \right) \Lambda^q$$

and

$$L^q - e^{ik} \sum_{\{s_k\}} \left(a^{q-(s_1+s_2)/2, s_1, s_2} \right)^\dagger L^{q-(s_1+s_2)/2} a^{q-(s_1+s_2)/2, s_1, s_2} = \Omega^q - \delta_{k,0} \left(\sum_{q'=p^{min}}^{p^{max}} \text{tr} \left(\Omega^{q'} \Lambda^{q'} \right) \right) \Xi^q.$$

Therefore K and L can be computed with a method that solves the previous equations iteratively in

$$\mathcal{O} \left(4N_{iter} P \max_q (D^q)^3 \right)$$

time. The algorithms for computing these inverses are presented in the pseudocode of algorithms 4.15 and 4.16 and are very similar to the algorithms 4.5 and 4.6 for the \mathcal{CT} invariant case.

Algorithm 4.15 Determine $(\mathbb{1} - e^{ik}\mathbb{E})^+$ acting on the right (\mathcal{T}^2 and gauge invariant case)

Input: $a, \Omega, k, \Xi, \Lambda$

Output: K .

```

1: function  $K = \text{INVTRANSRIGHT}(a, \Omega, k, \Xi, \Lambda)$ 
2:   if  $k = 0$  then
3:     for  $q = p^{\min} : p^{\max}$  do
4:        $\Omega^q \leftarrow \Omega^q - \delta_{k,0} \left( \sum_{q'=p^{\min}}^{p^{\max}} \text{tr} \left( \Xi^{q'} \Omega^{q'} \right) \right) \Lambda^q$ 
5:     end for
6:   end if
7:    $K = \text{bicgstab}(@\{K\}\text{ApplyTransRight}(K, a, k), \Omega)$ 
8: end function
9: function  $K' = \text{APPLYTRANSRIGHT}(K, a, k)$ 
10:  for  $q = p^{\min} : p^{\max}$  do
11:     $K'^q = K^q - e^{ik} \sum_{\{s_k\}} a^{q, s_1, s_2} K^{q+(s_1+s_2)/2} (a^{q, s_1, s_2})^\dagger$ 
12:  end for
13: end function

```

Algorithm 4.16 Determine $(\mathbb{1} - e^{ik}\mathbb{E})^+$ acting on the left (\mathcal{T}^2 and gauge invariant case)

Input: $a, \Omega, k, \Xi, \Lambda$

Output: L .

```

1: function  $L = \text{INVTRANSLEFT}(a, \Omega, k, \Xi, \Lambda)$ 
2:   if  $k = 0$  then
3:     for  $q = p_{\min} : p_{\max}$  do
4:        $\Omega^q \leftarrow \Omega^q - \delta_{k,0} \left( \sum_{q'=p^{\min}}^{p^{\max}} \text{tr} \left( \Omega^{q'} \Lambda^{q'} \right) \right) \Xi^q$ 

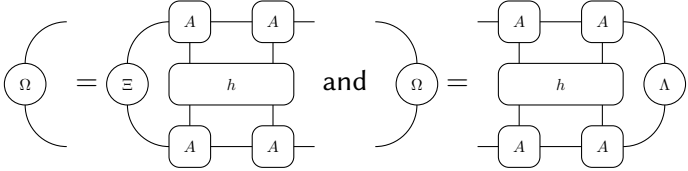
```

```

5:      end for
6:      end if
7:       $L = \text{bicgstab}(@L)\text{ApplyTransLeft}(L,a,k),\Omega$ 
8:  end function
9:  function  $L' = \text{APPLYTRANSLEFT}(L,a,k)$ 
10:     for  $q = p^{\min} : p^{\max}$  do
11:          $L'^q = L^q - e^{ik} \sum_{\{s_k\}} \left( a^{q-(s_1+s_2)/2, s_1, s_2} \right)^\dagger$ 
 $L^{q-(s_1+s_2)/2} a^{q-(s_1+s_2)/2, s_1, s_2}$ 
12:     end for
13: end function

```

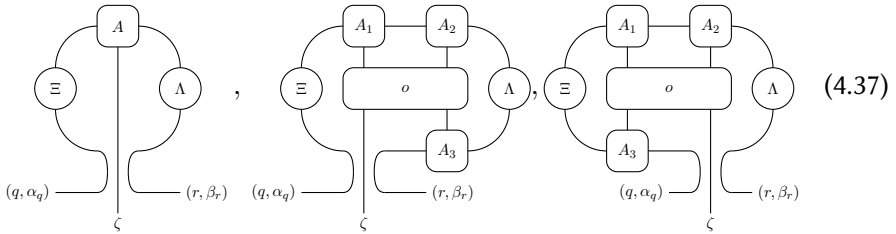
For the computation of K_0 and L_0 we need to apply the algorithms for



where Ω can be computed as in eq. (4.33).

(d) Efficient computation of $\nabla_{\bar{b}} H$

For the computation of $\nabla_{\bar{b}} H$ we need to compute the following type of diagrams:



where $\zeta = (s_1, p_1, s_2, p_2)$, $p_1 = q + (s_1 - 1)/2$, $r = p_2 = q + (s_1 + s_2)/2$, Ξ and Λ are block diagonal and A_n take the form eq. (4.34):

$$[\Xi]_{(q, \alpha_q); (r, \beta_r)} = \delta_{q,r} [\Xi^q]_{\alpha_q, \beta_r}, \quad [\Lambda]_{(q, \alpha_q); (r, \beta_r)} = \delta_{q,r} [\Lambda^q]_{\alpha_q, \beta_r}$$

$$[A_n^{s_1, p_1, s_2, p_2}]_{(q, \alpha_q); (r, \beta_r)} = \delta_{p_1, q + (s_1 - 1)/2} \delta_{p_2, q + (s_1 + s_2)/2} \delta_{r, p_2} [a_n^{q, s_1, s_2}]_{\alpha_q, \beta_r}.$$

For the first diagram we find

$$\begin{aligned}
 &= \left[\Xi^q a^{q, s_1, s_2} \Lambda^{q+(s_1+s_2)/2} \right]_{\alpha_q, \beta_r} \\
 &\quad \delta_{p_1, q+(s_1-1)/2} \delta_{r, p_2} \delta_{r, q+(s_1+s_2)/2}. \quad (4.38)
 \end{aligned}$$

with $\zeta = (s_1, p_1, s_2, p_2)$.

To compute the two other diagrams, as in subsection 2.1.3, we start with

$$\begin{aligned}
 &= \left[a_1^{q, s_1, s_2} a_2^{q+(s_1+s_2)/2, s_3, s_4} \right]_{\alpha_q, \beta_r} \\
 &\quad \delta_{p_1, q+(s_1-1)/2} \delta_{p_2, q+(s_1+s_2)/2} \delta_{p_3, q+(s_1+s_2+s_3-1)/2} \\
 &\quad \delta_{p_4, q+(s_1+s_2+s_3+s_4)/2} \delta_{r, p_4}
 \end{aligned}$$

($\zeta_k = (s_{2k-1}, p_{2k-1}, s_{2k}, p_{2k})$) and then apply o :

$$\begin{aligned}
 &= \sum_{\{s'_k\}} \langle s_1, s_2, s_3, s_4 | o^q | s'_1, s'_2, s'_3, s'_4 \rangle \left[c^{q, s'_1, s'_2, s'_3, s'_4} \right]_{\alpha_q, \beta_r} \\
 &\quad \delta_{p_1, q+(s_1-1)/2} \delta_{p_2, q+(s_1+s_2)/2} \delta_{p_3, q+(s_1+s_2+s_3-1)/2} \\
 &\quad \delta_{p_4, q+(s_1+s_2+s_3+s_4)/2} \delta_{r, p_4}
 \end{aligned}$$

($\langle s_1, s_2, s_3, s_4 | o^q | s'_1, s'_2, s'_3, s'_4 \rangle$ is defined in eq. (4.29)).

The outcome of the diagrams eq. (4.37) can now easily be computed:

Next, we perform the following contractions ($\zeta = (s_1, p_1, s_2, p_2)$)

$$\begin{aligned}
 (q, \alpha_q) \text{---} E \text{---} (r, \beta_r) &= \begin{array}{c} (q, \alpha_q) \text{---} D_{1,2} \\ | \quad | \quad | \\ | \quad | \quad | \\ \zeta \quad | \quad | \\ \quad \quad A_3 \\ \quad \quad | \\ \quad \quad (r, \beta_r) \end{array} \quad \Lambda \\
 &= \sum_{\{s'_k\}} \left[d_{1,2}^{q, s_1, s_2, s'_1, s'_2} \Lambda^{q+(s_1+s_2+s'_1+s'_2)/2} \right. \\
 &\quad \left. \left(a_3^{q+(s_1+s_2)/2, s'_1, s'_2} \right)^\dagger \right]_{\alpha_q, \beta_r} \\
 &\quad \delta_{p_1, q+(s_1-1)/2} \delta_{p_2, q+(s_1+s_2)/2} \delta_{r, p_2},
 \end{aligned}$$

$$\begin{aligned}
 (q, \alpha_q) \text{---} F \text{---} (r, \beta_r) &= \begin{array}{c} (q, \alpha_q) \text{---} \Xi \\ | \quad | \quad | \\ | \quad | \quad | \\ \zeta \quad | \quad | \\ \quad \quad A_3 \\ \quad \quad | \\ \quad \quad (q, \alpha_q) \end{array} \quad D_{1,2} \text{---} (r, \beta_r) \\
 &= \sum_{\{s'_k\}} \left[\left(a_3^{q-(s'_1+s'_2)/2, s'_1, s'_2} \right)^\dagger \Xi^{q-(s'_1+s'_2)/2} \right. \\
 &\quad \left. d_{1,2}^{q-(s'_1+s'_2)/2, s'_1, s'_2, s_1, s_2} \right]_{\alpha_q, \beta_r} \\
 &\quad \delta_{p_1, q+(s_1-1)/2} \delta_{p_2, q+(s_1+s_2)/2} \delta_{r, p_2},
 \end{aligned}$$

hence

$$\begin{aligned}
 \begin{array}{c} \Xi \text{---} A_1 \text{---} A_2 \text{---} \Lambda \\ | \quad | \quad | \\ | \quad | \quad | \\ \zeta \quad | \quad | \\ \quad \quad o \\ \quad \quad | \\ \quad \quad A_3 \\ \quad \quad | \\ \quad \quad (r, \beta_r) \end{array} &= (q, \alpha_q) \text{---} \Xi \text{---} E \text{---} (r, \beta_r) \\
 &= [\Xi^q e^{q, s_1, s_2}]_{\alpha_q, \beta_r} \delta_{p_1, q+(s_1-1)/2} \delta_{p_2, q+(s_1+s_2)/2} \delta_{r, p_2},
 \end{aligned}$$

$$\begin{aligned}
 & \text{Diagram with nodes } A_1, A_2, A_3, o, \Xi, \Lambda \text{ and legs } (q, \alpha_q), (r, \beta_r), \zeta \\
 &= (q, \alpha_q) - [F] - \Lambda - (r, \beta_r) \\
 & \quad \quad \quad \zeta \\
 &= \left[f^{q, s_1, s_2} \Lambda^{q+(s_1+s_2)/2} \right]_{\alpha_q, \beta_r} \\
 & \quad \delta_{p_1, q+(s_1-1)/2} \delta_{p_2, q+(s_1+s_2)/2} \delta_{r, p_2}
 \end{aligned}$$

The steps are summarized in algorithms 4.17 and 4.18. The algorithm 4.17 gives the outcome of the diagram

$$\text{Diagram (4.39)} \tag{4.39}$$

and algorithm 4.18 concerns the computation of the diagram

$$\text{Diagram (4.40)} \quad (\zeta = (s_1, p_1, s_2, p_2)). \tag{4.40}$$

Both diagrams result in a tensor A_* which has the same form as the A_n :

$$[A_*^{s_1, p_1, s_2, p_2}]_{(q, \alpha_q); (r, \beta_r)} = \delta_{p_1, q+(s_1-1)/2} \delta_{p_2, q+(s_1+s_2)/2} \delta_{r, p_2} [a_*^{q, s_1, s_2}]_{\alpha_q, \beta_r}.$$

The computation time scales with

$$\mathcal{O} \left(4^2 N_{iter} P \max_q (D^q)^3 \right).$$

Algorithm 4.17 Diagram (4.39) for gauge and \mathcal{T}^2 invariant MPS

Input: $a_1, a_2, a_3, \Xi, \Lambda, o$

Output: Outcome a_* of the diagram (4.39)

```

1: function  $a_* = \text{COMPUTEDIAGRAM1}(a_1, a_2, a_3, \Xi, \Lambda, o)$ 
2:   for  $q = p^{\min} : p^{\max}$  do
3:     for  $s_1, s_2, s_3, s_4 = -1, 1$  do
4:        $c_{1,2}^{q, s_1, s_2, s_3, s_4} = a_1^{q, s_1, s_2} a_2^{q + (s_1 + s_2)/2, s_3, s_4}$ 
5:     end for
6:   end for
7:   for  $q = p^{\min} : p^{\max}$  do
8:     for  $s_1, s_2, s_3, s_4 = -1, 1$  do
9:        $d_{1,2}^{q, s_1, s_2, s_3, s_4} = \sum_{\{s'_k\}} \langle s_1, s_2, s_3, s_4 | o^q | s'_1, s'_2, s'_3, s'_4 \rangle c_{1,2}^{q, s'_1, s'_2, s'_3, s'_4}$ 
10:    end for
11:  end for
12:  for  $q = p^{\min} : p^{\max}$  do
13:    for  $s_1, s_2 = -1, 1$  do
14:       $e^{q, s_1, s_2} = \sum_{\{s'_k\}} \left[ d_{1,2}^{q, s_1, s_2, s'_1, s'_2} \Lambda^{q + (s_1 + s_2 + s'_1 + s'_2)/2} \left( a_3^{q + (s_1 + s_2), s'_1, s'_2} \right)^\dagger \right]$ 
15:       $a_*^{q, s_1, s_2} = \Xi^q e^{q, s_1, s_2}$ 
16:    end for
17:  end for
18: end function

```

Algorithm 4.18 Diagram (4.40) for gauge and \mathcal{T}^2 invariant MPS

Input: $a_1, a_2, a_3, \Xi, \Lambda, o$

Output: Outcome a_* of the diagram (4.40)

```

1: function  $a_* = \text{COMPUTEDIAGRAM2}(a_1, a_2, a_3, \Xi, \Lambda, o)$ 
2:   for  $q = p^{\min} : p^{\max}$  do
3:     for  $s_1, s_2, s_3, s_4 = -1, 1$  do
4:        $c_{1,2}^{q, s_1, s_2, s_3, s_4} = a_1^{q, s_1, s_2} a_2^{q + (s_1 + s_2)/2, s_3, s_4}$ 
5:     end for
6:   end for
7:   for  $q = p^{\min} : p^{\max}$  do
8:     for  $s_1, s_2, s_3, s_4 = -1, 1$  do
9:        $d_{1,2}^{q, s_1, s_2, s_3, s_4} = \sum_{\{s'_k\}} \langle s_1, s_2, s_3, s_4 | o^q | s'_1, s'_2, s'_3, s'_4 \rangle c_{1,2}^{q, s'_1, s'_2, s'_3, s'_4}$ 
10:    end for
11:  end for
12:  for  $q = p^{\min} : p^{\max}$  do

```

```

13:   for  $s_1, s_2 = -1, 1$  do
14:      $f^{q,s} = \sum_{\{s'_k\}=-1,1} \left( a_3^{q-(s'_1+s'_2)/2, s'_1, s'_2} \right)^\dagger \Xi^{q-(s'_1+s'_2)/2}$ 
15:        $a_{1,2}^{q-(s'_1+s'_2)/2, s'_1, s'_2, s_1, s_2}$ 
16:      $a_*^{q, s_1, s_2} = f^{q, s_1, s_2} \Lambda^{q+(s_1+s_2)/2}$ 
17:   end for
18: end for

```

(e) TDVP algorithm for gauge and \mathcal{T}^2 invariant MPS

In algorithm 4.19 we present the ‘gauged \mathcal{T}^2 invariant version’ of algorithm 2.1. One notices that this algorithm is very similar to that of the previous section, algorithm 4.9. The input ‘stringGaugeFix’ is the desired form of the output b : ‘left’ if we want b to obey the left gauge fixing condition and ‘right’ if we want b to obey the right gauge fixing condition. The computation time of the algorithm, when $P, 2 \ll \max_q D^q$, scales with

$$\mathcal{O} \left(4^2 N_{iter} P \max_q (D^q)^3 \right).$$

Algorithm 4.19 Compute gradient TDVP for gauge and \mathcal{T}^2 invariant MPS

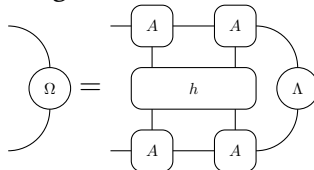
Input: a, Ξ, Λ, h , stringGaugeFix

Output: X, b

```

1: function  $[X, b] = \text{TDVPDIRECTION}(a, \Xi, \Lambda, h, \text{stringGaugeFix})$ 
2:    $a_1 = \text{computeDiagram1}(a, a, a, \Xi, \Lambda, h)$  ▷ Algorithm 4.17
3:    $a_2 = \text{computeDiagram2}(a, a, a, \Xi, \Lambda, h)$  ▷ Algorithm 4.18
4:   switch stringGaugeFix do
5:     case ‘right’

```



6: ▷ Eq. (4.33)

```

7:    $K_0 = \text{invTransRight}(A, \Omega, 0, \Xi, \Lambda)$  ▷ Algorithm 4.15

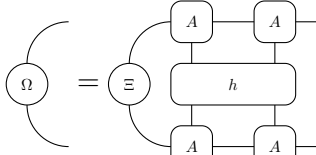
```

```

8:   for  $q = p^{min} : p^{max}$  do
9:     for  $s_1, s_2 = -1, 1$  do
10:       $a_3^{q, s_1, s_2} = \Xi^q a^{q, s_1, s_2} K_0^{q+(s_1+s_2)/2}$ 
11:       $(\nabla_{\bar{b}} H)^{q, s_1, s_2} = a_1^{q, s_1, s_2} + a_2^{q, s_1, s_2} + a_3^{q, s_1, s_2}$ 
12:     end for
13:   end for

```

```

14:       $v_R = \text{computeVR}(a, \Xi, \Lambda)$  ▷ Algorithm 4.13
15:      for  $q = p^{\min} : p^{\max}$  do
16:           $X^q = \sum_{\{s_k\}} \left[ (\Xi^q)^{-1/2} (\nabla_{\bar{b}} H)^{q, s_1, s_2} \right.$ 
 $\left. \left( \Lambda^{q+(s_1+s_2)/2} \right)^{-1/2} \left( v_R^{q, s_1, s_2} \right)^\dagger \right]$ 
17:      end for
18:      for  $q = p^{\min} : p^{\max}$  do
19:          for  $s_1, s_2 = -1, 1$  do
20:               $b^{q, s_1, s_2} = (\Xi^q)^{-1/2} X^q v_R^{q, s_1, s_2} \left( \Lambda^{q+(s_1+s_2)/2} \right)^{-1/2}$ 
21:          end for
22:      end for
23:      case 'left'
24:          
▷ Eq. (4.33)
25:           $L_0 = \text{invTransLeft}(a, \Omega, 0, \Xi, \Lambda)$  ▷ Algorithm 4.16
26:          for  $q = p^{\min} : p^{\max}$  do
27:              for  $s_1, s_2 = -1, 1$  do
28:                   $a_3^{q, s_1, s_2} = L_0^q a^{q, s_1, s_2} \Lambda^{q+(s_1+s_2)/2}$ 
29:                   $(\nabla_{\bar{b}} H)^{q, s_1, s_2} = a_1^{q, s_1, s_2} + a_2^{q, s_1, s_2} + a_3^{q, s_1, s_2}$ 
30:              end for
31:          end for
32:           $v_L = \text{computeVL}(a, \Xi, \Lambda)$  ▷ Algorithm 4.14
33:          for  $q = p^{\min} : p^{\max}$  do
34:               $X^q = \sum_{\{s_k\}} \left[ \left( v_L^{q-(s_1+s_2)/2, s_1, s_2} \right)^\dagger \left( \Xi^{q-(s_1+s_2)/2} \right)^{-1/2} \right.$ 
 $\left. (\nabla_{\bar{b}} H)^{q-(s_1+s_2)/2, s_1, s_2} \left( \Lambda^q \right)^{-1/2} \right]$ 
35:          end for
36:          for  $q = p^{\min} : p^{\max}$  do
37:              for  $s_1, s_2 = -1, 1$  do
38:                   $b^{q, s_1, s_2} = (\Xi^q)^{-1/2} v_L^{q, s_1, s_2} X^{q+(s_1+s_2)/2}$ 
 $\left( \Lambda^{q+(s_1+s_2)/2} \right)^{-1/2}$ 
39:              end for
40:          end for
41:      end switch
42: end function
    
```


Now we have rewritten the function ‘TDVPdirection’ we can use the algorithms 2.2 and 2.3 to perform a steepest descent or to perform real-time evolution.

When using algorithm 2.2 to find an optimal approximation $|\Psi_u[A]\rangle$ of the ground state of \mathcal{H} where now A is automatically gauge invariant,

$$\begin{array}{c} (q, \alpha_q) \text{---} \boxed{A} \text{---} (r, \beta_r) \\ | \\ (s_1, p_1, s_2, p_2) \end{array} = [a^{q, s_1, s_2}]_{\alpha_q, \beta_r} \delta_{p, q+(s_1-1)/2} \delta_{p_2, q+(s_1+s_2)/2} \delta_{r, p_2}$$

the steepest descent just keeps on computing $[X, b] = \text{TDVPdirection}(a, \Xi, \Lambda, h)$ and updates a according to

$$a^{q, s_1, s_2} \leftarrow a^{q, s_1, s_2} - b^{q, s_1, s_2} d\tau$$

for $d\tau$ small. The algorithm has converged to its optimal approximation when

$$\text{normGrad} = \sqrt{\sum_{q=p_{min}}^{p_{max}} \text{tr} \left((X^q)^\dagger X^q \right)}$$

is sufficiently small. Instead of normalizing with the general algorithm 1.1, we now have to use algorithm 4.11. With these comments, we can apply the algorithm 2.2 in exactly the same way, we refer to is pseudocode for the details.

In a similar way we can now apply algorithm 2.3 to perform real-time evolution with a time-independent Hamiltonian by invoking the function $[X, b] = \text{TDVPdirection}(a, \Xi, \Lambda, h)$ via algorithm 4.19. In this formulation it is hard to let the bond dimension grow during the evolution as the TDPV here is developed for an optimal evolution within the manifold of MPS with a fixed bond dimension. In general however, we expect the entanglement to grow with time during real-time evolution and it would thus be convenient to increase the bond dimension. Therefore we will rather use the iTEBD method that will be discussed in the next section.

4.2.5. Excitations in the tangent plane

Assume now we have found $|\Psi_u[A]\rangle$ with

$$\begin{array}{c} (q, \alpha_q) \text{---} \boxed{A} \text{---} (r, \beta_r) \\ | \\ (s_1, p_1, s_2, p_2) \end{array} = [a^{q, s_1, s_2}]_{\alpha_q, \beta_r} \delta_{p_1, q+(s_1-1)/2} \delta_{p_2, q+(s_1+s_2)/2} \delta_{r, p_2}$$

which is a \mathcal{T}^2 and gauge invariant MPS approximation for the ground state of \mathcal{H} . Then we can use the tangent vectors $|\Phi_k[B, A]\rangle$, see eq. (1.16), to

approximate the one-particle excitations with momentum $k \in [-\pi, \pi[$, see section 1.3. Gauge invariance is imposed if

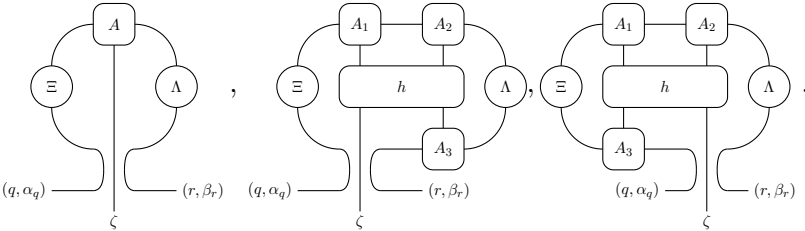
$$\begin{array}{c} (q, \alpha_q) \text{---} \boxed{B} \text{---} (r, \beta_r) \\ | \\ (s_1, p_1, s_2, p_2) \end{array} = [b^{q, s_1, s_2}]_{\alpha_q, \beta_r} \delta_{p_1, q+(s_1-1)/2} \delta_{p_2, q+(s_1+s_2)/2} \delta_{r, p_2}.$$

As in the general case, because the excitations should be orthogonal to the ground state we can impose either the right gauge fixing condition eq. (1.20) or the left gauge fixing condition eq. (1.19) on B . In both cases, it is then possible to parameterize B by a matrix X , see eq. (4.35) for the right gauge fixing condition and eq. (4.36) for the left gauge fixing condition. As discussed in section 2.2, the optimal approximation $|\Phi_k[B, A]\rangle$ for the excited states is found by solving the eigenvalue problem

$$\tilde{H}_k^{eff}(X) = E_k X$$

where $\tilde{H}_k^{eff}(X)$ can be found in eqs. (2.20) and (2.21).

Let us now assume that B obeys the left gauge fixing condition and thus that b is parameterized as in eq. (4.36). Then in eq. (2.20) \tilde{H}_k is computed and this involves computing diagrams of the form:



These can be computed as discussed in equation eq. (4.38) and algorithms 4.17 and 4.18. Note also that eq. (2.20) involves the computation of the pseudo inverses $(\mathbb{1} - e^{ik}\mathbb{E})^+$ which can be performed using the algorithms 4.15 and 4.16. After performing the contractions in eq. (2.20) we obtain the tensor $\tilde{H}_k[X]$ which takes the form

$$\left[\left(\tilde{H}_k[X] \right)^{s_1, p_1, s_2, p_2} \right]_{(q, \alpha_q), (r, \beta_r)} = \left[\left(\tilde{h}_k[X] \right)^{q, s_1, s_2} \right]_{\alpha_q, \beta_r} \delta_{p_1, q+(s_1-1)/2} \delta_{p_2, q+(s_1+s_2)/2} \delta_{r, p_2}.$$

Computing diagram (2.21) yields then that

$$\left[\tilde{H}_k(X) \right]_{(q, \alpha_q), (r, \beta_r)} = \delta_{q, r} \left[\left(\tilde{H}_k^{eff}(X) \right)^q \right]_{\alpha_q, \beta_r}$$

with

$$\left(\tilde{H}_k^{eff}(X)\right)^q = \sum_{\{s_k\}} \left[\left(v_L^{q-(s_1+s_2)/2, s_1, s_2}\right)^\dagger \left(\Xi^{q-(s_1+s_2)/2}\right)^{-1/2} \left(\tilde{h}_k[X]\right)^{q-(s_1+s_2)/2, s_1, s_2} \left(\Lambda^q\right)^{-1/2} \right].$$

The eigenvalue equation $\tilde{H}_k^{eff}(X) = \mathcal{E}_k X$ thus boils down to finding the blocks $X^q \in \mathbb{C}^{D^q \times D^q}$ of the block diagonal matrix X such that ,

$$\left(\tilde{H}_k^{eff}(X)\right)^q = \mathcal{E}_k X^q, q = p^{min}, \dots, p^{max}.$$

The pseudocode is presented in algorithm 4.20 and is similar to algorithms 2.4 and 4.10. The main function 'ElementaryExcitation' invokes the iterative eigensolver 'eigs' to find the lowest eigenvalues of 'ApplyHeff'. As discussed above, 'ApplyHeff' computes, given the block diagonal matrix X , $\left(\tilde{H}_k^{eff}(X)\right)^q$ in

$$\mathcal{O}\left(4^2 P N_{iter} \max_q (D^q)^3\right)$$

time where N_{iter} originates from the computation of L_0, L_2, L_3, L_4 and K_1 which also need an iterative method, see algorithms 4.15 and 4.16.

Algorithm 4.20 Excitations in the tangent plane for \mathcal{T}^2 and gauge invariant MPS

Input: a, k, h

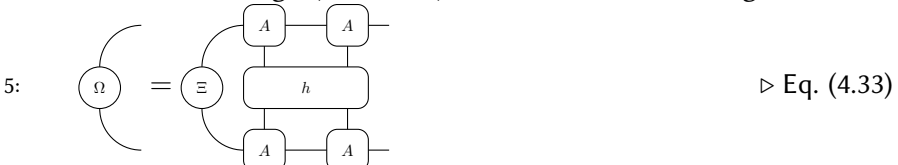
Output: $\{X_k\}, \{\mathcal{E}_k\}$

1: **function** $\{\{X_k\}, \{\mathcal{E}_k\}\} = \text{ELEMENTARYEXCITATION}(a, k, h)$

2: $[a, \Xi, \Lambda] = \text{normalizeUmps}(a)$ ▷ Algorithm 4.11



4: $K_0 = \text{invTransRight}(a, \Omega, 0, \Xi, \Lambda)$ ▷ Algorithm 4.15



6: $L_0 = \text{invTransLeft}(a, \Omega, 0, \Xi, \Lambda)$ ▷ Algorithm 4.16

7: $v_L = \text{computeVL}(a, \Xi, \Lambda)$ ▷ Algorithm 4.14

8: $[\{X_k\}, \{\mathcal{E}_k\}] = \text{eigs}(\text{@}(X)\text{ApplyHeff}(X, a, K_0, L_0, \Lambda, \Xi, v_L, h, k))$

9: **end function**

10: **function** $H_k^{\text{eff}}[X] = \text{APPLYHEFF}(X, a, K_0, L_0, \Lambda, \Xi, v_L, h, k)$

11: **for** $q = p^{\min} : p^{\max}$ **do**

12: **for** $s_1, s_2 = -1, 1$ **do**

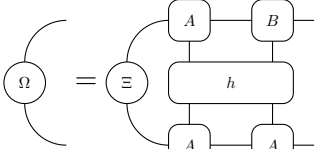
13: $b^{q, s_1, s_2} = (\Xi^q)^{-1/2} v_L^{q, s_1, s_2} X^{q+(s_1+s_2)/2} (\Lambda^{q+(s_1+s_2)/2})^{-1/2}$

14: **end for**

15: **end for**

16:  ▷ Eq. (4.33)

17: $L_2 = \text{invTransLeft}(a, \Omega, -k, \Xi, \Lambda)$ ▷ Algorithm 4.16

18:  ▷ Eq. (4.33)

19: $L_3 = \text{invTransLeft}(a, \Omega, -k, \Xi, \Lambda)$ ▷ Algorithm 4.16

20:  ▷ Eq. (4.27)

21: $L_4 = \text{invTransLeft}(a, \Omega, -k, \Xi, \Lambda)$ ▷ Algorithm 4.16

22:  ▷ Eq. (4.28)

23: $K_1 = \text{invTransRight}(a, \Omega, k, \Xi, \Lambda)$ ▷ Algorithm 4.15

24: Compute $\tilde{H}_k[X]$, eq. (2.20) ▷ Eq. (4.38), algorithms 4.17 and 4.18

25: **for** $q = p^{\min} : p^{\max}$ **do**

26:
$$\left(\tilde{H}_k^{\text{eff}}(X) \right)^q = \sum_{\{s_k\}} \left[\left(v_L^{q-(s_1+s_2)/2} \right)^\dagger \left(\Xi^{q-(s_1+s_2)/2} \right)^{-1/2} \left(\tilde{h}_k[X] \right)^{q-(s_1+s_2)/2, s_1, s_2} \left(\Lambda^q \right)^{-1/2} \right]$$

27: **end for**

28: **end function**

4.2.6. Application to the Schwinger model

In section 2.2 and section 3.3 of part I we apply this formalism to the Schwinger model with $\alpha \neq 0$, i.e. to the Hamiltonian

$$\mathcal{H} = \frac{g}{2\sqrt{x}} \left(\sum_{n=1}^{2N} [L(n) + \alpha]^2 + \frac{\sqrt{x}}{g} m \sum_{n=1}^{2N} (-1)^n (\sigma_z(n) + (-1)^n) + x \sum_{n=1}^{2N-1} (\sigma^+(n) e^{i\theta(n)} \sigma^-(n+1) + h.c.) \right).$$

By blocking sites $2n - 1$, $2n$ and link $2n - 1$ and link $2n$ into one effective site the Hamiltonian can be written as

$$\mathcal{H} = \sum_{n=1}^{N-1} (\mathcal{T}^2)^{n-1} h (\mathcal{T}^2)^{-n+1} \quad (N \rightarrow +\infty)$$

$$h = \frac{g}{2\sqrt{x}} \left([L(1) + \alpha]^2 + [L(2) + \alpha]^2 + \frac{\sqrt{x}}{g} m (-\sigma_z(1) + \sigma_z(2) + 2) + x (\sigma^+(1) e^{i\theta(1)} \sigma^-(2) + \sigma^+(2) e^{i\theta(2)} \sigma^-(3) + h.c.) \right).$$

For our applications we will be interested in the string tension σ_α which is the difference of the ground state energy for $\alpha \neq 0$ with the ground state energy for $\alpha = 0$ per unit of length. Therefore we will immediately subtract this contribution from the Hamiltonian. More specifically, if ϵ_0 is the ground state energy per site of \mathcal{H} with $\alpha = 0$, i.e. $\epsilon_0 = x\omega_0$ with ω_0 the energy density computed in eq. (4.24), then we renormalize h by

$$h \leftarrow h - 2\omega_0 \mathbb{1} \otimes \mathbb{1}.$$

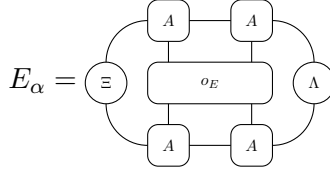
Using the TDVP, see subsection 4.2.4, we obtain the ground state approximation $|\Psi_u[A]\rangle$ with

$$[A^{s_1, p_1, s_2, p_2}]_{(q, \alpha_q); (r, \beta_r)} = [a^{q, s_1, s_2}]_{\alpha_q, \beta_r} \delta_{p_1, q+(s_1-1)/2} \delta_{p_2, q+(s_1+s_2)/2} \delta_{r, p_2}.$$

In our computations we stopped the steepest descent method when $normGrad \approx 5 \times 10^{-9} - 10^{-9}$. With this renormalized Hamiltonian the string tension equals

$$\sigma_\alpha = \frac{\sqrt{x}}{2} \left(\Xi \otimes \Lambda \right)$$

We will also be interested in the electric field



with

$$o_E = (L(1) + L(2))/2.$$

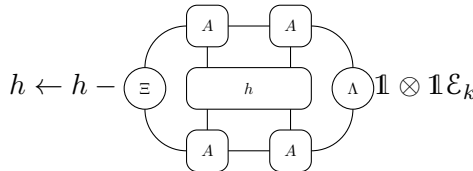
These diagrams can be computed using algorithm 4.12. Therefore we only need the matrix elements

$$\begin{aligned} \langle s_1, s_2, s_3, s_4 | h^q | s'_1, s'_2, s'_3, s'_4 \rangle &= \frac{g}{2\sqrt{x}} \left(\delta_{s_1, s'_1} \delta_{s_2, s'_2} \delta_{s_3, s'_3} \delta_{s_4, s'_4} \right. \\ &\quad \left((q + s_1 - 1)/2 \right)^2 + (q + s_1 + s_2)/2 \right)^2 + \frac{\sqrt{x}}{g} m(-s_1 + s_2 + 2) - 2x\omega_0 \Big) \\ &+ x \left(\delta_{s_1, s'_2} \delta_{s_1, s'_2} \delta_{s_1, -s'_1} \delta_{s_2, -s'_2} \delta_{s_3, s'_3} + \delta_{s_1, s'_1} \delta_{s_2, s'_3} \delta_{s'_2, s_3} \delta_{s_3, -s'_3} \delta_{s_2, -s'_2} \right) \delta_{s_4, s'_4} \Big) \\ \langle s_1, s_2, s_3, s_4 | o_E^q | s'_1, s'_2, s'_3, s'_4 \rangle &= \delta_{s_1, s'_1} \delta_{s_2, s'_2} \delta_{s_3, s'_3} \delta_{s_4, s'_4} \frac{q + s_1 - 1 + (s_2 + 1)/2}{2} \end{aligned}$$

see eq. (4.29).

The Schmidt spectrum is obtained as discussed in subsection 4.2.2. In particular we are interested in the renormalized entropy ΔS_α associated to a half cut of the lattice which is the difference of the entropy of the ground state of \mathcal{H}_α with $\alpha \neq 0$ with the entropy of the ground state of \mathcal{H}_0 with $\alpha = 0$. We always assume that the half cut is taken between an even and an odd site.

To find the excitations we put the ground state energy equal to zero, i.e.



and we apply then algorithm 4.20 to find the excitation energies \mathcal{E}_k and the corresponding approximations for the eigenstates $|\Phi_k[B, A]\rangle$ with

$$[B^{s_1, p_1, s_2, p_2}]_{(q, \alpha_q); (r, \beta_r)} = [b^{q, s_1, s_2}]_{\alpha_q, \beta_r} \delta_{p_1, q+(s_1-1)/2} \delta_{p_2, q+(s_1+s_2)/2} \delta_{r, p_2}.$$

4.2.7. Real-time evolution within the coherent state approximation

Using the one-particle excitations we can approximate real-time evolution within the one-particle spectrum of \mathcal{H}_α . If \mathcal{H}_{α_0} is the Hamiltonian in an electric background field α_0

$$\mathcal{H}_{\alpha_0} = \frac{g}{2\sqrt{x}} \left(\sum_{n=1}^{2N} [L(n) + \alpha_0]^2 + \frac{\sqrt{x}}{g} m \sum_{n=1}^{2N} (-1)^n (\sigma_z(n) + (-1)^n) \right. \\ \left. + x \sum_{n=1}^{2N-1} (\sigma^+(n) e^{i\theta(n)} \sigma^-(n+1) + h.c.) \right).$$

and \mathcal{H}_α is the Hamiltonian in an electric background field α , then we can write (up to an irrelevant constant)

$$\mathcal{H}_\alpha = \mathcal{H}_{\alpha_0} + \epsilon \mathcal{V}$$

where

$$\mathcal{V} = \frac{g}{\sqrt{x}} \sum_{n=1}^{2N} L(n)$$

and $\epsilon = \alpha - \alpha_0$. Now we approximate \mathcal{H}_α by a free bosonic Hamiltonian of the form

$$\mathcal{H}_\alpha = \int dk \left(\sum_m \mathcal{E}_m(k) a_m^\dagger(k) a_m(k) \right). \quad (4.41)$$

Here the integral goes over the momenta from $-\pi$ till π , the sum over m goes over all one-particle excitations and $\mathcal{E}_m(k)$ is positive. The operators a_m and a_m^\dagger are the annihilation and creation operators of the one-particle excitations with energy $\mathcal{E}_m(k)$ and momentum k which satisfy the canonical commutation relations

$$[a_n(k'), a_m^\dagger(k)] = \delta(k' - k) \delta_{m,n}, [a_m(k'), a_n(k')] = 0, [a_n^\dagger(k'), a_m^\dagger(k)] = 0.$$

Using the TDVP, algorithm 4.19, we have a uMPS approximation $|\Psi_u[A]\rangle$ for the ground state of \mathcal{H}_α and by using algorithm 4.20 we have a MPS approximation $|\Phi_k[B_m(k), A]\rangle$ for the m -th one-particle excitation with momentum k and energy $\mathcal{E}_m(k)$. They are normalized as

$$\langle \Psi_u[A] | \Psi_u[A] \rangle = 1 \quad (4.42a)$$

$$\langle \Psi_u[A] | \Phi_k[B_m(k), A] \rangle = 2\pi \delta(k) \delta_{m,0} N_{eff}^1[A, B_m(k)] \quad (4.42b)$$

$$\langle \Phi_{k'}[B_n(k'), A] | \Phi_k[B_m(k), A] \rangle = 2\pi \delta(k - k') \delta_{n,m} N_{eff}^2 [B_n(k'), B_m(k)] \quad (4.42c)$$

where N_{eff}^1 and N_{eff}^2 are finite values depending on the tensors of the MPS, see subsection 1.3.5. We will normalize the states such that $N_{eff}^2 = 1$. The delta-Dirac functions originate from the infinite lattice length and have to be read as

$$\delta(k - k') = \lim_{N \rightarrow +\infty} \frac{2N}{2\pi} \delta_{k,k'} \quad (4.43)$$

where $2N$ ($N \rightarrow +\infty$) is the number of sites on the lattice. In this approximation we have that

$$\mathcal{H}_\alpha |\Psi_u[A]\rangle = 0, \mathcal{H}_\alpha |\Phi_k[B_m(k), A]\rangle = \mathcal{E}_m(k) |\Phi_k[B_m(k), A]\rangle,$$

and

$$a_m(k)^\dagger |\Psi_u[A]\rangle = \frac{1}{\sqrt{2\pi}} |\Phi_k[B_m(k), A]\rangle, a_m(k) |\Psi_u[A]\rangle = 0. \quad (4.44)$$

We now want to express the ground state $|0\rangle_0$ of \mathcal{H}_{α_0} in terms of the ground state $|\Psi_u[A]\rangle$ and the excitations $|\Phi_k[B, A]\rangle$ of \mathcal{H}_α . Therefore, similar as eq. (4.41) we approximate \mathcal{H}_{α_0} up to second order in $(a_m(k), a_m^\dagger(k))$:

$$\begin{aligned} \mathcal{H}_{\alpha_0} = & \int dk \int dk' \left(\sum_{m,n} \mu_{m,n}(k, k') a_m(k)^\dagger a_n(k') \right) \\ & + \int dk \left(\sum_m c_m(k) a_m(k) + \sum_m \bar{c}_m(k) a_m^\dagger(k) \right). \end{aligned}$$

Because \mathcal{H}_{α_0} is Hermitian, $\mu_{m,n}$ should also be a Hermitian operator (in the indices (m, n)). Using the ground state $|\Psi_u[A]\rangle$ and the one-particle excitations $|\Phi_k[B_m(k), A]\rangle$ of \mathcal{H}_α it follows from eq. (4.41) and eq. (4.44) that we can compute the coefficients $\mu_{m,n}$ and c_m as

$$\mu_{m,n}(k, k') = \frac{1}{2\pi} \langle \Phi_k[B_m(k), A] | \mathcal{H}_\alpha | \Phi_{k'}[B_n(k'), A] \rangle \quad (4.45a)$$

$$c_m(k) = \frac{1}{\sqrt{2\pi}} \langle \Psi_u[A] | \mathcal{H}_\alpha | \mathcal{E}_m(k) \rangle \quad (4.45b)$$

If we renormalize \mathcal{H}_{α_0} such that

$$\langle \Psi_u[A] | \mathcal{H}_{\alpha_0} | \Psi_u[A] \rangle = 0$$

and normalize the states in (4.42) with $N_{eff}^2 = 1$, the right-hand side of eq. (4.45) is normalized as follows:

$$\langle \Phi_k[B_m(k), A] | \mathcal{H}_{\alpha_0} | \Phi_{k'}[B_n(k'), A] \rangle = 2\pi\delta(k - k') H_{eff}^1[B_m(k'), B_n(k)] \quad (4.46a)$$

$$c_m(k) = \langle \Psi_u[A] | \mathcal{H}_{\alpha_0} | \Phi_k[B_m(k), A] \rangle = 2\pi\delta(k) H_{eff}^2[A, B_m(k)] \quad (4.46b)$$

where H_{eff}^1 and H_{eff}^2 are finite quantities that can be computed from eqs. (1.29a) and (1.30i).

Using eq. (4.45) and (4.46) we rewrite \mathcal{H}_{α_0} now:

$$\mathcal{H}_{\alpha_0} = \int dk \left(\sum_{m,n} M_{m,n}(k) a_m^\dagger(k) a_n(k) + \sum_m c_m(k) a_m(k) + \sum_m \bar{c}_m(k) a_m^\dagger(k) \right)$$

where

$$M_{m,n}(k) = H_{eff}^1[B_m(k), B_n(k)], \quad (4.47a)$$

$$c_m(k) = \sqrt{2\pi} H_{eff}^2[A, B_m(0)] \delta(k). \quad (4.47b)$$

\mathcal{H}_{α_0} is now diagonalized by the following transformations:

$$b_r(k) = \sum_m \left(U_{r,m}(k) a_m(k) + \frac{U_{r,m}}{\mathcal{E}_r} \bar{C}_m(k) \right)$$

where $U(k)$ is the unitary transformation which diagonalize $M(k)$ and $\mathcal{E}(k)$ is the diagonal matrix containing the eigenvalues of $M(k)$, i.e. $M(k) = U(k)^\dagger \mathcal{E}(k) U(k)$. In vector notation we can write this transformation as

$$\mathbf{b}(k) = U(k) \mathbf{a}(k) + \mathcal{E}^{-1}(k) U(k) \bar{\mathbf{c}}(k) \quad (4.48)$$

or

$$\mathbf{a}(k) = U^\dagger(k) \mathbf{b}(k) - U^\dagger(k) \mathcal{E}^{-1}(k) U(k) \bar{\mathbf{c}}(k).$$

One easily verifies now that

$$\mathcal{H}_{\alpha_0} = \int dk \left(\sum_r \mathcal{E}_r(k) b_r^\dagger(k) b_r(k) - \sum_{m,n} [M^{-1}]_{m,n}(k) c_m(k) \bar{c}_n(k) \right).$$

Some remarks are in order here

- i. The last term in \mathcal{H}_{α_0} is a constant (divergent) term and can be omitted. This term is only necessary if we are doing computations in the eigenbasis of \mathcal{H}_α because it is this term which assures us that

$$\langle \Psi_u[A] | \mathcal{H}_\alpha | \Psi_u[A] \rangle = 0.$$

- ii. In the Hamiltonian there appear terms of the form $c_m(k)c_n(k)$ which is ill defined as $c_m(k) \propto \delta(k)$. One regularize this by replacing the Dirac-functions by $\delta(k) \rightarrow \delta_{k,0}2N/(2\pi)$ and the dk by $dk \rightarrow 2\pi/2N$ ($2N$ the number of sites on the lattice, $2N \rightarrow +\infty$).
- iii. $\mathcal{E}_r(k)$ should be positive, otherwise the quadratic expansion of \mathcal{H}_0 in the creation and annihilation operators $a_n^\dagger(k)$ and $a_n(k)$ is certainly not valid anymore.

Now we have diagonalized \mathcal{H}_{α_0} , the ground state $|0\rangle_0$ of \mathcal{H}_{α_0} is the state satisfying

$$b_r(k) |0\rangle_0 = 0, \forall k \in [-\pi, \pi[\text{ and } \forall r, \quad (4.49a)$$

or

$$a_m(k) |0\rangle_0 = d_m(k) |0\rangle_0 \quad (4.49b)$$

where

$$d_m(k) = - \sum_r [M(k)^{-1}]_{m,r} \bar{c}_r(k) \quad (4.49c)$$

as follows from (4.48). Note that if $k \neq 0$ that $d_m(k) = 0$, so for non-zero momenta (in this approach) \mathcal{H}_{α_0} and \mathcal{H}_α have the same vacuum. This can be interpreted as the fact that a translation invariant quench cannot create particles with non-zero momentum out of the vacuum. Again, in the calculation for $k = 0$, $d_m(k)$ involves a Delta-dirac distribution which can be regularized by (4.43).

Assume now we want to compute expectation values with respect to $|0\rangle_0$ of a translation invariant observable

$$\mathcal{O} = \sum_{n=1}^{2N} T^{n-1} o T^{-n+1}$$

where o has only support on sites 1 and 2. Then we expand this operator similar as \mathcal{H}_{α_0} quadratically in the annihilation and creation operators of \mathcal{H}_α

$$\begin{aligned} \mathcal{O} = \int dk \left(\sum_m o_{2,m}(k) a_m(k) + \bar{o}_{2,m}(k) a_m^\dagger(k) \right) \\ + \int dk \int dk' \left(\sum_{m,n} o_{1,m,n}(k,k') a_m^\dagger(k) a_n(k') \right). \end{aligned}$$

We renormalize \mathcal{O} such that $\langle \Psi_u[A] | \mathcal{O} | \Psi_u[A] \rangle = 0$. The coefficients can be extracted similar to (4.46):

$$\begin{aligned} o_{1,m,n}(k, k') &= \frac{1}{2\pi} \langle \Phi_k[B_m(k), A] | \mathcal{O} | \Phi_{k'}[B_n(k'), A] \rangle \\ &= \delta(k - k') O_{eff}^1[B_m(k), B_n(k')] \\ o_{2,m}(k) &= \frac{1}{\sqrt{2\pi}} \langle \Psi_u[A] | \mathcal{O} | \Phi_k[B_m(k), A] \rangle = \sqrt{2\pi} \delta(k) O_{eff}^2[A, B_m(k)] \end{aligned}$$

where O_{eff}^1 and O_{eff}^2 are finite quantities that can be computed from eqs. (1.29a) and (1.30i).

Hence we find

$$O = \sum_m \left(o_{2,m} a_m(0) + \bar{o}_{2,m} a_m^\dagger(0) \right) + \int dk \left(\sum_{m,n} o_{1,m,n}(k) a_m^\dagger(k) a_n(k) \right) \quad (4.50)$$

with

$$\begin{aligned} o_{1,m,n}(k) &= O_{eff}^1[B_m(k), B_n(k)], \\ o_{2,m} &= \sqrt{2\pi} O_{eff}^2[A, B_m(0)]. \end{aligned}$$

To perform real-time evolution with \mathcal{H}_α we will work in the Heisenberg picture. The creation- and annihilation operator $a_m^\dagger(k)$ and $a_m(k)$ satisfy the following differential equation

$$\dot{a}_m(k) = i[\mathcal{H}_\alpha, a_m(k)] = -i\mathcal{E}_m(k) a_m(k) \text{ and } \dot{a}_m^\dagger(k) = i\mathcal{E}_m(k) a_m^\dagger(k) \quad (4.51)$$

which can be solved as

$$a_m(k, t) = e^{-i\mathcal{E}_m(k)t} a_m(k) \text{ and } a_m^\dagger(k, t) = e^{i\mathcal{E}_m(k)t} a_m^\dagger(k).$$

In the Heisenberg picture (4.50) becomes

$$\begin{aligned} \mathcal{O}(t) &= \sum_m \left(o_{2,m} a_m(0, t) + \bar{o}_{2,m} a_m^\dagger(0, t) \right) \\ &\quad + \int dk \left(\sum_{m,n} o_{1,m,n}(k) a_m^\dagger(k, t) a_n(k, t) \right) \end{aligned}$$

and the expectation value with respect to $|0\rangle_0$, the vacuum of \mathcal{H}_{α_0} , see eq. (4.49), then reads

$$\begin{aligned} \langle 0 | \mathcal{O}(t) | 0 \rangle_0 &= \sum_m o_{2,m} d_m(0) e^{-i\mathcal{E}_m(0)t} + \sum_m \bar{o}_{2,m} \bar{d}_m(0) e^{i\mathcal{E}_m(0)t} \\ &\quad + \int dk \left(\sum_{m,n} o_{1,m,n} e^{i(\mathcal{E}_m(k) - \mathcal{E}_n(k))t} \bar{d}_m(k) d_n(k) \right) \end{aligned}$$

where we used eqs. (4.49) and (4.51). As already noted before, $d_m(k)$ involves a delta-Dirac contribution: $d_m(k) = \delta(k)d'_m$. The expression $\langle 0|\mathcal{O}(t)|0\rangle$ is regularized by $\delta(k) \rightarrow \delta_{k,0}2N/(2\pi)$ and $dk = 2\pi/2N$. This yields the following results:

$$\langle 0|\mathcal{O}(t)|0\rangle = \frac{2N}{2\pi} \left[\sum_m o_{2,m} d'_m e^{-i\varepsilon_m(0)t} + \sum_m \bar{o}_{2,m} \bar{d}'_m e^{i\varepsilon_m(0)t} + \left(\sum_{m,n} o_{1,m,n} e^{i(\varepsilon_m(0) - \varepsilon_n(0))t} \bar{d}'_m d'_n \right) \right].$$

Because $\mathcal{O} = \sum_{n=1}^{2N-1} T^{n-1} o T^{-n+1}$, $\langle 0|\mathcal{O}(t)|0\rangle$ will scale with the number of lattice sites. It follows that

$$\frac{1}{2N} \langle 0|\mathcal{O}(t)|0\rangle = \frac{1}{2\pi} \left[\sum_m o_{2,m} d'_m e^{-i\varepsilon_m(0)t} + \sum_m \bar{o}_{2,m} \bar{d}'_m e^{i\varepsilon_m(0)t} + \left(\sum_{m,n} o_{1,m,n} e^{i(\varepsilon_m(0) - \varepsilon_n(0))t} \bar{d}'_m d'_n \right) \right]$$

is the expectation value per site and is finite.

4.3. iTEBD for the Schwinger model

4.3.1. Real-time evolution

At $t = 0$ we assume that we have a uMPS approximation $|\Psi_u[A_{1,2}]\rangle$, see eq. (4.25), for the ground state of

$$\mathcal{H}_0 = \frac{g}{2\sqrt{x}} \left(\sum_{n=1}^{2N} [L(n) + \alpha_0]^2 + \frac{\sqrt{x}}{g} m \sum_{n=1}^{2N} (-1)^n \sigma_z(n) + x \sum_{n=1}^{2N-1} (\sigma^+(n) e^{i\theta(n)} \sigma^-(n+1) + h.c.) \right).$$

obtained by for instance using the TDVP, see subsection 4.2.4. Gauge invariance implies that $A_{1,2}$ takes the form

$$\begin{array}{c} (q, \alpha_q) \text{---} \boxed{A_{1,2}} \text{---} (r, \beta_r) \\ \text{---} \downarrow \text{---} \\ (s_1, p_1, s_2, p_2) \end{array} = \left[a_{1,2}^{q, s_1, s_2} \right]_{\alpha_q, \beta_r} \delta_{p_1, q+(s_1-1)/2} \delta_{p_2, q+(s_1+s_2)/2} \delta_{r, p_2},$$

with $q, r, p_2 \in \mathbb{Z}[p_{min}^1, p_{max}^1]$ and $p_1 \in \mathbb{Z}[p_{min}^2, p_{max}^2]$ and $a_{1,2}^{q,s_1,s_2} \in \mathbb{C}^{D_1^q \times D_1^r}$. Now we want to evolve the state with the Hamiltonian

$$\mathcal{H}_\alpha = \frac{g}{2\sqrt{x}} \left(\sum_{n=1}^{2N} [L(n) + \alpha]^2 + \frac{\sqrt{x}}{g} m \sum_{n=1}^{2N} (-1)^n \sigma_z(n) + x \sum_{n=1}^{2N-1} (\sigma^+(n) e^{i\theta(n)} \sigma^-(n+1) + h.c.) \right).$$

according to the Schrödinger equation: $|\Psi(t)\rangle = \exp(-i\mathcal{H}_\alpha t) |\Psi_u[A_{1,2}]\rangle$.

We will use the iTEBD algorithm to approximate the real-time evolution within the class of MPS. As discussed in section 2.3, the iTEBD algorithm expands the operator $\exp(-i\mathcal{H}_\alpha dt)$ through a Trotter-Suzuki decomposition [123] as a sequence of two-site gates $\mathcal{U}_{n,n+1}(dt') = \exp(-ih_{n,n+1} dt')$ ($dt' \leq dt < 1$) that are rearranged into the gates $\mathcal{V}_n = \bigotimes_{r \in \mathbb{Z}} \mathcal{U}_{2r+n, 2r+1+n}$, ($n = 1, 2$). In general $\exp(-i\mathcal{H}_\alpha dt)$ is then approximated by a sequence of the form

$$\exp(-i\mathcal{H}_\alpha dt) \approx \mathcal{V}_1(dt_1) \mathcal{V}_2(dt_2) \mathcal{V}_1(dt_3) \dots \mathcal{V}_2(dt_{2M}) \mathcal{V}_1(dt_{2M+1}).$$

After applying each of the gates the uMPS is updated as explained in section 2.3, see also algorithm 2.5. In fact we can just copy the whole section (but we won't do this) but now the special structure of the matrices implies that we can compute the following diagrams more efficiently:

$$\text{---} \boxed{B_n} \text{---} = \text{---} \bigcirc \Xi \text{---} \boxed{A_n} \text{---} \bigcirc \Lambda \text{---} \quad (4.52a)$$

$$\text{---} \boxed{B_{n,n+1}} \text{---} = \text{---} \boxed{A_n} \text{---} \boxed{A_{n+1}} \text{---} \quad (4.52b)$$

$$\text{---} \boxed{B_{n,n+1}} \text{---} = \begin{array}{c} \boxed{A_{n,n+1}} \\ \boxed{\mathcal{U}_{n,n+1}} \end{array} \quad (4.52c)$$

where $A_n^{s,p}$ lives on site n , $A_{n+1}^{s,p}$ lives on site $n+1$, $A_{n,n+1}^{s_1,p_1,s_2,p_2}$ lives on sites n and $n+1$ and $\mathcal{U}_{n,n+1}$ is a unitary operator acting on sites n and $n+1$. Gauge invariance imposes now the following block structure, see eq. (3.14),

$$\begin{array}{c} (q, \alpha_q) \text{---} \boxed{A_k} \text{---} (r, \beta_r) \\ | \\ (s, p) \end{array} = [a_k^{q,s}]_{\alpha_q, \beta_r} \delta_{r, q+(s+(-1)^k)/2} \delta_{r,p}, \quad k = n, n+1$$

with $a_k^{q,s} \in \mathbb{C}^{D_k^q \times D_{k+1}^r}$ ($q \in \mathbb{Z}[p_k^{\min}, p_k^{\max}]$, $r, p \in \mathbb{Z}[p_{k+1}^{\min}, p_{k+1}^{\max}]$),

$$\begin{array}{c} (q, \alpha_q) \text{---} \boxed{A_{n,n+1}} \text{---} (r, \beta_r) \\ \begin{array}{cc} | & | \\ (s_1, p_1) & (s_2, p_2) \end{array} \end{array} = \left[a_{n,n+1}^{q,s_1,s_2} \right]_{\alpha_q, \beta_r} \delta_{p_1, q+(s_1+(-1)^n)/2} \delta_{p_2, q+(s_1+s_2)/2} \delta_{r, p_2}$$

with $a_{n,n+1}^{q,s_1,s_2} \in \mathbb{C}^{D_n^q \times D_{k+2}^r}$ ($q \in \mathbb{Z}[p_k^{\min}, p_k^{\max}]$, $p_1 \in \mathbb{Z}[p_{k+1}^{\min}, p_{k+1}^{\max}]$, $r, p_2 \in \mathbb{Z}[p_{k+2}^{\min}, p_{k+2}^{\max}]$),

$$[\Xi]_{(q,\alpha);(r,\beta_r)} = \delta_{q,r} [\Xi^q]_{\alpha_q, \beta_r}, \quad [\Lambda]_{(q,\alpha);(r,\beta_r)} = \delta_{q,r} [\Lambda^q]_{\alpha_q, \beta_r}$$

with $\Xi^q \in \mathbb{C}^{D_n^q \times D_n^q}$ and $\Lambda^q \in \mathbb{C}^{D_{n+1}^q \times D_{n+1}^q}$.

In a similar way as in the previous sections we find that the diagrams eq. (4.52) result in tensors with a similar structure:

$$\begin{array}{c} (q, \alpha_q) \text{---} \boxed{B_n} \text{---} (r, \beta_r) \\ | \\ (s, p) \end{array} = [b_n^{q,s}]_{\alpha_q, \beta_r} \delta_{r, q+(s+(-1)^n)/2} \delta_{r, p}$$

$$\begin{array}{c} (q, \alpha_q) \text{---} \boxed{B_{n,n+1}} \text{---} (r, \beta_r) \\ \begin{array}{cc} | & | \\ (s_1, p_1) & (s_2, p_2) \end{array} \end{array} = \left[b_{n,n+1}^{q,s_1,s_2} \right]_{\alpha_q, \beta_r} \delta_{p_1, q+(s_1+(-1)^n)/2} \delta_{p_2, q+(s_1+s_2)/2} \delta_{r, p_2}.$$

For eq. (4.52a) we find

$$b_n^{q,s} = \Xi^q a_n^{q,s} \Lambda^{q+(s+(-1)^n)/2},$$

for eq. (4.52b) we find

$$b_{n,n+1}^{q,s_1,s_2} = a_n^{q,s_1} a_{n+1}^{q+(s_1+(-1)^n)/2, s_2}$$

and finally for eq. (4.52c) we have

$$b_{n,n+1}^{q,s_1,s_2} = \sum_{s'_1, s'_2 = \pm 1} \langle s_1, s_2 | u_{n,n+1}^q | s'_1, s'_2 \rangle a_{n,n+1}^{q,s'_1,s'_2}$$

where

$$\begin{aligned} \langle s_1, s_2 | \mathcal{U}_{n,n+1}^q | s'_1, s'_2 \rangle &= \langle s_1, p_1, s_2, p_2 | \mathcal{U}_{n,n+1} | s'_1, p'_1, s'_2, p'_2 \rangle \\ &\delta_{p_1, q+(s_1+(-1)^n)/2} \delta_{p_2, q+(s_1+s_2)/2} \delta_{p'_1, q+(s'_1+(-1)^n)/2} \delta_{p'_2, q+(s'_1+s'_2)/2} \\ &\delta_{s_1+s_2, s'_1+s'_2} \delta_{p_2, p'_2} \end{aligned} \quad (4.53)$$

as follows from gauge invariance of $\mathcal{U}_{n,n+1}$ and eq. (3.29).

The last issue we need to address is decomposing the tensors $A_{n,n+1}$ on sites n and $n + 1$ into tensors on site n and $n + 1$ as in eq. (2.25):

$$\text{---} \boxed{A_{n,n+1}} \text{---} \stackrel{(SVD)}{=} \text{---} \boxed{U_n} \text{---} \boxed{\Sigma_{n+1}} \text{---} \boxed{V_{n+1}} \text{---}$$

where

$$\begin{array}{c} \boxed{U_n} \\ \circlearrowleft \mathbb{1}_{D_n} \\ \boxed{U_n} \end{array} = \mathbb{1}_{D_{n+1}}, \quad \begin{array}{c} \boxed{V_{n+1}} \\ \circlearrowright \mathbb{1}_{D_{n+2}} \\ \boxed{V_{n+1}} \end{array} = \mathbb{1}_{D_{n+1}}$$

and $\Sigma_{n+1} \in \mathbb{C}^{D_{n+1} \times D_{n+1}}$ is a positive definite diagonal matrix.¹

If $A_{n,n+1}$ is of the form

$$\begin{array}{c} (q, \alpha_q) \\ \boxed{A_{n,n+1}} \\ (s_1, p_1) \quad (s_2, p_2) \end{array} \text{---} (r, \beta_r) = \left[a_{n,n+1}^{q,s_1,s_2} \right]_{\alpha_q, \beta_r} \delta_{p_1, q + (s_1 + (-1)^n)/2} \delta_{p_2, q + (s_1 + s_2)/2} \delta_{r, p_2}$$

then for every q for which $q - (s_1 + (-1)^n)/2, q + (s_2 + (-1)^{n+1})/2 \in \mathbb{Z}[p_{min}^n, p_{max}^n]$ we perform a singular value decomposition of $\tilde{a}^q \in \mathbb{C}^{F_{n+1}^q \times F_{n+1}^q}$, with

$$F_{n+1}^q = \sum_{s=-1,1} D_n^{q-(s+(-1)^n)/2} = \sum_{s=-1,1} D_n^{q+(s+(-1)^{n+1})/2}$$

and

$$[\tilde{a}^q]_{(\alpha, s_1)(\beta, s_2)} = [a_{n,n+1}^{q-(s_1+(-1)^n)/2, s_1, s_2}]_{\alpha, \beta}, \quad (4.54a)$$

$$\tilde{a}^q = \tilde{U}^q \Sigma_{n+1}^q \tilde{V}^q \quad (4.54b)$$

where $\tilde{U}^q \in \mathbb{C}^{F_{n+1}^q \times F_{n+1}^q}$ and $\tilde{V}^q \in \mathbb{C}^{F_{n+1}^q \times F_{n+1}^q}$ are unitary matrices and $\Sigma_{n+1}^q \in \mathbb{C}^{F_{n+1}^q \times F_{n+1}^q}$ is a positive diagonal matrix. Next, one defines

$$\begin{aligned} [U_n^{s,p}]_{(q,\alpha),(r,\beta)} &= \delta_{p, q+(s+(-1)^n)/2} \delta_{p,r} [u_n^{q,s}]_{\alpha,\beta} \\ \text{with } [u_n^{q,s}]_{\alpha,\beta} &= \left[\tilde{U}^{q+(s+(-1)^n)/2} \right]_{(\alpha,s),\beta} \end{aligned} \quad (4.54c)$$

$$\begin{aligned} [V_{n+1}^{s,p}]_{(q,\alpha),(r,\beta)} &= \delta_{p, q+(s+(-1)^{n+1})/2} \delta_{p,r} [v_{n+1}^{q,s}]_{\alpha,\beta} \\ \text{with } [v_{n+1}^{q,s}]_{\alpha,\beta} &= \left[\tilde{V}^q \right]_{\alpha,(\beta,s)} \end{aligned} \quad (4.54d)$$

1. Because we work in a translational invariant setting over two sites all equalities with respect to the site n have to be read modulo 2, for instance with D_{n+2} we mean D_n and if $n = 2$ then $n + 1$ means 1.

and

$$\left| \Phi_{q,\alpha_q}^{\mathcal{A}_1^n} \right\rangle \in \bigotimes_{j \in \mathcal{A}_1^n} \mathcal{H}_j \quad \text{and} \quad \left| \Phi_{q,\alpha_q}^{\mathcal{A}_2^n} \right\rangle \in \bigotimes_{j \in \mathcal{A}_2^n} \mathcal{H}_j$$

are orthonormal unit vectors,

$$\left\langle \Phi_{q,\alpha_q}^{\mathcal{A}_1^n} \middle| \Phi_{r,\beta_r}^{\mathcal{A}_1^n} \right\rangle = \delta_{q,r} \delta_{\alpha_q,\beta_r}, \quad \left\langle \Phi_{q,\alpha}^{\mathcal{A}_2^n} \middle| \Phi_{r,\beta_r}^{\mathcal{A}_2^n} \right\rangle = \delta_{q,r} \delta_{\alpha_q,\beta_r}.$$

To apply the iTEBD algorithm we note that gauge invariance of \mathcal{H}_α implies that $\mathcal{U}_{n,n+1}(dt') = \exp(-ih_{n,n+1}dt')$ has a similar form as eq. (4.53) and that

$$\langle s_1, s_2 | [\exp(-ih_{n,n+1}dt')]^q | s'_1, s'_2 \rangle = \langle s_1, s_2 | [\exp(-ih_{n,n+1}^q dt')] | s'_1, s'_2 \rangle$$

here $h_{n,n+1}^q \in \mathbb{C}^{(2 \otimes 2) \times (2 \otimes 2)}$ is the matrix with components

$$\begin{aligned} \langle s_1, s_2 | h_{n,n+1}^q | s'_1, s'_2 \rangle &= \langle s_1, p_1, s_2, p_2 | h_{n,n+1} | s'_1, p'_1, s'_2, p'_2 \rangle \\ &= \delta_{p_1, q + (s_1 + (-1)^n)/2} \delta_{p_2, q + (s_1 + s_2)/2} \delta_{p'_1, q + (s'_1 + (-1)^n)/2} \delta_{p'_2, q + (s'_1 + s'_2)/2} \\ &\quad \delta_{s_1 + s_2, s'_1 + s'_2} \delta_{p_2, p'_2}. \end{aligned}$$

For the Schwinger model we have that

$$\begin{aligned} \langle s_1, s_2 | h_{n,n+1}^q | s'_1, s'_2 \rangle &= \frac{g}{2\sqrt{x}} \left(\delta_{s_1, s'_1} \delta_{s_2, s'_2} \left((q + (s_1 + (-1)^n)/2 + \alpha)^2 \right. \right. \\ &\quad \left. \left. + (-1)^n \frac{\sqrt{x}}{g} m (s_1 + (-1)^n) \right) + x \delta_{s_1, -s_2} \delta_{s'_1, -s'_2} \delta_{s_1, s'_2} \delta_{s_2, s'_1} \right) (n = 1, 2). \end{aligned}$$

When we have at time t the state $|\Psi_u[A_{1,2}]\rangle$ and evolve it, using the iTEBD algorithm, this results in a state with a similar form at time $t + dt$. To compute expectation values or to normalize the state we can use the tools from section 4.2, see in particular algorithms 4.11 and 4.12. Note that the computation time of the iTEBD algorithm (for advancing with a step dt) scales with

$$\mathcal{O} \left(2^3 \max_q (D^q)^3 \right).$$

4.3.2. Thermal evolution

In subsection 3.4.1 we showed that to determine the Gibbs state $\rho = \mathcal{P}e^{\beta \mathcal{H}_\alpha}$ we need to apply imaginary time evolution within the class of states $|\Psi_u[A_1 A_2]\rangle$ that take the form eq. (3.26):

$$\begin{aligned} |\Psi_u[A_1 A_2]\rangle &= \begin{array}{c} \textcircled{v_L^i} \text{---} \textcircled{A_1} \text{---} \textcircled{A_2} \text{---} \dots \text{---} \textcircled{A_1} \text{---} \textcircled{A_2} \text{---} \dots \text{---} \textcircled{A_1} \text{---} \textcircled{A_2} \text{---} \textcircled{v_R} \\ \text{(\kappa_1, \kappa_1^a)} \quad \text{(\kappa_2, \kappa_2^a)} \quad \quad \quad \text{(\kappa_{2n-1}, \kappa_{2n-1}^a) (\kappa_{2n}, \kappa_{2n}^a)} \quad \quad \quad \text{(\kappa_{2N-1}, \kappa_{2N-1}^a) (\kappa_{2N}, \kappa_{2N}^a)} \end{array} \\ &\hspace{15em} (4.56a) \end{aligned}$$

$(N \rightarrow +\infty)$ with $\kappa_n = (s_n, p_n)$, $\kappa_n^a \in \{-1, 1\} \times \mathbb{Z}$ and

$$\begin{array}{c} (q, \alpha_q) - \boxed{A_n} - (r, \beta_r) \\ \downarrow \\ (s, p, s^a, p^a) \end{array} = [a_n^{q, s, s^a}]_{\alpha_q, \beta_r} \delta_{r, q+(s+(-1)^n)/2} \delta_{r, p} \delta_{p^a, q+(s^a+(-1)^n)/2}, \quad (4.56b)$$

$a_n^{q, s, s^a} \in \mathbb{C}^{D_n^q \times D_{n+1}^r}$, $q \in \mathbb{Z}[p_n^{\min}, p_n^{\max}]$, $p, r \in \mathbb{Z}[p_{n+1}^{\min}, p_{n+1}^{\max}]$. At $\beta = 0$ we set

$$a_n^{q, s, s^a} = \delta_{s, s^a} a_n$$

and we have to evolve the state according to

$$|\Psi(\beta)\rangle = e^{-\beta \mathcal{H}_\alpha/2} |\Psi_u[A_1 A_2]\rangle.$$

The Gibbs state is then obtained as

$$\rho(\beta) \propto \text{tr}_{\mathcal{H}^a} (|\Psi_u[A_{1,2}]\rangle \langle \Psi_u[A_{1,2}]|)$$

which means that we have to trace out the auxiliary indices s^a and p^a .

Comparing this ansatz eq. (4.56) with the ansatz eq. (4.25) we observe that the tensors have now the extra label s^a . This is not a physical index and will be traced out. As we will see, we can apply the machinery from the previous subsection but now there will be one or two extra loops with respect to the auxiliary spin indices s^a . To apply the iTEBD we need to discuss the following topics:

- (a) How the contractions in eq. (4.52) must be performed taking into account the block structure eq. (4.56b) and the fact that the operators are gauge invariant and act as the identity on the auxiliary indices s^a and p^a .
- (b) How to normalize the state, i.e. ensuring that $\text{tr}(\rho(\beta)) = 1$. As a nice byproduct we will obtain the free energy from the largest eigenvalue of the transfer matrix.
- (c) How to perform the singular value decomposition eq. (2.25).
- (d) How to compute expectation values of gauge invariant operators.

Because we work in a translational invariant setting over two sites all equalities with respect to the site n have to be read modulo 2, for instance with D_{n+2} we mean D_n and if $n = 2$ then $n + 1$ means 1.

(a) The contractions eq. (4.52)

Here we discuss how to perform the following contractions

$$\begin{array}{c} \boxed{B_n} \\ \downarrow \end{array} = \begin{array}{c} \textcircled{\Xi} \\ \downarrow \end{array} - \begin{array}{c} \boxed{A_n} \\ \downarrow \end{array} - \begin{array}{c} \textcircled{\Lambda} \\ \downarrow \end{array} \quad (4.57a)$$

$$\begin{array}{c} \text{---} \text{---} \text{---} \\ | \quad | \\ \text{---} \end{array} B_{n,n+1} = \begin{array}{c} \text{---} \text{---} \\ | \quad | \\ \text{---} \end{array} A_n \text{---} \begin{array}{c} \text{---} \text{---} \\ | \quad | \\ \text{---} \end{array} A_{n+1} \text{---} \quad (4.57b)$$

$$\begin{array}{c} \text{---} \text{---} \\ | \quad | \\ \text{---} \end{array} B_{n,n+1} = \begin{array}{c} \text{---} \text{---} \\ | \quad | \\ \text{---} \end{array} A_{n,n+1} \\ \text{---} \text{---} \\ | \quad | \\ \text{---} \end{array} \mathcal{U}_{n,n+1} \quad (4.57c)$$

where A_n^{s,p,s^a,p^a} lives on site n , A_{n+1}^{s,p,s^a,p^a} lives on site $n+1$, $A_{n,n+1}^{s_1,p_1,s_1^a,p_1^a,s_2,p_2,s_2^a,p_2^a}$ lives on sites n and $n+1$ and $\mathcal{U}_{n,n+1}$ is a unitary operator acting on sites n and $n+1$. Here the tensors have the following block structure, see eq. (4.56b),

$$\begin{array}{c} (q, \alpha_q) \text{---} \text{---} \\ | \\ (s, p, s^a, p^a) \end{array} A_k \text{---} \begin{array}{c} (r, \beta_r) \\ \text{---} \end{array} = \left[a_k^{q,s,s^a} \right]_{\alpha_q, \beta_r} \delta_{r, q+(s+(-1)^k)/2} \delta_r \delta_{p^a, q+(s^a+(-1)^k)/2},$$

($k = n, n+1$) with $a_k^{q,s,s^a} \in \mathbb{C}^{D_k^q \times D_{k+1}^r}$ ($q \in \mathbb{Z}[p_k^{\min}, p_k^{\max}]$, $r, p, p^a \in \mathbb{Z}[p_{k+1}^{\min}, p_{k+1}^{\max}]$),

$$\begin{array}{c} (q, \alpha_q) \text{---} \text{---} \\ | \quad | \\ (\kappa_1, \kappa_1^a) \quad (\kappa_2, \kappa_2^a) \end{array} A_{n,n+1} \text{---} \begin{array}{c} (r, \beta_r) \\ \text{---} \end{array} = \left[a_{n,n+1}^{q,s_1,s_2,s_1^a,s_2^a} \right]_{\alpha_q, \beta_r} \delta_{p_1, q+(s_1+(-1)^n)/2} \\ \delta_{p_2, q+(s_1+s_2)/2} \delta_{p_1^a, q+(s_1^a+(-1)^n)/2} \delta_{p_2^a, q+(s_1^a+s_2^a)/2} \delta_{r, p_2}$$

with $\kappa_i = (s_i, p_i)$, $\kappa_i^a = (s_i^a, p_i^a)$, $a_{n,n+1}^{q,s_1,s_2,s_1^a,s_2^a} \in \mathbb{C}^{D_k^q \times D_{k+2}^r}$ ($q \in \mathbb{Z}[p_k^{\min}, p_k^{\max}]$, $p_1 \in \mathbb{Z}[p_{k+1}^{\min}, p_{k+1}^{\max}]$, $r, p_2 \in \mathbb{Z}[p_{k+2}^{\min}, p_{k+2}^{\max}]$),

$$[\Xi](q, \alpha); (r, \beta_r) = \delta_{q,r} [\Xi^q]_{\alpha_q, \beta_r}, [\Lambda](q, \alpha); (r, \beta_r) = \delta_{q,r} [\Lambda^q]_{\alpha_q, \beta_r}$$

with $\Xi^q \in \mathbb{C}^{D_n^q \times D_n^q}$ and $\Lambda^q \in \mathbb{C}^{D_{n+1}^q \times D_{n+1}^q}$.

In a similar way as in the previous subsection we find that these diagrams result in tensors with a similar structure:

$$\begin{array}{c} (q, \alpha_q) \text{---} \text{---} \\ | \\ (s, p, s^a, p^a) \end{array} B_n \text{---} \begin{array}{c} (r, \beta_r) \\ \text{---} \end{array} = \left[b_n^{q,s,s^a} \right]_{\alpha_q, \beta_r} \delta_{r, q+(s+(-1)^n)/2} \delta_r \delta_{p^a, q+(s^a+(-1)^n)/2},$$

$$\begin{array}{c} (q, \alpha_q) \text{---} \text{---} \\ | \quad | \\ (\kappa_1, \kappa_1^a) \quad (\kappa_2, \kappa_2^a) \end{array} B_{n,n+1} \text{---} \begin{array}{c} (r, \beta_r) \\ \text{---} \end{array} = \left[b_{n,n+1}^{q,s_1,s_2,s_1^a,s_2^a} \right]_{\alpha_q, \beta_r} \delta_{p_1, q+(s_1+(-1)^n)/2} \\ \delta_{p_2, q+(s_1+s_2)/2} \delta_{p_1^a, q+(s_1^a+(-1)^n)/2} \delta_{p_2^a, q+(s_1^a+s_2^a)/2} \delta_{r, p_2}$$

For eq. (4.57a) we find

$$b_n^{q,s,s^a} = \Xi^q a_n^{q,s,s^a} \Lambda^{q+(s+(-1)^n)/2},$$

for eq. (4.57b) we find

$$b_{n,n+1}^{q,s_1,s_2,s_1^a,s_2^a} = a_n^{q,s_1,s_1^a} a_{n+1}^{q+(s_1+(-1)^n)/2,s_2,s_2^a}$$

and, finally, for eq. (4.57c) we have

$$b_{n,n+1}^{q,s_1,s_2,s_1^a,s_2^a} = \sum_{s'_1,s'_2=\pm 1} \langle s_1, s_2 | u_{n,n+1}^q | s'_1, s'_2 \rangle a_{n,n+1}^{q,s'_1,s'_2,s_1^a,s_2^a}$$

where $\langle s_1, s_2 | u_{n,n+1}^q | s'_1, s'_2 \rangle$ is defined in eq. (4.53). We indeed observe that the auxiliary indices s_1^a, s_2^a, s^a only serve as an additional label.

(b) Normalization of the state

If

$$\rho(\beta) \propto \text{tr}_{\mathcal{H}^a} (|\Psi_u[A_{1,2}]\rangle \langle \Psi_u[A_{1,2}]|)$$

then it follows that for all observables \mathcal{O} that the ensemble average equals

$$\text{tr}(\rho(\beta)\mathcal{O})/Z(\beta) = \langle \Psi_u[A_{1,2}] | \mathcal{O} | \Psi_u[A_{1,2}] \rangle / Z(\beta).$$

with $Z(\beta)$ the partition function,

$$Z(\beta) = \text{tr}(\rho(\beta)) = \langle \Psi_u[A_{1,2}] | \Psi_u[A_{1,2}] \rangle.$$

In order to compute these expectation values we thus need to normalize the uMPS $|\Psi_u[A_{1,2}]\rangle$. Within the iTEBD algorithm we will block the sites $2n - 1$ and $2n$ into one effective site but also the sites $2n$ and $2n + 1$ into one effective site. In both cases we need to normalize a uniform MPS $|\Psi_u[A_{n,n+1}]\rangle$ of the form eq. (1.12) where

$$\begin{aligned} \begin{array}{c} (q, \alpha_q) \text{---} \boxed{A_{n,n+1}} \text{---} (r, \beta_r) \\ \begin{array}{cc} | & | \\ (\kappa_1, \kappa_1^a) & (\kappa_2, \kappa_2^a) \end{array} \end{array} = \left[a_{n,n+1}^{q,s_1,s_2,s_1^a,s_2^a} \right]_{\alpha_q,\beta_r} \delta_{p_1,q+(s_1+(-1)^n)/2} \\ \delta_{p_2,q+(s_1+s_2)/2} \delta_{p_1^a,q+(s_1^a+(-1)^n)/2} \delta_{p_2^a,q+(s_1^a+s_2^a)/2} \delta_{r,p_2} \\ a_{n,n+1}^{q,s_1,s_2,s_1^a,s_2^a} = a_n^{q,s_1,s_1^a} a_{n+1}^{q+(s_1+(-1)^n)/2,s_2,s_2^a}. \end{aligned}$$

This is done by applying algorithm 1.1, but similar to algorithm 4.11 we can speed up the computation by exploiting the block structure of the tensors.

More specifically, as follows from algorithms 1.1 and 4.11 the crucial step is to implement the action of the transfer matrix

$$\mathbb{E}_{n,n+1} \equiv \sum_{\kappa_1, \kappa_1^a, \kappa_2, \kappa_2^a} A_{n,n+1}^{\kappa_1, \kappa_1^a, \kappa_2, \kappa_2^a} \otimes \overline{A}_{n,n+1}^{\kappa_1, \kappa_1^a, \kappa_2, \kappa_2^a}$$

with $\kappa_i = (s_i, p_i)$, $\kappa_i^a = (s_i^a, p_i^a) \in \{-1, 1\} \times \mathbb{Z}$.

If

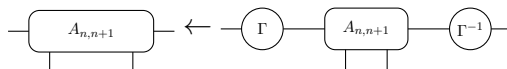
$$[\Xi]_{(q,\alpha);(r,\beta_r)} = \delta_{q,r} [\Xi^q]_{\alpha_q, \beta_r}, [\Lambda]_{(q,\alpha);(r,\beta_r)} = \delta_{q,r} [\Lambda^q]_{\alpha_q, \beta_r}$$

then we find for the left and the right action of the transfer matrix:

$$\begin{aligned} [\mathbb{E}_{n,n+1}^T(\Xi)]_{(q,\alpha);(r,\beta_r)} &= \text{Diagram: A circle containing the symbol } \Xi \text{ is connected to two boxes labeled } A_{n,n+1}. \text{ The top box has an output line labeled } (r, \beta_r). \text{ The bottom box has an input line labeled } (q, \alpha_q). \\ &= \delta_{q,r} \left(\sum_{\{s_k^a\}} \sum_{\{s_k\}} \left[\left(a_{n,n+1}^{q-(s_1+s_2)/2, s_1, s_2, s_1^a, s_2^a} \right)^\dagger \right. \right. \\ &\quad \left. \left. \Xi^{q-(s_1+s_2)/2} a_{n,n+1}^{q-(s_1+s_2)/2, s_1, s_2, s_1^a, s_2^a} \right]_{\alpha_q, \beta_r} \right) \end{aligned}$$

$$\begin{aligned} [\mathbb{E}_{n,n+1}(\Lambda)]_{(q,\alpha);(r,\beta_r)} &= \text{Diagram: A box labeled } A \text{ has an input line labeled } (q, \alpha_q). \text{ A box labeled } A_{n,n+1} \text{ has an input line labeled } (r, \beta_r). \text{ A circle labeled } \Lambda \text{ is connected to the right side of } A \text{ and the right side of } A_{n,n+1}. \\ &= \delta_{q,r} \left(\sum_{\{s_k^a\}} \sum_{\{s_k\}} \left[a_{n,n+1}^{q, s_1, s_2, s_1^a, s_2^a} \right. \right. \\ &\quad \left. \left. \Lambda^{q+(s_1+s_2)/2} \left(a_{n,n+1}^{q, s_1, s_2, s_1^a, s_2^a} \right)^\dagger \right]_{\alpha_q, \beta_r} \right). \end{aligned}$$

If we in algorithm 4.11 implement the functions ‘ApplyTransferLeft’ and ‘ApplyTransferRight’ as above and implement the MPS gauge transformation



as

$$a_{n,n+1}^{q,s_1,s_2,s_1^a,s_2^a} \leftarrow \Gamma^q a_{n,n+1}^{q,s_1,s_2,s_1^a,s_2^a} \left(\Gamma^{q+(s_1+s_2)/2} \right)^{-1}$$

for $q = p_n^{\min}, \dots, p_n^{\max}$, $s_i, s_i^a = -1, 1$ we can obtain the matrices Ξ_{n-1} and Λ_{n+1} corresponding to the left and right eigenvector of the transfer matrix $\mathbb{E}_{n,n+1}$ in

$$\mathcal{O} \left(2^4 N_{iter} \max_q (D_n^q)^3 \right)$$

time.

The matrices Ξ_{n-1} and Λ_{n+1} enable us to compute the Schmidt spectrum of the purification $|\Psi_u[A_{1,2}]\rangle$ of $\rho(\beta)$ and give thus no information about the entanglement properties of the Gibbs state $\rho(\beta)$. They are only useful to control the error when discarding Schmidt values during the iTEBD algorithm.

Every time we normalize the state we divide $A_{n,n+1}$ by $\sqrt{\eta}$ with η the leading eigenvalue of the transfer matrix in magnitude. It is useful to retain the values of η as they give us the free energy (up to an additive constant). If we would define for $\beta = 0$: $f = 0$ and every time we divide $A_{n,n+1}$ by η we update F' according to

$$f_\alpha(\beta) \leftarrow f_\alpha(\beta) + \log(\eta) \quad (4.58a)$$

then we have that

$$-\frac{1}{2\beta} f_\alpha(\beta) = \frac{F_\alpha(\beta)}{2N} + C(N \rightarrow +\infty) \quad (4.58b)$$

with C a constant and

$$F_\alpha(\beta) = (-1/\beta) \log(\text{tr}(\mathcal{P} e^{-\beta \mathcal{H}_\alpha})) \quad (4.58c)$$

the free energy. The reason that we only have the free energy up to a constant is that at $\beta = 0$ we cannot compute the free energy of $\rho(\beta) = \mathcal{P}$ because we would need to keep an infinite number of eigenvalues of $L(n)$. Fortunately, the constant C is independent of α and we can thus consider the finite renormalized quantities

$$\Delta F_\alpha(\beta) = F_\alpha(\beta) - F_0(\beta). \quad (4.58d)$$

More specifically we will be interested in the string tension which equals

$$\sigma_\alpha = \sqrt{x} \frac{\Delta F_\alpha(\beta)}{2N} = -\frac{\sqrt{x}}{2\beta} (f_\alpha(\beta) - f_0(\beta)) \quad (4.58e)$$

and is a UV finite quantity.

(c) The singular value decomposition eq. (2.25)

Here we discuss how we can decompose the tensors $A_{n,n+1}$ on sites n and $n + 1$ in tensors on site n and $n + 1$ as in eq. (2.25):

$$\text{---} \boxed{A_{n,n+1}} \text{---} \stackrel{(SVD)}{=} \text{---} \boxed{U_n} \text{---} \boxed{\Sigma_{n+1}} \text{---} \boxed{V_{n+1}} \text{---}$$

where

$$\begin{array}{c} \text{---} \boxed{U_n} \text{---} \\ | \\ \text{---} \boxed{\mathbb{1}_{D_n}} \text{---} \\ | \\ \text{---} \boxed{U_n} \text{---} \end{array} = \mathbb{1}_{D_{n+1}}, \quad \begin{array}{c} \text{---} \boxed{V_{n+1}} \text{---} \\ | \\ \text{---} \boxed{\mathbb{1}_{D_{n+1}}} \text{---} \\ | \\ \text{---} \boxed{V_{n+1}} \text{---} \end{array} = \mathbb{1}_{D_{n+1}}$$

and $\Sigma_{n+1} \in \mathbb{C}^{D_{n+1} \times D_{n+1}}$ is a positive definite diagonal matrix.

If $A_{n,n+1}$ is of the form

$$\underset{(s,p,s^a,p^a)}{\overset{(q,\alpha_q)}{\boxed{A_n}}}(r,\beta_r) = [a_n^{q,s,s^a}]_{\alpha_q,\beta_r} \delta_{r,q+(s+(-1)^n)/2} \delta_{r,p} \delta_{p^a,q+(s^a+(-1)^n)/2}$$

then for every q for which $q - (s_1 + (-1)^n)/2, q + (s_2 + (-1)^{n+1})/2 \in \mathbb{Z}[p_{min}^n, p_{max}^n]$ we perform a singular value decomposition of $\tilde{a}^q \in \mathbb{C}^{2F_{n+1}^q \times 2F_{n+1}^q}$, with

$$F_{n+1} = \sum_{s=-1,1} D_n^{q-(s+(-1)^n)/2} = \sum_{s=-1,1} D_n^{q+(s+(-1)^{n+1})/2}$$

and

$$\begin{aligned} [\tilde{a}^q]_{(\alpha,s_1,s_1^q)(\beta,s_2,s_2^q)} &= [a^{q-(s_1+(-1)^n)/2,s_1,s_2,s_1^q,s_2^q}]_{\alpha,\beta}, \\ \tilde{a}^q &= \tilde{U}^q \Sigma_{n+1}^q \tilde{V}^q \end{aligned}$$

where $\tilde{U}^q \in \mathbb{C}^{2F_{n+1}^q \times 2F_{n+1}^q}$ and $\tilde{V}^q \in \mathbb{C}^{2F_{n+1}^q \times 2F_{n+1}^q}$ are unitary matrices and $\Sigma_{n+1}^q \in \mathbb{C}^{2F_{n+1}^q \times 2F_{n+1}^q}$ is a positive diagonal matrix. Next, one defines

$$\begin{aligned} [U_n^{s,p,s^a,p^a}]_{(q,\alpha),(r,\beta)} &= \delta_{p,q+(s+(-1)^n)/2} \delta_{p^a,q^a+(s^a+(-1)^n)/2} \delta_{p,r} [u_n^{q,s,s^a}]_{\alpha,\beta} \\ &\text{with } [u_n^{q,s}]_{\alpha,\beta} = \left[\tilde{U}^{q+(s+(-1)^n)/2} \right]_{(\alpha,s,s^a),\beta} \end{aligned}$$

$$\begin{aligned} [V_{n+1}^{s,p,s^a,p^a}]_{(q,\alpha),(r,\beta)} &= \delta_{p,q+(s+(-1)^{n+1})/2} \delta_{p^a,q^a+(s^a+(-1)^{n+1})/2} \delta_{p,r} [v_{n+1}^{q,s,s^a}]_{\alpha,\beta} \\ &\text{with } [v_{n+1}^{q,s,s^a}]_{\alpha,\beta} = \left[\tilde{V}^q \right]_{\alpha,(\beta,s,s^a)} \end{aligned}$$

$$[\Sigma_{n+1}]_{(q,\alpha);(r,\beta_r)} = \delta_{q,r} [\Sigma_{n+1}^q]_{\alpha_q,\beta_r}$$

where $u_n^{q,s} \in \mathbb{C}^{D_n^q \times 2F_{n+1}^q}$ and $v_n^{q,s} \in \mathbb{C}^{2F_{n+1}^q \times D_{n+2}^q}$. With these definitions, we indeed recover

$$\text{---} \boxed{A_{n,n+1}} \text{---} \stackrel{(SVD)}{=} \text{---} \boxed{U_n} \text{---} \boxed{\Sigma_{n+1}} \text{---} \boxed{V_{n+1}} \text{---}$$

as in eq. (2.25).

Notice that if we allow on site n and on site $n + 2$ the eigenvalues $q \in \mathbb{Z}[p_n^{\min}, p_n^{\max}]$ of $L(n)$ that this implicitly means that we retain the eigenvalues $q \in \mathbb{Z}[p_{n+1}^{\min}, p_{n+1}^{\max}]$ of $L(n + 1)$ in our numerical scheme where

$$p_{n+1}^{\min} = p_n^{\min} - 1 \text{ if } n \text{ is odd, } p_{n+1}^{\min} = p_n^{\min} \text{ if } n \text{ is even,}$$

$$p_{n+1}^{\max} = p_n^{\max} + 1 \text{ if } n \text{ is even, } p_{n+1}^{\max} = p_n^{\max} \text{ if } n \text{ is odd.}$$

In this way we can dynamically expand the eigenvalues of $L(n)$ we keep in our numerical scheme. Also, similar to the general iTEBD algorithm, section 2.3, it follows that at site $n + 1$ the bond dimension equals

$$D_{n+1}^q = 2F_{n+1}^q = 2(D_n^q + D_n^{q+(-1)^n}) \sim 4D_n^q.$$

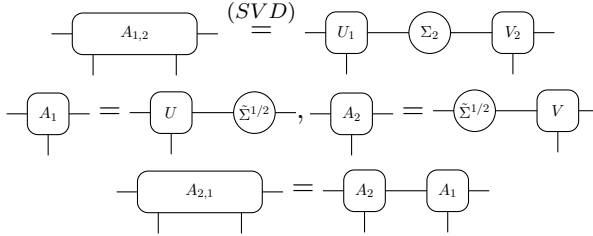
When applying the iTEBD algorithm and performing the singular value decompositions exactly this would lead to an exponential increase of D_{n+1}^q . Therefore one can discard the diagonal elements of Σ_n^q smaller than a tolerance ϵ . In particular, it is even possible to discard the sector corresponding to the eigenvalue q of $L(n + 1)$: if all singular values of Σ_{n+1}^q are smaller than ϵ we put $D_{n+1}^q = 0$. Note that discarding the singular values of Σ_{n+1}^q corresponds to a truncation in the Schmidt spectrum of the purification $|\Psi_u[A_{n,n+1}]\rangle$ of $\rho(\beta)$. The Schmidt values that we now obtain are thus only useful for numerical purposes but don't tell us anything about the entanglement properties of the Gibbs state $\rho(\beta)$.

(d) Expectation values of gauge invariant operators

Starting at inverse temperature β the state $|\Psi_u[A_{1,2}]\rangle$ is evolved using the iTEBD algorithm 2.5, but taking into account the special structure of the tensors by computing the contractions, performing the normalization and performing the singular value decomposition as discussed in (a), (b) and (c). The computation time of the iTEBD algorithm for advancing with a step $d\beta$ scales with

$$\mathcal{O}\left(2^6 \max_q (D^q)^3\right).$$

To compute expectation values we first decompose the tensor $A_{1,2}$ using the singular value decomposition discussed in (c) and reblock the sites $2n$ and $2n + 1$:



In the thermodynamic limit we have that $|\Psi_u[A_{1,2}]\rangle = |\Psi_u[A_{2,1}]\rangle$. If we now normalize both representations as discussed in (a) and the matrices Ξ_{n-1} and Λ_{n+1} correspond to the left and right eigenvector of the leading eigenvalue of the transfer matrix $\mathbb{E}_{n,n+1}$, then we find for an observable \mathcal{O} which is translation invariant over two sites,

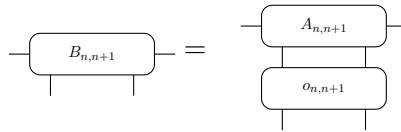
$$\mathcal{O} = \sum_{n=1}^{2N-1} o_{n,n+1}, o_{2n-1,2n} = \mathcal{T}^{2n-2} o_{1,2} \mathcal{T}^{-2n+2},$$

$$o_{2n,2n+1} = \mathcal{T}^{2n-2} o_{2,3} \mathcal{T}^{-2n+2},$$

for the ensemble average per site that

$$\lim_{N \rightarrow +\infty} \frac{1}{2N} \text{tr}(\mathcal{O} \rho(\beta)) = \frac{1}{2} \left(\begin{array}{c} \text{Diagram 1: } \Xi_2 \text{ connected to } A_1, A_2 \text{ and } o_{1,2} \\ \text{Diagram 2: } \Xi_1 \text{ connected to } A_2, A_1 \text{ and } o_{2,3} \end{array} \right).$$

Diagrams of these types are computed as before: first one computes



as discussed in (a). Then one computes

$$\Omega_{n-1}^q = \sum_{\{s_k\}} \sum_{\{s_k^a\}} b_{n,n+1}^{q,s_1,s_2,s_1^a,s_2^a} \Lambda_{n+1}^{q+(s_1+s_2)/2} \left(a_{n,n+1}^{q,s_1,s_2,s_1^a,s_2^a} \right)^\dagger$$

and we arrive at

$$\text{tr}(\Xi_{n-1}^q \Omega_{n-1}^q) = \sum_{q=p_n^{min}}^{p_n^{max}} \text{tr}(\Xi_{n-1}^q \Omega_{n-1}^q).$$

4.4. Confinement: from small to large distances

4.4.1. MPS ansatz

Here we discuss the simulations for confinement between static charges separated by a finite distance, see section 3.4 of part I. We consider a slightly more general setting where the Hamiltonian equals

$$\mathcal{H} = \frac{g}{2\sqrt{x}} \left(\sum_{n=-N_L}^{M+N_R-1} [L(n) + \alpha(n)]^2 + \frac{\sqrt{x}}{g} m \sum_{n=-N_L}^{M+N_R-1} (-1)^n \sigma_z(n) + x \sum_{n=-N_L}^{M+N_R-1} (\sigma^+(n) e^{i\theta(n)} \sigma^-(n+1) + h.c.) \right),$$

where

$$\alpha(n) = \alpha_L \text{ for } -N_L \leq n \leq m_L$$

$$\alpha(n) = \alpha_R \text{ for } m_R + 1 \leq n \leq M + N_R$$

with α_L, α_R independent of n and $-N_L \ll 1 \leq m_L \leq m_R \leq M \ll M + N_R$. For $m_L + 1 \leq n \leq m_R$ we allow $\alpha(n)$ to be any function of n . The thermodynamic limit is now obtained by taking the limits $N_L, N_R \rightarrow +\infty$ while keeping m_L, m_R and M fixed. Notice that this Hamiltonian takes the same form as the Hamiltonian discussed in section 2.4. Therefore, a MPS ansatz for the ground state is, see eq. (2.30),

$$|\Psi[B]\rangle = \begin{array}{c} \textcircled{B_0} - \textcircled{B_1} - \textcircled{B_2} - \dots - \textcircled{B_n} - \dots - \textcircled{B_{M-1}} - \textcircled{B_M} - \textcircled{B_{M+1}} \\ \downarrow \quad \downarrow \quad \downarrow \quad \quad \downarrow \quad \quad \quad \downarrow \quad \downarrow \quad \downarrow \\ (\kappa_{-N_L}, \dots, \kappa_0) \quad \kappa_1 \quad \kappa_2 \quad \quad \kappa_n \quad \quad \quad \kappa_{M-1} \quad \kappa_M \quad (\kappa_{M+1}, \dots, \kappa_{M+N_R}) \end{array} \quad (4.59a)$$

with $B_n^{\kappa_n} \in \mathbb{C}^{D_n \times D_{n+1}}$,

$$\begin{array}{c} \textcircled{B_0} - \\ \downarrow \\ (\kappa_{-N_L}, \dots, \kappa_0) \end{array} = \begin{array}{c} \textcircled{v_L^\dagger} - \textcircled{L_1} - \textcircled{L_2} - \dots - \textcircled{L_1} - \textcircled{L_2} - \\ \downarrow \quad \downarrow \quad \downarrow \quad \quad \downarrow \quad \downarrow \\ \kappa_{-N_L} \quad \kappa_{-N_L+1} \quad \quad \quad \kappa_{-1} \quad \kappa_0 \end{array} \quad (4.59b)$$

and

$$\begin{array}{c} - \textcircled{B_{M+1}} \\ \downarrow \\ (\kappa_{M+1}, \dots, \kappa_{M+N_R}) \end{array} = \begin{array}{c} - \textcircled{R_1} - \textcircled{R_2} - \dots - \textcircled{R_1} - \textcircled{R_2} - \textcircled{v_R} \\ \downarrow \quad \downarrow \quad \quad \downarrow \quad \downarrow \\ \kappa_{M+1} \quad \kappa_{M+2} \quad \quad \quad \kappa_{M+N_R-1} \quad \kappa_{M+N_R} \end{array} \quad (4.59c)$$

$\kappa_n = (s_n, p_n) \in \{-1, 1\} \times \mathbb{Z}[p_{n+1}^{min}, p_{n+1}^{max}]$ where R_n resp. L_n are the tensors corresponding to the MPS approximation $|\Psi_u[L_1 L_2]\rangle$ resp. $|\Psi_u[R_1 R_2]\rangle$ of the ground state of the Hamiltonian eq. (3.1) with a uniform electric

background field $\alpha(n) = \alpha_L$ resp. $\alpha(n) = \alpha_R$. We assume that L_n resp. R_n is in the left resp. right canonical form. As a MPS approximation for the ground state of a gauge invariant Hamiltonian they have the following block-structure:

$$\begin{array}{c} (q, \alpha_q) \text{---} \boxed{R_n} \text{---} (r, \beta_r) \\ | \\ \kappa \end{array} = [r_n^{q,s}]_{\alpha_q, \beta_r} \delta_{r, q+(s+(-1)^n)/2} \delta_{r,p} \quad (4.59d)$$

$$\begin{array}{c} (q, \alpha_q) \text{---} \boxed{L_n} \text{---} (r, \beta_r) \\ | \\ \kappa \end{array} = [l_n^{q,s}]_{\alpha_q, \beta_r} \delta_{r, q+(s+(-1)^n)/2} \delta_{r,p} \quad (4.59e)$$

for $r_n^{q,s} \in \mathbb{C}^{D_n^{R,q} \times D_{n+1}^{R,r}}$ and $l_n^{q,s} \in \mathbb{C}^{D_n^{L,q} \times D_{n+1}^{L,r}}$. Note also that we here assume that M and N_R are even and that N_L is odd. In order that the state obeys $G_n |\Psi[B]\rangle = 0$ we impose the same block structure on B_n :

$$\begin{array}{c} (q, \alpha_q) \text{---} \boxed{B_n} \text{---} (r, \beta_r) \\ | \\ \kappa \end{array} = [b_n^{q,s}]_{\alpha_q, \beta_r} \delta_{r, q+(s+(-1)^n)/2} \delta_{r,p} \quad (4.59f)$$

with $b_n^{q,s} \in \mathbb{C}^{D_n^q \times D_{n+1}^r}$, $D_1^q = D_1^{L,q}$, $D_{M+1}^q = D_1^{R,q}$.

4.4.2. DMRG

The ansatz eq. (4.59) is linear in each of the $b_n^{q,s}$, hence we can use the DMRG algorithm, see section 2.4 and in particular in algorithm 2.6, to find an optimal approximation for the ground state. We recall that the DMRG minimizes

$$H(B_1, \dots, B_M) = \frac{\langle \Psi[\bar{B}] | \mathcal{H} | \Psi[B] \rangle}{\langle \Psi[\bar{B}] | \Psi[B] \rangle}$$

with respect to B_n by sweeping from left to right, i.e. from site $n = 1$ until site $n = M$, and sweeping back, i.e. from site $n = M$ until site $n = 1$, thereby finding for every n the smallest eigenvalue and corresponding eigenvector of

$$\begin{aligned} & [\mathbb{H}_n]_{(\kappa', (q', \gamma_{q'}), (r', \delta_{r'})); (\kappa, (q, \alpha_q), (r, \beta_r))} \\ &= \frac{\partial}{\partial [B_n^{\kappa'}]_{(q, \alpha_q), (r, \beta_r)}} \frac{\partial}{\partial [\bar{B}_n^{\kappa'}]_{(q', \gamma_{q'}), (r', \delta_{r'})}} H(B_1, \dots, B_M), \end{aligned}$$

with

$$\begin{aligned} \kappa &= (s, p), \kappa' = (s', p') \in \{-1, 1\} \times \mathbb{Z}[p_{n+1}^{\min}, p_{n+1}^{\max}]; q, q' \in \mathbb{Z}[p_n^{\min}, p_n^{\max}]; \\ r, r' &\in \mathbb{Z}[p_{n+1}^{\min}, p_{n+1}^{\max}]; \alpha_q = 1, \dots, D_n^q; \gamma_{q'} = 1, \dots, D_n^{q'}; \\ &\beta_r = 1, \dots, D_{n+1}^r; \delta_{r'} = 1, \dots, D_{n+1}^{r'}. \end{aligned}$$

In our case B_n^κ takes the form eq. (4.59f), hence we need to minimize $H(B_1, \dots, B_M)$ with respect to the variational degrees of freedom b_n^κ . When now performing the sweeps we need to find for every n the smallest eigenvalue and corresponding eigenvector of

$$[\mathbb{H}_n]_{(q', s' \gamma_{q'}, \delta_{r'}) ; (q, s, \alpha_q, \beta_r)} = \frac{\partial}{\partial [b_n^{q, s}]_{\alpha_q, \beta_r}} \frac{\partial}{\partial [\bar{b}_n^{q', s'}]_{\gamma_{q'}, \delta_{r'}}} H(B_1, \dots, B_M).$$

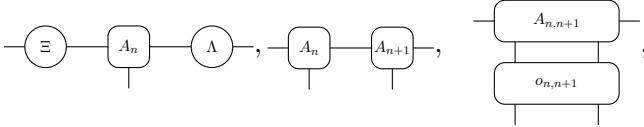
We can now apply algorithm 2.6 for the DMRG, but now taking into account the structure (4.59f) of B_n^κ . Specifically, this means that, similar to subsection 4.3.1 for the iTEBD algorithm, we have to contract the tensor network diagrams that occur in algorithm 2.6 on the level of the matrices $b_n^{q, s}$, $l_n^{q, s}$ and $r_n^{q, s}$. In subsection 4.3.1 we discussed already if A_n takes the form

$$\begin{array}{c} (q, \alpha_q) \text{---} \boxed{A_n} \text{---} (r, \beta_r) \\ | \\ (s, p) \end{array} = [a_n^{q, s}]_{\alpha_q, \beta_r} \delta_{r, q + (s + (-1)^n) / 2} \delta_{r, p},$$

and $A_{n, n+1}$ takes the form

$$\begin{array}{c} (q, \alpha_q) \text{---} \boxed{A_{n, n+1}} \text{---} (r, \beta_r) \\ | \quad | \\ (s_1, p_1) \quad (s_2, p_2) \end{array} = [a_{n, n+1}^{q, s_1, s_2}]_{\alpha_q, \beta_r} \delta_{p_1, q + (s_1 + (-1)^n) / 2} \delta_{p_2, q + (s_1 + s_2) / 2} \delta_{r, p_2}$$

how to contract tensor network diagrams of the form



see eq. (4.52), and how to perform the singular value decomposition,

$$\boxed{A_{n, n+1}} \stackrel{(SVD)}{=} \boxed{U_n} \text{---} \text{---} \text{---} \boxed{\Sigma_{n+1}} \text{---} \text{---} \text{---} \boxed{V_{n+1}},$$

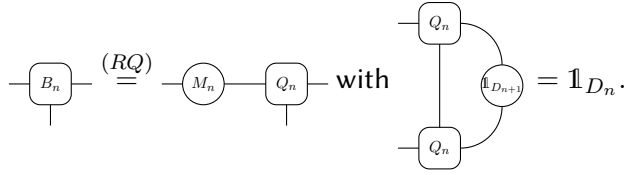
see eq. (4.54).

Looking at algorithm 2.6 we only need to discuss how

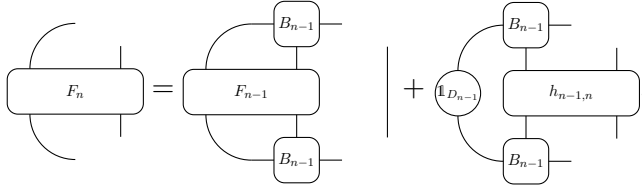
(a) to bring B_n in the left canonical form:

$$\boxed{B_n} \stackrel{(QR)}{=} \boxed{Q_n} \text{---} \text{---} \text{---} \boxed{M_n} \text{ with } \begin{array}{c} \text{---} \text{---} \text{---} \boxed{Q_n} \text{---} \\ | \\ \text{---} \text{---} \text{---} \boxed{Q_n} \text{---} \end{array} = \mathbb{1}_{D_{n+1}}.$$

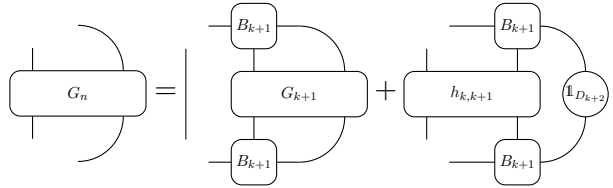
(b) to bring B_n in the right canonical form:



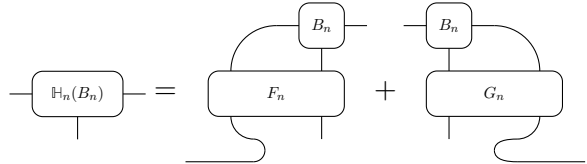
(c) to update F_n , see eq. (2.37),



(d) to update G_n , see eq. (2.37),



(e) to implement the action of H_n on $b_n^{q,s}$, see eq. (2.38),



(a) QR decomposition to put B_n in the left canonical form

When B_n takes the form

$$\begin{array}{c} (q, \alpha_q) \\ | \\ \boxed{B_n} \\ | \\ (s, p) \end{array} \begin{array}{c} (r, \beta_r) \\ | \\ \end{array} = [b_n^{q,s}]_{\alpha_q, \beta_r} \delta_{p, q + (s + (-1)^n)/2} \delta_{r, p}$$

then for every $q \in \mathbb{Z}[p_{min}^{n+1}, p_{max}^{n+1}]$ for which $q - (s + (-1)^n)/2 \in \mathbb{Z}[p_{min}^n, p_{max}^n]$ we perform a QR decomposition of $\tilde{b}_n^q \in \mathbb{C}^{F_n^q \times D_{n+1}^q}$, with

$$F_n = \sum_{s=-1,1} D_n^{q - (s + (-1)^n)/2}$$

and

$$\left[\tilde{b}_n^q \right]_{(\alpha,s),\beta} = [b_n^{q-(s+(-1)^n)/2,s}]_{\alpha,\beta},$$

$$\tilde{b}_n^q = \tilde{Q}_n^q \tilde{M}_n^q$$

where $\tilde{Q}_n^q \in \mathbb{C}^{F_n^q \times \tilde{D}_{n+1}^q}$ is an isometry,

$$(\tilde{Q}_n^q)^\dagger \tilde{Q}_n^q = \mathbb{1}_{\tilde{D}_{n+1}^q}, \tilde{D}_{n+1}^q = \min(F_n^q, D_{n+1}^q)$$

and $\tilde{M}_n^q \in \mathbb{C}^{\tilde{D}_{n+1}^q \times D_{n+1}^q}$. Next, one defines

$$[Q_n^{s,p}]_{(q,\alpha),(r,\beta)} = \delta_{p,q+(s+(-1)^n)/2} \delta_{p,r} [q_n^{q,s}]_{\alpha,\beta}$$

$$\text{with } [q_n^{q,s}]_{\alpha,\beta} = \left[\tilde{Q}^{q+(s+(-1)^n)/2} \right]_{(\alpha,s),\beta} \text{ and } [M_n]_{(q,\alpha),(r,\beta)} = \delta_{q,r} [M_n^q]_{\alpha,\beta},$$

where $q_n^{q,s} \in \mathbb{C}^{D_n^q \times \tilde{D}_{n+1}^q}$ and $M_n^q \in \mathbb{C}^{\tilde{D}_{n+1}^q \times D_{n+1}^q}$. With these definitions, we indeed recover

Notice that if we set b_n equal to Q_n and absorb M_n into B_{n+1} ,

$$\text{---} \boxed{B_{n+1}} \text{---} \leftarrow \text{---} \bigcirc M_n \text{---} \boxed{B_{n+1}} \text{---}, \text{ i.e. } b_{n+1}^{q,s} \leftarrow M_n^q b_{n+1}^{q,s},$$

that we change the bond dimension on site $n+1$ from D_{n+1}^q to $\tilde{D}_{n+1}^q = \min(D_{n+1}^q, F_{n+1}^q)$. This is not a truncation in the state but only a MPS gauge transformation. If B_1, \dots, B_{n-1} are in the left canonical form and B_{n+1}, \dots, B_M are in the right canonical form then we can compute from M_n^q the Schmidt values: if we denote with σ_{n,α_q}^q the eigenvalues of Σ_n^q (Σ_n^q) † ,

$$\Sigma_n^q = M_n^q / \left(\sqrt{\sum_{q=p_{n+1}^{\min}}^{p_{n+1}^{\max}} \text{tr} \left(M_n^q (M_n^q)^\dagger \right)} \right),$$

then the Schmidt decomposition of $|\Psi[B]\rangle$ with respect to the bipartition $\{\mathcal{A}_1^n = \mathbb{Z}[-N_L, \dots, n], \mathcal{A}_2^n = \mathbb{Z}[n+1, M+N_R]\}$ of the lattice reads ($1 \leq n \leq M$)

$$|\Psi[B]\rangle = \sum_{q=p_{n+1}^{\min}}^{p_{n+1}^{\max}} \sum_{\alpha_q=1}^{D_{n+1}^q} \sqrt{\sigma_{n,\alpha_q}^q} |\Phi_{q,\alpha_q}^{\mathcal{A}_1^n}\rangle \otimes |\Phi_{q,\alpha_q}^{\mathcal{A}_2^n}\rangle$$

where

$$1 \geq \sigma_{n,1}^q \geq \sigma_{n,2}^q \geq \dots \geq \sigma_{n,D_{n+1}^q}^q \geq 0, \quad \sum_{q=p_{n+1}^{min}}^{p_{n+1}^{max}} \sum_{\alpha_q=1}^{D_{n+1}^q} \sigma_{n,\alpha_q}^q = 1$$

and

$$\left| \Phi_{q,\alpha_q}^{\mathcal{A}_1^n} \right\rangle \in \bigotimes_{j \in \mathcal{A}_1^n} \mathcal{H}_j \quad \text{and} \quad \left| \Phi_{q,\alpha_q}^{\mathcal{A}_2^n} \right\rangle \in \bigotimes_{j \in \mathcal{A}_2^n} \mathcal{H}_j$$

are orthonormal unit vectors,

$$\left\langle \Phi_{q,\alpha_q}^{\mathcal{A}_1^n} \middle| \Phi_{r,\beta_r}^{\mathcal{A}_1^n} \right\rangle = \delta_{q,r} \delta_{\alpha_q,\beta_r}, \quad \left\langle \Phi_{q,\alpha}^{\mathcal{A}_2^n} \middle| \Phi_{r,\beta_r}^{\mathcal{A}_2^n} \right\rangle = \delta_{q,r} \delta_{\alpha_q,\beta_r}.$$

(b) RQ decomposition to put B_n in the right canonical form

When B_n takes the form

$$\begin{array}{c} (q, \alpha_q) \text{---} \boxed{B_n} \text{---} (r, \beta_r) \\ \text{---} \downarrow \text{---} \\ (s, p) \end{array} = [b_n^{q,s}]_{\alpha_q,\beta_r} \delta_{p,q+(s+(-1)^n)/2} \delta_{r,p}$$

then for every $q \in \mathbb{Z}[p_{min}^n, p_{max}^n]$ for which $q+(s+(-1)^n)/2 \in \mathbb{Z}[p_{min}^{n+1}, p_{max}^{n+1}]$ we perform a QR decomposition of $\tilde{b}_n^q \in \mathbb{C}^{F_{n+1}^q \times D_n^q}$, with

$$F_{n+1} = \sum_{s=-1,1} D_{n+1}^{q+(s+(-1)^n)/2}$$

and

$$\left[\tilde{b}_n^q \right]_{(\alpha,s),\beta} = \left[(b_n^{q,s})^\dagger \right]_{\alpha,\beta},$$

$$\tilde{b}_n^q = \tilde{Q}_n^q \tilde{M}_n^q$$

where $\tilde{Q}_n^q \in \mathbb{C}^{F_{n+1}^q \times \tilde{D}_n^q}$ is an isometry,

$$(\tilde{Q}_n^q)^\dagger \tilde{Q}_n^q = \mathbf{1}_{\tilde{D}_n^q}, \quad \tilde{D}_n^q = \min(F_{n+1}^q, D_n^q)$$

and $\tilde{M}_n^q \in \mathbb{C}^{\tilde{D}_n^q \times D_n^q}$. Next, one defines

$$[Q_n^{s,p}]_{(q,\alpha),(r,\beta)} = \delta_{p,q+(s+(-1)^n)/2} \delta_{p,r} [q_n^{q,s}]_{\alpha,\beta}$$

$$\text{with } [q_n^{q,s}]_{\alpha,\beta} = \left[(\tilde{Q}^q)^\dagger \right]_{\alpha,(\beta,s)} \quad \text{and} \quad [M_n]_{(q,\alpha),(r,\beta)} = \delta_{q,r} \left[(M_n^q)^\dagger \right]_{\alpha,\beta}$$

where $q_n^{q,s} \in \mathbb{C}^{\tilde{D}_n^q \times D_{n+1}^q}$ and $M_n^q \in \mathbb{C}^{D_n^q \times \tilde{D}_n^q}$. With these definitions, we indeed recover

The diagram shows an equality between two tensor networks. On the left, a box labeled B_n is connected to a circle labeled M_n , which is then connected to another box labeled Q_n . This is followed by the word "with". On the right, two boxes labeled Q_n are connected to a central circle labeled $\mathbb{1}_{D_{n+1}}$. The entire right-hand side is equated to $\mathbb{1}_{\tilde{D}_n}$.

Notice that if we set B_n equal to Q_n and absorb M_n into B_{n-1} ,

The diagram shows a box labeled B_{n-1} connected to a circle labeled M_n , which is then connected to another box labeled B_{n-1} . This is followed by the text "i.e. $b_{n-1}^{q,s} \leftarrow b_{n-1}^{q,s} M_n^{q+(s+(-1)^{n-1})/2}$ ".

that we change the bond dimension from D_n^q to $\tilde{D}_n^q = \min(D_n^q, F_n^q)$. If B_1, \dots, B_{n-1} are in the left canonical form and B_{n+1}, \dots, B_M are in the right canonical then we can compute from M_n^q the Schmidt values: if we denote with σ_{n-1, α_q}^q the eigenvalues of $\Sigma_{n-1}^q (\Sigma_{n-1}^q)^\dagger$,

$$\Sigma_{n-1}^q = M_n^q / \left(\sqrt{\sum_{q=p_n^{\min}}^{p_n^{\max}} \text{tr} \left(M_n^q (M_n^q)^\dagger \right)} \right)$$

then the Schmidt decomposition of $|\Psi[B]\rangle$ with respect to the bipartition $\{\mathcal{A}_1^{n-1} = \mathbb{Z}[-N_L, \dots, n-1], \mathcal{A}_2^{n-1} = \mathbb{Z}[n, M+N_R]\}$ of the lattice reads ($1 \leq n \leq M$)

$$|\Psi[B]\rangle = \sum_{q=p_n^{\min}}^{p_n^{\max}} \sum_{\alpha_q=1}^{D_n^q} \sqrt{\sigma_{n-1, \alpha_q}^q} \left| \Phi_{q, \alpha_q}^{\mathcal{A}_1^{n-1}} \right\rangle \otimes \left| \Phi_{q, \alpha_q}^{\mathcal{A}_2^{n-1}} \right\rangle$$

where

$$1 \geq \sigma_{n-1, 1}^q \geq \sigma_{n-1, 2}^q \geq \dots \geq \sigma_{n-1, D_n^q}^q \geq 0, \quad \sum_{q=p_n^{\min}}^{p_n^{\max}} \sum_{\alpha_q=1}^{D_n^q} \sigma_{n-1, \alpha_q}^q = 1$$

and

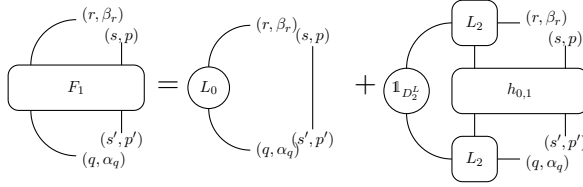
$$\left| \Phi_{q, \alpha_q}^{\mathcal{A}_1^{n-1}} \right\rangle \in \bigotimes_{j \in \mathcal{A}_1^{n-1}} \mathcal{H}_j \quad \text{and} \quad \left| \Phi_{q, \alpha_q}^{\mathcal{A}_2^{n-1}} \right\rangle \in \bigotimes_{j \in \mathcal{A}_2^{n-1}} \mathcal{H}_j$$

are orthonormal unit vectors,

$$\left\langle \Phi_{q, \alpha_q}^{\mathcal{A}_1^{n-1}} \middle| \Phi_{r, \beta_r}^{\mathcal{A}_1^{n-1}} \right\rangle = \delta_{q,r} \delta_{\alpha_q, \beta_r}, \quad \left\langle \Phi_{q, \alpha}^{\mathcal{A}_2^{n-1}} \middle| \Phi_{r, \beta_r}^{\mathcal{A}_2^{n-1}} \right\rangle = \delta_{q,r} \delta_{\alpha_q, \beta_r}.$$

(c) Computation of F_n

For F_1 we have that, see eq. (2.37)



where the expression of L_0 can be found in eq. (2.32). Note that L_0 can be computed efficiently using algorithm 4.16 and that L_0 is block diagonal

$$[L_0]_{(q, \alpha_q), (r, \beta_r)} = \delta_{q,r} = [L_0^q]_{\alpha_q, \beta_r}.$$

Therefore, it follows from gauge invariance of \mathcal{H} that F_1 takes the form

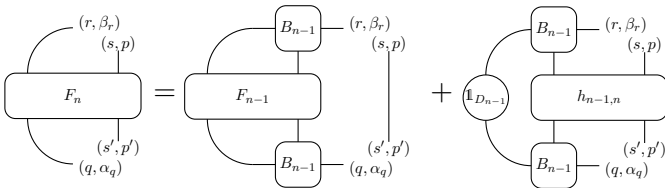
$$[F_1^{(s', p'), (s, p)}]_{(q, \alpha_q), (r, \beta_r)} = \delta_{p, p'} \delta_{r, q+(s'-s)/2} \left[f_1^{q, s', s} \right]_{\alpha_q, \beta_r} \quad (4.60a)$$

where

$$f_1^{q, s', s} = \delta_{s, s'} L_0^q + \sum_{t, t'=-1, 1} \delta_{t-t', s'-s} \langle t', s' | h_{0,1}^{q-(t'+1)/2} | t, s \rangle \left(\left[l_2^{q-(t'+1)/2, t'} \right]^\dagger l_2^{q-(t'+1)/2, t} \right). \quad (4.60b)$$

where the matrix elements $\langle t', s' | h_{n,n+1}^q | t, s \rangle$ are defined in eq. (3.29).

Similarly, it follows from



that

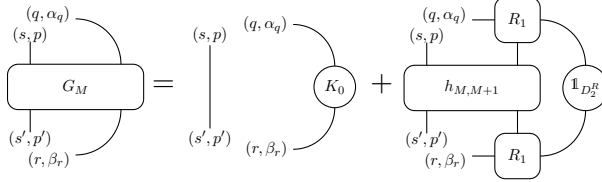
$$[F_n^{(s', p'), (s, p)}]_{(q, \alpha_q), (r, \beta_r)} = \delta_{p, p'} \delta_{r, q+(s'-s)/2} \left[f_n^{q, s', s} \right]_{\alpha_q, \beta_r} \quad (4.60c)$$

with

$$\begin{aligned}
 & f_n^{q,s',s} \\
 = & \delta_{s,s'} \sum_{t,t'=-1,1} \left[b_{n-1}^{q-(t'+(-1)^{n-1})/2,t'} \right]^\dagger f_{n-1}^{q-(t'+(-1)^{n-1})/2,t',t} b_{n-1}^{q-(t+(-1)^{n-1})/2,t} \\
 & + \sum_{t,t'=-1,1} \left[\delta_{t-t',s'-s} \langle t', s' | h_{n-1,n}^{q-(t'+(-1)^{n-1})/2} | t, s \rangle \right. \\
 & \left. \left(\left[b_{n-1}^{q-(t'+(-1)^{n-1})/2,t'} \right]^\dagger b_{n-1}^{q-(t'+(-1)^{n-1})/2,t} \right) \right]. \quad (4.60d)
 \end{aligned}$$

(d) Computation of G_n

For G_M we have that, see eq. (2.37)



where the expression of K_0 can be found in eq. (2.33). Note that K_0 can be computed efficiently using algorithm 4.15 and that K_0 is block diagonal

$$[K_0]_{(q,\alpha_q),(r,\beta_r)} = \delta_{q,r} = [K_0^q]_{\alpha_q,\beta_r}.$$

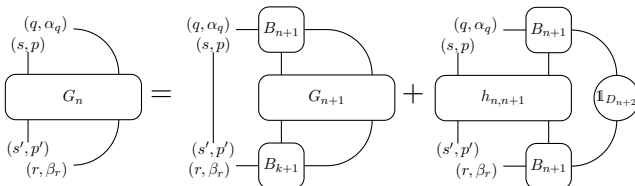
Therefore, it follows from gauge invariance of \mathcal{H} that F_1 takes the form

$$[G_M^{(s',p'),(s,p)}]_{(q,\alpha_q),(r,\beta_r)} = \delta_{p,p'} \delta_{r,q+(s'-s)/2} \left[g_M^{q,s',s} \right]_{\alpha_q,\beta_r} \quad (4.61a)$$

with

$$\begin{aligned}
 g_M^{q,s',s} &= \delta_{s,s'} K_0^q \\
 &+ \sum_{t,t'=-1,1} \delta_{t-t',s'-s} \langle s', t' | h_{M,M+1}^{q-(s+1)/2} | s, t \rangle \left(r_1^{q,t} \left[r_1^{q+(t-t')/2,t'} \right]^\dagger \right). \quad (4.61b)
 \end{aligned}$$

Similarly, it follows from



that

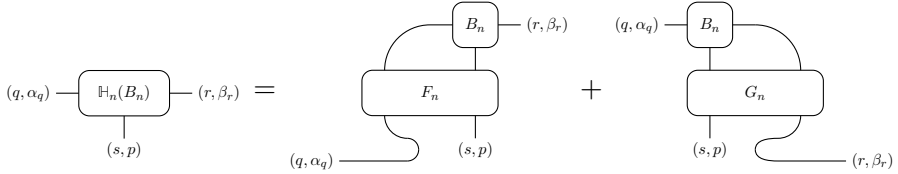
$$[G_n^{(s',p'),(s,p)}]_{(q,\alpha_q),(r,\beta_r)} = \delta_{p,p'} \delta_{r,q+(s'-s)/2} \left[g_n^{q,s',s} \right]_{\alpha_q,\beta_r} \quad (4.61c)$$

with

$$g_n^{q,s',s} = \delta_{s,s'} \sum_{t,t'=-1,1} b_{n+1}^{q,t} g_{n+1}^{q+(t+(-1)^{n+1})/2,t',t} \left[b_{n+1}^{q,t'} \right]^\dagger + \sum_{t,t'=-1,1} \left[\delta_{t-t',s'-s} \langle s',t' | h_{n,n+1}^{q-(s+(-1)^{n+1})/2} | s,t \rangle \left(b_{n+1}^{q,t} \left[b_{n+1}^{q+(t-t')/2,t'} \right]^\dagger \right) \right]. \quad (4.61d)$$

(e) Applying \mathbb{H}_n to $b_n^{q,s}$

Now we can compute F_n and G_n , we can implement the action of \mathbb{H}_n to $b_n^{q,s}$, see eq. (2.38). From



and the form of F_n and G_n , see eqs. (4.60) and (4.61), it follows that

$$\left[(\mathbb{H}_n(b_n))^{(s,p)} \right]_{(q,\alpha_q),(r,\beta_r)} = \delta_{p,q+(s+(-1)^n)/2} \delta_{r,p} [H_n^{q,s}(b_n)]_{\alpha_q,\beta_r}$$

with

$$[H_n^{q,s'}(b_n)] = \sum_{s=-1,1} f_n^{q,s',s} b_n^{q+(s'-s)/2,s} + \sum_{s=-1,2} b_n^{q,s} g_n^{q+(s+(-1)^n)/2,s',s}$$

for $q = p_n^{\min}, \dots, p_n^{\max}$ and $s = -1, 1$. Hence, when sweeping in the DMRG algorithm we need for every site n to invoke an iterative eigensolver to find the smallest eigenvalue \mathcal{E}_0 such that

$$H_n^{q,s}(b_n) = \mathcal{E}_0 b_n^{q,s}.$$

The computation time of $H_n^{q,s}(b_n)$ thus scales with

$$\mathcal{O} \left(2^4 \max_q (D_n)^q \right).$$

Bibliography

- [1] J. Schwinger, "Gauge invariance and mass. ii," *Phys. Rev.* **128**, 2425 (1962).
- [2] J. Schwinger, "Gauge invariance and mass," *Phys. Rev.* **125**, 397 (1962).
- [3] P. W. Anderson, "Plasmons, gauge invariance, and mass," *Phys. Rev.* **130**, 439 (1963).
- [4] J. Kogut and D. K. Sinclair, "(1 + 1)-dimensional models of quark confinement and final states in deep-inelastic scattering," *Phys. Rev. D* **10**, 4181 (1974).
- [5] S. Coleman, R. Jackiw, and L. Susskind, "Charge shielding and quark confinement in the massive schwinger model," *Annals of Physics* **93**, 267 (1975).
- [6] S. Coleman, "More about the massive schwinger model," *Annals of Physics* **101**, 239 (1976).
- [7] T. Banks, L. Susskind, and J. Kogut, "Strong-coupling calculations of lattice gauge theories: (1 + 1)-dimensional exercises," *Phys. Rev. D* **13**, 1043 (1976).
- [8] W. Fischler, J. Kogut, and L. Susskind, "Quark confinement in unusual environments," *Phys. Rev. D* **19**, 1188 (1979).
- [9] H. J. Rothe, K. D. Rothe, and J. A. Swieca, "Screening versus confinement," *Phys. Rev. D* **19**, 3020 (1979).

- [10] C. Hamer, J. Kogut, D. Crewther, and M. Mazzolini, "The massive schwinger model on a lattice: Background field, chiral symmetry and the string tension," *Nuclear Physics B* **208**, 413 (1982).
- [11] I. Bender, H. Rothe, and K. Rothe, "Monte carlo study of screening versus confinement in the massless and massive schwinger model," *Nuclear Physics B* **251**, 745 (1985).
- [12] J. E. Hetrick and Y. Hosotani, "Qed on a circle," *Phys. Rev. D* **38**, 2621 (1988).
- [13] S. Iso and H. Murayama, "Hamiltonian formulation of the schwinger model: Non-confinement and screening of the charge," *Progress of Theoretical Physics* **84**, 142 (1990).
- [14] M. A. E. Abdalla and K. Rothe, "Non-perturbative methods in two-dimensional quantum field theory," (World Scientific, Reading, Massachusetts, 1991) Chap. 10.3.5.
- [15] I. Sachs and A. Wipf, "Finite Temperature Schwinger Model," *ArXiv e-prints* (2010), arXiv:1005.1822 [hep-th] .
- [16] Y. Kluger, J. M. Eisenberg, B. Svetitsky, F. Cooper, and E. Mottola, "Fermion pair production in a strong electric field," *Phys. Rev. D* **45**, 4659 (1992).
- [17] J. V. Steele, A. Subramanian, and I. Zahed, "General correlation functions in the schwinger model at zero and finite temperature," *Nuclear Physics B* **452**, 545 (1995).
- [18] G. Grignani, P. Sodano, G. Semenoff, and O. Tirkkonen, "Charge screening in the finite temperature schwinger model," *International Journal of Modern Physics A* **11**, 4103 (1996).
- [19] R. Rodriguez and Y. Hosotani, "Anomalous behavior in the massive schwinger model," *Physics Letters B* **389**, 121 (1996).
- [20] R. Rodriguez and Y. Hosotani, "Confinement and chiral condensates in 2d QED with massive N-flavor fermions," *Physics Letters B* **375**, 273 (1996), hep-th/9602029 .
- [21] C. Adam, "Massive Schwinger Model within Mass Perturbation Theory," *Annals of Physics* **259**, 1 (1997), hep-th/9704064 .
- [22] C. Adam, "Charge screening and confinement in the massive Schwinger model," *Physics Letters B* **394**, 161 (1997), hep-th/9609155 .

- [23] C. Adam, “Normalization of the chiral condensate in the massive Schwinger model,” *Physics Letters B* **440**, 117 (1998), hep-th/9806211 .
- [24] S. Schmidt, D. Blaschke, G. Röpke, S. A. Smolyansky, A. V. Prozorkevich, and V. D. Toneev, “A Quantum Kinetic Equation for Particle Production in the Schwinger Mechanism,” *International Journal of Modern Physics E* **7**, 709 (1998), hep-ph/9809227 .
- [25] A. Armoni, J. Sonnenschein, and Y. Frishman, “The String Tension in Two-Dimensional Gauge Theories,” *International Journal of Modern Physics A* **14**, 2475 (1999), hep-th/9903153 .
- [26] Y. Hosotani and R. Rodriguez, “Bosonized massive n -flavour schwinger model,” *Journal of Physics A: Mathematical and General* **31**, 9925 (1998).
- [27] T. Byrnes, *Density Matrix Renormalization Group: A New Approach to Lattice Gauge Theory* (University of New South Wales, 2003).
- [28] P. Korcyl and M. Koren, “Screening in two-dimensional gauge theories,” *ArXiv e-prints* (2012), arXiv:1212.0569 [hep-lat] .
- [29] K. Cichy, A. Kujawa-Cichy, and M. Szyniszewski, “Lattice Hamiltonian approach to the massless Schwinger model: Precise extraction of the mass gap,” *Computer Physics Communications* **184**, 1666 (2013), arXiv:1211.6393 [hep-lat] .
- [30] M. C. Bañuls, K. Cichy, J. I. Cirac, and K. Jansen, “The mass spectrum of the Schwinger model with matrix product states,” *Journal of High Energy Physics* **11**, 158 (2013), arXiv:1305.3765 [hep-lat] .
- [31] F. Hebenstreit, J. Berges, and D. Gelfand, “Simulating fermion production in 1+1 dimensional QED,” *Phys. Rev. D* **87**, 105006 (2013), arXiv:1302.5537 [hep-ph] .
- [32] F. Hebenstreit and J. Berges, “Connecting real-time properties of the massless schwinger model to the massive case,” *Phys. Rev. D* **90**, 045034 (2014).
- [33] S. Kühn, J. I. Cirac, and M.-C. Bañuls, “Quantum simulation of the Schwinger model: A study of feasibility,” *Phys. Rev. A* **90**, 042305 (2014), arXiv:1407.4995 [quant-ph] .
- [34] M. C. Bañuls, K. Cichy, K. Jansen, and H. Saito, “Chiral condensate in the Schwinger model with Matrix Product Operators,” *ArXiv e-prints* (2016), arXiv:1603.05002 [hep-lat] .

- [35] P. Hauke, D. Marcos, M. Dalmonte, and P. Zoller, “Quantum simulation of a lattice schwinger model in a chain of trapped ions,” *Phys. Rev. X* **3**, 041018 (2013).
- [36] U.-J. Wiese, “Ultracold quantum gases and lattice systems: quantum simulation of lattice gauge theories,” *Annalen der Physik* **525**, 777 (2013), arXiv:1305.1602 [quant-ph] .
- [37] E. A. Martinez, C. A. Muschik, P. Schindler, D. Nigg, A. Erhard, M. Heyl, P. Hauke, M. Dalmonte, T. Monz, P. Zoller, and R. Blatt, “Real-time dynamics of lattice gauge theories with a few-qubit quantum computer,” *ArXiv e-prints* (2016), arXiv:1605.04570 [quant-ph] .
- [38] V. Kasper, F. Hebenstreit, M. Oberthaler, and J. Berges, “Schwinger pair production with ultracold atoms,” *ArXiv e-prints* (2015), arXiv:1506.01238 [cond-mat.quant-gas] .
- [39] P. Calabrese, J. Cardy, and B. Doyon, “Entanglement entropy in extended quantum systems introduction,” *Journal Of Physics A-Mathematical And Theoretical* **42** (2009).
- [40] S. Ryu and T. Takayanagi, “Holographic Derivation of Entanglement Entropy from the anti de Sitter Space/Conformal Field Theory Correspondence,” *Physical Review Letters* **96**, 181602 (2006), hep-th/0603001 .
- [41] E. Itou, K. Nagata, Y. Nakagawa, A. Nakamura, and V. I. Zakharov, “Entanglement in four-dimensional su(3) gauge theory,” **2016** (2016), 10.1093/ptep/ptw050.
- [42] P. Calabrese and J. Cardy, “Evolution of entanglement entropy in one-dimensional systems,” *Journal of Statistical Mechanics: Theory and Experiment* **4**, 04010 (2005), cond-mat/0503393 .
- [43] J. Haegeman, J. I. Cirac, T. J. Osborne, I. Pižorn, H. Verschelde, and F. Verstraete, “Time-Dependent Variational Principle for Quantum Lattices,” *Physical Review Letters* **107**, 070601 (2011), arXiv:1103.0936 [cond-mat.str-el] .
- [44] S. R. White, “Density matrix formulation for quantum renormalization groups,” *Phys. Rev. Lett.* **69**, 2863 (1992).
- [45] G. Vidal, “Efficient Classical Simulation of Slightly Entangled Quantum Computations,” *Physical Review Letters* **91**, 147902 (2003), quant-ph/0301063 .

- [46] J. D. Jackson and L. B. Okun, “Historical roots of gauge invariance,” *Reviews of Modern Physics* **73**, 663 (2001), hep-ph/0012061 .
- [47] C. N. Yang and R. L. Mills, “Conservation of isotopic spin and isotopic gauge invariance,” *Phys. Rev.* **96**, 191 (1954).
- [48] S. L. Glashow, “Partial-symmetries of weak interactions,” *Nuclear Physics* **22**, 579 (1961).
- [49] P. W. Higgs, “Broken symmetries and the masses of gauge bosons,” *Phys. Rev. Lett.* **13**, 508 (1964).
- [50] F. Englert and R. Brout, “Broken symmetry and the mass of gauge vector mesons,” *Phys. Rev. Lett.* **13**, 321 (1964).
- [51] H. Fritzsche, M. Gell-Mann, and H. Leutwyler, “Advantages of the color octet gluon picture,” *Physics Letters B* **47**, 365 (1973).
- [52] H. Fritsch, “The history of QCD,” *CERN Cour.* **52N8**, 21 (2012).
- [53] D. J. Gross and F. Wilczek, “Ultraviolet behavior of non-abelian gauge theories,” *Phys. Rev. Lett.* **30**, 1343 (1973).
- [54] H. D. Politzer, “Reliable perturbative results for strong interactions?” *Phys. Rev. Lett.* **30**, 1346 (1973).
- [55] L. Faddeev and V. Popov, “Feynman diagrams for the yang-mills field,” *Physics Letters B* **25**, 29 (1967).
- [56] V. Gribov, “Quantization of non-abelian gauge theories,” *Nuclear Physics B* **139**, 1 (1978).
- [57] A. G. Williams, “QCD, gauge-fixing, and the Gribov problem,” *Nuclear Physics B Proceedings Supplements* **109**, 141 (2002), hep-lat/0202010 .
- [58] K. G. Wilson, “Confinement of quarks,” *Phys. Rev. D* **10**, 2445 (1974).
- [59] K. G. Wilson, “The Origins of Lattice Gauge Theory,” *Nuclear Physics B Proceedings Supplements* **140**, 3 (2005), hep-lat/0412043 .
- [60] J. B. Kogut, “The lattice gauge theory approach to quantum chromodynamics,” *Rev. Mod. Phys.* **55**, 775 (1983).
- [61] M. Creutz, “Confinement and the critical dimensionality of space-time,” *Phys. Rev. Lett.* **43**, 553 (1979).
- [62] A. Ukawa, “Kenneth Wilson and Lattice QCD,” *Journal of Statistical Physics* **160**, 1081 (2015), arXiv:1501.04215 [hep-lat] .

- [63] G. S. Bali, “Overview from lattice QCD,” *Nuclear and particle physics with CEBAF at JLab. Proceedings, International Conference, Dubrovnik, Croatia, November 3-10, 1998, Fizika* **B8**, 229 (1999), arXiv:hep-lat/9901023 [hep-lat] .
- [64] Z. Fodor and C. Hoelbling, “Light hadron masses from lattice QCD,” *Reviews of Modern Physics* **84**, 449 (2012), arXiv:1203.4789 [hep-lat] .
- [65] C. McNeile, “Strong Coupling and Quark Masses from Lattice QCD,” *Modern Physics Letters A* **28**, 1360012 (2013), arXiv:1306.3326 [hep-lat] .
- [66] O. Philipsen, “The QCD equation of state from the lattice,” *Progress in Particle and Nuclear Physics* **70**, 55 (2013), arXiv:1207.5999 [hep-lat] .
- [67] K. Fukushima and T. Hatsuda, “The phase diagram of dense QCD,” *Reports on Progress in Physics* **74**, 014001 (2011), arXiv:1005.4814 [hep-ph] .
- [68] J. Kogut and L. Susskind, “Hamiltonian formulation of wilson’s lattice gauge theories,” *Phys. Rev. D* **11**, 395 (1975).
- [69] M. Creutz, “Gauge fixing, the transfer matrix, and confinement on a lattice,” *Phys. Rev. D* **15**, 1128 (1977).
- [70] B. E. Baaquie, “Lattice gauge theory: Hamiltonian, wilson fermions, and action,” *Phys. Rev. D* **33**, 2367 (1986).
- [71] M. B. Hastings, “An area law for one-dimensional quantum systems,” *Journal of Statistical Mechanics: Theory and Experiment* **8**, 08024 (2007), arXiv:0705.2024 [quant-ph] .
- [72] J. Eisert, M. Cramer, and M. B. Plenio, “*Colloquium* : Area laws for the entanglement entropy,” *Rev. Mod. Phys.* **82**, 277 (2010).
- [73] L. Masanes, “Area law for the entropy of low-energy states,” *Phys. Rev. A* **80**, 052104 (2009), arXiv:0907.4672 [quant-ph] .
- [74] R. Orús, “A practical introduction to tensor networks: Matrix product states and projected entangled pair states,” *Annals of Physics* **349**, 117 (2014), arXiv:1306.2164 [cond-mat.str-el] .
- [75] J. I. Cirac and F. Verstraete, “Renormalization and tensor product states in spin chains and lattices,” *Journal of Physics A Mathematical General* **42**, 504004 (2009), arXiv:0910.1130 [cond-mat.str-el] .

- [76] U. Schollwöck, “The density-matrix renormalization group in the age of matrix product states,” *Annals of Physics* **326**, 96 (2011), arXiv:1008.3477 [cond-mat.str-el] .
- [77] T. Nishino, “Nishino’s dmrg page,” [Http://quattro.phys.sci.kobe-u.ac.jp/dmrg.html](http://quattro.phys.sci.kobe-u.ac.jp/dmrg.html).
- [78] I. Affleck, T. Kennedy, E. H. Lieb, and H. Tasaki, “Rigorous results on valence-bond ground states in antiferromagnets,” *Phys. Rev. Lett.* **59**, 799 (1987).
- [79] M. Fannes, B. Nachtergaele, and R. Werner, “Finitely correlated states on quantum spin chains,” *Communications in Mathematical Physics* **144**, 443 (1992).
- [80] H. N. Phien, G. Vidal, and I. P. McCulloch, “Infinite boundary conditions for matrix product state calculations,” *Phys. Rev. B* **86**, 245107 (2012), arXiv:1207.0652 [quant-ph] .
- [81] T. Sugihara, “Matrix product representation of gauge invariant states in a \mathbb{Z}_2 lattice gauge theory,” *Journal of High Energy Physics* **7**, 022 (2005), hep-lat/0506009 .
- [82] E. Rico, T. Pichler, M. Dalmonte, P. Zoller, and S. Montangero, “Tensor Networks for Lattice Gauge Theories and Atomic Quantum Simulation,” *Physical Review Letters* **112**, 201601 (2014), arXiv:1312.3127 [cond-mat.quant-gas] .
- [83] S. Kühn, E. Zohar, J. I. Cirac, and M. C. Bañuls, “Non-Abelian string breaking phenomena with matrix product states,” *Journal of High Energy Physics* **7**, 130 (2015), arXiv:1505.04441 [hep-lat] .
- [84] P. Silvi, E. Rico, M. Dalmonte, F. Tschirsich, and S. Montangero, “Finite-density phase diagram of a (1+1)-d non-abelian lattice gauge theory with tensor networks,” *ArXiv e-prints* (2016), arXiv:1606.05510 [quant-ph] .
- [85] A. Milsted, “Matrix product states and the non-Abelian rotor model,” *Phys. Rev. D* **93**, 085012 (2016), arXiv:1507.06624 [hep-lat] .
- [86] N. Schuch, D. Pérez-García, and I. Cirac, “Classifying quantum phases using matrix product states and projected entangled pair states,” *Phys. Rev. B* **84**, 165139 (2011), arXiv:1010.3732 [cond-mat.str-el] .
- [87] J. Haegeman, B. Pirvu, D. J. Weir, J. I. Cirac, T. J. Osborne, H. Verschelde, and F. Verstraete, “Variational matrix product ansatz for

- dispersion relations,” *Phys. Rev. B* **85**, 100408 (2012), arXiv:1103.2286 [quant-ph] .
- [88] J. Haegeman, T. J. Osborne, and F. Verstraete, “Post-matrix product state methods: To tangent space and beyond,” *Phys. Rev. B* **88**, 075133 (2013), arXiv:1305.1894 [quant-ph] .
- [89] S. Elitzur, “Impossibility of spontaneously breaking local symmetries,” *Phys. Rev. D* **12**, 3978 (1975).
- [90] P. Calabrese and J. Cardy, “Entanglement entropy and quantum field theory,” *Journal of Statistical Mechanics: Theory and Experiment* **2004**, P06002 (2004).
- [91] J. Haegeman, S. Michalakis, B. Nachtergaele, T. J. Osborne, N. Schuch, and F. Verstraete, “Elementary Excitations in Gapped Quantum Spin Systems,” *Physical Review Letters* **111**, 080401 (2013), arXiv:1305.2176 [quant-ph] .
- [92] G. S. Bali, “QCD forces and heavy quark bound states,” *Phys. Rep.* **343**, 1 (2001), hep-ph/0001312 .
- [93] G. S. Bali and K. Schilling, “Static quark-antiquark potential: Scaling behavior and finite-size effects in su(3) lattice gauge theory,” *Phys. Rev. D* **46**, 2636 (1992).
- [94] C. Lang and C. Rebbi, “Potential and restoration of rotational symmetry in su (2) lattice gauge theory,” *Physics Letters B* **115**, 137 (1982).
- [95] J. D. Stack, “Heavy quark potential in su(2) lattice gauge theory,” *Phys. Rev. D* **27**, 412 (1983).
- [96] L. Griffiths, C. Michael, and P. Rakow, “Mesons with excited glue,” *Physics Letters B* **129**, 351 (1983).
- [97] S. W. Otto and J. D. Stack, “Su(3) heavy-quark potential with high statistics,” *Phys. Rev. Lett.* **52**, 2328 (1984).
- [98] A. Hasenfratz, P. Hasenfratz, U. Heller, and F. Karsch, “Rotational symmetry of the su(3) potential,” *Zeitschrift für Physik C Particles and Fields* **25**, 191 (1984).
- [99] D. Barkai, K. J. M. Moriarty, and C. Rebbi, “Force between static charges and universality in lattice qcd,” *Phys. Rev. D* **30**, 2201 (1984).

- [100] R. Sommer and K. Schilling, “Testing the rotational symmetry of the $su(3)$ potential,” *Zeitschrift für Physik C Particles and Fields* **29**, 95 (1985).
- [101] A. Huntley and C. Michael, “Static potentials and scaling in $su(2)$ lattice gauge theory,” *Nuclear Physics B* **270**, 123 (1986).
- [102] J. Hoek, “Wilson loops on 324 lattices and the $su(3)$ potential,” *Zeitschrift für Physik C Particles and Fields* **35**, 369 (1987).
- [103] S. Aoki, G. Boyd, R. Burkhalter, S. Ejiri, M. Fukugita, S. Hashimoto, Y. Iwasaki, K. Kanaya, T. Kaneko, Y. Kuramashi, K. Nagai, M. Okawa, H. P. Shanahan, A. Ukawa, T. Yoshié, and CP-PACS Collaboration, “The static quark potential in full QCD,” *Nuclear Physics B Proceedings Supplements* **73**, 216 (1999), hep-lat/9809185 .
- [104] G. S. Bali, B. Bolder, N. Eicker, T. Lippert, B. Orth, P. Ueberholz, K. Schilling, and T. Struckmann, “Static potentials and glueball masses from QCD simulations with Wilson sea quarks,” *Phys. Rev. D* **62**, 054503 (2000), hep-lat/0003012 .
- [105] C. Bernard, T. Burch, K. Orginos, D. Toussaint, T. A. DeGrand, C. Detar, S. Gottlieb, U. M. Heller, J. E. Hetrick, and B. Sugar, “Static quark potential in three flavor QCD,” *Phys. Rev. D* **62**, 034503 (2000), hep-lat/0002028 .
- [106] G. S. Bali, H. Neff, T. Düssel, T. Lippert, and K. Schilling (SESAM Collaboration), “Observation of string breaking in qcd,” *Phys. Rev. D* **71**, 114513 (2005).
- [107] R. Alkofer, D. Diakonov, J. Pawłowski, H. Reinhardt, V. Zakharov, D. Zwanziger, and J. Greensite, “Panel discussion: What *don't* we know about confinement?” *Proceedings, 9th Conference on Quark Confinement and the Hadron Spectrum, AIP Conf. Proc.* **1343**, 17 (2011), arXiv:1012.3192 [hep-th] .
- [108] R. Alkofer and J. Greensite, “Quark Confinement: The Hard Problem of Hadron Physics,” *J. Phys.* **G34**, S3 (2007), arXiv:hep-ph/0610365 [hep-ph] .
- [109] J. Greensite, “The confinement problem in lattice gauge theory,” *Progress in Particle and Nuclear Physics* **51**, 1 (2003).
- [110] H. Reinhardt, M. Engelhardt, K. Langfeld, M. Quandt, and A. Schäfer, in *American Institute of Physics Conference Series*, American Insti-

- tute of Physics Conference Series, Vol. 508 (2000) pp. 142–151, hep-th/9911145 .
- [111] M. E. Peskin and D. V. Schroeder, *An introduction to quantum field theory*, Advanced book program (Westview Press Reading (Mass.), Boulder (Colo.), 1995) autre tirage : 1997.
- [112] V. Zauner, M. Ganahl, H. G. Evertz, and T. Nishino, “Time Evolution within a Comoving Window: Scaling of signal fronts and magnetization plateaus after a local quench in quantum spin chains,” *ArXiv e-prints* (2012), arXiv:1207.0862 [cond-mat.str-el] .
- [113] A. Milsted, J. Haegeman, T. J. Osborne, and F. Verstraete, “Variational matrix product ansatz for nonuniform dynamics in the thermodynamic limit,” *Phys. Rev. B* **88**, 155116 (2013).
- [114] O. Philipsen and H. Wittig, “String breaking in non-abelian gauge theories with fundamental matter fields,” *Phys. Rev. Lett.* **81**, 4056 (1998).
- [115] M. Abramowitz, *Handbook of Mathematical Functions, With Formulas, Graphs, and Mathematical Tables*, (Dover Publications, Incorporated, 1974) Chap. 10.
- [116] H. Galic, “Fun and frustration with hydrogen in a 1+1 dimension,” *American Journal of Physics* **56** (1988).
- [117] A. Z. Capri and R. Ferrari, “Hydrogenic atoms in one-plus-one dimensions,” *Canadian Journal of Physics* **63**, 1029 (1985).
- [118] M. Pepe and U.-J. Wiese, “From Decay to Complete Breaking: Pulling the Strings in SU(2) Yang-Mills Theory,” *Physical Review Letters* **102**, 191601 (2009), arXiv:0901.2510 [hep-lat] .
- [119] F. Verstraete, J. J. García-Ripoll, and J. I. Cirac, “Matrix Product Density Operators: Simulation of Finite-Temperature and Dissipative Systems,” *Physical Review Letters* **93**, 207204 (2004), cond-mat/0406426 .
- [120] M. Zwolak and G. Vidal, “Mixed-State Dynamics in One-Dimensional Quantum Lattice Systems: A Time-Dependent Superoperator Renormalization Algorithm,” *Physical Review Letters* **93**, 207205 (2004), cond-mat/0406440 .
- [121] M. B. Hastings, “Solving gapped hamiltonians locally,” *Phys. Rev. B* **73**, 085115 (2006).

- [122] A. Molnar, N. Schuch, F. Verstraete, and J. I. Cirac, “Approximating gibbs states of local hamiltonians efficiently with projected entangled pair states,” *Phys. Rev. B* **91**, 045138 (2015).
- [123] N. Hatano and M. Suzuki, “Quantum annealing and other optimization methods,” (Springer Berlin Heidelberg, Berlin, Heidelberg, 2005) Chap. Finding Exponential Product Formulas of Higher Orders, pp. 37–68.
- [124] Y. Nambu, “Nobel lecture: Spontaneous symmetry breaking in particle physics: A case of cross fertilization*,” *Rev. Mod. Phys.* **81**, 1015 (2009).
- [125] N. Kawamoto and J. Smit, “Effective lagrangian and dynamical symmetry breaking in strongly coupled lattice {QCD},” *Nuclear Physics B* **192**, 100 (1981).
- [126] L. Y. Glozman, “Confinement, chiral symmetry breaking and the mass generation of hadrons,” *ArXiv e-prints* (2012), arXiv:1211.7267 [hep-ph]
- [127] P. O. Bowman, K. Langfeld, D. B. Leinweber, A. Sternbeck, L. von Smekal, and A. G. Williams, “Role of center vortices in chiral symmetry breaking in su(3) gauge theory,” *Phys. Rev. D* **84**, 034501 (2011).
- [128] C. Huscroft, R. Gass, and M. Jarrell, “Maximum entropy method of obtaining thermodynamic properties from quantum monte carlo simulations,” *Phys. Rev. B* **61**, 9300 (2000).
- [129] M. Troyer, S. Wessel, and F. Alet, “Flat histogram methods for quantum systems: Algorithms to overcome tunneling problems and calculate the free energy,” *Phys. Rev. Lett.* **90**, 120201 (2003).
- [130] S. Bi and N.-H. Tong, “Monte carlo algorithm for free energy calculation,” *Phys. Rev. E* **92**, 013310 (2015).
- [131] L. Onsager, “Crystal statistics. i. a two-dimensional model with an order-disorder transition,” *Phys. Rev.* **65**, 117 (1944).
- [132] N. D. Mermin and H. Wagner, “Absence of ferromagnetism or antiferromagnetism in one- or two-dimensional isotropic heisenberg models,” *Phys. Rev. Lett.* **17**, 1133 (1966).
- [133] R. Peierls and M. Born, “On Ising’s model of ferromagnetism,” *Proceedings of the Cambridge Philosophical Society* **32**, 477 (1936).
- [134] J. Schwinger, “On Gauge Invariance and Vacuum Polarization,” *Physical Review* **82**, 664 (1951).

- [135] D. Kawai, Y. Sato, and K. Yoshida, “Schwinger pair production rate in confining theories via holography,” *Phys. Rev. D* **89**, 101901 (2014), arXiv:1312.4341 [hep-th] .
- [136] G. Vidal, “Classical Simulation of Infinite-Size Quantum Lattice Systems in One Spatial Dimension,” *Physical Review Letters* **98**, 070201 (2007), cond-mat/0605597 .
- [137] L. Vanderstraeten, J. Haegeman, T. J. Osborne, and F. Verstraete, “S Matrix from Matrix Product States,” *Physical Review Letters* **112**, 257202 (2014), arXiv:1312.6793 [cond-mat.str-el] .
- [138] L. Vanderstraeten, F. Verstraete, and J. Haegeman, “Scattering particles in quantum spin chains,” *Phys. Rev. B* **92**, 125136 (2015), arXiv:1506.01008 [cond-mat.str-el] .
- [139] N. Linden, S. Popescu, A. J. Short, and A. Winter, “Quantum mechanical evolution towards thermal equilibrium,” *Phys. Rev. E* **79**, 061103 (2009).
- [140] J. Eisert, M. Friesdorf, and C. Gogolin, “Quantum many-body systems out of equilibrium,” *Nature Physics* **11**, 124 (2015), arXiv:1408.5148 [quant-ph] .
- [141] J.-S. Caux and R. M. Konik, “Constructing the Generalized Gibbs Ensemble after a Quantum Quench,” *Physical Review Letters* **109**, 175301 (2012), arXiv:1203.0901 [cond-mat.quant-gas] .
- [142] M. Friesdorf, A. H. Werner, W. Brown, V. B. Scholz, and J. Eisert, “Many-Body Localization Implies that Eigenvectors are Matrix-Product States,” *Physical Review Letters* **114**, 170505 (2015), arXiv:1409.1252 [quant-ph] .
- [143] M. C. Bañuls, J. I. Cirac, and M. B. Hastings, “Strong and Weak Thermalization of Infinite Nonintegrable Quantum Systems,” *Physical Review Letters* **106**, 050405 (2011), arXiv:1007.3957 [quant-ph] .
- [144] K. Van Acoleyen, N. Bultinck, J. Haegeman, M. Marien, V. B. Scholz, and F. Verstraete, “The entanglement of distillation for gauge theories,” *ArXiv e-prints* (2015), arXiv:1511.04369 [quant-ph] .
- [145] R. M. Soni and S. P. Trivedi, “Aspects of entanglement entropy for gauge theories,” *Journal of High Energy Physics* **1**, 136 (2016), arXiv:1510.07455 [hep-th] .

- [146] L. Vanderstraeten, J. Haegeman, F. Verstraete, and D. Poilblanc, “Quasiparticle interactions in frustrated Heisenberg chains,” *Phys. Rev. B* **93**, 235108 (2016), arXiv:1603.07665 [cond-mat.str-el] .
- [147] F. Verstraete and J. I. Cirac, “Renormalization algorithms for Quantum-Many Body Systems in two and higher dimensions,” *eprint arXiv:cond-mat/0407066* (2004), cond-mat/0407066 .
- [148] P. Corboz, R. Orús, B. Bauer, and G. Vidal, “Simulation of strongly correlated fermions in two spatial dimensions with fermionic projected entangled-pair states,” *Phys. Rev. B* **81**, 165104 (2010), arXiv:0912.0646 [cond-mat.str-el] .
- [149] P. Corboz, J. Jordan, and G. Vidal, “Simulation of fermionic lattice models in two dimensions with projected entangled-pair states: Next-nearest neighbor Hamiltonians,” *Phys. Rev. B* **82**, 245119 (2010), arXiv:1008.3937 [cond-mat.str-el] .
- [150] C. V. Kraus, N. Schuch, F. Verstraete, and J. I. Cirac, “Fermionic projected entangled pair states,” *Phys. Rev. A* **81**, 052338 (2010), arXiv:0904.4667 [quant-ph] .
- [151] V. Murg, F. Verstraete, and J. I. Cirac, “Variational study of hard-core bosons in a two-dimensional optical lattice using projected entangled pair states,” *Phys. Rev. A* **75**, 033605 (2007), cond-mat/0611522 .
- [152] J. Jordan, R. Orús, G. Vidal, F. Verstraete, and J. I. Cirac, “Classical Simulation of Infinite-Size Quantum Lattice Systems in Two Spatial Dimensions,” *Physical Review Letters* **101**, 250602 (2008), cond-mat/0703788 .
- [153] L. Vanderstraeten, M. Mariën, F. Verstraete, and J. Haegeman, “Excitations and the tangent space of projected entangled-pair states,” *Phys. Rev. B* **92**, 201111 (2015), arXiv:1507.02151 [cond-mat.str-el] .
- [154] H. N. Phien, J. A. Bengua, H. D. Tuan, P. Corboz, and R. Orús, “Infinite projected entangled pair states algorithm improved: Fast full update and gauge fixing,” *Phys. Rev. B* **92**, 035142 (2015), arXiv:1503.05345 [cond-mat.str-el] .
- [155] P. Corboz, “Variational optimization with infinite projected entangled-pair states,” *ArXiv e-prints* (2016), arXiv:1605.03006 [cond-mat.str-el] .
- [156] L. Vanderstraeten, J. Haegeman, P. Corboz, and F. Verstraete, “Gradient methods for variational optimisation of projected entangled-pair states,” *ArXiv e-prints* (2016), arXiv:1606.09170 [cond-mat.str-el] .

- [157] M. Lubasch, J. I. Cirac, and M.-C. Bañuls, “Algorithms for finite projected entangled pair states,” *Phys. Rev. B* **90**, 064425 (2014), arXiv:1405.3259 [quant-ph] .
- [158] L. Tagliacozzo, A. Celi, and M. Lewenstein, “Tensor Networks for Lattice Gauge Theories with Continuous Groups,” *Physical Review X* **4**, 041024 (2014), arXiv:1405.4811 [cond-mat.str-el] .
- [159] J. Haegeman, K. Van Acoleyen, N. Schuch, J. I. Cirac, and F. Verstraete, “Gauging Quantum States: From Global to Local Symmetries in Many-Body Systems,” *Physical Review X* **5**, 011024 (2015), arXiv:1407.1025 [quant-ph] .
- [160] E. Zohar, M. Burrello, T. B. Wahl, and J. I. Cirac, “Fermionic projected entangled pair states and local $U(1)$ gauge theories,” *Annals of Physics* **363**, 385 (2015), arXiv:1507.08837 [quant-ph] .
- [161] A. Milsted and T. J. Osborne, “Quantum Yang-Mills theory: an overview of a programme,” *ArXiv e-prints* (2016), arXiv:1604.01979 [quant-ph] .
- [162] P. Corboz, T. M. Rice, and M. Troyer, “Competing states in the t - j model: Uniform d -wave state versus stripe state,” *Phys. Rev. Lett.* **113**, 046402 (2014).
- [163] S. Albeverio and R. Høegh-Krohn, “Frobenius theory for positive maps of von neumann algebras,” *Communications in Mathematical Physics* **64**, 83 (1978).
- [164] D. Perez-Garcia, F. Verstraete, M. M. Wolf, and J. I. Cirac, “Matrix Product State Representations,” *eprint arXiv:quant-ph/0608197* (2006), quant-ph/0608197 .
- [165] W. Arnoldi, “The principle of minimized iterations in the solution of the matrix eigenvalue problem,” *Quarterly of Applied Mathematics* **9**, 17 (1951).
- [166] E. R. Davidson, “The iterative calculation of a few of the lowest eigenvalues and corresponding eigenvectors of large real-symmetric matrices,” *Journal of Computational Physics* **17**, 87 (1975).
- [167] Y. Saad and M. H. Schultz, “Gmres: A generalized minimal residual algorithm for solving nonsymmetric linear systems,” *SIAM Journal on Scientific and Statistical Computing* **7**, 856 (1986).

- [168] H. A. van der Vorst, “Bi-cgstab: A fast and smoothly converging variant of bi-cg for the solution of nonsymmetric linear systems,” *SIAM J. Sci. Stat. Comput.* **13**, 631 (1992).
- [169] P. A. M. Dirac, “Note on exchange phenomena in the thomas atom,” *Mathematical Proceedings of the Cambridge Philosophical Society* **26**, 376 (1930).
- [170] P. Kramer and M. Saraceno, “Group theoretical methods in physics: Proceedings of the ix international colloquium held at cocoyoc, méxico, june 23–27, 1980,” (Springer Berlin Heidelberg, Berlin, Heidelberg, 1980) Chap. Geometry of the time-dependent variational principle in quantum mechanics, pp. 112–121.
- [171] J. Haegeman, C. Lubich, I. Oseledets, B. Vandereycken, and F. Verstraete, “Unifying time evolution and optimization with matrix product states,” *ArXiv e-prints* (2014), arXiv:1408.5056 [quant-ph] .
- [172] J. Haegeman, M. Mariën, T. J. Osborne, and F. Verstraete, “Geometry of Matrix Product States: metric, parallel transport and curvature,” *ArXiv e-prints* (2012), arXiv:1210.7710 [quant-ph] .
- [173] “Practical mathematical optimization: An introduction to basic optimization theory and classical and new gradient-based algorithms,” (Springer US, Boston, MA, 2005) Chap. Line Search Descent Methods for Unconstrained Minimization.
- [174] A. Milsted, J. Haegeman, and T. J. Osborne, “Matrix product states and variational methods applied to critical quantum field theory,” *Phys. Rev. D* **88**, 085030 (2013), arXiv:1302.5582 [hep-lat] .
- [175] U. M. Ascher and L. R. Petzold, *Computer Methods for Ordinary Differential Equations and Differential-Algebraic Equations*, 1st ed. (Society for Industrial and Applied Mathematics, Philadelphia, PA, USA, 1998).
- [176] A. Bijl, J. de Boer, and A. Michels, “Properties of liquid helium ii,” *Physica* **8**, 655 (1941).
- [177] R. P. Feynman and M. Cohen, “Energy spectrum of the excitations in liquid helium,” *Phys. Rev.* **102**, 1189 (1956).
- [178] D. P. Arovas, A. Auerbach, and F. D. M. Haldane, “Extended heisenberg models of antiferromagnetism: Analogies to the fractional quantum hall effect,” *Phys. Rev. Lett.* **60**, 531 (1988).

- [179] S. Östlund and S. Rommer, “Thermodynamic limit of density matrix renormalization,” *Phys. Rev. Lett.* **75**, 3537 (1995).
- [180] W. Zimmermann, “On the bound state problem in quantum field theory,” *Il Nuovo Cimento (1955-1965)* **10**, 597 (1958).